THÈSE de DOCTORAT DE L'UNIVERSITÉ DE LYON
opérée au sein de l'École Centrale de Lyon

École Doctorale N°162
Mécanique Énergétique Génie Civil Acoustique

Spécialité de doctorat : Mécanique des fluides

Soutenue publiquement le 05/12/2022, par
Jean AL AM

Broadband noise predictions of a fan stage using large eddy simulations

Devant le jury composé de :

Pr.	Sanjosé, Marlène	ÉTS Montréal	Rapporteure
Dr.	Moureau, Vincent	CORIA	Rapporteur
Pr.	Balarac, Guillaume	LEGI Grenoble INP	Examinateur
Pr.	Fortes-Patella, Regiane	LEGI Grenoble INP	Examinatrice
Pr.	Bailly, Christophe	École Centrale de Lyon	Examinateur
Dr.	Boudet, Jérôme	École Centrale de Lyon	Directeur de thèse
Dr.	Giauque, Alexis	École Centrale de Lyon	Encadrant de thèse
Dr.	Clair, Vincent	École Centrale de Lyon	Encadrant de thèse
Dr.	Gea-Aguilera, Fernando	Safran Aircraft Engines	Invité
Dr.	Duchaine, Florent	CERFACS	Invité, encadrant de thèse

"Telle est bien la beauté et la noblesse de la science : désir sans fin de repousser les frontières du savoir, de traquer les secrets de la matière et de la vie sans idée préconçue des conséquences éventuelles."

Marie Curie

"Avec l'avion, nous avons appris la ligne droite."

Antoine de Saint-Exupéry

Remerciements

Je souhaite tout d'abord remercier les membres du jury d'avoir accepté d'évaluer mon travail de thèse. En particulier, je tiens à remercier chaleureusement mes directeurs de thèse Vincent Clair, Alexis Giauque, Jérôme Boudet et Fernando Gea-Aguilera pour la qualité de leur encadrement, leur implication exceptionnelle dans mon projet de thèse et leur disponibilité. Ce travail est le fruit d'un vrai travail d'équipe pluridisciplinaire, avec des expertises académiques et industrielles en acoustique et turbomachines.

Je souhaite ensuite remercier les différents chercheurs au laboratoire avec qui j'ai pu interagir pendant ces trois années. Du coté acoustique, je pense particulièrement à Michel Roger et Antonio Pereira pour leurs conseils notamment autour les modèles analytiques et l'analyse modal acoustique. Du coté turbomachines, je remercie particulièrement Stéphane Aubert, Pascal Ferrand et Pierre Duquesne pour leurs conseils continues pendant ces trois ans au cours des réunions hebdomadaires de recherche (RHR turbo). Je tiens à remercier aussi les expérimentateurs avec qui j'ai pu discuter, particulièrement Xavier Ottavy, Christoph Brandstetter et Edouard Salze. Je pense aussi à Christophe Bailly, notamment pour les différents discussions lors des réunions ARENA et du café scientifiques et particulièrement pour son commentaire "calculs merveilleux", adressé aux calculs réalisés pendant cette thèse. J'adresse tous mes remerciements à Fatima El Boukhrissi et Marie-Gabrielle Perriaux pour leur disponibilité et à Laurent Pouilloux pour son efficacité, son implication sans faille dans la vie du laboratoire et surtout pour sa bonne humeur lors de chacune de ses visites.

De même, je tiens à particulièrement remercier les ingénieurs chez Safran Aircraft Engines avec qui j'ai pu discuter. Je pense particulièrement à Helene De-Laborderie avec qui j'ai pu pas mal discuter autour de l'outil Optibrui. Je tiens aussi à remercier les collègues au Cerfacs qui nous ont fournit le code de calcul AVBP et qui étaient toujours à
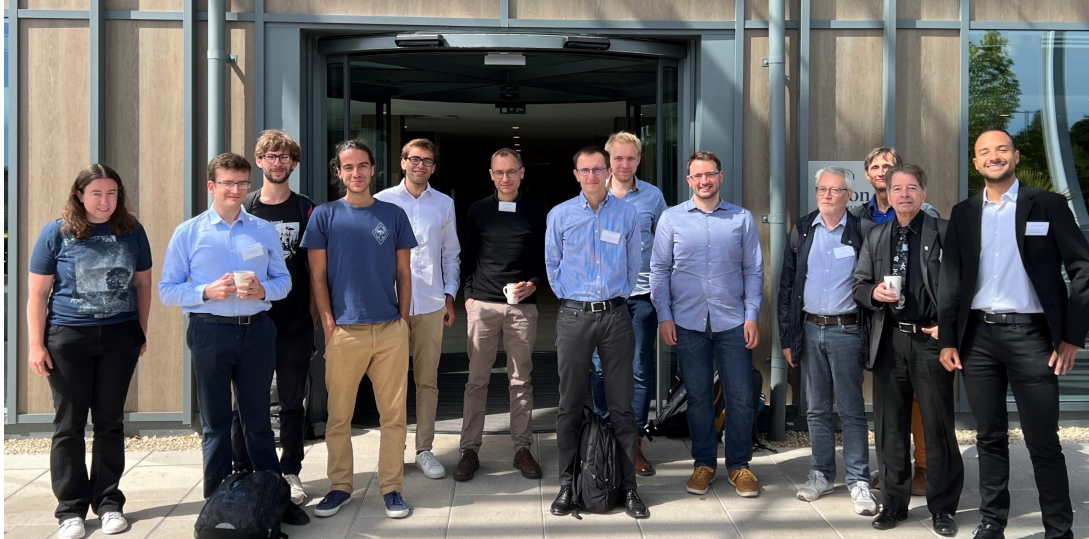
Equipe LMFA à la conférence AIAA-CEAS 2022 !

l'écoute en cas de problèmes liés au code. Je pense aussi aux divers échanges avec l'équipe acoustique à Sherbrooke, particulièrement avec Stéphane Moreau et Marlène Sanjosé.

Arrivant maintenant aux doctorants. Je trouve que c'est grâce à cette belle ambiance au labo qu'on peut bien avancer dans nos thèses. Je remercie donc tous les doctorants avec qui j'ai pu interagir, tant sur le plan scientifique que sur le plan humain, et que je considère désormais comme des amis et des copains et non pas que des collègues. Je vais particulièrement remercier Danny qui m'a beaucoup aider pendant ma thèse, qui m'a appris beaucoup de choses et avec qui j'ai pu beaucoup discuter. Je remercie aussi Léo, pour les discussions sur les modes acoustiques, mais aussi le ski et le Tennis :). Je continue avec mes co-bureau et je remercie aussi Gabriele et Giovanni pour leur bonne humeur au quotidien, ainsi que Emmanuele et Laura que je peux tout simplement les considérer parmi mes meilleurs amis au labo. Je pense aussi particulièrement à Hugo pour les discussions toujours très intéressantes autour des calculs et d'avoir assez apprécier mes résultats de thèse, ainsi que pour l'accompagnement muscu :). Je pense aussi aux doctorants turbo et particulièrement à Valdo Pagès qui m'a aidé notamment sur la géométrie ECL5 et à Anne-Lise Fiquet. Nombre d'autres doctorants et post-doctorants ont contribué à rendre cette expérience mémorable et je les en remercie : Etienne (avec sa présence assez utile et particulière au labo :)), Elina (pour ces conseils particulièrement utiles pour l'après thèse), Arthur (qui siège à mon coté au conseil du labo :)) Pierre, Daher, Yann, David, Nacio, Codor, Ariane, Mathieu (pour la LES en marche :)), Alexis, Igor, Marie, Simon, Jules, Loïc, Estelle, Yuling, Mohcene, Allan, Courtney, Amal, Daniel et Wesley. Je remercie aussi le "quartier italien" et je pense particulièrement à Livia, Marilina, Stéphano, Anika et Jean (même s'il est français :)).

Je pense aussi aux différents échanges que j'ai eu au cours des conférence avec des chercheurs du monde entier, particulièrement Andrea Arroyo Ramo, Fernanda Leticia dos Santos et Laura Botero Bolívar de l'ISAE-SUPAERO et de l'Université de Twente.

Finalement, je tiens à remercier ma famille, mon père qui a fait un long trajet pour être présent à ma soutenance, ainsi que tous mes copains à Lyon, avec qui j'ai passé les meilleurs moments pendant ces trois ans !

Abstract

Decreasing the noise emitted by turbofan engines is now one of the main constraints for aircraft engine manufacturers. The fan/Outlet Guide Vane (OGV) stage is considered as one of the major contributors to the total noise radiated by aero-engines, especially for future architectures, such as ultra-high by-pass ratio engines. A lot of work has been dedicated to the tonal components of fan/OGV stage noise, whereas the broadband component has received less attention. At subsonic operating points, the main sources of broadband noise originate from the interaction of the turbulent flow with solid surfaces such as the blades and vanes. In the present work, fully-compressible large eddy simulations (LES) are performed on a realistic fan/OGV stage to compute both the turbulent flow and the acoustic emissions in the fan stage. To this end, three configurations of increasing complexity and computational cost are considered: a radial-slice periodic sector, then, a full-span periodic sector, and finally, a 360° full-stage configuration. The LES numerical parameters are carefully chosen based on a parametric study carried out using flat plates configurations. Several noise sources are studied using these configurations by (i) either analyzing the LES direct noise propagation in the fan stage, (ii) or separating the contributions of each noise source using a hybrid method coupling the LES results with an acoustic analogy. The numerical results are compared with predictions from available analytical models informed by the LES. Comparable results are observed between the two approaches. Some discrepancies can be explained by additional noise sources present in the LES that are not considered by the analytical models. Finally, the increase of noise levels in the full-span sector simulation, due to the periodic boundary condition, is evaluated by comparison to the 360° configuration.

Keywords: aeroacoustics, turbomachinery, fan noise, broadband noise, large eddy simulation, secondary flows, direct noise computation.

Résumé

La réduction du bruit des turboréacteurs est un enjeu important pour les fabricants de moteurs d'avion. L'étage soufflante/redresseur est considéré comme l'une des principales sources de bruit d'un turboréacteur, particulièrement pour les nouvelles architectures de moteurs d'avion, tel que les moteurs à très haut taux de dilution. Un grand nombre de travaux de recherche a été dédié aux composantes tonales du bruit des turboréacteurs, tandis que le bruit à large bande a reçu une attention moindre. En régime subsonique, les principales sources de ce bruit à large bande sont associées à l'interaction de l'écoulement turbulent avec les surfaces solides du moteur, telles que les aubes de la soufflante et du redresseur. Dans la présente étude, des simulations aux grandes échelles (SGE) compressibles sont effectuées sur un étage soufflante/redresseur réaliste pour modéliser l'écoulement turbulent et les émissions acoustiques dans l'étage de soufflante. A cette fin, trois configurations de complexité et de coût de calcul croissants sont considérées : une tranche radiale d'un secteur périodique, puis un secteur périodique à envergure complète, et enfin un étage à circonférence complète (360°). Les paramètres numériques des SGE sont soigneusement choisis en se basant sur une étude paramétrique effectuée sur des configurations simples de plaques planes. Différentes sources de bruit sont étudiées en utilisant ces configurations, (i) soit en analysant la propagation directe par la SGE dans l'étage de soufflante, (ii) soit en séparant les contributions de chaque source de bruit à l'aide d'une méthode hybride couplant les résultats des SGE avec une analogie acoustique. Les résultats numériques sont comparés aux prédictions obtenues par des modèles analytiques issus de la littérature, dont les données d'entrée sont extraites des SGE. Certaines différences peuvent être expliquées par des sources acoustiques présentes dans les SGE qui ne sont pas considérées dans les modèles analytiques. Enfin, la surestimation du bruit dans le calcul secteur à envergure complète, due aux conditions limites périodiques, est évaluée par comparaison à la configuration à 360°.

Mots clés: aéroacoustique, turbomachine, bruit de soufflante, bruit à large bande, simulation aux grandes échelles, écoulements secondaires, prédiction acoustique directe.

Contents

List of Figures

List of Tables

Nomenclature

Acronyms

2D	Two dimensional
3D	Three dimensional
ACARE	Advisory Council for Aviation Research and Innovation in Europe
AR	Aspect Ratio
BBN	BroadBand Noise
BPF	Blade Passing Frequency [Hz]
CAA	Computational Aero-Acoustics
CD	Controlled Diffusion
CFD	Computational Fluid Dynamics
CFL	Courant–Friedrichs–Lewy
DES	Detached Eddy Simulation
DNS	Direct Numerical Simulation
EoS	Equation of State
FWH	Ffowcs Williams and Hawkings
HBR	High Bypass Ratio
HSV	Horse-Shoe Vortex
ICAO	International Civil Aviation Organization
IV	Induced Vortex
LBM	Lattice-Boltzmann Method
LBR	Low Bypass Ratio
LE	Leading Edge
LES	Large Eddy Simulation
LESCOTT	Large Eddy Simulations COnfiguration Tool for Turbomachinery
MPT	Multiple Pure Tones
NSCBC	Navier Stokes Characteristic Boundary Condition
OGV	Outlet Guide Vane
PSD	Power Spectral Density
RANS	Reynolds-Averaged Navier-Stokes
RMS	Root Mean Square
RSI	Rotor-Stator Interaction
SDT	Source Diagnostic Test

SGS	Sub-Grid Scale
SWL	Sound poWer Level
TE	Trailing Edge
TEN	Trailing Edge Noise
TI	Turbulence Intensity
TIN	Turbulence Interaction Noise
TLV	Tip Leakage Vortex
TSV	Tip Separation Vortex
UHBR	Ultra-High Bypass Ratio
URANS	Unsteady Reynolds-Averaged Navier-Stokes
WALE	Wall-Adapting Local Eddy-viscosity
WM	Wall-Modeled
WR	Wall-Resolved

Latin characters

(x,y,z)	Cartesian coordinates (axial, transverse and spanwise coordinates, respectively)
(x^+,y^+,z^+)	Dimensionless wall distance (axial, transverse and spanwise coordinates, respectively)
(r,θ,x)	Cylindrical coordinates (radial, azimuth and axial coordinates, respectively)
$\mathbf{F}$	Net force vector
$\mathbf{q}$	Heat flux vector
$\mathbf{u}$, $\overrightarrow{u}$	Velocity vector
$\widetilde{\mathbf{u}}$	Resolved velocity vector
$\mathbf{u'}$	Velocity fluctuation vector
$\mathbf{U}$	Velocity vector without its acoustic part
A_{mj}	Modal amplitude of the duct mode (m,j)
B	Blade count
c	Vane or blade chord length [m]
c_0	Speed of sound [m/s]
c_f	Friction coefficient
C_p	Pressure coefficient
c_p	Specific heat capacity at constant pressure [J/kg.K]
c_v	Specific heat capacity at constant volume [J/kg.K]
d	Non-overlapping area [m^2]
d_c	Cell local characteristic length [m]
e	Thickness [m]
E	Internal energy [J/kg]
f	Frequency [Hz]
f_c	Cut-off frequency [Hz]
$f(r)$	Radial function for modal decomposition
$g(\theta)$	Azimuthal function for modal decomposition
G	Green's function
G_0	Free-field Green's function in a medium at rest
h	Intervane channel height [m]
$h(x)$	Axial function for modal decomposition

IQ_v, IQ_a	Mesh quality indicators
J_m	Bessel function of first kind of order m
$k = \frac{\omega}{c_0}$	Acoustic wavenumber [m^{-1}]
k_c	Cut-off wavenumber [m^{-1}]
k_{mj}	Axial wavenumber of the duct mode (m,j)
K_{mj}	Eigenvalue of the duct mode (m,j)
k_t	Turbulent kinetic energy [m^2/s^2]
k_x	Axial wavenumber [m^{-1}]
k_z	Spanwise wavenumber [m^{-1}]
L	Span length [m]
l_0	Integral length scale [m]
l_z	Spanwise correlation length [m]
m	Azimuthal order
$\dot{m}$	Mass flow rate [kg/s]
M	Mach number
M_0	Freestream Mach number
M_w	Molecular weight of the gas [mole]
n	Order of a harmonic
N_{ite}	Number of required iterations for convergence
P	Static pressure [Pa]
p'	Pressure fluctuations [Pa]
P_{t0}	Freestream total pressure [Pa]
P_t	Total pressure [Pa]
Q	Q-criterion
$\dot{Q}$	Volume heat source [J/s]
r_s	Specific mixture gas constant m^2.s^{-2}.K^{-1}
R	Universal gas constant [J.K^{-1}.mol^{-1}]
Re	Reynolds number
Re_c	Chord-based Reynolds number
R_h	Hub radius [m]
R_m	Mean radius [m]
R_s	Shroud radius [m]
S_b	Surfaces of the blades and vanes [m^2]
R_{pp}	Cross spectrum function of the pressure fluctuations
t	Time [s]
T	Static temperature [K]
T_{t0}	Freestream total temperature [K]
T_{phys}	Physical time [s]
T_t	Total temperature [K]
T_{ij}	Lighthill's tensor [Pa]
u	Streamwise velocity component [m/s]
U_0	Freestream velocity [m/s]
u_c	Convective velocity [m/s]
U_c	Wake centerline axial velocity [m/s]
u_d	Wake axial velocity deficit [m/s]
U_d	Maximum wake axial velocity deficit [m/s]
U_e	External velocity [m/s]
u^+	Dimensionless wall velocity

u_τ	Friction velocity [m/s]
v	Transverse velocity component [m/s]
V	Vane count
v_0	Velocity scale of the turbulence integral scale [m/s]
v_η	Velocity scale of the turbulence Kolmogorov scale [m/s]
V_r	Radial velocity component [m/s]
V_x	Axial velocity component [m/s]
V_θ	Azimuth velocity component [m/s]
w	Upwash velocity fluctuation [m/s]
x_i	Observer coordinates
y_i	Noise source coordinates
Y_m	Bessel function of second kind of order m

Greek characters

α	Angle of attack [°]
$\beta = \sqrt{1 - M^2}$	Compressibility parameter
κ_s	Stagger angle [°]
λ_{ac}	Acoustic wavelength [m]
λ_c	Cut-off wavelength [m]
λ_f	Longitudinal turbulence length scale [m]
λ_t	Turbulence length scale [m]
λ_{Ta}	Taylor micro-scale [m]
λ_{th}	Thermal conductivity
δ	Boundary layer thickness [m]
δ_1	Boundary displacement layer thickness [m]
δ_2	Boundary momentum layer thickness [m]
δ_{ij}	Kronecker delta
Δf	Frequency step [Hz]
Δt	Time step [s]
Δr	Strip thickness [m]
ϵ	Energy dissipation rate [J/s]
η	Kolmogorov length scale [m]
γ^2	Coherence function of the pressure
$\gamma^2_{u_i}$	Coherence function of the velocity component u_i
$\gamma^2_{u_i p}$	Coherence function of the velocity component u_i and the pressure
μ	Dynamic viscosity [Pa.s]
μ_0	Freestream dynamic viscosity [Pa.s]
μ_t	Turbulent viscosity [Pa.s]
ν	Kinetic viscosity [m²/s]
ν_t	SGS eddy kinetic viscosity [m²/s]
$\phi(r, \theta, x)$	Acoustic potential
ϕ_{pp}	Wall-pressure spectrum [dB/Hz]
$\Phi_{u_i u_i}$	PSD of the u_i velocity fluctuations [dB/Hz]
ψ	Solidity
Ω	Rotational speed [RPM]

$\overrightarrow{\Omega_v}$	vorticity vector.
Ω_n	Nominal rotational speed [RPM]
ω	Angular frequency [Hz]
ω_c	Cut-off angular frequency [Hz]
ω_t	Dissipation rate of the turbulent kinetic energy [m^2/s^2]
ρ	Density [Kg/m^3]
ρ'	Density fluctuations [Kg/m^3]
σ	Ratio of the hub to shroud radii
τ_{ij}	Viscous stress tensor [Pa]
τ_{ij}^{SGS}	Sub-grid scale stress tensor [Pa]
τ_{mj}	Attenuation rate of the duct mode (m,j)
τ_w	Wall shear stress [Pa]

Subscripts

0	Freestream
rms	Root mean square

Introduction

General context

According to an annual report of the International Civil Aviation Organization (ICAO) in 2018, the number of air passengers is increasing (an annual increase of 4.5% to 8.7% from 2010 to 2018). In parallel to this important growth of air traffic, the urbanization of areas in the vicinity of airports is expanding, leading to a stronger opposition of the population to pollution and noise emissions caused by airplanes. In order to respond to this population exposure, more constraining pollutant and noise emission regulations have been established. For this reason, three main axes of action were identified by the ICAO, (i) the reduction of the emission of greenhouse gas on a global scale, (ii) the reduction of pollutants emitted by aero-engines on a local scale, and (iii) the reduction of the noise pollution. The present PhD addresses the latter axis.

In Europe, for instance, the Advisory Council for Aviation Research and Innovation in Europe (ACARE) has set objectives of 50% and 65% noise reduction for the airplanes constructed in 2020 and 2050 respectively, compared to airplanes from the 2000's. These objectives must be ensured for three certification points (as prescribed by the International Civil Aviation Organization, ICAO) shown in Figure 1: approach, sideline and fly-over.

Over the last fifty years, important progress has been achieved in the aim of reducing aircraft noise. In the 1940's, the first aero-engines were single-flux engines characterized by high speed exhaust hot gas to produce thrust. The noise emissions from such aero-engines were thus related to the jet flow, for which the resulting acoustic power evolves as the eighth power of the flow speed [147, 148]. With the development of double flux reactors (also called turbofan engines), the airplane noise has been constantly decreasing over the years. For turbofan aero-engines, the air flow is distributed between the main core flow and the bypass flow, as shown in Figure 2. For this type of aero-engines, the thrust generation is mainly based on the increased momentum in the bypass flow. Concurrently, the speed of the exhaust hot gas is reduced, leading to lower noise emissions.

To further improve the efficiency of aero-engines, the bypass ratio (ratio between the mass-flow rates of the bypass and core flows) has been increased over the years. The new generation of aero-engines, known as ultra-high bypass ratio (UHBR) engines, is characterized by bypass ratios between 12 and 20, whereas the bypass ratio is around 11 for present aero-engines [166].
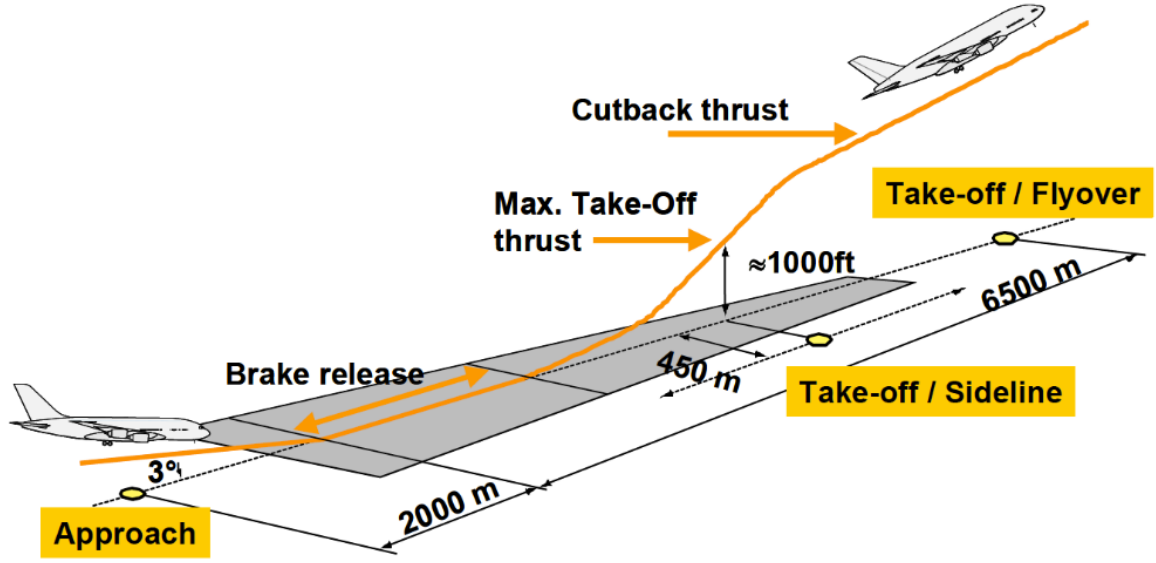
Figure 1: Acoustic certification flight paths and control points. (adapted from [40]).
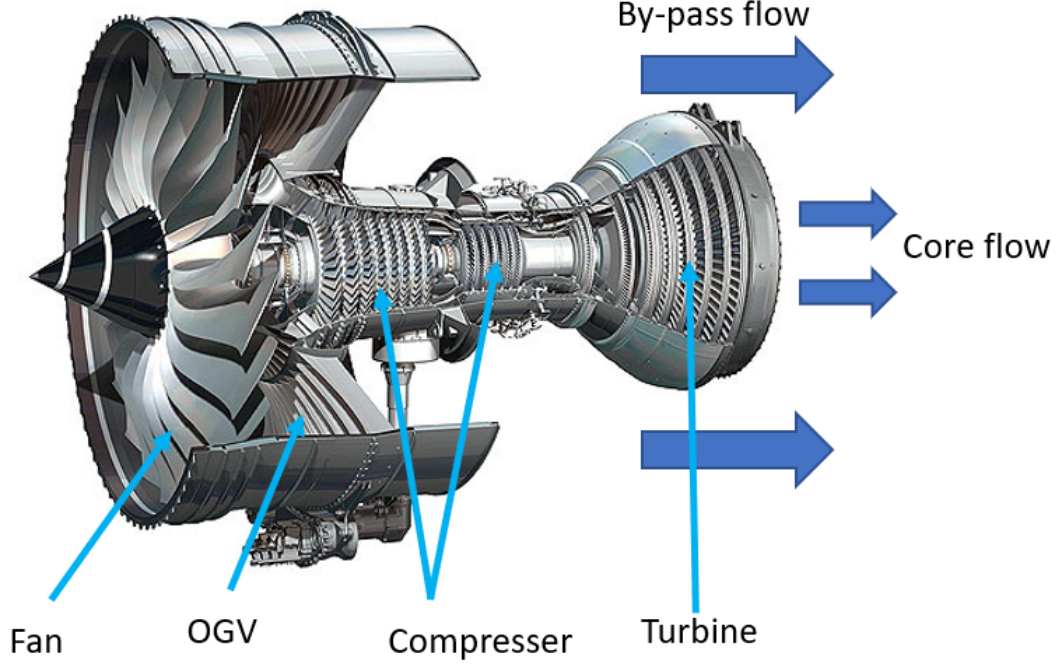
Figure 2: Double-flux turbofan engine. OGV stands for "outlet guide vanes".
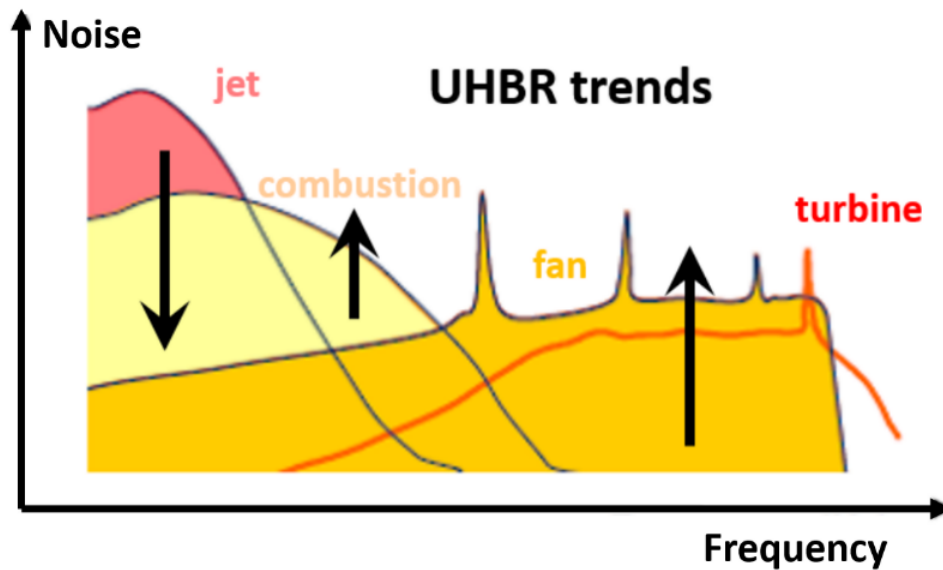
Figure 3: Typical noise spectrum of an UHBR engine [166]. The arrows represent evolution trends over the years.

Noise contributors

A typical noise spectrum of a classical UHBR aero-engine is shown in Figure 3, where the main noise contributions can be noted.

- Jet noise. The jet noise is generated by the mixing of hot high speed gases emitted by the nozzle with the ambient air. Jet noise produces a low frequency broadband noise component and mainly radiates downstream of the aero-engine.

- Fan stage noise. The fan stage of an aero-engine produces tonal and broadband noise components. The tonal noise is usually characterized by rays at the blade passing frequencies (BPF). The broadband noise component is related to the turbulent flow in the fan stage and the different broadband noise sources are extensively described in this work.

- Combustion noise. Combustion noise is usually decomposed into direct and indirect combustion noise. The direct combustion noise comes from the unsteady flame in the combustion chamber, associated with strong fluctuations of the local density. Indirect combustion noise is generated by the acceleration of pockets of hot gas through the turbine stage. The combustion noise is characterized by a broadband acoustic signature at low to mid frequencies, and mainly radiates in the downstream direction. This noise source is usually masked by the fan and jet noise sources.

- Compressor and turbine noise sources. These noise sources are characterized by a similar acoustic signature as the fan noise, with significant contributions at larger frequencies. Usually, these noise sources are not preponderant. Additionally, the high frequencies are less penalizing with regard to acoustic certifications. The compressor noise is usually masked by the fan noise contribution upstream of the aero-engine and the turbine noise by the jet and fan noise contributions in the downstream direction.
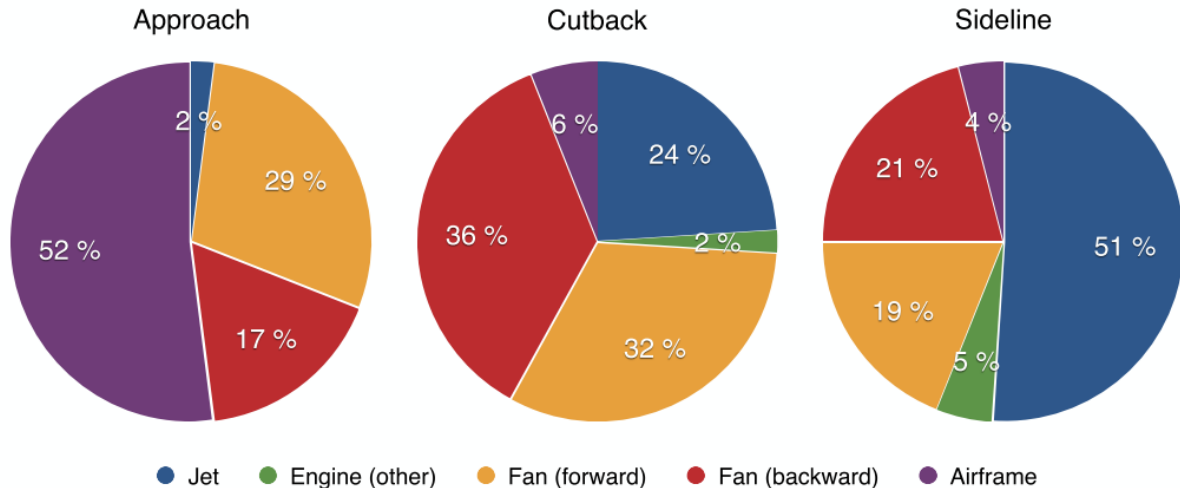
Figure 4: Example of noise source sensitivity on a typical Long Range aircraft with 4 recent engines, at the three certification points [100].

The evolution of the noise contributions with the increase of the bypass ratio is also shown in Figure 3 and the energy distribution of these contributions is presented in Figure 4, for observers at the different certification points, sideline, approach and flyover. The jet noise is seen to be dominant at sideline, whereas at approach and cutback conditions, the fan stage becomes the main noise contributor if the aero-engine.

Overview of the PhD

This brief discussion of the different noise sources of an aero-engine shows that the fan stage of modern aero-engines is one of the major contributors to the total noise radiated by an aircraft, whether tonal or broadband, at both approach and take-off operating points. This may become even more important for future aero-engines, such as UHBR aero-engines. The understanding of the different fan noise mechanisms of the future generation of aero-engines is an important step in the reduction of these noise sources and thus a direct way to tackle the problem of aircraft noise pollution.

PhD thesis objectives

The main objective of this PhD is the prediction of different noise mechanisms, described in details in Chapter 1: (i) the rotor/stator interaction (RSI) noise, (ii) the trailing edge (TE) noise, (iii) the laminar separation noise and (iv) the tip gap noise, of a fan/OGV (rotor + stator) stage using large eddy simulations (LES). The present work mainly focuses on the study of the broadband component of these noise mechanisms of a fan/OGV stage, exclusively at approach conditions. Different noise prediction approaches are used in order to assess their validity, but also to discriminate between the contributions of these sources. These approaches are:

- LES-informed analytical models.

- Hybrid numerical methods coupling the LES results with an integral method.

- LES direct noise computation.

More specifically, the present study aims to:

- draw the LES numerical requirements allowing for a good prediction of several broadband noise mechanisms, using a direct noise computation approach in a fan/OGV stage at approach condition.

- develop a fast pre-dimensioning tool that allows the user to estimate the mesh size in each region of interest of the computational domain (boundary layers, wakes, tip gap region, acoustic propagation regions) and provides a quick estimation of the computational time of LES for fan/OGV stage applications.

- study in details the complex flow topology of secondary flows at partial regimes, such as recirculation bubbles and complex tip leakage flows.

- evaluate the direct noise computation in a fan stage using LES.

- compare direct noise predictions from the LES with advanced analytical models, which are fed by LES data.

- assess the contributions of the different noise sources to the total noise emissions.

- perform a first of its kind 360° fan/OGV LES that is able to properly compute both the turbulent flow in the boundary layers and wakes, and the acoustic field around the fan stage.

- use the 360° LES data to analyze the modal content of the acoustic field radiated by the fan stage and the blade-to-blade correlations of the turbulent flow. Such analyses are not possible with more classical simulations performed on a periodic sector of a fan stage.

- improve the physical understanding of the complex broadband noise mechanisms, and clearly identify the main noise sources in a fan stage.

PhD thesis structure

The present manuscript is structured as follows. Chapter 1 is dedicated to a literature review. This chapter provides an overview of the main concepts and some fundamental knowledge that allow to carry out broadband noise predictions in a fan stage. It also clearly defines the scope of this study. The main noise sources in a fan/OGV stage at approach condition, and several numerical and analytical approaches to estimate the noise resulting from these sources, are briefly described. A particular focus is made on the numerical methods and the analytical models that are used in the following chapters.

Chapter 2 presents the numerical parameters used in this work. It gathers all mesh related information of the different configurations considered in this work. The specific geometry, operating conditions and numerical setup of each configuration are presented.

Chapter 3 investigates the numerical requirements for a correct description of (i) the flow in boundary layers and wakes and (ii) the prediction of two main noise mechanisms, the rotor-stator interaction noise and the trailing edge noise. Several LES computations are performed using flat plate configurations. The results of this chapter enable to guide the design of turbomachinery meshes that meet the prescribed turbulent and acoustic criteria. They led to the development of a pre-dimensioning tool for LES in turbomachinery applications.

The following chapters investigate four main broadband noise sources of the ECL5 ultra-high bypass ratio fan/OGV stage at approach conditions; (i) the laminar separation noise, (ii) the tip gap noise, (iii) the rotor-stator interaction noise and (iv) the trailing edge noise.

Chapters 4 and 5 improve our current understanding of the unsteady aerodynamic characteristics and noise generation mechanisms of two secondary flows on the rotor blades in fan/OGV stages: a recirculation bubble that can appear close to the leading edge of the rotor blades at approach condition, and the tip leakage flow. Chapter 4 particularly focuses on the effects of the mass flow rate, i.e. the angle of attack, on the characteristics of the recirculation bubble and its acoustic signature. Additionally, the influence of the inlet turbulence injection rate on the properties of the recirculation bubble, and the capability of wall-modeled LES to properly capture these properties, are assessed.

The flow topology and the main noise sources in the blade tip region are investigated in Chapter 5. The different noise generation mechanisms in this region are extensively analyzed by means of steady and unsteady flow investigations, a correlation analysis and a dynamic mode tracking technique. The contribution of each noise mechanism in the blade tip region to the total noise emissions from the rotor blade is also studied.

Finally, Chapter 6 presents an aerodynamic and aeroacoustic analysis of the ECL5 fan stage using LES. A first of its kind 360° LES is compared to a periodic sector configuration in terms of mean and turbulent flows as well as the acoustic field in the fan stage. The broadband noise is directly computed from the fully-compressible LES solver and compared with predictions from available analytical models. An acoustic analogy, based on the pressure fluctuations on the solid surfaces of the blades, is used to separate the noise contributions of different noise mechanisms to the total noise emissions. Finally, aeroacoustic results are compared between the 360° and the periodic sector LES configurations. A mode decomposition technique over the duct acoustic modes is also performed, using unsteady pressure fluctuations obtained by the 360° LES.

Due to the large scope of physical mechanisms studied in the present work, including the study of a large variety of noise mechanisms in a fan stage using different numerical and analytical approaches, Chapters 4, 5 and 6 contain a state of the art of the specific mechanisms studied in these chapters, complementing what is presented in Chapter 1.

PhD thesis dissemination

The work performed during this PhD has led to the following dissemination:

Patent application

A patent application has been prepared (ref. e-soleau: DSO2022009163).

Journal Articles

Two journal articles have been published during the PhD thesis.

- J. Al-Am, V. Clair, A. Giauque, J. Boudet, and F. Gea-Aguilera. On the effects of a separation bubble on fan noise. Journal of Sound and Vibration, vol. 537, 2022. https://doi.org/10.1016/j.jsv.2022.117180.

- J. Al-Am, V. Clair, A. Giauque, J. Boudet, and F. Gea-Aguilera. A parametric study on the LES numerical setup to investigate fan/OGV broadband noise. International Journal of Turbomachinery, Propulsion and Power, 6(2) :12, 2021. https://doi.org/10.3390/ijtpp6020012.

Conference proceedings

Three conference papers have been published during the PhD thesis.

- J. Al-Am, V. Clair, A. Giauque, J. Boudet, and F. Gea-Aguilera. Direct noise predictions of fan broadband noise using LES and analytical models. 28th AIAA/CEAS Aeroacoustics Conference, 2022.
  https://doi.org/10.2514/6.2022-2882.

- J. Al-Am, V. Clair, A. Giauque, J. Boudet, and F. Gea-Aguilera. Effet du débit sur le bruit propre d'un étage soufflante/redresseur en régime d'approche, Congrès Français de l'Acoustique, 2022.

- J. Al-Am, V. Clair, A. Giauque, J. Boudet, and F. Gea-Aguilera. Fan/OGV broadband noise predictions using LES. EuroHPC Summit Week 2022, Paris, France.

- J. Al-Am, V. Clair, A. Giauque, J. Boudet, and F. Gea-Aguilera. A parametric study on the LES numerical setup to investigate fan/OGV broadband noise. 14th European Conference on Turbomachinery Fluid dynamics & Thermodynamics Conference, 2021.

Awards

Two awards have been received during this PhD thesis.

- PRACE project (LESFOS, id.2021240101) award of 30 million CPUh to perform a first of its kind high fidelity computation on a full fan/OGV stage of future generation.
  https://prace-ri.eu/hpc-access/project-access/project-access-awarded-projects/projects-awarded-under-prace-project-access-call-23/#Engineering.

- Top 5 paper award at the European Turbomachinery Conference 2021 (ETC14).

Table 5: Distribution of CPU hours consumption (in millions of CPU hours) during the PhD thesis, over the different clusters.

	Newton	Occigen	Irene-Cines	Irene-Prace	Total
year 1	1.0	1.5	0.0	0.0	3.5
year 2	0.4	6.8	2.0	0.0	8.8
year 3	0.0	0.0	9.0	30	39
Total	1.4	8.3	11	30	50.7

General public communications

Several general public communications were achieved during this PhD.

- Article published in the "Tribune de Lyon" journal, December 2022. Une simulation lyonnaise inédite pour réduire le bruit des moteurs d'avions. https://tribunedelyon.fr/sciences-innovation/une-simulation-lyonnaise-inedite-pour-reduire-le-bruit-des-moteurs-davions/.

- Chronic radio at "RCF", octobre 2022. L'étude de la réduction du bruit des nouveaux moteurs d'avion. https://www.rcf.fr/culture-et-societe/dis-pourquoi-rcf-lyon?episode=294504.

- Articles on the websites of the Ecole Centrale de Lyon and the CNRS. Simulation haute fidélité d'un étage complet de soufflante aéronautique (360°), Octobre 2022. ECL: https://www.ec-lyon.fr/actualites/2022/simulation-haute-fidelite-etage-complet-soufflante-aeronautique-360deg. CNRS: https://www.rhone-auvergne.cnrs.fr/fr/cnrsinfo/simulation-haute-fidelite-dun-etage-complet-de-soufflante-aeronautique-360deg).

Computational hours

The computations performed during this PhD thesis have used about 51 million CPU hours on different clusters,

- Newton, which is a local cluster at Ecole Centrale de Lyon.

- Occigen, which is a cluster operated by the CINES in France. The access to this cluster was obtained through French national allocations of GENCI (projects 2A05039).

- Irene, which is a cluster operated by the CEA in France. The access to this cluster was obtained through French national allocations of GENCI (projects 2A05039) and the European PRACE project LESFOS.

The distribution of the CPU hours consumption is given in Table 5.

Chapter 1

State of the Art

> **Introduction**
>
> Modern and future generations of aero-engines are usually considered as a major contributor to the total noise radiated by aircrafts, as highlighted in the introduction. The reduction of noise from aircraft engines close to airports, particularly during take-off and approach, is one of the main objectives of engine manufacturers, to meet current and future stringent regulations. It is then important to study the multiple mechanisms that generate noise.
>
> The objective of this chapter is to provide some fundamentals and a theoretical background of the aeroacoustic phenomena involved in a fan-OGV stage. It aims to identify the available numerical and analytical tools to carry out broadband noise studies and to justify the choices made in the following chapters.
>
> This Chapter can be divided into three main parts. In the first part, an overview of the dominant tonal and broadband noise mechanisms, encountered in a fan stage, are presented. The second part presents the main aspects of the different numerical tools used in this work, with a particular focus on the LES approach. The third part shows the different noise prediction approaches adopted in the present work.

Contents

1.1 Turbofan engines

A modern turbofan engine, shown in Figure 2, is an axial flow turbomachine, that produces thrust to power an aircraft through four main phases: (i) ingestion of the ambient air, (ii) compression of the air, (iii) combustion and (iv) expansion of the hot gas. The incoming flow is first driven by a ducted fan that uses part of the mechanical energy absorbed by the turbine to accelerate the flow. Then, the flow is divided into two streams: a primary or core stream and a bypass or secondary stream. The core flow is first compressed in the compressor stages, then it is burnt with fuel in the combustion chamber. Then, the resulting hot gas undergoes expansion in the turbine stages, where a part of its energy provided in the compression and combustion stages, is recovered to drive the fan and the compressors. The core gas is then ejected through a nozzle and forms a hot jet. The secondary or bypass flow is accelerated in the fan/OGV stage, where its direction is also adjusted. Finally, it is ejected through the exhaust nozzle and mixed with the hot gas.

All modern civil airplane aero-engines are turbofans. They combine the high speed capability of turbojets with the fuel efficiency and appropriate acceleration characteristics of propellers. The main difference between turbofans is the bypass ratio, which corresponds to the ratio between the mass flow rate passing through the fan to that passing through the core engine. Actual high bypass ratio turbofans are characterized by bypass ratios of 10. The next generation of turbofans tends to further increase the bypass ratio and leads to ultra high bypass ratio (UHBR) engines with bypass ratios of 15 or more.

1.2 Aeroacoustic sources

Aeroacoustic noise sources can have different origins related to different noise production mechanisms. These can usually be modeled using three main equivalent source models [147, 148, 277]:

- Monopole sources, which originate from volume flow variation during the motion of surfaces. The noise resulting from these sources is usually characterized by wavenumbers much larger than the geometric dimensions of the source.

- Dipole sources, which originate from the interaction of aerodynamic force fluctuations in the flow with solid surfaces.

- Quadrupole sources, which correspond to the internal fluctuating stress in the fluid.

10

(a) Subsonic case, approach condition.   (b) Transonic case, take-off condition.
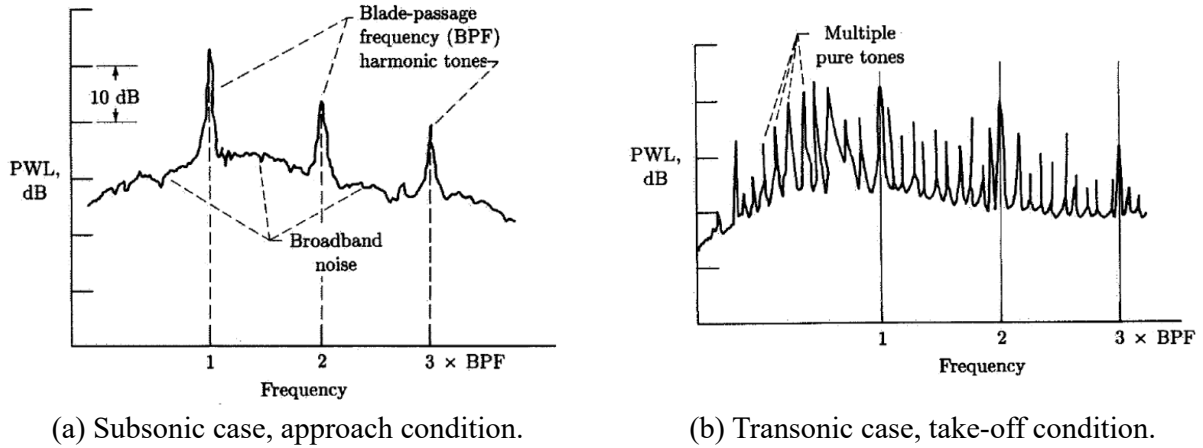
Figure 1.1: Typical acoustic spectra of a fan-OGV stage, extracted from [99].

1.3   Fan noise sources

Typical sound power spectra resulting from fan noise sources are presented in Figure 1.1 for two operating points, approach and take-off conditions. The fan stage produces both tonal and broadband noise components. The tonal noise component is generated from periodic phenomena and appears at multiple discrete frequencies. The broadband noise (BBN) results from random fluctuations related to the turbulent flow. Over the whole frequency range, the BBN extends continuously. Different behaviors are observed for these two components depending on the operating point. At approach condition (Figure 1.1 (a)), the flow remains subsonic all along the blade and the tonal noise is mainly produced by the periodic interaction of the fan wakes with the OGVs, creating tones at the Blade Passing Frequency (BPF) and its harmonics. At take-off condition (Figure 1.1 (b)), the flow becomes transsonic at the rotor tip. Shock waves are then formed, which leads to the apparition of tones in the acoustic spectrum, as shown in Figure 1.1 (b). These tones are known as Multiple Pure Tones and constitute the so-called buzz saw noise, which is characterized by a quadrupole noise contribution at transsonic regimes.

The tonal part of the fan-OGV stage noise emissions is widely addressed in previous studies and many solutions have been proposed to reduce it. For example, specially designed nacelle and acoustic liners at the duct exhaust can be implemented to damp propagating tones [141]. The fan and OGV count can also be properly chosen to take advantage of duct filtering [260] and cut-off the blade passing frequency. At partial regimes though, the BBN of the fan/OGV stage becomes a major contributor to the total noise emissions [192, 193].

BBN is less studied in the literature due to its stochastic nature associated with the fine structures of the turbulence in boundary layers of the fan blades and the OGVs, and in the wakes of the fan. Due to the large range of cut-on modes, this noise mechanism is hard to control [193]. BBN noise originates from several mechanisms, such as (i) the interaction of the inlet turbulence with the rotor blades, (ii) the fan tip gap noise, (iii) the trailing edge (TE) noise and (iv) the rotor/stator interaction (RSI) noise. The tip gap noise is associated with the highly unsteady flow that develops in the gap between the tip of the fan blades and the casing. This highly unsteady flow may then be diffracted at the trailing edge corner of the blade tip, or interact with the following blades to generate noise. TE noise is generated when the turbulent flow in boundary layers encounters the

11
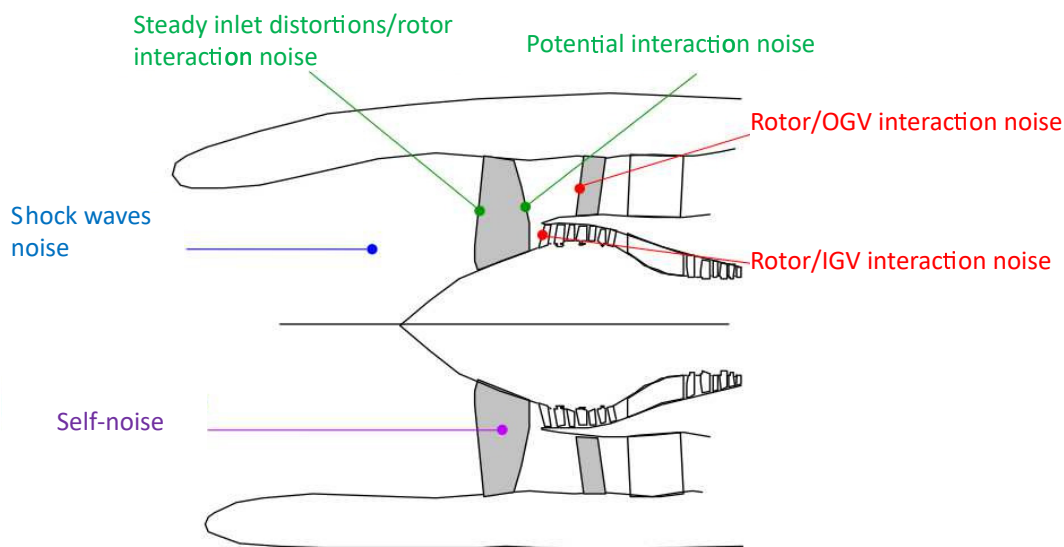
Figure 1.2: Tonal noise sources of a high bypass ratio engine (modified from [14]).

TE of the blade or the vane. RSI noise results from the interaction of turbulence in the rotor wakes with the leading edge of the stator, which generates an unsteady loading on the vanes. The RSI noise mechanism is usually considered as the dominant noise source in a fan stage at approach condition [193, 144].

1.3.1 Tonal noise sources

The main noise mechanisms that generate tonal sources are presented in Figure 1.2 and described in the following.

- Shock wave noise. At take-off conditions, the flow is supersonic at the blade tip. Shock waves are thus formed. The small blade-to-blade angles irregularities result in the detachment of the shock waves, that propagate upstream of the duct and lead to tones at multiples of the rotational shaft frequency instead of the BPF and its harmonics (associated to the Buzz Saw Noise in Figure 1.1 (b)).

- Rotor/stator interaction noise. At subsonic operating points, the fan stage noise is mainly generated by the impact of the periodic mean velocity deficit induced by the rotor wakes, on the stator vanes. For an observer in the stator reference frame, the rotating wakes are generated at the blade passing frequency (BPF) and lead to a periodic variation of the loading on the stator vanes. This interaction is expected to generate noise at the BPF harmonics $\omega = nB\Omega$, where n is an integer denoting the order of the BPF harmonic and Ω is the rotation speed. From the Tyler & Sofrin rule [261], the acoustic duct modes that are generated by this interaction noise have azimuthal orders m given as,

$$m = nB - kV \tag{1.1}$$

where k is an integer and V is the vanes count.

Due to its periodic nature, tonal noise results in narrow peaks in the far-field noise spectrum, as seen in Figure 1.1 (a). This mechanism has been extensively studied
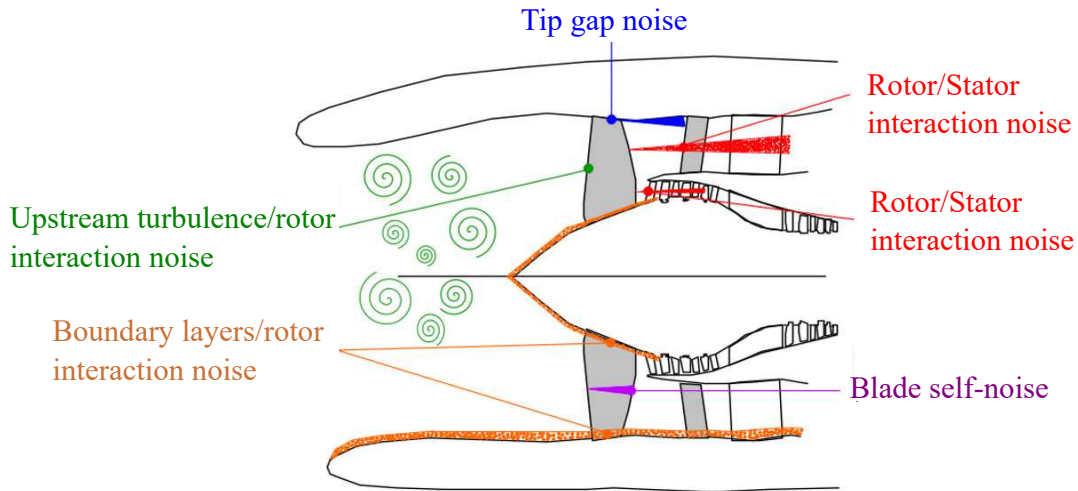
Figure 1.3: Broadband noise sources of a high bypass ratio engine (modified from [14]).

in the literature [137, 72, 50, 80, 238, 195, 239, 111], and considerably reduced over the past decades.

- Inlet distortions/rotor interaction noise. At subsonic regimes, this mechanism arises from the interaction of steady inlet flow distortions induced by installation or ground effects with the rotor blades. Tonal contribution at the BPF and its harmonics is associated to this noise mechanism.

- Potential interaction noise. The stator vanes induce a steady distortion of the streamlines, which leads to pressure fluctuations on the rotor blades. The potential effect decreases quite rapidly in the upstream direction and is known to become negligible for distances larger than 0.3 times the chord length [188, 196]. For future engine generation, with the reduction of the distance between the rotor and the stator, this mechanism may become important. In this case, the trailing edge of the rotor encounters a periodic potential field imposed by the stator. This induces load fluctuations on the rotor blade surface that are converted into tonal noise at the BPF harmonics. The acoustic modes generated by this mechanism are also given by the Tyler & Sofrin rule [261] equation (Eq. 1.1), with the difference that the mode orders of the sources is fixed to the multiple of the number of vanes kV.

1.3.2 Broadband noise sources

At subsonic operating conditions, the broadband noise component, which is related to the turbulent flow, becomes a significant contributor to the total noise emissions. The different BBN noise mechanisms are shown in Figure 1.3 and described as follows,

- Blade/Vane self-noise. The self-noise is associated with the turbulent flow that develops in the boundary layers of the blades and vanes, all along their span. When the flow remains attached along the surface of an airfoil with a sharp trailing edge, the turbulent eddies developing in the boundary layer are diffracted when passing the trailing edge and generate noise. This mechanism is referred as trailing edge noise (TE noise) [7, 276, 95, 223, 171, 224, 170, 84] and is mostly present in the case

of a fan stage at its nominal operating regime. If the fan operates at a lower regime, for example at approach conditions, a separation region may appear in the vicinity of the fan blades' leading edge, which leads to the formation of a recirculation bubble in that region. This phenomenon and its contribution to self-noise have been extensively studied experimentally [168, 142, 54, 248, 98, 211, 163, 136] and numerically [5, 219, 218, 113, 283, 283, 52, 249].

- Rotor/Stator interaction noise, also known as turbulence interaction noise or leading edge noise, is produced when the turbulent flow in the wakes of the fan blades, formed by the mixing of both the suction and pressure side boundary layers at the trailing edge, impinge on the OGVs. The coherent and periodic components of the wakes give rise to tonal noise at the blade passing frequency, whereas the stochastic part of the wakes' turbulent flow generate a broadband component. This noise source is identified as one of the major contributors to the broadband noise radiated by modern aircraft engines [193], and has been extensively studied both experimentally [58, 101, 102, 200, 201, 158, 11, 259, 24, 159] and numerically [276, 95, 171, 170, 84, 209, 181, 213, 265, 208, 62, 207, 93, 145, 25, 221, 127, 89, 81, 79, 203, 198, 107, 66, 65, 92] over the past decades.

- Upstream turbulence/rotor interaction noise. The interaction of the atmospheric upstream turbulence with the rotor leading edge can also be considered as a BBN source [92, 190].

- Boundary layers/rotor interaction noise. The interaction of the turbulent boundary layers on the shroud and the hub with the rotor blades generates BBN. At the shroud, the boundary layer is thick and interacts with the tip gap of the blade. This may lead to the formation of a horse shoe vortex at the blade leading edge at the tip. At the hub, the boundary layer interacts with the blade and leads to the formation of a corner vortex.

- Tip gap noise. The tip gap of the rotor blade leads to aerodynamic losses and noise generation. The pressure gradient between the pressure and suction side on the blade tip generates a tip clearance flow. This region is characterized by a high speed and turbulent flow, that exists in the gap as a cross-flow jet and interacts with the surrounding flow. Consequently, two main vortices are generally formed (as shown in Figure 1.4), (i) the tip leakage vortex (TLV), generated at the leading edge of the rotor, and (ii) the tip separation vortex (TSV), formed at mid-chord. These vortices interact with the outer flow and the surrounding walls of the blades and the shroud. Such interactions generate two highly turbulent pressure fluctuation zones, leading to broadband self-noise production [106, 26, 108, 87].

  - The first zone corresponds to a jet-like flow, that generates a quadrupolar noise source when leaving the clearance region, directly and by interacting with the blade tip edge [106].

  - The second zone corresponds to the tip vortices, the TLV and TSV, that induce loading fluctuations when interacting with the suction side of the blade they originated from or the pressure side of the neighboring blades [87]. The tip vortices are also diffracted at the TE and contribute to the TE noise, thus forming a local dipole source that is much more coherent than the distributed TE noise.
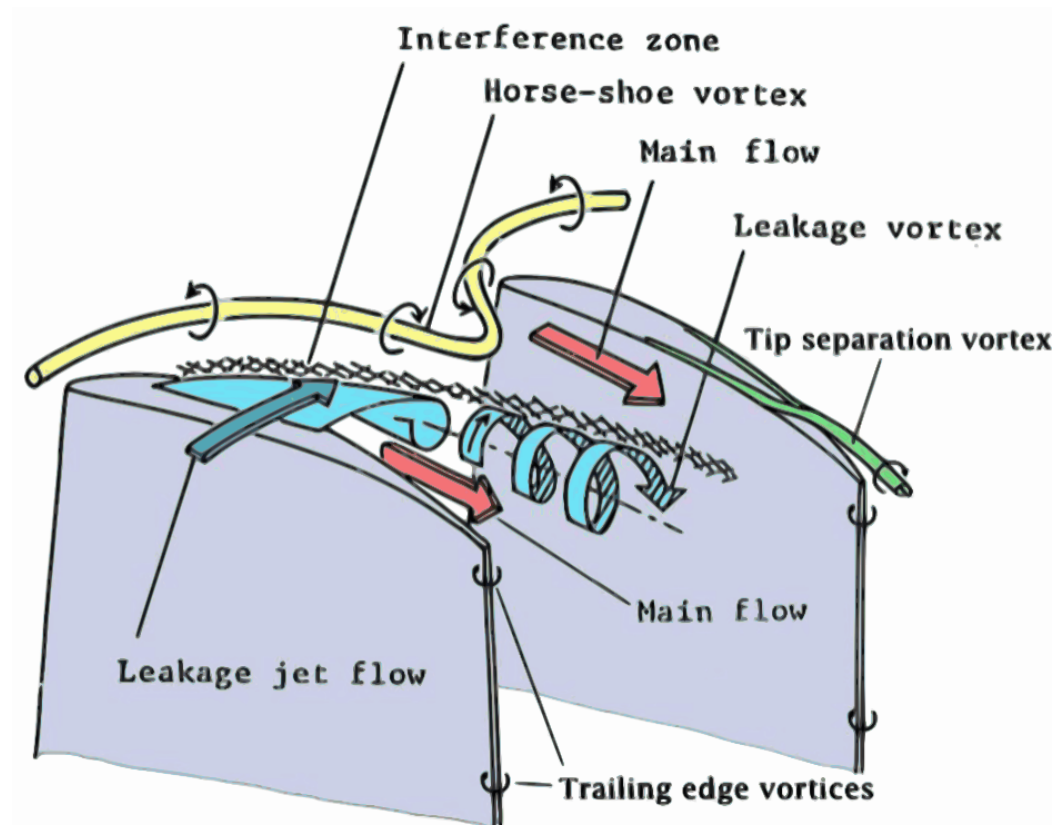
Figure 1.4: Schematic view of the rotor tip clearance flow (from [104]).

The tip noise is usually characterized by large broadband humps in the acoustic spectra. These humps occur at frequencies independent from the BPF and its harmonics and correspond to quasi-tonal spectral features [150, 172]. These features result from the mixing of highly coherent flow structures (the tip leakage vortex) with uncorrelated flow structures (the turbulent flow), which leads to the spectral humps. The tip vortices may also interact with the stator vanes with a noise signature at the BPF harmonics, thus contributing to the RSI noise.

The present work focuses on four broadband noise mechanisms.

- Rotor-stator interaction noise.

- Trailing edge noise.

- Laminar separation noise.

- Tip gap noise.

Fan stage noise sources ———————————————————— **Summary**

In this section, the main mechanisms generating both broadband and tonal noise sources in a fan/OGV stage of a turbofan engine have been described. In this work, the fan is operating at approach condition. The fan stage is thus the main noise

contributor of the aero-engine and the sources related to the transsonic regime, like the shock wave noise, are not considered. Since the Mach number remains below 0.6 at this regime, monopole and quadrupole sources are neglected and dipole sources, mainly corresponding to aerodynamic force fluctuations on solid walls, are particularly studied. Different mechanisms, such as the rotor/stator interaction noise, the blade/vane self-noise and the tip gap noise, have appeared as significant broadband and tonal noise sources, justifying the need to further study these mechanisms.

1.4   Numerical tools

In the present study, the fan stage noise is studied using numerical simulations. Experimental methods, usually considered as the most accurate approaches, are very expensive and require complex measurement tools. However, computational fluid dynamics (CFD) methods allow to extract data anywhere in the flow field with a reduced cost compared to experimental investigations. The increase of available computational resources has allowed the use of high-fidelity numerical methods to perform fluid dynamics studies in complex flow configurations with a fairly suitable precision. In this section, a brief overview of the existing CFD methods is presented, with a highlight on both the level of flow description and the computational cost of each of the methods.

1.4.1   Governing equations

The general equations of fluid dynamics are the compressible Navier-Stokes equations, which can be decomposed into three main equations, (i) mass conservation or continuity equation, (ii) momentum conservation equation and (iii) total energy conservation equation. The system is composed of 7 unknowns (density ρ, pressure p, temperature T, three components of the velocity vector $\mathbf{u}$, total energy E of the considered fluid and three components of the heat flux vector $\mathbf{q}$). If the fluid is subjected to a net force vector F, and to a volume heat source $\dot{Q}$, the Navier-Stokes equations can be given as,

$$\frac{\partial \rho}{\partial t} + \frac{\partial}{\partial x_j}(\rho u_j) = 0 \tag{1.2}$$

$$\frac{\partial(\rho u_i)}{\partial t} + \frac{\partial}{\partial x_j}(\rho u_i u_j + p\delta_{ij} - \tau_{ij}) = \rho F_i \quad i = 1,2,3 \tag{1.3}$$

$$\frac{\partial(\rho E)}{\partial t} + \frac{\partial}{\partial x_j}(\rho E u_j + p u_j - \tau_{ij}u_j + q_j) = \rho F_j u_j + \dot{Q} \quad i = 1,2,3 \tag{1.4}$$

In order to obtain a closed system three assumptions are usually made:

- Ideal gas. If an ideal gas is considered, its thermodynamic properties can be described through the ideal gas Equation of State (EoS), given as,

$$\frac{p}{\rho} = r_s T \tag{1.5}$$

where $r_s = R/M_w = c_p - c_v$ is the specific mixture gas constant ($r_s = 287 \mathrm{m}^2.\mathrm{s}^{-2}.\mathrm{K}^{-1}$ for air mixture), R the universal gas constant ($R = 8.3145$ J.K^{-1}.mol^{-1}) and M_w the molecular weight of the gas. c_p and c_v are the constant pressure and volume

specific heat capacities, respectively. They can be considered as constant for perfect gases such as air if the temperature does not evolve significantly.

- Fourier law. It relates the heat flux q with the temperature gradient,

$$q_i = -\lambda_{th} \frac{\partial T}{\partial x_i} \tag{1.6}$$

where λ_{th} is the thermal conductivity of the considered fluid.

- Newtonian fluid. The Newtonian fluid assumption allows to obtain a linear relation between the viscous stresses τ_{ij} and the local strain rate:

$$\tau_{ij} = \mu \left(\frac{\partial u_i}{\partial x_j} + \frac{\partial u_j}{\partial x_i} \right) - \frac{2}{3} \mu \left(\frac{\partial u_i}{\partial x_i} \right) \tag{1.7}$$

where μ is the dynamic viscosity of the fluid that can be obtained through Sutherland's law as,

$$\mu(T) = \mu_{ref} \left(\frac{T}{T_{ref}} \right)^{\frac{3}{2}} \frac{T_{ref} + S}{T + S} \tag{1.8}$$

where $\mu_{ref} = 1.711.10^{-5}$ kg.m^2.s^{-1} is the dynamic viscosity at reference temperature $T_{ref} = 273.15$ K and the constant for air $S = 110.4$ K is obtained experimentally.

1.4.2 Turbulent scales and modeling

Multiple modeling and numerical approaches exist to solve the Navier-Stokes equations, which mainly differ in the turbulence modeling. As the Reynolds number increases, the flow transitions from a laminar to a turbulent state. The latter is characterized by a non-deterministic behavior, which generates a large range of length scales, described in the following.

- Large eddies, which derive their energy from the mean flow are anisotropic. These eddies are unstable and break-up into smaller eddies.

- At the scales of the smallest eddies, the turbulent energy is dissipated through heat. The behavior of the small eddies is more universal in nature than the large eddies and their sizes are mainly determined by the viscosity.

- Intermediate scales between the large and small eddies.

The turbulent kinetic energy is transferred from the largest eddies to the smallest ones. This transfer is known as the turbulence cascade and is mainly described by Kolmogorov's universal equilibrium theory that was originally stated in the form of three hypothesis, recalled here.

- Kolmogorov's hypothesis of local isotropy. The small scale turbulent structures are statistically isotropic.

- Kolmogorov's first similarity hypothesis. The small scale structures have a universal form that is only determined by the kinematic viscosity ν and the energy dissipation rate ϵ.
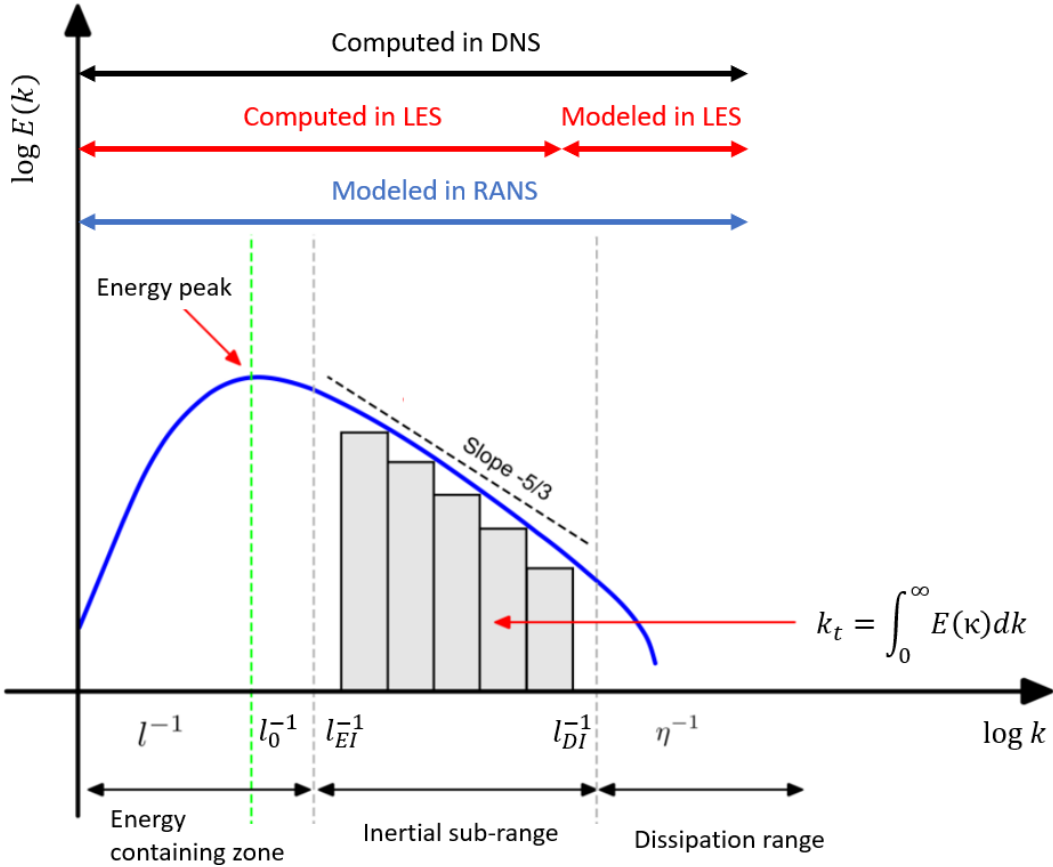
Figure 1.5: Energy spectrum of turbulence in function of wavenumber k, with indication of the range of application of the DNS, LES and RANS models.

- Kolmogorov's second similarity hypothesis. The statistics of the motions between the large and small scales have a universal form that is only determined by ϵ, and is independent of ν.

Consequently, the velocity and time scales decrease as the size of the eddies decreases. Based on these hypotheses and using dimensional analysis, the smallest length η and velocity v_η scales (known as Kolmogorov scales) can be given as,

$$\eta = \left(\frac{\nu^3}{\epsilon}\right)^{\frac{1}{4}} \qquad v_\eta = (\nu\epsilon)^{\frac{1}{4}} \qquad (1.9)$$

The largest length l_0 and velocity v_0 scales (known as the integral scales) can then be determined as,

$$\frac{l_0}{\eta} \propto Re_T^{1/4} \qquad \frac{v_0}{v_\eta} \propto Re_T^{1/4} \qquad (1.10)$$

where Re_T is the Reynolds number related to the integral scales; $Re_T = \frac{k_t l_0}{\nu}$ with $k_t = \frac{1}{2}\overline{u_i'^2}$ is the turbulent kinetic energy and u_i' are the three components of the velocity fluctuation vector **u'**.

Between these two ranges there are eddies that are too small to behave as integral length scales and too large to behave as Kolmogorov eddies. This range is known as the inertial range, where the motion of the eddies is determined by inertial effects (viscous effects are negligible) and the second Kolmogorov's similarity hypothesis is valid. The

eddies found in this range are characterized by the Taylor microscale, given as,

$$\lambda = \left(\frac{10 \nu k_t}{\epsilon} \right)^{1/2} \tag{1.11}$$

The Taylor microscale can also be related to the largest and smallest scales as follows,

$$\frac{\lambda}{l_0} = \sqrt{10} Re_T^{-1/2} \qquad\qquad \frac{\lambda}{\eta} = \sqrt{10} Re_T^{1/4} \tag{1.12}$$

The three main zones (the energy containing zone, the inertial sub-domain and the dissipation zone) that follow the energy cascade are shown by a typical isotropic turbulence spectrum depicted in Figure 1.6 [204]. In the inertial sub-range, the energy resulting from the breaking-up of the larger structures is transferred successively down to smaller structures. The associated energy spectrum decreases following Kolmogorov's law ($E \propto k^{-5/3}$). This range is limited by the scales $l_{EI} = l_0/6$ and $l_{DI} = 60\eta$. The inertial and dissipation ranges are characterized by statistical universality. The main part of the information about the mean flow and the boundary conditions are embedded in the large structures. Consequently, the different numerical approach, described in the following, are sorted with respect to the range of captured turbulent scales.

Reynolds-Averaged Navier-Stokes RANS

RANS simulations consist in modeling the turbulence in a statistical approach. Navier-Stokes equations are averaged over the whole spectrum of turbulent fluctuations, associating a statistically averaged solution to any specific flow configuration. Using this approach, one assumes that each flow variable can be decomposed into a mean part and a fluctuating part. This allows to define the Reynolds stress tensor, adding six unknowns to the Navier-Stokes equations.

In order to close the system, a modeling process should be applied. Many models with different levels of complexity can be used. They are usually based on Boussinesq's closure method, that links the Reynolds stress tensor to the strain and aims to model the turbulent viscosity μ_t. The most widely used models for turbomachinery applications are the Spalart-Allmaras model with one transport equation for μ_t, $k - \epsilon$ and $k - \omega$ models with two transport equations, and the Reynolds stress model with a transport equation for each tensor component. These models use several assumptions, such as an isotropic turbulence, and an equilibrium between turbulence production and dissipation. Additionally, the constants used in these models are usually obtained from calibrations performed on canonical configurations. Consequently, none of them can produce reliable flow simulations in all flow configurations. In turbomachinery applications, the choice of the turbulence model can have a significant impact on the flow field, mainly in highly turbulent flow regions and in the presence of flow separations.

Two approaches can be considered when performing RANS computations: steady and unsteady RANS. The steady approach is limited to a time averaged solution of the equations. Thus, it is not adapted for flows exhibiting an important unsteadiness. The unsteady RANS (URANS) approach, widely used for turbomachinery applications [238, 195, 75, 76, 78, 77], is an extension of the steady approach that allows to obtain a time dependent statistically averaged flow solution. However, the considered unsteadiness in the flow is limited to periodic and deterministic phenomena (tonal noise, vortex shedding)

and the turbulence chaotic fluctuations are still modeled statistically.

Direct numerical simulation DNS

Direct numerical simulations (DNS) are high-fidelity numerical methods and are usually considered as a reference to other types of simulations. This approach directly solves the Navier-Stokes equations by computing all the turbulent scales, from the largest ones in the integral zone, down to the smallest dissipation scales (Kolmogorov scale). All the turbulent spectrum is thus solved and no modeling process is involved. This method is limited to academic and canonical configurations (such as for the simulation of low Reynolds channel flows [125] or for low-pressure turbines [284, 162, 279, 160, 235]) due to two main constraints:

- It requires very dense meshes since the smallest cells should at least be two times smaller than the Kolmogorov length scale. The mesh size is proportional to $Re_T^{9/4}$ ($Re_T = \frac{k_t l_0}{\nu}$). In a fan-OGV stage, this leads to almost 10^{16} cells for Reynolds numbers based on the rotor chord length of 10^6, which is out of reach considering the current available computational power.

- It requires high-order discretization schemes in order to minimize the dissipation and dispersion of the flow structures and the acoustic waves.

Large eddy simulation LES

LES is a high-fidelity approach that can be considered as an alternative to DNS and RANS approaches. This method is based on the assumption that small turbulent eddies mainly contribute to the dissipation rate. These eddies are assumed to have an isotropic behavior that can be predicted by a model called sub-grid scale model. However, the large structures, that mainly produce the turbulent energy, have a behavior that depends on the geometry of the problem.

The idea of the LES approach is to use a spatial filtering, where the large scales are solved down to a given scale. The smaller scales (down to the Kolmogorov scale) are modeled by a sub-grid scale model. Indeed, these scales are responsible for the prohibitive cost of the DNS approach. Modeling them allows to significantly reduce the computational cost of the simulation compared to DNS. LES approach still enables to recover the unsteady behavior of the turbulent flow and most of the turbulent energy. The mesh size is proportional to Re_T^2 ($Re_T = \frac{k_t l_0}{\nu}$) [39]. In a fan-OGV stage, this leads to almost 10^{11} cells for Reynolds numbers based on the rotor chord length of 10^6.

A significant reduction of the computational cost is thus allowed by this method compared to DNS. However, LES approach is still quite expensive for industrial applications. One method to further reduce the computational cost is to use a wall law for the boundary layers close to the walls. This method is known as "Wall-Modeled LES" (WM-LES). It consists in imposing the values of the velocity and velocity gradients on the wall surface through a model. The first mesh cell near the surface is usually set in the logarithmic layer instead of the inner viscous layer, thus avoiding to solve the full boundary layer. Even though this method yields drastic reduction in the mesh density, it adds a source of inaccuracy to the simulation, since important flow mechanisms are modeled. This approach was shown to provide good results when compared to experimental data, in the case of compressors [268], turbines [269, 270, 267] and fan stages [143, 213, 184, 122].

Hybrid RANS-LES approaches

In hybrid approaches, RANS is used to model the flow near the walls, whereas LES is used otherwise. Several hybrid approaches have been developed, such as the so-called Detached Eddy Simulation (DES) [13, 253], which models the flow near the walls with a RANS approach, as far as the flow remains attached to the solid wall. The remaining part of the computational domain is treated with a LES approach. A similar approach has been used by Bonneau *et al.* [15] in the context of a fan-OGV stage.

1.4.3 Large Eddy Simulation

In the present work, the large eddy simulation (LES) approach is adopted to solve both the turbulent flow and the acoustic field inside the fan stage. This section presents the main principles of LES, in terms of the resolved equations and the modeling process of the unresolved turbulent eddies, in a more detailed way than in the previous section.

General description

As explained previously, the main principle of LES is to filter the small dissipative turbulent scales from the turbulent flow. The larger turbulent eddies that contain most of the turbulent kinetic energy are solved for. In practice, the Navier-Stokes equations are filtered either using an explicit spatial filtering or by the mesh itself that behaves as an implicit filter. For the different LES performed in this work, the latter filtering approach is used. A mesh grid of local characteristic length d_c of dimension (d_x, d_y, d_z) in the three dimensions (x, y, z),

$$d_c = (d_x d_y d_z)^{1/3}, \tag{1.13}$$

induces cut-off wavenumber of the order of:

$$k_c = \frac{2\pi}{\lambda_c} = \frac{\pi}{d_c} \tag{1.14}$$

where λ_c is the cut-off wavelength.

Consequently, all the turbulent eddies with a wavelength larger than λ_c are resolved. The eddies with smaller wavelengths, referred to as sub-grid scales, are filtered. An illustration of the low-pass filter in the wavenumber domain induced by the mesh is presented in Figure 1.6. For a given mesh, the cut-off wavenumber k_c must ideally be set between the integral length scale and the Taylor microscale. This ensures that k_c lies in the inertial range. The closer k_c is from the Taylor microscale, the more accurate the simulation is expected to be. Chapter 3 presents a parametric study to specify the mesh size as a function of the Taylor microscale.

The LES approach can also be divided into two categories, depending on the way the sub-grid scales are treated.

- Explicit LES, for which an extra term referred to as Sub-Grid Scale (SGS) model is introduced to model the filtered small scales turbulence.

- Implicit LES, which does not rely on SGS models but uses numerical dissipation to account for the effect of small scale turbulence.

For the different LES performed in this work, the LES explicit approach is adopted.
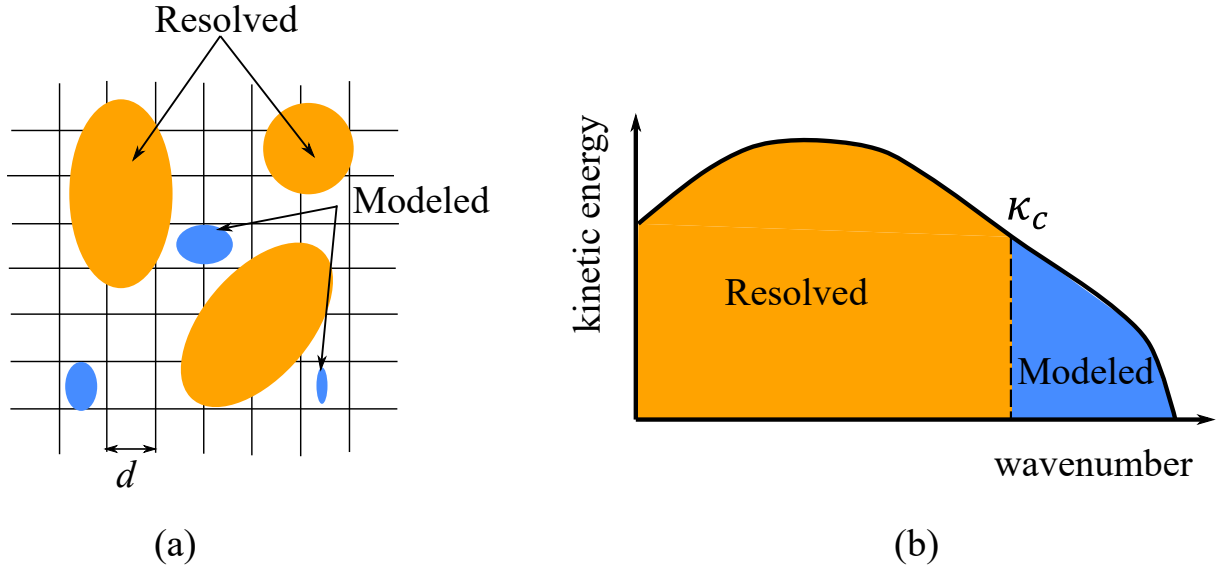
Figure 1.6: Schematic view of the implicit filtering induced by the mesh: grid and theoretical filters are the same, yielding a sharp cutoff filtering in Fourier space between the resolved and sub-grid scales. Adapted from [232].

Filtered Navier-Stokes equations

Any flow quantity ϕ can be split into two parts, a resolved part $\overline{\phi}$ and a modeled part ϕ' so that,

$$\phi = \overline{\phi} + \phi' \tag{1.15}$$

The filtered compressible Navier-Stokes equations are then deduced by resorting to the Favre decomposition as follows,

$$\phi = \tilde{\phi} + \phi'' \tag{1.16}$$

where $\tilde{\phi} = \frac{\overline{\rho\phi}}{\overline{\rho}}$ and $\overline{\rho\phi''} = 0$.

Filtering Navier-Stokes equations, we obtain,

$$\frac{\partial \overline{\rho}}{\partial t} + \frac{\partial}{\partial x_j}(\overline{\rho}\tilde{u}_j) = 0 \tag{1.17}$$

$$\frac{\partial(\overline{\rho}\tilde{u}_i)}{\partial t} + \frac{\partial}{\partial x_j}(\overline{\rho}\tilde{u}_i\tilde{u}_j + \overline{p}\delta_{ij} - \overline{\tau_{ij}} - \tau_{ij}^{SGS}) = 0 \quad i = 1,2,3 \tag{1.18}$$

$$\frac{\partial(\overline{\rho}\tilde{E})}{\partial t} + \frac{\partial}{\partial x_j}(\overline{\rho}\tilde{E}\tilde{u}_j + \overline{p}\tilde{u}_j - \tilde{u}_i\tilde{\tau}_{ij} + \tilde{u}_i\tau_{ij}^{SGS} + \overline{Q_j} + Q_j^{SGS}) = 0 \quad i = 1,2,3 \tag{1.19}$$

where τ_{ij}^{SGS} is the sub-grid scale stress tensor and Q_j^{SGS} the sub-grid scale heat flux. It is here assumed that $\overline{p}$ can be directly computed from $\overline{\rho}$ and $\tilde{E}$ using the ideal gas EoS.

Sub-grid scale model

The non resolved sub-grid scale terms in equations 1.18 and 1.19, need to be modeled in order to solve the Navier-Stokes equations.

The turbulent sub-grid scale stress tensor $\tau_{i,j}{}^{SGS}$ is expressed as,

$$\tau_{i,j}{}^{SGS} = -\overline{\rho}(\widetilde{u_j u_i} - \tilde{u}_i\tilde{u}_j) \tag{1.20}$$

22

Different SGS models have been developed in previous works in the literature. Most of these models use an eddy-viscosity assumption known as the Boussinesq's hypothesis. Thus, the SGS tensor is given as follows,

$$\tau_{i,j}{}^{SGS} = 2\overline{\rho}\nu_t\overline{S_{ij}} \tag{1.21}$$

where $\overline{S_{ij}}$ is the filtered scale strain rate tensor, $\delta_{ij} = 1$ for $i = j$ and 0 otherwise, and ν_t is called the SGS eddy viscosity.

For the different LES performed in this work, three different SGS models are used, the Smagorinsky [250] and dynamic Smagorinsky [165] models, the wall adapting local-eddy viscosity (WALE) model [182], and the SIGMA model [183].

Beginning by the simplest SGS model for LES, the Smagorinsky model has the advantage to be easy to implement, robust, and is often used in conjunction with wall modeling. The expression for the turbulent viscosity ν_t reads,

$$\nu_t = (C_S\Delta)^2\sqrt{2\overline{S_{ij}S_{ij}}} \tag{1.22}$$

where Δ is the filter width (which depends on the mesh size) and C_S is the Smagorinsky coefficient equal to 0.18. Despite its limitations reported in [164], this model is widely used as a SGS closure in LES of turbomachinery flows. Some improvements of this model use a modified value of the coefficient C_S or add artificial and often ad hoc damping functions.

The WALE's model, developed by Nicoud and Ducros [182], aims to capture the significant change of the scale sizes close to walls. The turbulent viscosity is computed in this model as,

$$\nu_t = (C_W\Delta)^2\frac{(s_{ij}^d s_{ij}^d)^{3/2}}{(\overline{S_{ij}S_{ij}})^{5/2}(s_{ij}^d s_{ij}^d)^{5/4}} \tag{1.23}$$

where s_{ij}^d is given by

$$s_{ij}^d = \frac{1}{2}(\widetilde{g}_{i,j}^2 + \widetilde{g}_{j,i}^2) - \frac{1}{3}\widetilde{g_{kk}}^2\delta_{ij}$$

with $\widetilde{g}_{i,j} = \frac{\partial\widetilde{u}}{\partial x_j}$ the filtered velocity gradient, and C_W the model coefficient equal to 0.5.

Finally, the SIGMA model is developed by Nicoud et al. [183] as an improved version of the WALE model. Its operator is based on the singular values (σ_1 , σ_2 , σ_3) of the velocity gradient tensor and ν_t is then given as,

$$\nu_t = C_m\Delta_S D_m(\widetilde{u}) \tag{1.24}$$

where $C_m = 1.35$ is the model constant, Δ_S is the model differential operator that depends on the resolved field $\widetilde{u}$. D_m is given as,

$$D_m = \frac{\sigma_3(\sigma_1 - \sigma_2)(\sigma_2 - \sigma_3)}{\sigma_1^2} \tag{1.25}$$

In addition to the modeling of the unresolved scale effects on the resolved flow field, the SGS operator is desired to fulfill certain universal turbulent flow properties. Based on practical and physical considerations, one can list the following properties [183].

- (**P0**) Positiveness and locality. The operator should be defined locally, which is useful in terms of both implementation in general purpose LES solvers and physical

Table 1.1: Summary of the ability of the three SGS models used in this study to satisfy the desired properties described above

	P0	P1	P2	P3
Smagorinsky	YES	NO	NO	NO
WALE	YES	YES	NO	NO
SIGMA	YES	YES	YES	YES

interpretation of the results. Moreover, it is desirable that the differential operator generates only positive values for stability reasons.

- (**P1**) Cubic behavior near solid boundaries. The turbulence should be damped near walls due to the no-slip boundary condition. Thus, the differential operator should tend to zero in near-wall regions. Additionally, the operator and thus the eddy-viscosity should decay with the third power of the distance to the solid boundary [34].

- (**P2**) Zero for any two-component or two-dimensional flows. The operator and thus the turbulent eddy viscosity should vanish in the case of a flow in solid rotation and in the case of a pure shear.

- (**P3**) Zero for axi-symmetric or isotropic expansion-contraction. The SGS eddy viscosity should be zero in a case for which the resolved scales are either in pure axi-symmetric or isotropic expansion (or contraction).

Satisfying property P0 is always required, whereas property P1 is only essential for wall-resolved LES. Property P1 is less constraining when a wall-law is used since no attempt is made for the SGS model to provide the wall shear stress. Even though, when property P1 is respected, better results near the walls are expected. Table 1.1 summarizes the desired properties that are satisfied by the three SGS models used in this work. The improvements made by the SIGMA model are thus well highlighted compared to the other models.

Numerical tools ———————————————————————— **Summary**

The main numerical simulations approaches are briefly presented. These approaches differ by their level of description of the flow. This can be measured through the way they deal with turbulence.

- Direct Numerical Simulation. This approach resolves all the turbulent scales from the largest turbulent eddies, which are characterized by the integral length scale and produce most of the turbulent energy, to the smallest eddies, which are characterized by the Kolmogorov length scale and dissipate the kinetic energy.

- RANS. This approach is the most widely used approach for flow computations. It solves the averaged fields of the flow solution, in which all the turbulent structures are modeled. The Unsteady RANS approach (URANS) enables

> to take into account additional deterministic phenomena. All the stochastic phenomena related to turbulence remain modeled.
>
> - LES. This approach resolves the large turbulent eddies of the flow and models the non-resolved scales through the use of a sub-grid scale model that reproduces their universal behavior. A non-exhaustive list of sub-grid scale models is presented with their respective assets and drawbacks.

1.5 Noise prediction methods

Several methods are available in the literature to predict the noise generated in a fan/OGV stage. These methods can be classified as follows,

- Analytical and semi-analytical approach. Analytical models informed by LES data are used to estimate the rotor-stator interaction noise and the trailing edge noise mechanisms in the present work.

- Hybrid numerical approaches. This method is particularly used in the present work to separate and compare between the contributions of the different noise mechanisms.

- Direct noise computation. This method is used for the different noise mechanisms studied in the present work.

The rotor-stator interaction noise and the trailing edge noise have been the subject of extensive research studies over the past decades with the aim of developing predictive tools. The other noise sources studied in this work, the laminar separation noise and the tip gap noise, have received less attention in previous studies in the literature, particularly in terms of analytical and semi-analytical modeling. In the following sections, the principles of the acoustic propagation in an annular duct are presented and the different predictive methods are detailed with a particular focus on the rotor-stator interaction and the trailing edge noise mechanisms.

1.5.1 Acoustic propagation in a duct

The predictive tools listed above and presented in the following sections rely on different approaches for acoustic propagation. This is particularly the case for analytical models. Some of them consider radiation in a free-field whereas others consider an in-duct propagation. The present section shows the specific features related to the propagation of acoustic waves in an annular duct with the aim of emphasizing the fundamental differences with free-field propagation conditions.

Additionally, in the present work, the acoustic field upstream of the rotor and downstream of the stator can also be directly predicted by the fully-compressible LES. The acoustic field calculated can thus be projected over the duct modal basis that is defined in this section.

Solution to the Helmholtz equation

All the acoustic potentials $\phi(r, \theta, x)$ should satisfy the Helmholtz convective equation in cylindrical coordinates (r,θ,x). For an axial mean flow of subsonic Mach number M, the Helmholtz equation can be written as,

$$\Delta\phi - \frac{1}{c_0^2}\frac{D^2\phi}{Dt^2} = \frac{\partial^2\phi}{\partial r^2} + \frac{1}{r^2}\frac{\partial^2\phi}{\partial\theta^2} + (1-M^2)\frac{\partial^2\phi}{\partial x^2} + \frac{\partial\phi}{\partial r} + 2ikM\frac{\partial\phi}{\partial x} + k^2\phi, \tag{1.26}$$

where $k = \frac{\omega}{c_0}$, $\frac{D}{Dt} = \frac{\partial}{\partial t} + \mathbf{W}\cdot\nabla$ and $\mathbf{W} = W_x e_x = Mc_0 e_x$ (e_x is the unit vector in the x direction).

This equation should satisfy the radial boundary conditions given as,

$$\frac{\partial\phi}{\partial r} = 0 \quad\text{for}\quad r \in [R_h, R_s],$$

where R_h and R_s are the hub and the shroud radii respectively.

The convective Helmholtz equation can be solved using the Fourier method, which uses a variable separation technique of the solution function. Consequently, this function can be written as,

$$\phi(r, \theta, x) = f(r)g(\theta)h(x)$$

and Eq 1.26 can then be given as,

$$\frac{r^2}{f}\left(\frac{d^2f}{dr^2} + \frac{1}{r}\frac{df}{dr}\right) + \frac{1}{g}\frac{d^2g}{d\theta^2} + r^2\left[(1-M^2)\frac{1}{h}\frac{d^2h}{dx^2} + 2ikM\frac{1}{h}\frac{dh}{dx}\right] + k^2r^2 = 0 \tag{1.27}$$

Eq.1.27 can be written as a sum of three constants equal to three terms only involving the functions f, g and h and their associated variables.

The azimuthal function $g(\theta)$ satisfies the following relation,

$$\frac{1}{g}\frac{d^2g}{d\theta^2} = m^2 \Rightarrow g(\theta) = \alpha e^{im\theta} + \beta e^{-im\theta} \tag{1.28}$$

In an annular duct, a 2π-periodicity condition is satisfied for the angle θ. Thus, the solutions only correspond to discrete values of m ($m \in \mathbb{N}$). A rigid boundary condition should be used at the walls of the blades and vanes. Consequently g should respect the following boundary condition (assuming zero thickness),

$$\frac{dg}{d\theta} = 0, \text{for } \theta = 2\pi/V \tag{1.29}$$

where V is the vanes count. This condition implies an expression for g given as,

$$g(\theta) = A\cos(n_q\theta), \ n_q = qV/2 \tag{1.30}$$

where q is an integer.

The function $h(x)$ is solution of the equation,

$$(1-M^2)\frac{1}{h}\frac{d^2h}{dx^2} + 2ikM\frac{1}{h}\frac{dh}{dx} = -\kappa^2 \tag{1.31}$$

where κ is a constant. When the axial function is written as $h(x) = ae^{ik_x x}$, the character-

istic equation becomes,

$$k_x^2 + 2k\frac{M}{\beta^2}k_x - \frac{\kappa^2}{\beta^2} = 0 \tag{1.32}$$

where $\beta^2 = 1 - M^2$. Eq. 1.32 has the following solutions,

$$k_x^{\pm} = -\frac{Mk}{\beta^2} \pm \sqrt{\frac{\kappa^2}{\beta^2} + \frac{M^2k^2}{\beta^4}}.$$

Thus, the function $h(x)$ can be written as,

$$h(x) = Ce^{ik_x^+ x} + De^{ik_x^- x} \tag{1.33}$$

The radial function is a solution of a Bessel equation,

$$\frac{\mathrm{d}^2 f}{\mathrm{d}r^2} + \frac{1}{r}\frac{\mathrm{d}f}{\mathrm{d}r} + \left(K^2 - \frac{n^2}{r^2}\right)f = 0 \tag{1.34}$$

where $K^2 = k^2 - \kappa^2$. This equation is associated with the following boundary conditions of a rigid walls annular duct,

$$\frac{\mathrm{d}f(r)}{\mathrm{d}r} = 0, r \in [R_h, R_s].$$

The Bessel equation depends on two parameters m and K. The fundamental solutions of this equation are the Bessel functions of order m of first and second kind, respectively noted $J_m(Kr)$ and $Y_m(Kr)$. Each solution $f(r)$ can thus be written as,

$$f(r) = AJ_m(Kr) + BY_m(Kr).$$

The constants A, B and K can be determined using the boundary conditions equation given as,

$$\frac{\mathrm{d}f(r)}{dr} = A'J_m(Kr) + B'Y_m(Kr) = 0, r \in [R_h, R_s]. \tag{1.35}$$

Consequently, the solution only exists for certain discrete values of B/A and K chosen from Eq. 1.35. These values are denoted (m,j) for the azimuthal and radial directions, respectively. Using the Bessel functions, the radial function can be given as,

$$f_{mj}(r) = N_{mj}(cos(\tau_{mj})J_m(K_{mj}r) - sin(\tau_{mj})Y_m(K_{mj}r), \ \ \tau_{mj} = \arctan\left(\frac{J_m'(K_{mj})}{Y_m'(K_{mj})}\right) \tag{1.36}$$

where N_{mj} is the normalization term given as,

$$N_{mj} = \frac{0.5\sqrt{2}\pi K_{mj}}{\left[\frac{1-m^2/K_{mj}^2}{J_m'(K_{mj})^2+Y_m'(K_{mj})^2} - \frac{1-m^2/(K_{mj}\sigma)^2}{J_m'(K_{mj}\sigma)^2+Y_m'(K_{mj}\sigma)^2}\right]^{0.5}}$$

and $\sigma = R_h/R_s$.

For circular ducts $(R_h = 0)$, one of the boundary conditions disappears. However, the function Y_m yields a non-physical solution, since it presents a singularity at $r = 0$. In this case, only the contribution of the Bessel's function of first kind is kept in the expression

of $f(r)$.

Due to the discrete nature of the radial solution $f(r)$, each particular solution of the complete equation $f(r)g(\theta)h(z)$ is subject to the condition $K = K_{mj}$. κ^2 should then take a discrete value, $\kappa_{mj}^2 = k^2 - K_{mj}^2$. Consequently, the axial wavenumbers $k_x^\pm$ can only take discrete values $k_{mj}^\pm$, determined by the angular frequency ω and the eigen values K_{mj}. Thus, the axial wavenumber can be written as,

$$k_{mj}^\pm = \frac{-Mk \pm \overline{k_{mj}^\pm}}{\beta^2}, \quad \overline{k_{mj}^\pm} = \sqrt{k^2 - \beta^2 K_{mj}^2}. \tag{1.37}$$

The general solution of Eq. 1.26 can finally be written as,

$$\phi(r,\theta,x,t) = \sum_{n=-\infty}^{\infty} \sum_{j=0}^{\infty} (A_{mj}^+ e^{\mathrm{i}k_{mj}^+ x} + A_{mj}^- e^{\mathrm{i}k_{mj}^- x}) f_{mj}(r) e^{\mathrm{i}m\theta} e^{-\mathrm{i}\omega t} \tag{1.38}$$

where A_{mj}^+ and A_{mj}^- represent the modal amplitudes of the waves propagating in the same and opposite directions of the flow, respectively.

Indeed, the acoustic field propagating in an annular duct is a combination of eigen modes of the form,

$$f_{mj}(r) e^{\mathrm{i}m\theta} e^{\mathrm{i}k_{mj}^\pm x} e^{-\mathrm{i}\omega t} \tag{1.39}$$

These modes depend on the boundary conditions and are totally determined by the azimuthal and radial indices (m,j).

A mode of order (m,j) is composed of a stationary structure in the radial direction, $f_{mj}(r)$, which is due to successive reflexions on the walls, and a phase term, $e^{\mathrm{i}m\theta} e^{\mathrm{i}k_{nj}^\pm x} e^{-\mathrm{i}\omega t}$, which represents the wave propagation of the mode. For given values of r and x, and for $m \neq 0$, the wave is reduced to a rotating mode. ω/m corresponds to the rotational speed of the mode m to the azimuthal wavenumber and $|m|$ to the number of lobes of the mode.

Mode cut-off condition

Eq. 1.37 reveals that not all the modes can propagate in the duct and that the cut-off angular frequency can be given by,

$$\omega_c = c_0 \beta K_{mj}. \tag{1.40}$$

- If $\omega \geq \omega_c$, the axial wavenumber is real and the corresponding mode is then propagating with no attenuation (since rigid walls are considered). This mode is referred to as cut-on mode.

- If $\omega < \omega_c$, the axial wavenumber $\overline{k_{mj}^\pm}$ is an imaginary number. In this case, the acoustic wave is attenuated with an exponential decay of:

$$\overline{k_{mj}^\pm} = \mathrm{i}\sqrt{\beta^2 K_{mj}^2 - k^2}.$$

The corresponding mode is then classified as being a cut-off mode and is often designated as an "evanescent wave". The attenuation rate of a mode is defined by the imaginary part of the axial wavenumber $k_{mj}^\pm$. Over a distance dx, the attenuation rate τ_{mj} of a mode can be given as,

$$\tau_{mj} = \exp(-1/\beta^2 \sqrt{\beta^2 K_{mj}^2 - k^2} dx). \tag{1.41}$$

28

Consequently, a mode of order (m,j) can only propagate if its frequency is larger than the cut-off frequency $f_c = \omega_c/(2\pi)$. This frequency depends on the hub-to-shroud ratio and the speed of the flow. As the Mach number increases, the cut-off frequency reduces. Thus, the increase of the Mach number allows the propagation of additional modes for the same frequency. The decay of cut-off modes is an important feature of duct acoustics. Indeed, it limits the number of acoustic modes that will propagate from a source to the duct exit, where they can radiate to the far field. This property of the duct has been extensively exploited in the engine design process to cut-off the first modes at the BPF, which has significantly reduced the tonal noise radiated. However, for broadband noise, such noise reduction concepts are not as easily applicable. Therefore, the noise sources have to be directly damped.

1.5.2 Analytical models for RSI noise

For early development stages of new aero-engines, analytical models are usually used to provide closed-form expressions of the sound field. They take the advantage of their low cost. However, this low-cost noise evaluation is at the price of drastic assumptions, which possibly lead to substantial errors. A careful assessment of the modeling techniques should also be made, for instance by comparing the results to dedicated laboratory experiments or to high fidelity numerical simulations.

Several models have been developed to analytically predict the rotor-stator interaction noise mechanism in a fan/OGV stage at approach condition [176, 174]. The noise is generated from the interaction of the turbulent structures (in the rotor wakes or in the background) with the stator vanes cascade. Then, an acoustic analogy is usually used to propagate the noise generated to the far-field. In this section, an overview of the available analytical models is first presented. The general concepts used by the analytical models and the two cascade models adopted in this work are briefly described.

The first type of analytical models focuses on the interaction of a perturbation imping-ing on an isolated airfoil. The general idea of this type of models is to consider an incident gust (harmonic perturbation) normal to the airfoil. The gust is convected until reaching the leading edge of the airfoil, creating an unsteady loading and generating broadband noise. Sears [246] calculated the two-dimensional aerofoil response to parallel sinusoidal gusts in a specific case of incompressible flows. Sears's [246] response function is only valid at low frequency. Filotas [60] extended the analysis of Sears [246] to include skewed sinusoidal gusts in incompressible flows. Amiet [8] developed a compressible response function. Paterson and Amiet [190] extended this theory to take into account trailing-edge back-scattering. Then, Moreau *et al.* [169] and Roger *et al.* [225] extended this theory to three-dimensional aerodynamic gusts with subcritical and supercritical gusts. In these models the airfoil is considered as an infinitely thin flat plate immersed in a uniform in-viscid flow with zero incidence, neglecting camber and mean loading effects. The latter effects were introduced by Myers and Kerschen [178] and Evers and Peake [59].

These models are well adapted for low solidity rotors without external casing, such as helicopter rotors or propellers. However, modern ducted fan-OGV stages, such as UHBR fan stages, display a large number of vanes with substantial overlapping, questioning the isolated vane assumption. In such configurations, the influence of the neighboring vanes on the acoustic propagation, which can be referred to as cascade effect, cannot be neglected.

Another range of models analytically solve the integral equation of the problem to obtain the cascade response through the use of the Wiener-Hopf technique [151, 131,
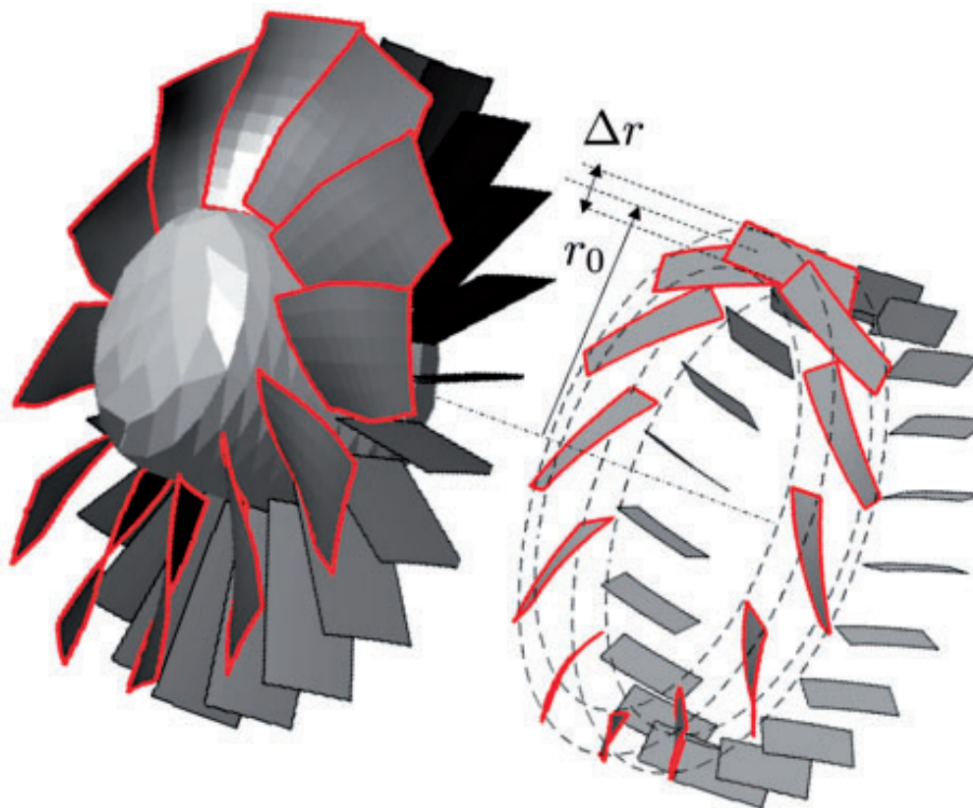
Figure 1.7: Definition of an annular strip of mean radius r_0 for analytical modeling, assuming homogeneous conditions over the span length Δr. Source [176].

191, 69]. The model of Glegg [69] considers a three-dimensional cascade response. This response function does not rely on a direct computation of the acoustic sources on the vanes to obtain the acoustic field outside of the cascade. Hanson and Horan [91] and Hanson [93] extended the model of Glegg [69] by using a new formalism to take into account complex geometry features and spanwise variations of the flow and the blades and vanes geometry through the use of the strip theory (Figure 1.7). Additionally, Posson *et al.* [209, 207] extended the model of Glegg [69] to allow for the computation of the unsteady loading on the vanes. As for the model of Hanson [93], Posson's model [209, 207] also allows to consider complex geometries and spanwise varying flow conditions by using the strip theory. The computed unsteady loading is used as a dipole source in Goldstein's analogy [71]. Posson's model [209, 207] has then been extended to consider swirl effects by Masson *et al.* [153] using the generalized Green's function proposed by Posson and Peake [206] for homentropic flows. Posson's model [209, 207] is also extended by Mathews and Peake [154], who recently developed a Green's function for a more general isentropic flow with a lined duct. More recently, Baddoo *et al.* [10] developed a model that allows to take into account some geometric features of a realistic airfoil, such as the camber and the thickness if they are small enough. They have found that these parameters can have significant impact on the radiated noise of the cascade.

Basics of the analytical models

The basic concepts used in the previously described analytical models are established in [176, 174] and are summarized in the following.
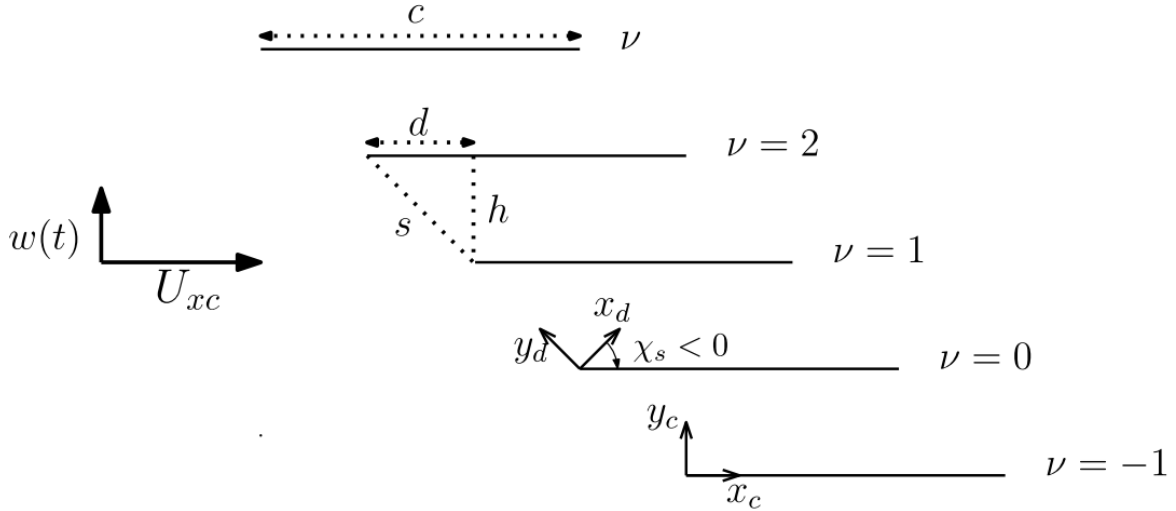
Figure 1.8: Geometric features for an unwrapped strip. ν is the vane number, U_{xc} the incoming axial velocity component and $w(t)$ the impinging gust. Source [51].

- Geometric properties. The duct is considered annular and of infinite length. The rotor blades and stator vanes are modeled as zero thickness flat plates with finite chord and span. The considered fan stage is split into annular strips. In each strip, the geometry is assumed to be homogeneous along the span, so that the aeroacoustic phenomena are locally described in the unwrapped annulus in cartesian coordinates.

  An adequate radial evolution of the equivalent flat plates is considered in a way to match the pitch and spanwise stackings of the real geometry. This allows to conserve the main geometrical parameters of the blade design, such as the stagger, lean and sweep angles. Indeed, these geometric features have significant influence on the fan stage noise [137, 82].

  The other parameters inherent to the cascade, such as the chord length c, the intervane channel height h, the solidity c/s with $s = 2\pi R_m / v$ (R_m is the mean radius and V the vane count), and the non-overlapping area d (as shown is Figure 1.8) are also replicated with this approach.

- Impinging flow. The incoming flow is considered to be homogeneous along the span of each strip. Over each strip, the real incident flow is modeled as a gust convected by a mean flow. The flow is considered in the form of a harmonic perturbation by using time and spatial Fourier transforms. The harmonic amplitude is defined using mean and turbulent characteristics of the flow at the considered radius. These parameters aim to reproduce as closely as possible the actual flow impinging on the stator vanes and generating rotor-stator interaction noise. For that, the radial distribution of mean and turbulent parameters of the flow is typically extracted from CFD computations (or experiments). These parameters are listed in the following.

  - Axial velocity component.
  - Magnitude of the absolute velocity.
  - Wake half-width.
  - Turbulence intensity in the wakes and in the background.
  - Integral length scale in the wakes and in the background.

31

Using these parameters, a turbulent spectrum is computed at each strip to describe the turbulent behavior of the flow.

- Acoustic sources. Some models explicitly compute the cascade response and provide the unsteady loading distribution on the vanes. As discussed earlier, the unsteady loading can either be computed using an isolated airfoil or a cascade response approach that take into account the neighboring vanes.

- Sound radiation. When the unsteady loading is computed, it can be used as an equivalent dipole source distribution in a chosen acoustic analogy to recover the acoustic power upstream and downstream of the studied cascade. For instance, a free-field acoustic analogy is used in the model of Hanson [93], an in-duct analogy in the model of Posson *et al.* [209, 207], and an in-duct with swirling flow in the model of Masson *et al.* [153].

Hanson's model

Hanson's model [93] is based on the cascade model of Glegg [69]. The main features of this model are listed as follows.

- Hanson's model uses the strip theory, in which the geometry is divided into several cylindrical cuts of thickness Δ_r.

- This model is able to consider a realistic impinging flow by taking into account the in-homogeneity and the anisotropy that characterize the flow in the inter-stage.

- This model is able to take into account the specific features of complex blade geometries (variable stagger, sweep and lean angles).

- This model is developed in the cylindrical framework, which allows to consider wavenumbers in the duct coordinate system with the actual number of blades and vanes.

- For each strip, the acoustic power is computed and radiated only within the considered Δ_r strip based on the Glegg's approach [69] and using a free-field acoustic analogy. The contributions of each strip are then summed up incoherently.

Posson's model

Posson's model [209, 207, 208] is based on the cascade model of Glegg [69] and includes the developments made by Hanson's model [93]. The main features of this model are listed as follows.

- Posson's model [209, 207, 208] uses the strip theory. In each strip, a rectilinear cascade of zero-thickness flat plates of infinite span is subjected to a 3D impinging gust.

- This model allows to compute the unsteady pressure jump across the vanes, which can then be considered as an equivalent distribution of dipoles along the vane's surface.

- The vane cascade responses subject to each gust are added up to obtain the noise source distribution corresponding to that of the actual impinging flow.

- These noise sources are then radiated using an in-duct acoustic analogy (Goldstein's analogy [71]).

- The contributions of each strip are then summed up incoherently.

1.5.3 Analytical models for trailing edge noise

The first study of the broadband trailing edge noise is attributed to Powell [210] in 1959. It consists of an experimental study that aimed to develop a semi-empirical model for the trailing edge noise. The power spectral density of the far-field acoustic pressure is proportional to U^α, with $\alpha = 4 - 6$, where U is a characteristic flow velocity magnitude, and to ω^{-3} (ω is the angular frequency) at high frequencies. Other empirical models were also proposed in previous studies in the literature [63, 23]. These models can neither be extended to airfoil configurations nor to radiation angles that are not in the database used to produce the model, which limit their usage.

In the 1970s the first analytical models were proposed in the study of Ffowcs Williams and Hall [276] being followed by Amiet's [7] and Howes's [95] theories among others. In the review of Howe [95], these methods are classified in three main families differing by the way by which the perturbation interacts with the plate's trailing edge and can be summarized as follows.

- Theories based on Lighthill's acoustic analogy [148] in the case of a particular vortex in the vicinity of the trailing edge. We can particularly note the works of Crighton & Leppington [47] and Ffowcs Williams and Hall [276]. In this latter, a non-viscous isentropic flow in a uniform medium is considered. This allows to obtain an evolution of the PSD of the acoustic pressure as U^5.

- Theories based on the resolution of compressible linearized fluid dynamics equations. They aim to link the far-field radiated sound spectrum to hydrodynamic pressure fluctuations measured at or close to the trailing-edge. Chase [35, 36] and Chandiramani [33] decomposed the hydrodynamic pressure fluctuation into several harmonics. The far-field radiated pressure is then obtained using Lighthill's acoustic analogy [148].

  Contrary to previous studies, Amiet [7] proposes a model for a fixed plate in a medium with motion using a strategy similar to the rotor-stator interaction noise model [8].

- Ad hoc models. They suppose an *a priori* distribution of dipoles whose strengths and types are generally determined empirically (Tam & Yu [258]).

Finally, Howe [95] proposed an analytical model synthesizing the previously proposed models mentioned earlier. Howe's model [95] is based on a half-plane Green's function for a source close to the trailing edge and an observer placed in the far-field. All these models produce similar predictions for small Mach numbers and lead to a U^5 scaling law.

These formulations are developed for a semi-infinite flat plate ignoring the leading edge. The given argument for this assumption is that the scattering process is of the order of magnitude of the convected vortical eddies on the trailing edge, which are much smaller than the chord length. Therefore, they are limited to high frequencies. The first attempt to take into account the leading edge scattering effect was introduced by Howe [96]

who proposed a formulation of the Green's function for an arbitrary finite airfoil chord by performing several scattering computations at high frequencies. More recently, the scattering effect was addressed by Roger & Moreau [223] who extended Amiet's theory [7] by adding a leading-edge back-scattering correction and a three-dimensional extension of the original formulation. This was done using a two-step Schwarzschild's procedure [8, 7] and yields a modified chordwise distribution of the acoustic sources. Thus, the directivity is slightly modified with the apparition of secondary lobes. It is equivalent to the formulation of Howe [96] in the case of a vanishing Mach number and can also be used for high speed subsonic flows.

Input data

In the present work, Amiet's model [7] with the back-scattering correction [223] is adopted for the trailing edge noise, using the strip theory. The flow state in the boundary layers at the trailing edge is described using two main parameters, (i) the wall pressure spectrum and (ii) the spanwise correlation length. These parameters can be directly extracted from the LES computation or modeled using empirical and semi-empirical models. In the present work, Goody's [73] and Rozenberg's [228] models are used for the wall pressure spectrum. The different models used for the spanwise correlation length are (i) Corcos's model [44], (ii) Guedel's model [88], (iii) Efimtsov's model [57] and (iv) Salze's model [233]. These models are briefly described in Chapter 3. The input data for these models are recalled in the following.

- Boundary layers thicknesses: boundary layer thickness, displacement thickness and momentum thickness.

- Convection velocity.

- Friction velocity.

- Wall shear stress.

- Adverse pressure gradient.

In the present work, these parameters are extracted from the LES computations at each strip radius. The wall pressure spectrum and the spanwise correlation length can then be estimated by the previously mentioned empirical models and compared to direct predictions from the LES.

1.5.4 LES-informed analytical models

This method couples a CFD computation, a LES in the present work, with one of the analytical models described earlier. The CFD computation is used to obtain the flow parameters that characterize the properties of the impinging flow upstream of the vanes and the boundary layers close to the trailing edge to feed the analytical models. Some of these models, such as Amiet's [8, 7] and Posson's [209, 207] models, use the CFD data to compute the unsteady loading on the surfaces. This loading is then considered as an equivalent dipole source distribution in an acoustic analogy in order to compute the associated radiated noise [213, 146].

1.5.5 Hybrid numerical approach

Hybrid numerical approaches are based on a two-step process that separates the computation of the acoustic sources from the noise propagation. It couples a fully compressible CFD simulation, a LES in the present work, with an acoustic analogy, such as the Ffowcs Williams and Hawkings [277] analogy. The flow simulation is used to compute the acoustic sources on a control surface. In the case of thin airfoil noise, the noise radiated is mostly of dipolar nature and is related to the unsteady loading on the surfaces of the blades and vanes. The loading is then used in the acoustic analogy to compute the acoustic far field. The main drawback of such approaches is that the Green's function is only known for canonical cases (free-field, uniform flow, annular cylindrical ducts, with possible but complex extensions to slowly varying ducts, lined ducts, mean swirl flows). Consequently, some specific flow features are ineluctably neglected, as in the case of sheared flows for example. This can impact the accuracy of the method. Moreover, such an approach only consider dipolar sources, is only a valid assumption at low Mach numbers.

Acoustic analogy - Lighthill's equation

The concept of an acoustic analogy is to rewrite the full equations of fluid dynamics (presented in Section 1.4.1) as an equivalent wave equation in a homogeneous medium at rest or in uniform motion. The methodology is first introduced by Lighthill [147, 148] and aims to apply the standard Green's function technique to derive approximate solutions.

Starting from the gas dynamics equations and performing some mathematical manipulations, the Lighthill's equation [147, 148] can be given as,

$$\frac{\partial^2 \rho}{\partial t^2} - c_0^2 \frac{\partial^2 \rho}{\partial x_i \partial x_i} = \frac{\partial^2 T_{ij}}{\partial x_i \partial x_j}, \tag{1.42}$$

where $T_{ij} = \rho u_i u_j + (p - c_0^2 \rho)\delta_{ij} - \tau_{ij}$ is the so-called Lighthill's stress tensor. When applied to a pure acoustic problem, all the right-hand side terms in Eq.1.42 can be neglected at large distances from the flow (according to reasonable assumptions related to the propagation of acoustic waves, such as the assumption of small-amplitude acoustic waves, isentropic motion, etc.). Consequently, Eq.1.42 reduces to a homogeneous wave equation.

The double divergence of the Lighthill's stress tensor T_{ij} appears as the source term in Eq. 1.42. Lighthill's equation is exact and accounts for all the aeroacoustic processes, including (i) the sound generation by the flow non-homogeneities, (ii) the sound propagation through the flow and (iii) the sound dissipation by viscosity or heat conduction.

This equation can not be solved explicitly since the right-hand side term contains the acoustic field to be determined. To overcome this difficulty, several assumptions are applied and summarized in the following.

- At large Reynolds numbers, viscous effects are much smaller than inertial effects so that the viscous stress tensor τ_{ij} can be neglected when compared to the Reynolds stresses $\rho u_i u_j$.

- For non-reactive flows at large Reynolds numbers and low Mach numbers, the thermal effects $p - c_0^2 \rho$ can also be neglected when compared to the Reynolds stresses $\rho u_i u_j$.

- At low fluctuating Mach numbers, the vortical flow develops as nearly incompressible

and T_{ij} finally reduces to $T_{ij} = \rho_0 U_i U_j$, **U** being the velocity field without its acoustic part.

Using these assumptions, Lighthill's equation indicates that non-linear aerodynamic interactions induce density fluctuations at low order of magnitude, which propagate as sound. This equation becomes explicit and possible to solve using the standard Green's function technique.

Ffowcs Williams & Hawkings acoustic analogy

The Lighthill's analogy is well adapted for modeling the noise radiated by free-field turbulence (e.g. jet mixing noise). However, it does not directly address the question of physical boundaries. A convenient way to overcome this limitation is to replace the surfaces by additional equivalent sources supposed to radiate in free field. This method is an extension of the Lighthill's analogy [147, 148] to account for fixed solid boundaries, and moving boundaries with mean axial flow. This approach is first introduced by Curle [48] and Ffowcs Williams & Hawkings [277].

Starting from the equations of gas dynamics and using a rigid wall boundary condition (no-crossing flow boundary condition) on the surface, a formal procedure can be used to derive an equation for the fluctuating density ρ', given as,

$$\frac{\partial^2 \rho'}{\partial t^2} - c_0^2 \frac{\partial^2 \rho'}{\partial x_i \partial x_i} = \frac{\partial^2 T_{ij}}{\partial x_i \partial x_j} + \frac{\partial}{\partial x_i}\left(\sigma'_{ij}\delta(f)\frac{\partial f}{\partial x_j}\right) + \frac{\partial}{\partial t}\left(\rho_0 V_{S_i}\delta(f)\frac{\partial f}{\partial x_i}\right) \tag{1.43}$$

where $\sigma'_{ij} = \tau_{ij} - (P - P_0)\delta_{ij}$ is the stress tensor, δ stands for the Dirac delta function, V_{S_i} is the velocity field of a point on the surfaces and $f(\mathbf{x}, t) = 0$ is an equation defining the kinematics of the surfaces.

The right-hand side terms in Eq. 1.43 can be considered as noise sources that generate density fluctuations and can be defined as follows.

- The first term represents noise generation due to a volume distribution of quadrupole sources in a limited area enclosing the sources.

- The second term represents the loading noise, produced by the exertion of a net unsteady force on the fluid, and can be assimilated to a distribution of dipole noise sources.

- The last term corresponds to the thickness noise resulting from the unsteady volume displacement effects of the surface. It is equivalent to a surface distribution of monopoles.

Approximations

In order to solve Eq.1.43 using the Green's function technique, some approximations should be considered to simplify the right-hand side terms.

- The Reynolds number of the flow is relatively large and the characteristic Mach number of the fluctuating part of the flow is relatively small.

- When computing the noise sources, the pressure fluctuations due to the flow inhomogeneities are much larger than the acoustic pressure fluctuations. Consequently,

the second term at the right-hand side of Eq.1.43 reduces to only the blade loading forces (lift and drag). This term can thus be determined by unsteady CFD simulations (a LES in the present work).

- The third term at the right-hand side of Eq.1.43 does not require any approximation, since it is completely defined by the kinematics of the surfaces, assumed to be known.

Using these assumptions, the right-hand side of Eq. 1.43 becomes independent of the desired density field and the equation can be solved using the Green's function technique.

In the specific case of subsonic fan configurations, which is the case of the computations in the present work, the quadrupole (first term) and monopole (last term) sources can both be neglected since the Mach number does not exceed 0.5 at approach conditions [277, 71].

Using all these approximations, the solution of Eq.1.43 can be given as,

$$\rho'(\mathbf{x}, t) = \frac{1}{c_0^2} \int_{-T}^{T} \int_{S_b(\tau)} F_i \frac{\partial G(\mathbf{x}, t | \mathbf{y}, \tau)}{\partial y_i} dS(\mathbf{y}) d\tau \tag{1.44}$$

where S_b is the surfaces of the blades and vanes, $\mathbf{x} = (x_1, x_2, x_3)$ and $\mathbf{y} = (y_1, y_2, y_3)$ are the observer and source coordinates respectively, t and τ are the observer time and source time respectively, $\mathbf{F}$ is the force loading on the surfaces, and G is the Green's function.

The Green's function in the free-field for a moving medium can be given as,

$$G(\mathbf{x}, t | \mathbf{y}, \tau) = \frac{\delta(\tau - t + R_e/c_0)}{4\pi R_s}, \tag{1.45}$$

where

$$R_s^2 = (x_1 - y_1)^2 + \beta^2 \left[(x_2 - y_2)^2 + (x_3 - y_3)^2 \right] \;\; ; \;\; \beta^2 = 1 - M^2$$

$$R_e = \frac{1}{\beta^2} [R_s - M(x_1 - y_1)] \;\; ; \;\; M = U/c_0.$$

1.5.6 Direct noise computation

The direct noise computation approach requires to perform an unsteady simulation, an LES in the present work, to compute both (i) the turbulent flow near the fan blades and OGVs and (ii) the acoustic field in the fan stage. Fan stage broadband noise is generated due to the interaction of turbulent flows with solid walls. Consequently, the unsteady simulation should be able to capture the inherent stochastic nature of turbulence and its modeling must be as limited as possible. Thus, unsteady statistical approaches, such as URANS, can not be used for broadband noise predictions since turbulence is entirely modeled. Such approaches can only be used for the prediction of tonal noise sources, since the deterministic sources can be captured.

A higher fidelity numerical approach should be adopted for broadband noise predictions, such as DNS and LES. Due to its high computational cost, direct noise computation using a DNS approach is limited to cases at low to moderate Reynolds numbers (i.e. channel flows [126], low-pressure turbines with limited span [285, 162, 280, 161, 236] , and compressor and fan blades [173, 283]. As an alternative, the LES approach seems to be better adapted for direct noise computation, thanks to the significant increase of computational resources. The variety of LES approaches (wall-resolved LES, wall-modeled LES, hybrid RANS/LES) makes it a more versatile tool than DNS that can be applied to a wider range of flow configurations for direct noise computation.

One main difficulty for direct noise computation using LES is to properly propagate the acoustic waves up to a certain distance in the fan stage, particularly at the high frequencies of interest. Indeed, at subsonic Mach numbers, the magnitude disparity between hydrodynamic and acoustic disturbances is significantly large. Only a very small fraction of the flow energy effectively radiates into the far-field [46]. The numerically captured acoustic waves are then prone to numerical errors. The accuracy of the numerical setup, particularly the properties of the numerical scheme, the mesh type and the boundary conditions, appear as a stringent requirement for direct noise computation. Additionally, artificial dissipation is generally used in the LES approaches for stability purposes. If the rate of artificial dissipation is relatively large, acoustic waves may be significantly damped due to their low magnitude and propagative nature.

Consequently, to correctly transport the acoustic waves without damping and distortion, (i) high-order discretization schemes with suitable dissipation and dispersion properties, (ii) a well refined mesh and (iii) low artificial dissipation rates are required. Since the numerical requirements for the LES setup are not well documented in previous works in the literature, a parametric study is carried out in Chapter 3 to define best practices for the choice of LES parameters to properly predict the fan stage broadband noise mechanisms using a direct noise computation approach.

Noise prediction methods ——————————————— Summary

In this section, the main available approaches for the prediction of fan stage broadband noise are presented:

- LES-informed analytical models.

- Hybrid numerical methods.

- Direct noise computation.

The duct modes and the duct cut-off conditions are first introduced. The available analytical models for the two broadband noise mechanisms, the rotor-stator interaction noise and the trailing edge noise, are briefly described, with an emphasis on the models used in the following chapters. The concept of acoustic analogy is also presented, with a particular focus on the Ffowcs Williams & Hawkings [277] analogy. This analogy computes the noise propagation in the free-field for an axial flow. It is used in Chapters 5 and 6 to separate the contributions of different noise mechanisms.

Analytical models

An overview of the available analytical models for the RSI noise and the TE noise is briefly presented. A particular interest is focused on the models used in Chapter 6, the models of Hanson [93] and Posson [209, 207, 208] for the RSI noise, and the model of Amiet [7, 223] for the TE noise.

For the different models, the fan stage is split into annular strips. In each strip, the geometry and the incoming flow are assumed homogeneous along the span. The models consider the blades and vanes as a cascade of flat plates and compute the

blade or vane response induced by an incident flow in a radial strip. The surface response is then used as an equivalent dipole source in an acoustic analogy. The Hanson's and Posson's models mainly differ by the noise propagation step (free-field for Hanson's model and in-duct propagation for Posson's model).

Hybrid numerical approach

For hybrid numerical approaches, the computation of aerodynamic sources and the noise propagation step are decoupled. In the following chapters, this approach is based on the coupling between a scale resolving simulation (LES) and the acoustic analogy of Ffowcs Williams & Hawkings [277]. It is mainly used to separate the contributions of different noise mechanisms in the fan stage.

Direct noise computation

For direct noise computation approaches, the aerodynamic sources as well as the acoustic field in the fan stage are computed. The specific constraints of such approaches, in terms of numerical scheme, artificial dissipation, grid type and mesh refinements are highlighted.

1.6 Conclusions

This chapter introduces the main concepts required to perform broadband noise predictions in a fan/OGV stage.

1.6.1 Fan noise mechanisms

Several tonal and broadband noise mechanisms encountered in a fan stage are first briefly described. The different noise mechanisms studied in the following Chapters are highlighted.

- Rotor-stator interaction noise, which is generated by the interaction of the rotor wakes with the stator vanes. This noise mechanism is studied for flat plate configurations in Chapter 3 and for an UHBR fan stage configuration in Chapter 6.

- Trailing edge noise, which is generated by the diffraction of turbulent boundary layers when passing the trailing edge of the blades and the vanes. This noise mechanism is studied for flat plate configurations in Chapter 3 and for an UHBR fan stage in Chapter 6.

- Separation noise, which is generated due to pressure and velocity fluctuations in a recirculation bubble close to the leading edge of the rotor blade at partial regimes. This noise mechanism is studied in Chapter 4 on a radial slice of an UHBR fan stage.

- Tip gap noise, which is generated by the interactions of the tip flow vortices, mainly the tip leakage vortex, with the rotor blades. This noise mechanism is studied in Chapter 5 on an UHBR fan stage configuration.

The multiple numerical simulation approaches, from statistical methods to fully turbulent resolving methods, are also described and compared in terms of accuracy and computational costs.

1.6.2 Prediction methods

Different noise prediction techniques used in the following chapters are presented and briefly summarized in the following.

- LES-informed analytical models. These methods have the advantage to provide fast noise estimates. This allows us to carry out reasonably accurate noise pre-design or optimization studies in an industrial context. In the present work, the analytical models are fed with LES data. Different models for RSI and TE noise predictions are briefly described, with an emphasis on the models adopted in the following Chapters of this work.

- Hybrid numerical methods. These methods decouple the computation of the aerodynamic field, which contains the acoustic sources, and the acoustic propagation. The aerodynamic field is obtained using a LES and the acoustic propagation is computed using the Ffowcs Williams & Hawkings [277] analogy. This method is used to separate between the contributions of different noise mechanisms encountered in the fan stage and compare them to the total far-field noise.

- Direct noise prediction. This approach is based on a fully unsteady simulation (a LES) that resolves both the turbulent flow around the blades and the vanes and the acoustic waves in the fan stage. It relies on much less modeling than the analytical models and the hybrid numerical approaches. This makes it the most precise tool to investigate the flow mechanisms responsible for the acoustic field. It also allows to assess the validity of the hypotheses made in the analytical models. Nevertheless, it requires the use of a specific numerical setup and important computational resources, which have so far limited its use for aeroacoustic studies in turbomachinery applications.

Chapter 2

Configurations and numerical setup

Introduction

The main objective of this PhD thesis is the prediction of fan stage broadband noise using LES and analytical models. To this end, the work has been split into 2 parts or phases.

- Phase 1 corresponds to LES of several flat plate configurations. A parametric study for different LES numerical parameters is performed and LES results are compared with analytical models. Figure 2.1 (a) presents an illustration of the computational domain of the flat plate configuration.
  The objective of these LES simulations is to define the proper numerical LES setup for an appropriate description of the flow topology and a direct noise prediction in a fan/OGV stage without making any assumptions for the noise propagation.

- Phase 2 corresponds to LES and RANS computations of the ECL5 fan stage, which has been designed at École Centrale de Lyon. Figure 2.1 (b) presents the fan stage of the ECL5 configurations.
  The main objectives of these LES simulations are the following.

  - Investigation of the flow topology and noise mechanisms of the ECL5 fan stage at approach condition.

  - Direct prediction of the acoustic levels from the fan stage, using a well-refined mesh, which is based on the results from phase 1.

  - Assessment of numerically-informed analytical models by comparing the direct LES acoustic results with the results of the models.

The objective of this chapter is to facilitate the reading of the manuscript by gathering all mesh related information of the different configurations considered in the following chapters. This chapter also presents a summary of the configurations on which the simulations and noise predictions in the following chapters have been performed. The geometry and operating conditions of each configuration of the two phases are described. Additionally, the numerical setups are presented, including the computational domain, numerical parameters (CFD solver, numerical schemes, boundary conditions) and the mesh parameters. Finally, the mesh quality for the different cases of phase 2 is analyzed.

Contents

2.1   Phase 1: flat-plate configurations

The simulations of the flat plate were performed at a freestream velocity of $U_0 = 100\,\mathrm{m/s}$, and atmospheric conditions ($\rho_0 = 1.177\,\mathrm{kg/m^3}$, $T_{t0} = 300\,\mathrm{K}$, $\mu_0 = 1.81\,10^5\,\mathrm{kg\,m^{-1}s^{-1}}$).

In this phase, two cases are investigated; case 1 is dedicated to the study of the turbulence interaction noise, which is also called Leading Edge (LE) noise from a flat plate interacting with an oncoming turbulent flow, and case 2 focuses on the study of Trailing Edge (TE) noise from a flat plate with a sharp TE.

For both cases, the unsteady three-dimensional flow around the plate is computed with the LES approach using the AVBP compressible solver developed by CERFACS [245]. The SIGMA SGS model [183] is adopted with the Two steps Taylor Galerkin TTGC scheme [43], which is a third-order convective numerical scheme in space and time. The Jameson's artificial viscosity sensor is adopted.

2.1.1   Case 1: leading edge noise

In this section, the numerical setup for the simulations of case 1, dedicated to the study of LE noise, is presented. Furthermore, the different mesh resolutions are described.
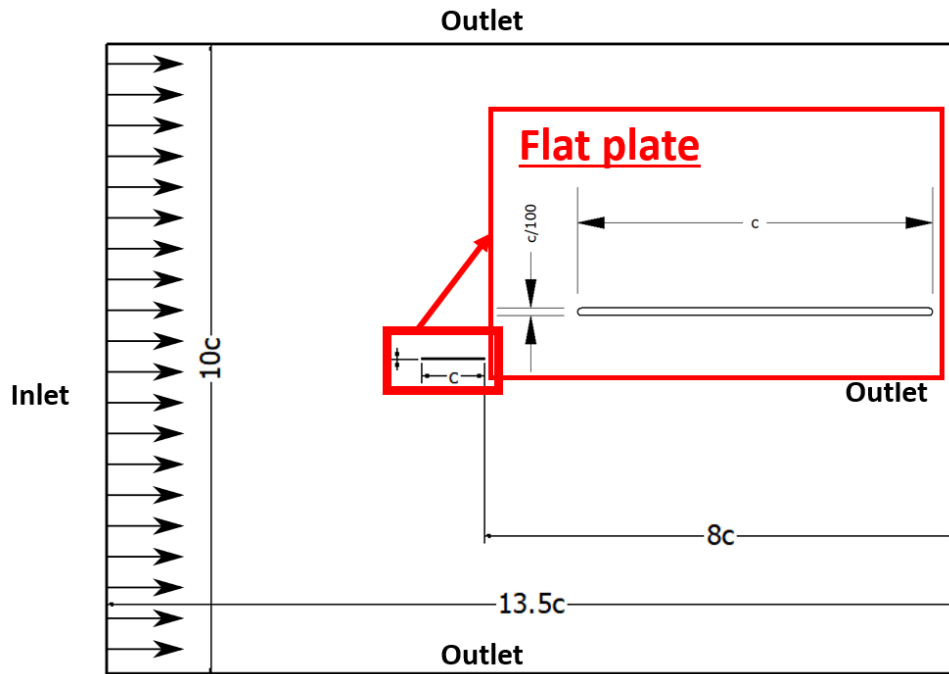
(a)
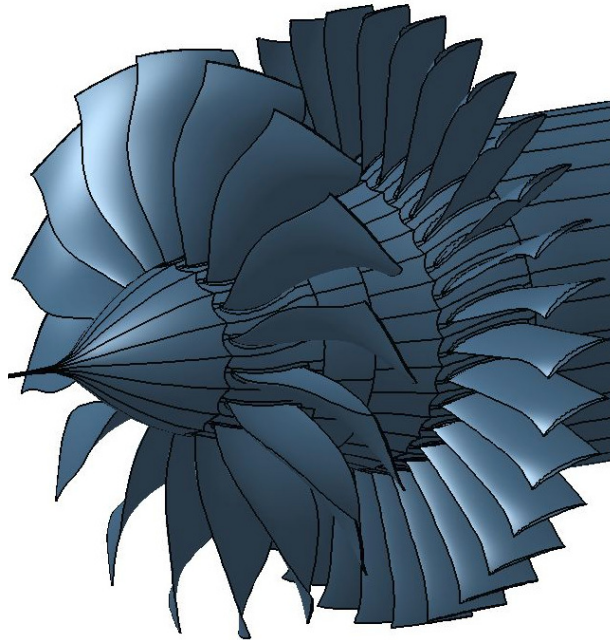
(b)

Figure 2.1: Illustration of the (a) Phase 1 and (b) Phase 2 configurations.

(a)

(b)
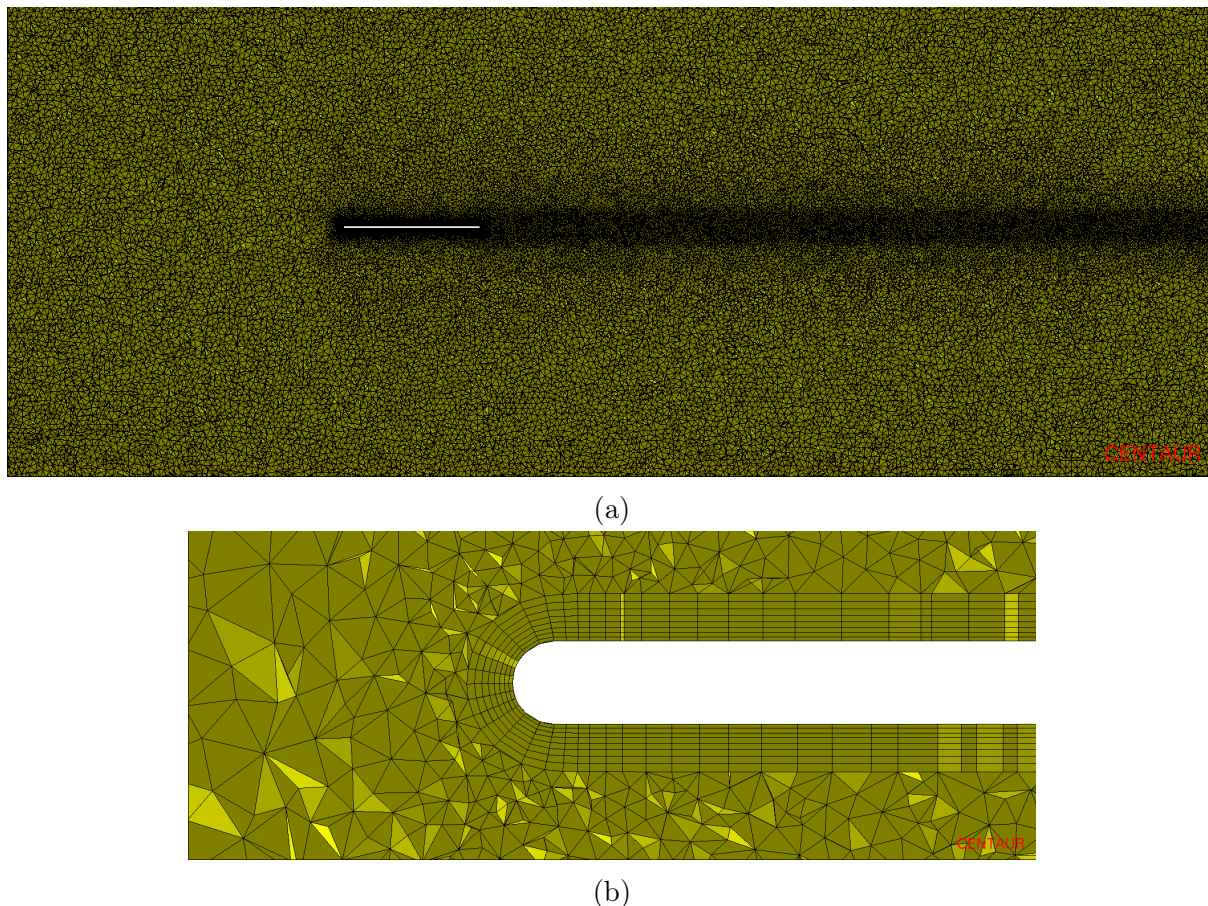
Figure 2.2: (a) Mesh view for MESH1. (b) Mesh refinement close to the leading edge.

Configuration

The computational domain size extends $20c$ in the x-direction (streamwise direction) and $25c$ in the y-direction (normal direction), where c stands for the chord length. The spanwise extension is 10% of the chord length, which represents about five times the displacement thickness of the boundary layer at the TE. The chord length is set to $c = 0.1\,\mathrm{m}$ and the plate thickness is $e = c/100$. The Reynolds number based on the chord length is $Re_c = 10^6$.

Mesh description

Five different meshes are considered, which are composed of prismatic cells around the plate surface, tetrahedral cells away from the walls, and pyramidal cells in the transition between prismatic and tetrahedral cells. A mesh representation at mid-span is presented in Figure 2.2. At the plate surface, 8 layers of prismatic cells have been imposed. The wall-normal spacing is the smallest for the first layer near the wall and increases progressively with a geometric ratio of 1.1. The properties of the different meshes are presented in Chapter 3. For all the cases, a wall model is imposed, with a mean value of the non-dimensional wall normal cell-size, y^+, over the flat plate surface of 25 [266]. Since only the leading edge noise is studied in this case, it is not necessary to increase the resolution of the boundary layers on the flat plate surface. Upstream of the flat plate, the mesh is sufficiently refined to convect the oncoming turbulence from the inlet to the leading edge.

Boundary conditions

The boundary conditions used in the present simulations are presented below.

- Inlet boundary condition. A Navier Stokes Characteristic Boundary Condition (NSCBC) [202] is specified at the inlet section. Synthetic turbulence is injected based on a spectral approach. The mean flow speed is $U_0 = 100\,\mathrm{m/s}$. Upstream of the LE (at $0.02c$ from the LE), the turbulence spectrum can be fitted by a Von-Karman spectrum with a turbulent intensity of $4\,\%$ and an integral length scale of $5\,\mathrm{mm}$. Thus, the integral length scale corresponds to 5% of the chord length, which is considered to be representative of the turbulence length scales in the fan/OGV interstage. The cut-off wavelength is equal to two times the largest cell size according to Shannon's principle. The number of Fourier modes that compose the random velocity perturbation is 50.

- Outlet boundary condition. A NSCBC boundary condition is specified at the outlet section. An adequate relaxation factor, as described in Ref. [149], is set to limit acoustic wave reflections that may be generated due to the presence of turbulent structures in the wake of the plate at the outlet section. A static target pressure of $101325\,\mathrm{Pa}$ has also been set at the outlet section.

- Spanwise boundary condition. Periodic boundary conditions are applied at the boundaries in the spanwise direction.

- Wall boundary condition. A no-slip boundary condition is used on the plate surface. A wall model is used, with a dimensionless wall velocity $u^+ = \frac{1}{\kappa}\ln(Ay^+)$ for $y^+ > 11.45$ with $\kappa = 0.41$ and $A = 9.2$.

Estimation of the computational time

Let us consider an estimation of the computational time as:

$$\mathrm{cost} = \frac{N_{\mathrm{ite}}}{\mathrm{perfo}} \tag{2.1}$$

where "perfo" is the mean efficiency of the cluster for a given total number of cells in the mesh (in other terms, "perfo" is the number of iterations per second for all the processors for a given mesh size) and N_{ite} is the number of required iterations for convergence.

The number of iterations required is the ratio of the physical time by the time step used by the numerical code. The physical time T_{phys} should be taken as the sum of the time $T_{1,\mathrm{phys}}$ needed to ensure convergence and the time $T_{2,\mathrm{phys}}$ required to have a sufficient resolution of the acoustic spectra in the frequency domain, i.e. $T_{\mathrm{phys}} = T_{1,\mathrm{phys}} + T_{2,\mathrm{phys}}$.

$T_{1,\mathrm{phys}}$ is proportional to the residence time, T_{res}, in the domain and can be given by,

$$T_{1,\mathrm{phys}} = \alpha T_{\mathrm{res}} = \alpha \frac{V}{Q} \tag{2.2}$$

where α is a constant taken equal to 5, Q is the volume flow rate and V is the total volume of the domain. Replacing by the numerical values, we obtain $T_{1,\mathrm{phys}} = 0.0675\,\mathrm{s}$.

Let us consider Δf as the target frequency step for the acoustic spectra. The PSD is calculated by averaging the unsteady recordings using M segments. Thus, $T_{2,\mathrm{phys}}$ is given

(a)

(b)   (c)
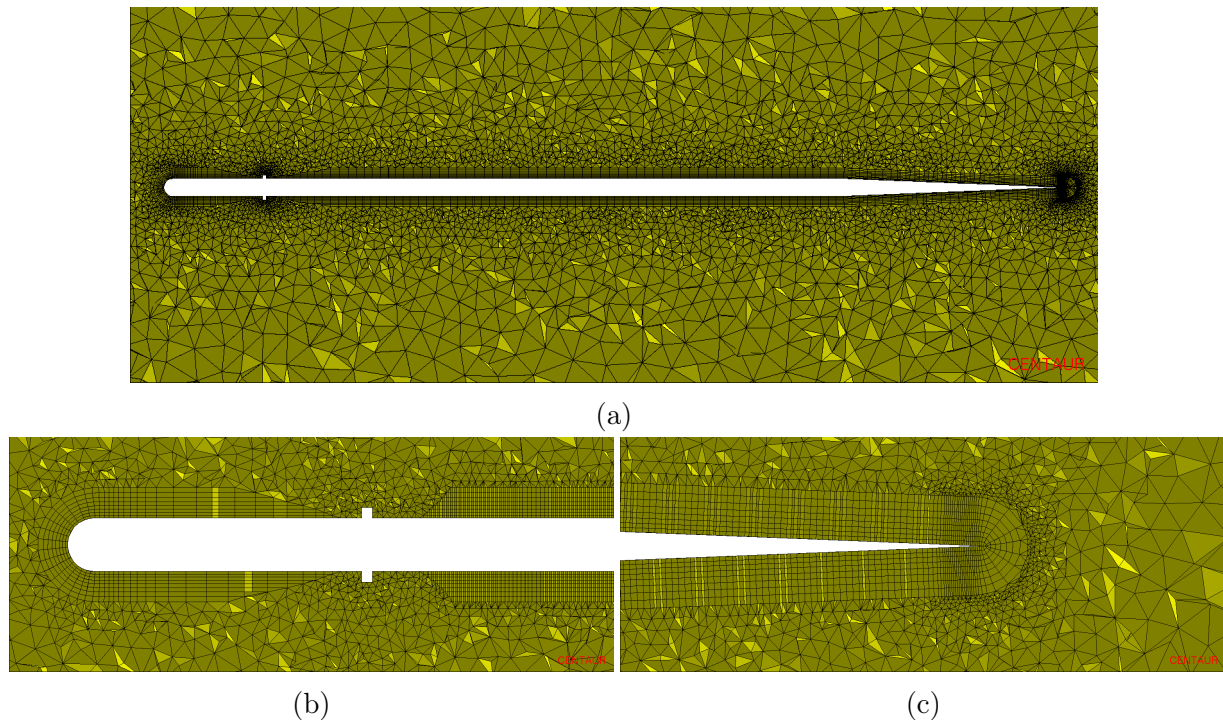
Figure 2.3: (a) Mesh view in the mid-span plane, around the flat plate. Mesh refinements near the LE (b) and the TE (c).

as,

$$T_{2,\text{phys}} = M/\Delta f \tag{2.3}$$

In the following, M will be taken equal to 5 and Δf equal to $40\,\text{Hz}$, so that $T_{2,\text{phys}} = 0.125\,\text{s}$.

The time step Δt of the AVBP LES solver is limited by the propagation of acoustic waves and can be estimated using the CFL criterion as follow:

$$\text{CFL} = \frac{|U_0 + c_0|_{\text{max}}\Delta t}{\Delta x_{\text{min}}} = 0.7 \tag{2.4}$$

where c_0 corresponds to the speed of sound.

2.1.2 Case 2: Trailing edge noise

In this case, the trailing edge of the plate is sharp and a square trip (as shown in Figure 2.3) is used on the flat plate surface to force the transition of the boundary layers to turbulence. Since the trailing edge noise is directly related to the turbulent eddies close to the trailing edge of the flat plate, a good description of the boundary layers is required.

Mesh description

The mesh is mostly composed of unstructured tetrahedral elements and is carefully clustered near the flat plate surface to achieve a good spatial resolution. A mesh representation at mid-span is presented in Figure 2.3. Near the wall, two types of elements are compared, tetrahedral and prismatic. Particularly, 10 layers of prisms are imposed for

46
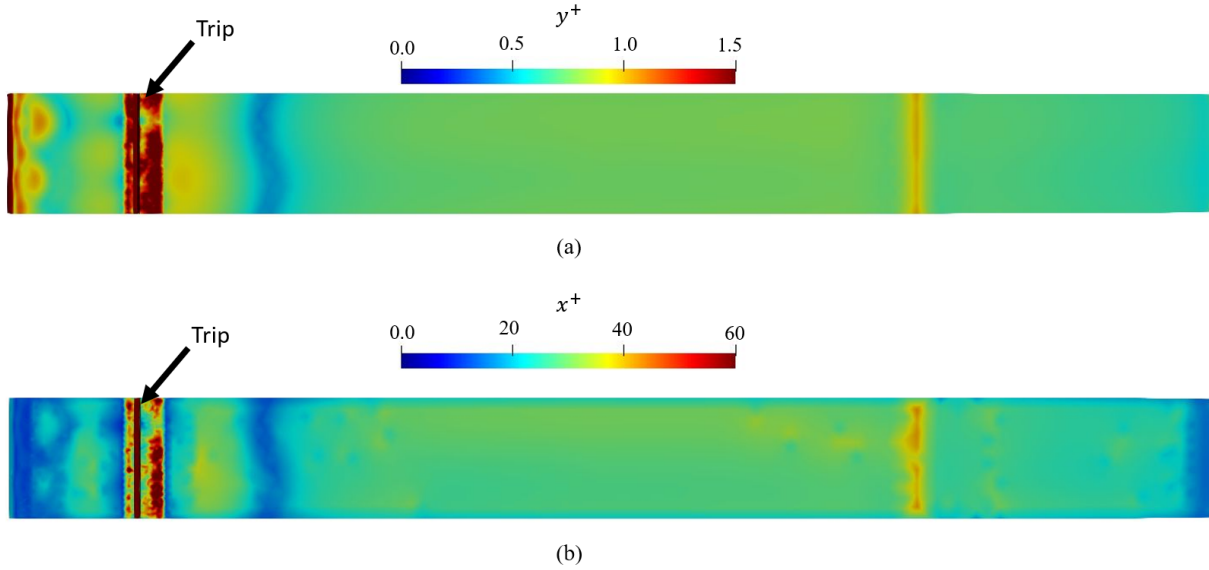
Figure 2.4: y^+ (a) and $x^+ = z^+$ (b) values on the upper surface of the plate for the WR cases of the flat plate using the TE configuration.

Wall-Modeled (WM) cases and 16 layers for Wall-Resolved (WR) cases. The smallest wall normal spacing corresponds to the first layer near the wall. The spacing increases progressively with a geometric ratio of 1.1. In all the cases, a square trip is used and the mesh around the geometric trip is tetrahedral in order to avoid very small cells, which would lead to small timesteps (see Figure 2.3 (b)). For the WR cases, the mean value of y^+ is kept below 1 (except close to the trip and to the leading edge) and the mean values of x^+ and z^+ below 35 (as shown in Figure 2.4). For the WM cases, the mean value of y^+ is kept below 30 and x^+ and z^+ below 150 (as shown in Figure 2.5). The properties of the different meshes used in this study are described in Chapter 3.

Boundary conditions

NSCBC [202] are used at the inlet and outlet planes of the domain, as well as at the upper and lower boundaries. At the inlet section a mean flow speed ($U_0 = 100 \, \text{m/s}$) is imposed. At the outlet section, a static pressure ($P = 101325 \, \text{Pa}$) is specified. An adequate relaxation factor is specified at the inlet and outlet conditions to limit wave reflections from the domain boundaries [149]. A no-slip wall boundary condition is used at the surfaces of the plate. Unless otherwise noted, periodic boundary conditions are used in the spanwise direction.

Phase 1: flat plate configurations ———————— **Summary**

Computational domain

- Flat plate configurations.

- Plate thickness $e = c/100$, where $c = 100 \, \text{mm}$.
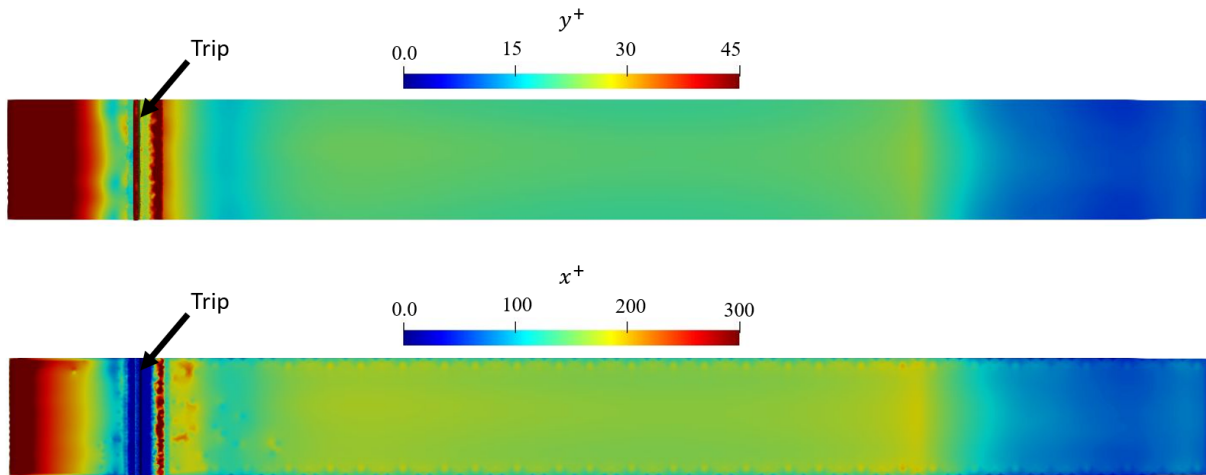
Figure 2.5: y^+ (a) and $x^+ = z^+$ (b) values on the upper surface of the plate for the WM cases of the flat plate using the TE configuration.

- For the TE noise configuration, the TE is sharp and a square trip is added on the surface of the plate close to the LE.

Numerical parameters

- Solver: AVBP (CERFACS).

- LES approach.

- Subgrid-scale model: Sigma.

- Convection scheme: TTGC (third order in time and space).

- Artificial viscosity sensor: Jameson.

- Inlet boundary condition: NSCBC non-reflective. A synthetic turbulence injection is used at the inlet section for LE noise configuration.

- Outlet boundary condition: NSCBC non-reflective.

- Side boundary condition: periodic.

- Solid wall boundary condition: adiabatic walls with no-slip condition.

Meshes

- Hybrid unstructured meshes: prismatic cells on solid surfaces and tetrahedra in the rest of the domain.

- Different mesh refinements.

- Wall-modeled and wall-resolved (for the TE noise configuration) LES.
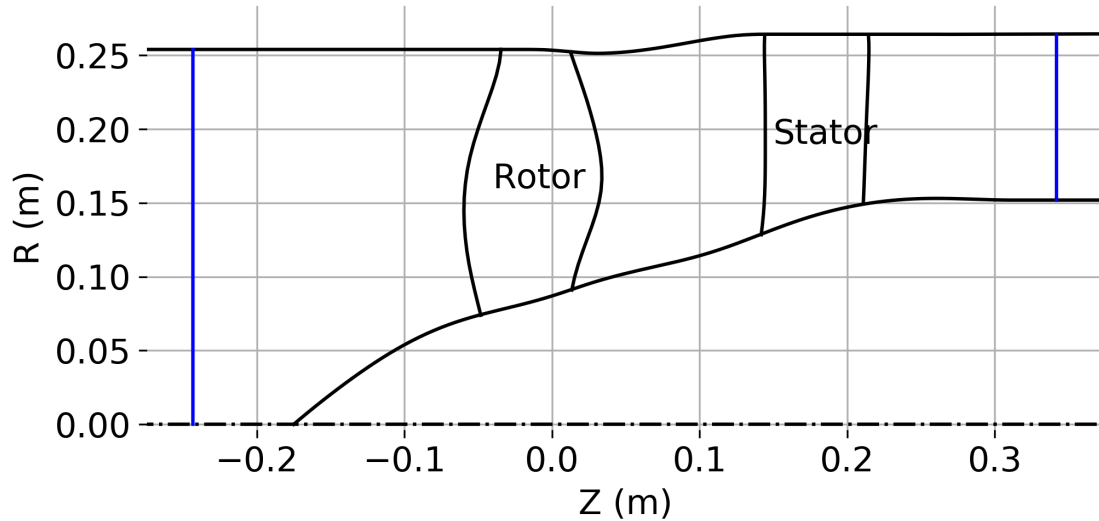
Figure 2.6: Meridian view of the ECL5 fan stage.

2.2 ECL5 configuration

The configuration used in the phase 2 of this PhD thesis is the ECL5 fan/OGV stage, which is an open test-case designed by École Centrale de Lyon that will be tested at the ECL-B3 test rig [22, 187]. The ECL5 is an Ultra High Bypass Ratio (UHBR) low-speed fan stage design, without core flow, which has been designed based on technical requirements for a commercial mid-range aircraft.

2.2.1 Geometric properties

This state-of-the-art fan stage is composed of 16 rotor blades and 31 stator vanes (as shown in Figure 2.1 (b)). It should be noted that this low-count OGV is expected to be cut-on for the blade passing frequency (BPF), which leads to a significant tonal noise contribution. Figure 2.6 shows a cross-section of the ECL5 fan stage and presents the main geometric characteristics. The hub-to-tip ratio at the fan LE position is set to 0.29. The minimum rotor-stator distance is 110 mm (slightly larger than one mid-span rotor chord length), which is expected to minimize potential effects. The hub and shroud radii are respectively $R_H = 72$ mm and $R_S = 250$ mm upstream of the rotor, and $R_H = 150$ mm and $R_S = 252$ mm downstream of the stator. The tip clearance at approach condition is 0.965 mm ($0.011c$) at the LE and 1.27 mm ($0.014c$) at the TE, with a linear evolution from the LE to the TE. To reduce the effect of a relatively large tip clearance on the tip leakage flow, the pressure ratio at the fan blade tip was minimized. The stator vanes are fixed on the hub and shroud without any clearance. The ECL5 fan is highly twisted, which is a direct consequence of the small hub-to-tip ratio. The stagger angle varies from 2° at the hub to -58° at the tip.

The fan airfoil sections for different radial locations are presented in Figure 2.7. The hub corresponds to a spanwise position of 0% and the fan tip to 100%. The design of theses airfoil sections is based on the flow conditions at the design speed. Highly cambered airfoils are located at a spanwise position of 20%. At this position, the flow is subsonic. For airfoils at higher spanwise positions, the camber is reduced. This is due to the flow near
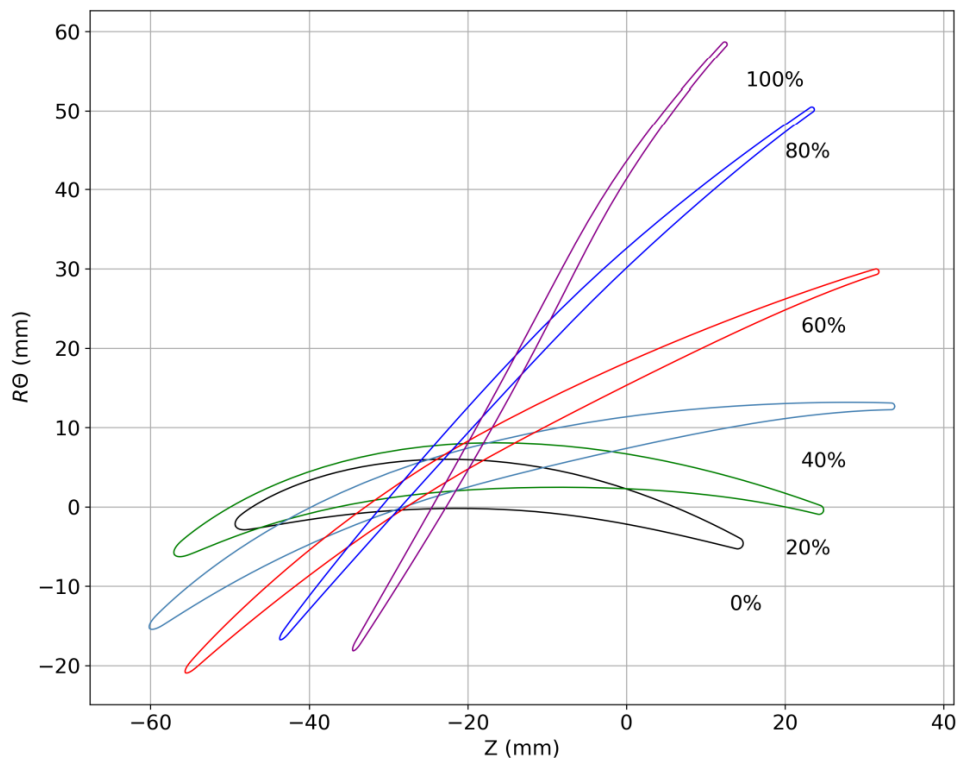
Figure 2.7: Rotor profiles for different heights.

the fan tip, where the flow speed is transonic and the pressure gradient is highly influenced by the presence of shock waves. This affects the design. Particularly, the airfoil at the fan tip (100%) presents a change in the slope of the mean camber line between the LE and the maximum camber position. At the fan tip, the airfoil is relatively flat near the LE and the position of the maximum camber is set to 70% of the chord length. These properties are characteristic for airfoils operating at transonic speeds regimes and are expected to have important effects on the flow topology in the tip gap region.

The main geometric parameters of the rotor blades and stator vanes at four different spanwise positions (root, mid-span, 80%-span and tip) are shown in Table 2.1. The solidity $\psi = c/g$, where $g = 2\pi r/N$ is the blade-to-blade spacing, r is the radius, and N is the number of rotor blades or stator vanes, is larger than 1 at almost all locations. The thickness decreases as a function of the radial location in order to reduce blade deformation due to centrifugal forces and limit the flow acceleration at the tip.

2.2.2 Operating conditions

The nominal rotational speed of the ECL5 fan is $\Omega_n = 11000$ RPM. RANS simulations are performed to study the aerodynamic behavior of the stage at different operating points, including the nominal rotational speed (100%Nn), to a partial regime (80%Nn) and to approach conditions at a low rotational speed (55%Nn). LES are only performed at approach conditions (55%Nn). At this operating point, the rotational speed is $\Omega = 6050$ RPM, which corresponds to an azimuthal Mach number of 0.48 at the blade tip and a blade passing frequency BPF $= 1613$ Hz. The inflow axial Mach number is about 0.3 and the relative Mach number at the blade tip is 0.56. Thus, the fan operates in a fully subsonic regime at approach conditions. The reference mass flow rate is $\dot{m} = 20$ kg/s

Table 2.1: Main geometric parameters at different spanwise positions. κ_s corresponds to the stagger angle, and ψ to the solidity.

	Position	c [mm]	Thickness [% c]	κ_s [°]	ψ
Rotor	Hub	64	4.8	2.0	1.99
	Mid-span	101	1.9	-23	1.54
	80%-span	95	1.2	-45	1.10
	Tip	90	1.0	-58	0.90
Stator	Hub	73	1.9	15	2.68
	Mid-span	69	2.2	12	1.74
	80%-span	70	3.0	12	1.49
	Tip	73	3.3	21	1.40

and the total pressure ratio (defined as the ratio between the outlet total pressure and the inlet total pressure) is 1.1. The Reynolds number based on the rotor mid-span chord length is approximately 10^6.

2.3   Phase 2: ECL5 configuration - RANS setup

In this section, the numerical setup of the RANS computations is described. The steady RANS simulations are performed for a full-span periodic sector of the ECL5 fan stage, as shown in Figure 2.8 (a).

2.3.1   Computational domain and mesh description

A multi-block structured mesh is adopted, with 5.1×10^6 grid points. The mesh is generated using the commercial software *Autogrid V5*, developed by *Numeca International* (called now *Cadence*). The mesh uses an O4H block topology, which is a standard block topology for turbomachinery applications and allows for a mesh refinement in certain regions, such as boundary layers and wakes. The mesh of the computational domain is shown in Figure 2.8. The domain extends from 3.75 fan chord lengths upstream of the fan leading edge to 4.25 vane chord lengths downstream of the OGV. The duct is divided using a mixing plane in the rotor/stator interface, at a constant axial position shown in Figure 2.8 (a).

The near-wall mesh is sufficiently refined to capture boundary layers without using a wall model. The normalized wall-normal distance y^+ varies between 1 and 3 on a large portion of the blade and vane surfaces with a maximum of 4 at the LE, as shown in Figure 2.9. The total cell count in the rotor domain is approximately 3.4 millions, with 131 layers in the radial direction. The fan tip-clearance region is discretized using 31 points in the radial direction to correctly capture the flow features in this region. For the stator domain, 1.8 million cells are used, including 105 layers in the radial direction. The mesh is refined in the rotor wake region, where around 20 points per aerodynamic wavelength (based on the Taylor micro-scale) are used.
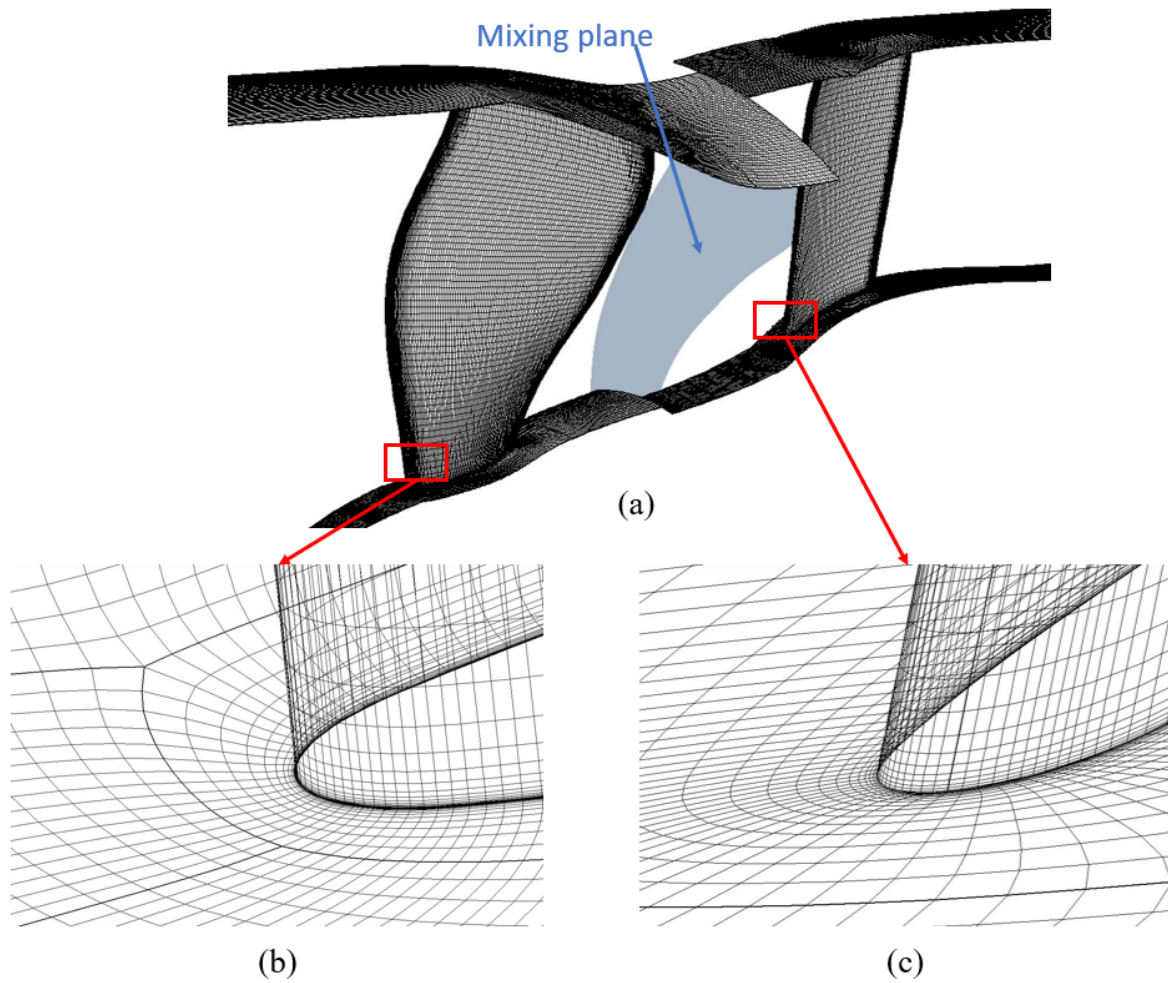
Figure 2.8: Mesh description for the RANS computations. (a) mesh view around the walls of the rotor, the stator, the shroud and the hub. Mesh refinement around the LE of the rotor (b) and the stator (c).
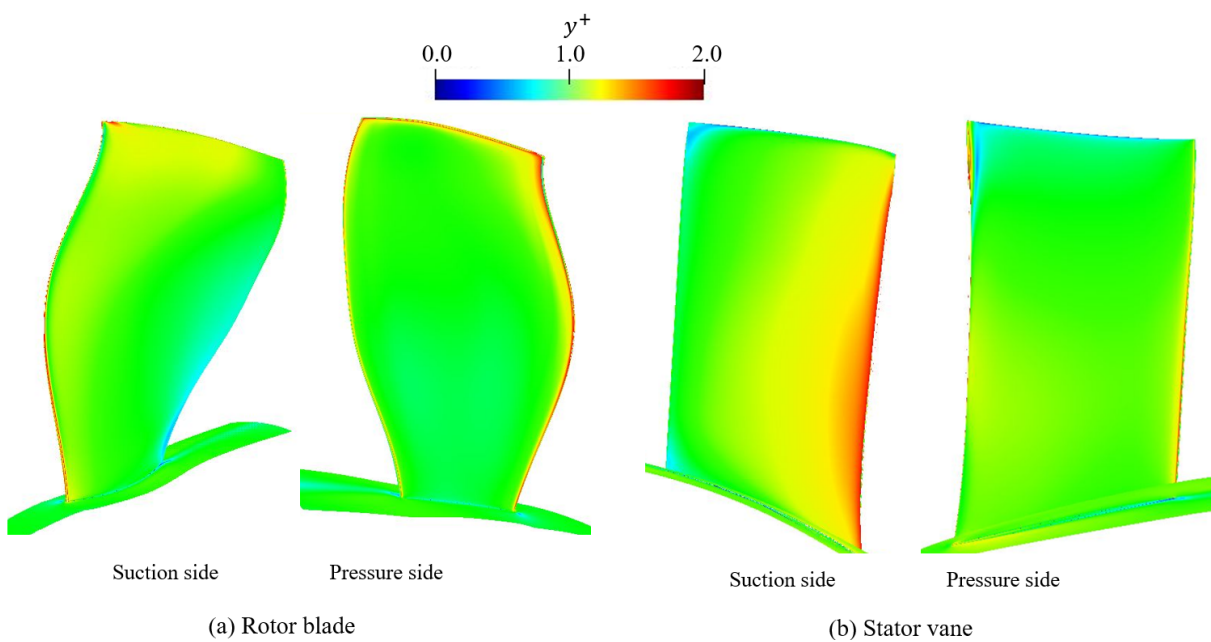
Figure 2.9: y^+ values on the rotor blade (a) and stator vane (b).

52
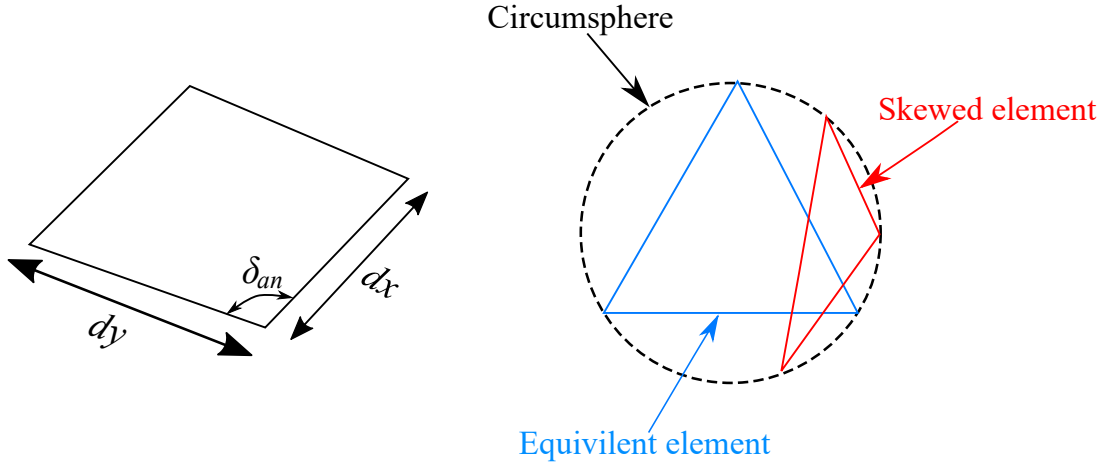
Figure 2.10: Illustration of the grid skewness definition.

2.3.2 Numerical parameters

The RANS simulations are performed using the *FineTurbo* solver developed by *Numeca International*, using a mixing plane between the fan and the OGVs, and the Jameson-Schmidt-Turkel numerical scheme [110]. Menter's $k-\omega$ SST turbulence model is used [157], which provides improved flow predictions in the presence of adverse pressure gradients in comparison to the Wilcox $k-\omega$ model [275]. Similar input flow conditions are used for both the LES and RANS simulations, i.e. standard total flow quantities are imposed at the inlet section (total pressure $P_{t0} = 101325$ Pa, total temperature $T_{t0} = 300$ K) with a uniform turbulent flow (turbulence intensity of $TI = 0.5$ % and a turbulence length scale of $\lambda_t = 0.05$ m). These values of TI and λ_t are based on available hot-wire measurements at the ECL-B3 facility and are expected to be representative of the turbulent flow downstream of a TCS (Turbulence Control Screen) and upstream of the fan LE. On the solid surfaces, a non-slip adiabatic wall boundary condition is used. Finally, periodic boundary conditions are imposed on the lateral surfaces of the computational domain.

2.3.3 Mesh quality

The mesh quality can be studied based on two parameters described below.

- Cell Aspect Ratio (AR): defined as the ratio of the longest edge length to the shortest one of a given cell. In an ideal case, AR is equal to 1 for a square (structured mesh) or an equilateral triangle (tetrahedral cells). Acceptable values of the aspect ratio are in the limit of 100. Large values of AR in the high gradient regions of the flow (like flow separation, recirculation, and reattachment regions) may deteriorate the accuracy of the numerical result and lead to poor convergence. For the RANS mesh, the mean value of the AR is 1.11 and the maximum value is 105 in the blade tip region close to the LE. The percentage of elements with AR> 50 is 0.002% of the total cell count.

- Cell skewness or grid distortion. For structured meshes, the cell skewness evaluates the angle between consecutive grid lines (for exemple, see the angle δ_{an} in Figure 2.10 on the left), where an angle of about 90° is the ideal value. For triangles and

tetrahedral elements, the skewness ($skew$) can be defined as follow,

$$skew = \frac{V_{equi} - V_{ac}}{V_{ac}} \qquad (2.5)$$

where V_{equi} is the volume of an (ideal) equilateral tetrahedron having the same circumsphere of the actual tetrahedron and V_{ac} is the volume of the current tetrahedron (an illustration for a 2D case is shown in Figure 2.10 on the right). A value of skewness equal to 0 indicates a square, or an equilateral cell (ideal case), whereas a value of 1 indicates a very low quality (worst case). The skewness values should be low (ideally below 0.5) for stability reasons. The mean skewness value for the current mesh is 0.15 and the maximum value is 0.92 (in the fan tip region close to the leading edge). The percentage of elements with skewness > 0.85 is 0.01% of the total cell count.

For the RANS simulations, the structures grid indicators are used.

Phase 2: ECL5 configuration - RANS setup ——————————— **Summary**

Computational domain

- ECL5 fan/OGV stage.

- 1 rotor blade -1 stator vane configuration.

Numerical parameters

- Solver: FineTurbo (*Numeca International*).

- Mixing plane approach.

- Turbulence modeling: Menter's $k - \omega$ SST turbulence model.

- Inlet boundary condition: total pressure and temperature with uniform turbulent flow parameters.

- Outlet boundary condition: mass-flow rate is imposed.

- Lateral boundary condition: periodic.

- Wall boundary condition: adiabatic and non-slip wall condition.

Mesh

- Multi-block structured mesh using a O4H block topology is adopted.

- Wall-resolved simulation.

- The adopted mesh quality criteria are in the acceptable range for a reliable simulation (averaged AR = 1.11, maximum AR<105; averaged $skew$ = 0.15, maximum $skew$<0.92).

2.4 Phase 2: ECL5 configuration - LES setup

The geometry used for the present LES is also the ECL5 fan/OGV stage [22, 187]. LES are only performed at approach condition (55%Nn). In this section, the LES numerical setups for the different configurations are presented.

2.4.1 Configurations

Three different configurations are considered as shown in Figure 2.11:

- radial-slice sector LES.

- (full-span) sector LES.

- (full-span) 360° LES.

For the first two cases, a periodic fan/OGV sector is simulated to reduce the computational cost of the LES. The AVBP solver that is used for the LES in this work requires the same angular extent for the rotor and stator domains. Thus, the original 31 vanes configuration is adapted to 32 vanes to allow for a $2\pi/16$ angular periodicity and reduce the size of the computational domain. According to Rai *et al.* [215], the stage performance is kept constant by adjusting the vane chord length to maintain the same solidity. To assess the influence of the reduced-chord vanes on the flow topology, a comparison between the two configurations is carried out using RANS simulations. Theses are shown in Appendix C, where both configurations show a similar flow topology and aerodynamic performance, which validates the modified vane count for the present study.

For the radial-slice sector LES, only a radial slice that corresponds to 12% of the complete span (i.e. a span length of 12 mm) is simulated. The slice is centered at a radial position that corresponds to 80% of the hub-to-tip distance, and both the blade and vane airfoil sections are kept constant throughout the span. According to the full-span RANS results, three-dimensionnal effects, such as the radial velocity component, are minimized at 80% of the span.

Overviews of the computational domains of the radial-slice sector LES and the (full-span) sector LES are respectively shown in Figures 2.12 and 2.13. For all the cases, the domain extends from 3.75 fan chord lengths upstream of the fan to 4.25 vane chord lengths downstream of the stator.

2.4.2 LES numerical parameters

In the present study, the LES governing equations are solved using the AVBP solver, which is an explicit unstructured fully-compressible LES solver developed by CERFACS [245]. For turbomachinery applications, two LES domains are coupled. The first one is the rotor domain that contains the fan blades, and the second one is the stator domain that contains the stator vanes. The coupler CWIPI is used for the data exchange between the two domains, based on an overlapping grid method [267] and a third order interpolation, which is consistent with the order of the adopted numerical scheme.

A third order, finite-volume, Two-Step Taylor Galerkin Convective TTGC [43] scheme is used to solve the filtered Navier-Stokes equations. The SIGMA sub-grid scale model [183] is used for the closure of the unresolved turbulent eddies. NSCBC [202] are used at the inlet and the outlet sections. At the inlet section, a uniform mean flow is injected in the

Rotor **Stator** **Periodic sector**

(full-span) 360° LES **(full-span) sector LES**

Radial slice sector LES
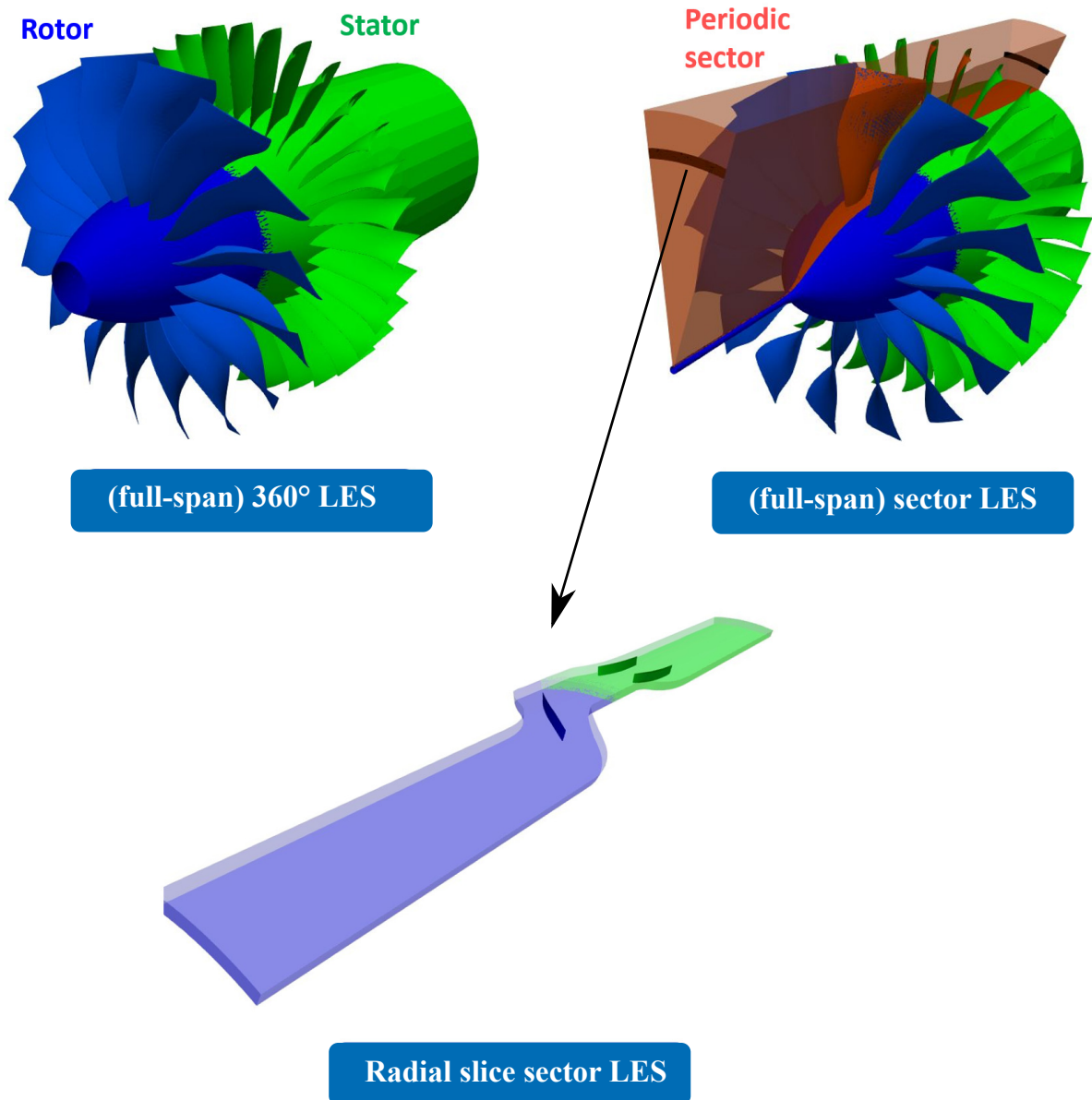
Figure 2.11: LES configurations.

Periodic boundary conditions

Inlet

357

44.9° 95

65

72 43

11.33°

68.9

292

Outlet

Rotor Stator
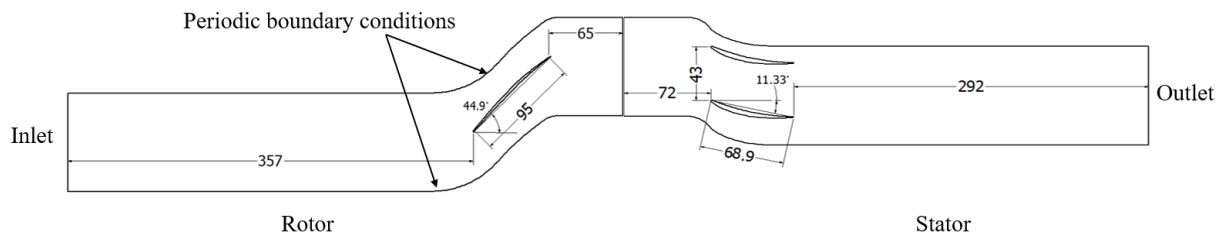
Figure 2.12: An overview of the computational domain of the radial-slice sector LES case. Dimensions are given in mm. Angles are given in degrees.
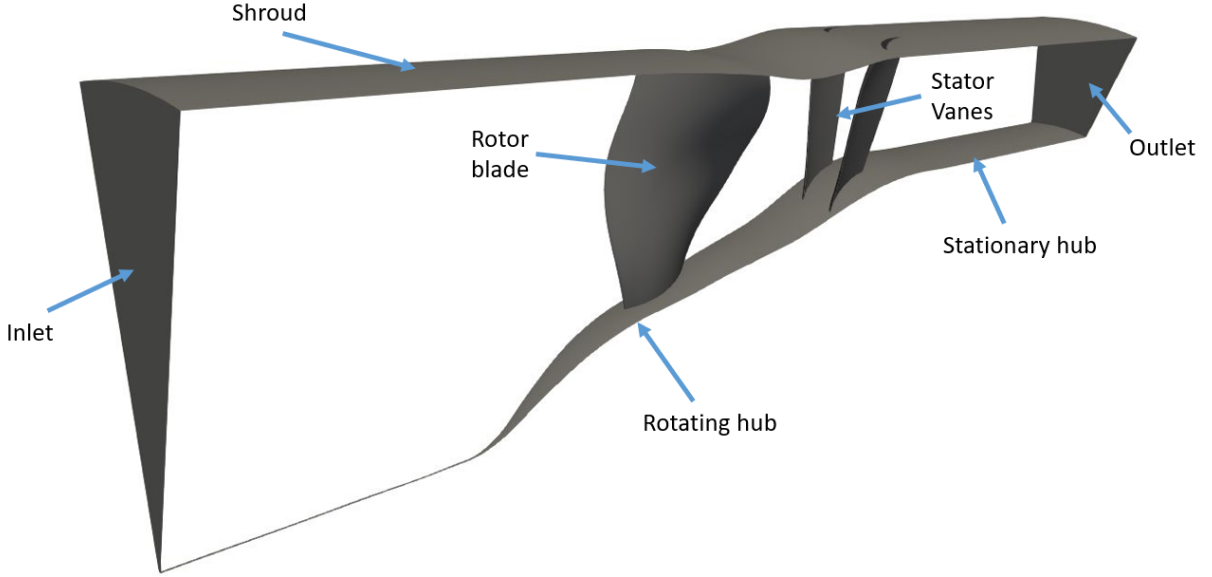
Figure 2.13: An overview of the computational domain of the (full-span) sector LES case.

axial direction, the total pressure is set to P_0=101325 Pa and the total temperature is set to T_0=300 K. At the outlet section, the pressure is adjusted to obtain the correct mass flow rate. For the sector configurations, periodic boundary conditions are used on both sides of the computational domain. On the wall surfaces of the blades, the vanes, the shroud and the hub, a no-slip boundary condition is used. For the wall-modeled (WM) cases, the boundary layer is modeled using a wall law [244] with a dimensionless wall velocity $u^+ = \frac{1}{\kappa}\ln(Ay^+)$ for $y^+ > 11.45$, with $\kappa = 0.41$ and $A = 9.2$. For lower values of y^+, a linear law is imposed. For the radial-slice case, a slip wall boundary condition is used at the boundaries in the radial direction.

2.4.3 Temporal convergence

For unsteady simulations, temporal convergence is mandatory to ensure proper physical analysis. For the different LES computations in this work, numerical and statistical convergence studies are performed. Numerical convergence corresponds to the end of the transient state. Statistical convergence corresponds to the convergence of the flow statistics. A convergence analysis methodology introduced by Boudet *et al.* [17] is used to ensure the numerical and statistical convergence. This analysis is applied for the different cases in the following chapters. The number of rotor rotations required to reach temporal convergence is summarized in Table 2.2. Once temporal convergence is reached, the unsteady pressure, velocity components and density are collected using monitor points to compute the acoustic field. The number of rotations used to compute the acoustic field is also presented in Table 2.2.

2.4.4 Mesh characteristics

An overview of the mesh at mid-span is shown in Figure 2.14 for the radial-slice LES and in Figure 2.15 for both the (full-span) sector LES and the (full-span) 360° LES. For these cases, a view of the mesh in the tip gap region is also presented. The hybrid unstructured mesh is composed of prismatic cells on the blade walls, tetrahedral cells
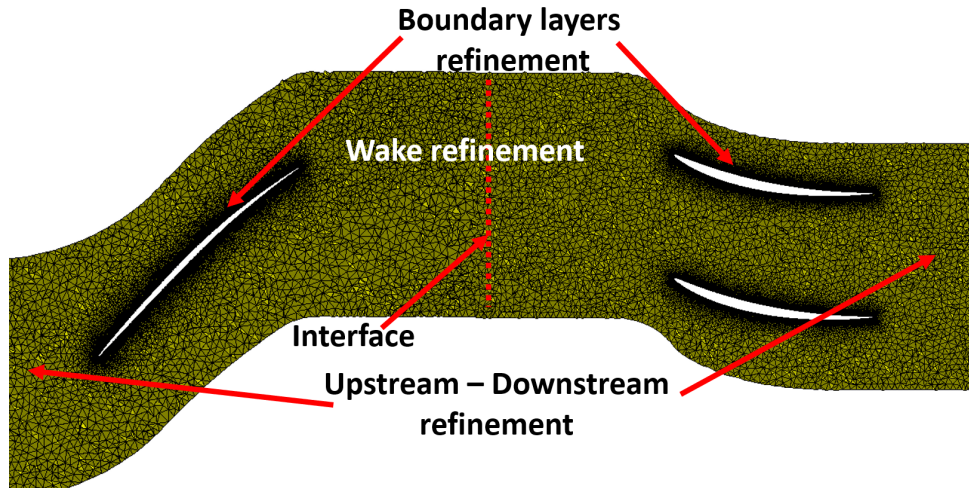
(a)
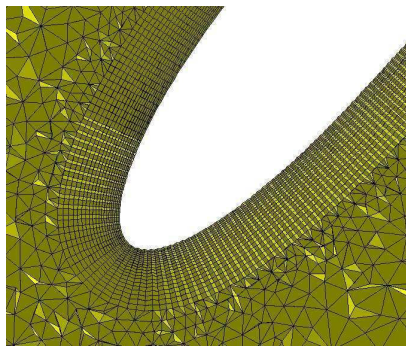
(b)
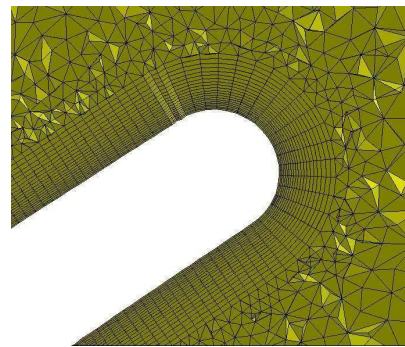
(c)
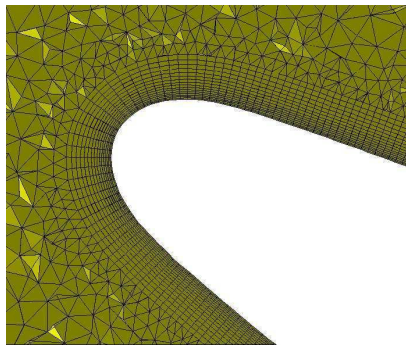
(d)
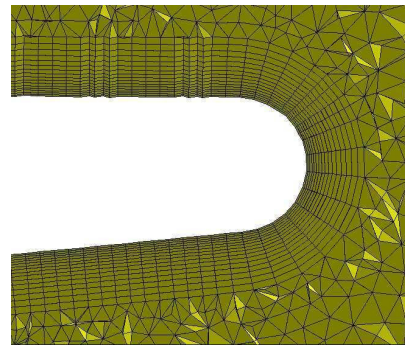
(e)

Figure 2.14: (a) Mesh view at mid-span for the radial-slice sector LES. Mesh refinements around the rotor LE (b), rotor TE (c), stator LE (d) and stator TE (d).

Table 2.2: Temporal convergence in number of rotor rotations.

	Radial-slice LES	(full-span) sector LES	(full-span) 360° LES
Statistical convergence	1.5	1.5	1.5
Numerical convergence	5	4.5	4.5
Acoustic recording	4	4	1.0

58

Figure 2.15: (a) Mesh view at mid-span for the (full-span) sector and 360° LES. Mesh refinements around the rotor LE (b), rotor TE (c), stator LE (d), stator TE (e), and in the rotor tip gap region (f).
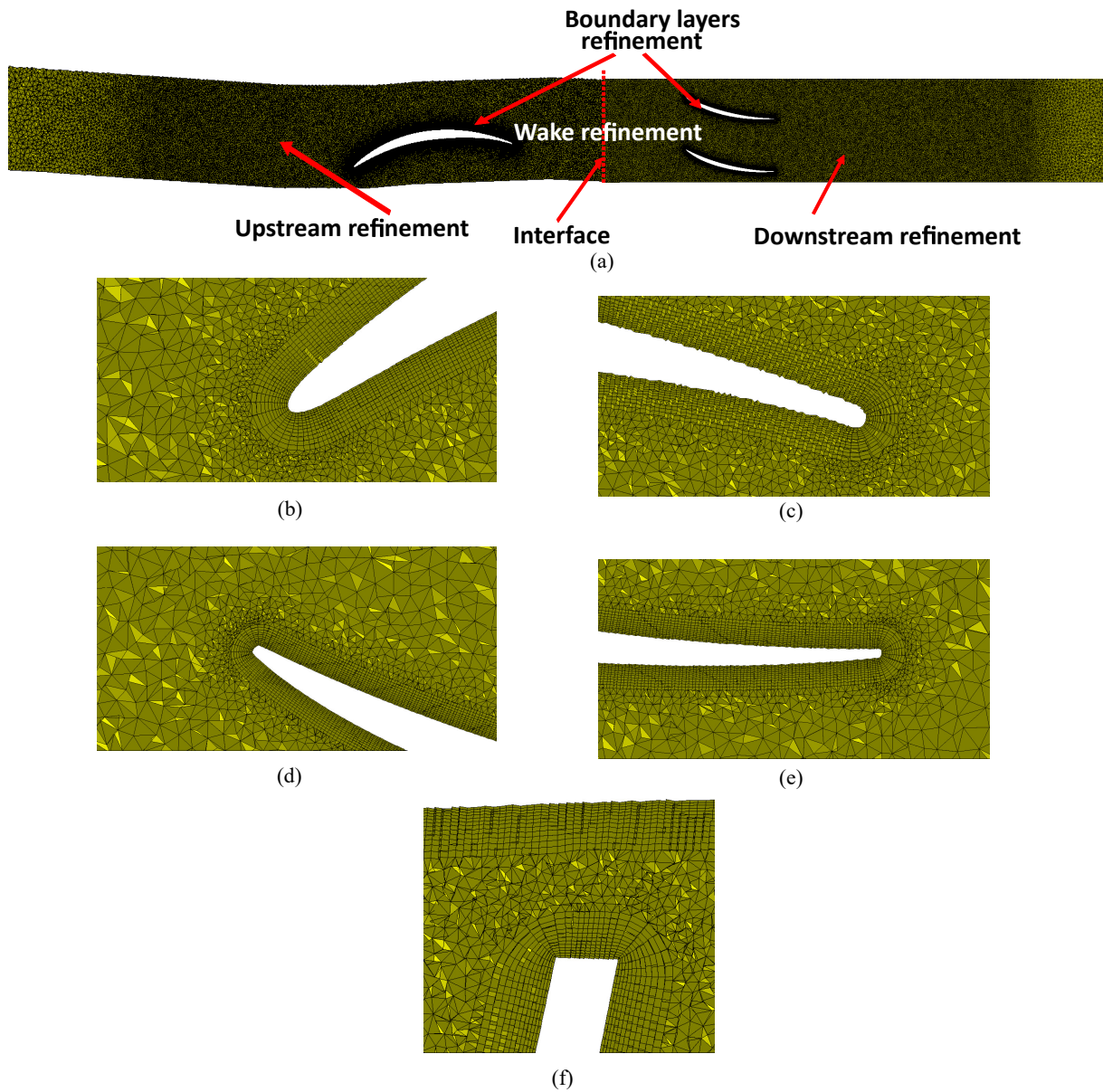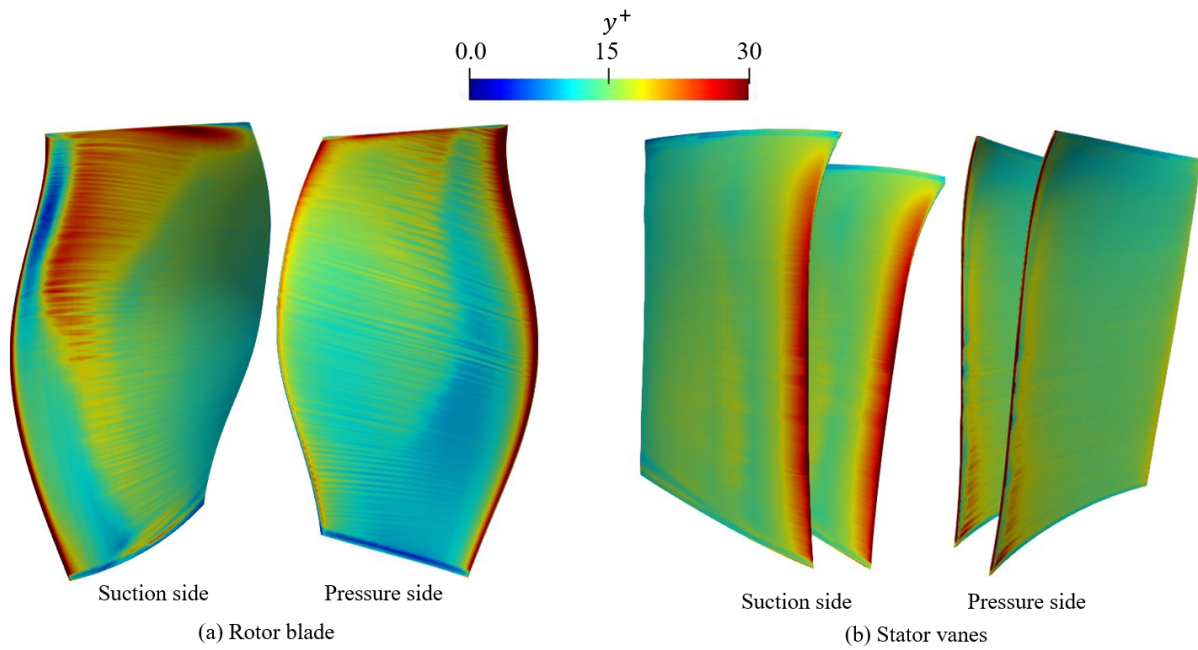
Figure 2.16: y^+ values on the rotor blade (a) and stator vanes (b) for the (full-span) sector LES (WM).
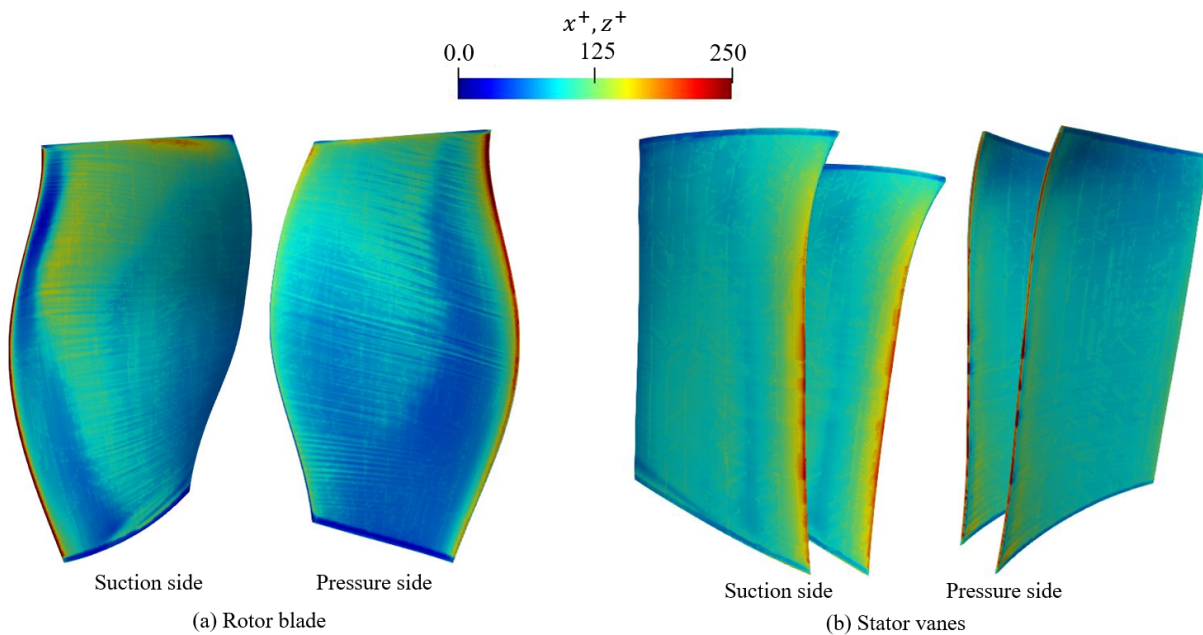
Figure 2.17: $x^+ = z^+$ values on the rotor blade (a) and stator vanes (b) for the (full-span) LES sector (WM).
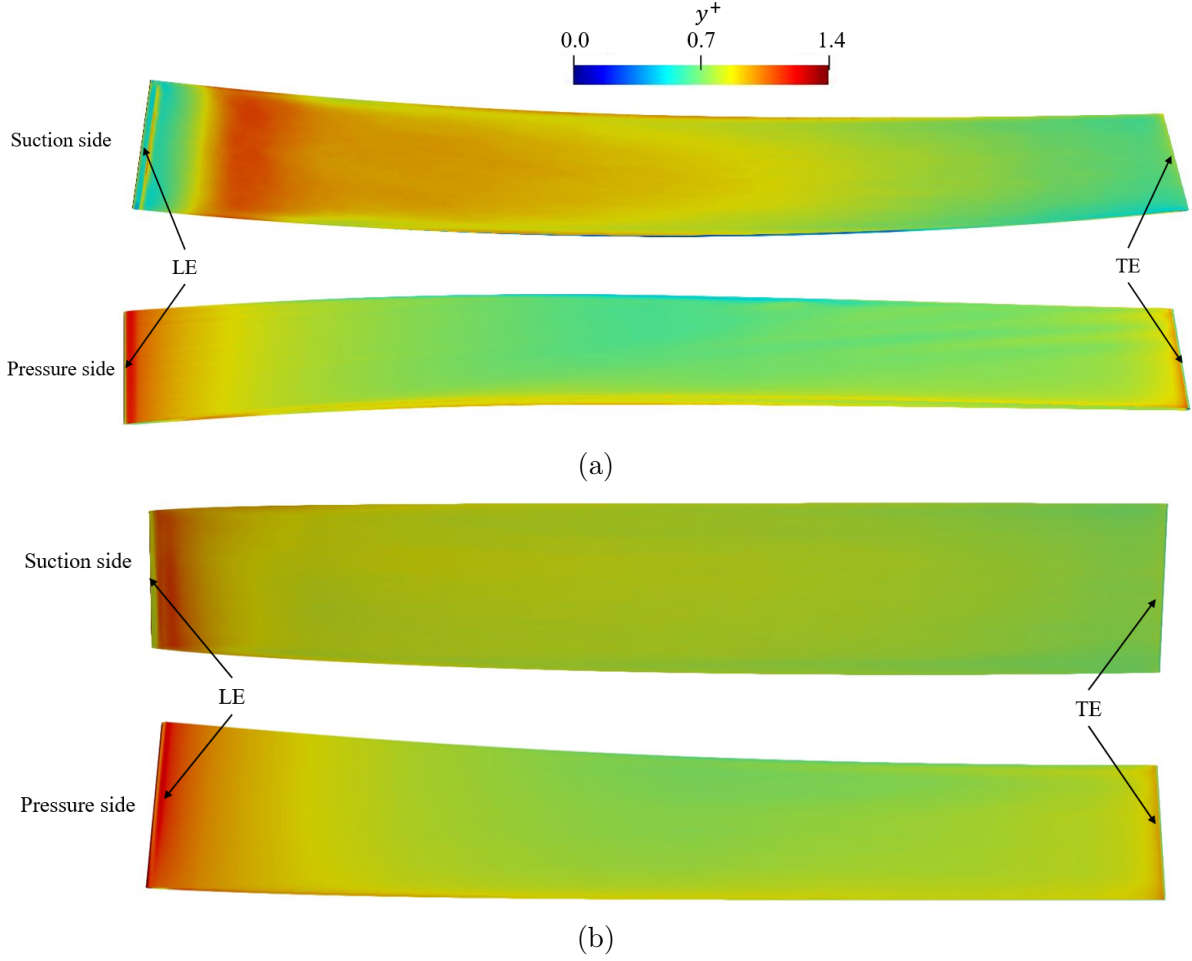
Figure 2.18: y^+ values on the rotor blade (a) and stator vanes (b) for the radial-slice LES (WR).

away from the blades, and pyramidal cells in the transition region between the prismatic and the tetrahedral cells. The mesh was designed based on turbulent and acoustic criteria established in Chapter 3. In order to obtain a suitable spatial resolution to resolve the boundary layers on the airfoil surfaces, the mesh is particularly refined in these regions. The first layer near the wall corresponds to the smallest spacing normal to the wall, and the cell size increases progressively away from the wall. Using prism layers on the walls, the values of x^+, y^+ and z^+ can be chosen in the appropriate ranges for WM and WR LES. For the WM cases, the y^+ values are kept smaller than 30 (Figure 2.16 for the (full-span) sector LES) and x^+ and z^+ values smaller than 250 (Figure 2.17). For the WR cases, y^+ values are kept smaller than 1 (Figure 2.18) and x^+ and z^+ values smaller than 40 (Figure 2.19).

Away from the walls, the mesh resolution is controlled by two main criteria:

- The number of points per acoustic wavelength $\lambda_{ac} = \frac{c_0(1-M)}{f_c}$, where c_0 is the speed of sound, M is a mean Mach number, and f_c is the desired mesh cut-off frequency.

- A constant "A_{Ta}" that is the ratio of the mesh size to the Taylor micro-scale $\lambda_{Ta} = (10\frac{\nu k_t}{\epsilon})^{1/2}$, where ν is the kinetic viscosity, k_t the turbulent kinematic energy, and ϵ the turbulent dissipation rate.

According to the parameter study from Chapter 3, using a similar mesh topology and
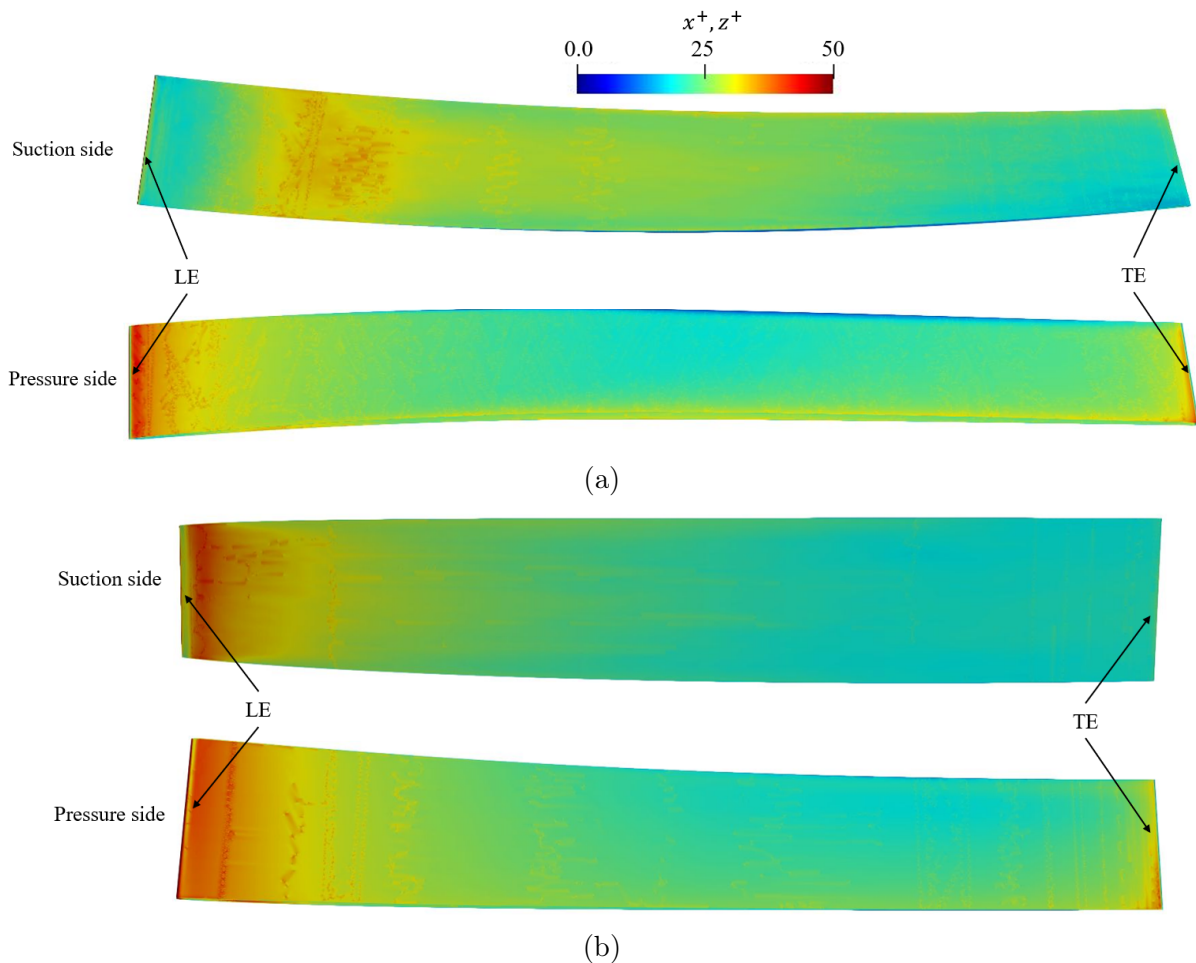
Figure 2.19: $x^+ = z^+$ values on the rotor blade (a) and stator vanes (b) for the radial-slice LES (WR).

numerical scheme, 13 points per λ_{ac} and a value of $A_{Ta} = 30$ are set. This implies that the mesh size is limited to 30 times the Taylor micro-scale to reduce the computational cost while providing a good resolution of the turbulent structures. This relationship between the mesh size and the Taylor microscale ensures that the cut-off frequency of the LES lies within the inertial region of the turbulent spectrum. The refined mesh regions that follow the above criteria are listed below.

- Upstream of the rotor and downstream of the stator. The mesh is refined over one blade chord length upstream of the LE of the rotor and one vane chord length downstream of the TE of the stator in order to ensure a correct acoustic propagation in these regions up to $f_c = 30$ kHz for the radial-slice sector LES and up to $f_c = 20$ kHz for the (full-span) sector and 360° LES.

- Rotor-stator interstage. The mesh resolution at the interstage ensures that the fan wakes are correctly convected between the TE of the fan blades and the LE of the vanes.

- Around the blades. A smooth transition region between the prismatic layers and the tetrahedral cells has been ensured for all the meshes used in this study.

Table 2.3: Assessment of mesh quality criteria for the LES of the ECL5 fan stage.

		Radial-slice LES	(full-span) sector LES	(full-span) 360° LES
Aspect ratio	Mean value	1.1	1.15	1.18
	Maximum value	160	270	285
	Percentage of cells with AR >100	$3 \times 10^{-6}\%$	$8 \times 10^{-6}\%$	$9 \times 10^{-6}\%$
Cell skewness	Mean value	0.18	0.25	0.27
	Maximum value	0.99	0.99	0.99
	Percentage of cells with skewness >0.85	$1 \times 10^{-2}\%$	$2 \times 10^{-2}\%$	$2 \times 10^{-2}\%$
Minimum dihedral angle (DiA)	Mean value [°]	65	54	52
	Minimum value [°]	7	4	3
	Percentage of cells with DiA $<10°$	$2 \times 10^{-4}\%$	$6 \times 10^{-4}\%$	$7 \times 10^{-4}\%$
Maximum dihedral angle (DiA)	Mean value [°]	90	93	98
	Maximum value [°]	174	176	177
	Percentage of cells with DiA $>170°$	$2 \times 10^{-5}\%$	$5 \times 10^{-5}\%$	$7 \times 10^{-5}\%$
Sliver	Mean value	1.13	1.19	1.22
	Maximum value	31	50	62
	Percentage of cells with sliver >10	$2 \times 10^{-5}\%$	$7 \times 10^{-5}\%$	$9 \times 10^{-5}\%$

Using these mesh refinement criteria, different mesh zones are shown in Figures 2.14 (a) and 2.15 (a). In the tip region, considering prism and tetrahedral cells, 30 points are imposed in the radial direction, as shown in Figure 2.15 (f).

2.4.5   Mesh quality

For the LES meshes, different criteria are used to ensure the accuracy of the numerical results. In addition to examining the aspect ratio and the cell skewness criteria used for the RANS mesh (see section 2.3.3), the dihedral angles and the cell sliver are checked.

- The dihedral angle is the angle between two faces of a given tetrahedron. Acceptable values are between 10° and 170°.

- The cell *sliver* (Eq. 2.6) is the ratio of the volume of an equivalent equilateral tetrahedron with the same average edge length (L_{avg}) as the current tetrahedron, to the volume of the current tetrahedron (V_{ac}). Acceptable values are below 10.

$$sliver = \frac{\sqrt{2}}{12} \frac{L_{\mathrm{avg}}^3}{V_{ac}} \qquad (2.6)$$

The mesh quality criteria are assessed in Table 2.3 for the different LES configurations. All the criteria are shown to be within the acceptable ranges according to the the standards from the literature.
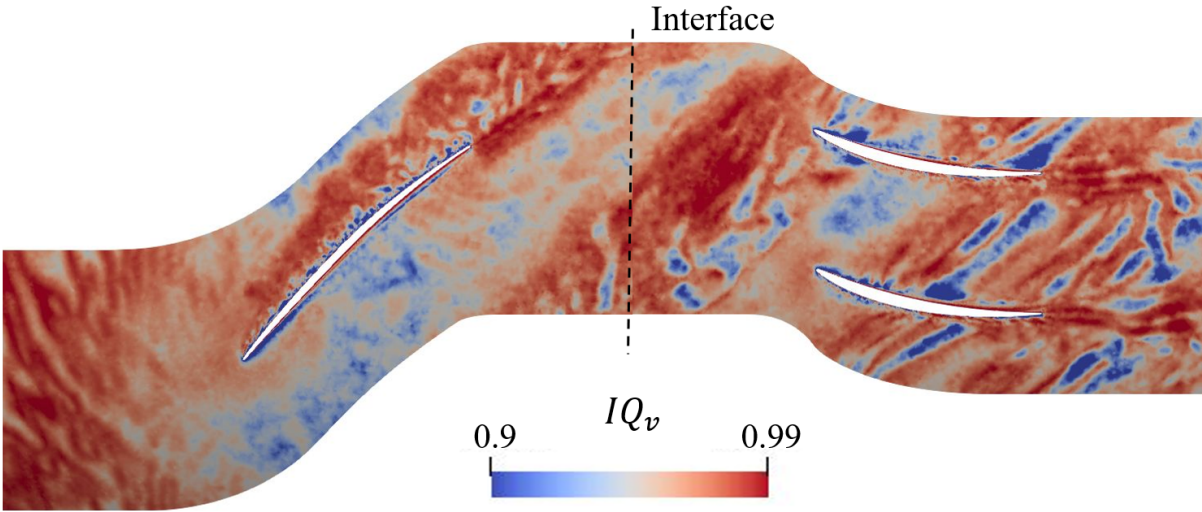
Figure 2.20

Figure 2.21: Mesh quality indicator IQ_v for the WR radial-slice sector LES at mid-span.
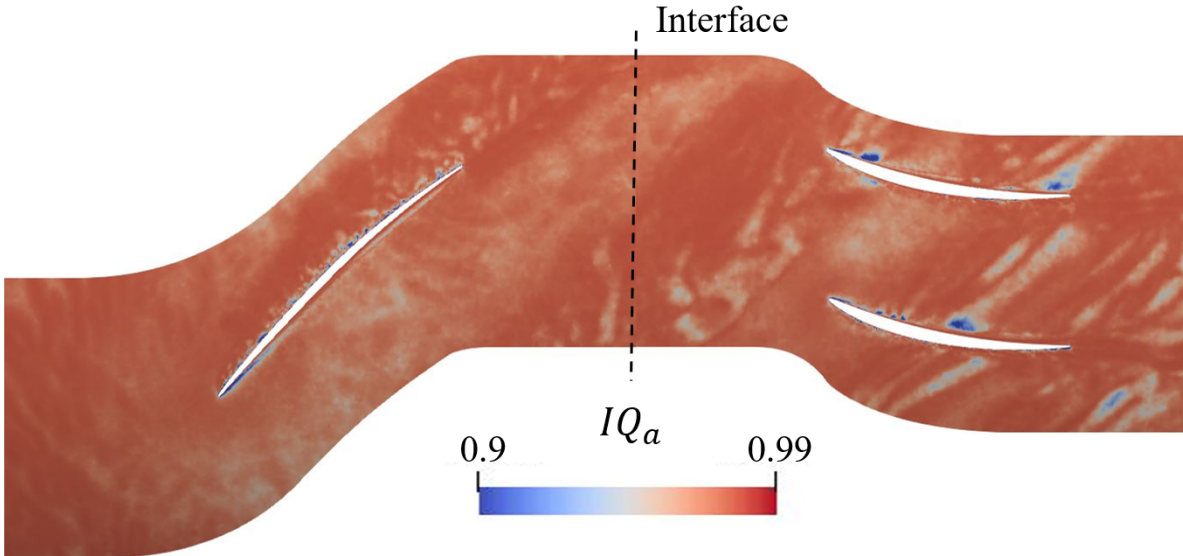
Figure 2.22: Mesh quality indicator IQ_a for the radial-slice sector LES at mid-span.

(a)
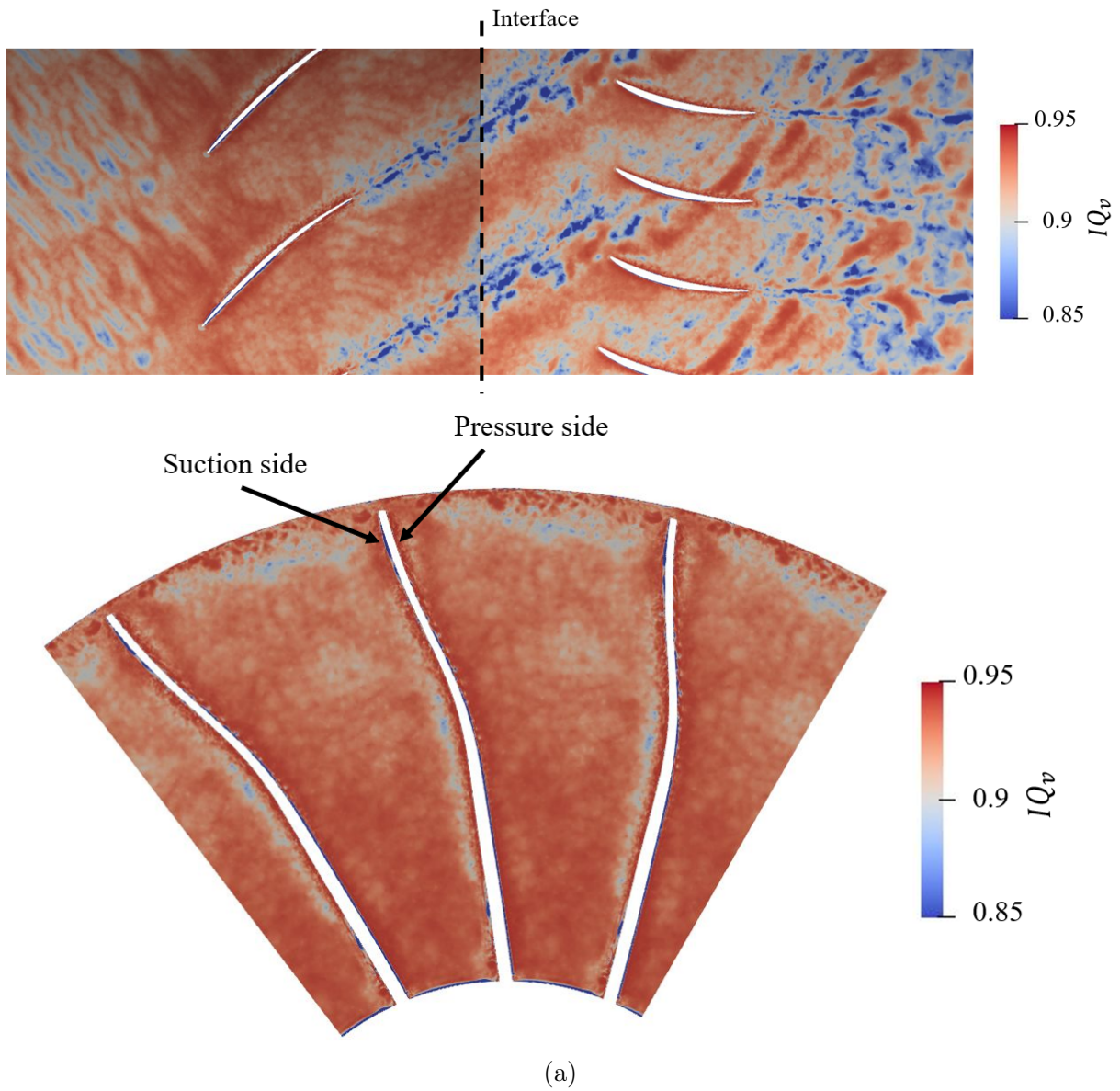
Figure 2.23: Mesh quality indicator IQ_v for the (full-span) sector LES case. (a) Section at a span position of 80% of the hub-to-tip ratio. (b) Section at an axial position of 60% of the chord length.
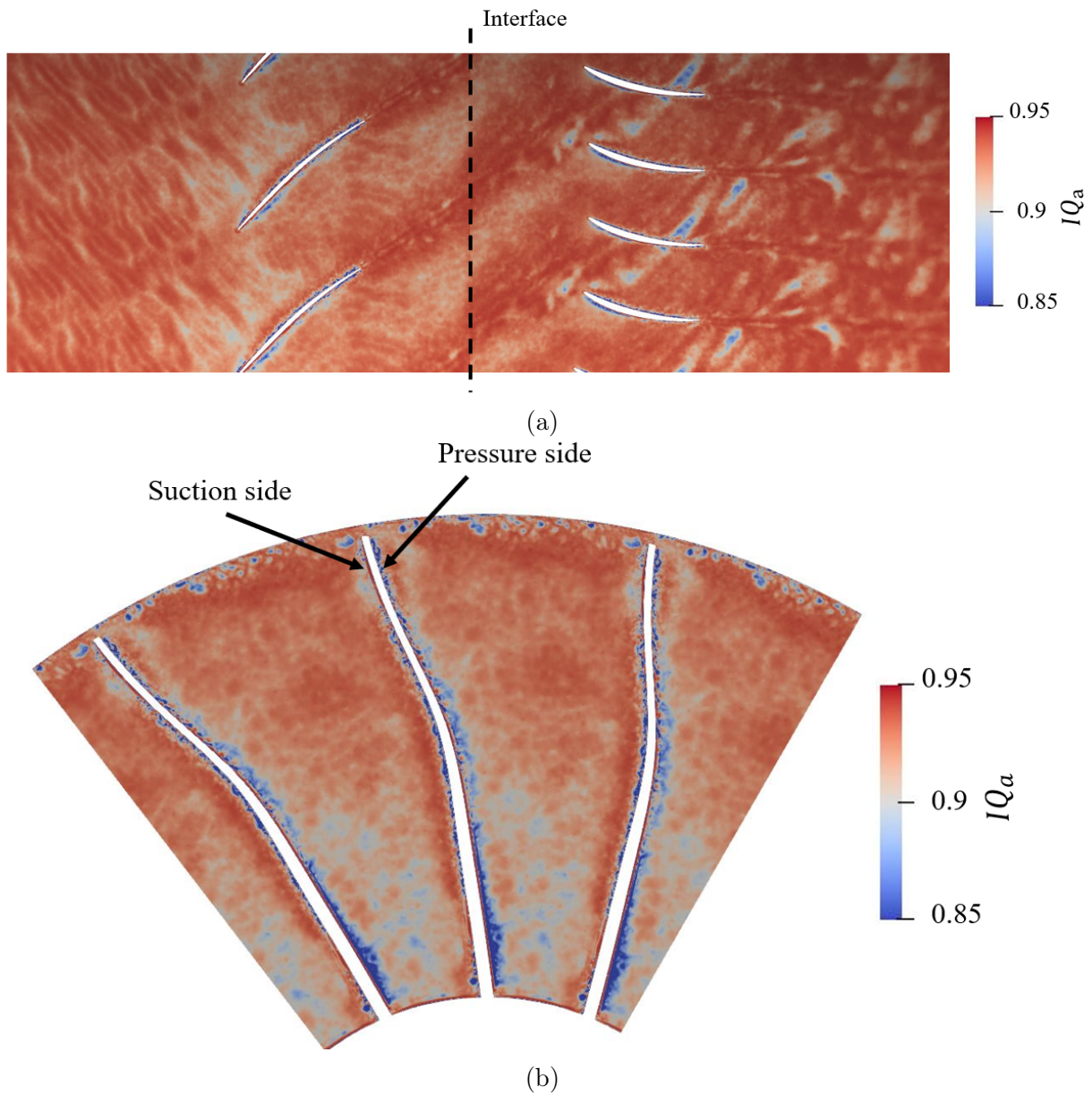
Figure 2.24: Mesh quality indicator IQ_a for the (full-span) sector LES case. (a) Section at a span position of 80% of the hub-to-tip ratio. (b) Section at an axial position of 60% of the chord length.

To further investigate the mesh resolution of the LES computations, the mesh criterion IQ_v, which was proposed by Celik *et al.* [32], is used. This criterion (as defined in Eq. 2.7) allows us to quantify the mesh resolution by comparing the turbulent viscosity calculated by the sub-grid scale model μ_{sgs} and the molecular viscosity of the fluid μ.

$$IQ_v = (1 + \alpha_v(\mu_{\text{sgs}}/\mu)^n)^{-1} \tag{2.7}$$

where $\alpha_v = 0.05$ and $n = 0.5$. A well resolved LES corresponds to $IQ_v > 0.8$ and a DNS to $IQ_v > 0.95$.

Another mesh criterion IQ_a is also introduced to compare the artificial viscosity μ_{artif} to the molecular viscosity of the fluid. This criterion can be defined as,

$$IQ_a = (1 + \alpha_a(\mu_{\text{artif}}/\mu)^n)^{-1} \tag{2.8}$$

where $\alpha_a = 0.05$ and $n = 0.5$. A well resolved LES corresponds to $IQ_a > 0.8$ and a DNS to $IQ_a > 0.95$.

The IQ_v and IQ_a criteria are shown in Figures 2.21 and 2.22 for the WR radial-slice sector LES at mid-span, and in Figures 2.23 and 2.24 for the WM (full-span) sector LES on a radial cut section at 80% of the hub-to-tip distance and on an axial cut at 60% of the chord length. Both the IQ_v and IQ_a criteria are calculated based on an instantaneous field obtained after statistical and numerical convergence. For both cases, IQ_v and IQ_a values are larger than 0.85 in almost all of the computational domain. The lowest values are located in the boundary layers and in the wakes. In these regions, the flow is highly turbulent. It can be noted that the computation is well resolved in the rotor wake region, which ensures the propagation of the wake properties from the rotor trailing edge to the stator leading edge. Thus, the main noise sources, which are related to the diffraction of the boundary layers near the trailing edge, the rotor-stator interaction, and the tip leakage flow, are expected to be well captured in both the WM and WR cases.

The mesh is also designed to propagate the acoustic waves over a distance of one chord length upstream of the rotor and downstream of stator, up to a frequency of 30 kHz for the radial slice-sector LES, and to 20 kHz for the (full-span) sector and 360° LES. These criteria have also been verified and will be further discussed when analyzing the acoustic spectra in the following chapters. Consequently, the turbulent and acoustic criteria presented in 2.4.4 are suitable to assess the mesh quality for LES simulations of fan noise.

Phase 2: ECL5 configuration - LES setup ———————————————— **Summary**

Configurations

- Radial-slice sector LES: 1 rotor blade - 2 stator vanes configuration with rescaled vanes to maintain the stage performance. The radial slice is extracted at 80% of the fan span with an extent of 12% of the full span.

- (full-span) sector LES: 1 rotor blade - 2 stator vanes configuration with rescaled vanes to maintain the stage performance.

- (full-span) 360° LES: 16 rotor blades - 31 stator vanes.

Numerical parameters

- Solver: AVBP (CERFACS).

- Subgrid scale model: SIGMA model.

- Inlet and outlet boundary conditions: NSCBC are used at the inlet and the outlet sections. At the inlet section, total pressure and temperature are imposed with a uniform flow. At the outlet section, the pressure is adjusted to obtain the correct mass flow rate.

- Lateral boundary conditions: periodic boundary conditions are used for both the radial-slice and the full-span sector LES.

- Wall boundary condition: non-slip wall. For the WM cases, the boundary layers are modeled using a wall law.

Mesh

- Hybrid unstructured mesh: prismatic cells on solid surfaces, tetrahedral cells away from the walls, and pyramidal cells in the transition between the prismatic and the tetrahedral cells.

- For the radial-slice sector cases: WM and WR LES are performed.

- For the (full-span) sector and 360° LES cases: WM LES are performed.

- The assessment of several mesh quality parameters ensures reliable simulations.

2.5   Conclusion

This chapter introduced the different configurations for the numerical simulations. The computations can been split into 2 different phases.

The first phase focuses on the numerical setup and best practices for LES of broadband noise from a flat plate, which allows us to compare the results with analytical models. This is useful to define relevant parameters for the mesh and to ensure the quality of the LES of rotor-stator configurations.

The second phase corresponds to an aeroacoustic analysis of the ECL5 fan stage using RANS and LES on three different configurations, a radial-slice sector LES, a (full-span) sector LES, and a (full-span) 360° LES. The flow conditions and the main geometric parameters for each configuration have been presented. The RANS and LES numerical setups have been described, including details on the CFD solvers, the numerical schemes,

modeling assumptions, and the meshing strategy. The mesh quality for the different configurations has been investigated based on the non-dimensional wall distances and several mesh parameters, to assess that the generated meshes respect the quality requirements for a WR RANS and, WM LES and WR LES.

Chapter 3

Flat plate configurations - Parametric study

> **Introduction**
>
> The main objective of this chapter is to investigate the numerical requirements for a correct description of the turbulence interaction noise (TIN) and trailing edge noise (TEN) mechanisms with LES. Comparisons to analytic models are preferred to avoid any experimental or numerical uncertainty in the reference data. Consequently, each noise mechanism is investigated separately on a dedicated flat-plate configuration that satisfies the hypotheses of the corresponding model. Flow conditions are chosen to be representative of a fan stage at approach conditions, with a significant chord-based Reynolds number ($Re_c = 10^6$) and a freestream Mach number of about $M_0 = 0.3$. Beyond the investigation of the numerical parameters, this study is also the opportunity to clarify the dependency of broadband noise on the main physical parameters.
>
> The chapter is organized as follows. In Section 3.1, Amiet's model is briefly presented for both TIN and TEN mechanisms. Sections 3.2 and 3.3 present the results of the parametric studies for the leading edge noise case and the trailing edge noise case, respectively. In Section 3.2, the effects of several numerical and physical parameters on the TIN are presented. The investigated parameters are:
>
> - Numerical parameters: the cell size and the sub-grid scale model.
>
> - Physical parameters: the plate thickness and the angle of attack.
>
> In Section 3.3, the influence of several numerical parameters on the boundary layer characteristics and on the TEN is described. The studied parameters are:
>
> - The near-wall modeling.
>
> - The grid topology and refinement in the near-wall and wake regions.
>
> - The domain extent and the boundary conditions in the spanwise direction.
>
> - The tripping methodology.

Contents

3.1 Analytical models

The analytical models used in this study are based on Amiet's theory for single airfoils. In this section, the assumptions and the formulation of this theory are briefly recalled.

3.1.1 Assumptions of Amiet's models

The assumptions used in the formulation of Amiet's theory can be classified as follows.

- **Airfoil geometrical parameters**. The scattering effects are only considered for airfoils with small thickness, camber and angle of attack. To consider the camber effect, Moreau *et al.* [169] have proposed semi-empirical corrections by modifying the surface loading as a function of the geometrical parameters. However, this effect is moderate (difference of 1 to 2 dB for a camber of 12° to 24°). The influence of the thickness is more significant. Noise levels decrease in a quasi-linear way as a function of the thickness [169, 190, 83]. This reduction is more important for smaller upstream velocities.

- **Far Field Assumptions**. In the models presented here, the observers are assumed to be in the acoustical and geometrical far field. The influence of these assumptions is studied in the PhD of J. Christophe [41]. It is shown that the geometrical far-field assumption yields similar results to the exact formulation for an observer at a distance larger than two times the span length (assuming that the span length is sufficiently larger than the chord length). The acoustical far-field assumption yields acceptable results for an observer at a distance greater than ten times the acoustic wavelength. Extensions of this theory have led to consider near field effects [134].

- **Uniform upstream flow conditions**. In Amiet's theory, the incident velocity is considered uniform and turbulence is assumed to be frozen, which leads to a uniform turbulence intensity and integral length scale. To account for spanwise-varying flow conditions along the airfoil, a strip method can be applied. This method consists in a discretization of the airfoil span in strips, having their own upstream flow conditions [134, 41].

3.1.2   Amiet model

The TIN model considered in this work was first proposed by Amiet (1975) [8]. The incident wake impinging on the LE is assumed to be frozen turbulence and is described as a sum of spatial Fourier modes in the streamwise and spanwise directions. Assuming a large span to chord aspect-ratio, the resulting far-field sound at an observer position in the midspan plane $(x,0,z)$ is given by

$$S_{pp}(\mathbf{x}, \omega) = (\frac{kz\rho_\infty c}{2S_0^2})^2 \frac{U_0 L\pi}{2} \mathcal{L}(x, k_x, 0)^2 \Phi_{ww}(k_x, 0), \qquad (3.1)$$

where k_x is the axial wavenumber, Φ_{ww} is the Power Spectral Density (PSD) of the upwash velocity fluctuations, and $\mathcal{L}(x, k_x, 0)$ is the total aeroacoustic transfer function. For a frozen turbulent velocity field $k_x = \omega/U_0$. More details about the derivation of TIN Amiet model are given in Appendix A.

The TEN model [7] describes the scattering of pressure fluctuations from an incident boundary layer at the sharp TE [223]. Assuming a large span to chord aspect ratio, the PSD of the acoustic far-field, for an angular frequency ω and an observer at $\mathbf{x} = (x,y,z)$, is given by

$$S_{pp}(\mathbf{x}, \omega) = (\frac{kcz}{4\pi S_0^2})^2 2\pi L \Pi_0(\frac{\omega}{u_c}, k_z)|I(\frac{\overline{\omega}}{u_c}, \overline{k}_z)|^2, \qquad (3.2)$$

where k is the acoustic wavenumber, $\overline{k} = kc/2$, c is the chord length, L is the span length, k_z is the spanwise wavenumber, S_0 represents a convection-corrected distance, and u_c is the convective velocity. Π_0 is a statistical function related to the wall-pressure spectrum ϕ_{pp} slightly upstream of the TE, assuming homogeneous boundary layer turbulence. l_z is the associated spanwise correlation length,

$$\Pi_0(\frac{\omega}{u_c}, k_z) = \frac{1}{\pi}\Phi_{pp}(\omega)l_z(k_z, \omega) \qquad l_z(k_z, \omega) = \int_0^{+\infty} \sqrt{\gamma^2(\Delta z, \omega)}\cos(k_z\Delta z)d\Delta z \quad (3.3)$$

where γ^2 is the spanwise coherence of the pressure fluctuations between points separated by a distance Δz. In Equation (3.2), I is the aeroacoustic transfer function that can be considered as the sum of the contribution of the main scattering from the TE I_1 and the LE scattering correction I_2. Detailed expressions can be found in [223].

3.2   Case 1: leading edge noise

The simulations address the flow around a flat plate for a freestream velocity of $U_0 = 100\,\text{m/s}$, in atmospheric conditions ($\rho_0 = 1.177\,\text{kg/m}^3$, $T_0 = 300\,\text{K}$, $\mu_0 = 1.81.10^5$). A synthetic turbulence is prescribed at the inlet section based on a spectral approach [133, 251].
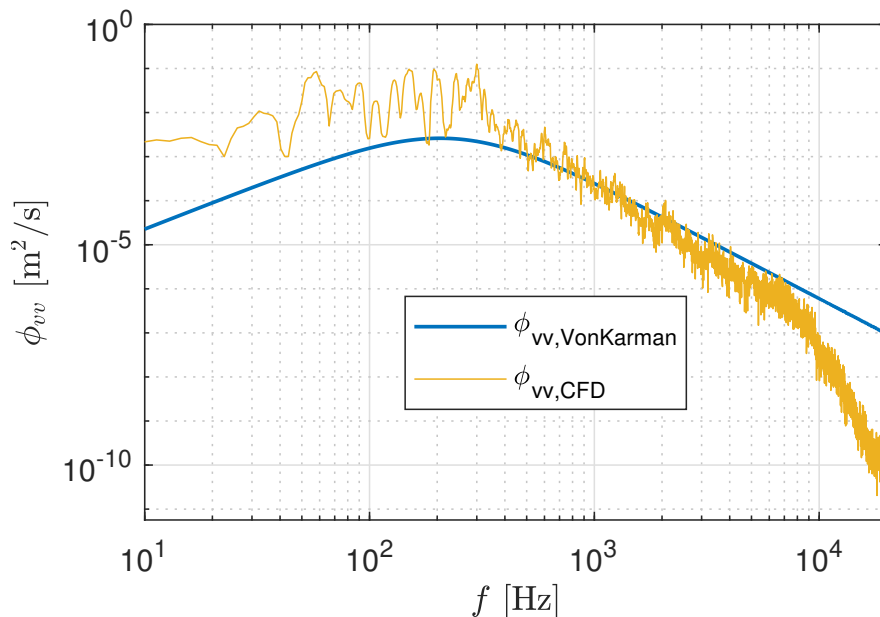
Figure 3.1: Upstream turbulent energy spectrum (close to the inlet section). The numerical spectrum obtained by LES with MESH4 ($\phi_{vv,CFD}$) is compared to a fit of Von Karman spectrum ($\phi_{vv,VonKarman}$ Eq. 3.5).

The turbulent spectrum can be fitted by a Von-Karman spectrum with a turbulent intensity of 4 % and an integral length scale of 5 mm (5% of the chord length), as shown in Figure 3.1.

3.2.1 Mesh description

In this case, five different meshes are considered. The main parameters of these meshes are summarized in Table 3.1. The first four meshes (MESH1 to MESH4) have the same refinement near the plate surface and different refinements in the far-field region. MESH5 has the same far-field mesh refinement as MESH4 and a coarser mesh close to the plate surface. For all cases, a wall law is imposed near the plate surface, with a mean normalized wall-normal spacing of $y^+ = 25$ (except for MESH5 where $y^+ = 35$). As mentioned in chapter 2, the description of the boundary layer is not the main objective of this case.

3.2.2 Pressure and velocity fluctuations

Figure 3.2 shows an instantaneous field of the normal velocity fluctuations, and the root mean square (RMS) of the pressure fluctuations P_{rms} around the plate for MESH4. The upstream synthetic turbulence, revealed by the velocity fluctuations, is seen to impinge on the LE of the plate. Consequently, a dipolar distribution of P_{rms} is observed at the LE, which is in good agreement with the assumptions of Amiet's model. These pressure fluctuations allow to locate the TIN source around the blade LE.

The distribution of P_{rms} along the upper side of the plate is also presented in Figure 3.3 for MESH4 and MESH5, which differ by their near wall mesh refinement. In both cases, a peak of P_{rms} at the LE is observed, which reveals the TIN source distribution. When comparing the two meshes, it can be observed that MESH4 allows to capture a larger peak of P_{rms} at the LE. Also, moderate oscillations can be noticed for MESH5 at $0 < x/c < 0.05$.

Table 3.1: Mesh parameters used in the LES simulations for case 1. N is the total number of cells, $\Delta y_{\min}$ the minimum mesh size, Δx_{ff} the mesh size in the far-field, Δt the minimum time step, and CPU h an estimation of the computational time.

	Parameters	MESH1	MESH2	MESH3	MESH4	MESH5
Mesh Parameters	N (10^6)	0.9	1.2	1.65	2.35	2.01
	Δy_{min} [mm]	0.13	0.13	0.13	0.13	0.18
	Δx_{ff} [%c]	5.5	3.6	2.1	1.7	1.7
	y^+	25	25	25	25	35
CPU Estimation	CFL	0.7	0.7	0.7	0.7	0.7
	Δt [10^{-7}s]	1.5	1.5	1.5	1.5	2.1
	Δf_{min} [dB]	40	40	40	40	40
	T_{phys} [ms]	125	125	125	125	125
	CPU h	663	1238	1702	2424	1700
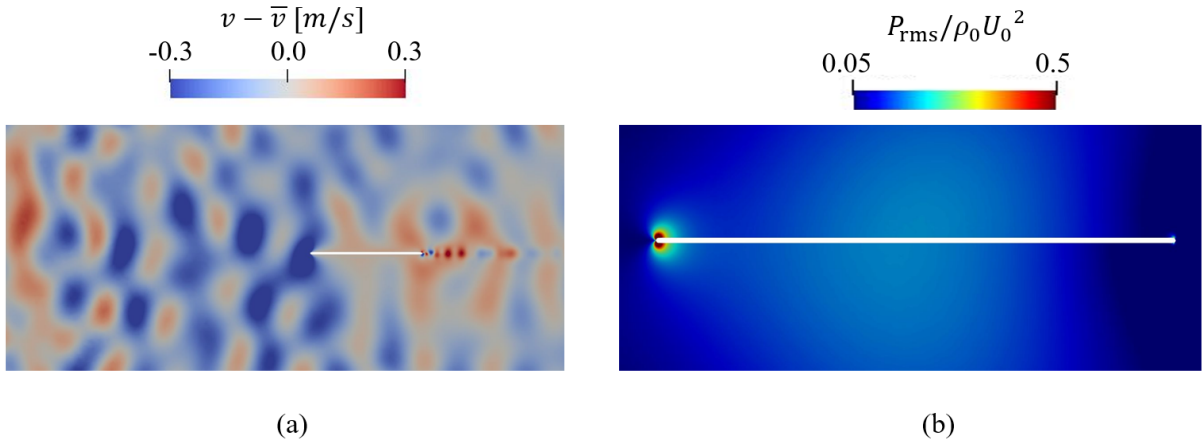
Figure 3.2: (a) Instantaneous snapshot of the transverse velocity fluctuations and (b) RMS pressure fluctuations, P_{rms}, around the plate.
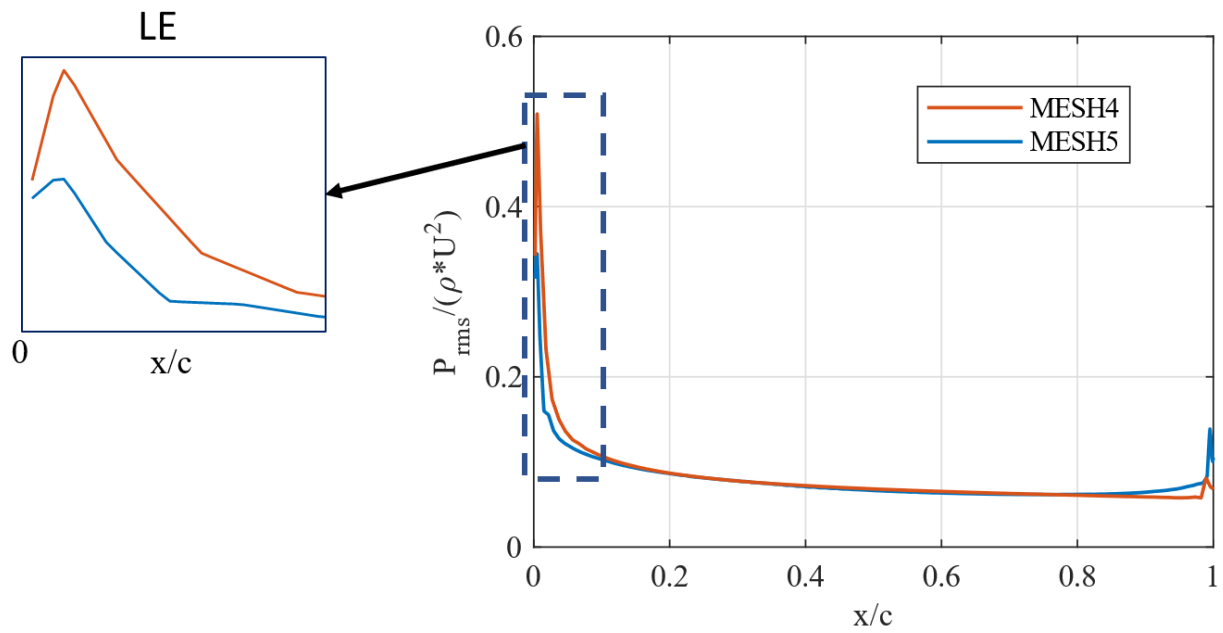
Figure 3.3: Evolution of P_{rms} along the upper side of the plate for MESH4 and MESH5.
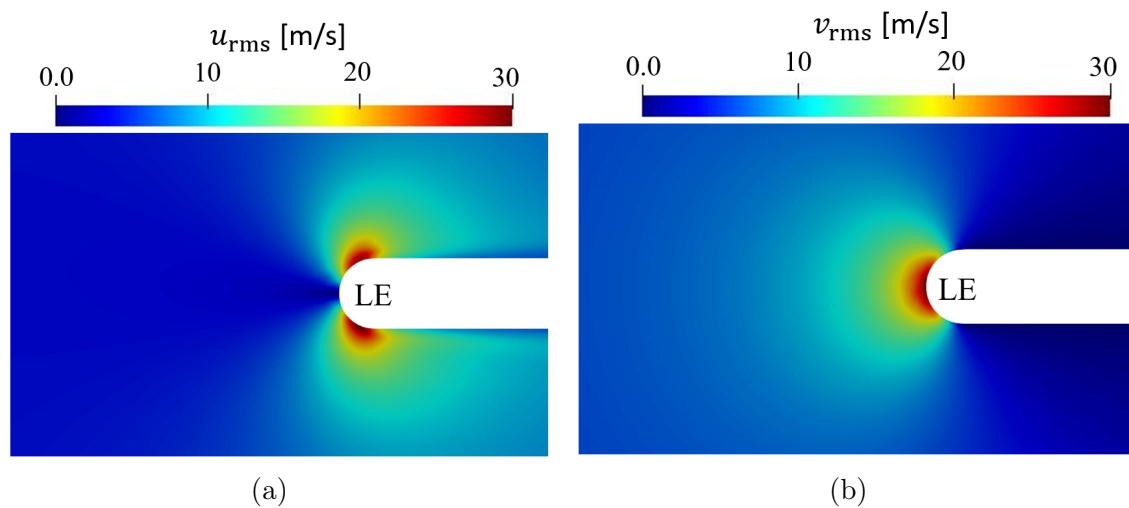
Figure 3.4: Contours of streamwise (a) and transverse (b) RMS velocity fluctuations around the LE of the plate for MESH4.
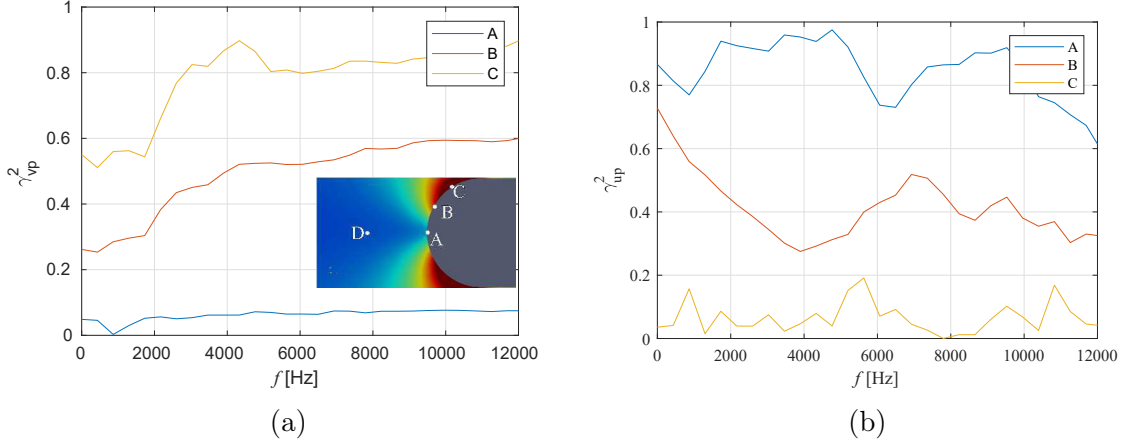
Figure 3.5: Coherence between the pressure fluctuations at three different locations (A, B, and C) on the surface of the plate and (a) transverse and (b) streamwise velocity fluctuations, respectively, upstream of the LE (location D, $x/c = -0.02$ along the stagnation line). Inserted field corresponds to an enlarged view of P_{rms} at the LE.

The small peak at the TE is due to the abrupt transition from the wall condition to the free field. The TE peak is limited when using the refined mesh (MESH4).

Figure 3.4 shows contours of the streamwise and transverse components of the RMS velocity fluctuations around the LE of the plate. The streamwise component, u_{rms}, decreases in the stagnation region. This is due to the reduction of the axial velocity and the axial Mach number in the cross-section of the plate, which restricts the velocity fluctuations in the streamwise direction. However, the transverse component, v_{rms}, is increased in the stagnation region as pointed out by Gill *et al.* [68] and Kim *et al.* [124]. This decay of u_{rms} and the increase of v_{rms} along the stagnation line means that a certain amount of turbulent kinetic energy in the streamwise direction is transferred into the transverse direction. This process is significant near the LE of the plate at a distance below $0.005c$. According to Santana *et al.* [241], the strongest turbulence distortion occurs at a distance of the order of the LE radius, which is consistent with the results shown here.

For a further study of the relationship between the velocity fluctuations in the vicinity of the LE, and the unsteady pressure response on the plate surface, the coherence $\gamma^2_{u_i p}$ is calculated. It is defined as,

$$\gamma^2_{u_i p}(f) = \frac{|S_{u_i p}(f)|^2}{S_{u_i u_i}(f) S_{pp}(f)} \tag{3.4}$$

where $S_{u_i u_i}$ is the power spectral density (PSD) of a velocity fluctuation component (u' and v' in the streamwise and transverse directions, respectively) in the vicinity of the LE, S_{pp} is the PSD of the pressure fluctuations p' on the plate surface, and $S_{u_i p}$ is the cross-spectral density between u_i' (the i-th velocity fluctuation component) and p'. Figure 3.5 shows the coherence between the streamwise and transverse velocity fluctuations at position D ($x/c = -0.02$) along the stagnation line, and the pressure fluctuations on the plate surface at the locations A, B and C. Pressure fluctuations at the stagnation point (location A) are mainly generated by streamwise velocity fluctuations, with $\gamma^2_{up} \approx 0.92$ and $\gamma^2_{vp} \approx 0.08$ at almost all frequencies. As pointed out from Figure 3.4 (a), turbulence intensity in the streamwise direction is attenuated in the vicinity of the LE and the noise is not radiated from the stagnation point A. Moving away from the stagnation point (locations B and C), the coherence between transverse velocity fluctuations and the unsteady pressure response
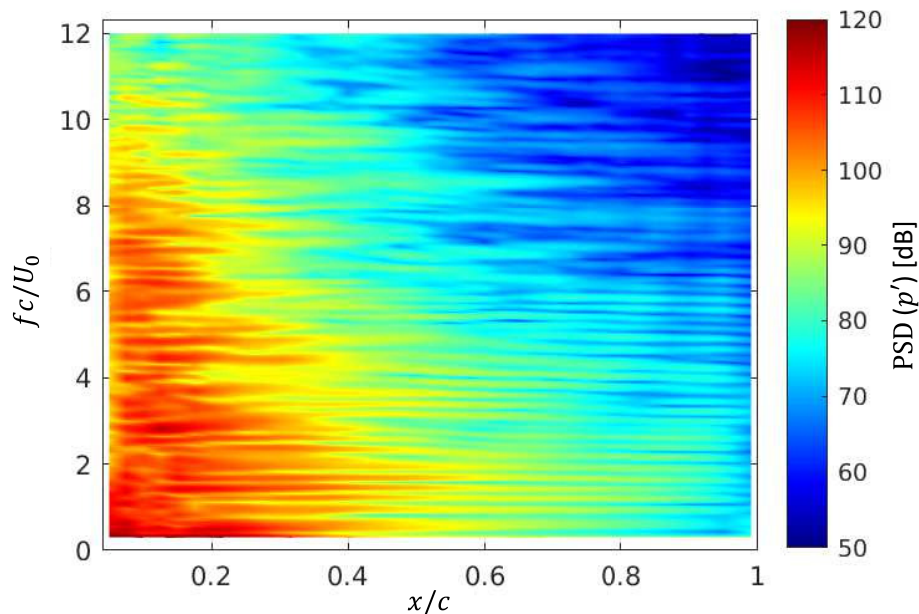
Figure 3.6: PSD of the unsteady pressure fluctuations on the upper surface of the plate. LE and TE correspond to $x/c = 0$ and $x/c = 1$, respectively.

increases significantly corresponding to an important increase in P_{rms} shown in Figure 3.3. The transverse fluctuating velocity component is thus at the origin of the radiated TIN.

The distribution of P_{rms} presented in Figures 3.2 (b) and 3.3 is important to locate noise sources, but does not provide any information about their frequency content. For that, the PSD of pressure fluctuations along the upper surface of the plate is presented in Figure 3.6, showing the spectral decomposition of the pressure response. PSD are obtained by a periodogram method, using segments of size 2^{10} time steps and a 50% overlap. A Hann window is also applied. The reference pressure is 2.10^{-5} Pa. As in Figure 3.3, it can be observed that noise sources are mainly located near to the plate LE ($x/c < 0.3$). The noise is mainly radiated at low reduced frequencies ($fc/U_0 < 6$), which are the major contributors to TIN source. Additionally, the axial extent of the region of large pressure fluctuations on the plate surface is more important at low frequencies than at high frequencies.

Pressure and velocity fluctuations ———————————————— **Summary**

- A dipolar noise source is observed at the plate LE, characterized by a peak of P_{rms} that depends on the mesh resolution close to the LE.

- The P_{rms} peak at the LE is mostly related to the transverse velocity fluctuations.

- Noise is mainly radiated at low to mid frequencies ($fc/U_0 < 6$).
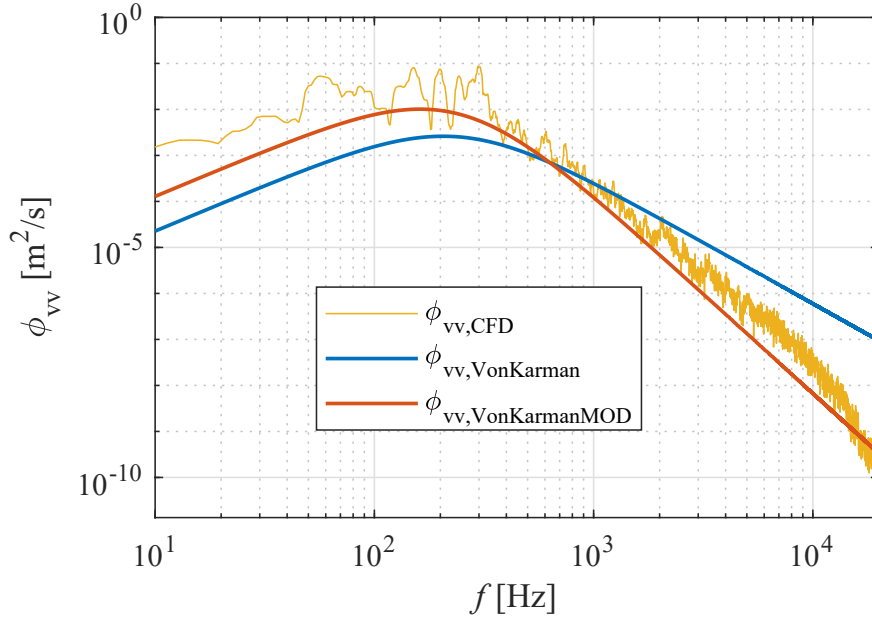
Figure 3.7: Upstream turbulent energy spectrum (at $x/c = -0.02c$). The numerical spectrum obtained by LES from MESH4 ($\phi_{vv,\text{CFD}}$) is compared to a fit of Von Karman spectrum ($\phi_{vv,\text{VonKarman}}$ Eq. 3.5) and to the modified version of Von Karman spectrum ($\phi_{vv,\text{VonKarmanMod}}$, Eq. 3.7).

3.2.3 Influence of numerical parameters

In this section, the effects of two numerical parameters, the mesh size in the far-field region and the sub-grid scale model, are investigated. Numerical results from the different meshes are compared to analycal noise predictions from Amiet's model.

Processing of flow variables for Amiet's model

Far-field noise predictions with TIN Amiet's model (described in section 3.1) require, as an input, the turbulent energy spectrum of the flow upstream of the airfoil. This spectrum is usually modeled by either a Von Karman or a Liepmann spectrum [262, 27]. The use of these spectra coupled with Amiet's theory has been validated in several applications [8, 190, 226, 3]. A modified version of Von Karman spectrum, which will be presented in the following, is considered in this study to fit the LES results. The Von Karman model is formulated as,

$$\phi_{vv}(k_x, k_y) = \frac{4}{9\pi} \frac{\overline{u^2}}{k_e^2} \frac{\hat{k}_x^2 + \hat{k}_y^2}{(1 + \hat{k}_x^2 + \hat{k}_y^2)^{7/3}} \tag{3.5}$$

where $\hat{k}_i$ are the wave-numbers made dimensionless by k_e defined as

$$k_e = (\sqrt{\pi}/\Lambda_f)\Gamma(5/6)/\Gamma(1/3) \tag{3.6}$$

The two relevant parameters of this model spectrum are the average of the squared velocity fluctuations u^2, which is directly available from the flow computation, and the longitudinal turbulence length scale λ_f, the only remaining parameter that allows us to adjust the spectrum model to fit the LES spectrum. At relatively close distances from the plate LE, the flow is largely distorted due to the plate thickness and the spectrum of the incoming

79
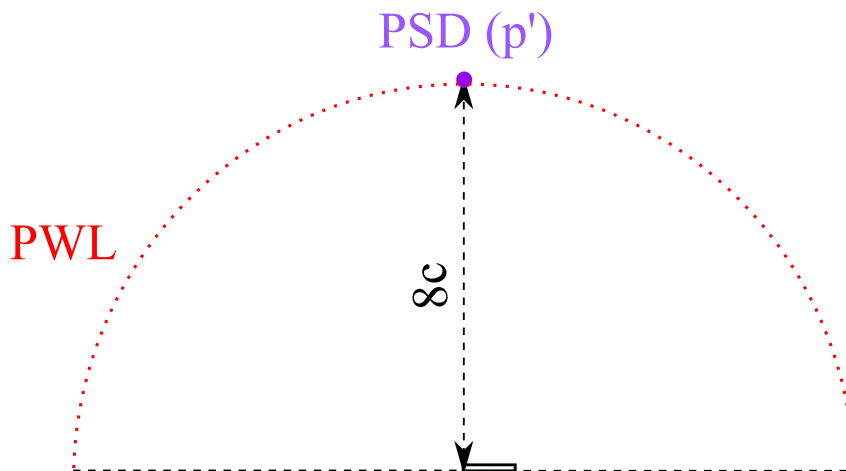
Figure 3.8: Distribution of the monitor points used to compute the PSD of the pressure fluctuations and the PWL.

flow is largely influenced by the airfoil body. For that, a modification of the Von Karman spectrum is proposed by J. Chritophe [41] to take into account flow deformation. This modification is based on the generalization of the rapid distortion theory for turbulent flows around bluff bodies and can be given as,

$$\phi_{vv}(k_x, k_y) = \frac{91}{36\pi} \frac{\overline{u^2}}{k_e^2} \frac{\hat{k}_x^2 + \hat{k}_y^2}{(1 + \hat{k}_x^2 + \hat{k}_y^2)^{19/6}} \tag{3.7}$$

Figure 3.7 shows the turbulent energy spectrum ϕ_{vv} directly obtained from the LES (MESH4) at a distance of $0.02c$ upstream of the plate LE. The Von Karman spectrum ($\phi_{vv,\text{VonKarman}}$, Eq. 3.5) and its modified version ($\phi_{vv,\text{VonKarmanMod}}$, Eq. 3.7) are used to fit the numerical spectrum ($\phi_{vv,\text{CFD}}$) and are also presented in Figure 3.7. An integral length-scale of 5 mm (5% of the chord length) and a turbulent intensity of 4% are used for these two spectra. The modified spectrum better fits the LES spectrum than the original Von Karman spectrum. This fit is used for the far-field predictions with Amiet's model in the following.

Influence of the far-field mesh refinement

Figure 3.9 shows the numerical acoustic power level spectra (PWL) for the different meshes. The PWL is computed by integrating over a circle of radius $8c$ centered at the leading edge, as shown in Figure 3.8. A reference value of 1.10^{-12}W is adopted. For the comparison with Amiet's model, ϕ_{vv} is taken as a fit of the modified version of Von Karman spectrum (Eq. 3.7). All the other parameters are directly taken from the LES. Apart from slight differences at low frequencies, a very good agreement is observed with the analytical model for all cases up to $4\,\text{kHz}$. All meshes have the same structure and the same minimum cell size near the plate LE, where the TIN source is located. The far-field grid refinement influences the propagation and consequently the cut-off frequency of the spectrum, such that the most refined mesh can propagate a larger range of frequencies.

The acoustic cut-off wave-lengths ($\lambda_c = c_0/f_c$, where f_c is the cut-off frequency obtained from Figure 3.9) obtained for the different meshes are presented in Figure 3.10, as
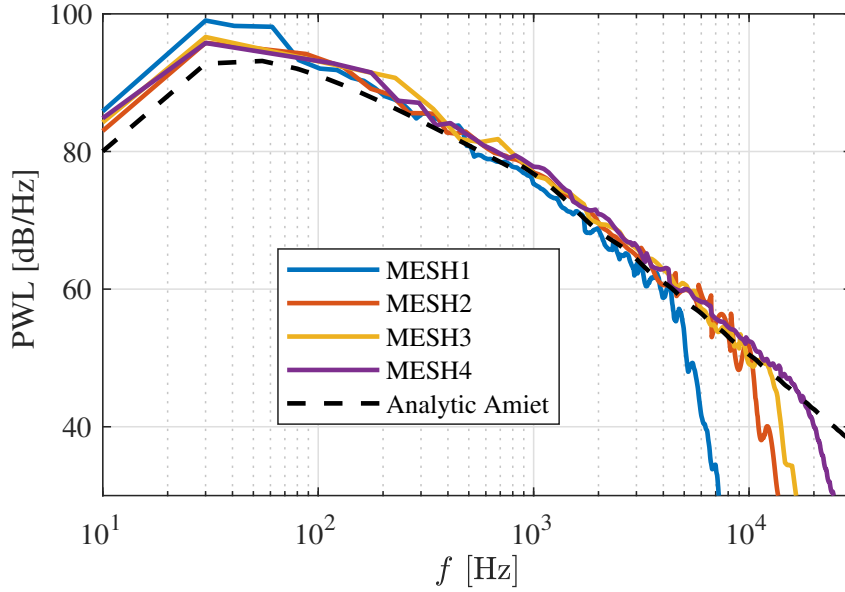
Figure 3.9: Comparison of the power spectral levels PWL for the different meshes, at a distance of $8c$, with the analytical solution of Amiet's theory.
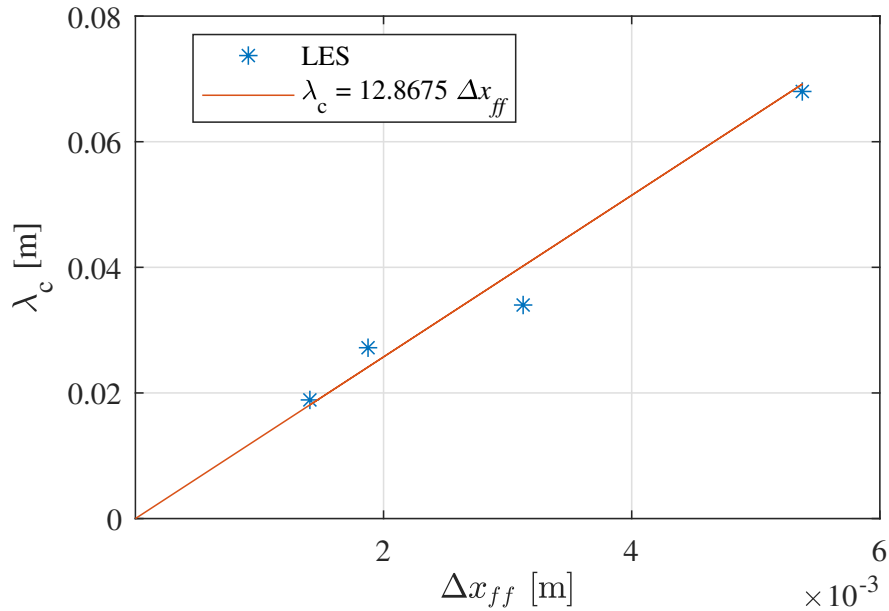
Figure 3.10: Cut-off acoustic wave-length λ_c as a function of the mesh size Δx_{ff}, for different meshes, and a linear fit.
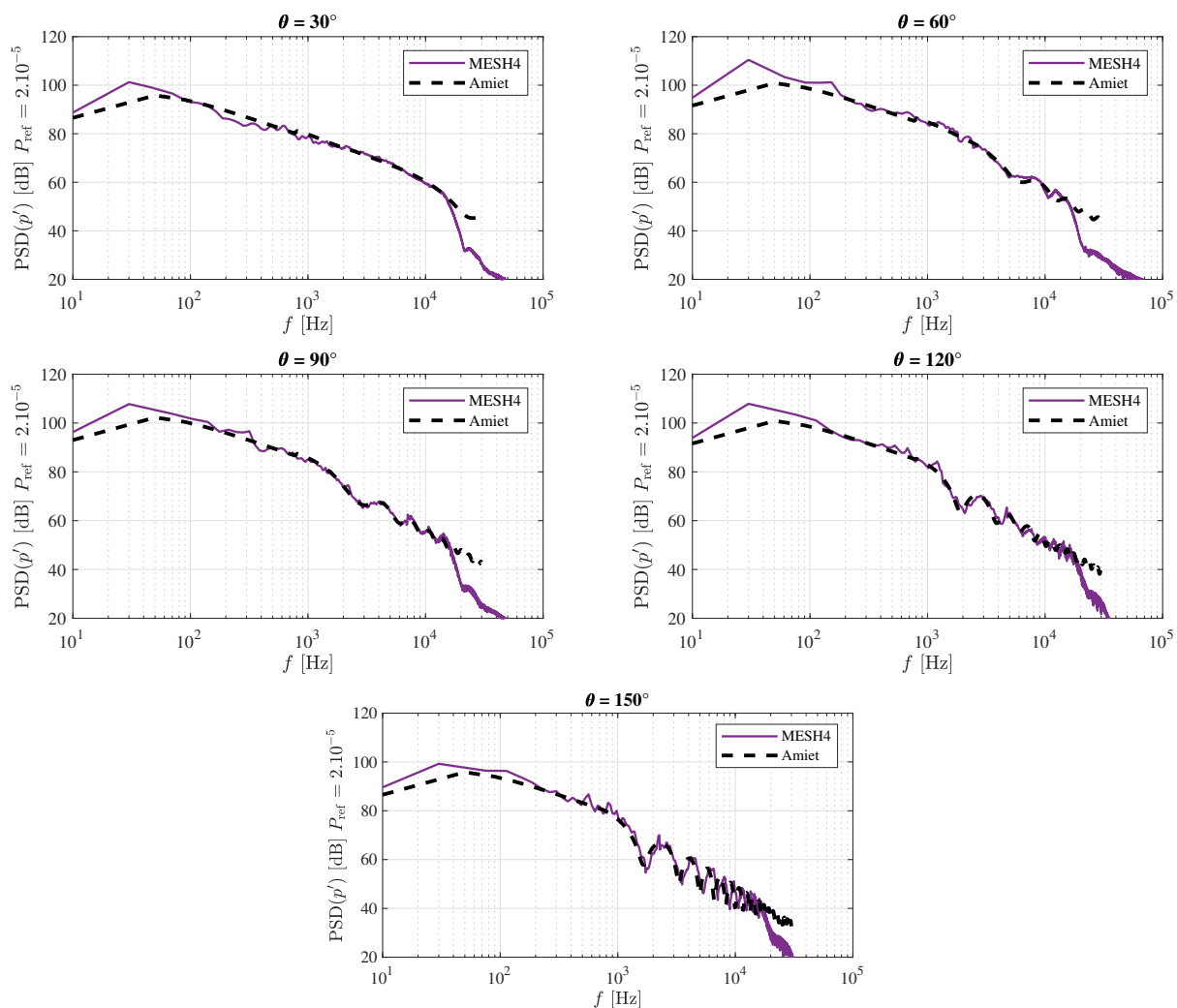
Figure 3.11: Comparison between numerical (MESH4) and analytical results of the PSD spectra of the pressure fluctuations at $R = 8c$ and different angles θ measured counter-clockwise from the main flow direction.

a function of the far-field mesh size Δx_{ff} given in Table 3.1. A linear trend is observed, and for the present numerical setup (particularly for the third order numerical scheme TTGC), one can infer that 13 points per wavelength are required to accurately capture acoustic waves up to a distance of $8c$ from the leading edge of the plate. This means that for a cell size of $\lambda_c/13$ with $f_c = 20\,\mathrm{kHz}$, the amplitudes of the pressure spectra are successfully captured up to a frequency of $20\,\mathrm{kHz}$ at a distance of 47 acoustic wavelengths with the present numerical setup. This valuable information will be used in the future to set up aeroacoustic-oriented LES simulations.

To study the noise propagation around the plate, five monitor points are located on a semi-circle around the plate LE in the mid-span plane, at a radius of $R = 8c$ and at angles of $\theta = 30°$, $60°$, $90°$, $120°$, and $150°$, where R originates from the LE of the plate and θ is measured counter-clockwise from the freestream flow direction. Figure 3.11 shows a comparison of the PSD of the pressure fluctuations from MESH4 determined at these five monitor points and the analytical TIN Amiet solution at the same positions. A
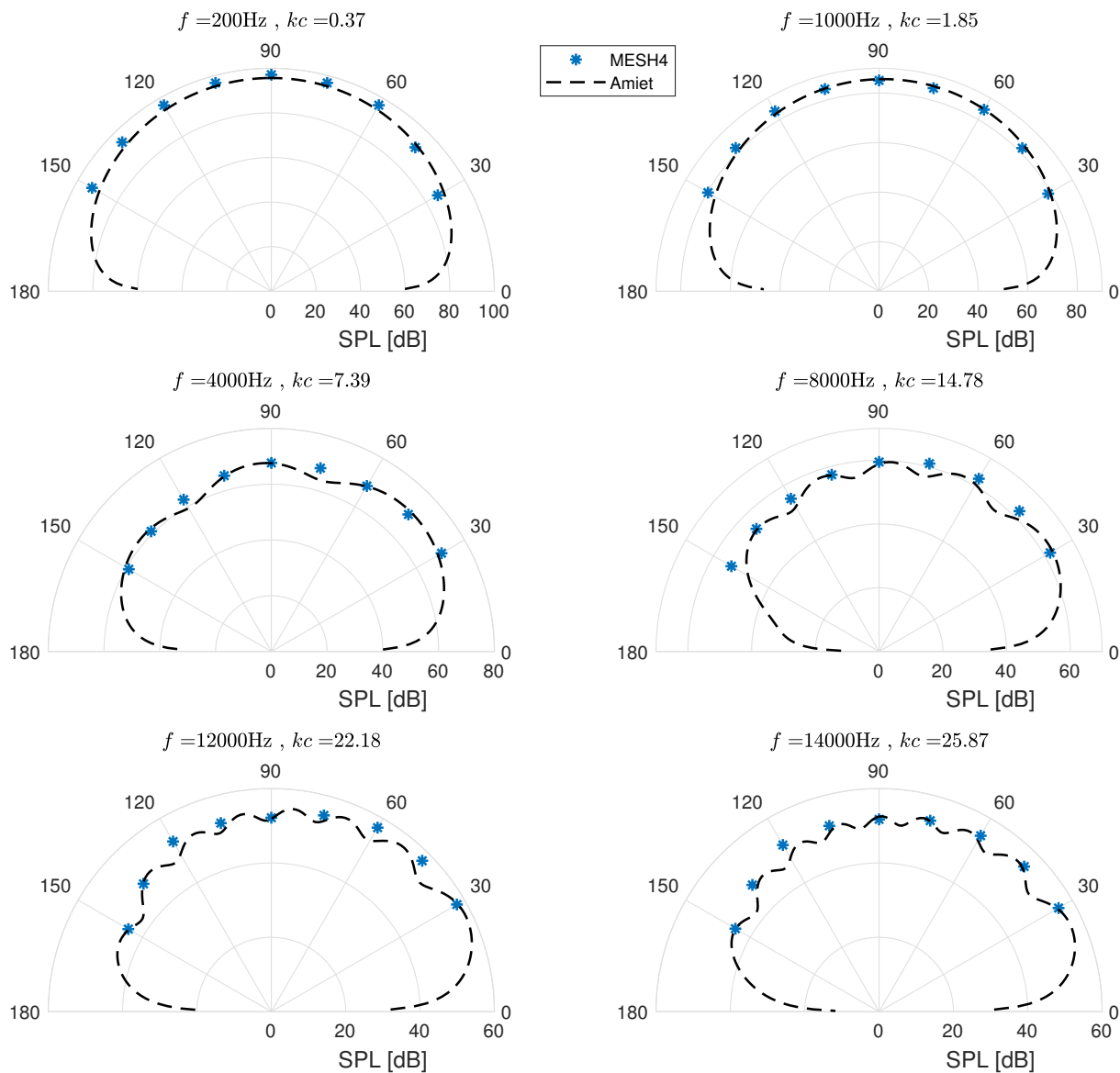
Figure 3.12: Comparison between numerical (MESH4) and analytical results of the directivity of the sound power level, at $R = 8c$ and for six frequencies.
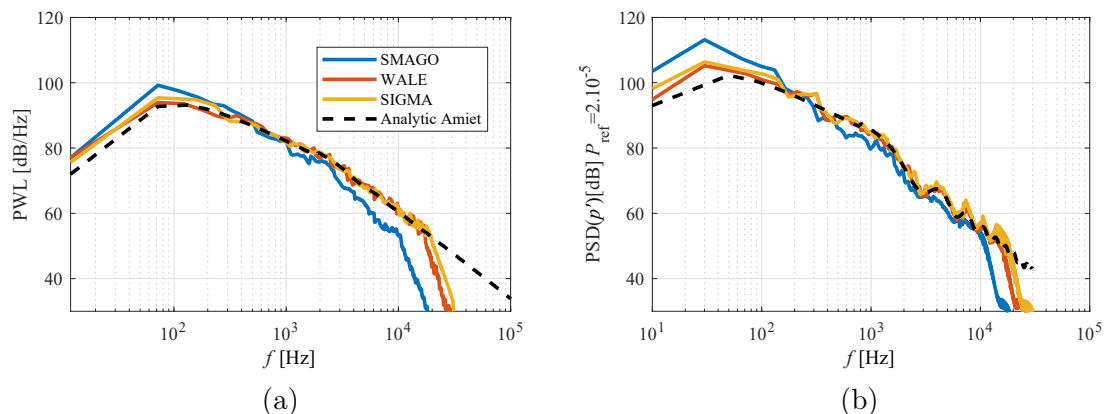
Figure 3.13: Comparison between three different SGS models and TIN Amiet model. (a) Power spectral level PWL at a distance of $8c$. (b) PSD of the pressure fluctuations at a distance of $8c$ normal to plate LE.

good agreement can be noticed for the captured frequency range for the different angles around the LE of the plate. The numerical PSD spectra nicely reproduce the lobes of the analytical solution, which are due to the non-compactness of the acoustic sources on the plate surface.

Moreover, Figure 3.12 shows directivity plots around the plate for different reduced wavenumbers kc, where $k = 2\pi f/c_0$ is the acoustic wavenumber and c_0 the speed of sound in the freestream flow. As kc increases, the non-compactness effects become more important. The directivities are calculated for the sound power spectra at $R = 8c$ for MESH4, and compared to results obtained with Amiet's TIN model. Since the radiated noise is symmetric, only the upper part is represented. For small values of the reduced frequency ($kc = 0.37$ and $kc = 1.86$), the plate is sufficiently compact relatively to the gust wavelength ($\lambda/c = 17$ and $\lambda/c = 3.4$ for $kc = 0.37$ and $kc = 1.86$, respectively) and the acoustic field can be assimilated to a unique dipole, as observed for the first two wavenumbers plotted in Figure 3.12. As the frequency increases, kc increases and the wavelength relative to the chord length decreases. Directivities become more and more complex and multiple lobes start to appear highlighting non-compactness effects related to the finite chord length of the plate. These effects can be observed in Figure 3.12 for frequencies larger than 4000 Hz ($kc > 7.39$ and $\lambda/c < 0.85$). In all cases, a good agreement between numerical and analytical results is observed.

Influence of sub-grid scale (SGS) model

Three different SGS models are compared, Smagorinisky (SMAGO) [250], wall adapting local-eddy viscosity (WALE) [182] and SIGMA [183] models. Figure 3.13 shows a comparison of the PWL and the PSD of the pressure fluctuations at a distance of $8c$ in the direction normal to the LE, between the different SGS models and the analytical solution obtained by Amiet's TIN model. MESH4 (Table 3.1) is used for the three numerical cases. Results obtained by WALE and SIGMA models are very similar and match very well the analytical solution. A slight increase of the cut-off frequency is noticed by the SIGMA model. However, significant differences can be observed for the SMAGO model, which overestimates the sound level at low frequencies (below 500 Hz) and underestimates it at larger frequencies (beyond 2000 Hz).

Compared to the spectra obtained using WALE and SIGMA models, when using SMAGO model, the linear slope in the spectrum at mid to high frequencies is not well predicted and the cut-off frequency is reduced. Thus, for the same mesh refinement, SMAGO model appears to be too dissipative. In addition, by observing the PSD of the pressure fluctuations (Figure 3.13 (b)), the lobes corresponding to non-compactness effects are also better reproduced by the SIGMA and the WALE models than by the SMAGO model. Consequently, for the same computational cost, the WALE and SIGMA models are more accurate in the far-field noise prediction than the SMAGO model, especially in the high frequency range.

Influence of numerical parameters ———————————— **Summary**

Comparison with Amiet's TIN model

- Turbulent energy spectrum: a modified Von Karman spectrum is used to fit the numerical spectrum as an input for Amiet's model.

- All other inputs are directly taken from the numerical simulations.

Parametric study

- Far-field mesh refinement: for a cell size of $\lambda_c/13$ with $f_c = 20\,\text{kHz}$, the amplitudes of the pressure spectra are successfully captured up to a frequency of 20 kHz at a distance of 47 acoustic wavelengths with the present numerical setup (mainly with the third order numerical scheme TTGC).

- Influence of subgrid scale model: the WALE and SIGMA models allow to obtain similar noise predictions in good agreement with the analytical model, while the Smagorinsky model underestimates the acoustic levels at mid and high frequencies.

3.2.4 Influence of physical parameters

Following the successful validation of the numerical LES approach in the prediction of the TIN of a flat plate, the effects of two physical parameters on the predicted noise are investigated, the plate thickness e and the flow angle of attack α. The other geometrical parameters, the operating conditions and the turbulence synthesizing method are kept unchanged in this section. MESH4 is used for this study.

Influence of the plate thickness

The effects of the plate thickness on the generated TIN are investigated by performing LES for four different thicknesses, $e/c = 1\%, 2\%, 4\%$ and 8%. The PWL obtained from the LES noise predictions for the various thicknesses are compared with Amiet analytical model in Figure 3.14, for which the input data are taken from the LES corresponding to thickness $e/c = 1\%$. It can be noticed that noise reduction induced by thickness is more pronounced at high frequencies for thicker plates, which agrees with reported findings in
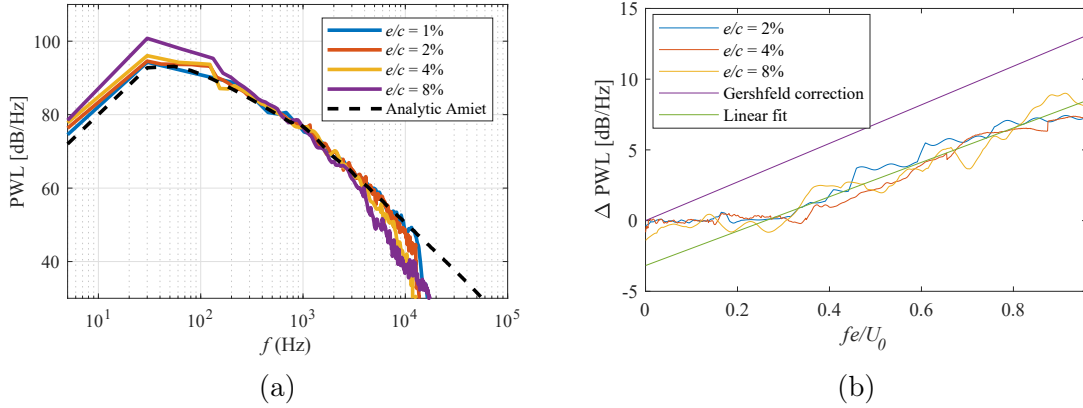
Figure 3.14: (a) Comparison of the power spectral level PWL predictions for the different plate thicknesses, with the analytical solution of Amiet's theory. (b) Noise reduction $\Delta\text{PWL} = \text{PWL}_{e=0} - \text{PWL}_e$ due to plate thickness.

the literature [68, 254, 189]. The frequency above which the noise becomes sensitive to the thickness of the plate is about $4\,\text{kHz}$ for $e/c = 8\%$, whereas it is about $7.8\,\text{kHz}$ for $e/c = 4\%$. This shows that the frequency for which the plate response varies due to the thickness effects is reduced when the plate's thickness is increased. In addition, slight increase of the noise at low frequencies can also be noticed with the increase of thickness.

To further study the trend of TIN when varying the plate thickness, the noise reduction is quantified by calculating $\Delta\text{PWL} = \text{PWL}_{e=0} - \text{PWL}_e$, where the subscript $e = 0$ refers to the Amiet solution for a flat plate and the subscript e refers to the numerical solutions for each thickness. Figure 3.14 (b) shows ΔPWL as a function of the reduced frequency based on the thickness, $K_t = fe/U_0$. In addition to the numerical predictions, the correction factor proposed by Gershfeld [67] is plotted. This factor is used to account for the effects of thickness on TIN, and is given by:

$$\Delta\text{PWL} = 10log_{10}(exp(\pi\frac{fe}{U_0})) = log_{10}(exp(10\pi))\frac{fe}{U_0} \tag{3.8}$$

It can be noticed that contributions from the various plate thicknesses collapse onto a single trend. This suggests that $K_t = fe/U_0$ is a good non-dimensional parameter for ΔPWL and is the dominant factor that controls the noise reduction due to thickness. For $K_t > 0.4$, a linear slope, similar to Gershfeld's correction term [67], is observed for the different thicknesses. Although the slope is similar, Gershfeld's model [67] significantly over-predicts noise reduction at high frequencies for the cases studied here. Alternatively, a representative estimation of ΔPWL can be obtained by using a least-squares method to linearly fit the numerical predictions. The best fit for ΔPWL in dB for the cases studied here is also showed in Figure 3.14 (b) and is given as,

$$\Delta PWL \approx 0; \quad Kt < 0.3$$
$$\Delta PWL = -3.18 + 12.16 * \frac{fe}{U_0}; \quad Kt > 0.3 \tag{3.9}$$

The mechanism underlying noise reduction due to the increase of the plate thickness is investigated here. Figure 3.15 shows a comparison of P_{rms} distributions along the upper surface of the front 20% of the chord length of the plate. P_{rms} values have all been
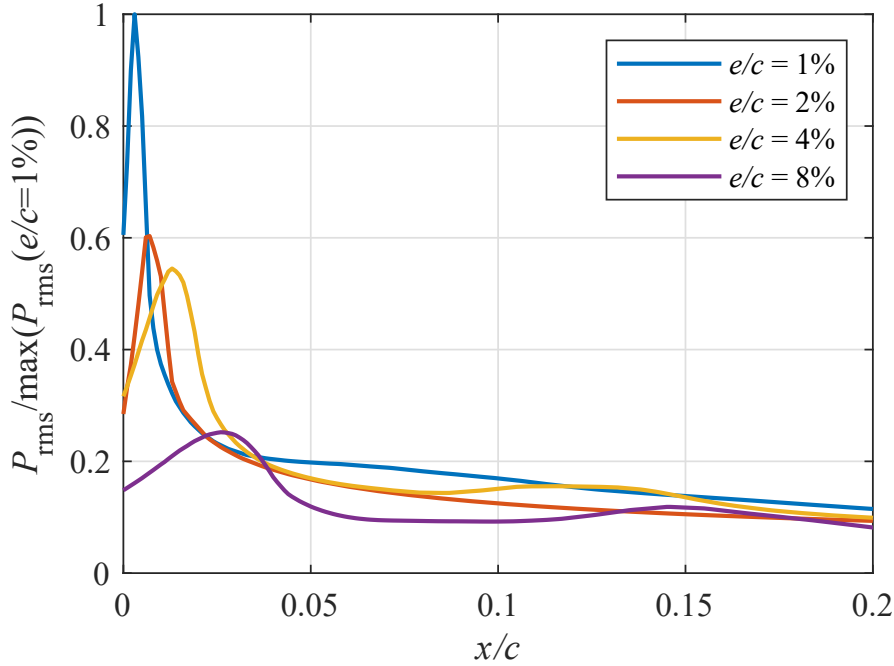
Figure 3.15: Axial distribution of P_{rms} for the different thicknesses along the upper surface of the plate.

normalized by the maximum P_{rms} for the case $e/c = 1$ %. As the thickness increases, the peak of P_{rms} close to the LE decreases and moves further downstream. This decrease of the surface pressure response may explain the reduction of the far-field noise predictions with the plate thickness, and agrees with the conclusions of Chiang and Fleeter [38] who used an analytical method to study the effects of thickness on the surface pressure response of an oscillating airfoil.

P_{rms} reduction with the thickness can be explained by the flow distortion in the stagnation region of the plate leading edge. Figure 3.16 shows the distribution of the mean streamwise velocity component, u, normalized by the freestream velocity magnitude, U_0, at different locations upstream of the plate LE for different thicknesses. For the first location, at 25% of the chord length upstream of the LE ($x/c = -0.25$ and $y/c = 0$), u/U_0 shows a small reduction of about 5% of the freestream value for $e/c = 8$%, which means that a small distortion of the turbulent structures would be expected at this location. Closer to the LE, the streamwise velocity component becomes more affected by the presence of the LE. At $0.02c$ upstream of the LE, a reduction of 50% of u/U_0 can be noticed for $e/c = 8$%, whereas this reduction is about 25% for $e/c = 4$%. Thus, the distortion of turbulent structures is shifted further upstream in the larger stagnation region near the leading edge as the thickness increases. Consequently, the magnitude of the turbulent velocities interacting with the plate and generating noise is expected to decrease with the thickness as it was pointed out by previous studies in the literature [68, 124]. This is verified in Figure 3.17 by plotting the distribution of the RMS transverse velocity fluctuations, v_{rms}, at different locations upstream of the plate LE for different thicknesses. As the thickness increases, the maximum value of v_{rms} decreases in the stagnation region of the plate. Thus, with the increase of the plate thickness, the incident turbulent velocity is more distorted by the velocity gradients in the stagnation region such that the distribution of the velocity fluctuations across the leading edge is smoothed and its amplitude
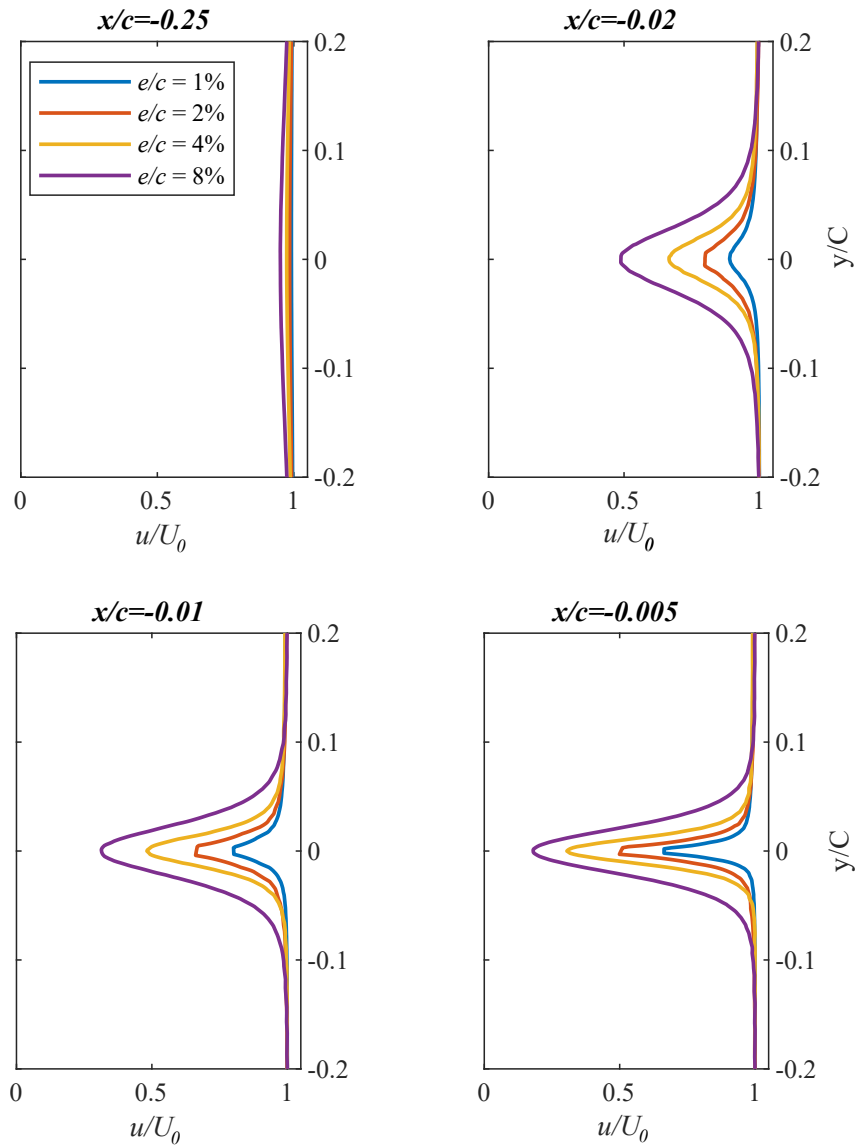
Figure 3.16: Transverse distribution of the normalized streamwise velocity u/U_0, at different axial positions upstream of the plate LE.
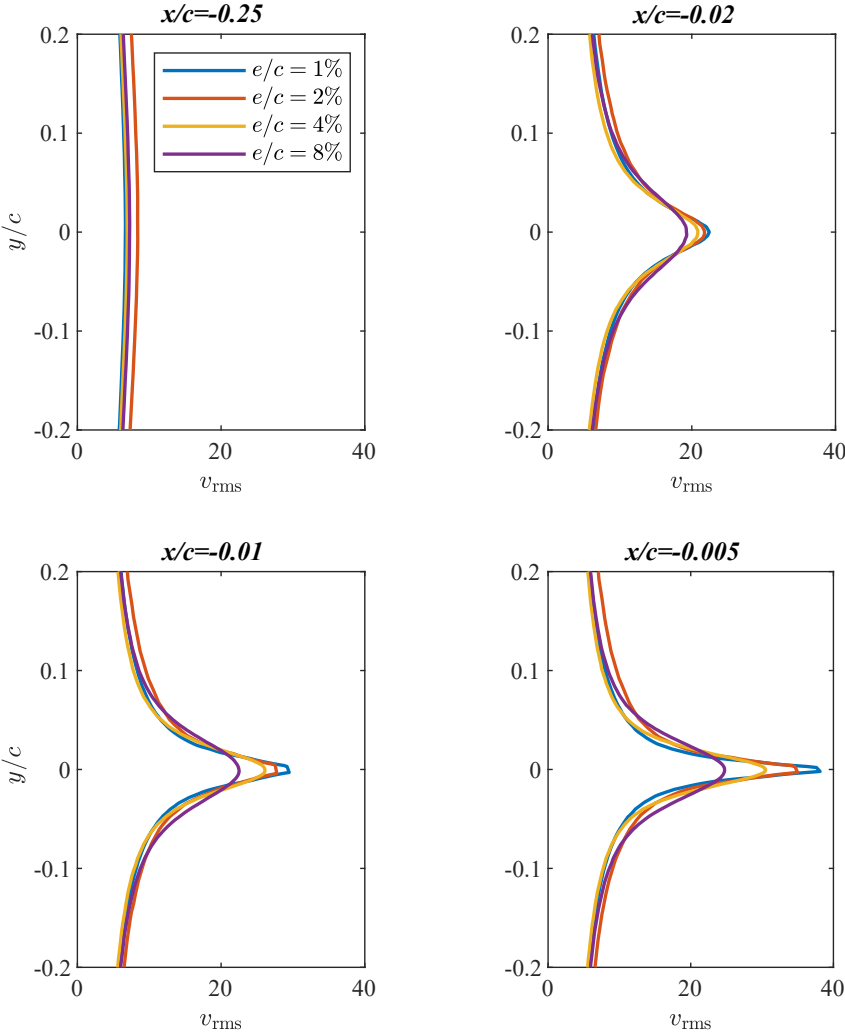
Figure 3.17: Transverse distribution of the RMS transverse velocity fluctuations v_{rms}, at different axial positions upstream of the plate LE.
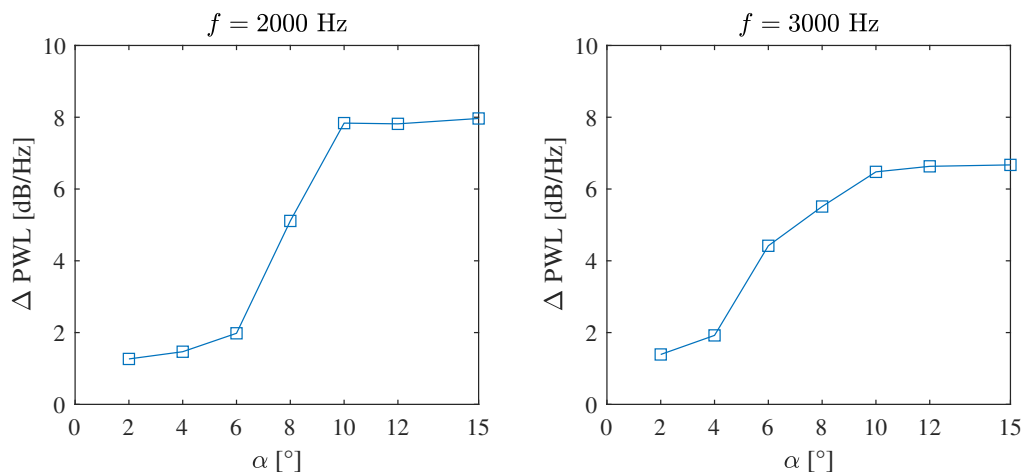
Figure 3.18: Effect of the angle of attack on the noise radiated in terms of $\Delta\text{PWL} = \text{PWL}_{\text{AoA}} - \text{PWL}_{\text{AoA}=0}$ for two different frequencies, $f = 2$ KHz (left) and $f = 3$ KHz (right).

is reduced.

Influence of the angle of attack

The effects of the angle of attack on the generated TIN are investigated by performing LES for different angles of attack of the flow upstream of the plate, $\alpha = 2°, 4°, 6°, 8°, 10°, 12°, 15°$. Figure 3.18 shows $\Delta\text{PWL} = \text{PWL}_{\alpha} - \text{PWL}_{\alpha=0°}$, the variation in PWL between the corresponding angle of attack, α, and the solution obtained by Amiet's model, $\alpha = 0°$, at two different frequencies, 2 kHz and 3 kHz. Three regimes can be identified. The increase of PWL is first negligible for low angles of attack (below 6°), then it significantly grows and saturates for the larger angles, beyond 10°.

To understand the origin of the additional noise, the flow field around the plate is investigated using instantaneous fields of the streamwise velocity component u around the plate, at different angles of attack, in Figure 3.19. The increase of α eventually leads to a separation and the formation of vortices at the plate LE. However, for $\alpha < 6°$, no significant vortex can be noticed. From 6° to 10°, the LE separation vortex is well formed and the flow exhibits a local separation at the LE followed by a reattachment close to the TE. Beyond 10°, the vortex detaches from the plate. These observations, combined with the noise level trend observed in Figure 3.18, suggest that the fast increase of the noise (from $\alpha = 6°$ to $\alpha = 10°$) is associated with the onset of the leading-edge vortex. This also indicates that, for high angles of attack, the TIN is not the dominant noise source. When the vortex leaves the plate, the noise generation mechanism is modified, which may explain the slope change of ΔPWL for $\alpha > 10°$.

Influence of physical parameters ———————————————— **Summary**

Influence of the plate thickness (e).

- The increase of the thickness leads to a reduction of the noise at high frequencies.
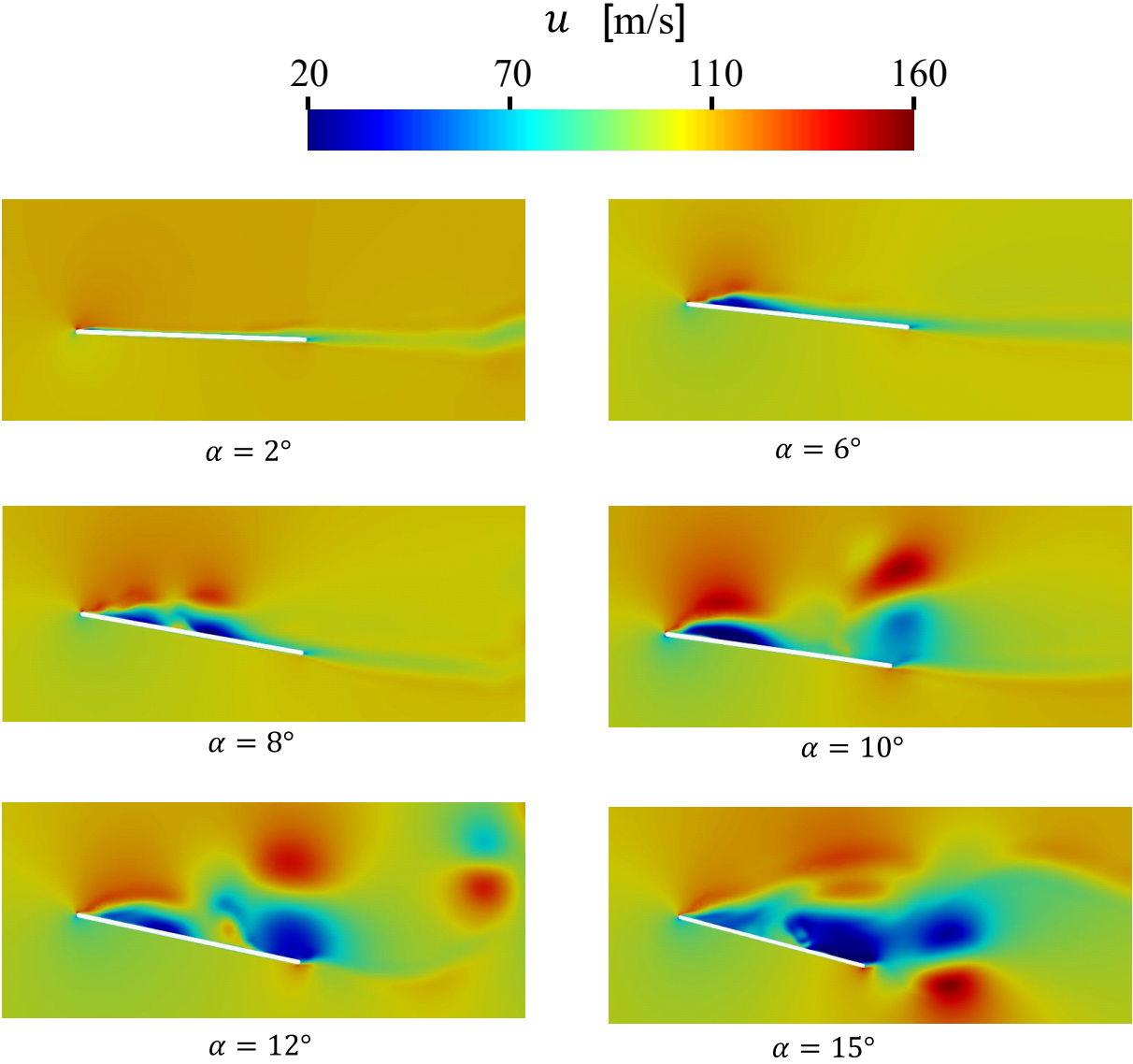
Figure 3.19: Instantaneous fields of the streamwise velocity component for different angles of attack around the plate.

- As the thickness increases, the frequency above which the noise becomes sensitive to the thickness decreases.

- The noise reduction due to the thickness is controlled by the parameter $K_t = fe/U_0$. All the reductions from the various plate thicknesses collapse onto a single trend when plotting ΔPWL in function of K_t.

Influence of the angle of attack (α).

- The angle of attack leads to a far-field noise increase.

- With the increase of α, three regimes can be identified,

  - $\alpha < 6°$: the noise increase is relatively small.
  - $6° < \alpha < 10°$: the noise significantly increases with α.
  - $\alpha > 10°$: saturation of the noise increase.

- The additional noise due to the increase of the angle of attack is explained by the formation of a separation vortex close to the LE of the plate.

3.3 Case 2: Trailing edge noise

This case considers the flow around a flat plate with a sharp TE for a freestream velocity $U_0 = 100$ m/s, at atmospheric conditions ($\rho_0 = 1.177$ kg/m^3, $T_0 = 300$ K, $\mu_0 = 1.81 \times 10^{-5}$ Pa.s). The chord length is $c = 0.1$ m and the plate thickness is $e = c/100$. The Reynolds number based on the chord length is Re$_c = 10^6$.

3.3.1 Input parameters for Amiet TEN model

In this section, the main parameters used as input for Amiet's TEN model (given in Eq. 3.2), as well as some analytical and empirical approaches from the literature to model these parameters, are briefly presented.

Turbulent boundary layer

TEN is directly related to the turbulent boundary layer characteristics. For flows around airfoils, the boundary layers are considered laminar for low Reynolds numbers (Re $\lesssim 10^5$), where Re is based on the external velocity and a characteristic length (usually the chord length). For higher Reynolds numbers, a transition zone appears, and is followed by a turbulent flow. This latter is characterized by a chaotic and non-linear motion with a rotational and three-dimensional velocity field.

The real difficulty of the numerical resolution of a turbulent boundary layer is the large variety of characteristic length, velocity and pressure scales encountered in this region. A two-layer model is widely used to analyze the turbulent boundary layer. Near the wall, small turbulent structures are found, and the motion is related to the fluid viscosity and
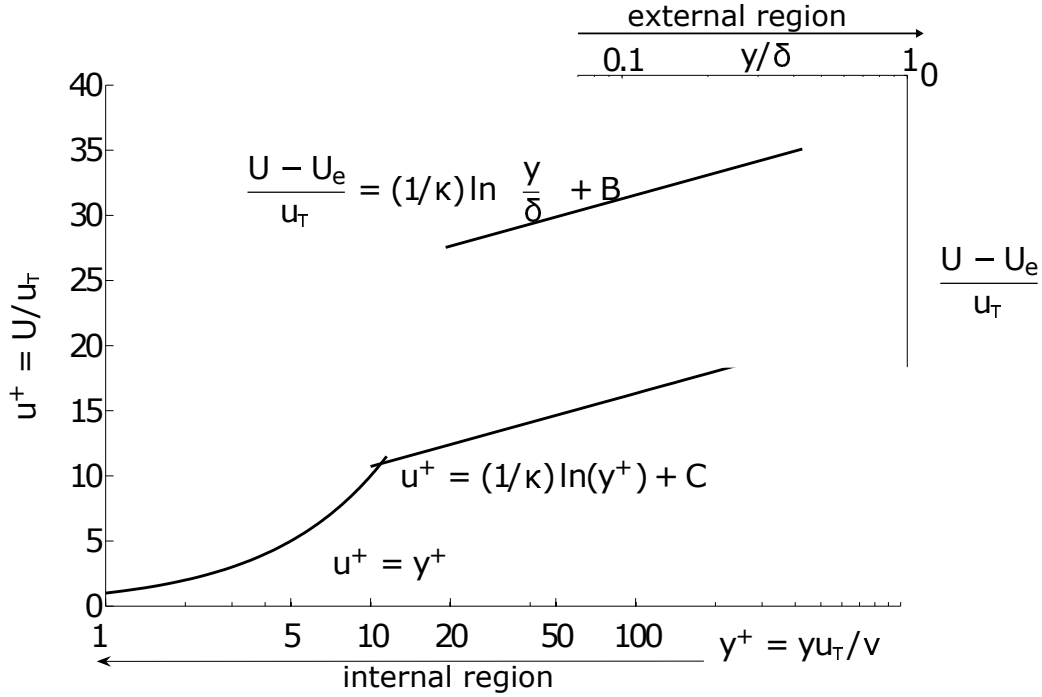
Figure 3.20: Dimensionless velocity profiles in the internal and external regions of a boundary layer. Source: J. Cousteix [45]

the wall shear stress τ_w defined as,

$$\tau_w = \mu \frac{du}{dy}\bigg|_{y=0} \tag{3.10}$$

where μ is the fluid dynamic velocity and y is the coordinate normal to the wall.

Larger structures are found for distances further away from the wall, where the behavior of the boundary layer is controlled by the external velocity U_e and the boundary layer thickness δ. This latter is usually defined as the distance from the wall for which the mean streamwise velocity reaches 99 % of its external value $u(y = \delta) = 0.99 U_e$.

The inner region is usually described by two dimensionless variables known as the inner variables, the normalized streamwise velocity, $u^+ = u/u_\tau$, and the dimensionless normal wall distance, $y^+ = y u_\tau/\nu$, where $u_\tau = \sqrt{\tau_w/\rho}$ is the friction velocity. This region can be divided into three zones.

- The laminar sub-layer, also called the viscous sub-layer, characterized by a linear evolution of the velocity with the distance to the wall, such that $u^+ = y^+$ for $y^+ < 7$.

- The inertial logarithmic zone, characterized by a logarithmic evolution of the velocity, such that $u^+ = (1/\kappa)ln(y^+) + C$, where $\kappa = 0.41$ is the Von Kármán constant and $C = 5.1$, for $y^+ > 20$.

- The buffer layer between the viscous sub-layer and the logarithmic zone ($7 < y^+ < 20$).

These regions are illustrated in Figure 3.20.

93
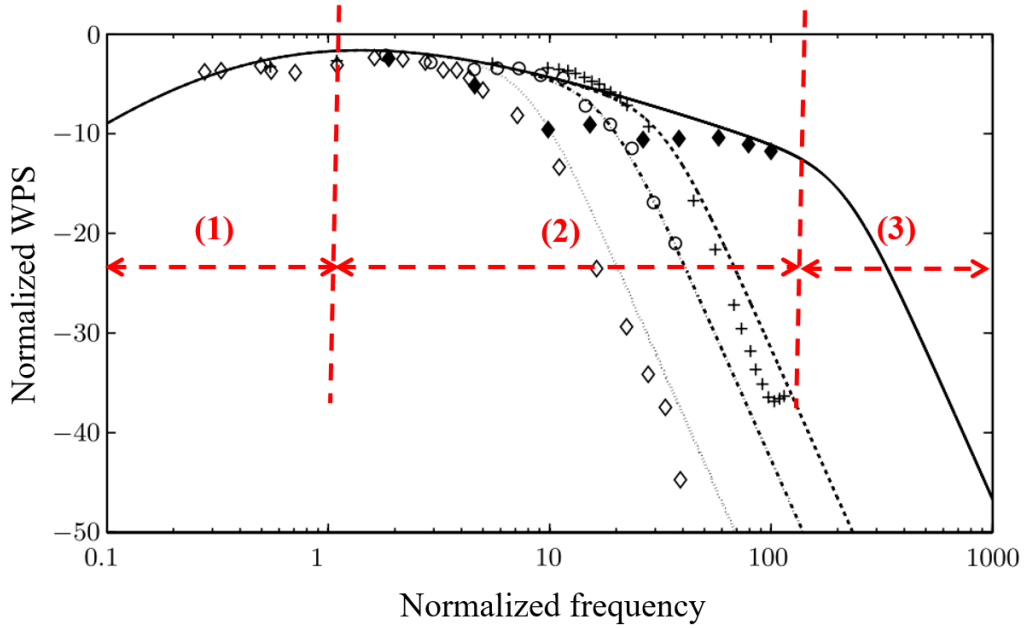
Figure 3.21: Typical experimental normalized wall pressure spectra. Source: Y. Rozenberg *et al.* [228]

Van Driest [263] provided an universal streamwise velocity profile based on an analysis that yields a continuous streamwise velocity and shear stress distribution for the turbulent flow near a smooth wall, given by,

$$u^+ = \int_0^{y^+} \frac{2dy^+}{1 + \sqrt{1 + K^2 y^{+2}[1 - exp(-y^+/A^+)]^2}} \qquad (3.11)$$

where $A^+ = 27$ and $K = 0.4$ are constants. This analytical expression will be used for validation purposes in the following sections.

The boundary layer can also be described by integral variables, the boundary layer displacement thickness δ_1 and the momentum thickness δ_2, defined as:

$$\delta_1 = \int_0^{\delta} 1 - \frac{\rho U(y)}{\rho_0 U_0} dy \qquad \delta_2 = \int_0^{\delta} \frac{\rho U(y)}{\rho_0 U_0}(1 - \frac{\rho U(y)}{\rho_0 U_0})dy. \qquad (3.12)$$

Physically, the displacement thickness represents the loss in mass flow in the region occupied by the boundary layer compared to an inviscid flow. The momentum thickness δ_2 is defined such that the total loss of momentum flux is equivalent to the removal of momentum through a distance δ_2. We can also define the form factor $H_{12} = \delta_1/\delta_2$, which characterizes the type of the boundary layer, whether it is laminar ($H_{12} = 2.6$), turbulent ($H_{12} \approx 1.4$) or at the separation point ($H_{12} = 2.76 \pm 0.23$) [31].

Wall Pressure Spectrum models

Typical Wall Pressure Spectra (WPS) are presented in Figure 3.21 for different Reynolds numbers. WPS exhibit three main slopes, (i) a positive slope at low frequencies (region (1) in Figure 3.21), (ii) a slightly negative slope in the overlap region of the spectrum (region (2) in Figure 3.21), and a strong negative slope at high frequencies (region (3) in

Figure 3.21).

In the early models [120], the WPS is either normalized by the internal variables of the boundary layer (τ_w and u_τ), which leads to an acceptable description of experimental data at high frequencies, or by the external variables (U_e, δ, δ_1), which leads to good agreement with experimental data at low frequencies. In more recent models [37, 74, 228], both the effects of the internal and external parameters are considered. Among the models existing in the literature, four of them are briefly described here, (i) the models of Amiet [7], (ii) Chase–Howe [37], (iii) Goody [74], and (iv) Rozenberg [228]. The models of Goody [74] and Rozenberg [228] are used for validation purposes of the numerical WPS obtained from the different LES performed in this chapter and in Chapter 6. For more details about the semi-empirical models for turbulent boundary-layer WPS, the reader is referred to Hwang *et al.* [103]. All the WPS, ϕ_{pp}, presented in the following use the single-sided convention, $\overline{p'^2} = \int_0^\infty \phi_{pp}(\omega)d\omega$.

- Amiet's model [7]. Based on experimental wall-pressure fluctuations beneath a turbulent boundary layer collected by Willmarth and Roos [278], Amiet [7] proposed an analytical formulation for the WPS (ϕ_{pp}) using the outer variables, given as follows:

$$\frac{\phi_{pp}(\omega)}{\rho_0^2 \delta U_e^3} = 2.10^{-5} \frac{F(\tilde{\omega})}{2} \tag{3.13}$$

where $F(\tilde{\omega}) = (1 + \tilde{\omega} + 0.217\tilde{\omega}^2 + 0.00562\tilde{\omega}^4)^{-1}$ with $\tilde{\omega} = \omega\delta_1/U_e$ and for $0.1 < \tilde{\omega} < 20$. When compared to experimental data, this model presents good results at low frequencies.

- Chase–Howe's model [97]. Using a mix of both internal and external variables, Howe [97] suggests the following formulation for the WPS based on a theoretical approach developed by Chase [37]:

$$\frac{\phi_{pp}(\omega)U_e}{\tau_w^2 \delta_1} = \frac{2\tilde{\omega}^2}{(\tilde{\omega}^2 + 0.0144)^{3/2}} \tag{3.14}$$

This model is applicable at low Mach numbers [97]. Compared to Amiet's model [7] that only uses outer variables, Chase–Howe's model [97] yields better agreement with experimental data due to the use of mixed variables. The Chase–Howe's model [97] scales well at low frequencies (slope of ω^2) and in the overlap region (slope of ω^{-1}), where both inner- and outer-layer scalings can be used. However, the third slope for high frequencies is not correctly captured.

- Goody's model [74]. Goody [74] proposed a semi-empirical model based on the WPS model of Chase–Howe [97, 37], considering the effects of the Reynolds number on the WPS. This model is based on the following criteria.

  1. ϕ_{pp} is proportional to ω^{-5} as ω tends to infinity.
  2. In the overlap region, the spectrum decay is of the order of $\omega^{-0.7}$.
  3. The increase of the Reynolds number increases the extent of the overlap region.
  4. A mix of inner and outer variables are used. For the characteristic length of the outer variables, the boundary layer thickness δ is used instead of the displacement thickness δ_1, considering that the largest coherent structures sizes are of the order of δ.

Consequently, the WPS is formulated as follows,

$$\frac{\phi_{pp}(\omega)U_e}{\tau_w^2\delta} = \frac{C_2(\omega\delta/U_e)^2}{[(\omega\delta/U_e)^{0.75} + C_1]^{3.7} + [C_3(\omega\delta/U_e)]^7} \tag{3.15}$$

where C_1, C_2 and C_3 are empirical constants usually taken as $C_1 = 0.5$, $C_2 = 3$ and $C_3 = 1.1R_T^{-0.57}$, with $R_T = (\delta/U_e)/(\nu/u_\tau^2)$ the ratio of the outer to inner boundary layer time scales. Compared to experimental results, Goody's model [74] shows acceptable results over the whole frequency range, for zero pressure-gradient turbulent boundary layers, for a wide range of Reynolds numbers [103].

- Rozenberg's model [228]. Rozenberg *et al.* [228] have extended Goody's model [74] to consider the effects of adverse pressure gradients. With respect to the model of Goody [74], the following modifications are included:

  1. The displacement thickness δ_1 is used instead of the boundary layer's thickness δ to normalize the WPS.

  2. For an adverse pressure gradient flow, the wall shear stress is replaced by the maximum shear stress along the normal direction in the boundary layer.

  3. In the overlap region, the spectrum decays with a slope larger than 0.7.

  4. At high frequencies, the spectrum can decay with a slope larger than 5.

  5. The global level of fluctuating pressure increases as the pressure gradient increases.

Consequently, the final formulation of Rozenberg's model [228] is given by,

$$\frac{\phi_{pp}(\omega)U_e}{\tau_w^2\delta_1} = \frac{[2.82\Delta^2(6.13\Delta^{-0.75} + F_1)^{A_1}][4.2(\frac{0.8(\beta_c+0.5)^{0.75}}{\Delta}) + 1]\tilde{\omega}^2}{[4.76\tilde{\omega}^{0.75} + F_1]^{A_1} + [C_3\tilde{\omega}]^{A_2}} \tag{3.16}$$

where $\Delta = \delta/\delta_1$ and $\beta_c = (\delta_2/\tau_w)(\mathrm{d}p/\mathrm{d}x)$ are the pressure gradient parameters, $A_1 = 3.7 + 1.5\beta_c$, $A_2 = \min(3, 19/\sqrt{R_t}) + 7$ and $F_1 = 4.76(\frac{1.4}{\Delta})^{0.75}[0.375A_1 - 1]$. Rozenberg's model model is not used in this chapter since zero pressure-gradient flat plates are simulated. However, this model is used in Chapter 6.

Convection velocity

The convection velocity u_c is usually taken as a constant (60 or 70 % of the streamwise external velocity). However, u_c depends on the frequency and can be deduced from a linear interpolation of the phase of the streamwise cross correlation spectrum obtained from LES data.

The convection velocity can also be predicted from the following empirical law developed by Smol'yakov [252],

$$\frac{u_c}{U_e} = a\frac{\omega_{\delta_1}}{1 + b\omega_{\delta_1}^2} + c \tag{3.17}$$

where $\omega_{\delta_1} = \omega\delta_1/U_e$, $a = 1.6$, $b = 16$ and $c = 0.6$.

It was shown that this empirical model is suitable for zero pressure-gradient flows [252, 233].

Correlation and coherence

The space-time correlation of the pressure fluctuations on the airfoil surface can be used to study the spatial and temporal evolution of the turbulent scales in the boundary layer and is given as,

$$C(x, t, r, \tau) = <p(x,t)p(x+r, t+\tau)> \tag{3.18}$$

The coherence length scale of the source field in the spanwise direction can be used to compute the spanwise correlation length, which is a direct input parameter of Amiet's TEN model. This coherence length scale represents the size of the source region that radiates independently from neighboring sources, at a given frequency, in a statistical sense. The coherence function γ between two points at a position $\mathbf{x}$ and separated by a distance r can be obtained as follow,

$$\gamma^2(\mathbf{x}, \mathbf{r}, \omega) = \frac{|R_{pp}(\mathbf{x}, \mathbf{r}, \omega)|^2}{R_{pp}(\mathbf{x}, 0, \omega) R_{pp}(x + \mathbf{r}, 0, \omega)} \tag{3.19}$$

The cross spectrum function, R_{pp}, is the Fourier transform of the space-time cross-correlation function and is defined as,

$$R_{pp}(\mathbf{x}, \mathbf{r}, \omega) = \int_{-\infty}^{\infty} C(\mathbf{x}, t, \mathbf{r}, \tau) e^{-i\omega\tau} d\tau \tag{3.20}$$

Spanwise correlation length scale

The spanwise correlation length, l_z, can be calculated from the coherence function as,

$$l_z(k_z, \omega) = \int_0^{+\infty} \sqrt{\gamma^2(\Delta z, \omega)} \cos(k_z \Delta z) d\Delta z \tag{3.21}$$

Several empirical models are found in the literature allowing to provide a quick prediction of the spanwise correlation length, l_z, used in Amiet's TEN model. The first model developed by Corcos [44] considers a decrease of l_z with a rate of ω^{-1} and is given as,

$$l_z(\omega) = \frac{\alpha u_c}{\omega} \tag{3.22}$$

where α is usually between 1.4 and 2.1. This model is only valid at high frequencies.

Another model introduced by Guedel *et al.* [88], which was obtained by averaging experimental data performed on airfoils at different angles of attack, is given as,

$$l_z(\omega) = \delta_1 \frac{(0.05 + 6.8\tilde{\omega}^2)}{0.12 + 5\tilde{\omega}^3} \tag{3.23}$$

where $\tilde{\omega} = \omega\delta_1/u_c$.

In order to correct the low-frequency scales predicted by the model of Corcos [44], an empirical model has been proposed by Efimtsov [57] that introduces the effects of the boundary layer thickness on the WPS. The results obtained by Efimtsov [57] are derived from an extensive series of measurements on airfoils, over a range of Mach number $0.41 < M < 2.1$. For $M < 0.75$, l_z is given as,

$$l_z(\omega) = \delta[(\frac{a_1 \omega_e}{u_c/u_\tau})^2 + \frac{a_2^2}{\omega_e^2 + (a_2/a_3)^2}]^{-1/2} \tag{3.24}$$

where $\omega_e = \omega\delta/u_\tau$, $a_1 = 0.77$, $a_2 = 548$ and $a_3 = 13.5$.

Finally, Salze *et al.* [233] derived a model based on Efimtsov's model [57] to correctly evaluate l_z over the whole frequency range, by replacing δ by δ_1 and recasting the expression of l_z as follows,

$$l_z(\omega) = \delta_1 \left[\left(\frac{a_1 \omega_{\delta_1}}{u_c/U_e} \right)^2 + \frac{a_2^2}{\omega_{\delta_1}{}^2 (H_1^2 U_e^+)^2 + (a_2/a_3)^2} \right]^{-1/2} \tag{3.25}$$

where $H_1 = \delta/\delta_1$ and $U_e^+ = U_e/u_\tau$. The nominal values of a_1 to a_3 provided by Efimtsov have also to be modified. To ensure consistency between the models of Efimtsov [57] and Salze [233], the constants $a1$, $a2$ and $a3$ proposed by Salze *et al* [233] ($a_1 = 0.85$, $a_2 = 100$ and $a_3 = 1$) are considered for the two models.

3.3.2   Parameter study nomenclature

A parameter study is performed in order to study the influence of the near-wall modeling, the grid topology and refinement in the near-wall and wake regions, the domain extent and boundary conditions in the spanwise direction, and the tripping methodology. Table 3.2 shows the mesh characteristics and the computational time estimations (CPU time) for the different cases using the SIGMA sub-grid scale model [183].

The nomenclature for these cases is as follows,

[trip method]X[trip position]H[trip height]-[cell type][y$^+$]W[wake cell size]-[span BC/extension]-[SGS]:

- [trip method]: Geom or Source (defined in Section 3.3.3);

- [trip position]: position of the trip as a percentage of the chord length from the LE;

- [trip height]: height of the trip relative the boundary-layer displacement thickness δ_1;

- [cell type]: near-wall cell type, 'P' for prisms and 'T' for tetrahedra;

- [y$^+$]: value of y^+ at the wall. A value around 1 is used for wall-resolved (WR) simulations, while larger values of y^+ indicate wall-modeled (WM) simulations. In the latter cases, a simple wall-model is used, with a dimensionless wall velocity $u^+ = \frac{1}{\kappa} ln(Ay^+)$ for $y^+ > 11.45$, with $\kappa = 0.41$ and $A = 9.2$;

- [wake cell size]: cell size in the wake relative to the Taylor scale, estimated in the wake far from the TE of the plate and given as $\lambda_w = (10\nu k_t/\epsilon)$, where k_t is the turbulence kinetic energy and ϵ is the turbulence dissipation rate;

- [spanwise BC]: 'PERIO' for periodic (by default), 'SYM' for symmetry;

- [spanwise extension]: 'Sp0.1c' and 'Sp1.0c' for 10% and 100% of the chord length, respectively;

- [SGS]: sub-grid scale model. 'SIGMA' for Sigma model [183] (by default), 'WALE' for wall adapting local-eddy viscosity model [182], 'SMAGO-DYN' for Dynamic Smagorinsky model [165].

Table 3.2: Mesh parameters used for the LES cases. N is the total number of cells, Δt the minimum time step, and CPU time an estimation of the computational time.

Mesh	N (10^6)	x^+	y^+	z^+	wake size	Δt $[10^{-9}\text{s}]$	CPU time $[10^3\text{h.NbProc}]$
GeomX10H1-P01W30	3.05	30	1	30	30	6.545	47.9
GeomX10H2-P01W30	3.09	30	1	30	30	6.676	46.9
GeomX10H4-P01W30	3.08	30	1	30	30	6.851	46.1
SourceX10H4-P01W30	3.06	30	1	30	30	6.851	45.8
GeomX10H1-P25W30	2.16	250	25	250	30	49.3	5.77
GeomX10H2-P25W30	2.21	250	25	250	30	73.8	3.93
GeomX10H4-P25W30	2.15	250	25	250	30	77.0	3.66
GeomX10H4-T25W30	2.36	250	25	250	30	64.2	4.84
GeomX10H4-T10W30	3.43	150	10	150	30	22.0	20.52
GeomX10H4-P25W15	3.50	250	25	250	15	77.0	5.98
GeomX10H4-P25W100	1.80	250	25	250	30	77.0	3.07

3.3.3 Influence of numerical parameters

The influence of the different numerical parameters described in section 3.3.2 is presented here.

Influence of the Mesh Type and Refinement at the Wall

The influence of the mesh type near the wall is studied by comparing tetrahedral and prismatic meshes. The trip height corresponding to H4 is used for this comparison since it gives the best transition in WM cases (as it will be shown in the next section). Figure 3.22 shows u^+, the mean streamwise velocity u normalized by the shear velocity u_τ, as a function of the distance to the wall y^+, in wall units, at $x/c = 70\%$. LES results are compared to the analytical solution of VanDriest [263]. The WR case (GeomX10H4-P01W30) shows the best agreement as expected, with a slightly larger value of u^+ in the buffer region when compared to the WM cases. In the WM cases, for the same value of $y^+ = 25$ at the wall and the same CPU cost, a better agreement is found for the prismatic mesh when compared to the tetrahedral one. In order to reach a similar agreement, the tetrahedral mesh needs to be 2.5 times finer at the wall, which leads to $y^+ = 10$.

The influence of the mesh near the wall on the wall pressure spectrum (WPS) in the vicinity of the trailing edge is also analyzed. Figure 3.23 shows the WPS obtained from the LES data, for prismatic and tetrahedral meshes, compared to the empirical solution proposed by Goody [74]. The numerical WPS are normalized by $U_0/\tau_w^2\delta$ and plotted against the reduced frequency $\omega\delta/U_0$. It should be noticed that the WPS is quite sensitive to the mesh type and refinement close to the wall. A very good agreement with the empirical model is obtained in the WR case (GeomX10H4-P01W30), while some discrepancies can be found for the WM cases. For the tetrahedral cases (GeomX10H4-T10W30 and GeomX10H4-T25W30), more discrepancies are visible, particularly at high frequencies.
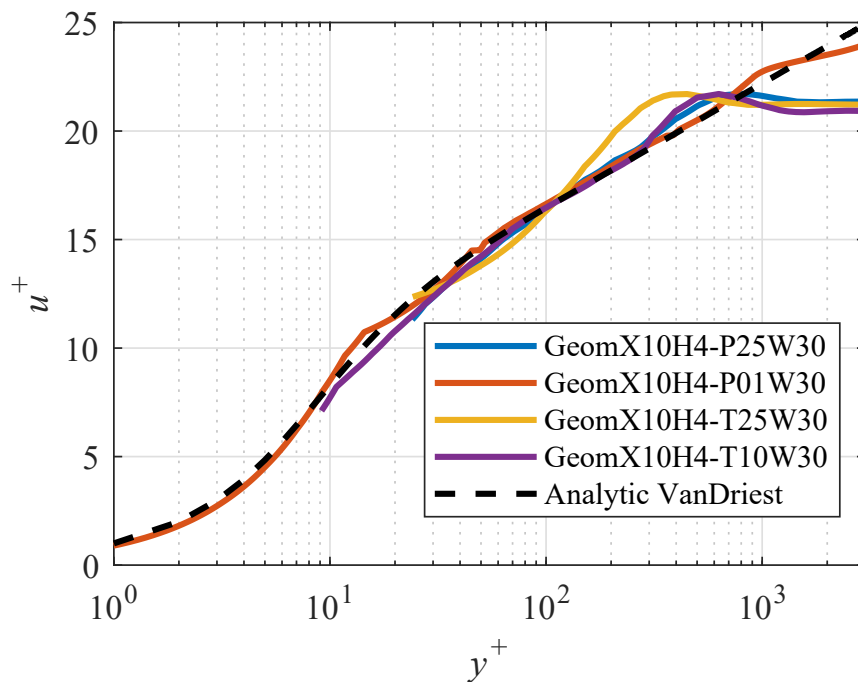
Figure 3.22: Mean velocity as a function of y^+ for different LES cases using different near-wall mesh type and refinements.

Influence of the Tripping Methodology

Two tripping methods are compared in this study. The first one corresponds to a geometric trip on the plate surface, with a rectangular step shape, which requires a dedicated mesh. The second one involves a source term introduced in the streamwise momentum and energy equations, which has been designed to mimic the presence of a rugosity in the flow [16, 17]. The root-mean-square (RMS) velocity profiles u_{rms} for the two tripping methods are compared in Figure 3.24 for WR simulations, at a streamwise position corresponding to $\text{Re}_{\delta_2} = 1968$ (Reynolds number based on the momentum thickness of the boundary layer δ_2). They are also compared to the DNS data from Jimenez [112], available at the same Re_{δ_2} value. Although the large geometric trip ("H4") overestimates the turbulent intensity in the boundary layer, a very good agreement with the DNS data in terms of shape and amplitude is obtained using the source term. Thus, the source term seems to allow for a correct transition without requiring a modification of the geometry and the adaptation of the mesh near the geometrical trip.

Influence of the Trip Height

The influence of the trip height is studied in WM and WR cases. Three heights are considered for each case: $\frac{H_{\text{trip}}}{\delta_1} = 1$, 2, and 4. The instantaneous flow topology is shown in Figure 3.25 for the trip heights H1 (a) and H4 (b), using iso-surfaces of Q-criterion from the LES computations. A transitional and turbulent boundary layer is found on both sides of the plate. The transition is triggered by the geometric trip, with small structures appearing close to the reattachment point. Although similar turbulent structures are observed for both trip heights in the WR cases (not shown here), the WM simulation with the larger trip (H4) shows finer structures than that with the H1 trip. Note that for
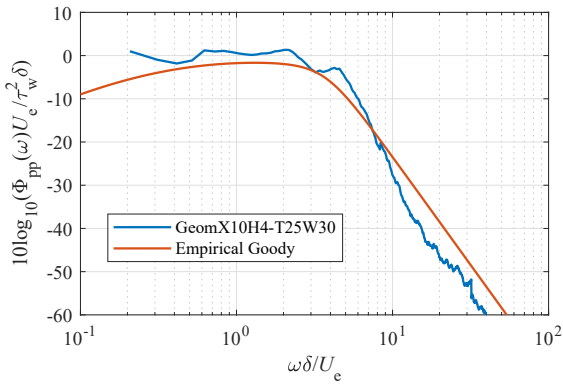
(a) GeomX10H4-T25W30
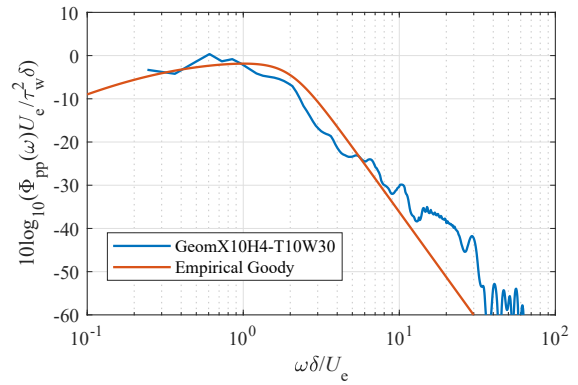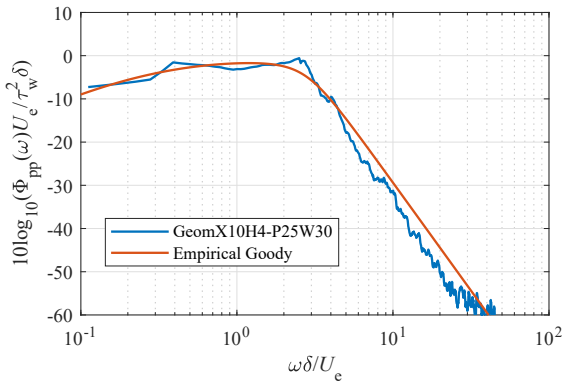
(b) GeomX10H4-T10W30
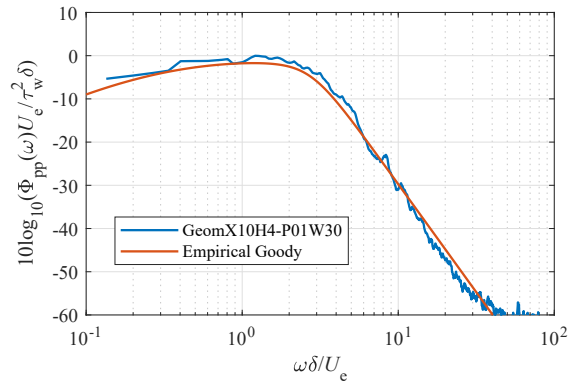
(c) GeomX10H4-P25W30

(d) GeomX10H4-P01W30

Figure 3.23: Wall pressure spectra (WPS) in the vicinity of the plate trailing edge (at 98% of the chord from the leading edge), for (a) GeomX10H4-T25W30, (b) GeomX10H4-T10W30, (c) GeomX10H4-P25W30 and (d) GeomX10H4-P01W30
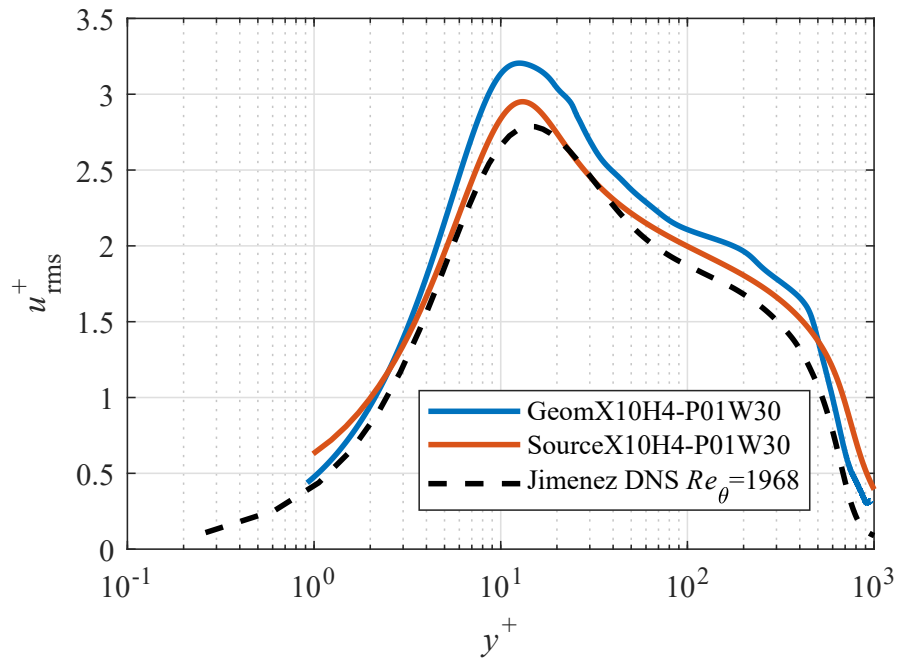
Figure 3.24: RMS velocity as a function of y^+ for two LES cases using different tripping methods.
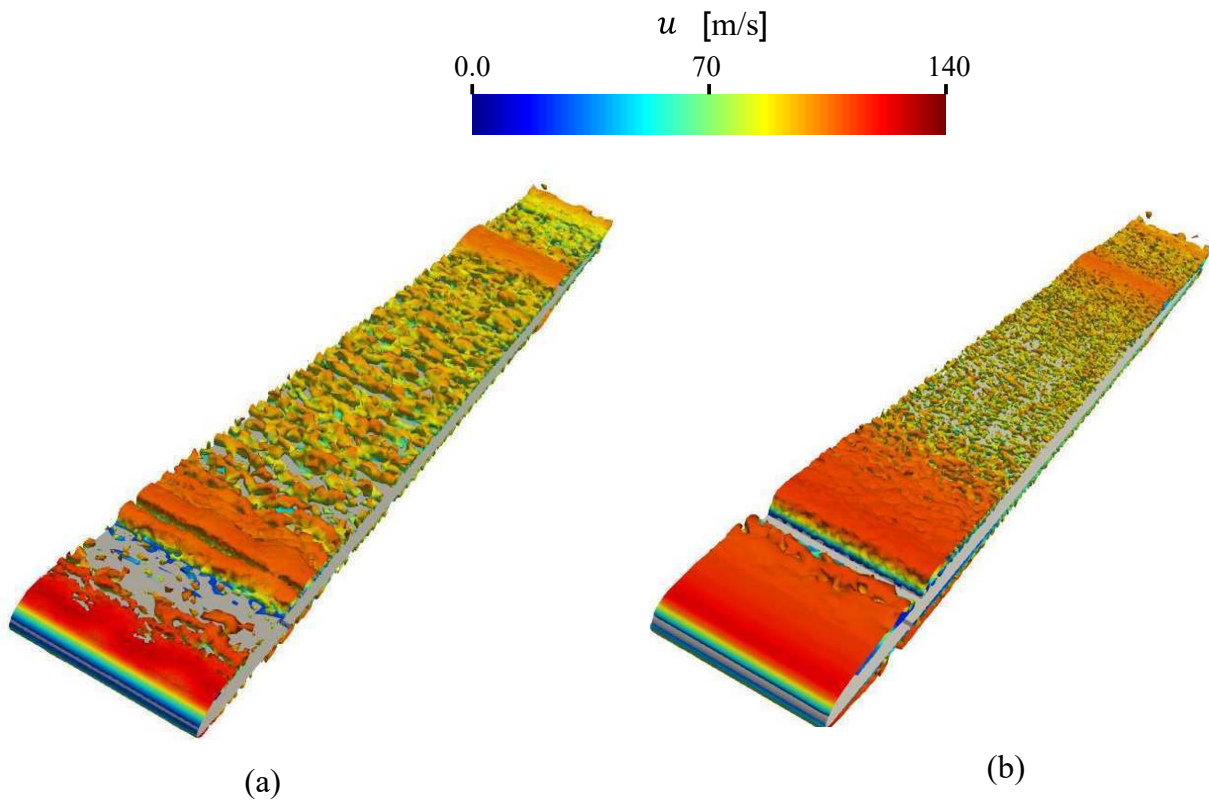
Figure 3.25: Iso-surfaces of Q-criterion ($QC^2/U^2 = 1000$), colored by the velocity magnitude, for (a) GeomX10H1-P25W30 simulation and (b) GeomX10H4-P25W30 simulation.
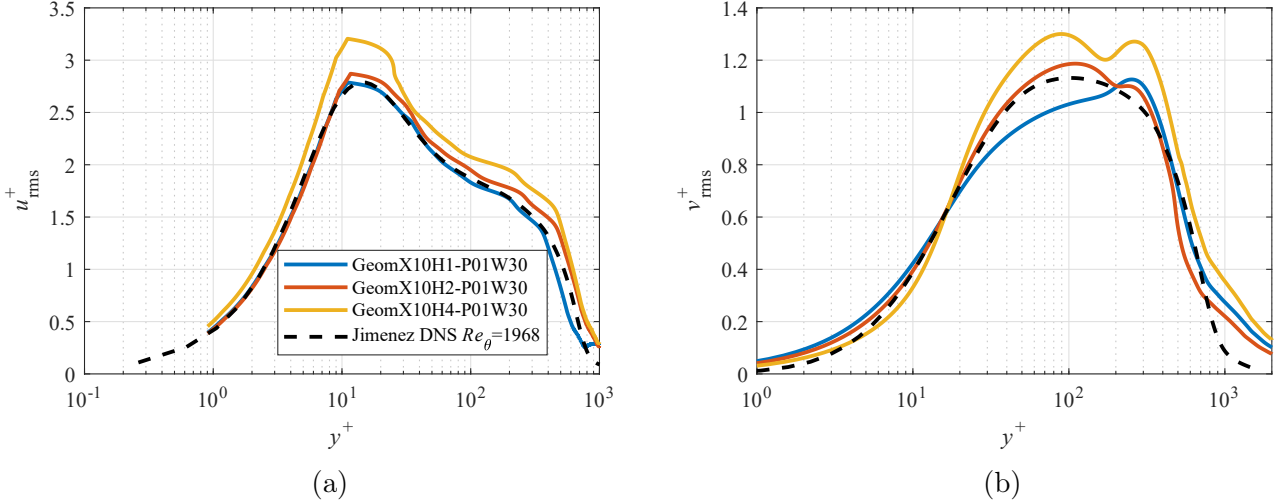
Figure 3.26: Axial (a) and normal (b) RMS velocities as a function of y^+ for different WR LES cases using different trip heights.

the WM cases, the small trip height (H1) is of the order of the first layer of prisms.

Figures 3.26 (a) and (b) show the normalized rms velocity profiles in the boundary layer, for WR cases, at a streamwise position corresponding to a Reynlods number $Re_{\delta_2} = 1968$. The LES results for the different trip heights are compared to DNS data from Jimenez [112] at the same Re_{δ_2}. While very good agreement is found for the cases "H1" and "H2" with the DNS data, a small overestimation of the turbulent intensity can be noticed when using the highest trip "H4".

The development of the turbulent boundary layer is then analyzed in Figure 3.27 by comparing the normalized velocity profiles and the WPS near the trailing edge for the different trip heights. Identical velocity profiles are obtained for the WR cases with the three trip heights, in very good agreement with the analytical solution. However, as it can be seen in Figure 3.27 (a) for the WM cases, the simulation corresponding to the largest trip "H4" shows a better agreement with the analytical solution. Thus, for WM simulations, the trip height must be sufficiently larger than the boundary layer displacement thickness in order to ensure an adequate boundary-layer transition. This effect on the boundary-layer transition can also be found by comparing the WPS in Figure 3.27 (b). Only slight differences are obtained between the WR cases. However, for the WM cases, the highest trip (H4) shows a reduction in the WPS amplitude by about 10 dB/Hz compared to H1 and H2 trips at low to moderate frequencies, but an increased intensity at high frequencies, with a slope closer to the WR cases.

Influence of trip position

The influence of the trip position on the transition of the boundary layer is addressed by considering two axial trip positions, $x = 0.1c$ (GeomX10H4-P25W30) and $x = 0.2c$ (GeomX20H4-P25W30), where $x = 0$ corresponds to the plate LE.

The flow topology is first studied using Q criterion in Figure 3.28. The flow topology corresponds to that observed in the previous section. The boundary layer transition occurs further downstream in the X20 case and slightly bigger turbulent structures are observed.

The boundary-layer normalized velocity profiles are compared with VanDriest analytic model [263] in Figure 3.29. Comparing the different positions for the trip, a better

(a) (b)
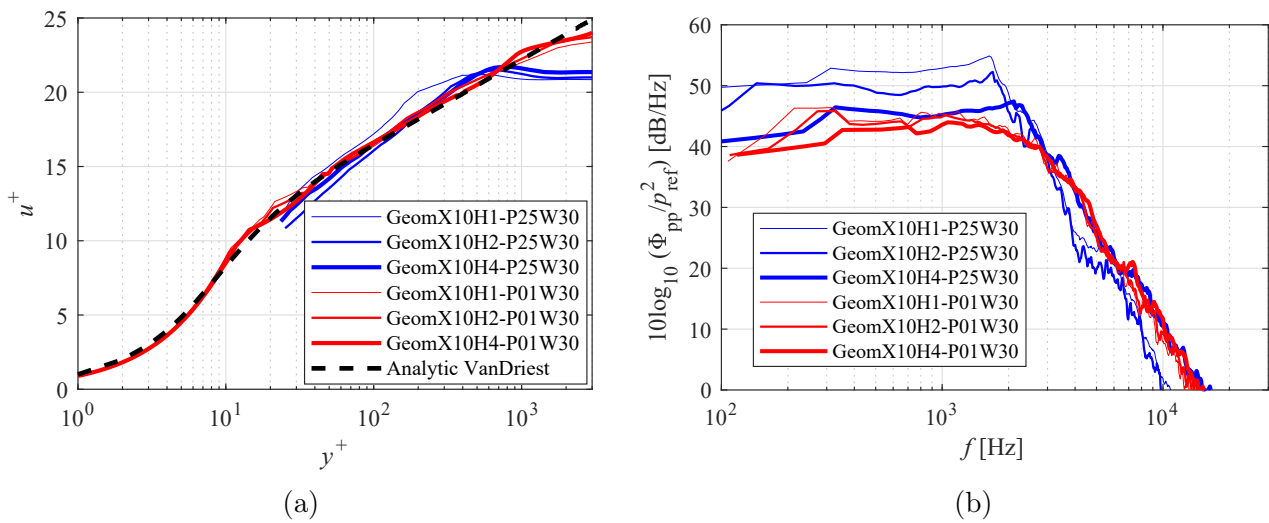
Figure 3.27: Comparison of the mean velocity profiles (a) and WPS (b) in the vicinity of the trailing edge, between LES simulations using different trip heights.

(a) (b)
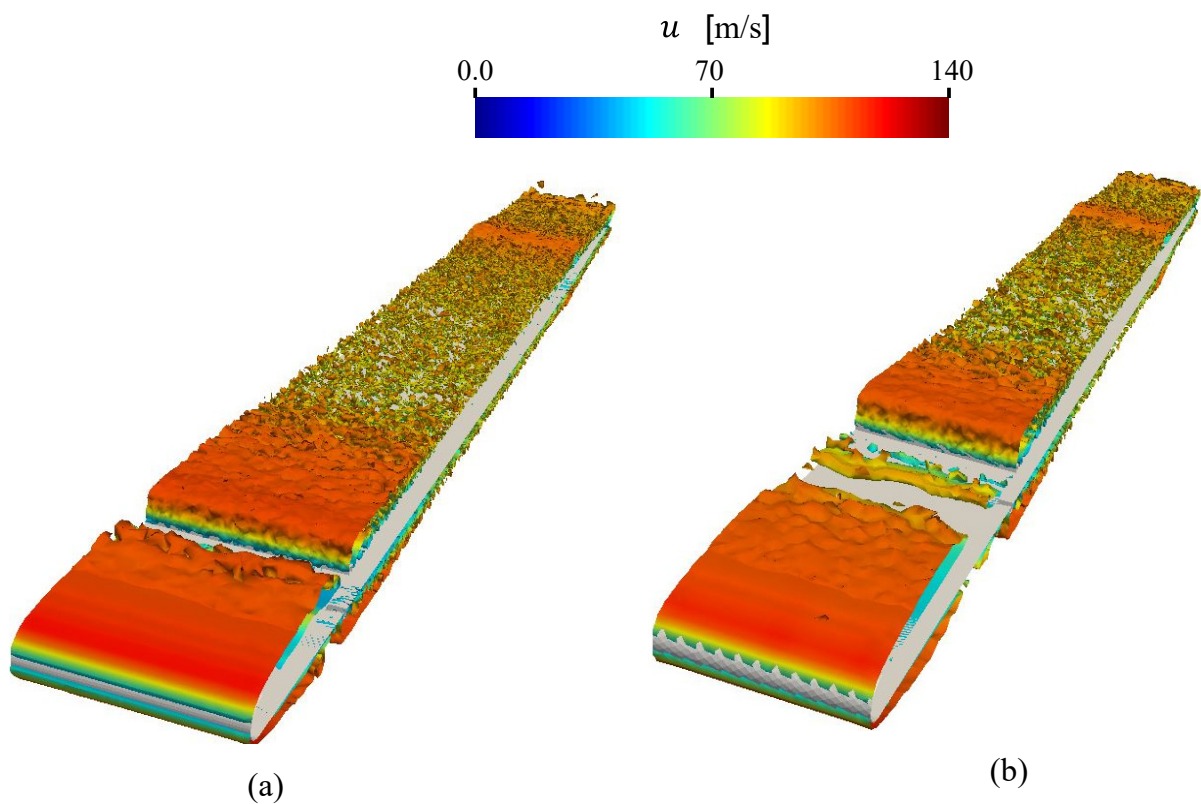
Figure 3.28: Iso-surfaces of Q-criterion ($QC^2/U^2 = 1000$), colored by the velocity magnitude, for (a) GeomX10H4-P25W30 simulation and (b) GeomX20H4-P25W30 simulation.
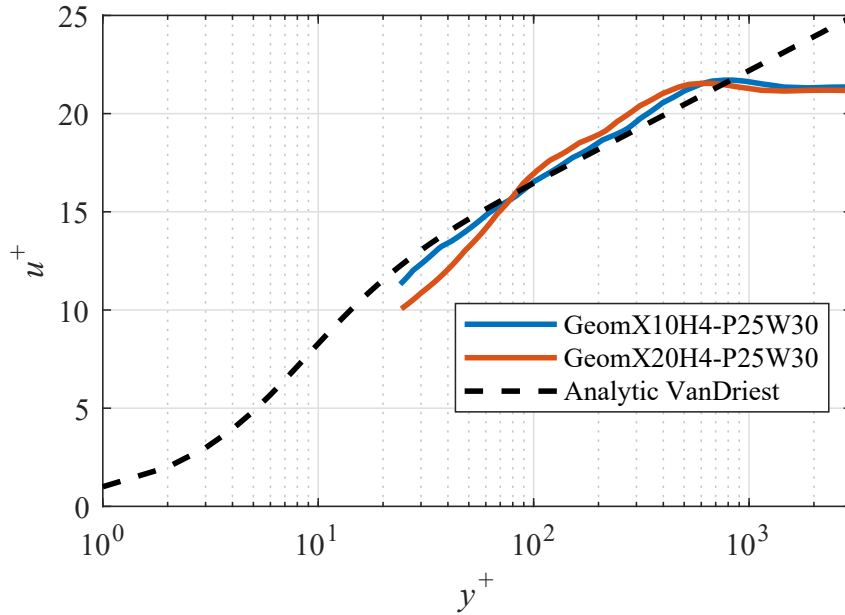
Figure 3.29: Comparison of the normalized velocity profiles between LES cases differing by the streamwise position of the trip.

agreement is obtained for the case X10, showing the necessity of an earlier tripping of the boundary layer. As a consequence, the trip is located at $x = 0.1c$ in all other cases.

Influence of the spanwise boundary condition

The influence of the spanwise boundary condition on the spanwise correlation length, l_z, is examined through a set of WM simulations corresponding to GeomX10H4-P25W30. Periodic ("PERIO") and symmetry ("SYM") boundary conditions are considered. l_z is calculated using the spanwise coherence γ^2 as showed in Eq. 6.9 and Eq. 3.19. Comparisons of γ^2 and l_z between the two boundary conditions are shown in Figures 3.30 and 3.33 respectively. In addition, l_z obtained from a WR case is given in Figure 3.33 (a) as a reference. The LES results are compared to Corcos [44], Guedel [88], Efimtsov [57] and Salze [233] empirical models. The four models use input data from the LES simulations, which slightly differ between WM and WR, leading to some differences in l_z even if the same model is used in both cases. Thus, WR and WM cases cannot be displayed in the same plot.

Except for the models of Efimtsov [57] and Salze [233] that give slightly closer results for l_z, large differences can be found with the other models. For the WR case, a good agreement of the LES with the model of Salze [233] is observed for high frequencies and a slight over-prediction at low to mid frequencies is found, probably due to the domain spanwise extent. The model of Salze [233] can, thus, be used as a reference for the WM cases.

From Figure 3.33 (b), it can be noticed that periodic boundary conditions lead to larger spanwise coherence at low frequencies compared to symmetry boundary condition. Furthermore, periodic boundary conditions lead to a relatively better agreement with the model of Salze [233] at high frequencies ($f > 4\,\text{kHz}$) compared to symmetric boundary conditions, while a slightly higher over-prediction at low to mid frequencies can be noticed. When periodic boundary conditions are used, a perfect correlation is imposed between the
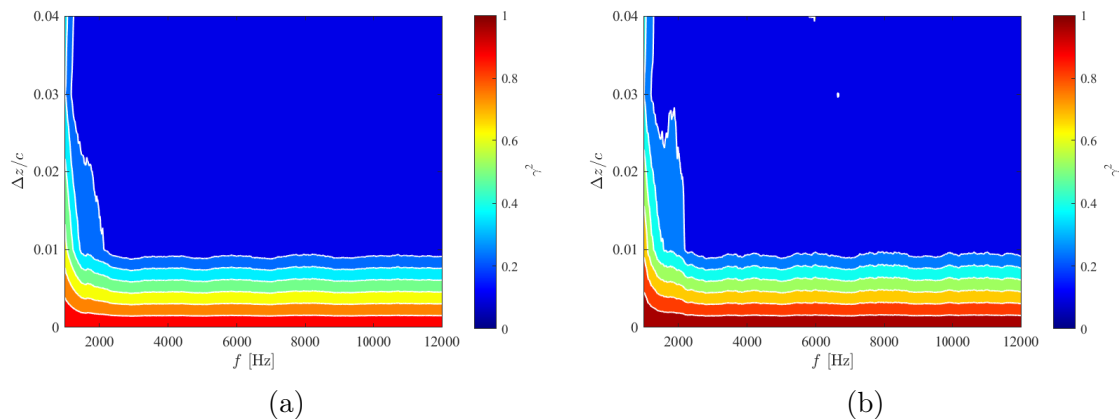
Figure 3.30: Contours of spanwise coherence of the fluctuating pressure on the surface of the plate as a function of frequency and spanwise separation, at streamwise locations $x/c = 0.98$, for computations (a) Geom-X10H4-P25W30-PERIO and (b) Geom-X10H4-P25W30-SYM.

boundaries, but velocity fluctuations normal to the boundary are also allowed. This may explain why l_z is overestimated at low frequencies, which correspond to length scales of the order of the spanwise extent of the domain, and is correctly estimated at intermediate and high frequencies, which are mainly controlled by small scale turbulence. Periodic boundary conditions are used for all the other cases.

Influence of the Spanwise Extent

The influence of the spanwise extent on the flow topology and spanwise correlation length l_z is addressed through a set of WM simulations corresponding to GeomX10H4-P25W30. Two span extents (10% (Sp0.1c) and 100% (Sp1.0c) of the chord length) are investigated. The flow topology is first illustrated using an iso-surface of Q criterion in Figure 3.31 for the two span extents. Both computations present similar flow behaviors. The turbulent structures, formed after the trip, seem to have similar size and intensity in both cases, which proves that the small span extent (Sp0.1c) is able to properly reproduce the turbulent boundary layer development on the surface of the plate.

The comparison between the spanwise correlation lengths for the two span lengths is presented in Figures 3.32 and 3.33 (b). Even if the spanwise extent of the computational domain ($L_{\text{LES}} = 10\,\text{mm} = 0.1c$) appears sufficient when compared to the maximum correlation length ($l_{z,\text{max}} = 3.5$ mm), a larger extent leads to a smaller correlation length at low frequencies, closer to Salze's and Efimtsov's models. It can be observed that the spanwise coherence γ^2 and the correlation length l_z are significantly reduced, particularly at low and mid frequencies, when the large span is considered. However, compared to the model of Salze [233], the range where l_z is over-predicted is restricted to lower frequencies. Consequently, in order to limit computational cost, the shorter span extent is retained.

Influence of the sub-grid scale model

The influence of the sub-grid scale (SGS) turbulence model is studied by considering the dynamic Smagorinsky (SMAGO-DYN) [165], the wall adapting local-eddy viscosity (WALE) [182] and the SIGMA [183] models.

106
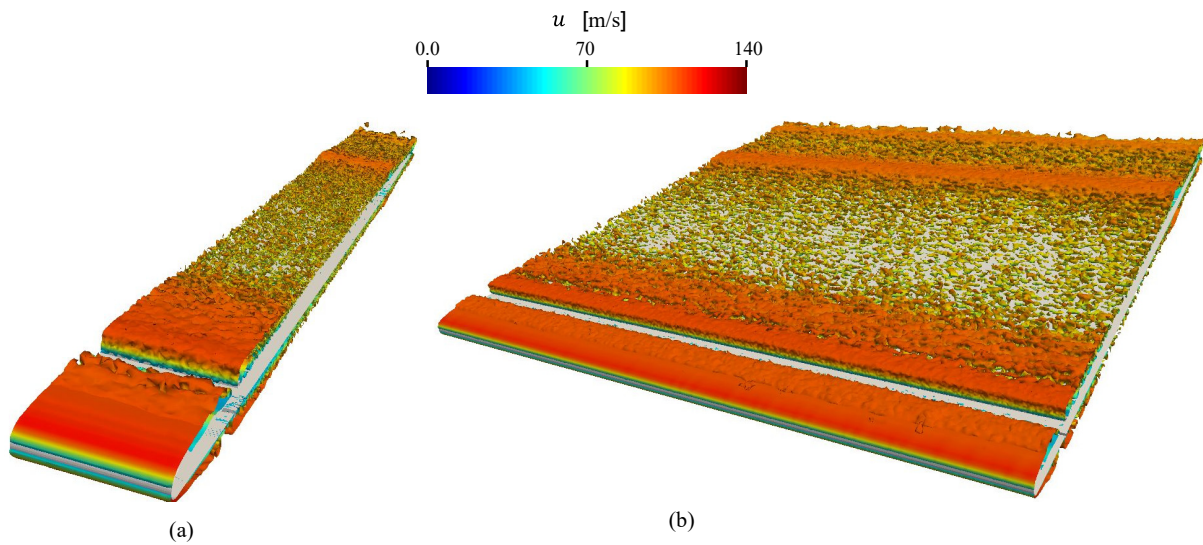
Figure 3.31: Iso-surfaces of Q-criterion ($QC^2/U^2 = 1000$), colored by the velocity magnitude, for (a) GeomX10H4-P25W30-Sp0.1c simulation and (b) GeomX10H4-P25W30-Sp1.0c simulation.
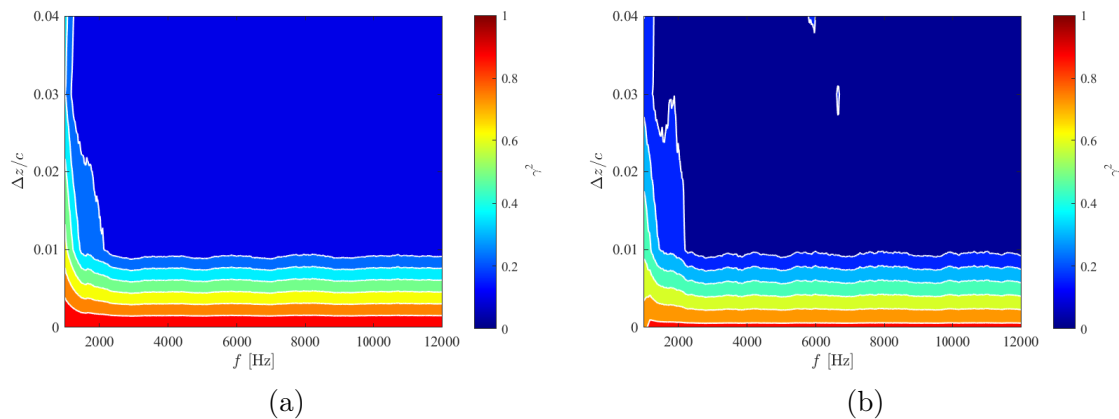
Figure 3.32: Contours of spanwise coherence of the pressure fluctuations on the surface of the plate as a function of frequency f and spanwise separation Δz, at streamwise location $x/c = 0.98$, for computations (a) Geom-X10H4-P25W30-Sp0.1c and (b) Geom-X10H4-P25W30-Sp1.0c.
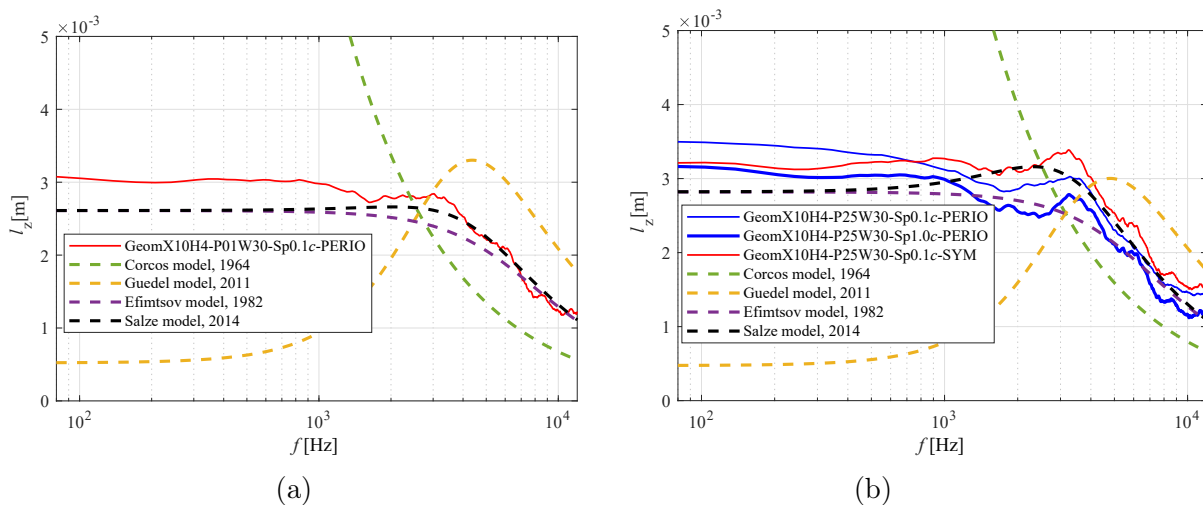
Figure 3.33: Spanwise correlation length, l_z, for WR (a) and WM (b) cases, for different spanwise boundary conditions and different spanwise extents, in comparison with empirical models.
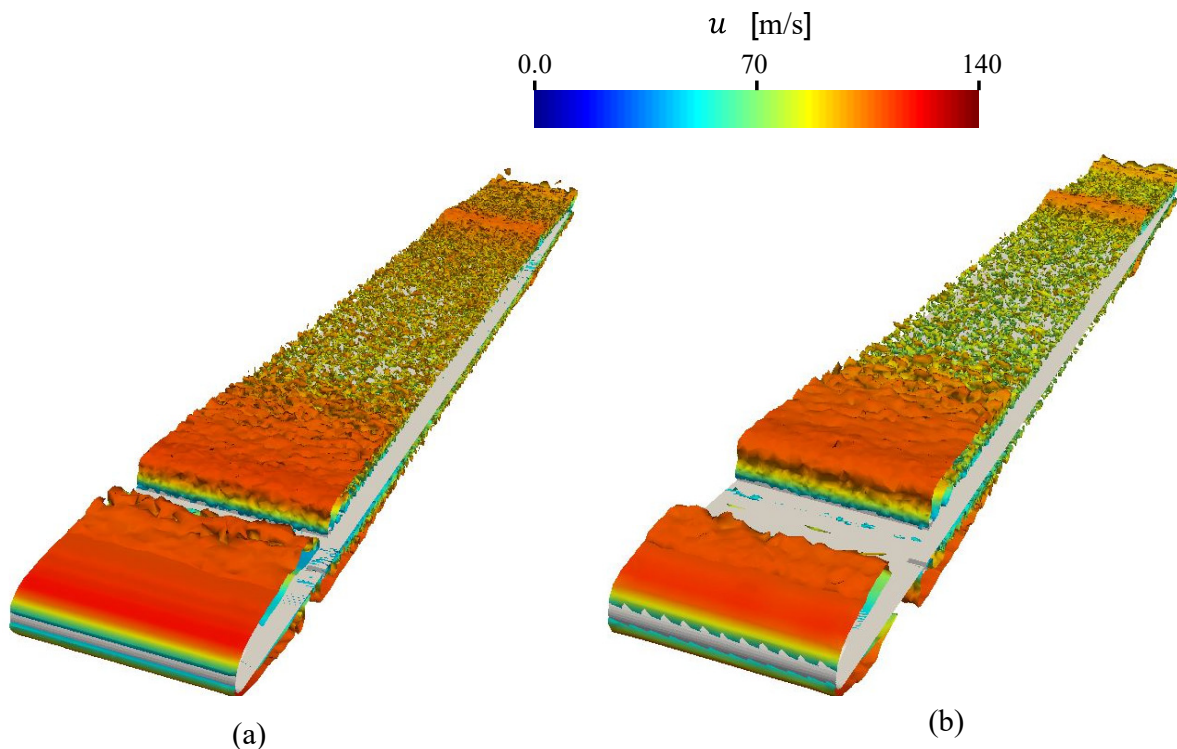
Figure 3.34: Iso-surfaces of Q-criterion ($QC^2/U^2 = 1000$), colored by the velocity magnitude, for (**a**) GeomX10H4-P25W30-SIGMA simulation and (**b**) GeomX10H4-P25W30-SMAGO-DYN simulation.
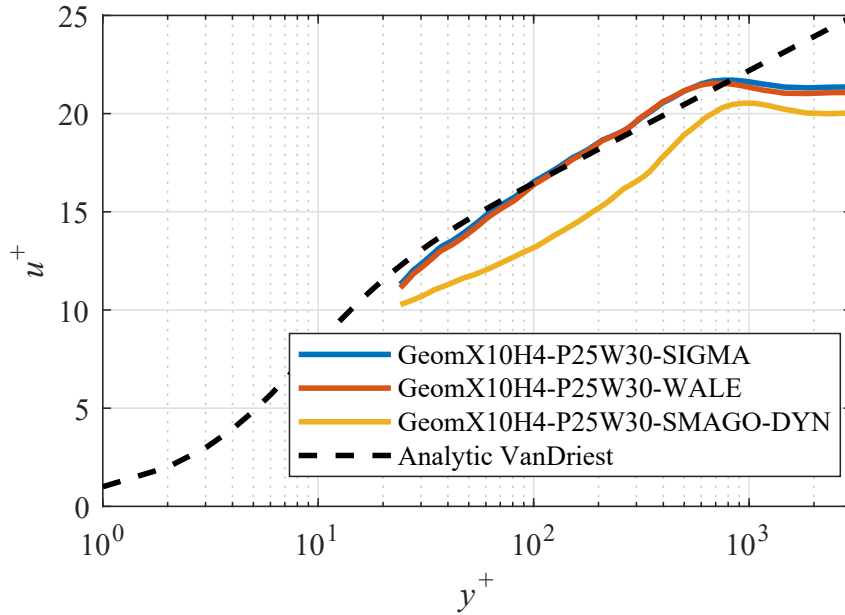
Figure 3.35: Comparison of the normalized velocity profiles between LES cases differing by the SGS turbulence model.

The flow topology is first studied using an isosurface of Q criterion in Figure 3.34 for SIGMA and SMAGO-DYN models. Smaller flow structures and larger velocities are noticed when using the SIGMA model. Similar flow structures are found when comparing the SIGMA and WALE models.

The boundary-layer transition is also studied by comparing the normalized velocity profiles in the boundary layer between the three SGS models in Figure 3.35. Similar profiles are obtained for SIGMA and WALE models, with a very good agreement with the Van Driest analytic solution. However, the velocity profile is underestimated by the SMAGO-DYN model. The latter seems to be very dissipative and not able to properly predict the turbulent boundary-layer properties.

Influence of the mesh in the wake region

For a fan/OGV stage, the wakes formed downstream of the fan reach the LE of the stator and generate rotor-stator interaction noise, which is the dominant source in such configurations. Thus, the numerical setup should allow for correct modeling and propagation of the fan wakes in the inter-stage. After some distance downstream of the TE of the fan blade, the wake reaches an asymptotic state. Once this length scale is known, the wake can be decomposed into three different regions: "near wake", "intermediate wake", and "far wake". The asymptotic far wake stage is reached when all turbulent flow statistics follow universal distributions that are independent of the TE conditions. Here, numerical results obtained from the LES cases are compared to empirical models or universal distributions in each wake region.

Three mesh refinements are considered in the wake region, denoted "W100", "W30", and "W15". The WM case corresponding to the mesh type and refinement at the wall "P25" is used for all three cases. Figure 3.36 shows the streamwise development of the center-line velocity (U_c) for the three mesh refinements in the near wake region. The shear velocity $u_{\tau 0}$ is computed at the trailing edge of the plate and the kinematic viscosity ν
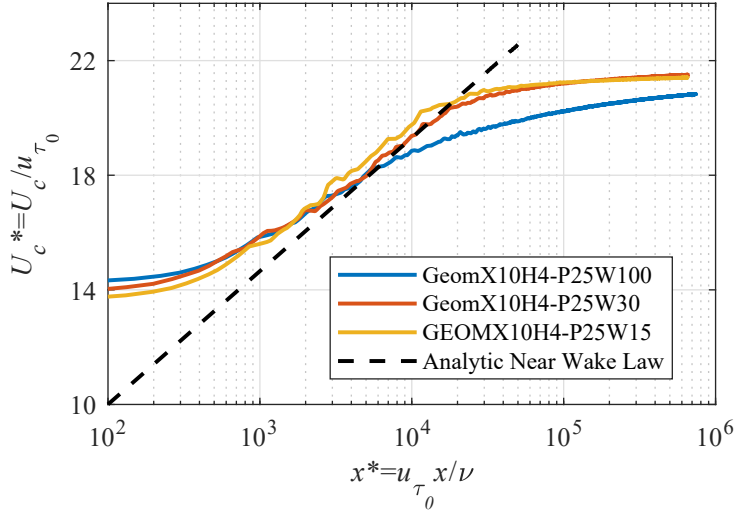
Figure 3.36: Axial development of the normalized centerline velocity U_c^* in the near-wake for the three mesh refinements in the wake region, and comparison with the corresponding analytic solution.

is equal to its averaged value at each location. The LES results are compared with the near-wake analytic model proposed by Ramaprian *et al.* [217],

$$U_c/u_{\tau 0} = (1/\kappa)[lng(x^*) - \gamma] + B \tag{3.26}$$

$$U/u_{\tau 0} = (1/\kappa)lny^* + B + (1/\kappa)E_1(\psi) \tag{3.27}$$

where $x^* = u_{\tau 0}x/\nu$, $y^* = \frac{u_{\tau 0}y}{\nu}$, $\psi = y/g(x)$, $E_1(\psi) = \int_\psi^\infty \frac{e^{-t}}{t}dt$, the function g is defined as $g(\alpha)[ln(g(\alpha)) - 1] = \kappa^2\alpha$, and $\gamma = 0.5772157$ is the Euler-Mascheroni constant. κ and B are model constants equal to 0.418 and 5.5, respectively. It can be noted that beyond a certain streamwise position ($x^* = 2 \times 10^3$), a good agreement is found between the LES results and the analytical solution, although U_c is under-predicted for the coarsest mesh "W100".

Figure 3.37 shows the velocity profiles, for different streamwise positions, for the different mesh refinements in the near wake region. Comparisons with analytic solutions are also shown. δ_{2f} is the momentum thickness in the far-wake. The streamwise position $x/\delta_{2f} = 28$ ($x^* \approx 2.10^4$) corresponds to approximately the upper limit of the near wake region, as noticed experimentally [21, 6]. Beyond $x/\delta_{2f} = 10$, a good agreement is obtained between the profiles of the cases W30 and W15 and the analytic solution.

The intermediate-wake characteristics are analyzed for the "W30" case by comparing the normalized deficit velocity and the Reynolds stress profiles, for different streamwise positions, in Figures 3.38 (a) and (b) respectively. In this region, the flow is expected to follow the asymptotic behavior given by [217],

$$u_d/U_d = exp(-4\eta^2 ln2) \tag{3.28}$$

$$G = \overline{uv} = 8ln2(\nu_t/U_d b)\eta \exp(-4\eta^2 ln2), \tag{3.29}$$

where $\eta = y/b$, u_d is the velocity deficit at a normal coordinate y and U_d the maximum velocity deficit. The profiles are plotted against y normalized by the local wake half-

110
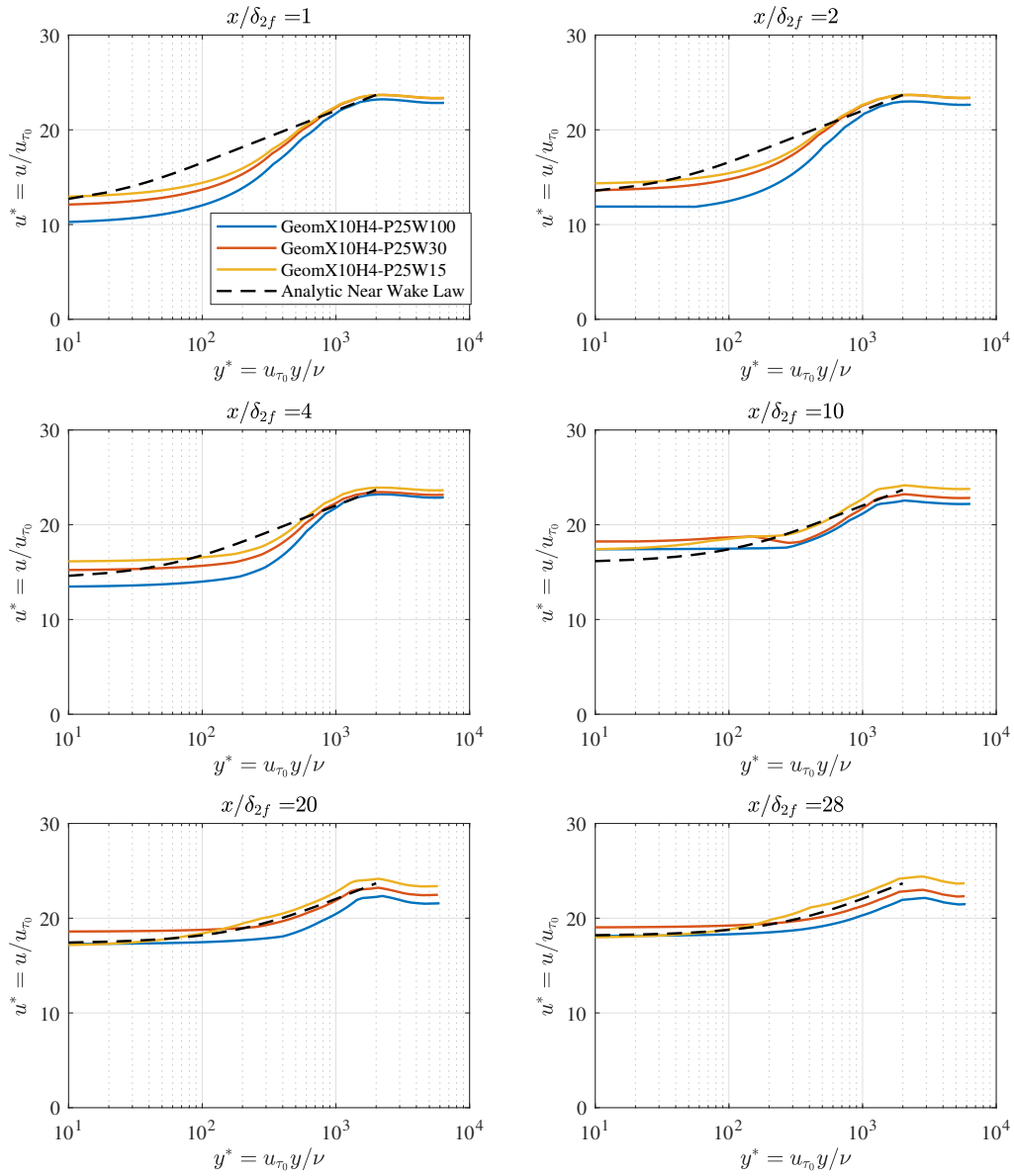
Figure 3.37: Normalized velocity profiles in the near-wake, for the three mesh refinements in the wake region, and comparison with the corresponding analytic solution.

(a)

(b)
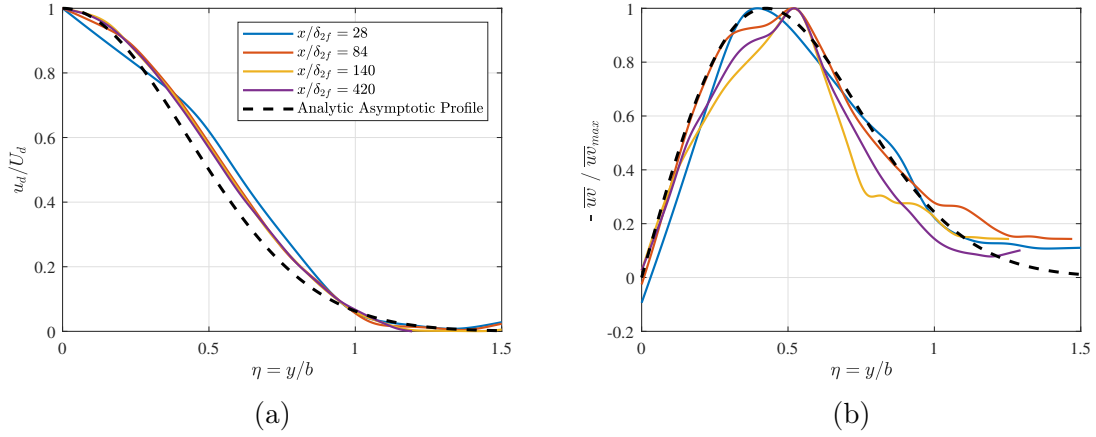
Figure 3.38: Comparison of the wake characteristics with empirical models in the intermediate-wake region, for the computation GeomX10H4-P25W30, at different streamwise positions x/δ_{2f}. (a) Normalized velocity deficit (u_d/U_d) profiles and (b) Reynolds stress ($\overline{uv}/\overline{uv}_{\max}$) profiles.

(a)

(b)
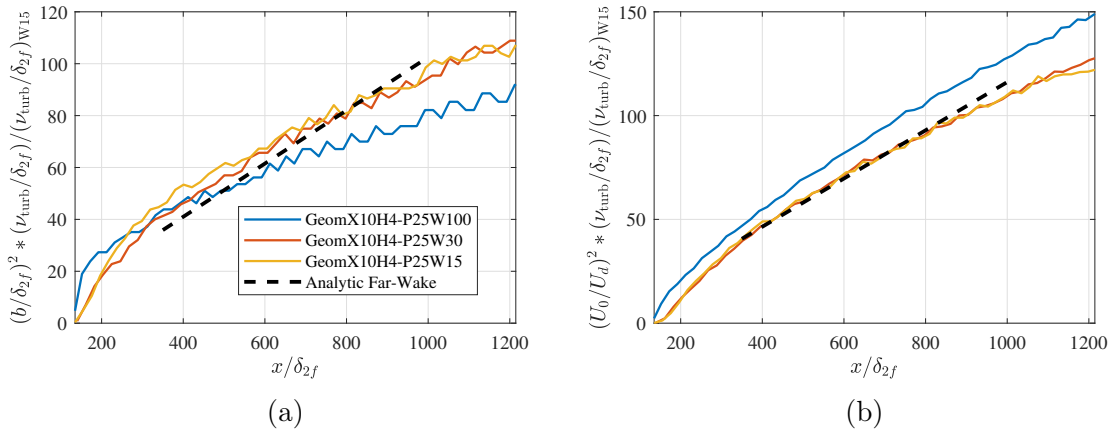
Figure 3.39: Asymptotic evolution of the wake parameters, for the three mesh refinements in the wake region, and comparison with the corresponding analytical solution.

width b. At distances above $x/\delta_{2f} = 28$, a good agreement for the normalized velocity deficit is found between the numerical results and the analytical solution, with a slight over-prediction between $\eta = 0.3$ and $\eta = 0.8$. For $\eta < 1$, the normalized Reynolds stress profiles are quite similar and fit well with the analytical solution. For larger values of η (i.e., $y > b$), the analytical solution predicts a turbulent intensity that tends to zero, while the Reynolds stress from the numerical results approaches its value outside of the wake region.

The far-wake properties are investigated in Figure 3.39. The asymptotic behavior is reached approximately beyond $x/\delta_{2f} = 350$. The results in the far-wake can be compared to the half-power laws for the half-width b and maximum velocity deficit U_d, which are given by

$$(b/\delta_{2f})^2 = 16(\nu_t/U_0\delta_{2f})\ln 2(x/\delta_{2f}) \qquad (U_0/U_d)^2 = 4\pi(\nu_t/U_0\delta_{2f})(x/\delta_{2f}). \qquad (3.30)$$

In the case of the refined meshes "W30" and "W15", the power laws for b and U_d

are well predicted and the product $U_d b/U_0 \delta_{2f}$ approaches the predicted constant value 0.9394 [217]. For these cases, $\nu_t/U_0\delta_{2f}$ approximately tends to 0.032 and G_{max} is slightly less than 0.0487 (see [217]). The mesh resolution "W100" seems to be too coarse in the wake region. Thus, it can be concluded that the mesh resolution "W30" is sufficient to properly predict the flow in the wake region beyond a certain streamwise position, with an acceptable computational cost.

Influence of numerical parameters on the WM-LES results — Summary

- Mesh type at the wall: prismatic cells show better agreement with Van Driest analytical model than tetrahedral cells.

- Mesh refinement at the wall: a value of $y^+ = 25$ allows to properly capture the boundary layer mean and fluctuating parameters.

- Trip height: a trip height equal to four times the displacement thickness of the boundary layer yields a good transition of the boundary layer to turbulence.

- Spanwise boundary condition: at mid and high frequencies, periodic boundary conditions show a better agreement of the spanwise correlation length with the empirical model of Salze than symmetry boundary conditions.

- Spanwise extent: the spanwise extent of $1c$, compared to the one of $0.1c$, allows to reduce the spanwise correlation length and to obtain a better agreement with the model of Salze, especially at low frequencies. However, the extent of $0.1c$ is sufficient at mid- and high-frequency.

- Trip position: a trip at an axial position of $x = 0.1c$ ($x = 0$ corresponds to the LE position) shows better boundary layer mean streamwise velocity profiles than the one at $x = 0.2c$.

- Subgrid scale model: similar boundary layer properties are obtained for Wale and Sigma models, whereas large discrepancies are noticed when using the dynamic Smagorinsky model.

- Mesh refinement in the wake region: a mesh size equal to 30 times the mean Taylor scale in the wake region is sufficient to properly propagate the wake properties.

3.3.4 Acoustic Far-Field Predictions

The acoustic far-field predicted using the LES results from the GeomX10H4-P25W30 and GeomX10H4-P01W30 simulations (both ensuring 13 points per wavelength in the far-field and a total number of points of 3.1 and 13 millions, respectively) is compared to Amiet's TEN model (see Equation (3.2)). For the analytical predictions, the convection velocity u_c is computed as the slope of the phase of the wall-pressure cross-spectrum between two streamwise locations in the vicinity of the trailing edge. The calculated values are between $u_c/U_0 = 0.63$ and $u_c/U_0 = 0.7$. The wall-pressure PSD in the vicinity of the
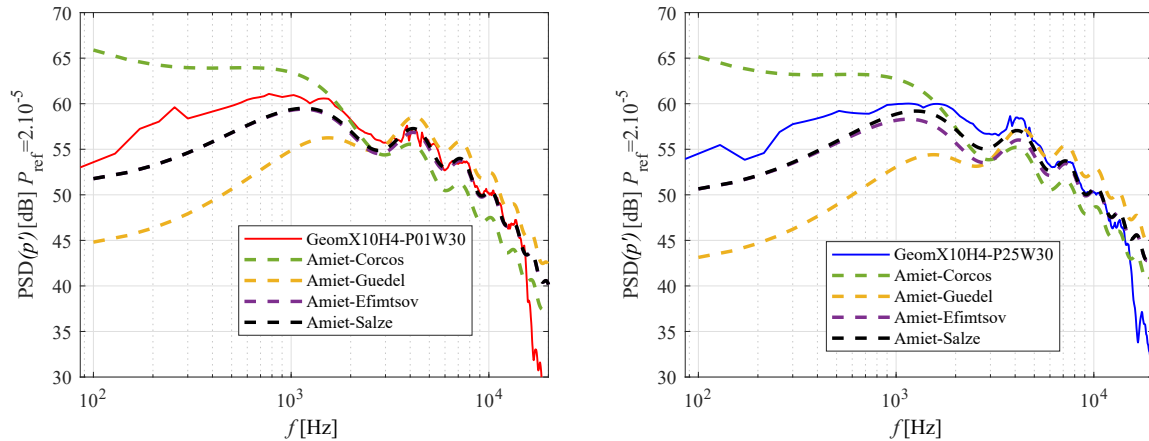
Figure 3.40: Direct prediction of the far-field PSD of pressure fluctuations from LES, in comparison to Amiet's theory (various correlation laws), for an observer at 90° and a distance of $8c$ from the plate.

trailing edge ϕ_{pp} is extracted from the LES computation and is fitted to a Goody model, which can be used as an input in the TEN model. The spanwise integral lengthscale, l_z, is modeled using the analytical models shown in Figure 3.33. For the direct numerical prediction, both the turbulent flow and the acoustic wave propagation are modeled by the LES solver.

A comparison between the LES predictions and the analytical solutions of the PSD of the pressure fluctuations in the far-field, at 90°and a distance of $8c$ from the trailing edge of the plate, is shown in Figure 3.40. The mesh cut-off frequency can be observed around 15 kHz. The analytical prediction is very sensitive to the model used for l_z. Both WR and WM results show a good agreement with the model of Salze [233] at mid-to-high frequencies, but seem to overestimate the low frequency levels. This can be explained by the domain confinement in the spanwise direction, as shown for l_z in Figure 3.33.

3.4 Conclusion

A parametric study of the effects of several numerical parameters on the flow development around a flat plate and the associated noise generation has been conducted using LES simulations. The main noise mechanisms are investigated separately: turbulence inter-action noise and trailing edge noise. The upstream flow properties for the leading edge noise case and the geometric parameters of the plate are chosen to approach as close as possible the assumptions made in Amiet's acoustic models.

Comparison with analytical models and DNS data show very good results for the boundary layer characteristics and the far-field noise prediction. These results allow the definition of an adequate numerical set-up in order to prepare LES simulations of the broadband noise generated by an UHBR turbofan fan stage.

The main results of the parametric studies can be summarized as follows,

- Mesh design. The computational domain can be divided into three main regions:

  - Near wall region. In order to properly describe the properties of the boundary layers, prismatic cells are preferred than tetrahedral cells on the wall surfaces. For WM-LES, a value of y^+ of 25 is seen to be appropriate.

– Wake region. In order to properly transport the turbulent wakes from the trailing edges of the fan to the leading edges of the OGV, a ratio of the cell size to the Taylor micro-scale of about 30 is required.

– Far-field region. In order to properly propagate the acoustic waves in the fan stage (upstream of the fan and downstream of the OGV), 13 cells per acoustic wavelength are required for the specific numerical setup adopted in this study (particularly for the third-order numerical scheme TTGC).

• Trip design. The effects of the trip height and its streamwise position on the development of the boundary layers are assessed.

– Trip height. Three trip heights (δ_1, $2\delta_1$ and $4\delta_1$) are compared. The best boundary layer transition is found for the biggest trip of height $4\delta_1$.

– Trip streamwise position. Two streamwise positions ($0.1c$ and $0.2c$) are compared. The trip at $0.1c$ shows better transition of the boundary layer.

• Sub-grid scale model. The boundary-layer properties obtained with the models SIGMA [183] and WALE [182] are similar and match well with the analytical results.

• Spanwise boundary conditions. Periodic and symmetric boundary conditions are compared. When periodic boundary conditions are used, the spanwise correlation length, which is an important input for Amiet's trailing edge model [7], is closer to Salze's model [233], compared to the one obtained when using symmetry boundary conditions.

• Spanwise extent. Two spanwise extents ($0.1c$ and c) are compared. An extent of $0.1c$ (about 5δ) is seen to be sufficient at mid to high frequencies.

With the numerical parameters selected in the analysis above, good predictions of the far field noise are achieved, in comparison to Amiet's TIN and TE noise models.

Note 1

The results of this Chapter were presented at the European Conference of Turbomachinery (ETC14) in 2021. The scientific publication was in the top-5 of the best contributions to the conference and was selected for publication in the International Journal of Turbomachinery, Propulsion and Power (IJTPP) [3].

Note 2

The results of this Chapter were used to develop a pre-dimensionning tool for LES in turbomachinery, called LESCOTT. LESCOTT allows to evaluate the mesh size in each region of interest of the computational domain, based on both turbulent and acoustic criteria, for a given numerical scheme and mesh topology. It provides also a quick estimation of the computational time of LES for fan/OGV stage applications. The main principles of this tool are presented in Appendix B.

Chapter 4

On the effects of a separation bubble on fan noise

Introduction

The main objective of the present chapter is to improve our current understanding of the unsteady aerodynamic characteristics and the noise generation mechanisms of a recirculation bubble. Such a phenomenon can appear close to the leading edge of the rotor blades in a state-of-the-art fan stage, at approach conditions. Particularly, this chapter focuses on the effects of the mass flow rate, i.e. the angle of attack, on the evolution of the bubble and its acoustic signature. Additionally, the influence of the inlet turbulence injection rate on the recirculation bubble characteristics is assessed.

This is achieved by performing a number of WR LES with varying mass flow rates and turbulent injection rates. Moreover, the capability of WM LES to properly capture the presence and the properties of the recirculation bubble is investigated by comparing two additional WM LES, with and without a roughness region close to the LE (called trip), with a WR case. To limit the computational cost, the radial slice sector LES case, described in Chapter 2, is considered. Meshes are designed such that the acoustic propagation is resolved by the LES up to one chord length (c) upstream of the fan and downstream of the OGV. The effects of the mass flow rate are analyzed in terms of the steady and unsteady characteristics of the flow in the vicinity of the fan blades and vanes and the noise contributions related to the recirculation bubble. To this end, a Dynamic Mode Tracking (DMT) method is used to examine the behavior of the flow at any frequency of interest for the recirculation bubble.

The chapter is organized as follows. Section 6.1 presents a literature review on the previous studies performed on a laminar separation bubble. The capability of the WM assumption for the prediction of some aerodynamic characteristics of the recirculation bubble is assessed in Section 4.2. The influence of the turbulence rate in the incoming flow on some aerodynamic properties of the recirculation bubble is investigated in Section 4.3. Finally, the effects of the mass flow rate on the formation of the recirculation bubble and its acoustic signature in the rotating and in the stationary domains are presented in Section 4.4.

Contents

4.1   Laminar separation bubble

For a fan stage operating at its nominal regime, the Reynolds number exceeds one million and the flow remains attached along the surface of the blades. The turbulent eddies in the boundary layer are diffracted when passing the TE and generate noise. At low fan speeds, such as at approach conditions, a flow separation region may appear close to the LE of the fan blades even at moderate adverse pressure gradient. If the flow transitions to turbulence and reattaches, a laminar recirculation bubble is formed. The recirculation bubble generally influences the fan performance by increasing the losses of the fan stage.

4.1.1   Mechanism of a laminar separation bubble

Figure 4.1 shows the basic mechanism of a boundary layer separation and the formation of a recirculation bubble close to the LE of the blade. Upstream of the separation region, the laminar boundary layer encounters an adverse pressure gradient due to a high angle of attack. The magnitude of the pressure gradient is sufficiently high to cause the separation of the flow. The separation region can be divided into two zones (a dividing shear layer separates the two zones in Figure 4.1). Close to the blade surface, a recirculating flow is generated, which leads to the formation of a reverse flow vortex. Away from the wall, the boundary layer undergoes a transition to turbulence due to disturbance amplification occurring in the unstable laminar layer. The turbulent mixing between these two zones enhances the exchange of momentum between the inner and outer parts of the wall-bounded shear layer, which can lead to flow reattachment. The described mechanism of separation, transition and reattachment results in the formation of a recirculation bubble close to the LE of a fan blade at approach condition [186, 54, 237, 53]. After the reattachment, a turbulent boundary layer develops. As the Reynolds number decreases,
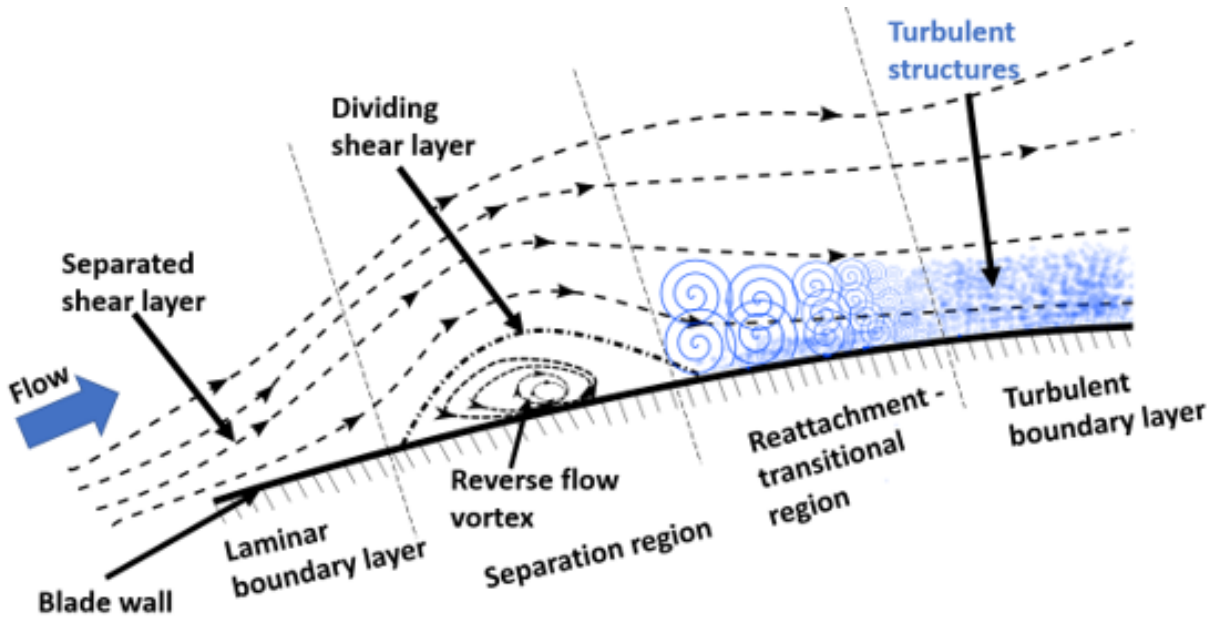
Figure 4.1: Laminar separation bubble formation on the suction side of an airfoil (adapted from [186]).

the transition and reattachment points on the blade suction side are shifted. At sufficiently large angles of attack and low Reynolds numbers, the separated shear layer fails to reattach, thus stalling the airfoil.

4.1.2 Literature review

This phenomenon and its contribution to self-noise have been extensively studied experimentally [168, 142, 54, 248, 98, 211, 163, 136] and numerically [219, 218, 113, 283, 283, 52, 249] on a single airfoil configuration.

Direct Numerical Simulations (DNS) of the airflow around a NACA0012 airfoil were performed by Sandberg *et al.* [219, 218] at Reynolds and Mach numbers of $Re = 5 \times 10^4$ and $M = 0.4$, respectively. Sandberg *et al.* [219, 218] observed that a laminar separation bubble can be found on the suction side of an airfoil at low Reynolds number and non-zero angle of attack. This separation bubble is followed by a transition to turbulence and a reattachment of the boundary layer. The acoustic results from the DNS indicate the presence of an additional noise source on the suction side that is not located at the TE and can change significantly the noise directivity. Similar conclusions were reached by Jones *et al.* [113], who observed that this additional noise source is dominant at high frequencies.

Another DNS study was performed by Wu *et al.* [283], who investigated the flow around a Controlled-Diffusion (CD) airfoil at $\alpha = 8°$, $Re = 1.5 \times 10^4$ and $M = 0.25$. Downstream of the LE, the flow is laminar and spanwise coherent structures are generated due to the Kelvin-Helmholtz instability [94, 273, 53]. This is related to a short recirculation bubble that triggers the laminar to turbulent transition of the boundary layer. Downstream of the transition region, the size of the turbulent structures decreases as they are convected, and turbulence is fully developed at the TE. Inside the separation region, a hump is observed in the amplitude of the wall pressure spectra. In this region, the space-time correlation of the fluctuating pressure shows a periodic pattern in time and significant

levels of correlation in space due to large coherent spanwise structures. Similar results were obtained by Sanjosé *et al.* [173] using the Lattice-Boltzmann method with a DNS resolution for low Mach and Reynolds numbers and by Deuse *et al.* [52] and Shubham *et al.* [249] using Large Eddy Simulations (LES). The axial position of the separation region and the velocity fluctuations in this region are observed to significantly oscillate, generating additional noise.

Experimental studies using airfoils at low Mach and Reynolds numbers and high angles of attacks [211, 163, 136, 240, 109] have shown an increase in the amplitude of the velocity fluctuations in the separation region. This occurs close to the LE and is due to the onset of a recirculation bubble in the separation region. Experimental results from Kurelek *et al.* [136] exhibit evidence of a triple peak pattern for the wall-normal profiles of the Root-Mean-Square (RMS) streamwise velocity fluctuations, and a significant increase in the RMS velocity fluctuations normal to the airfoil surface. Additionally, Michelis *et al.* [163] show a dominant broadband peak in the Power Spectral Density (PSD) of the velocity fluctuations in the bubble region, which is related to Kelvin-Helmholtz instabilities. Another experimental study by O'meara and Mueller [211], performed on a NACA00012 airfoil for a range of $0.65 \times 10^5 < Re < 4.5 \times 10^5$ and $\alpha = 2°$, investigates the feedback effects due to tonal noise emission in a laminar separation bubble formed on the suction side of an airfoil. A particular frequency is detected that is related to roll-up vorticies forming in the recirculation bubble region and passing over the TE of the airfoil.

Based on the observations discussed above, high angles of attack can be found at the fan LE at approach conditions, a major difference when compared to cruise conditions. This is related to the reduced freestream Mach number and fan rotational speed at approach conditions, which can result in local flow separations and the appearance of a recirculating bubble near the LE [213, 145, 146]. Recirculation bubbles play an important role in the boundary layer transition to turbulence on the fan blade surface and produce an additional noise source that can be associated to a highly unsteady flow in the bubble region [146]. It should be noted that a classical solution to suppress laminar separation bubbles consists in increasing the roughness (e.g. using a tripping band) near the LE in order to force the transition to turbulence before the flow separation [30, 247]. However, the use of a tripping band near the LE to prevent separation bubbles at approach conditions increases aerodynamic losses at cruise conditions.

Although the presence of recirculation bubbles has been observed and suggested as a significant noise contributor to fan noise [146], a detailed analysis of the flow in such bubbles and their acoustic signature in aero-engine applications has received limited attention.

4.2 Numerical assessment of the WM-LES

To assess the validity of the wall-modeled (WM) LES assumption in the prediction of some aerodynamic quantities in a separation region, WM and WR LES are compared at the reference mass flow rate $\dot{m} = 20\,\text{kg/s}$ and a rotational speed corresponding to 50% of the nominal speed ($\Omega = 5500\,\text{RPM}$). The properties of the three meshes compared in this study are shown in Table 4.1. The "WM-TRIP" mesh is constructed from the WM mesh by adding a square geometrical trip at 10% of the chord length (trip height around four times the boundary layer displacement thickness at the position of the trip, which is deemed sufficient for an adequate transition of the boundary layer to turbulence, as shown in Chapter 3).

Table 4.1: Mesh properties for the different WM and WR LES. x^+, y^+ and z^+ are the dimensionless wall distances in the streamwise, normal and spanwise directions, respectively.

	WM	WM-TRIP	WR
Number of cells [10^6]	40	41	80
$x^+ = z^+$	250	250	35
y^+	25	25	1.0
Number of prismatic layers	10	10	16
Stretching ratio [%]	10	10	6
Time step [10^{-8}s]	4.4	4.35	0.8
CPUh/blade passage [10^3]	50	51	280

The turbulent structures on the suction surface of the rotor blade are shown in Figure 4.2, for the different meshes, using iso-surfaces of the Q-criterion ($Qc^2/U_0^2 = 1500$, where U_0 is the free-stream velocity magnitude) colored by the vorticity magnitude. The value of the iso-surface of Q-criterion is chosen in a way to clearly identify the turbulent structures in the boundary layers. For all the cases, a laminar boundary layer is formed near the LE, followed by a transition region, where a recirculation bubble is identified. This bubble is characterized by a significant level of vorticity and forces the transition of the boundary layer to turbulence. Downstream of the recirculation bubble, the flow reattaches to the airfoil and remains attached down to the TE. When comparing with the WR case, the use of a wall model appears to delay the apparition of the recirculation bubble and leads to larger turbulent structures in the separation region and in the downstream direction, even when a trip is added.

The flow topology around the rotor blades is then analyzed by means of the mean streamwise velocity component, u, (Figure 4.3) and the turbulent kinetic energy, k_t, (Figure 4.4), which are averaged in the rotating reference frame. The averaged values are computed over 3.5 rotations of the fan. On the blade suction side, near the LE, a zone of negative velocity and high turbulent kinetic energy can be found. This recirculation region corresponds to the bubble identified by the Q-criterion iso-surfaces in Figure 4.2, which leads to the boundary layer transition to turbulence. By comparing the flow topology obtained from the different cases, we can observe that, for the WM cases compared to the WR case, the bubble is longer in the streamwise direction and its position is shifted downstream over the suction side. However, smaller values of the maximum turbulent kinetic energy are observed when a wall model is used, which delays the transition to turbulence. Consequently, both the boundary layer and the wake thicknesses increase for the WM cases. These differences between the WM and WR cases are less pronounced when adding a trip. In this case, the axial position of the bubble onset on the suction side of the blade is imposed by the trip position.

The distributions of isentropic Mach number, M_{is}, which is related to the static pressure distribution on the blade, and the RMS of the pressure fluctuations (P_{rms}), along the blade, are presented in Figure 6.1. The isentropic Mach number M_{is} is defined as,

$$M_{is} = \sqrt{\left(\left(\frac{P_0}{P}\right)^{\frac{\gamma-1}{\gamma}} - 1\right)\frac{2}{\gamma-1}},$$

Figure 4.2: Iso-surfaces of Q-criterion ($Qc^2/U_0^2 = 1500$), colored by the vorticity magnitude, for the different meshes, (a) WR, (b) WM, and (c) WM-TRIP.
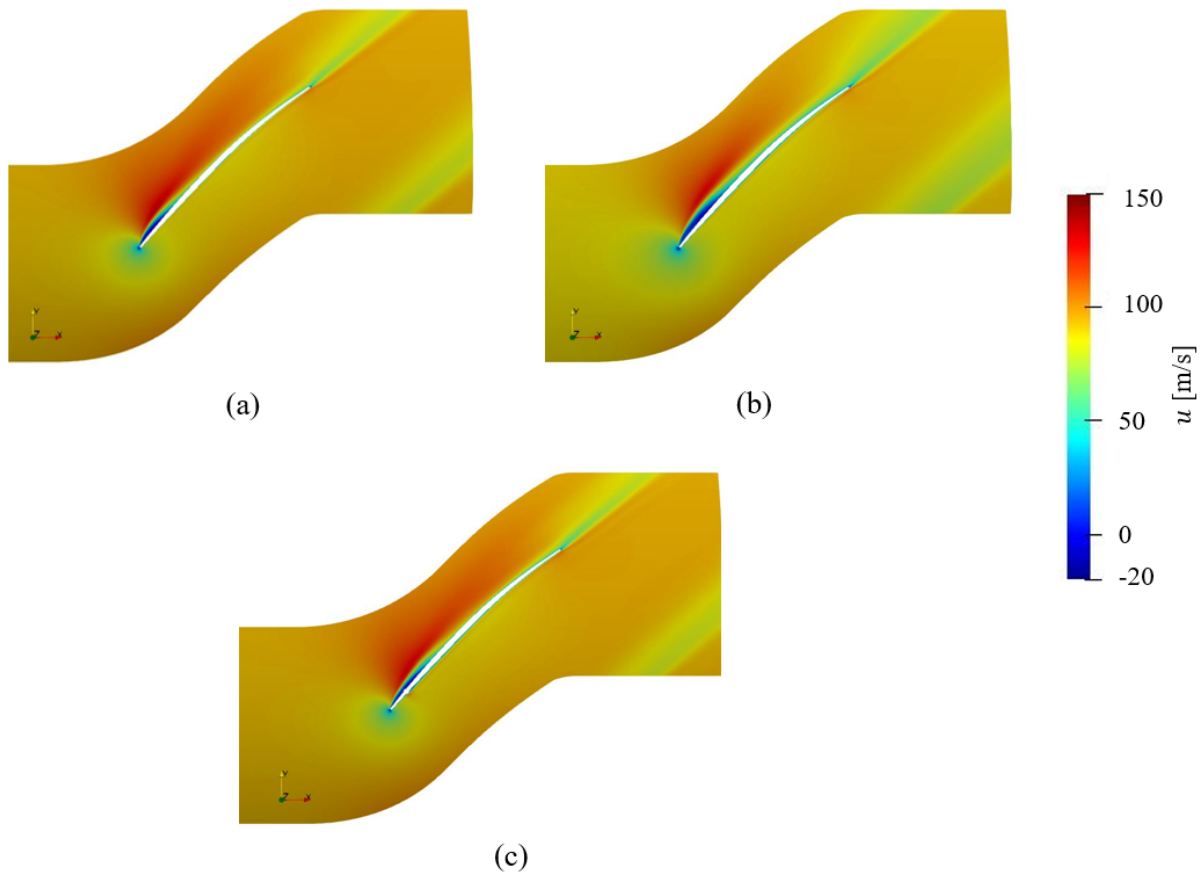
Figure 4.3: Contours of averaged streamwise velocity u around the rotor blade, for the different meshes, (a) WR, (b) WM, and (c) WM-TRIP.
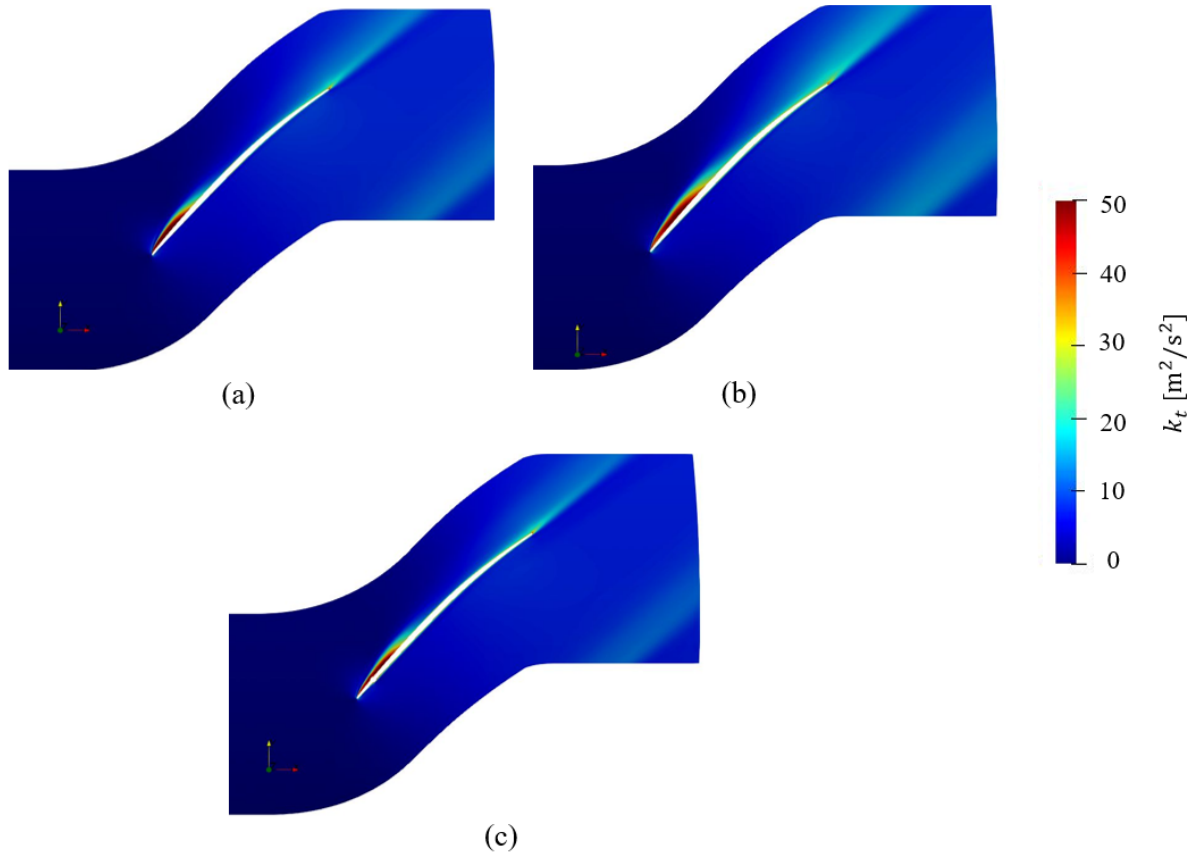
Figure 4.4: Contours of turbulent kinetic energy k_t around the rotor blade, for the different meshes, (a) WR, (b) WM, and (c) WM-TRIP.

Figure 4.5: Average isentropic Mach number M_{is} (a) and RMS pressure fluctuations P_{rms} (b) along the rotor blade for the different meshes.

Figure 4.6: Average friction coefficient C_f along the rotor blade for the different meshes. (a) suction side. (b) pressure side.

where P_0 is the total pressure in the free-stream outside the boundary layers, P is the static pressure and γ is the ratio of specific heats (in this case $\gamma = 1.4$). On the suction side, a plateau of M_{is} can be observed near the LE, which indicates the presence of the recirculation bubble. Downstream of the bubble region, the turbulent boundary layer is subjected to an adverse pressure gradient down to the TE. The bubble region also exhibits large P_{rms} values, as shown in Figure 6.1 (b). It can be observed that, when a wall law is used, the bubble is shifted downstream and its size increases, compared to the WR case. This is consistent with the previous observations on the flow topology. The strength of the additional self-noise source due to the recirculation bubble can be partly related to the P_{rms} levels. The maximum value of P_{rms} is lower for the WM cases compared to the WR case, but the width of the peak is larger. By adding a trip to the WM case, the position and the fluctuations of the recirculation bubble becomes closer to the WR case (LES WR). However, the mean pressure level is different, which shows that the outlet pressure needs to be rescaled in case a trip is added.

The friction coefficient, C_f, can also provide useful information about the recirculation bubble. A comparison of C_f between the different meshes is presented in Figure 4.6, over the suction side (a) and the pressure side (b) of the rotor blade. For all the cases, a region of negative friction coefficient is observed close to the LE of the blade on the suction side, related to the presence of the bubble. Downstream of this region, C_f remains positive along the suction side down to the TE. The locations where C_f reaches zero can be considered as the initial and end points of the bubble, respectively, which allows us to define the size of the bubble. As for the analysis of M_{is} in Figure 6.1, the reattachment point is shifted downstream when a wall law is used, which leads to a larger recirculation bubble. On the pressure side, the friction coefficient is slightly negative for the WM case with trip (WM-TRIP), directly after the trip position, which indicates that a small recirculation appears in this region caused by the trip. For the other cases, the distribution of C_f is quite similar and remains positive, which suggests that the flow is attached all along the pressure side.

Numerical assessment of the WM-LES ──────────── **Summary**

Configuration.

- Radial slice sector LES.

- LES are performed at approach condition (50Nn) without turbulence injection and at a mass flow rate of $\dot{m} = 20\,\mathrm{kg/s}$.

Assessment of the WM-LES

- Assessment of the WM LES assumption to predict the aerodynamic characteristics of a recirculation bubble that appears close to the LE of the rotor blade.

- The results of two WM LES, with and without a rugosity step (trip) close to the LE of the blade, are compared to results of WR LES without a trip in terms of steady and unsteady characteristics of the flow in the vicinity of the blade surface.

- When WM LES is used, the recirculation bubble is shifted downstream and its length is increased. The maximum value of P_rms is lower for the WM cases compared to the WR case, but the width of the peak is larger.

- When a trip is used, the differences with the WR LES case are reduced. However, the pressure level is different and the size and position of the trip have to be defined beforehand.

4.3 Influence of the turbulence injection rate

In this section, the effects of the inlet turbulence rate on the characteristics of the recirculation bubble are studied by comparing the results for three different turbulence injection rates, $TI = U_\mathrm{rms}/U$ of 0.8%, 1.2% and 2.1%, with the case without turbulence injection at the inlet section. Wall-resolved LES at the reference mass flow rate ($\dot{m} = 20$ kg/s) are performed for this study.

As for the first case of the study on the flat plates in Chapter 3, synthetic turbulence is injected based on a spectral approach first introduced by Kraichnan [133], where an isotropic turbulent velocity field is generated using random Fourier modes and extended by A. Smirnov *et al* [251] for spatially developing in-homogeneous, anisotropic turbulent flows. At a distance of $0.05c$ upstream of the LE, the turbulent spectrum can be fitted by a Von-Karman spectrum with a turbulence intensity of TI and an integral length scale of $5\,\mathrm{mm}$ (5% of the chord length). The cut-off wavelength is equal to two times the largest cell size according to Shannon's principle. The number of Fourier modes that compose the random velocity perturbation is 250.

In order to properly transport the turbulent flow from the inlet section down to the rotor blade, the mesh is carefully refined in the upstream region. A view of the rotor domain mesh at mid-span is presented in Figure 4.7. The main properties of the mesh corresponding to the WR cases with turbulence injection are given in Table 4.2 and
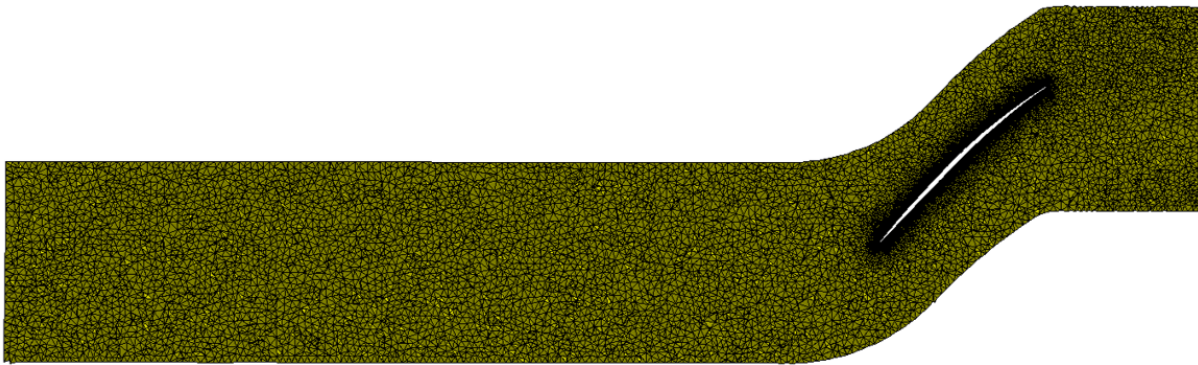
Figure 4.7: Grid in a blade-to-blade view of the rotor domain at mid-span for the radial-slice sector LES case with turbulence injection. The presented grid is four times coarser than the current grid.

Table 4.2: Mesh properties for the WR-LES cases with and without turbulence injection.

	WR	WR-Turb
Number of cells $[10^6]$	80	90
$x^+ = z^+$	35	35
y^+	1.0	1.0
Number of prismatic layers	16	16
Stretching ratio [%]	6	6
Time step $[10^{-8}\text{s}]$	0.8	0.8
CPUh/blade passage $[10^3]$	280	320

compared to the mesh for the WR cases without turbulence injection. The computational cost is increased by 14% for the mesh with turbulence injection, due to the increase of the mesh size and the additional model for turbulence injection.

The turbulent structures on the suction surface of the rotor blade are shown in Figure 4.8, for different turbulence intensity rates at the inlet section, using iso-surfaces of the Q-criterion ($Qc^2/U_0^2 = 1500$, where U_0 is the free-stream velocity magnitude) colored by the vorticity magnitude. For all the cases, a recirculation bubble appears close to the LE and leads to the transition of the boundary layer to turbulence, as discussed for Figure 4.2. When comparing the different cases, the transition of the boundary layer to turbulence appears earlier on the suction side of the rotor blade when the turbulence intensity is increased. This leads to smaller turbulent structures in the separation region and in the downstream direction. Even for the highest turbulence injection rate, the boundary layer remains laminar close to the LE and the boundary layer separation is observed.

The distributions of isentropic Mach number, M_{is}, which is related to the static pressure distribution on the blade, and RMS of the pressure fluctuations (P_{rms}), are presented in Figure 4.9. As in Figure 6.1, the recirculation bubble is identified by the plateau of M_{is} in Figure 4.9 (a), and the large P_{rms} values in Figure 4.9 (b), for the different turbulence injection rates. It can be observed that, as the turbulence injection rate increases, the bubble is shifted upstream and its size decreases, which is consistent with our previous findings from the flow topology. The strength of the additional self-noise source due to the recirculation bubble can be partly related to the P_{rms} levels. When the injection rate increases, the maximum value of P_{rms} is larger, but the width of the peak decreases.
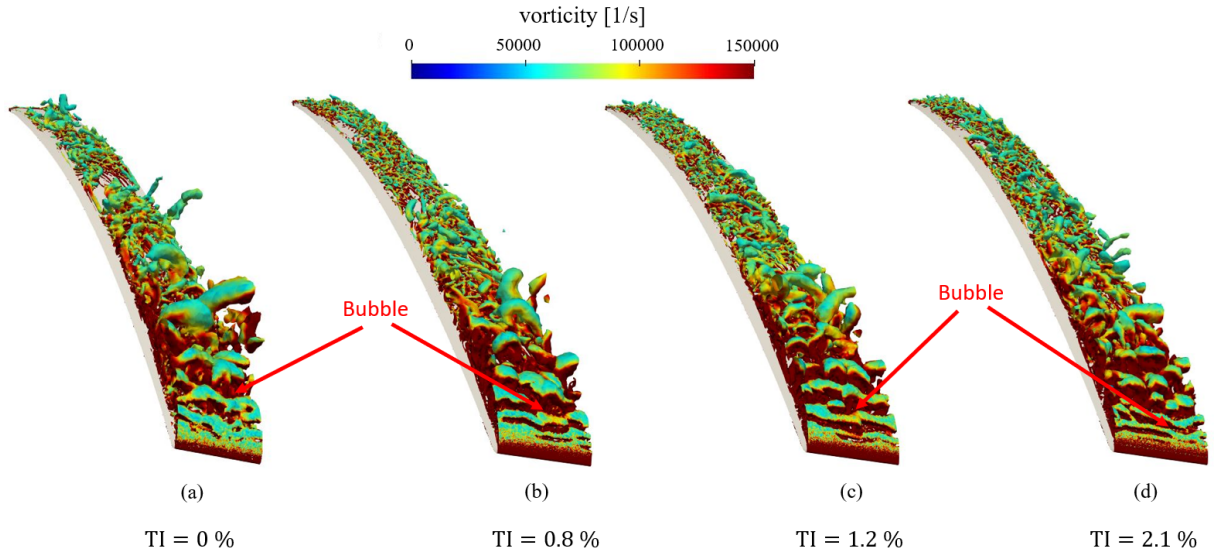
Figure 4.8: Iso-surfaces of Q-criterion ($Qc^2/U_0^2 = 1500$), colored by the vorticity magnitude, for different values of the turbulence intensity injected at the inlet section.
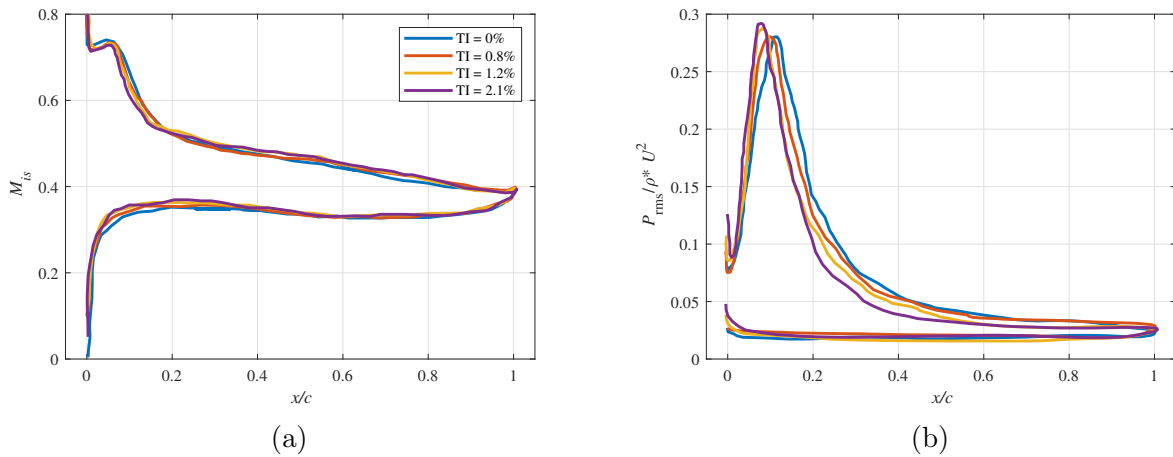
Figure 4.9: Average isentropic Mach number M_{is} (a) and RMS pressure fluctuations P_{rms} (b) along the rotor blade for the different values of the turbulence intensity injected at the inlet section.
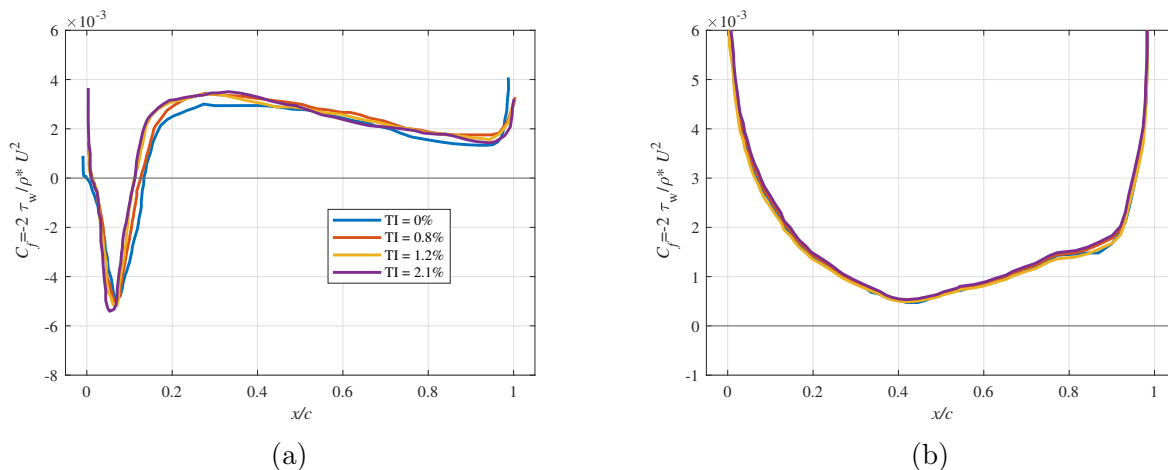
Figure 4.10: Average friction coefficient C_f along the rotor blade for the different values of the turbulence intensity injected at the inlet section. (a) suction side. (b) pressure side.

However, these changes remain below 3% of the maximum value of P_{rms} and are expected to have a small impact on the noise radiated.

As in Section 4.2, the friction coefficient, C_f, is used to characterize the size of the recirculation bubble. A comparison of C_f between the different turbulence injection rates is presented in Figure 4.10, over the suction side (a) and the pressure side (b) of the rotor blade. For all the cases, the recirculation bubble is identified by a region of negative friction coefficient close to the LE of the blade on the suction side, and the size of the bubble is obtained from the locations where C_f reaches zero. As for the analysis of M_{is} in Figure 4.9, the reattachment point is shifted upstream as the turbulence injection rate increases, which leads to a smaller recirculation bubble. On the pressure side, the distribution of C_f is quite similar for the different turbulence injection rates and remains positive, which indicates that the flow is attached all along the pressure side.

Influence of the turbulence injection rate ———————— Summary

- The computational cost is increased by 14% for the cases with turbulence injection, when compared to the cases without turbulence injection at the inlet section. This is due to the increase of the mesh size and the model of turbulence injection at the inlet.

- For the various turbulence injection rates:

  – The recirculation bubble is characterized by a region of negative friction coefficient, high pressure fluctuations, and a plateau in the distribution of isotropic Mach number, over the suction side of the rotor blade.

  – The boundary layer reattaches before the trailing edge of the blade in a fully turbulent state.

Table 4.3: Mesh properties for the different LES. x^+, y^+ and z^+ are the dimensionless cell sizes in the streamwise, normal and spanwise directions, respectively.

	WR-Mesh1	WR-Mesh2	WR-Mesh3
Number of cells [10^6]	68	80	100
$x^+ = z^+$	35	35	35
y^+	1.0	1.0	1.0
Number of prismatic layers	8	16	24
Stretching ratio [%]	12	6	3
Time step [10^{-8}s]	0.8	0.8	0.8
CPUh/blade passage [10^3]	238	280	350

- When the turbulence injection rate increases:

  - The length of the bubble and the region of high RMS pressure fluctuations over the suction side of the rotor blade slightly decrease.

  - The bubble is shifted upstream over the suction side of the rotor blade.

  - The peak of RMS pressure fluctuations in the separation region increases.

- The differences in the recirculation bubble characteristics between the different turbulence injection rates remain small.

4.4 Influence of the mass flow rate

In this section, the effects of the mass flow rate on the characteristics of the recirculation bubble and the generated noise are studied by comparing the results for four different mass flow rates ranging from 19 to 22 kg/s. Based on the results of the two previous sections, WR LES without turbulence injection are performed in this study. First, the grid and time convergences of the LES are presented. Then the aerodynamic and aeroacoustic results are discussed.

4.4.1 LES convergence criteria

Grid convergence

In this section, the mesh convergence of the LES is assessed by comparing the results from the 3 meshes presented in Table 4.3, for the reference mass flow rate $\dot{m} = 20\,\text{kg/s}$.

The near wall refinements (x^+, y^+ and z^+) are taken as small as possible within the range of a refined Wall-Resolved (WR) LES [266, 199, 282]. It should be noted that even a slight refinement of the near-wall surface mesh would lead to a significant increase in the computational cost of the simulation. The values of y^+ and $x^+ = z^+$ over the suction side of the rotor blade are shown in Chapter 2 and recalled in Figure 4.11 for $\dot{m} = 19$ kg/s. These values satisfy stringent guidelines for wall-resolved meshes in LES according to state-of-the-art literature review [266, 199, 282].

In the present work, the sensitivity of the recirculation bubble to the stretching ratio is assessed. This parameter is not explicitly addressed in the literature and is expected
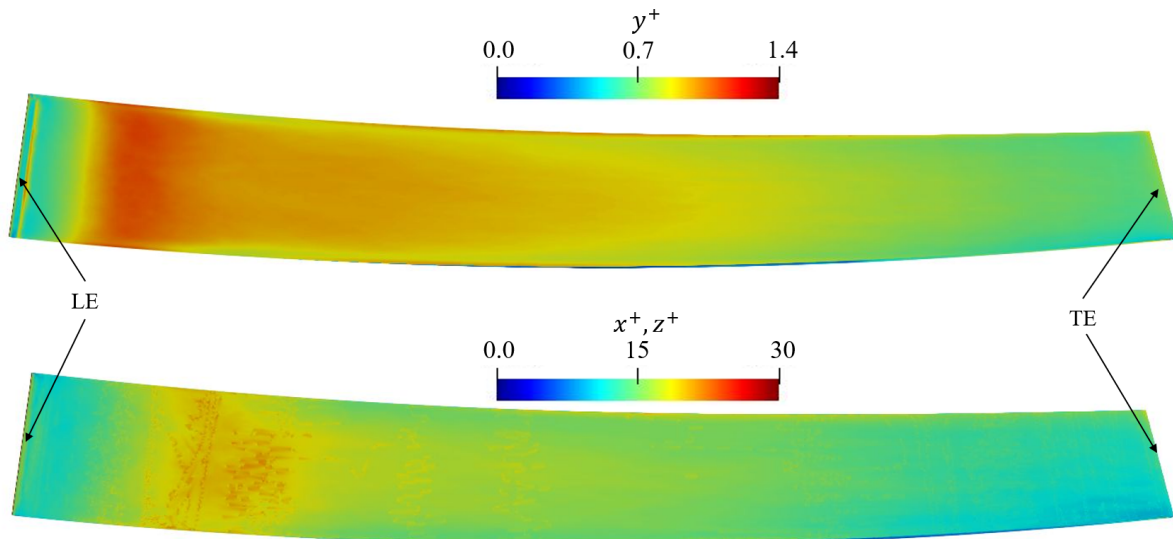
Figure 4.11: (a) y^+ and (b) $x^+ = z^+$ values over the suction side of the rotor for $\dot{m} = 19$ kg/s.

to have an effect on the recirculation bubble properties.

Figure 4.12 shows a comparison between the different meshes for several quantities characterizing the mean flow (isentropic Mach number, friction coefficient, boundary layer thickness) and the fluctuations (RMS pressure fluctuations P_rms) in the vicinity of the fan blade surface. The friction coefficient C_f and boundary layer displacement thickness δ_1 are shown for the suction side only, where the separation bubble appears. Overall, the results show a fairly good agreement between the different meshes along the blade chord length. The distributions of M_{is} and P_rms on the pressure side are close for the 3 meshes. On the suction side, near the LE, a separation zone can be associated with the region of negative friction coefficient and the plateau of isentropic Mach number. It should be noted that high pressure fluctuations are also observed in that region. Some discrepancies between WR-Mesh1 and WR-Mesh2 results can be seen for all the quantities in Figure 4.12, particularly in the separation region. These differences are more pronounced for δ_1 over the whole suction side, where WR-Mesh1 predicts a faster increase of the thickness of the boundary layer. This may be due to differences in the transition to turbulence, which may lead to cumulative discrepancies. When comparing WR-Mesh2 and WR-Mesh3, similar results are obtained for the different quantities in Figure 4.12 along the whole blade surface. This justifies the use of WR-Mesh2 to study the effects of the mass flow rate in the following.

Temporal convergence

Temporal convergence is necessary to ensure proper physical analysis. Two different types of temporal convergence are studied here for the mesh WR-Mesh2 at a mass flow rate of $\dot{m} = 20$ kg/s. The first type of convergence is referred to as numerical convergence and corresponds to the end of the transient state. The second type of convergence is referred to as statistical convergence and corresponds to the convergence of the flow statistics. Unsteady velocity samples are collected for the convergence analysis. These are obtained from the suction side boundary layer near the fan TE, at a normalized wall-normal distance of $y^+ = 50$. Based on the convergence analysis methodology introduced by Boudet *et al.* [17], the velocity signal is split into four segments and the statistical estimates on the
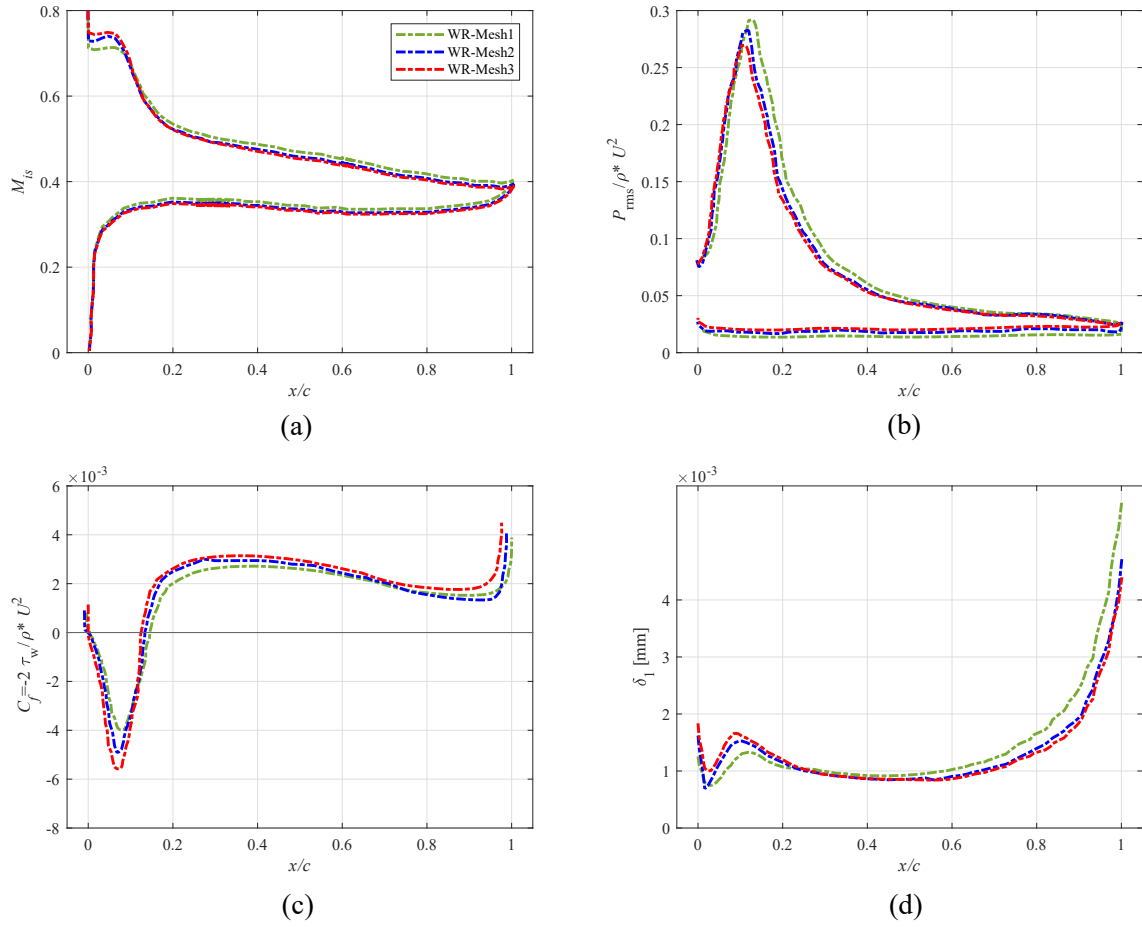
Figure 4.12: Grid convergence. (a) Isentropic Mach number M_{is} and (b) RMS pressure fluctuations P_{rms} along the rotor blade. (c) Friction coefficient C_f and (d) boundary layer displacement thickness δ_1 along the suction side of the rotor blade. ρ is the density and τ_w is the wall shear stress.
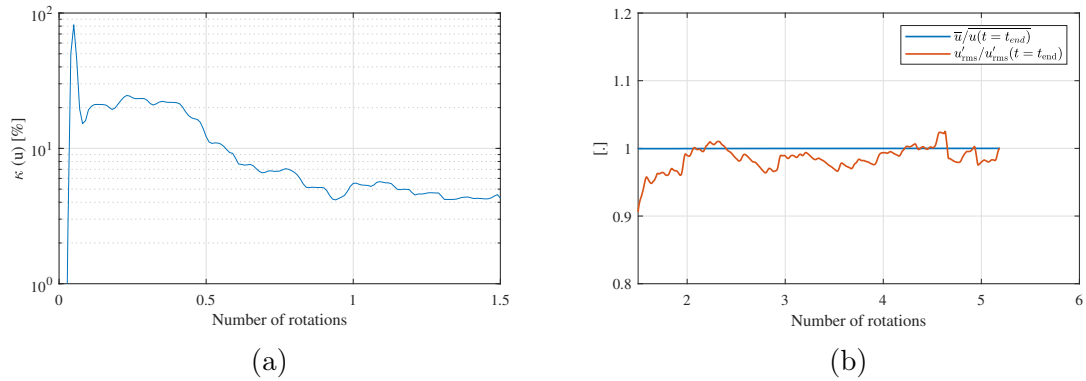
Figure 4.13: Temporal convergence for the WR-Mesh2 case. (a) Numerical convergence. The number of rotations corresponds to the end of the first segment. (b) Statistical convergence. The mean value ($\bar{u}$) and the standard deviation (u'_{rms}) of the streamwise velocity component are normalized by their values at the end of the simulation ($t = t_{end}$, where "t" corresponds to the time).

131

last three segments are compared. The numerical convergence is estimated by introducing the function

$$\kappa(u) = \max\left(\max_{i,j=2..4}\left(\left|\frac{\overline{u}^{(i)} - \overline{u}^{(j)}}{\overline{u}^{(4)}}\right|\right), \max_{i,j=2..4}\left(\left|\frac{u_{RMS}^{\prime(i)} - u_{RMS}^{\prime(j)}}{u_{RMS}^{\prime(4)}}\right|\right)\right) \times 100 \qquad (4.1)$$

where $\overline{u}^{(i)}$ and $u_{RMS}^{\prime(i)}$ are the average of a velocity component and the RMS velocity fluctuations, respectively, calculated over the i-th segment. The evolution of $\kappa(u)$ is presented in Figure 4.13 (a). Numerical convergence is reached when κ stabilizes within a few per cent (4% in this case). The statistics are then calculated from this point, at the end of the first segment.

The statistical convergence is considered to be reached when the statistics reach a constant value. Figure 4.13 (b) shows the evolution of the mean ($\overline{u}$) and the standard deviation (u'_{rms}) of the streamwise velocity component (u), both normalized by values at the end of the simulation. It can be observed that the simulation is well converged after 1.5 rotations.

Grid and temporal convergence ———————————— **Summary**

Configuration.

- Radial-slice sector LES.

- LES are performed at approach condition (55Nn) without turbulence injection.

Grid convergence.

- A grid convergence analysis is performed assessing the influence of the stretching ratio in the direction normal to the wall on the recirculation bubble characteristics.

- The adopted unstructured mesh consists of 80×10^6 cells with $y^+ = 1$, $x^+ = z^+ = 35$ (which are consistent with the state of the art requirements) and a stretching ratio of 6%.

Temporal convergences.

- The numerical and statistical convergences are ensured after 1.5 fan rotations.

4.4.2 Aerodynamic results

The decrease of the fan blade angle of attack α when the mass flow rate $\dot{m}$ increases (shown in Table 4.4) is expected to cause variations of the recirculation bubble characteristics,

Table 4.4: Fan blade angle of attack α for various mass flow rates $\dot{m}$.

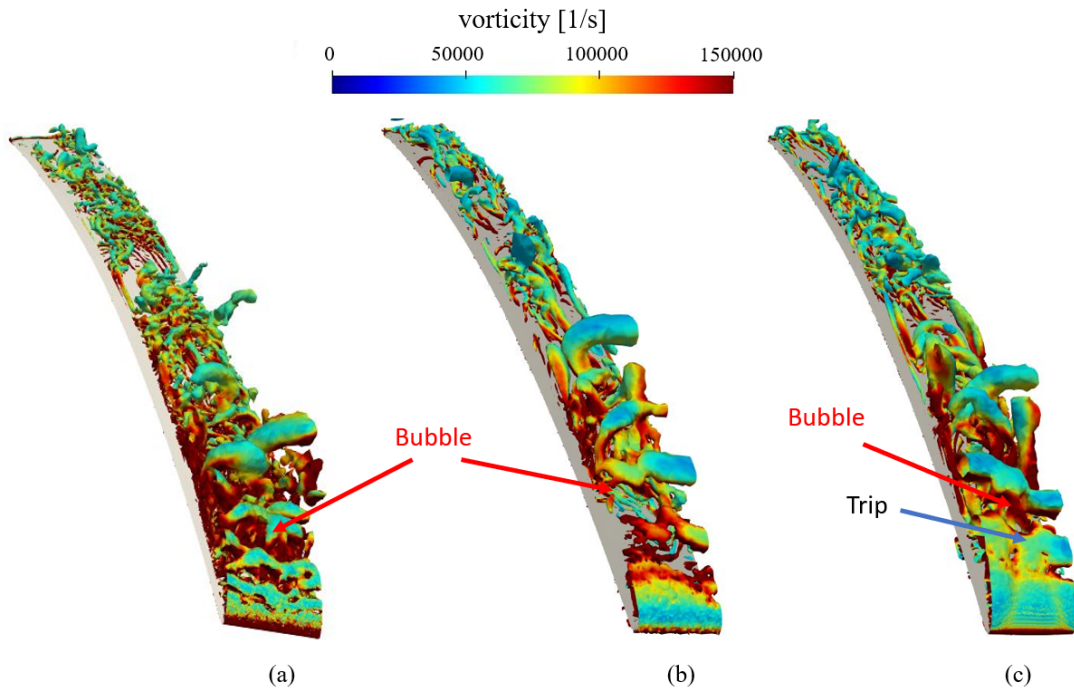| $\dot{m}$ [kg/s]	19	20	21	22
α [°]	12.5	9.10	7.40	5.30
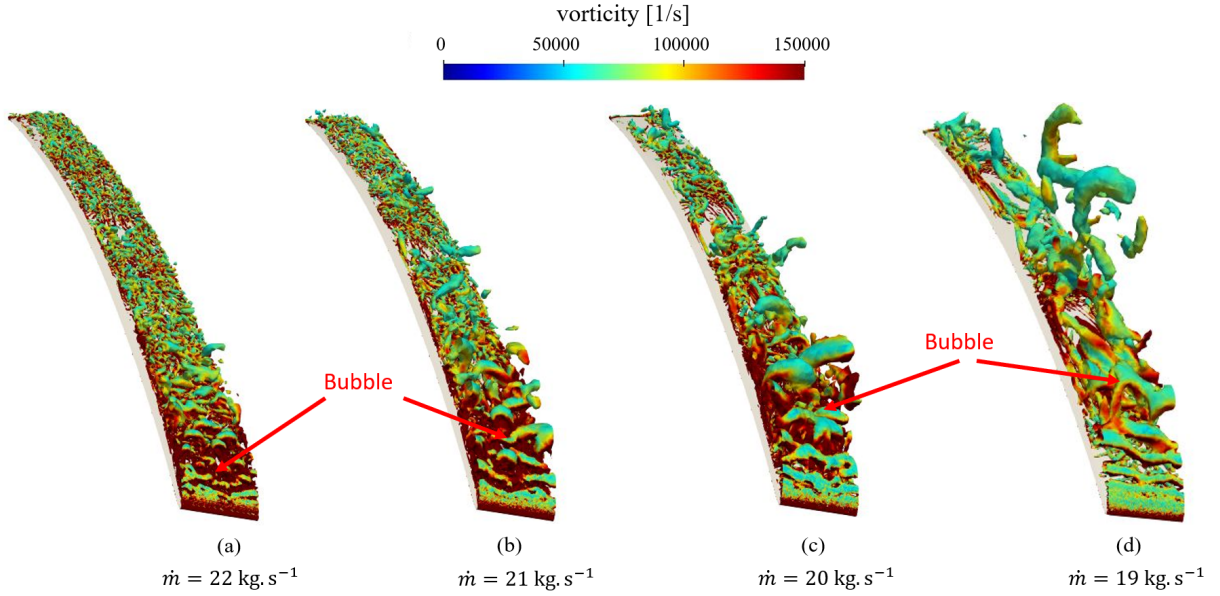
Figure 4.14: Iso-surfaces of Q-criterion ($Qc^2/U_0^2 = 1500$), colored by the vorticity magnitude, for the different mass flow rates. The cases are shown by decreasing mass flow rate, and increasing angle of attack of the fan blade.

which are detailed in the following.

The turbulent structures on the suction surface of the rotor blade are shown in Figure 4.14, for the different mass flow rates, using iso-surfaces of the Q-criterion ($Qc^2/U_0^2 = 1500$, where U_0 is the free-stream velocity magnitude) colored by the vorticity magnitude. For all the cases, a recirculation bubble appears close to the LE and leads to the transition of the boundary layer to turbulence, as discussed for Figure 4.2. When comparing the different cases, the reduction of the mass flow rate delays the boundary layer transition and leads to larger turbulent structures in the separation region and in the downstream direction.

The flow topology around the rotor blades is then analyzed by means of the mean streamwise velocity component, u, (Figure 4.15) and the turbulent kinetic energy, k_t, (Figure 4.16), which are averaged in the rotating reference frame. The averaged values are computed over 3.5 rotations of the fan. As shown in Figures 4.3 and 4.4, the recirculation bubble is identified by a zone of negative velocity and high turbulent kinetic energy for the different mass flow rates. By comparing the flow topology obtained from the different cases, we can observe that as the mass flow rate decreases, the bubble position is shifted downstream over the suction side and the size of the bubble increases. However, smaller values of the maximum turbulent kinetic energy are observed when the mass flow rate decreases. Consequently, both the boundary layer and the wake thicknesses increase when the mass flow rate is reduced.

The distributions of isentropic Mach number, M_{is}, and the RMS of the pressure fluctuations, P_{rms}, along the blade, are presented in Figure 4.17. As shown in Figure 6.1, the
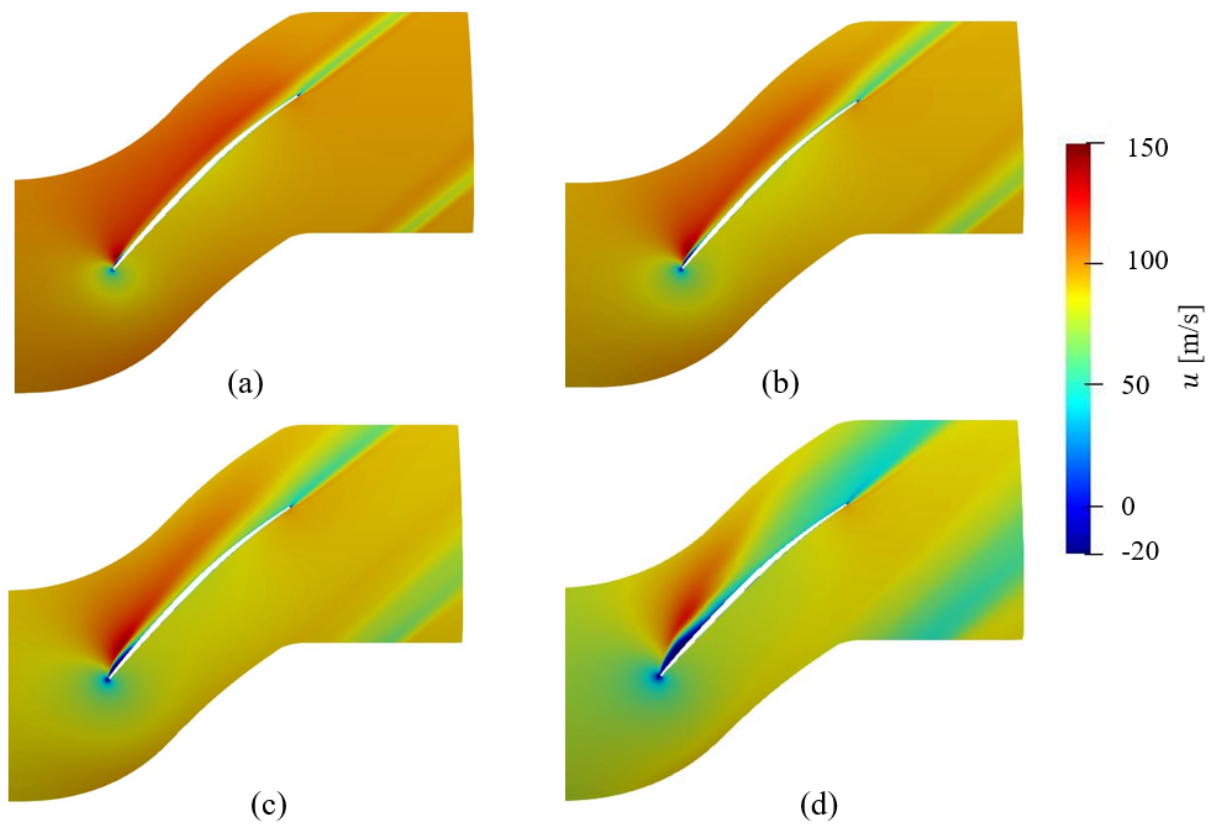
Figure 4.15: Contours of averaged streamwise velocity u around the rotor blade, for various mass flow rates, (a) $\dot{m} = 22$ kg/s, (b) $\dot{m} = 21$ kg/s, (c) $\dot{m} = 20$ kg/s and (d) $\dot{m} = 19$ kg/s.
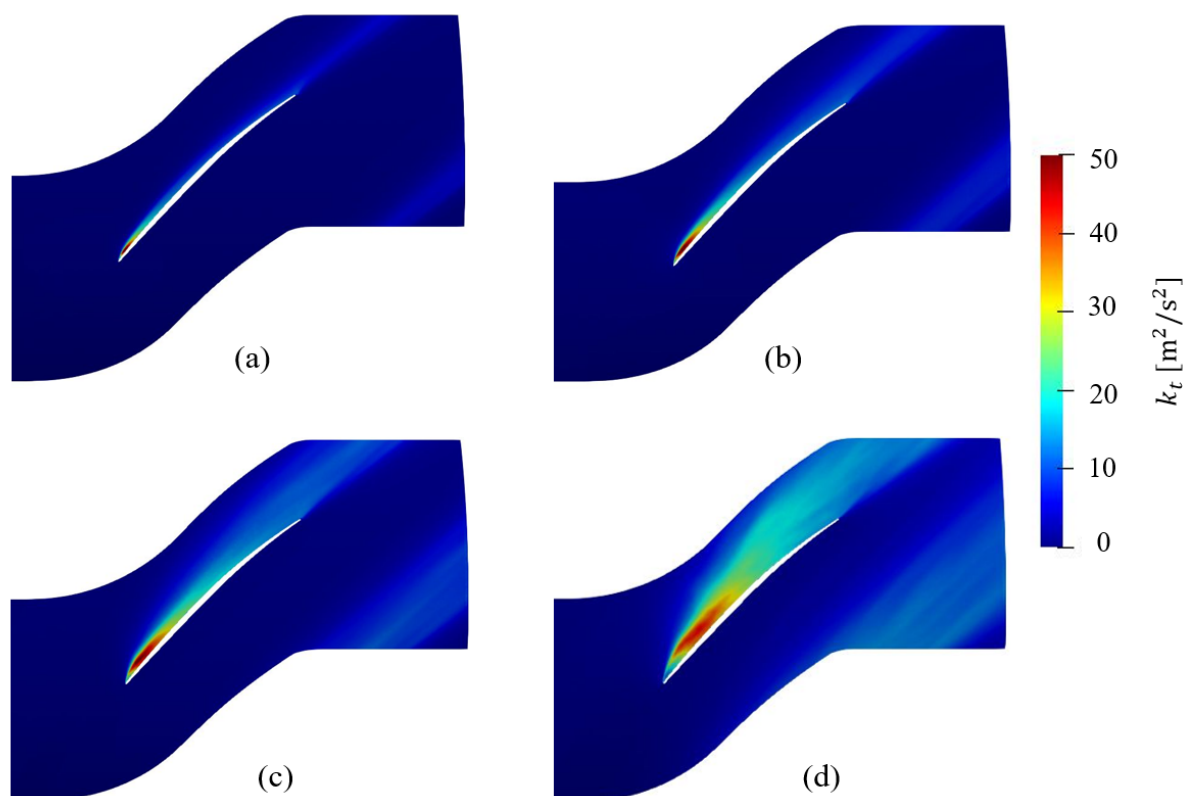
Figure 4.16: Contours of turbulent kinetic energy k_t around the rotor blade, for various mass flow rates, (a) $\dot{m} = 22\,\mathrm{kg/s}$, (b) $\dot{m} = 21\,\mathrm{kg/s}$, (c) $\dot{m} = 20\,\mathrm{kg/s}$ and (d) $\dot{m} = 19\,\mathrm{kg/s}$.
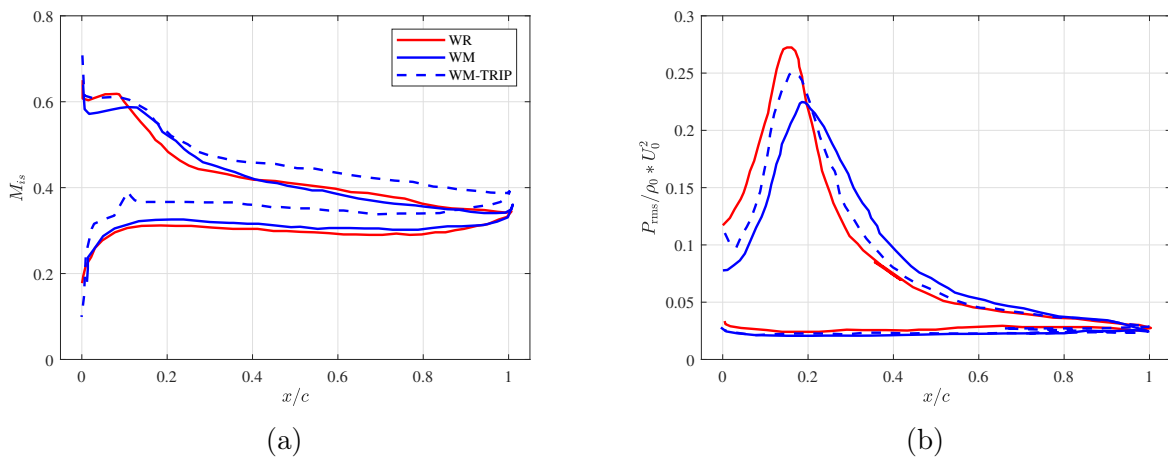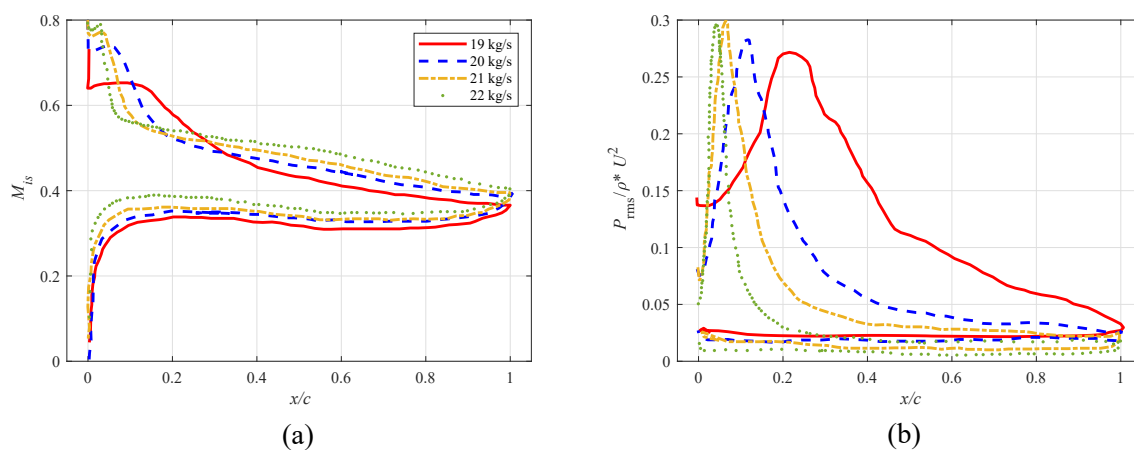

Figure 4.17: Average isentropic Mach number M_{is} (a) and RMS pressure fluctuations P_{rms} (b) along the rotor blade for various mass flow rates.
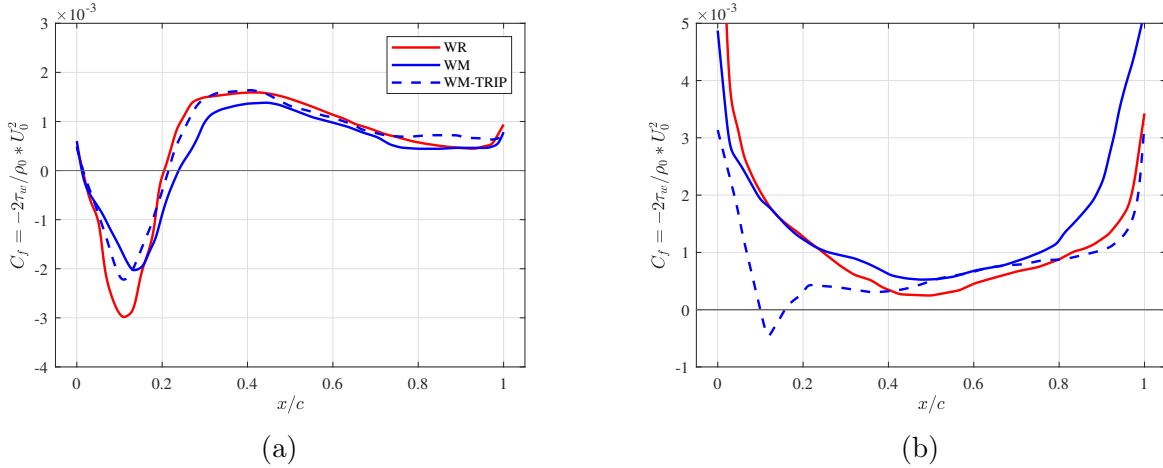
135
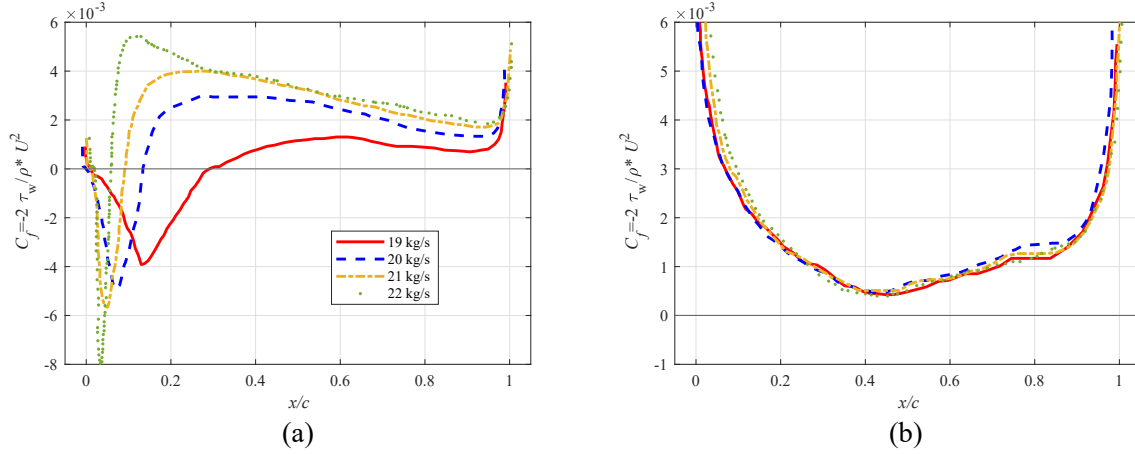
Figure 4.18: Average friction coefficient C_f along the rotor blade for various mass flow rates. (a) suction side. (b) pressure side.

recirculation bubble is identified by the plateau of M_{is} in Figure 4.17 (a), and the large P_{rms} values in Figure 4.17 (b), for the different mass flow rates. It can be observed that, as the mass flow rate decreases, the bubble is shifted downstream and its size increases, which is consistent with our previous findings from the flow topology. The strength of the additional self-noise source due to the recirculation bubble can be partly related to the P_{rms} levels. When the mass flow rate decreases, the maximum value of P_{rms} is lower, but the width of the peak increases. These changes are expected to have an impact on the noise radiated by this additional noise source.

As in Section 4.2, the friction coefficient, C_f, is used to characterize the size of the re-circulation bubble. A comparison of C_f between the different mass flow rates is presented in Figure 4.18, over the suction side (a) and the pressure side (b) of the rotor blade. For all the cases, the recirculation bubble is identified by a region of negative friction coefficient close to the LE of the blade on the suction side, and the size of the bubble is obtained from the locations where C_f reaches zero. As for the analysis of M_{is} in Figure 4.17, the reattachment point is shifted downstream as the mass flow rate decreases, which leads to a larger recirculation bubble. On the pressure side, the distribution of C_f is quite similar for the different mass flow rates and remains positive, which suggests that the flow is attached all along the pressure side.

Several boundary layer parameters are computed on the suction side of the rotor blade for the different mass flow rates and compared in Figure 4.19. The displacement thickness is defined as,

$$\delta_1 = \int_0^\delta (1 - \frac{\rho U}{\rho_0 U_0}) \mathrm{d}n. \tag{4.2}$$

The momentum thickness is defined as,

$$\delta_2 = \int_0^\delta \frac{\rho U}{\rho_0 U_0} (1 - \frac{U}{U_0}) \mathrm{d}n, \tag{4.3}$$

and the shape factor $H_{12} = \delta_1/\delta_2$, where n is the wall normal distance to the suction side surface of the blade, ρ_0 is the freestream density, and ρ and U are the density and the velocity magnitude in the boundary layer, respectively. The development of the boundary layer can be divided into three main regions, (i) the separation region, (ii) the
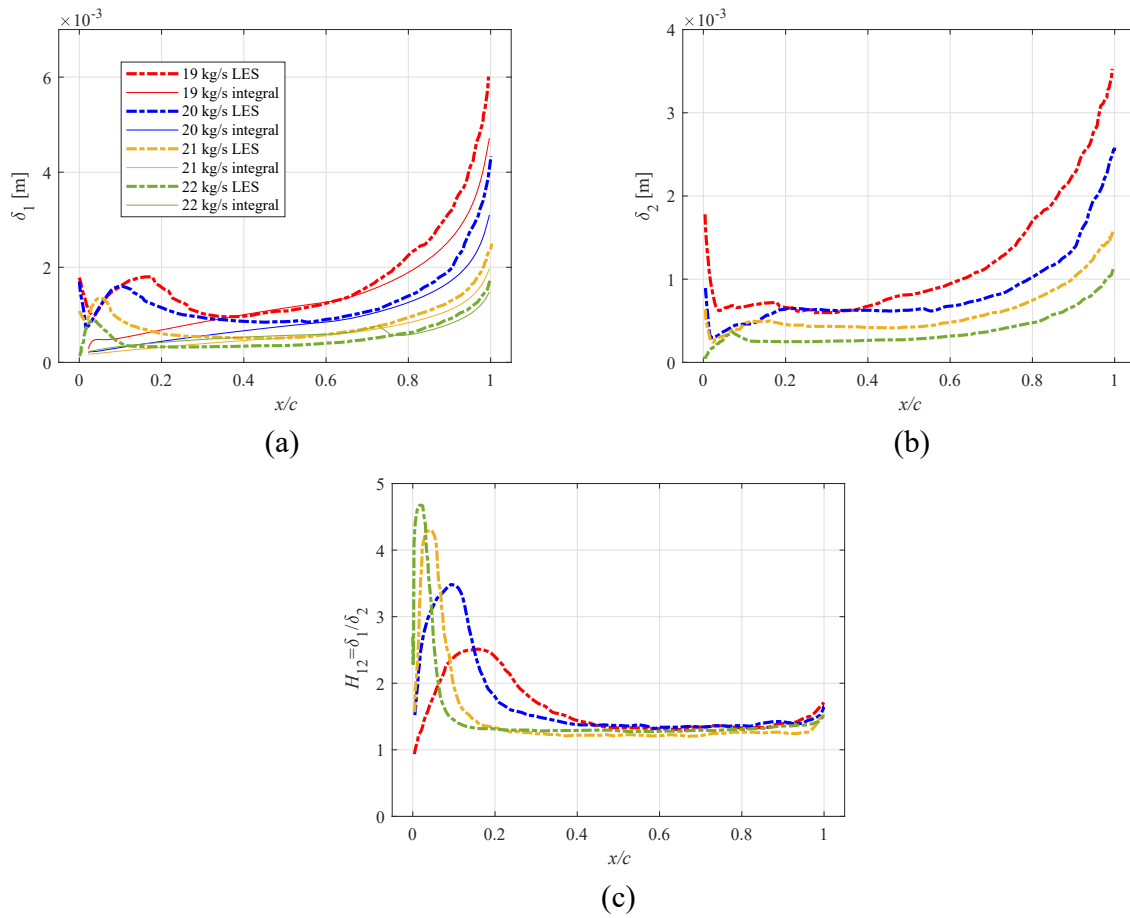
Figure 4.19: Comparison of boundary layer parameters on the suction side of the rotor blade for various mass flow rates. (a) Boundary layer displacement thickness δ_1, (b) momentum thickness δ_2, (c) and shape factor H_{12}.
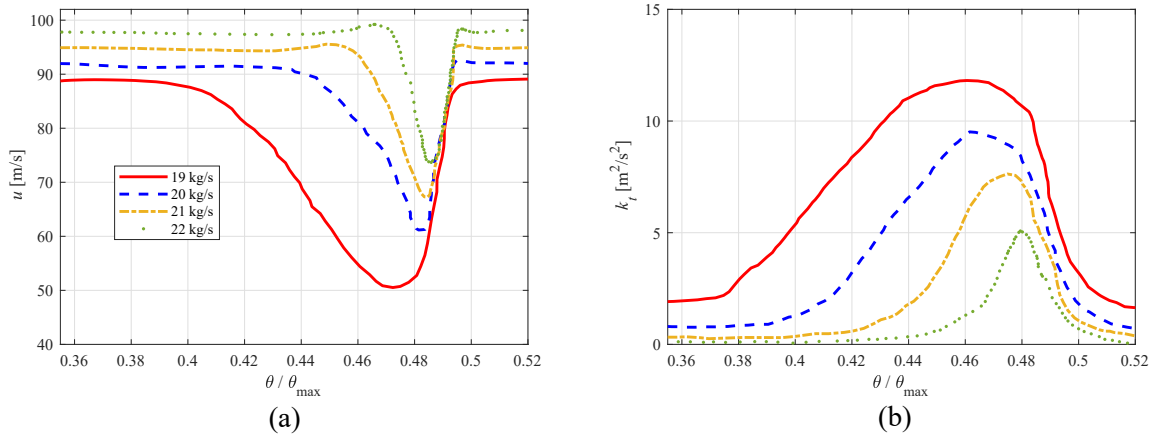
Figure 4.20: Comparison of the streamwise velocity component u (a) and k_t (b) profiles in the wake of the rotor blade, at one chord length from the TE.

reattachment region and (iii) the adverse pressure-gradient region. For all cases, near the LE, the displacement thickness δ_1 reaches a local maximum in the recirculation bubble, while the momentum thickness δ_2 is almost constant. Thus, in this region, large values of the shape factor H_{12} are reached. Downstream of the recirculation bubble, the boundary layer is reattached and the shape factor decreases significantly. As previously discussed, the streamwise location of the reattachment point varies significantly with the mass flow rate, and consequently the end of the H_{12} hump varies from $0.1c$ for the largest mass flow rate ($\dot{m} = 22$ kg/s) to $0.35c$ for the smallest mass flow rate ($\dot{m} = 19$ kg/s). After the reattachment, a plateau is observed for the boundary layer parameters. The size of this plateau increases with the mass flow rate. At further downstream locations, the combined effects of the adverse pressure gradient and the friction lead to an increase in both the displacement and momentum thicknesses while the shape factor remains nearly constant. By comparing the different cases, it can be observed that decreasing the mass flow rate leads to a thicker boundary layer with a larger separation region, and a reattachment point that is shifted further downstream.

The evolution of the boundary layer is controlled by several parameters, including the separation region due to the recirculation bubble, the pressure gradient and the skin friction. In order to study the effect of the recirculation bubble on the boundary layer, the displacement thickness has also been computed using the integral formulation available in the numerical software Xfoil [56, 55], neglecting the influence of periodicity. The results are compared to the LES computations for the different mass flow rates in Figure 4.19 (a). When using the integral formulation in Xfoil, the boundary layer is assumed to be fully turbulent from the LE, such that there is no recirculation bubble. The levels of δ_1 obtained from the integral formulation are consequently adjusted to match the values of δ_1 in the LES at a given axial position by adding a constant value. This allows for the comparison of the δ_1 distribution, taking into account the effect of the bubble on the boundary layer thickness. The differences in the δ_1 distributions for the different mass flow rates are mainly due to differences in the angle of attack and Reynolds number. The results from the LES and the integral formulation for the different mass flow rates show similar trends once the boundary layer is reattached, whereas significant differences can be found in the separation and reattachment regions. This is particularly true for the large mass flow rates (21 kg/s and 22 kg/s), which suggests that downstream of the
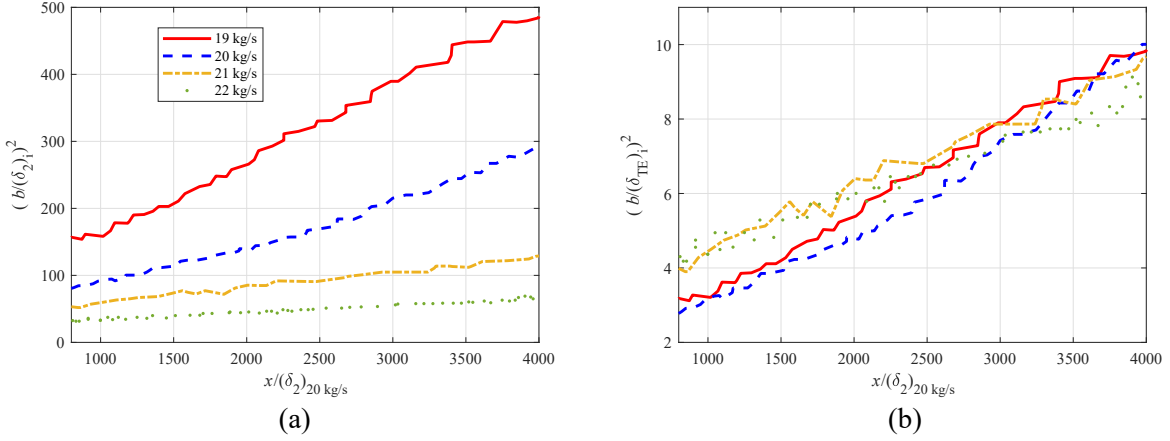
Figure 4.21: Streamwise evolution of the wake half-width b, normalized by the momentum thickness in the far wake δ_2 (a), and the boundary layer thickness at the blade TE δ_{TE} (b). x is the streamwise direction and $x = 0$ m corresponds to the blade TE.

bubble, the boundary layer is fully turbulent and that its thickness is only controlled by the pressure gradient and the skin friction. For small mass flow rates, discrepancies become significant due to the presence of a large recirculation bubble, which affects the boundary layer development over a larger region of the blade. Once the flow is reattached, the δ_1 distributions have similar trends despite the differences in absolute value.

Finally, the effect of the mass flow rate on the rotor wakes is studied. Figure 4.20 shows the distributions of the streamwise velocity component u and the turbulent kinetic energy k_t at a distance of one chord length from the TE of the rotor blade. θ_{max} is the angular sector of a single fan blade passage, which corresponds to $2\pi/16$. When the mass flow rate decreases, the wake becomes thicker whereas both the velocity deficit and turbulent kinetic energy increase, which is consistent with the results in Figures 4.15 and 4.16. For the largest mass flow rate case ($22\,\mathrm{kg/s}$), it seems that a symmetric Gaussian function could fit the circumferential distribution of k_t, whereas cases with a low mass flow rate show skewed wake profiles towards the suction side. The wake is further analyzed by calculating the wake half-width, b, which can be defined as the width of the wake where the velocity reaches 50% of the maximum velocity deficit. The axial evolution of the wake half-width is shown in Figure 4.21 (a), in which the variables are normalized by the momentum thickness in the far-wake, which is assumed to be constant for each case. It should be noted that the momentum thickness in the far-wake can be computed from Eq.D.11, which can be rewritten as $\delta_2 = \int_0^{\delta_w} \frac{\rho u}{\rho_0 U_0}(1 - \frac{u}{U_0})\mathrm{dn}$, where u corresponds to the streamwise component of the mean velocity in the wake, U_0 corresponds to the freestream velocity magnitude outside the wake and δ_w corresponds to wake width. Results in Figure 4.20 (a) are shown for the far-wake region ($x/\delta_2 > 800$), where the wake properties are assumed to have an asymptotic behavior and δ_2 is nearly constant. A linear increase of b^2 with the downstream distance can be observed for the different cases. Furthermore, the wake half-width also increases as the mass flow rate decreases, which is consistent with the trends in the boundary layer thicknesses in Figure 4.19. Figure 4.21 (b) shows the evolution of b normalized by the boundary-layer thickness at the TE of the fan blade, δ_{TE}, which is defined as the wall-normal distance from the blade surface where the velocity reaches 99% of the freestream velocity. All cases seem to collapse onto a single trend, particularly beyond a streamwise distance where the wake is fully developed

$(x/\delta_2 > 2500)$. In this case, the evolution of the fan wake is controlled by the boundary layer thickness at the TE of the blade.

Influence of the mass flow rate: aerodynamic results ——————— Summary

- For the various mass flow rates:

  – The recirculation bubble is characterized by a region of negative streamwise velocity and friction coefficient, high turbulent fluctuations and a plateau in the distribution of isotropic Mach number over the suction side of the rotor blade.

  – The boundary layer is reattached before the trailing edge of the blade in a fully turbulent state.

  – The wake width scales with the boundary layer thickness at the trailing edge of the rotor blade.

- When the mass flow rate is reduced:

  – The length of the bubble and the extent of the region of high RMS pressure fluctuations over the suction side of the rotor blade are increased.

  – The bubble is shifted downstream over the suction side of the rotor blade.

  – The peak of RMS pressure fluctuations in the separation zone is decreased.

  – The boundary layer displacement and momentum thicknesses and the wake width are increased.

4.4.3 Aeroacoustic results

Contours of the instantaneous dilatation rate $(\nabla \cdot \mathbf{u})$ for $\dot{m} = 20 \, \text{kg/s}$ are shown in Figure 4.22, along with iso-surfaces of Q-criterion $(Qc^2/U_0^2 = 100)$ colored by the vorticity magnitude. The development of turbulent structures around the blades and in the wakes can be observed. The contours of instantaneous dilatation rate show wave-fronts generated by the TE and the bubble region near the LE. The present simulations are able to capture the noise generation mechanisms at the TE and in the bubble region, as well as the acoustic wave propagation in the refined-mesh region around the fan stage. It should be noted that there is no acoustic reflection from the upstream and downstream boundaries of the domain. The turbulence in the fan wakes near the TE in Figure 4.22 does not seem to contribute to the radiated noise from the fan stage, which indicates that quadrupole noise sources from the wake are not dominant when compared to dipole noise sources from the blades.

The acoustic field is directly computed in the LES simulations up to one rotor chord length upstream of the rotor blades, in the mesh refinement region. A comparison of the PSD of the pressure fluctuations (p') for various mass flow rates is showed in Figure 4.23
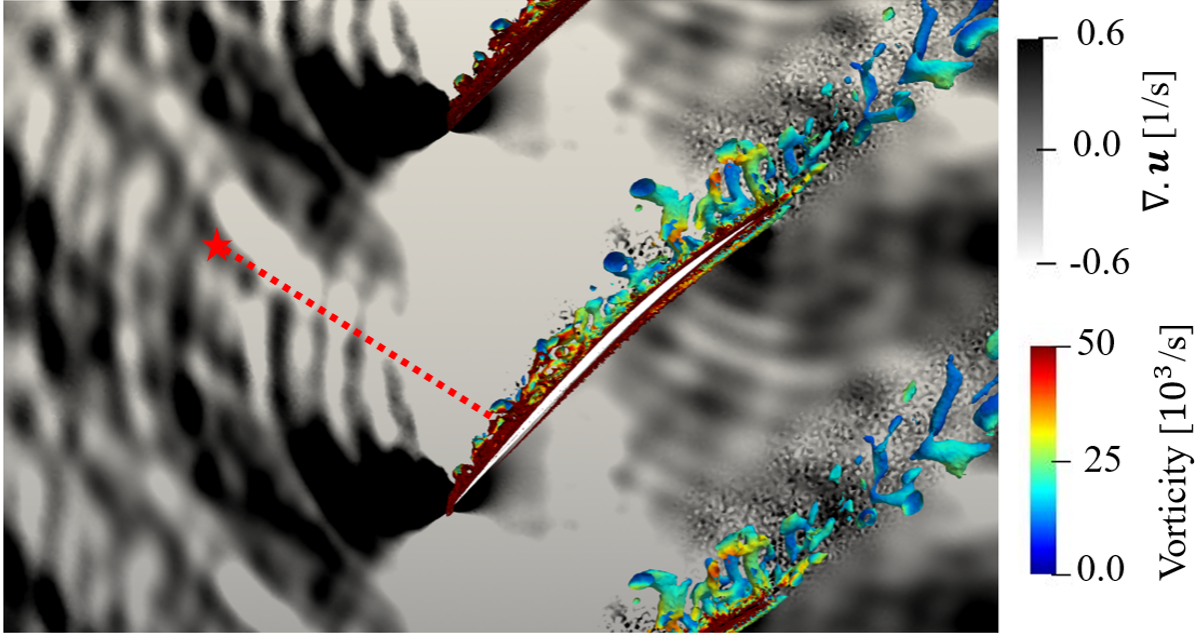
Figure 4.22: Instantaneous contours of dilatation rate and iso-surfaces of Q-criterion ($Qc^2/U_0^2 = 100$) colored by the vorticity magnitude, at $\dot{m} = 20$ kg/s. The star symbol indicates the location of the monitor point where unsteady pressure samples are collected for the PSD computation. The dashed-line shows the location of the monitor points used for the calculation of the coherence.

(a). All the PSD spectra are obtained by multiplying the pressure signals by a Hanning window with 50% overlap and by averaging the signals using 5 segments of length 2^{10}. A pressure reference of $P_{\text{ref}} = 2.10^{-5}$ Pa is adopted. The location of the monitor point used for the unsteady data collection is indicated by the star symbol in Figure 4.22. For the different cases, tones at 3200 Hz and 6400 Hz can be observed. The frequencies at which these tones appear are independent of the mass flow rate and correspond to the first two harmonics of the Vane Passing Frequency VPF $= V\Omega/60$, where Ω is the rotation speed in RPM, and $V = 32$ corresponds to the number of vanes in the full stage. The presence of tones at harmonics of the VPF for a monitor point that is rotating with the rotor domain can be associated with the noise emitted by the periodic interaction of the rotor blade wakes with the stator vanes. For a monitor point in the stator domain, this interaction is expected to generate noise at the BPF and its harmonics $\text{BPF}_n = nB\omega$, where $\omega = \Omega/60$ and n corresponds to the order of the BPF harmonic. Using the Tyler and Sofrin rule [261], the acoustic modes that are generated by the interaction noise have azimuthal orders $m = nB - kV$, where k is an integer. If the monitor point is in a rotating reference frame, its angular position θ varies with time, such that $\theta(t) = \omega t$. Thus, for a duct mode of order m, the phase term of the pressure fluctuation that depends on θ and t in the rotating reference frame can be written as,

$$\text{e}^{\text{i}(m\theta(t)-\omega t)} = \text{e}^{\text{i}([nB-kV]\omega t - nB\omega t)} = \text{e}^{-\text{i}kV\omega t} \tag{4.4}$$

where i is the imaginary unit and the frequency $kV\omega$ corresponding to the VPF harmonics can be recognized.

At higher frequencies, between 10 kHz and 13 kHz, a peak is visible for each case, except for the largest mass flow rate ($\dot{m} = 22$ kg/s). This peak is referred to as HFP^{1st} in

141

(a)

(b)
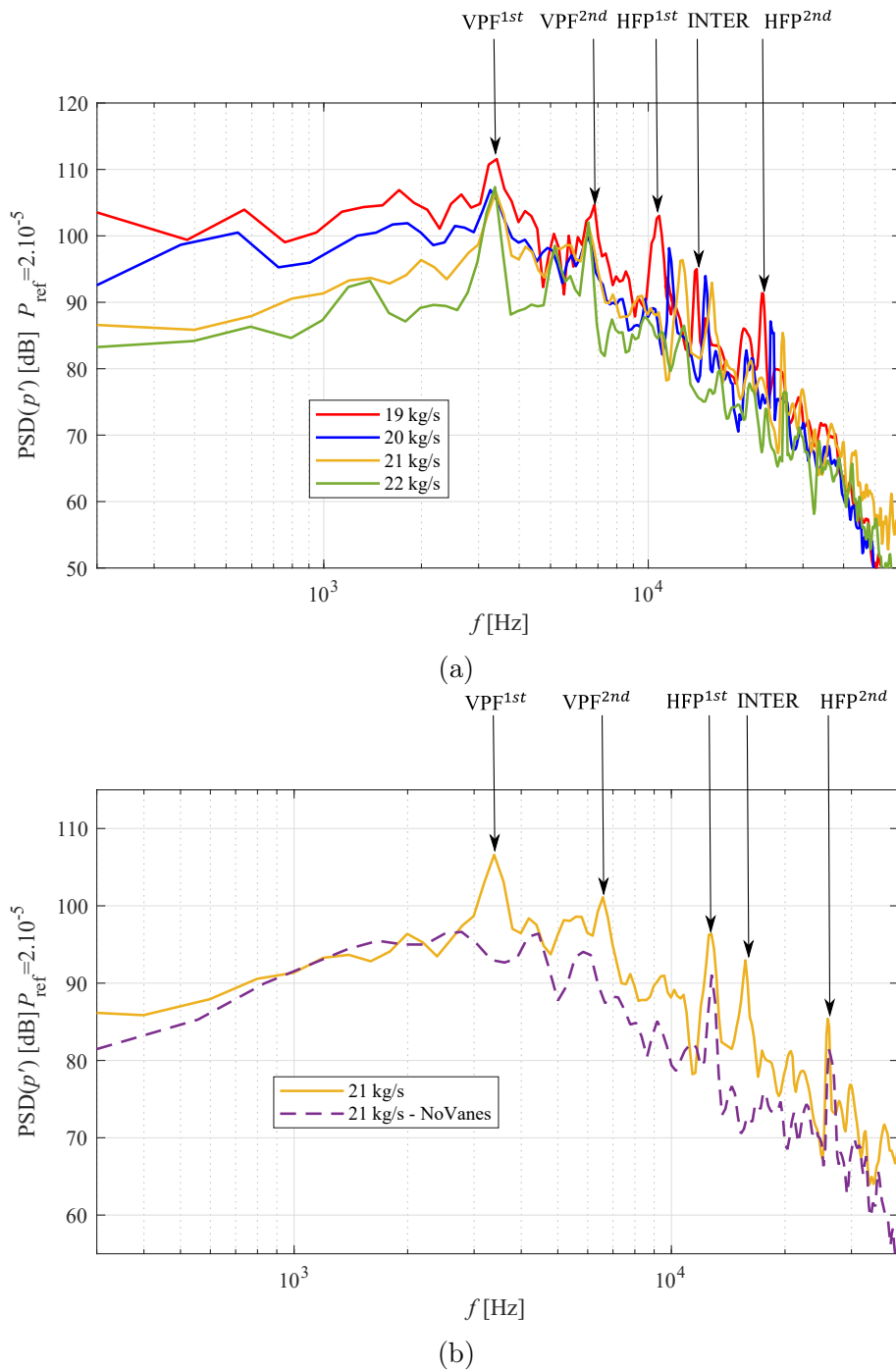
Figure 4.23: PSD of the pressure fluctuations from a monitor point normal to the rotor surface at one chord length from the rotor LE (indicated by a star in Figure 4.22) in the rotating frame of reference. (a) Rotor-stator simulations at various mass flow rates. (b) Comparison with a rotor-only simulation at $\dot{m} = 21\,\mathrm{kg/s}$.

142
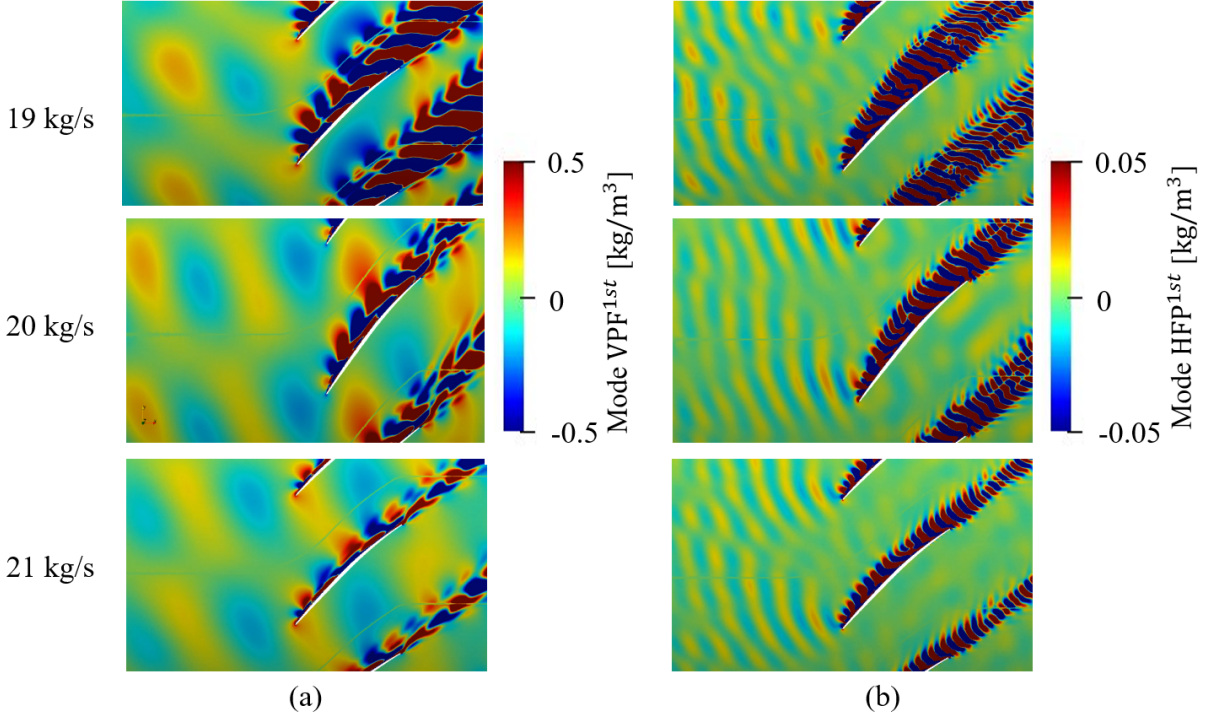
Figure 4.24: Spatial distribution of the density modes using the DMT technique. (a) VPF^{1st}. (b) HFP^{1st}.

Figure 4.23. Its second harmonic, denoted HFP^{2nd}, can also be observed in Figure 4.23. When the mass flow rate increases, the frequency of these High Frequency Peaks (HFP) increases (e.g. from 10.5 kHz to 12.8 kHz for HFP^{1st}) whereas their amplitude decreases. For each case where HFP peaks are present, an additional peak denoted INTER in Figure 4.23 can be observed at a frequency $\text{INTER} = \text{HFP}^{1st} + \text{VPF}^{1st}$. The HFP peaks are related to a noise mechanism associated with the recirculation bubble, and are discussed below, whereas the INTER peak is an interaction tone between HFP^{1st} and VPF^{1st}.

The effects of the stator on the generated noise can also be shown when comparing the acoustic spectra from the different mass flow rates in Figure 4.23 (a). When the mass flow rate is reduced, the turbulent kinetic energy in the boundary layers on the suction side of the rotor and in the rotor wakes is increased. Consequently, the trailing edge noise and the rotor-stator interaction noise are amplified. In Figure 4.23 (a), we can observe that the broadband noise component is increased with the reduction of the mass flow rate, and thus with the increase of the size and turbulent intensity of the recirculation bubble. This can be partly explained by the rotor-stator interaction noise, showing the effects of the stator on the generated noise.

The separation noise contribution can be compared to the rotor-stator interaction noise, which is the noise source that is usually considered as the dominant source in fan/OGV configurations at approach conditions. The amplitudes of the peaks VPF^{1st} and HFP^{1st} are compared in Table 4.5 for various mass flow rates. For the different cases, the contribution of the rotor-stator interaction noise is shown to be dominant. As the mass flow rate decreases, the amplitude of the VPF^{1st} peak increases. This is due to the increase of the width of the rotor wakes and the turbulence intensity in the wakes, with the increase of the recirculation bubble strength, which leads to an increase of the rotor-stator interaction noise. It is also interesting to compare the amplitude of the peak

Table 4.5: Comparison of the amplitudes of the peaks VPF^{1st} and HFP^{1st} for different mass flow rates.

$\dot{m}$ [kg/s]	$\|\text{VPF}^{1st}\|$ [dB]	$\|\text{HFP}^{1st}\|$ [dB]	$\Delta(\|\text{VPF}^{1st}\| - \|\text{HFP}^{1st}\|)$ [dB]
19	111.0	103.5	7.5
20	107.0	98.6	8.4
21	106.2	96.6	9.6
22	106.0	86.5	19.5
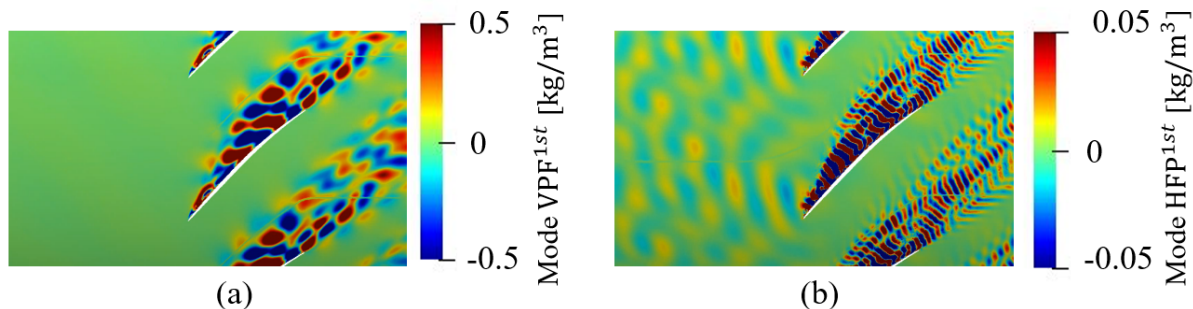
Figure 4.25: Spatial distribution of the density modes using the DMT technique for the case at $\dot{m} = 21$ kg/s without stator vanes. (a) VPF^{1st}. (b) HFP^{1st}.

HFP^{1st} from the lowest mass flow rate ($\dot{m} = 19$ kg/s) with the amplitude of the peak VPF^{1st} from the largest mass flow rate ($\dot{m} = 22$ kg/s), for which the bubble has limited influence on the rotor wakes. The contribution of the peak HFP^{1st} ($\dot{m} = 19$ kg/s) is comparable to VPF^{1st} ($\dot{m} = 22$ kg/s) with a difference of 2.5dB, which suggests that the noise associated to the recirculation bubble can be of the same order of magnitude as the rotor-stator interaction noise in a stage without the presence of a recirculation bubble.

In order to better understand the effects of a recirculation bubble on the fan noise, an additional LES is performed at $\dot{m} = 21$ kg/s without the stator vanes. Nevertheless, the stator domain without vanes that is downstream of the rotor is kept in the simulation in order to maintain the same length of the computational domain. The PSD of the pressure fluctuations obtained from the simulations at 21 kg/s, with and without the stator vanes, are compared in Figure 4.23 (b). As expected, the peaks at the VPFs and INTER frequencies are not present in the spectrum for the simulation without stator vanes. However, the HFPs can still be seen in the noise spectrum. The frequencies at which these tones appear are quite similar between the two cases, with and without the stator vanes, while the amplitudes are reduced in the case without stator vanes (a reduction of 5 dB for HFP^{1st} and 4 dB for HFP^{2nd}). In addition, the removal of the stator vanes leads to a broadband noise reduction of 5 to 8 dB over the frequency range starting from 3 kHz up to the cut-off frequency (30 kHz). This shows that the rotor-stator interaction noise, which is due to the interaction of the rotor wakes with the stator vanes, is significant.

The tones observed in Figure 4.23 can be further investigated using a mode decomposition technique, which is known as Dynamic Mode Tracking (DMT) [214]. The DMT has been developed to study the spatial and temporal features of the flow at a given frequency. It has the advantage to be an "on-the-fly" method, which is useful to reduce the computational expense and data storage requirements. Figure 4.24 shows DMT results
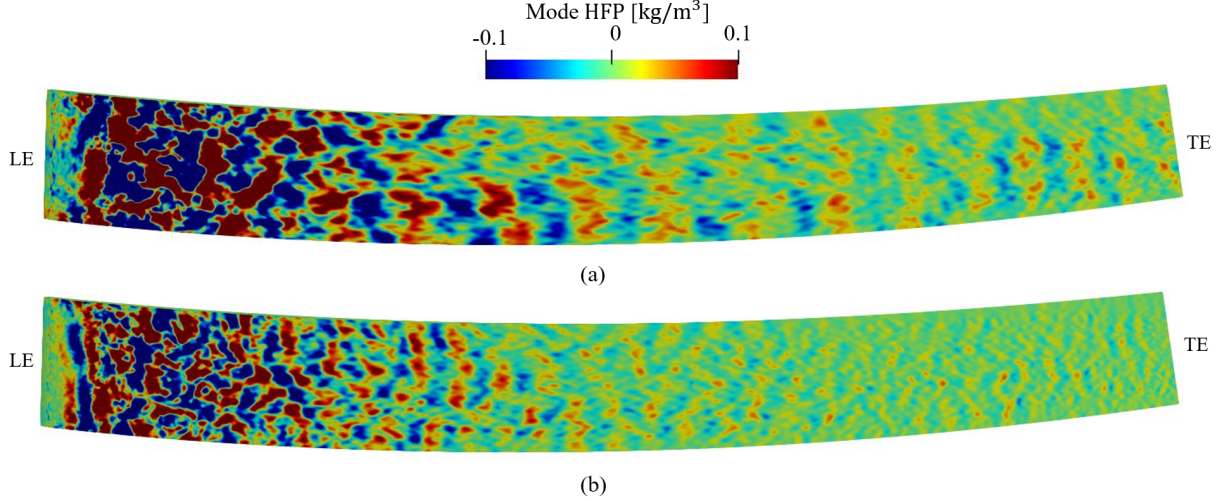
Figure 4.26: Spatial distribution of the density modes using the DMT technique on the suction side of the rotor blade at $\dot{m} = 19$ kg/s. (a) HFP^{1st}. (b) HFP^{2nd}.

calculated from the density in the LES with the stator vanes, at VPF^{1st} and HFP^{1st}, for various mass flow rates. Figure 4.25 shows the DMT results for the simulation without the stator vanes, at $\dot{m} = 21$ kg/s. For the simulations with stator vanes, the mode that is related to the VPF^{1st} shows wave-like fluctuations coming from downstream of the rotor and propagating in the upstream direction, through the blade passage. For the simulation without the stator vanes, the upstream propagating density fluctuations are not observed in Figure 4.25(a). Thus, the behavior of this mode at the VPF^{1st} confirms that the peaks observed at this frequency in Figure 4.23 are associated with the interaction tones between the periodic rotor wakes and the stator vanes.

The DMT results computed at the HFP^{1st} in Figures 4.24 and 4.25 show a density mode in the boundary layer that is convected by the flow, and another mode generated in the bubble region that propagates in the upstream direction. The latter can be associated with acoustic waves and confirms that the HFP^{1st} peak observed in Figure 4.23 is generated by a noise source located in the bubble region.

In Figure 4.26, the spatial distribution of the density modes from the DMT technique at HFP^{1st} and HFP^{2nd} is shown on the suction side of the rotor blade for a mass flow rate $\dot{m} = 19$ kg/s. The maximum amplitudes can be found in the separation region close to the LE and the modes travel towards the TE. Thus, the TE noise is expected to be affected by disturbances that are generated by the recirculation bubble.

In order to better understand the noise sources, the coherence between pressure fluctuations in the separation region of the rotor blade and pressure fluctuations at several positions upstream of the rotor is calculated for $\dot{m} = 20$ kg/s and $\dot{m} = 21$ kg/s. The location of the 100 monitor points is shown by a dashed line in Figure 4.22. The coherence between the signals is defined as,

$$\gamma_{p_w p'}^2(f) = \frac{|S_{p_w p'}(f)|^2}{S_{p_w p_w}(f) S_{p' p'}(f)}, \tag{4.5}$$

where $S_{p_w p_w}$ is the spectral density of the wall pressure fluctuations p_w in the separation region, $S_{p' p'}$ is the spectral density of the pressure fluctuations p' at a probe location upstream of the rotor blade, and $S_{p_w p'}$ is the cross-spectral density between p_w and p'. The resulting coherences are presented in Figure 4.27 (a) and (b) as a function of the frequency
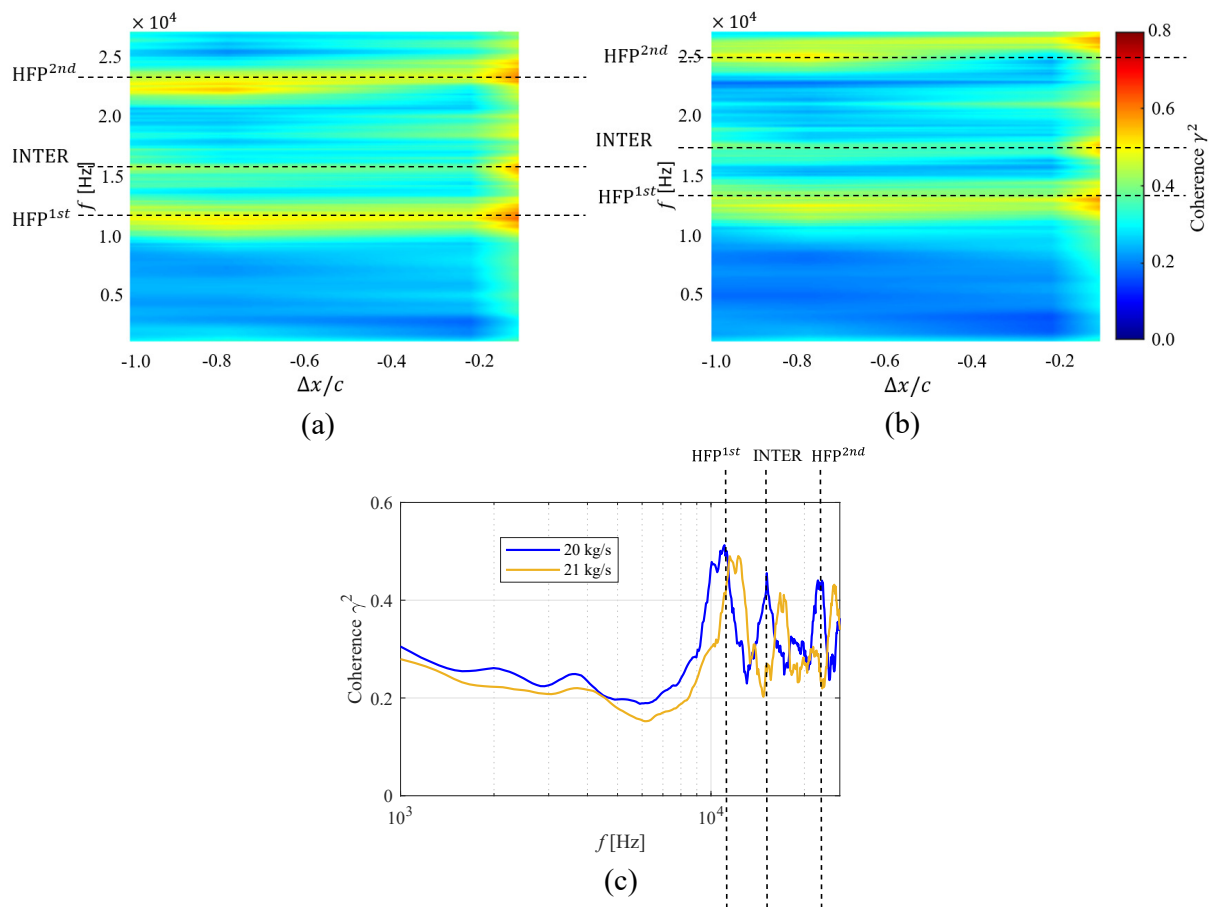
Figure 4.27: Coherence between the pressure fluctuations in the bubble region and the pressure fluctuations upstream of the rotor blade. (a) $\dot{m} = 20$ kg/s and (b) $\dot{m} = 21$ kg/s. (c) Coherence at $\Delta x/c = -1$. The origin of the Δx axis is the rotor LE.

Table 4.6: Strouhal number St parameters for various mass flow rates. $\delta_{1,\text{bubble}}$ corresponds to the local maximum of the boundary layer displacement thickness δ_1 in the separation region.

$\dot{m}$ [kg/s]	U_0 [m/s]	$\delta_{1,\text{bubble}}$ [mm]	HFP^{1st} frequency [kHz]	St
19	80	1.81	10.5	0.237
20	84	1.61	11.6	0.222
21	88	1.38	12.8	0.201
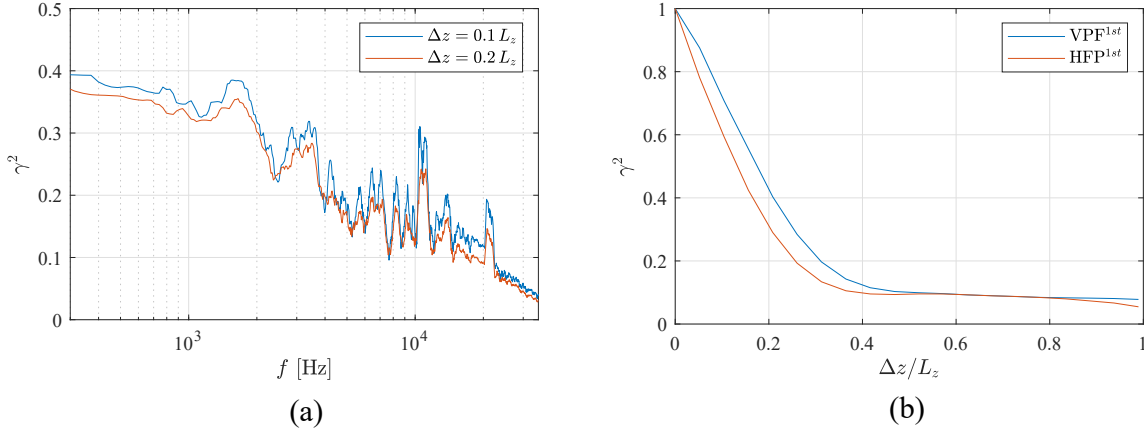
Figure 4.28: Spanwise coherence of the pressure fluctuations on the suction side of the blade, in the recirculation bubble region, for $\dot{m} = 19$ kg/s. (a) Coherence between two points separated by distances $\Delta_z = 0.1\,L_z$ and $\Delta_z = 0.2\,L_z$. (b) Coherence plotted against spanwise separation, Δz, for peak frequencies VPF^{1st} and HFP^{1st}.

and the distance $\Delta x/c$ between the reference point on the blade surface and the monitor point located in the upstream direction. Additionally, the coherence spectrum farthest from the blade surface (at $\Delta x/c = -1$) is plotted in Figure 4.27 (c) for $\dot{m} = 20$ kg/s and $\dot{m} = 21$ kg/s. All cases show high coherence levels and large peaks in the spectra at the high frequency peaks HFP^{1st}, HFP^{2nd} and INTER up to a large distance away from the recirculation bubble.

The results from the coherence analysis confirm the observations made using the DMT technique (Figures 4.24 and 4.26). Thus, the bubble region can be considered as an additional source of fan noise that produces high frequency peaks in the noise spectra. The low coherence in Figure 4.27 at the VPF^{1st} and VPF^{2nd} also confirms that the bubble region does not contribute to the peaks observed in the acoustic spectra at these frequencies. In Figure 4.27 (c), the frequencies of the peaks HFP^{1st}, HFP^{2nd} and INTER are increasing with the mass flow rate, which can be related to the reduced size of the bubble and is consistent with the acoustic spectra in Figure 4.23. The coherence of the peaks is slightly larger for the lowest mass flow rate. Since the noise produced by the bubble region at the HFPs is larger for the reduced mass flow rates, a significant contribution to the overall noise level at these frequencies can be attributed to the bubble region, which leads to high coherence levels in Figure 4.27.

At this point, it is interesting to show that the spanwise extent of the computational domain is sufficient. For that, the spanwise coherence of the pressure field, γ^2, and the spanwise correlation length, l_z, are calculated at a streamwise position in the recirculation
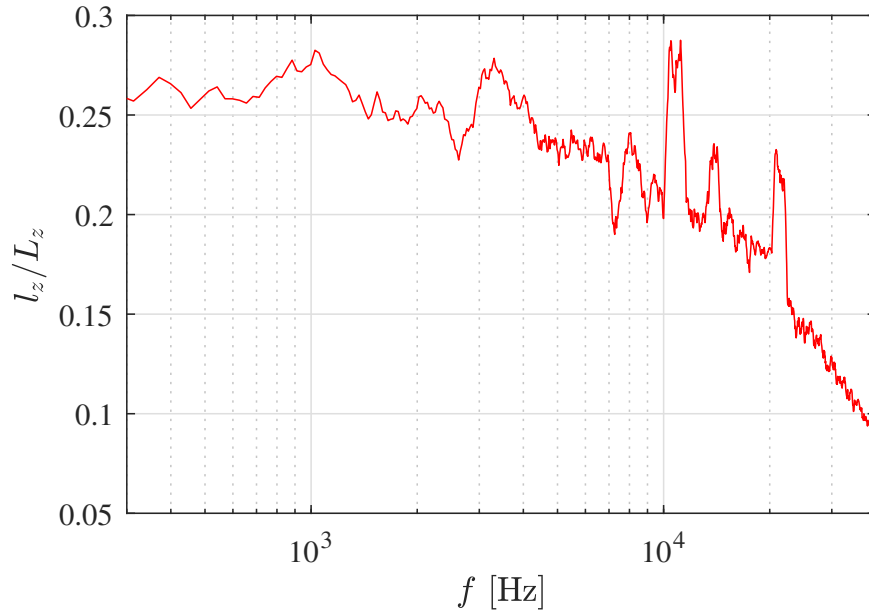
Figure 4.29: Spanwise correlation length of the pressure fluctuations on the suction side of the blade, in the recirculation bubble region, for $\dot{m} = 19$ kg/s.

bubble region and are presented in Figures 4.28 and 4.29 for the smallest mass flow rate $\dot{m} = 19$ kg/s (corresponding to the largest bubble). l_z is normalized by the total spanwise extent of the domain L_z. The coherence levels are observed to decay with the spanwise separation for the whole frequency range. In particular, for the two frequencies VPF^{1st} and HFP^{1st}, this decay is clearly shown in Figure 4.28 (b), down to negligible values over less than half of the domain size. This justifies that the current computational domain span allows to capture a statistically independent acoustic source region. The acoustic source signature of the recirculation bubble is also observed in Figures 4.28 (a) and 4.29. The highest correlation length corresponds to HFP^{1st} and constitutes 28.5% of the spanwise length. The present spanwise extent of 3.5 times the turbulence correlation length is considered sufficient.
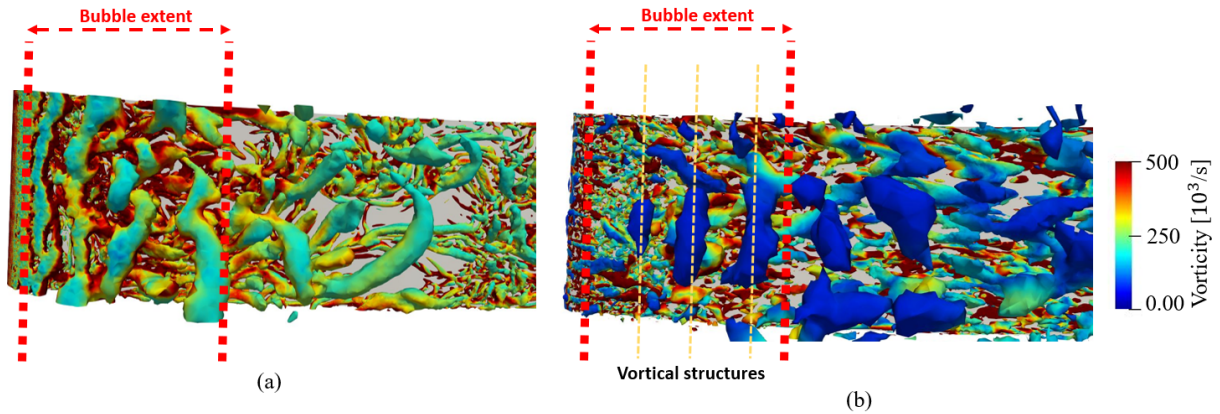
Figure 4.30: Iso-surfaces of Q-criterion ($Qc^2/U_0^2 = 5000$), colored by the vorticity magnitude, for the mass flow rate $\dot{m} = 20$ kg/s. (a) Instantaneous flow field. (b) Mode using the DMT technique at HFP^{1st}.

148

The physical mechanism which causes the HFPs in the acoustic spectra is also investigated. To this end, a snapshot of the turbulent structures is shown in Figure 4.30 (a) near the LE of the blade for the mass flow rate $\dot{m} = 20$ kg/s. Note that similar turbulent structures are obtained for other mass flow rates. The laminar boundary layer close to the leading edge detaches in the presence of a strong pressure gradient, and nearly bi-dimensional vortices are formed. Then, the vortical structures are subject to strong spanwise deformations as they are convected in the downstream direction. In order to investigate the relation between these vortical structures and the noise at the HFPs, Figure 4.30 (b) shows iso-surfaces of Q-criterion based on the filtered flow field from the DMT at HFP^{1st}. Turbulent structures at this frequency can thus be identified. 2D structures are visible again in the bubble region and are convected in the downstream direction. This indicates that the HFP^{1st} in the acoustic spectra is related to a mechanism of vortex shedding in the bubble region. A Strouhal number, defined as $St = f_v L/U_0$, where f_v is the frequency of the vortex shedding, L is a length scale, and U_0 is the relative free-stream velocity magnitude upstream of the fan, is calculated for each case. For a vortex shedding mechanism, the length scale is usually chosen as a characteristic length in the direction normal to the incoming flow. Here, we propose to use the local maximum of the boundary layer displacement thickness δ_1 in the separation region, as shown in Figure 4.19 (a). For a vortex shedding at the HFP^{1st}, the Strouhal numbers calculated for each case are shown in Table 4.6. The values obtained are typical of a vortex shedding mechanism ($St \approx 0.2$). This confirms that the noise radiated from the bubble region at the HFP^{1st} is associated with a vortex shedding mechanism.

Influence of the mass flow rate: aeroacoustic results ———— Summary

- For the various mass flow rates:

    - Two main self-noise sources can be observed from the rotor blade, the trailing edge noise and the separation noise.

    - Tones can be observed in the PSD spectra upstream of the rotor at the first two harmonics of the vane passing frequency, which are related to the tonal contribution of the rotor-stator interaction noise.

    - Except for the largest mass flow rate ($\dot{m} = 22$ kg/s), high frequency peaks can be observed in the PSD spectra upstream of the rotor.

    - By applying a dynamic mode tracking (DMT) technique and analyzing the coherence function between the pressure fluctuations in the bubble region and the pressure fluctuations upstream of the rotor, these high frequency peaks are related to acoustic waves due to fluctuations in the recirculation bubble.

    - By analyzing the turbulent structures obtained from a DMT solution, the high frequency peaks are associated to a vortex shedding mechanism.

- When the mass flow rate is reduced:

– The amplitude of the high frequency peaks is increased and their frequency is reduced.

– Higher broadband levels can be observed.

– The rotor-stator interaction noise is amplified due to the increase of the turbulence intensity in the rotor wake and the increase of the wake width.

• When the stator vanes are removed:

– The harmonics of the VPF are suppressed, but the high frequency peaks remain.

– The frequencies at which the high frequency peaks appear are quite similar between the cases with and without stator vanes.

– The amplitudes of the high frequency peaks are reduced.

– The broadband noise levels are reduced by 5 to 8 dB over the frequency range starting from 3 kHz up to the cut-off frequency (30 kHz).

4.4.4 Signature of the bubble in the stator domain

Aerodynamic results

The turbulent structures in the rotor wakes and in the boundary layers of the stator vanes are presented in Figure 4.31, for the different mass flow rates, using iso-surfaces of the Q-criterion ($Qc^2/U_0^2 = 500$) colored by the vorticity magnitude. For all the cases, the rotor wakes interact with the stators and generate the rotor-stator interaction noise. As the mass flow rate decreases, bigger turbulent structures are observed in the rotor wakes, which correspond to the big turbulent structures appearing downstream of the bubble in Figure 4.14 for the small mass flow rates. When the stator vane is not impacted by the rotor wake (upper vane in the figure), transition occurs near the LE, expect for the highest mass flow rate. When the vane is impacted by the wake, transition is promoted neat the LE for all the mass flow rates. For the smallest mass flow rate ($\dot{m} = 19$ kg/s), shown in Figure 4.31 (d), large turbulent structures are formed, which occupy all the interblade region between the stator vanes.

The flow topology around the stator vanes is then analyzed by means of the mean streamwise velocity component, u, (Figure 4.32) and the turbulent kinetic energy, k_t, (Figure 4.33), which are averaged in the stationary reference frame. The averaged values are computed over 3.5 rotations of the fan. Except for the lowest mass flow rate ($\dot{m} = 19$ kg/s), the flow remains attached on the suction side of the vanes. The high turbulent kinetic energy region close to the leading edge for $\dot{m} = 21$ kg/s and $\dot{m} = 20$ kg/s (positions 1 and 2 in Figure 4.33) indicate the transition of the boundary layer to turbulence, which is also observed in Figures 4.31 (b) and (c), respectively. For $\dot{m} = 19$ kg/s (Figure 4.33 (d)), a region of high turbulent kinetic energy and low streamwise velocity over the suction side of the stator vanes can observed. This region corresponds to a flow separation and leads to the formation of the large turbulent structures identified by the Q-criterion iso-surfaces in Figure 4.31 (d). This separation is due to the increase of the incidence on the vanes when the mass flow rate is reduced.

The distributions of isentropic Mach number, M_{is}, and the RMS of the pressure fluctuations ($P_{\rm rms}$), along the vane, are presented in Figure 4.34. For the different cases, the
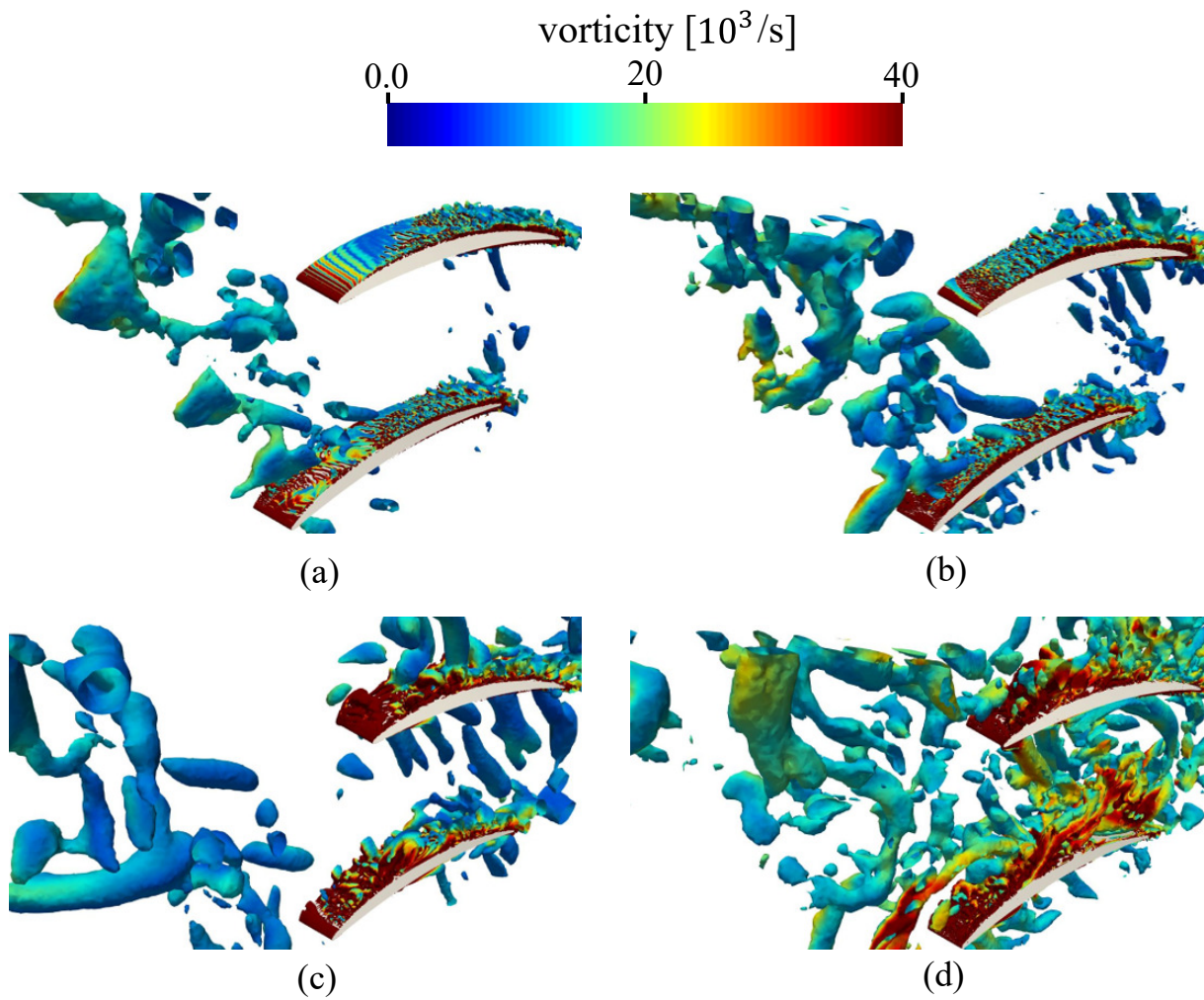
Figure 4.31: Iso-surfaces of Q-criterion ($Qc^2/U_0^2 = 500$), colored by the vorticity magnitude, for the different mass flow rates. The cases are shown by decreasing mass flow rate, and increasing angle of attack of the fan blade. (a) 22 kg/s. (b) 21 kg/s. (c) 20kg/s. (d) 19 kg/s.
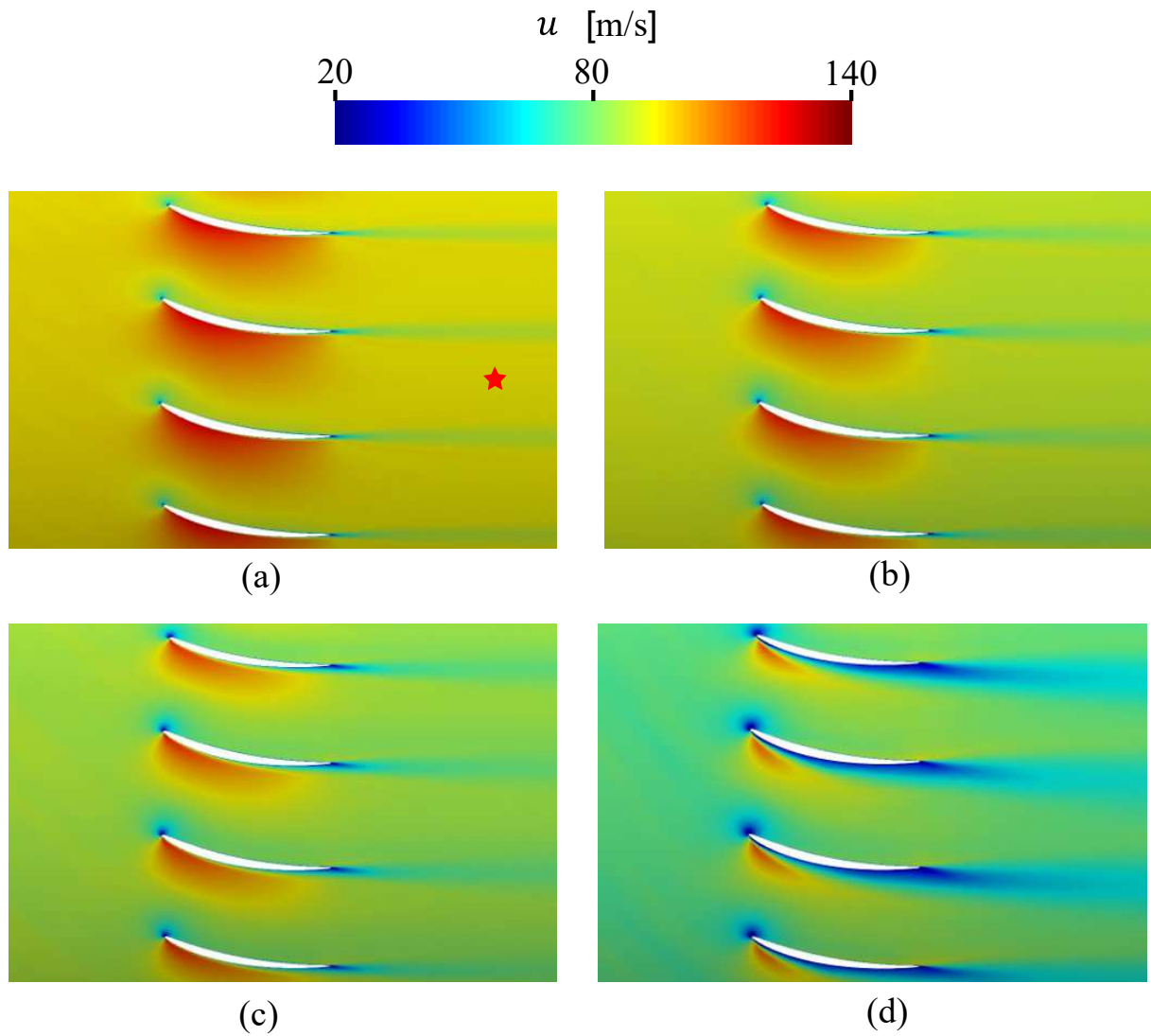
Figure 4.32: Contours of averaged streamwise velocity u around the stator vanes, for various mass flow rates, (a) $\dot{m} = 22$ kg/s, (b) $\dot{m} = 21$ kg/s, (c) $\dot{m} = 20$ kg/s and (d) $\dot{m} = 19$ kg/s. The star symbol indicates the location of the monitor point where unsteady pressure samples are collected for the PSD computation.
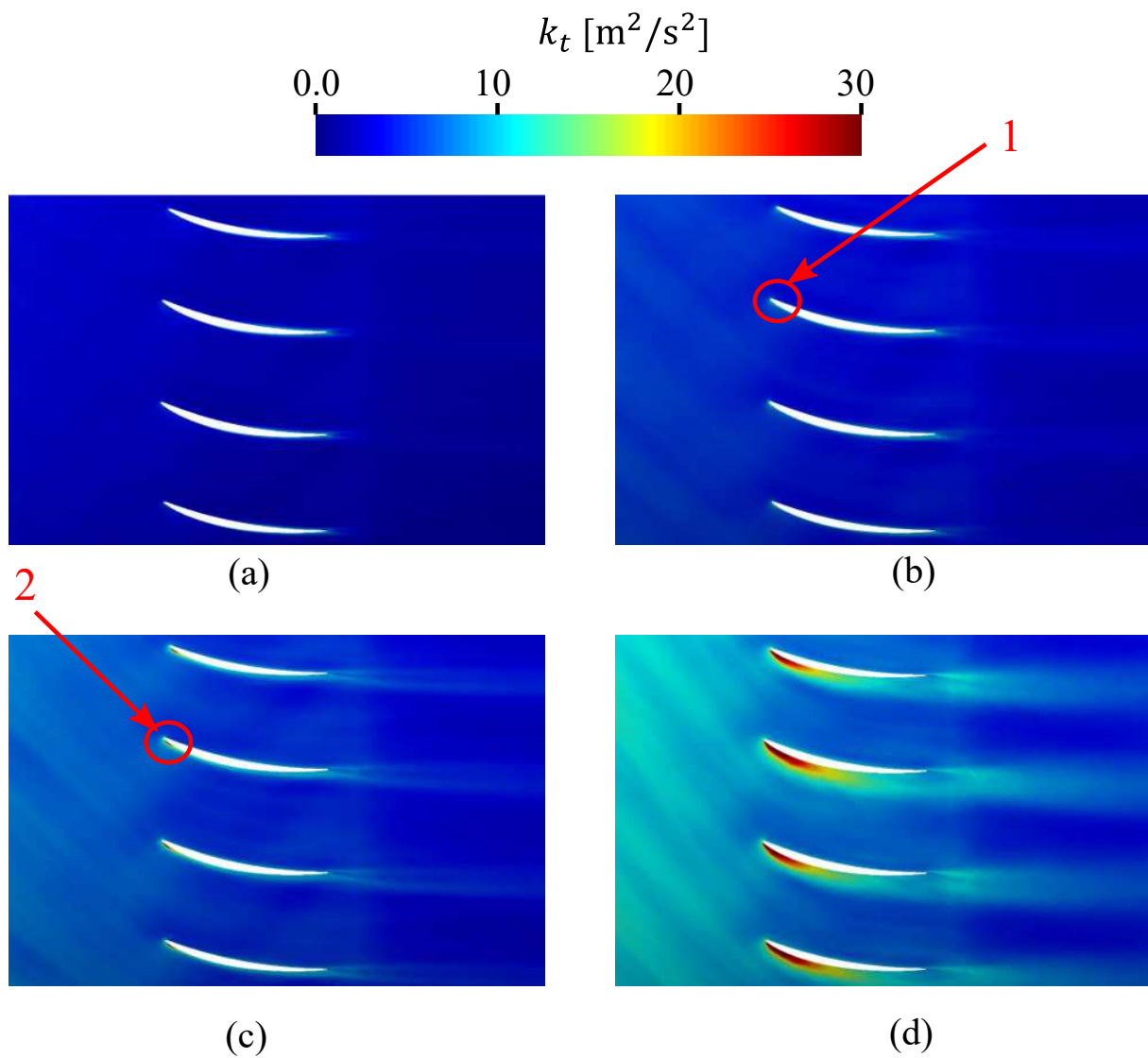
Figure 4.33: Contours of turbulent kinetic energy k_t around the stator vanes, for various mass flow rates, (a) $\dot{m} = 22\,\text{kg/s}$, (b) $\dot{m} = 21\,\text{kg/s}$, (c) $\dot{m} = 20\,\text{kg/s}$ and (d) $\dot{m} = 19\,\text{kg/s}$.
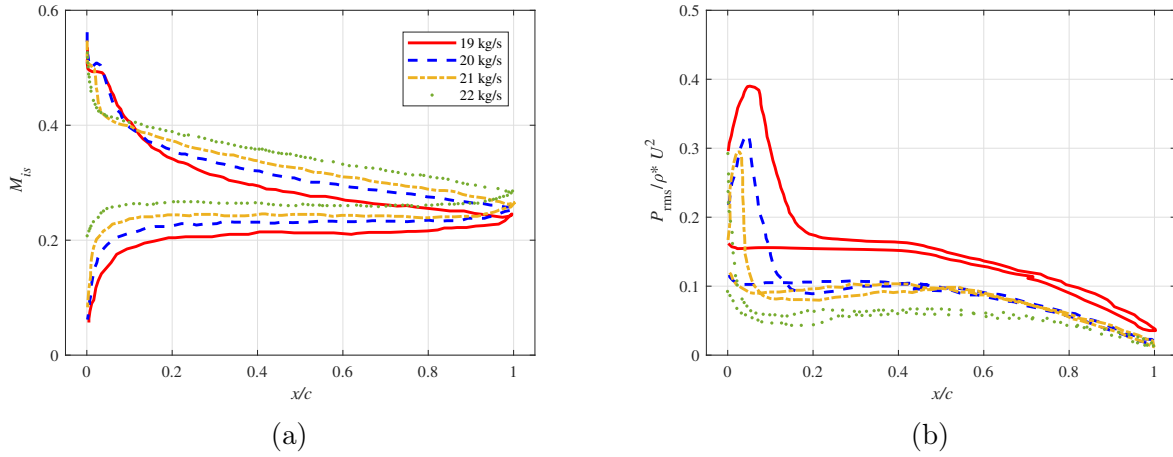
Figure 4.34: Average isentropic Mach number M_{is} (a) and RMS pressure fluctuations P_{rms} (b), along a stator vane, for the different mass flow rates.
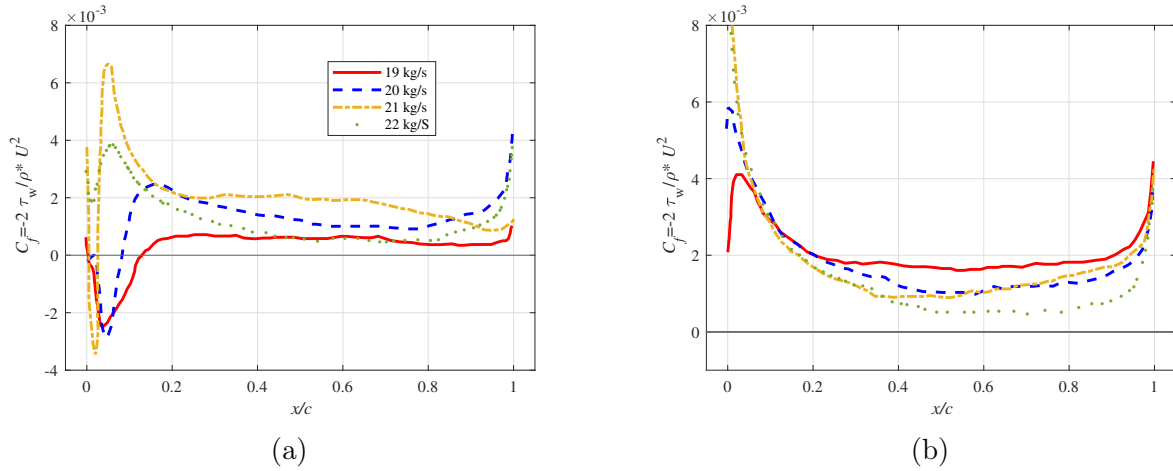
Figure 4.35: Average friction coefficient C_f along the stator vanes for various mass flow rates. (a) suction side. (b) pressure side.

pressure side shows a favorable pressure gradient. Except for the highest mass flow rate ($\dot{m} = 22$ kg/s), a plateau of M_{is} can be observed near the LE on the suction side, which indicates a small recirculation bubble. Downstream of this region, the turbulent boundary layer is subjected to an adverse pressure gradient right down to the TE. The front part of the suction side also exhibits high P_{rms} values, as shown in Figure 4.34 (b), which are produced by the small recirculation bubble and the interaction of the rotor wakes with the stator LE. However, the influence of the bubble is assumed to be small on the vane, since the bubble is small compared to the blade wake width.

The strength of the rotor-stator interaction noise source can be partly related to the P_{rms} levels. It can be observed that, as the mass flow rate decreases, the maximum value of P_{rms} close to the LE is higher, which indicates an increase of the intensity of the rotor-stator interaction noise. For the lowest mass flow rate ($\dot{m} = 19$ kg/s), high P_{rms} values can be observed over the whole vane chord, down to the TE. This suggests that even the strength of the trailing edge noise is increased when the rotor wake's width and turbulence intensity are amplified due to a larger and more turbulent recirculation bubble close to the rotor LE.
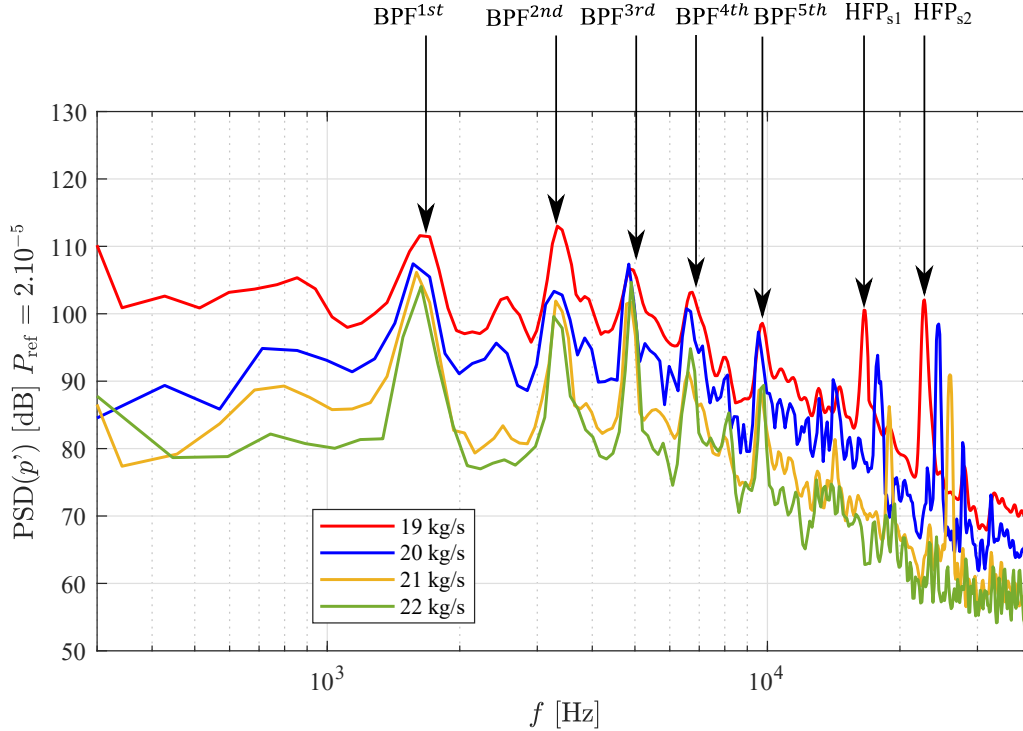
Figure 4.36: PSD of the pressure fluctuations from a monitor point at one chord length from the stator trailing edge, located by the star symbol in Figure 4.32 (a), at various mass flow rates.

The friction coefficient, C_f, also provides useful information about the boundary layer transition. A comparison of C_f between the different mass flow rates is presented in Figure 4.35, over the suction side (a) and the pressure side (b) of the stator vane. Except for the highest mass flow rate ($\dot{m} = 22$ kg/s), a region of negative friction coefficient is observed close to the LE of the vane on the suction side, which is related to the separation bubble. Downstream of this region, C_f remains positive along the suction side right down to the TE. As the mass flow rate decreases, the incidence on the vanes increases, which leads to a larger recirculation bubble. For $\dot{m} = 22$ kg/s, the flow remains attached over the whole vane surface, as observed in Figures 4.31, 4.32 and 4.33. On the pressure side, the distribution of C_f is quite similar for the different mass flow rates and remains positive, which suggests that the flow is attached all along the pressure side.

Aeroacoustic results

The acoustic field is directly computed in the LES simulations up to one stator chord length downstream of the stator vanes, in the mesh refinement region. A comparison of the PSD of the pressure fluctuations (p') for various mass flow rates is presented in Figure 4.36. All PSD spectra are obtained by multiplying the pressure signals by a Hanning window with 50% overlap and by averaging the signals using 5 segments of length 2^{10}. A reference pressure of $P_{\text{ref}} = 2.10^{-5}$ Pa is adopted. The location of the monitor point used for the unsteady data collection is indicated by the star symbol in Figure 4.32 (a). For the different cases, tones at 1650 Hz, 3200 Hz, 4800 Hz, 6000 Hz can be observed. The frequencies at which these tones appear are independent of the mass flow rate and correspond to the first four harmonics of the blade passing frequency BPF $= B\Omega/60$, where Ω is the rotation speed that is given in RPM, and $B = 16$ corresponds to the

Table 4.7: Comparison of the frequencies and the amplitudes of the tones BPF^{1st}, HFP_{s1} and HFP_{s2} for different mass flow rates.

$\dot{m}$ [kg/s]	19	20	21
BPF^{1st} [kHz]	1.65	1.65	1.65
$\|BPF^{1st}\|$ [dB]	112	106	103
HFP_{s1} [kHz]	16.7	17.8	19.91
$\|HFP_{s1}\|$ [dB]	100	94	85
HFP_{s2} [kHz]	22.7	24.5	26.1
$\|HFP_{s2}\|$ [dB]	102	97	91
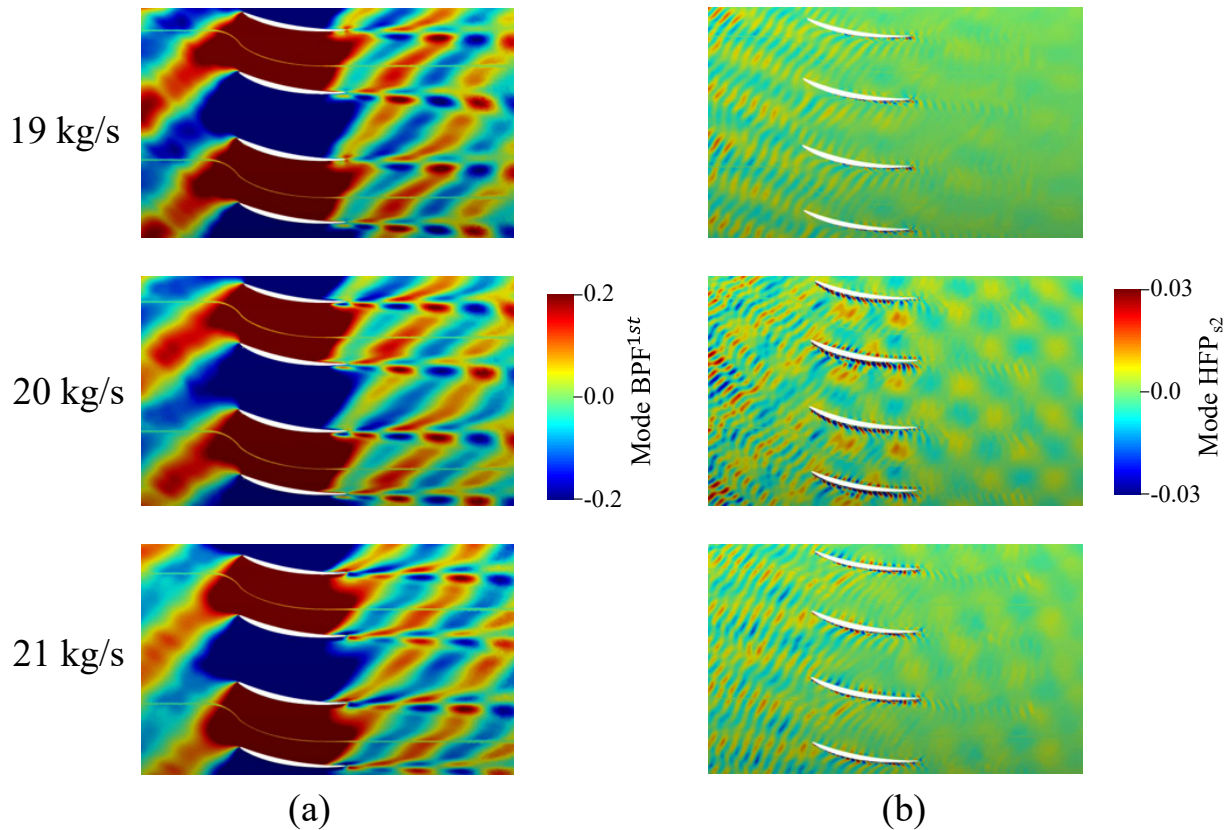
Figure 4.37: Spatial distribution of the density modes around the stator vanes using the DMT technique. (a) BPF^{1st}. (b) HFP_{s2}.

number of blades in the full stage.

At higher frequencies, except for the largest mass flow rate ($\dot{m} = 22$ kg/s), two main tones are visible for each case. The first tone is observed between 16 kHz and 20 kHz and is referred to as HFP$_{s1}$ in Figure 4.36. The second tone, denoted HFP$_{s2}$, can also be observed in Figure 4.36. The frequencies and the amplitudes of the different tones are presented in Table 4.7. When the mass flow rate increases, the frequency of these high frequency peaks increases whereas their amplitude decreases. Following the analysis made for the peaks appearing in Figure 4.23 (a), the high frequency peaks are related to a noise mechanism associated with the recirculation bubble on the rotor.

The tones observed in Figure 4.36 can be further investigated using the DMT technique [214]. Figure 4.37 shows DMT results calculated from the density in the LES around the stator vanes, at BPF^{1st} and HFP$_{s2}$, for various mass flow rates. At BPF^{1st}, the stage encounters a resonance phenomenon, which is a direct consequence of the blade and vane counts of the full stage (16 blades and 32 vanes). At HFP$_{s2}$, the predominant mode appears to have 16 lobes upstream of the stator for the different mass flow rates in Figure 4.37 (b). These figures correspond to $1/8^{th}$ of the full circumference. Thus, a predominant mode of azimuthal order 128 can be identified at this frequency. Downstream of the stator, the modes of azimuthal orders -32 and 32 can be identified by the four lobes in Figure 4.37 (b) in opposite directions. A further detailed analysis needs to be performed in order to quantitatively identify the modes in the stator domain that are related to the recirculation bubble.

Influence of the mass flow rate in the stator domain ————— Summary

- Except for the largest mass flow rate, the boundary layer transition to turbulence occurs close to the leading edge due to a small separation bubble. In all the cases, transition occurs earlier when a blade wake impacts the vane near the LE.

- For the different mass flow rates, a peak of RMS pressure fluctuations is observed close to the leading edge, which can be related to the separation bubble and the rotor-stator interaction.

- When the mass flow rate is reduced, the RMS pressure fluctuations and the extent of the flow separation region close to the leading edge are increased.

- In the PSD spectra, tones at the blade passing frequency and its harmonics appear for the different cases.

- Except for the largest mass flow rate, high frequency tones appear in the spectra. When the mass flow rate is reduced, the amplitude of theses tones is increased and their frequency is reduced.

- These tones may correspond to the separation noise related to the recirculation bubble that appears close to the leading edge of the rotor blade.

4.5   Conclusion

In this chapter, a set of wall-resolved LES are performed over a radial slice of a scale model UHBR fan stage at approach conditions, for different values of the turbulent injection rate and mass flow rate. In order to limit the computational cost, a periodic sector with a single blade and two OGVs is considered. The meshes are designed to ensure that the acoustic waves can be propagated to all the monitor points in the frequency range of interest. The capability of the wall-modeled LES assumption to predict some characteristics of the recirculation bubble is also assessed. When using a wall-model assumption, the flow around the rotor blade is seen to be well predicted, compared to the results of wall-resolved LES, with however some discrepancies in the recirculation bubble region.

For the different cases, a laminar separation bubble is observed on the suction side near the blade leading edge, which causes the boundary layer transition to turbulence. On one hand, the influence of the turbulence injection at the inlet on the flow topology around the rotor blade, and particularly on the recirculation bubble characteristics, is found to be moderate. On the other hand, the size and position of the recirculation bubble, as well as the amplitude of the pressure disturbances in the separation region, appear to vary significantly with the mass flow rate. As the mass flow rate decreases, the size of the bubble increases, the bubble shifts downstream, and high levels of wall pressure fluctuations can be found along the suction side of the blade. The development of the boundary layer and the wake is influenced by the presence of a recirculation bubble and its size. For a low mass flow rate and a large recirculation bubble, both the boundary layer thickness on the suction side and the wake width increase. However, the boundary layer on the pressure side appears to be unchanged for all mass flow rates. It is found that the wake width far downstream of the fan blade scales with the boundary layer thickness at the trailing edge.

Two different self-noise mechanisms are identified in the rotating frame: the trailing-edge noise generated by the scattering of the turbulent boundary layer at the trailing edge, and an additional noise source due to the recirculation bubble near the leading edge. High frequency peaks in the noise spectra are associated with the recirculation bubble. This noise generation mechanism is studied in details by using a DMT technique. It is found that the acoustic waves that are related to the first harmonic of the high frequency peak come from the bubble region. This finding is consistent with the results of the coherence between the wall pressure fluctuations in the recirculation bubble region and pressure fluctuations away from the blade.

The frequencies of the tones from the bubble decrease when the mass flow rate decreases, and the amplitudes of the tones increase. An interaction tone between the recirculation bubble and the stator vanes is found by analyzing an additional simulation performed without the stator vanes. Additionally, the broadband noise levels are found to increase for the low mass flow rates over the whole frequency range.

Iso-surfaces of Q-criterion are computed using the DMT technique at the first high frequency peak to investigate the physical mechanism of the noise from the recirculation bubble. This analysis suggests that a vortex shedding from the bubble explains the noise radiated at this frequency.

Finally, the influence of the mass flow rate and the effects of the rotor recirculation bubble in the stator are investigated. High frequency tones, which are related to the noise due to the recirculation bubble, can be identified in the PSD spectra downstream of the stator vanes.

It is shown that the noise radiated from a recirculation bubble can be a significant contributor to the fan noise. This noise source can be found at approach conditions, as the mass flow rate of an aero-engine is reduced. Thus, it might be useful to identify the presence of a recirculation bubble on fan blades using high-fidelity models to reduce this noise source during design.

> **Note**
>
> The results of this Chapter are published in the Journal of Sound of Vibrations [5] and were presented at the 16me Congrès Français d'Acoustique [4] and at the Congrès des Jeunes Chercheurs en Mécanique - Méca-J [1]

Aeroacoustic analysis of the tip leakage flow of an UHBR turbofan

---

Introduction

This chapter presents an aerodynamic and aeroacoustic analysis of the flow in the fan tip region of the (full-span) sector LES configuration. The flow topology in the blade tip region is first analyzed through mean and turbulent flow parameters, such as the velocity components, the rms velocity fluctuations, and the vorticity magnitude. Two tip leakage vortices are identified in this region, which is characterized by a deficit in the streamwise velocity component and significant levels of turbulent kinetic energy. The noise sources are then identified using the velocity dilatation rate and rms pressure fluctuations over the blade surface. The dominant noise sources in the tip gap region are observed at the trailing edge of the blade due to interactions of the tip leakage vortices with the trailing edges. The wall pressure spectra in the tip gap region and the coherence of pressure fluctuations between monitor points at different positions in this region show an acoustic contribution of the tip leakage flow mainly in two frequency ranges. The first range corresponds to medium frequencies between 2 kHz and 9 kHz, and the second range corresponds to high frequencies between 10 kHz and 25 kHz. A dynamic mode tracking technique is used to follow the evolution of modes identified at given frequencies. The far-field noise is computed using the Ffowcs Williams and Hawkings' (FWH) analogy from the solid surface of the blade. This surface is spilled into two parts; the tip region (outer 15% of span) and the rest of the blade (lower 85% of the span) in order to analyze the acoustic contributions of these two regions separately. Medium and high frequency contributions of the tip leakage flow are also observed and analyzed.

Contents

5.1 State of the art

The current chapter focuses on the tip gap noise of the ECL5 fan stage.

The tip gap noise is related to the leakage flow in the tip gap region of the rotor blades. To avoid any contact between the fan rotating blades and the casing, a radial clearance between the fan blade tip and the shroud is essential for the operation of the fan stage. The existence of such a clearance induce the development of a highly turbulent and three-dimensional unsteady secondary flow, due to a pressure difference between the pressure and suction sides of the rotor blade in the tip region. This complex flow is responsible for aerodynamic losses and noise emissions.

The first studies on the tip leakage flow, performed by Rains [216], have shown that the flow at the blade tip is perpendicular to the camber line, when passing from the pressure side to the suction side. When interacting with the main flow, this leakage flow is rolled up, which leads to the formation of a tip leakage vortex (TLV). This latter is characterized by highly vortical structures [257], which may interact with the trailing edge of the rotor blades and with the mainstream flow, and yield strong unsteady mechanisms. This leads to aerodynamic losses [286, 121] and noise emissions [115].

The influence of the tip leakage vortex on the aerodynamic performance of a turbomachine has been extensively studied in the literature [61, 212, 255, 289, 257, 286, 19]. Indeed, the efficiency of a rotating machine is very sensitive to the size of the tip gap, and it is strongly reduced when the tip clearance is increased. An experimental study was performed by Inoue *et al.* [105] on the rotor of an axial compressor, for various tip gap sizes, ranging from $\epsilon_s = 0.5\%$ to $\epsilon_s = 5\%$, where ϵ_s is the tip gap size normalized by the rotor span. It was shown that, when the tip gap size increases, both the efficiency and the compression rate of the rotor decrease. This is partly due to the thickening of the boundary layers at the casing, which generates a blockage effect and leads to a reduction of the tangential velocity component at the tip. For the smallest tip gap size, the strongest interaction between the tip leakage flow and the main flow occurs. It was also

noticed that, when the gap size increases, the location of the maximum pressure difference between the suction and pressure side moves towards the trailing edge of the blade. Also, for the largest gap size, a strong recirculation region appears in the tip gap. Similar findings were obtained experimentally by Kameier & Neise [116, 115] and numerically by Lallier-Daniels *et al.* [139] who have studied the effects of the tip gap size on a low speed fan at a high compression ratio. It was found that a reduction of ϵ_s by a factor of 4 leads to an efficiency gain of 7 %. In addition, the influence of the tip gap size on the generated noise was highlighted. When going from $\epsilon_s = 1.4\%$ to $\epsilon_s = 2.8\%$, an increase of the noise levels of 15 dB was observed around 370 Hz.

Several experimental studies [28, 287, 288] have been performed on the fan rig of the University of Siegen to analyze the influence of the tip leakage flow on the aerodynamic performance and the noise emissions. Different normalized tip gap sizes were investigated, varying from $\epsilon_s = 0.5\%$ to $\epsilon_s = 5\%$. At nominal operating speed, when increasing from $\epsilon_s = 0.5\%$ to $\epsilon_s = 5\%$, the far-field noise levels (for a microphone at 1.3 m upstream of the rotor) increased by 10dB. Tones also appeared in the far-field acoustic spectrum at frequencies lower than the blade passing frequency. The generated noise was attributed to interactions between the coherent structures formed in the tip region with the blade tip. These coherent structures are rotating at a speed lower than the rotation speed of the blades.

Many experimental [26, 85, 86, 86, 87, 106, 108] and numerical [19, 288, 140, 128] studies have been performed on isolated airfoil configurations to analyze the characteristics of the tip leakage flow, independently from other complex mechanisms occurring in a turbomachine. A parametric study has been performed on a NACA 5510 profile placed between two plates [85]. The effects of the incoming velocity magnitude, the angle of attack and the tip gap size (ϵ_s varying from 1% to 12%) on the topology of the tip leakage flow and the noise emissions have been investigated. The incoming velocity magnitude has shown little effects on the tip leakage flow topology, whereas a significant influence of the angle of attack and the tip gap size was found. For larger angles of attack, the aerodynamic loading of the profile increases and the tip leakage flow appears closer to the leading edge on the airfoil. Additionally, it was observed that, as the tip gap size increases, the position of the maximum velocity magnitude in the tip leakage flow moves towards the trailing edge. Two main noise sources were identified in the far-field acoustic spectrum. The first noise source, which has been identified at frequencies ranging from 0.7 kHz to 3.5 kHz, is of dipolar nature and corresponds to turbulent structures generated due to the flow separation in the tip gap region, and passing over the trailing edge. The second noise source, identified at frequencies ranging from 4 kHz to 7 kHz, is of a quadripolar nature and is associated to vortices in the shear layers of the tip leakage flow. Different numerical approaches, such as large eddy simulation [130], zonal large eddy simulation [19], and lattice Boltzmann Method [152], have shown that the main noise source at the tip is located between the mid-chord and the trailing edge. The main contribution of the tip gap noise was observed around 2 kHz and 6 kHz, with a stronger directivity on the pressure side.

In order to approach real turbomachinary configurations, several studies have been performed on linear compressor cascades. Experimental studies carried out by Kang & Hirsh [118, 117, 119] over a cascade of 7 NACA 65-1810 airfoils, with varying tip gap size, have shown the formation of three tip vortices, (i) a tip leakage vortex (TLV) formed close to the leading edge, (ii) a tip separation vortex (TSV) formed along the tip pressure side edge and exiting the clearance around mid-chord, and (iii) a secondary vortex develop-

ing at the tip suction side edge, which interacts with the TSV. An induced vortex (IV) can also be identified alongside the TLV and rotates in the opposite direction [286, 19]. The trajectory of the TLV was identified by Storer & Cumpsty [257] based on the minimum values of the static pressure on the casing. The aerodynamic characteristics of the TLV were also investigated in a series of experiments at Virginia Tech. [177, 272, 274] in a low-speed linear compressor cascade with stationary and moving endwalls. The TLV was characterized by a region of strong velocity gradients and high levels of turbulent kinetic energy. Furthermore, several numerical simulations [286, 222, 264, 231, 129] have been performed on a linear compressor cascade with a tip clearance to investigate the tip leakage flow topology and the associated noise sources. You *et al.* [286] have performed incompressible LES on a linear compressor cascade with a moving endwall. The tip leakage vortex was identified by a region of important streamwise and pitchwise vorticity magnitudes. The viscous losses in the cascade endwall region were mainly associated to the spanwise and pitchwise velocity gradients. It was also suggested that these losses can be reduced by using a rib-like structure or a vortex generator to change the direction of the tip-leakage jet such that the associated spanwise and pitchwise derivatives of the mean velocity are reduced. Ventosa-Molina *et al.* [264] have studied the effects of the relative motion between the casing and the blade in a linear compressor cascade using direct numerical simulations. In the presence of a relative motion, the TLV is shifted toward the middle of the passage, which results in the formation of secondary vortices behind it. Koch *et al.* [129] have performed a wall-resolved compressible LES on a linear compressor cascade to study the aerodynamic and aeroacoustic behavior of the TLV. The main tip noise mechanisms were identified through an aerodynamic analysis coupled with the Ffowcs Williams & Hawkings analogy and a dynamic mode decomposition technique. The main noise sources were identified at around 75% of the chord length at frequencies between 5 kHz and 6 kHz.

In order to take into account all the complex mechanisms in turbomachinery configurations, such as the effects of the rotation, several studies have been performed on rotating compressors and fans [281, 58, 138, 64, 213, 121, 123]. A comparison of the tip leakage flow topology between an axial compressor and a linear cascade configuration has been performed by Lakshminarayana *et al.* [138]. It was seen that, in the case of a linear cascade, the TLV formation due to the roll up of the tip leakage flow occurs in the vicinity of the suction side, which leads to an increase of the static pressure on the pressure side and induces significant losses. In the case of an axial compressor, the high speed jet coming from the leakage interacts with the main flow stream and generates a strong separation region. The TLV may also interact with the adjacent blades at the trailing edge and generate a significant noise source due to high fluctuation levels in the TLV [64]. Experimental studies have been performed on a fan stage, known as the source diagnostic test (SDT) configuration of NASA and GE Aviation [101], with a normalized tip gap size of $\epsilon_s = 0.1$ %, to investigate the flow topology [200, 201] and the noise sources [281, 58]. More recently, LES have also been performed on the SDT configuration [213, 121, 123]. Comparisons between the noise levels from the fan/outlet guide vanes (OGV) stage configuration and the fan-only configuration (without OGV), have permitted to separate the contributions of the main noise sources, the rotor-stator interaction noise and the tip leakage noise [174]. The contribution of the tip leakage noise source appears to be dominant below 6 kHz. Additionally, a comparison of the tip flow topology and the associated noise between approach and cutback operating conditions has been performed by Kholodov *et*
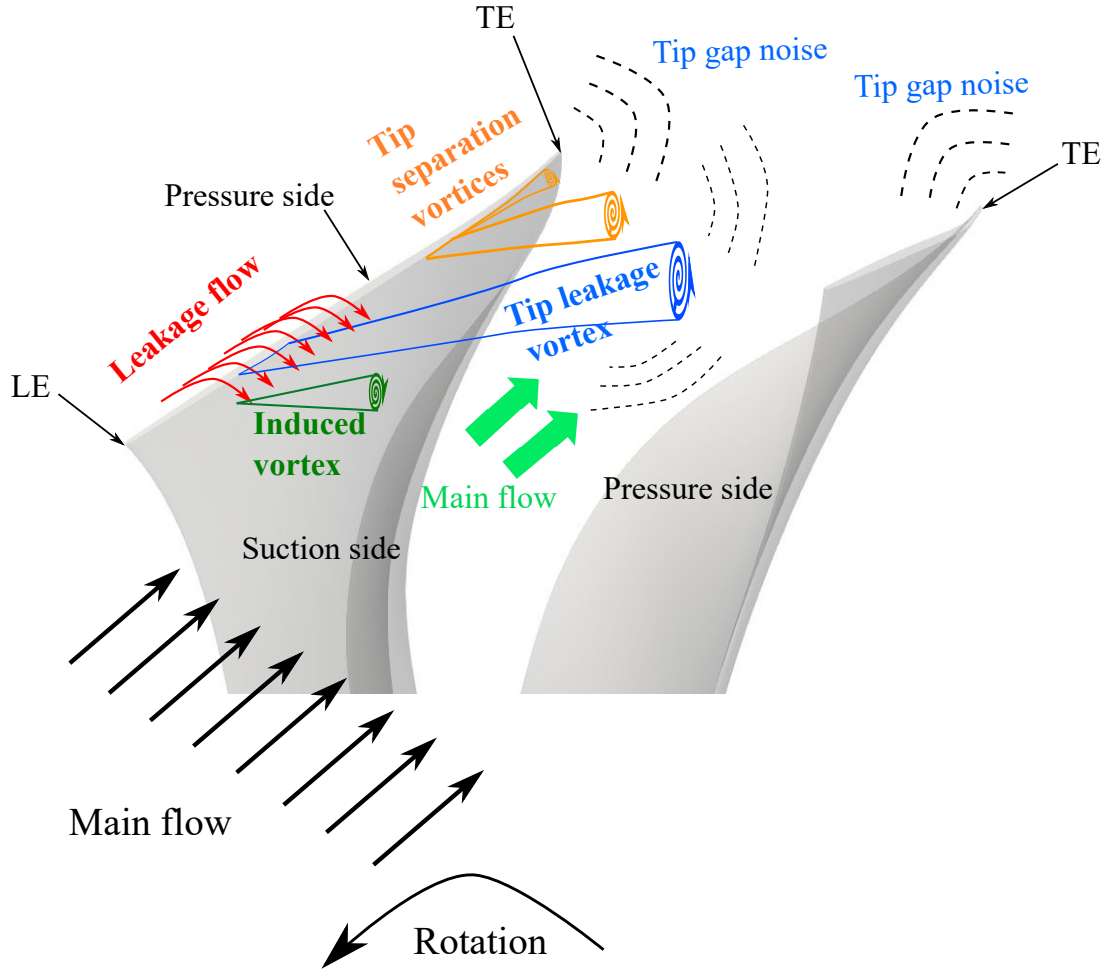
Figure 5.1: Schematic of the flow topology and the associated noise generation mechanisms in the tip gap region.

al. [123] using LES. A stronger TLV but with a smaller angle with the blades was observed at cutback condition, compared to approach condition.

5.2 Tip leakage flow noise mechanisms

In this section, the different tip vortices and the mechanisms of noise generation for a classical tip leakage flow are presented in a simplified way, based on the literature review from Section 5.1. A schematic view of the different tip vortices in the tip gap region and the associated noise mechanisms are presented in Figure 5.1. The view is taken from upstream of the fan. Due to the pressure difference between the pressure and suction sides at the blade tip, a tip leakage flow is formed. This flow rolls up and forms a tip leakage vortex. An induced vortex may also be formed alongside the tip leakage vortex, rotating in the opposite direction. A separation of the flow at tip may occur, leading to the formation of tip separation vortices. In this complex flow topology, several noise generation mechanisms can be identified and are listed as follows,

- The interaction of the tip leakage flow with the main flow and with the tip separation vortices in the interblade region. The sound mechanism related to this source is quadrupolar and is expected to be mostly significant for large Mach number ap-
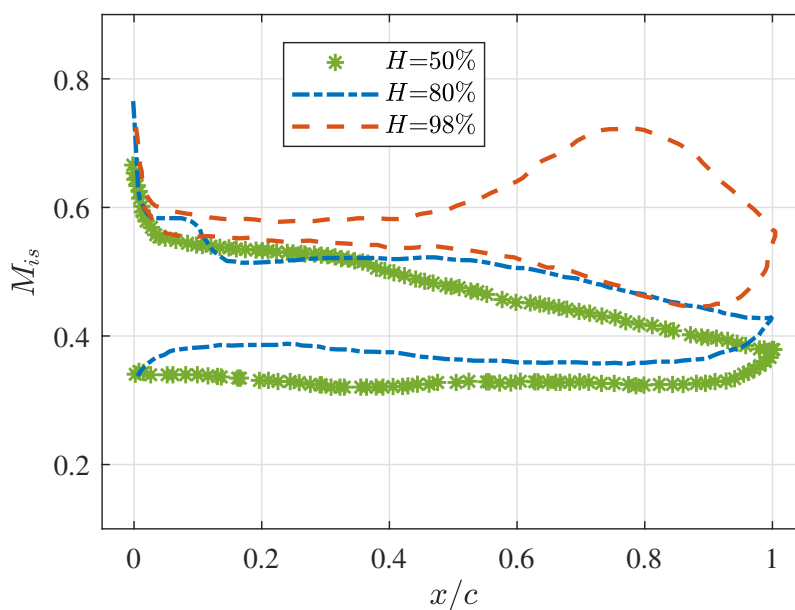
Figure 5.2: Averaged isentropic Mach number M_{is} along the rotor blade for different spanwise positions H.

plications.

- The interaction of the tip leakage vortex generated on one blade with the trailing edge of the adjacent blade. The sound mechanism related to this source is dipolar in nature.

- The interaction of the tip separation vortices generated on each blade with the trailing edge of the same blade. The sound mechanism related to this source is dipolar in nature.

5.3 Aerodynamics

5.3.1 Tip flow topology

The distribution of isentropic Mach number, M_{is}, which is related to the static pressure distribution on the blade, is presented in Figure 5.2 at three spanwise positions, mid-span, 80% and 98% of the rotor span. Similar distributions are obtained at mid-span and $H = 80\%$ of the rotor span. A difference between these two positions ($H = 50\%$ and $H = 80\%$) is found close to the leading edge, where a plateau of M_{is} at $H = 80\%$ indicates the presence of a small recirculation bubble in this region. When comparing these two spanwise positions ($H = 50\%$ and $H = 80\%$), it is also seen that, as the radius increases, the blade loading is shifted towards the trailing edge. A different behavior is observed at $H = 98\%$, which corresponds to a spanwise position much closer to the tip gap region. From the leading edge to a chordwise position of about 50% of the chord length, the pressure difference is quite small, compared to the other spanwise positions ($H = 50\%$ and $H = 80\%$). Starting at about 60% of the chord length, a significant increase of the pressure difference between the sides of the blade is observed. This behavior can be associated to the blade shape at the tip, that was designed to operate at transonic regimes,
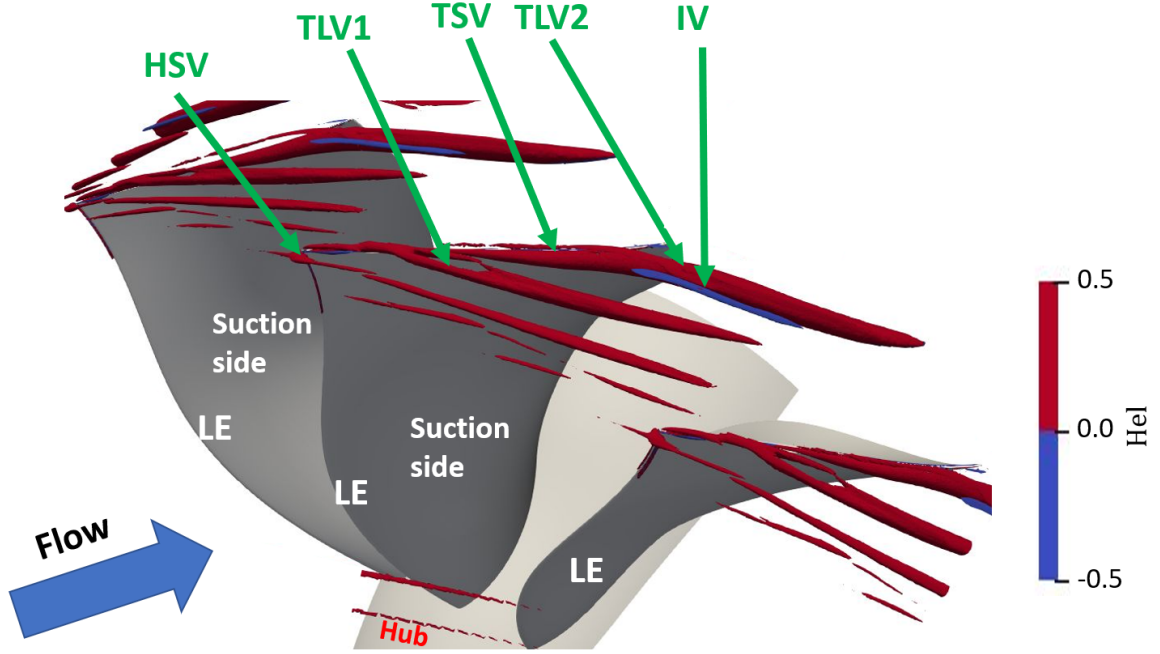
Figure 5.3: Averaged iso-surfaces of Q-criterion ($Qc^2/U_0^2 = 500$) in the tip gap region, colored by the normalized helicity.

and for which the blade loading is expected to be ensured by the shock waves. However, the operating point in the present simulation corresponds to a fully-subsonic regime at approach condition. The blade profile at the tip presents a significant camber evolution. Between the leading edge and the maximum camber position, the airfoil is relatively flat and thin, and the position of the maximum camber is located at 70% of the chord length, which is unusual for subsonic airfoils.

The flow structures in the tip gap region are visualized in Figures 5.3 and 5.4 using averaged and instantaneous iso-surfaces of the Q-criterion ($Qc^2/U_0^2 = 500$, where U_0 is the free-stream velocity magnitude), respectively. They are colored by the normalized helicity, which is defined as,

$$\text{Hel} = \frac{\overrightarrow{\Omega_v} \cdot \vec{u}}{||\overrightarrow{\Omega_v}|| \cdot ||\vec{u}||} \tag{5.1}$$

where $\overrightarrow{\Omega_v}$ and $\vec{u}$ are the vorticity and the velocity vectors, respectively. The helicity identifies the direction of rotation of a vortex; positive values means that the vortex rotates in the clockwise direction with respect to the flow (as seen from upstream), and negative values means that the vortex rotates in the counter clockwise direction. The flow direction is from the left to right. Several vortical structures are observed in the tip leakage region. A first tip leakage vortex (denoted "TLV1" in Figures 5.3 and 5.4) is formed at about 25% of the chord length due to the roll up of the tip leakage jet coming from the pressure side in this region.

A horseshoe vortex (denoted "HSV" in Figures 5.3 and 5.4) appears just upstream of the leading edge. The HSV generated on each blade interacts with the adjacent blade at about 25% of the chord length (region "A" in Figure 5.4) and seems to feed the tip leakage jet that forms the TLV1.

Downstream of the tip leakage vortex TLV1, tip separation vortices (denoted "TSV" in Figures 5.3 and 5.4) develop on the blade tip. These vortices separate from the blade
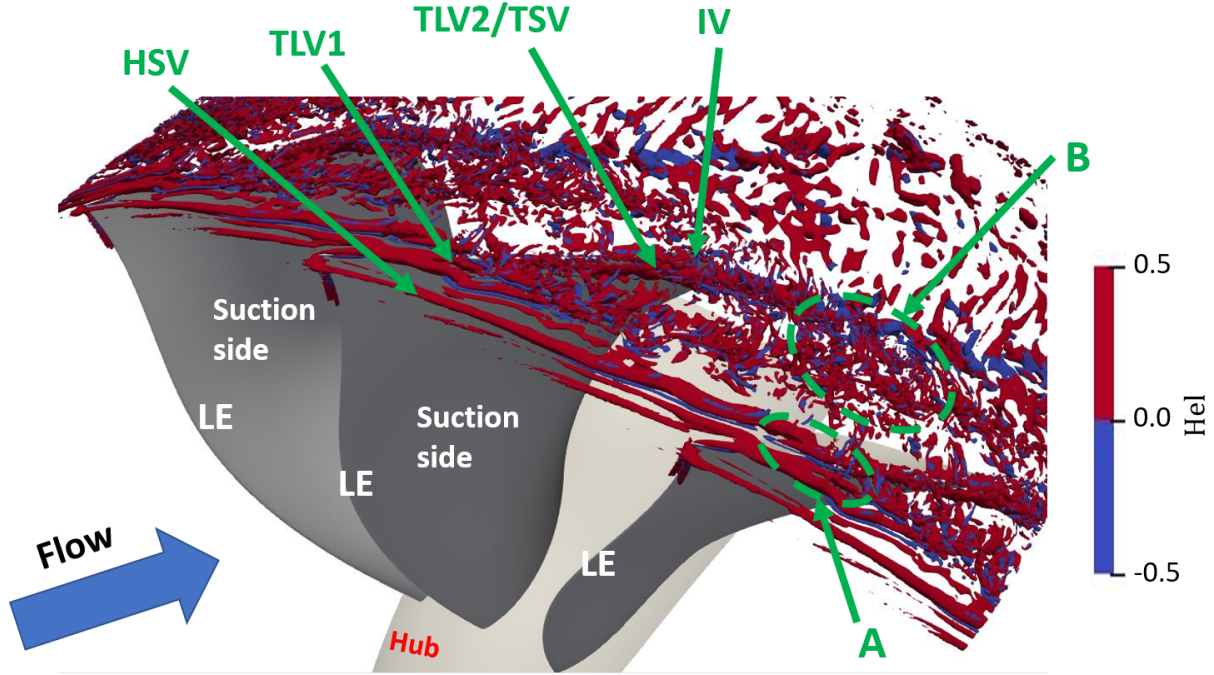
Figure 5.4: Instantaneous snapshot of iso-surfaces of Q-criterion ($Qc^2/U_0^2 = 500$) in the tip gap region, colored by the normalized helicity.

at about 70% of the chord length, in the region where the pressure difference is relatively important (Figure 5.2). The formation and topology of the TLV1 and TSV are classically observed in previous studies of the literature [286, 18, 121, 140].

Another tip leakage vortex (denoted "TLV2" in Figures 5.3 and 5.4) is generated at about 75% of the chord length due to the strong pressure difference in this region. Its root is fed by a part of the TLV1 coming from the adjacent blade. This phenomenon is known as double leakage. Additionally, an induced vortex (denoted "IV" in Figures 5.3 and 5.4) is observed alongside the TLV2, with an opposite direction of rotation.

After leaving the tip gap region, the first tip leakage vortex, TLV1, is convected in the interblade passage and interacts with the other tip flow vortices. The first interaction occurs with the tip vortices TLV2, IV and TSV (region "B" in Figure 5.4). All the vortices are then convected downstream. Another part of the TLV1 drifts towards the trailing edge of the adjacent blade. The TLV1 also interacts with the adjacent blade at about 70% of the chord length, in the region of high pressure gradient.

This complex flow topology in the tip gap region may be related to (i) the blade tip geometry, which was designed to operate at transsonic regimes, and to (ii) the tip gap size, which is larger than 1% of the chord length and increases towards the trailing edge.

To further analyze the flow topology in the tip gap region, the mean vortical topology of the tip leakage flow is presented in Figure 5.5, by using several isosurfaces of the mean Q-criterion colored by the vorticity magnitude. For the smallest value of the Q-criterion ($\overline{Q}c^2/U_0^2 = 500$ in Figure 5.5 (a)), the different tip flow vortices observed in Figures 5.3 and 5.4 can be identified. When increasing the value of the Q-criterion, less vortices can be observed. As the value of Q-criterion increases, the rotational effect of a vortex becomes more and more important compared to its strain effect. For $\overline{Q}c^2/U_0^2 = 750$ in Figure 5.5 (b), the tip vortices TLV1, TLV2, IV and TSV can still be identified, whereas the HSV is not well observed. Because of the relatively thin leading edge of the fan blade,
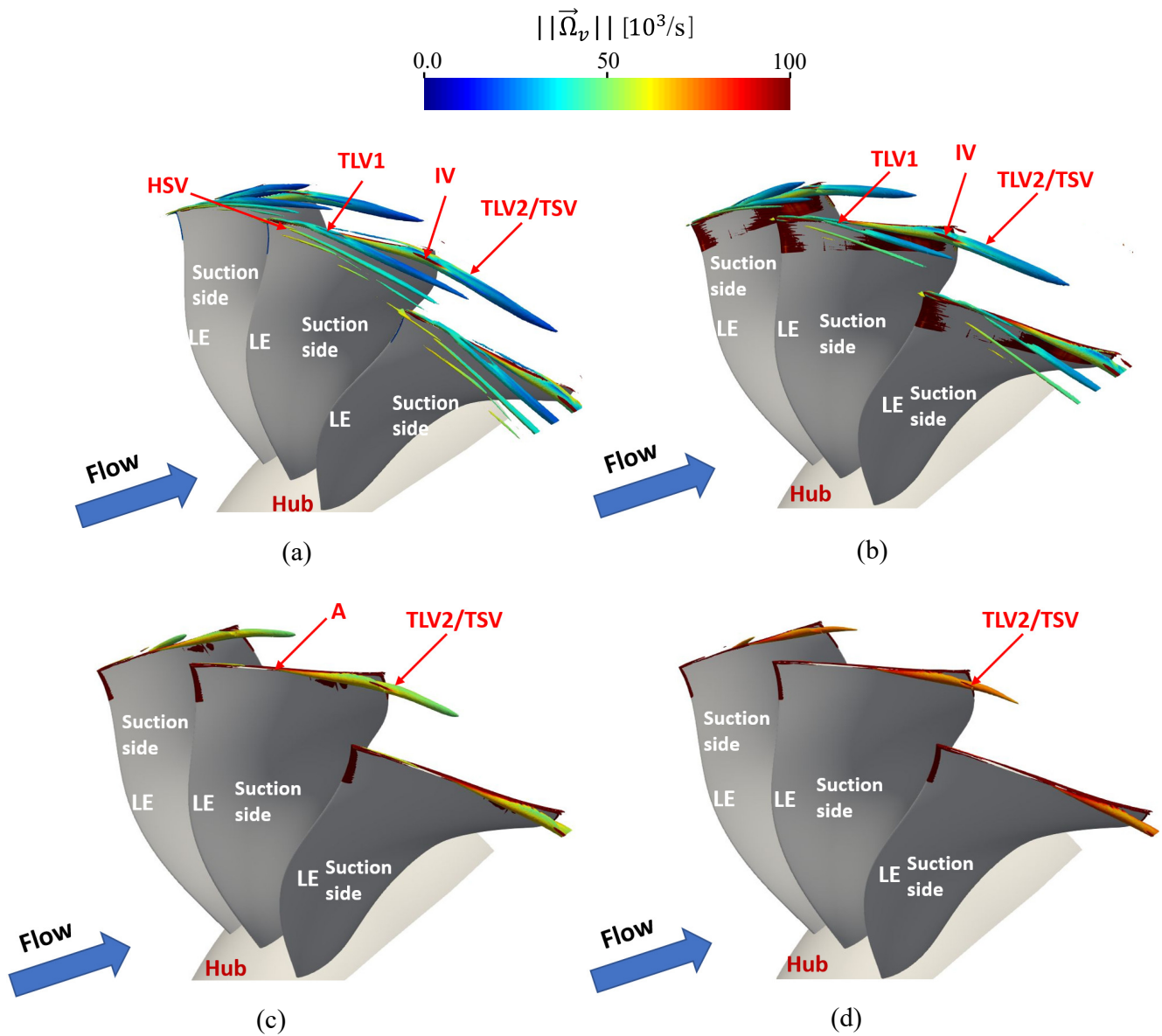
Figure 5.5: Averaged Q-criterion in the tip gap region, colored by the vorticity magnitude for different iso-surface value, (a) $\overline{Q}c^2/U_0^2 = 500$, (b) $\overline{Q}c^2/U_0^2 = 750$, (c) $\overline{Q}c^2/U_0^2 = 1000$, and (d) $\overline{Q}c^2/U_0^2 = 1250$.
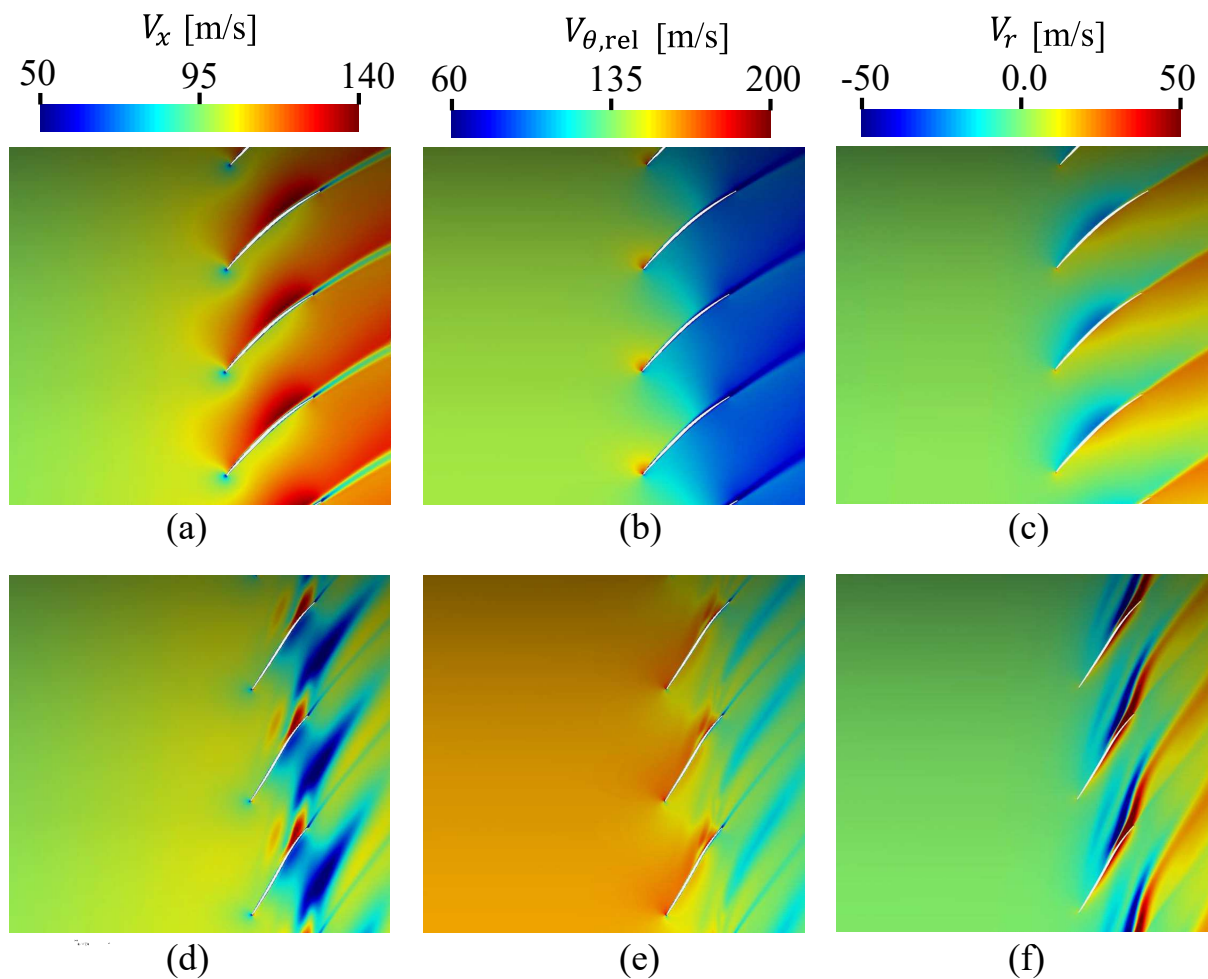
Figure 5.6: Contours of the averaged velocity components around the rotor blade for two spanwise positions, (a,b,c) 80%, (d,e,f) 99%.

particularly at the tip, the horseshoe vortex formed at the leading edge is weak and can only be properly observed at low isosurface values of the Q-criterion. For $\overline{Q}c^2/U_0^2 = 1000$ in Figure 5.5 (c), the TLV1 disappears and the onset of the flow separation that yields the formation of the TSV can be clearly observed. Only the TLV2 and the TSV can be observed for $\overline{Q}c^2/U_0^2 = 1250$ in Figure 5.5 (d). Furthermore, as the value of the isosurface of the Q-criterion is increased, the turbulent structures are characterized by larger vorticity magnitudes. Consequently, the rotational effect and the vorticity levels of the tip vortices TLV2 and TSV (which appear at about 70% of the chord length in the high pressure difference region as shown in Figure 5.2), are larger than that of the first tip leakage vortex TLV1. Indeed, the tip vortices TLV2 and TSV are fed by a much more turbulent boundary layer and a stronger tip flow leakage, due to the significant pressure difference.

5.3.2 Mean quantities

Figure 5.6 presents contour plots of the averaged velocity components around the rotor blade for two spanwise positions, 80% and 99%. For the latter position, which corresponds to the tip leakage region, a region of large axial velocity deficit, which leads to a flow blockage region, develops along the line joining the trailing edges of the blades. Upstream
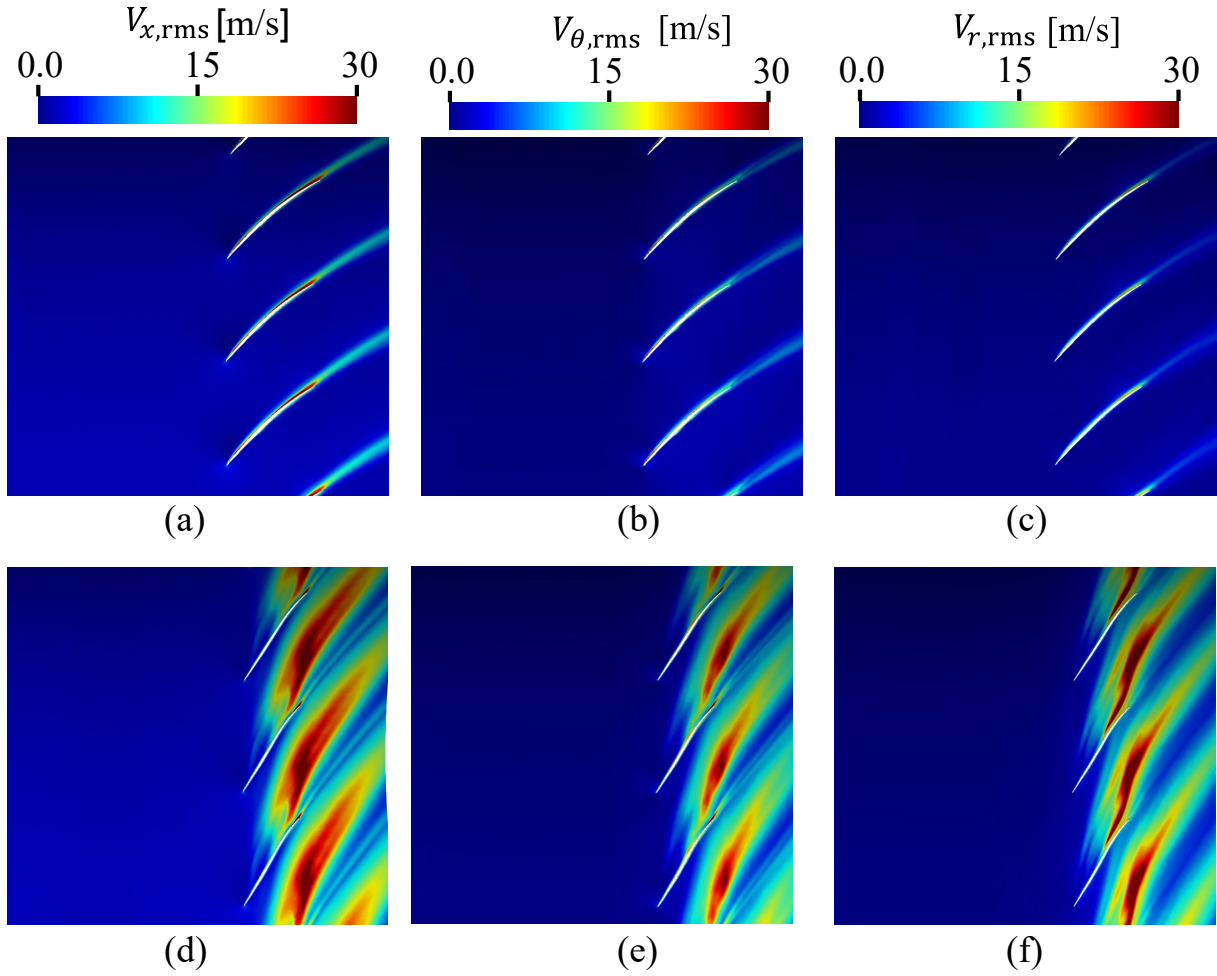
Figure 5.7: Contours of the components of the RMS velocity fluctuations around the rotor blade for two spanwise positions, (a,b,c) 80%, (d,e,f) 99%.

of the blockage region, a strong increase of the axial velocity component close to the suction surface at about 70% of the chord length appears, showing the onset of the tip vortices TLV2, IV and TSV. Large values of the axial velocity component can also be observed in the blade passage upstream of the flow blockage, which highlight the presence of the TLV1. The flow blockage due to the tip leakage and tip separation vortices is also seen through a deficit of the relative tangential velocity ($V_{\theta,\mathrm{rel}}$) in the interstage region downstream of the rotor blades. $V_{\theta,\mathrm{rel}}$ reaches large values at about 70% of the chord length in the region where the tip vortices TLV2, IV and TSV appear. The radial velocity component (V_r) exhibits a steep variation in the region where the tip vortices TLV2, IV and TSV appear. Upward and downward flow motions are observed in this region, indicating a circulating tip leakage vortex. A similar behavior is observed for the TLV1 with smaller V_r values. At 80% of the rotor span, the tip leakage vortices do not show any influence on the flow topology. At this spanwise position, large values of V_x are observed from about 60% to 80% of the chord length, indicating the region of the blade loading.

Figure 5.7 presents the three components of the rms velocity fluctuations at two span-wise positions, 80% and 99%. At a spanwise position of 80%, the tip vortices do not have any influence. At 99% of the rotor span, a region of large RMS velocity fluctuations is observed in the interstage region, starting at about 80% of the rotor chord length. It
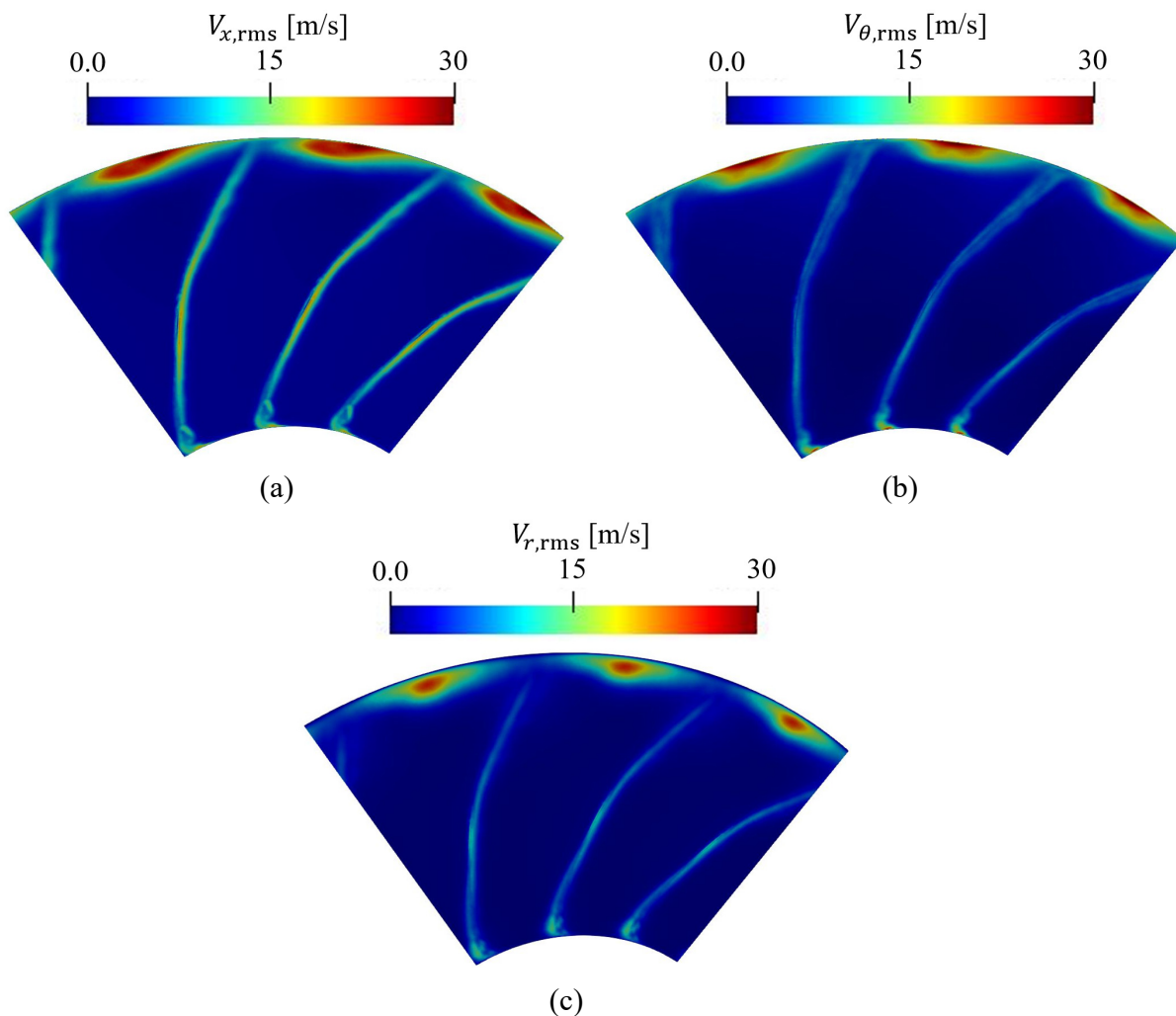
Figure 5.8: Contours of the components of the RMS velocity fluctuations at an axial plane directly downstream of the rotor trailing edge.

corresponds to the region of streamwise and tangential velocity deficits in Figures 5.6 (d) and (e). This region can be associated to the velocity fluctuations generated by the interaction of the vortices TLV1, TLV2, IV and TSV with the main flow. The vortices generated from one blade seem to interact with the trailing edge and the wake of the adjacent blade. The levels of the velocity fluctuations due to the tip vortices are much larger than the levels in the rotor blade boundary layers and wakes.

The three components of the RMS velocity fluctuations are also presented at an axial cut directly downstream of the rotor trailing edge in Figure 5.8. Significant levels of RMS velocity fluctuations are observed in the tip leakage region (representing roughly 10% of the channel height). It can also be noted that the velocity fluctuations in this region are more important than those in the wakes and in the corner separation region close to the hub. The tip leakage flow is the dominant contributor to the velocity fluctuations related to secondary flows.

Figure 5.9 presents the contours of the turbulent kinetic energy, k_t, the loss in turbulent kinetic energy, LIKE, and the RMS pressure fluctuations, P_{rms}, around the rotor blade at two spanwise positions, 80% and 99%. The parameter LIKE was first introduced by Daviller *et al.* [49], and is defined as the sum of the dissipation produced by resolved and
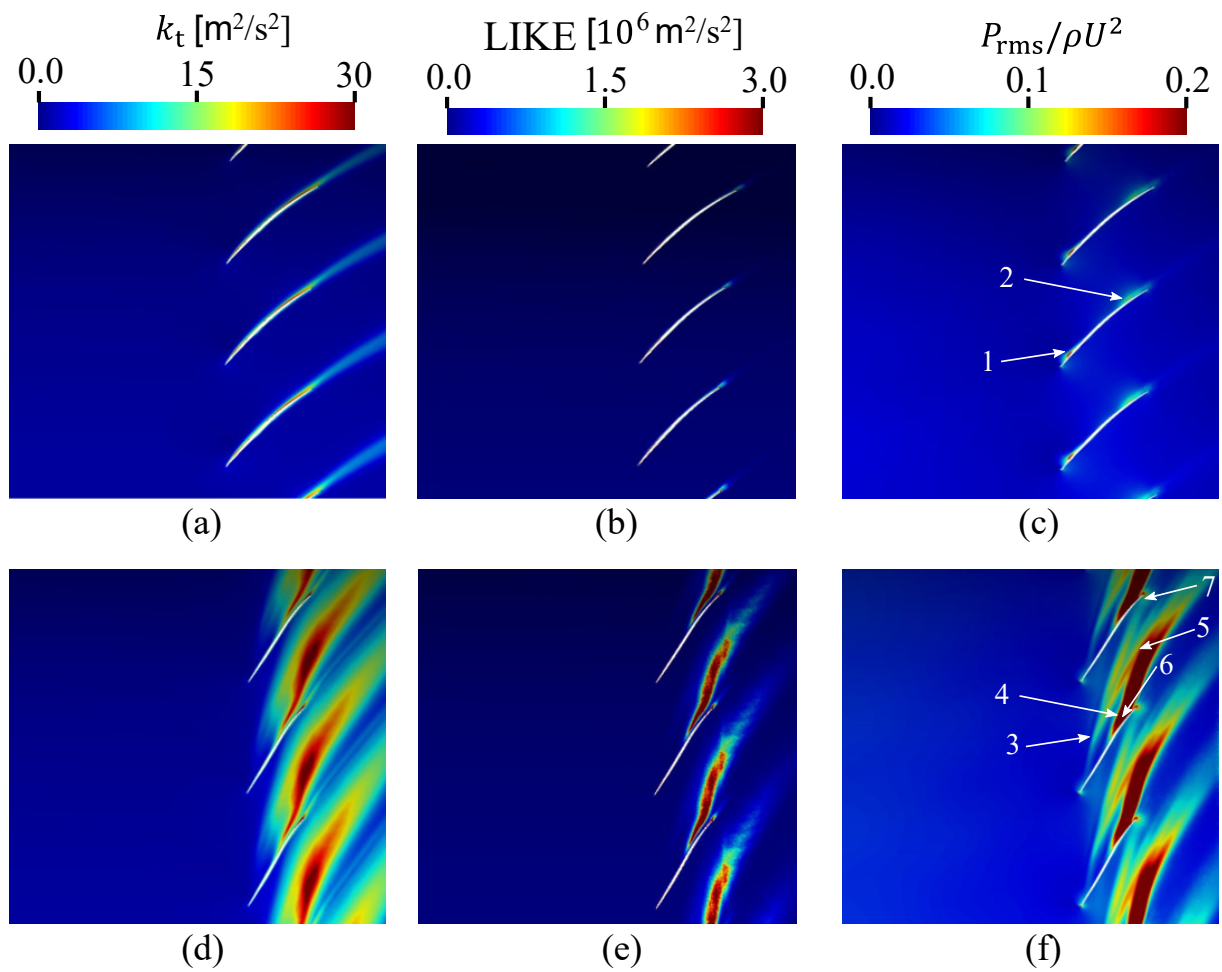
Figure 5.9: Contours of (a,d) turbulent kinetic energy, (b,e) loss in turbulent kinetic energy [49] and (c,f) RMS pressure fluctuations around the rotor blade for two spanwise positions, (a,b,c) 80%, (d,e,f) 99%.

modeled fluctuations and is given as,

$$\text{LIKE} = (\mu + \mu_t) \left(\frac{\partial \tilde{u}_i}{\partial x_j} + \frac{\partial \tilde{u}_j}{\partial x_i} \right)^2 \tag{5.2}$$

where $\tilde{u}_i$ correspond to each velocity component. The term $\mu \left(\frac{\partial u_i}{\partial x_j} + \frac{\partial u_j}{\partial x_i} \right)^2$ is present in the transport equations of both the turbulent kinetic energy [271] and the entropy [12, 132, 155]. This term corresponds to the viscous dissipation in the equation of the turbulent kinetic energy and to the losses induced by the fluid friction irreversibilities in the entropy equation. Since LES does not resolve all spatial scales, LIKE is computed using the filtered velocity components, and both the contributions of the fluctuations resolved by the LES ($\mu \left(\frac{\partial \tilde{u}_i}{\partial x_j} + \frac{\partial \tilde{u}_j}{\partial x_i} \right)^2$) and those modeled ($\mu_t \left(\frac{\partial \tilde{u}_i}{\partial x_j} + \frac{\partial \tilde{u}_j}{\partial x_i} \right)^2$) are added.

At the tip, the second tip leakage vortex, TLV2, the induced vortex, IV, and the tip separation vortices, TSV, are responsible for the major part of k_t and LIKE. The loss in turbulent kinetic energy is localized at the core of the TLV2 and TSV and quickly decreases downstream of the rotor.

The fan noise sources can be partly related to the RMS pressure fluctuations. At 80% of the rotor span, two regions of significant P_{rms} values are identified. The first region (region "1" in Figure 5.9 (c)) corresponds to the fluctuations in the recirculation bubble that appears at the suction side of the rotor blade, close to the leading edge, between 60% to 90% of the rotor span, as shown in Chapter 6. The second region (region "2" in Figure 5.9 (c)) corresponds to a small flow separation produced on the suction side of the blade, downstream of the maximum camber position. The influence of the tip vortices can be observed in Figure 5.9 (f). The first tip leakage vortex TLV1 and the tip vortices TLV2, TSV and IV can be identified (regions "3" and "4" in Figure 5.9 (f), respectively). The interaction between the TLV1 and the tip vortices TLV2, TSV and IV is observed at position "5" in Figure 5.9 (f). Important levels of P_{rms} are observed on the suction side from 70% of the chord length down to the trailing edge (position "6" in Figure 5.9 (f)), which are generated due to the interaction of the TLV2, TSV and IV with the blade surface. Additionally, a part of the TLV1 of each blade interacts with the trailing edge of the adjacent blade (position "7" in Figure 5.9 (f)), which generates large P_{rms} levels at the trailing edge on the pressure side. Thus, the main noise source is expected to be located at the trailing edge, due to these two interaction mechanisms. Finally, when the two spanwise positions are compared, it can be noticed that the size of the region of strong turbulent activity and pressure fluctuations is more important in the tip gap region than in the rotor wakes and in the recirculation bubble.

The tip leakage vortex is often identified by a region of high vorticity magnitude. Figure 5.10 shows contour plots of the averaged vorticity magnitude at different spanwise positions, from 94% to 99% of the rotor span. At 99% of the rotor span, large vorticity values are obtained close the blade surface at about 75% of the chord length (position "1" in Figure 5.10 (f)), which corresponds to the onset region of the tip flow vortices TLV2, TSV and IV. The main core of these vortices is convected downstream with two direction changes. From position 1 to position 2, the TSV under the influence of the pressure gradient starts to shift from the suction side. In this region, the TLV2 is not yet well formed and the TSV remains parallel to the blade chord. Between positions 2 and 3, the TLV2 now fully formed interacts with the TSV. Consequently, the tip vortices TSV and TLV2 are shifted and form an angle of about 30° with the blade chord. Finally,
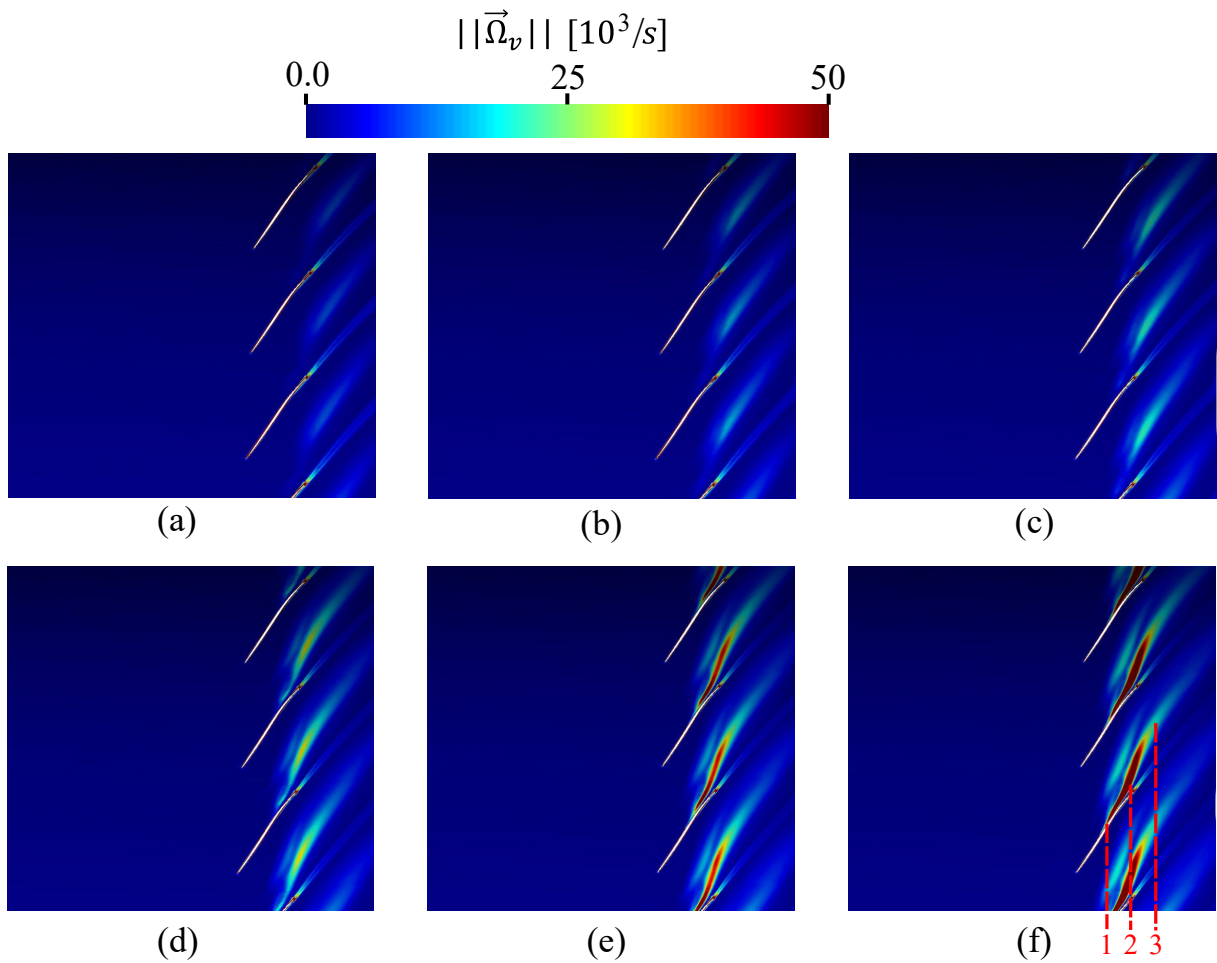
Figure 5.10: Contours of the averaged vorticity magnitude around the rotor blade for different spanwise positions, (a) 94% (b) 95% (c) 96% (d) 97% (e) 98% and (f) 99%.
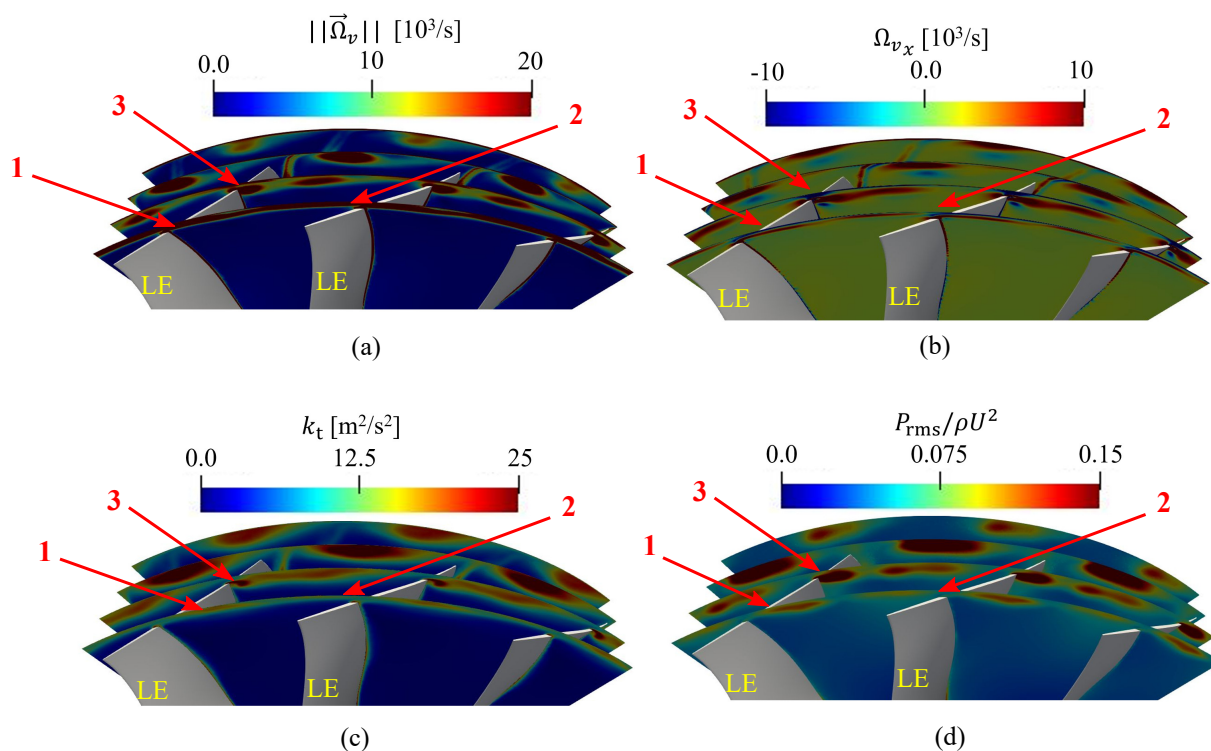
Figure 5.11: Contours of averaged (a) vorticity magnitude, (b) axial vorticity component, (c) turbulent kinetic energy and (d) RMS pressure fluctuations at four different axial cuts in the blade passage.

at position 3, these tip vortices are deviated after interacting with the main flow and with TLV1 and are convected in a direction parallel to the blade's wake. As the radius decreases, the maximum vorticity in the tip vortices is reduced and the position of the tip vortices core is shifted downstream.

The trajectory of the different tip vortices is further analyzed in Figure 5.11 through averaged contours of the vorticity magnitude, the axial vorticity component, the turbulent kinetic energy, k_t, and the RMS pressure fluctuations, P_{rms}, on four different axial cuts. The cuts are at 20%, 70%, 90% and 120% of the chord length starting from the leading edge. The different tip flow vortical structures can be identified. At 20% of the chord length, the region of large k_t and P_{rms} values close to the blade suction side (position "1" in Figure 5.11) corresponds to the apparition of the TLV1. When convected downstream, the TLV1 can still be observed at 70% of the chord length in the middle of the passage with lower vorticity magnitude, k_t and P_{rms} values. Close to the pressure side (position "2" in Figure 5.11), a small region of large vorticity magnitude highlights the interaction of the horseshoe vortex HSV coming from the suction side of the adjacent blade with the pressure side of the current blade. At 70% of the chord length, the tip vortices TSV, TLV2 and IV start to appear close to the blade suction side (position "3" in Figure 5.11). The region of negative axial vorticity component at this location shows the apparition of the induced vortex IV. These vortices are convected downstream; the tip vortices TSV and TLV2 can be identified through large positive values of Ω_{v_x}, whereas IV can be detected by large negative values of Ω_{v_x}.

The vorticity magnitude and vorticity components at an axial cut directly downstream of the rotor trailing edge are presented in Figure 5.12. As discussed in Figure 5.10, the tip gap region is characterized by high vorticity magnitudes. The influence of the tip vortices
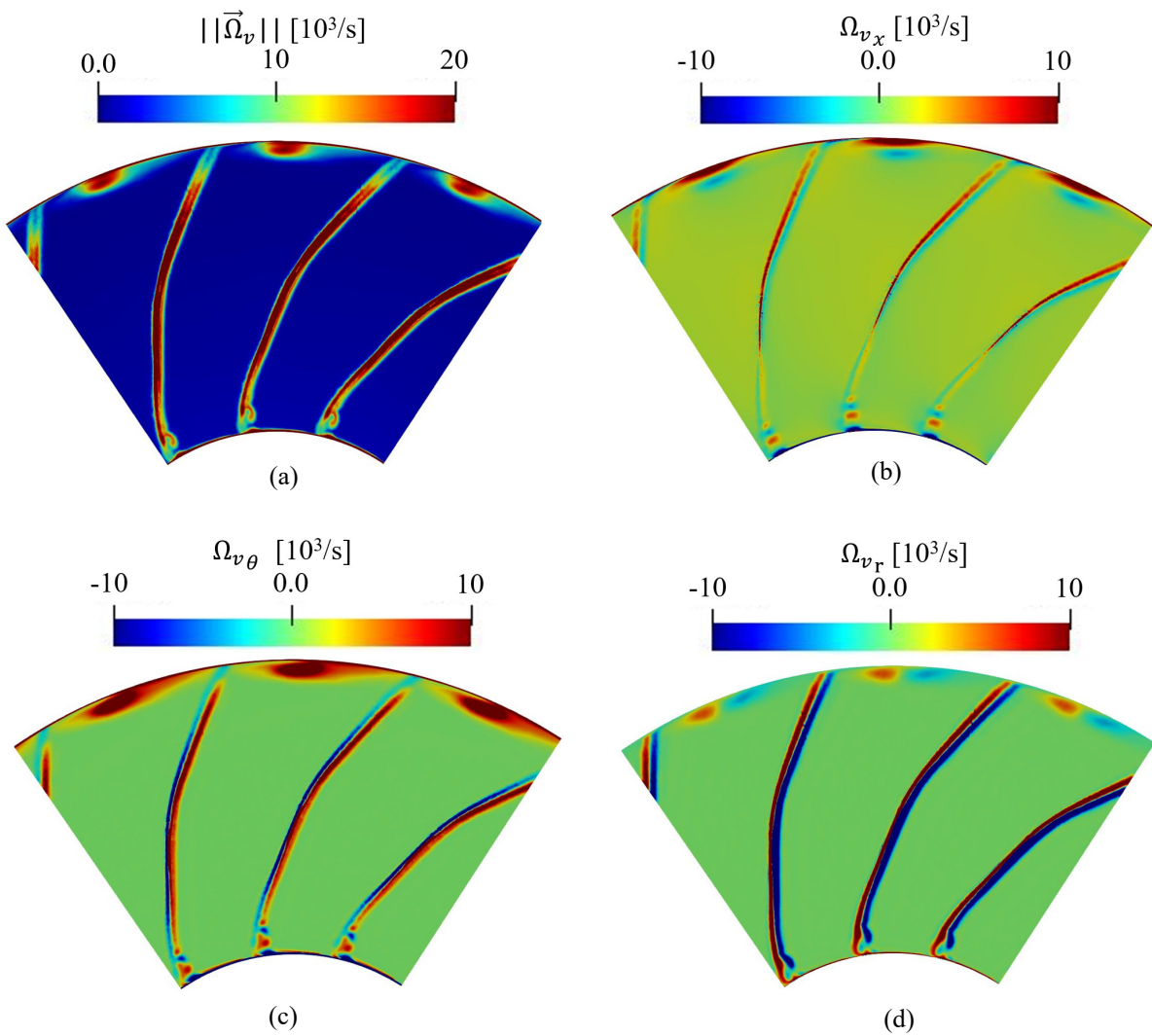
Figure 5.12: Contours of the averaged vorticity magnitude and vorticity components on an axial cut directly downstream of the trailing edge of the rotor.
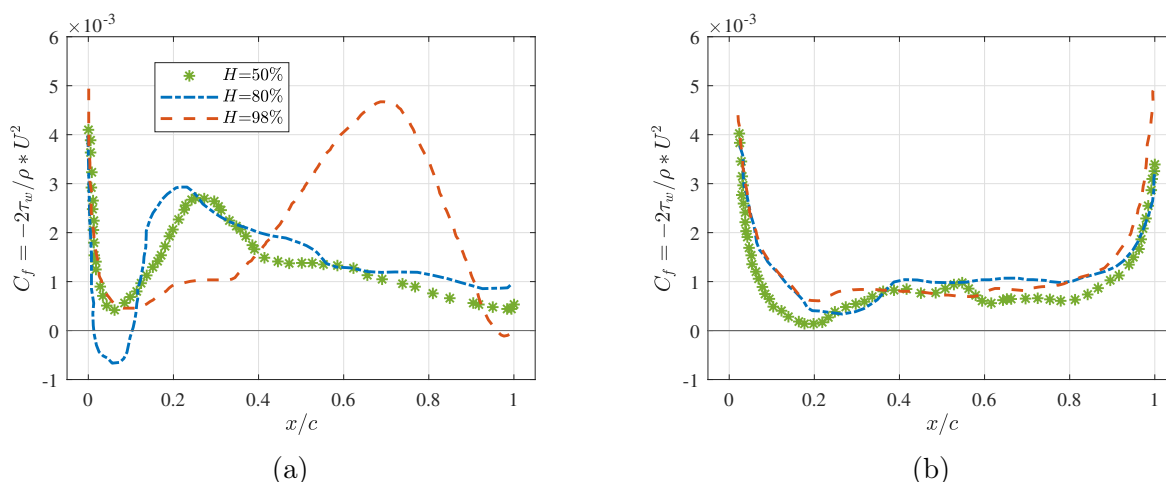
Figure 5.13: Average friction coefficient C_f along the rotor blade for different spanwise positions. (a) suction side. (b) pressure side.

is limited to the last 10% of the channel height towards the rotor casing. The vorticity field is dominated by the streamwise (Ω_{v_x}) and tangential (Ω_{v_θ}) components, associated to the direction of the vortices. The negative region of the axial vorticity component can be associated to the induced vortex IV. Finally, the radial vorticity component seems to be dominant in the boundary layers on the pressure and suction surfaces of the blade, compared to its values in the tip gap region.

A comparison of the friction coefficient, C_f, over the suction side and the pressure side of the rotor blade is presented in Figure 5.13 at different spanwise positions. For all the spanwise positions, positive values of C_f are obtained at the pressure side, where the boundary layers remain attached. At 50% of the rotor span, C_f remains positive over the suction side. A region of negative friction coefficient is observed close to the leading edge of the blade at 80% of the rotor span, related to the presence of a recirculation bubble. Downstream of this region, C_f remains positive along the suction side down to the TE. At 98% of the rotor span, a slight increase of C_f is observed at about 20% of the chord length, followed by a region of large C_f between 50% and 85% of the chord length. This corresponds to the formation of the tip vortices TSV, TLV2 and IV at about 65% of the chord length due to the high pressure difference observed in Figure 5.2.

Tip leakage flow: aerodynamic analysis ———————————— **Summary**

- The maximum blade loading and pressure difference at the blade tip are obtained between 50% and 90% of the chord length.

- Several vortical structures are identified in the tip region:

    - A horse shoe vortex (HSV) is identified at the leading edge of the blades.

    - A first tip leakage vortex (TLV1) forms at about 20% of the chord length due to a leakage flow from the pressure to the suction side.

    - A tip separation vortex (TSV) and a second tip leakage vortex (TLV2)

form at about 70% of the chord length in the region of large pressure difference.

– An induced vortex (IV) forms alongside the second tip leakage vortex (TLV2) and rotates in the opposite direction.

- The tip vortices are characterized by streamwise and pitchwise velocity deficits and significant variations of the radial velocity component.

- The tip gap region is characterized by large velocity fluctuations and strong turbulent kinetic energy levels.

- Important levels of RMS pressure fluctuations are observed at the blade suction side beyond 70% of the chord length, at the trailing edge and in the interblade region due to three interaction mechanisms:

  – The interaction of the tip vortices TLV2, TSV and IV with the first tip leakage vortex TLV1.

  – The interaction of the tip leakage vortex TLV1 generated at one blade with the trailing edge of the adjacent blade.

  – The interaction of the tip vortices TLV2, TSV and IV generated at one blade with the trailing edge of the same blade.

- The trajectory of the tip vortices TLV2, IV and TSV is characterized by three distinct orientations:

  – Between 60% and 70% of the chord length, the tip vortices are parallel to the blade chord.

  – Between 70% and 110% of the chord length, the angle between the tip vortices and the profile is approximately 30°.

  – Beyond 110% of the chord length, the tip vortices are convected parallel to the blade wakes.

- The influence of the tip leakage flow is limited to 10% of the span in the shroud region.

5.4 Aeroacoustics

5.4.1 Noise sources

Contours of instantaneous dilatation rate ($\nabla \cdot \mathbf{u}$) on an azimuthal cut crossing the rotor blade are shown in Figure 5.14, along with iso-surfaces of Q-criterion ($Qc^2/U_0^2 = 100$) colored by the vorticity magnitude in the tip gap region. The flow is coming from left to right and the view is taken by an observer downstream of the fan looking at the suction side of the blades. The flow topology in the tip gap region and the different tip vortices, described in Section 6.3, can be identified. Based on the wave-fronts that appear in the contours of the instantaneous dilatation rate, an important noise source is present in the tip gap region. These wave-fronts propagate in the upstream and downstream directions
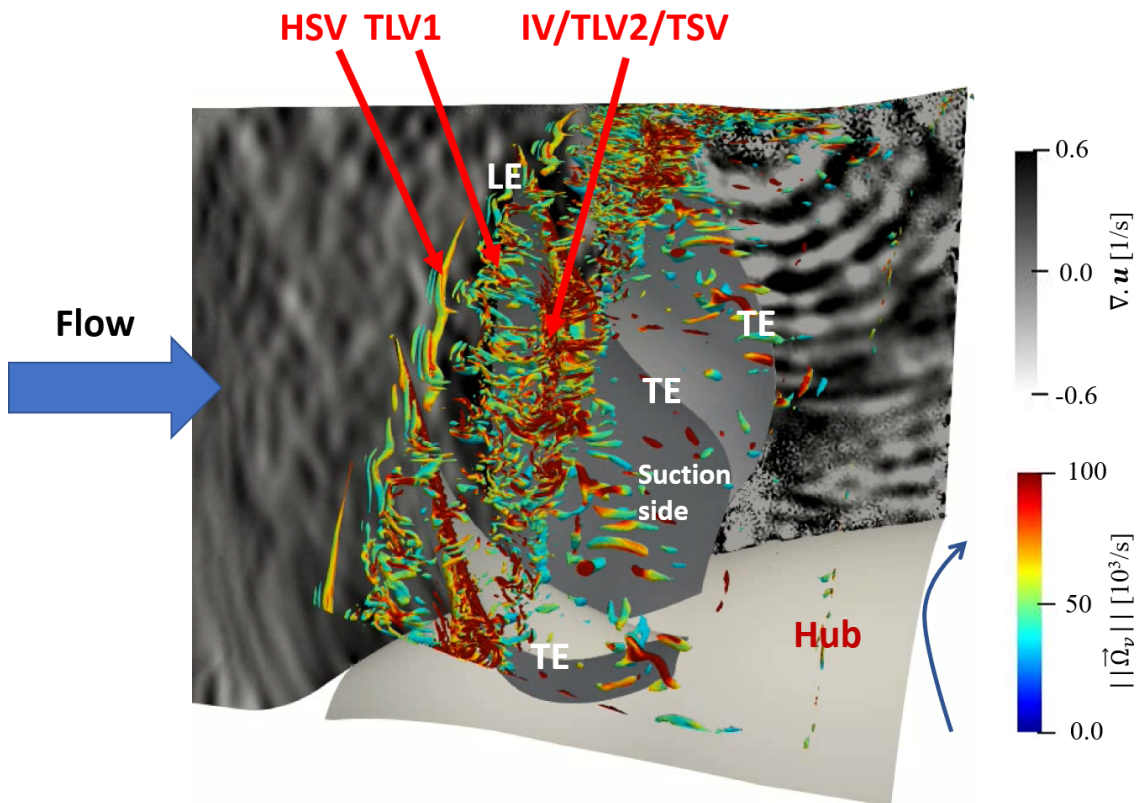
Figure 5.14: Instantaneous contours of dilatation rate on an azimuthal cut, and iso-surfaces of Q-criterion ($Qc^2/U_0^2 = 100$) colored by the vorticity magnitude in the tip gap region.

and the corresponding tip gap noise source seems to be the dominant fan noise source in this configuration at approach conditions.

In order to further investigate (i) the turbulent structures in the tip gap region and (ii) the associated noise sources and to compare them to other fan noise sources, contours of the instantaneous dilatation rate ($\nabla \cdot \mathbf{u}$) at two spanwise positions around the rotor blades are shown in Figure 5.15, along with iso-surfaces of Q-criterion ($Qc^2/U_0^2 = 100$) colored by the vorticity magnitude. The flow is coming from left to right and the view is taken from the shroud. The development of turbulent structures around the blades and in the wakes can be observed.

At 80% of the rotor span, a small recirculation bubble appears near to the leading edge and triggers the transition of the boundary layer to turbulence. Small turbulent structures are thus formed on the suction side of the blade. These structures are diffracted at the trailing edge, which generates trailing edge noise. The contours of instantaneous dilatation rate show wave-fronts generated at the trailing edge associated with this noise source.

At 98% of the rotor span, the different tip vortices (HSV, TLV1, TSV, TLV2 and IV) discussed in Section 6.3 are observed. After the interaction between TLV1 and the other tip vortices IV, TLV2 and TSV (position "1" in Figure 5.15 (b)), a part of TLV1 interacts with the trailing edge of the adjacent blade. Additionally, the highly turbulent structures related to the tip vortices IV, TLV2 and TSV interact with the suction side of the rotor blade they come from. Some of these structures are diffracted at the trailing edge of the blade. The wave-fronts identified using contours of instantaneous dilatation rate show that the main noise sources are located at the trailing edge, generated by two mechanisms, (i) the interaction of a part of the TLV1 from one blade with the trailing edge of the adjacent blade, and (ii) the interaction of the tip vortices IV, TLV2 and TSV from each blade with the trailing edge of the same blade. It should also be noted that the noise contribution due to the interaction between the different tip vortices at position "1" in Figure 5.15 (b) is negligible when compared to the interaction of the tip vortices with the trailing edges.

Comparing the two spanwise positions, larger values of the dilatation rate are observed in the tip gap region, which are associated to turbulent structures with larger vorticity magnitudes when diffracted at the trailing edges.

Due to the relatively low Mach number in the current study and to the absence of shock waves, dipolar noise sources, which are related to force fluctuations at the blade surface, are expected to dominate [90, 135]. Consequently, the location of the noise sources from the fan blade can be roughly estimated from the RMS pressure fluctuations, P_{rms}, along the rotor suction and pressure sides at three different spanwise positions, as shown in Figure 5.16. At 50% of the rotor span, on the suction side, the small increase of P_{rms} at about 16% of the chord length indicates the position of the boundary layer transition to turbulence. The bubble region, which appears at 80% of the rotor span close to the leading edge, also exhibits high P_{rms} values. In the tip region, a strong increase of P_{rms} is observed on the suction side starting from 60% of the chord length down to the trailing edge. This corresponds to the development of the tip vortices TLV2 and IV and the detachment of the tip separation vortex TSV in the region of high pressure difference. At the pressure side, large values of P_{rms} are observed close to the trailing edge, due to the impact of the TLV1 from the adjacent blade. Since the tip vortices IV, TLV2 and TSV are characterized by larger vorticity magnitudes and turbulent intensities than TLV1 (see Figures 5.9 and 5.10), the suction side exhibits larger P_{rms} levels than the pressure side at the trailing edge. Even though the levels of P_{rms} are not directly related to the

(a)

(b)
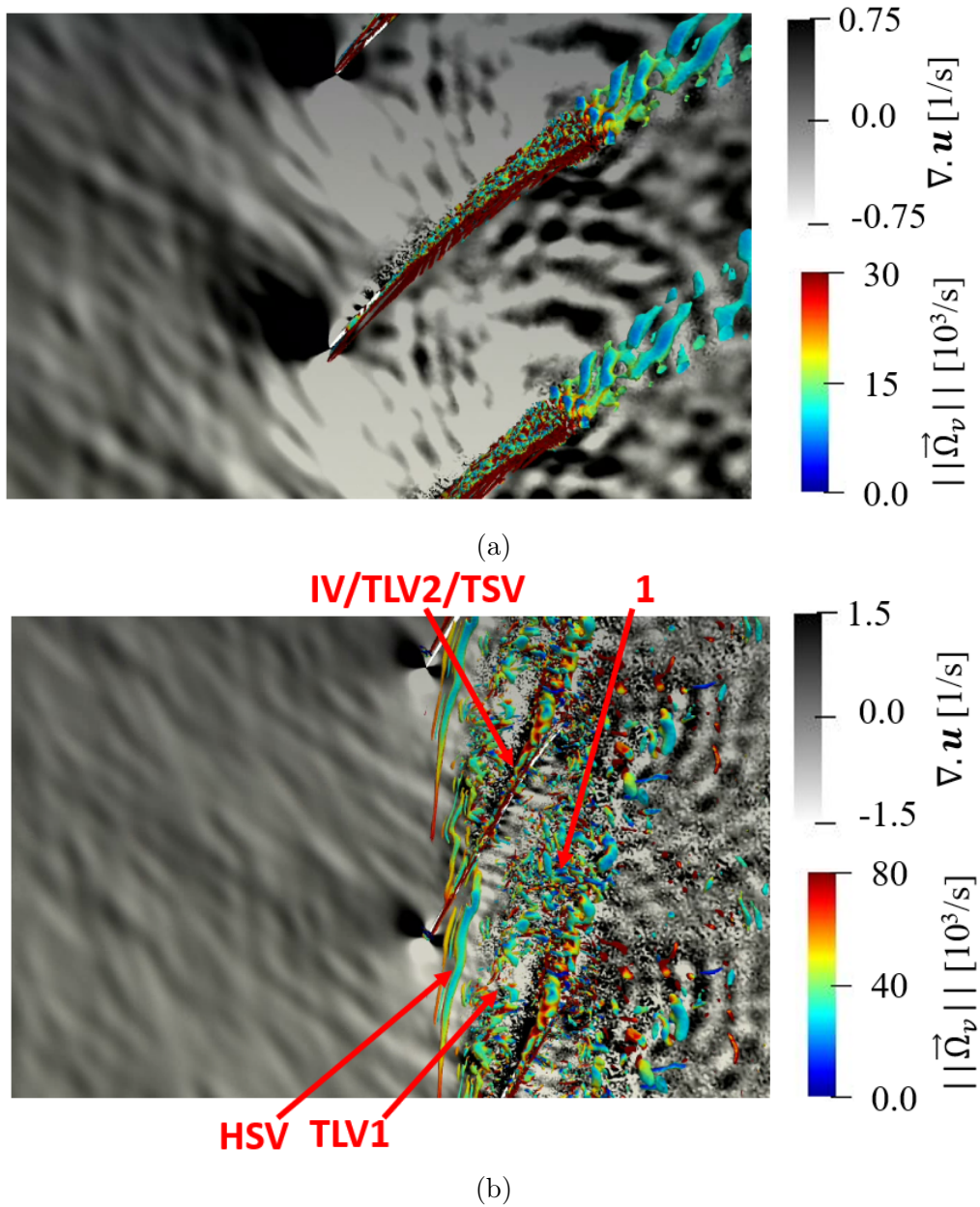
Figure 5.15: Instantaneous contours of dilatation rate and iso-surfaces of Q-criterion $(Qc^2/U_0^2 = 100)$ colored by the vorticity magnitude around the rotor blades at two spanwise positions, (a) 80% and (b) 98%.
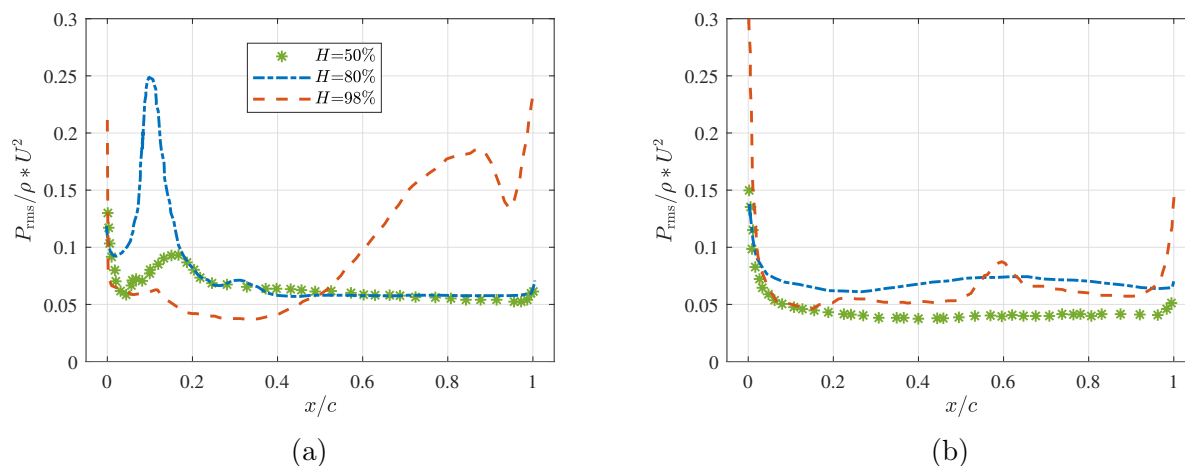
Figure 5.16: RMS pressure fluctuations P_{rms} along the rotor blade for different spanwise positions. (a) suction side. (b) pressure side.
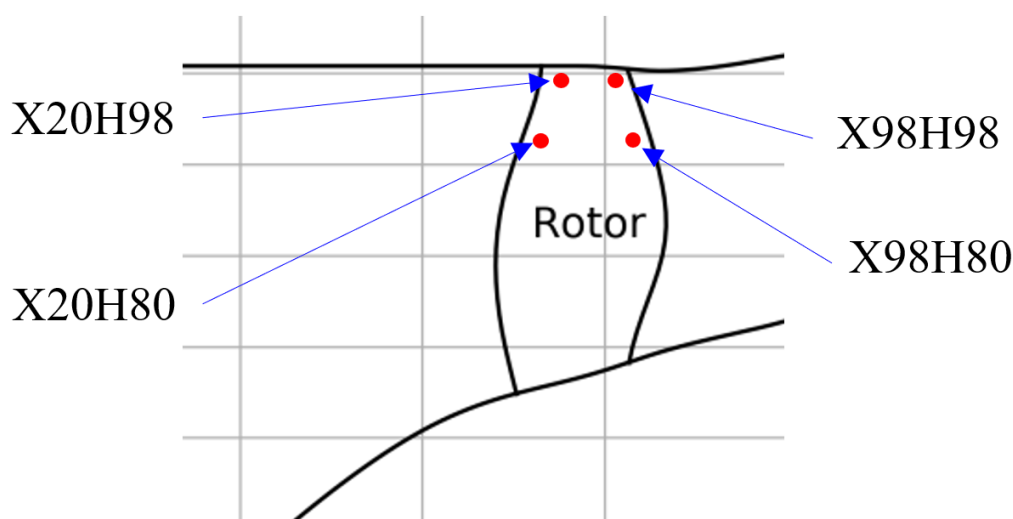
Figure 5.17: Position of unsteady monitor points used to compute the wall pressure spectra on the blade suction side at four different positions.

intensity of the noise sources, they can give an idea on the contribution of each noise source. Consequently, the dominant noise mechanism in the tip gap region for the present configuration seems to be the interaction of the tip vortices IV, TLV2 and TSV generated at about 70% of the chord length with the trailing edge of the same blade.

Finally, a small hump in the P_{rms} distribution can be observed on the pressure side from 50% to 70% of the chord length, which may be due to the interaction of some turbulent structures from the TLV1 of the adjacent blade. This region also corresponds to the apparition of the tip vortices IV, TLV2 and TSV, that are fed by these turbulent structures originating from the adjacent TLV1.

5.4.2 Wall pressure spectra

The wall pressure spectrum (WPS) is a key parameter to describe the state of the boundary layers and to characterize the different noise sources. The positions of the monitor
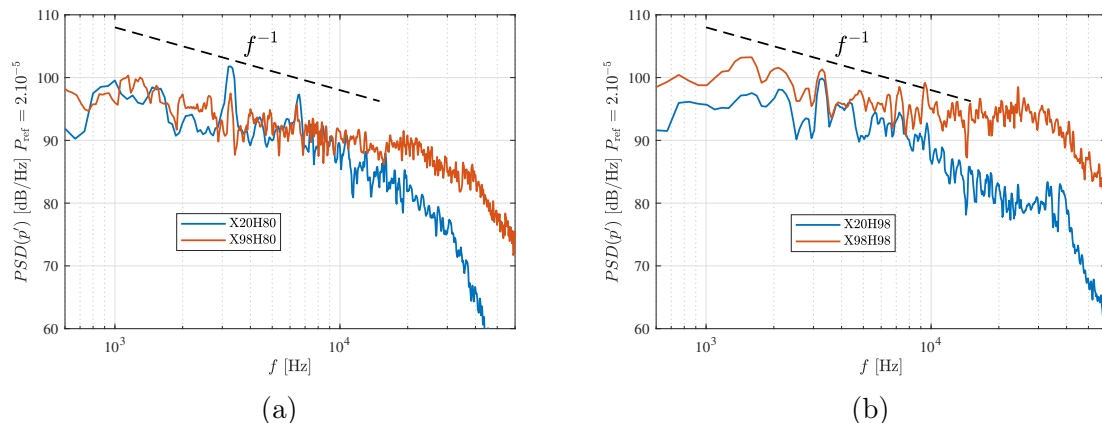
Figure 5.18: Wall pressure spectra (WPS) on the suction surface of the blade at four different positions. (a) 80% and (b) 98% of the rotor span.

points on the suction side used for the unsteady recordings to compute the WPS, are presented in Figure 5.17. For the nomenclature, the value after "X" corresponds to the chordwise position of the monitor point as a percentage of the chord length from the leading edge, and the value after "H" to the spanwise position as a percentage of the rotor span.

The WPS obtained using these four monitor points are presented in Figure 5.18. At 80% of the rotor span, similar WPS levels are obtained up to 10 kHz, with a slope of about f^{-1}, which corresponds to the large turbulent structures in the boundary layer. In the frequency range corresponding to this slope, universal spectra can be obtained for the WPS using internal and external variables of the boundary layer, as discussed in Chapter 3. This region is known as the overlap region and is related to turbulent activity in the inertial logarithmic zone of the boundary layer. The size of this region increases with the Reynolds number of the flow in the boundary layer. This slope has been observed experimentally [156, 230, 228, 227] and numerically [179, 129] and has been justified analytically by Bradshaw [20].

The monitor point at $20\%c$ is located in the recirculation bubble region, where large levels of RMS pressure fluctuations are observed (Figure 5.16). This may explain the comparable levels of the WPS at this monitor point with that at the trailing edge, for which a more turbulent boundary layer is expected.
The overlap region of the spectrum extends for the WPS close to the trailing edge up to about 16 kHz, whereas this region is limited to 10 kHz at $20\%c$. This is due to a larger Reynolds number at $98\%c$ compared to the Reynolds number at $20\%c$.

At 98% of the rotor span, larger WPS levels are obtained close to the trailing edge compared to the levels obtained at $20\%c$, over the whole frequency range. These differences are more pronounced at high frequencies ($f > 10$ kHz). The overlap region extends from about 1.5 kHz up to 7 kHz for the WPS at 20% of the chord length, whereas it extends from 1.5 kHz to 15 kHz at 98% of the chord length. After the overlap region, a significant hump is observed in the spectrum close to the trailing edge. This must be an effect of the tip flow, as it will be pointed out in the following.

In order to further investigate the pressure fluctuations in the tip leakage region, several monitor points are located on the blade tip surface for different chordwise positions, X30, X50, X70 and X90, the value after "X" being the chordwise position of the monitor point as a percentage of the chord length from the leading edge. The wall pressure spectra at
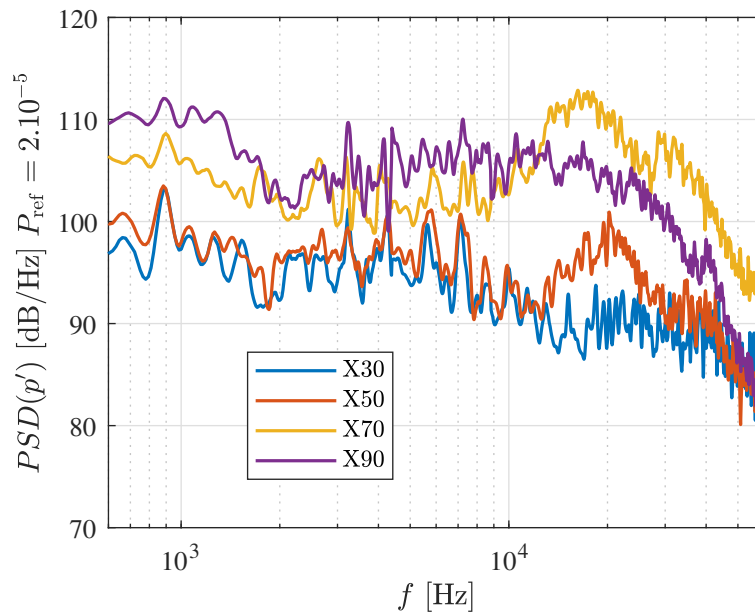
Figure 5.19: Wall pressure spectra (WPS) on the surface of the blade tip, at four different chordwise positions.

these positions are presented in Figure 5.19.

Similar spectra are obtained at 30% and 50% of the chord length, up to 12 kHz. For higher frequencies, the spectrum at X30 exhibits a plateau up to 30 kHz, whereas at X50 a significant hump is observed from 12 kHz to 25 kHz. Indeed, at 50% of the chord length, the TSV starts to separate from the blade and small turbulent structures are identified (Figures 5.3 and 5.4). This hump is more pronounced at X70 and is identified from 9 kHz to 30 kHz. At this position, the pressure difference between pressure and suction side reaches important values (Figure 5.2) and several tip vortices appear, TLV2, IV and TSV (Figures 5.3 and 5.4).

At X90, a hump in the WPS appears on a large range of frequency, from 2 kHz up to 25 kHz. At this position, two interaction mechanisms are identified; (i) the interaction of the TLV1 generated on the adjacent blade with the blade tip, and (ii) the interaction of the tip vortices TLV2, IV and TSV with the blade tip. By observing the spectra at X50 and X70, where only the interaction mechanism between the tip vortices TLV2, IV and TSV with the blade tip occurs, the hump observed at X90 between 9 kHz to 25 kHz can be attributed to this last mechanism, as it will be further investigated in the following. From 2 kHz to 9 kHz, the hump in the spectrum may be associated to the interaction between the TLV1 generated close to the leading edge of the adjacent blade and the blade tip, as pointed out in the following. This hump is also observed in the literature in more classical configurations where the tip leakage vortex TLV1 is the dominant tip leakage structure [18, 128, 140].

Since the TLV1 travels through all the blade passage before interacting with the trailing edge of the adjacent blade, the TLV1 is more diffused and widened than the tip vortices TLV2, TSV and IV, when interacting with the blade's surface. This may explain the lower frequency range induced by the interaction of the TLV1 with the adjacent blade compared to the range induced by the interaction of the tip vortices TLV2, TSV and IV with the blade surface, they originate from.
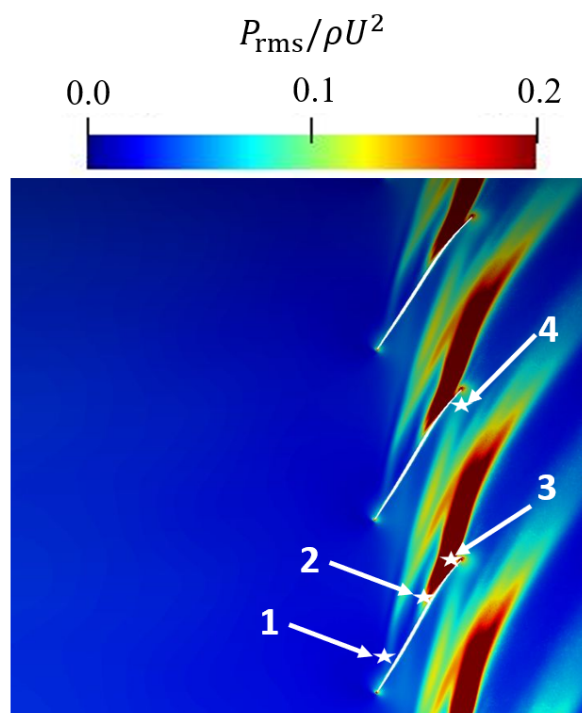
Figure 5.20: Contours of RMS pressure fluctuations around the rotor blade at 98% of the rotor span. The stars show the position of the monitor points used for the computation of the coherence in the tip gap region.

Due to the large range of turbulent coherent scales in the tip leakage vortices (particularly at the position X90), the frequency range of the hump is relatively large and this range is larger at X90 than at X50 and X70 (due to the contribution of the adjacent TLV1 at X90).

In order to further analyze the origin of these humps, the coherence between different points in the tip gap region is computed. Figure 5.20 presents the position of the monitor points used for the computation of the coherence. The coherence between monitor points 1 and 4 and between monitor points 2 and 3 are presented in Figure 5.21 (a) and (b) respectively. The monitor point 1 corresponds to the onset of the TLV1 and the monitor point 4 is located near the trailing edge on the pressure side. The coherence between these two positions (1 and 4) corresponds to the mechanism of interaction of the TLV1 generated at one blade with the trailing edge of the adjacent blade on the pressure side. This coherence presents large values between 2 kHz and 9 kHz, which support the analysis made in Figure 5.19 relating the hump at X90 from 2 kHz to 9 kHz to the impact of the adjacent TLV1 with the pressure side.

The monitor point 2 corresponds to the onset of the tip vortices TLV2 and IV and the detachment of the TSV from the blade surface, and the monitor point 3 is located near the trailing edge on the suction side. The coherence between these two positions (2 and 3) corresponds to the mechanism of interaction of the tip vortices TLV2, IV and TSV with the trailing edge of the blade on the suction side, and presents large values between 10 kHz and 25 kHz. This coherence study is consistent with the analysis made in Figure 5.19 regarding the origin of the high frequency hump from 9 kHz to 25 kHz, attributed to the interaction of the tip vortices TLV2, TSV and IV with the suction side.
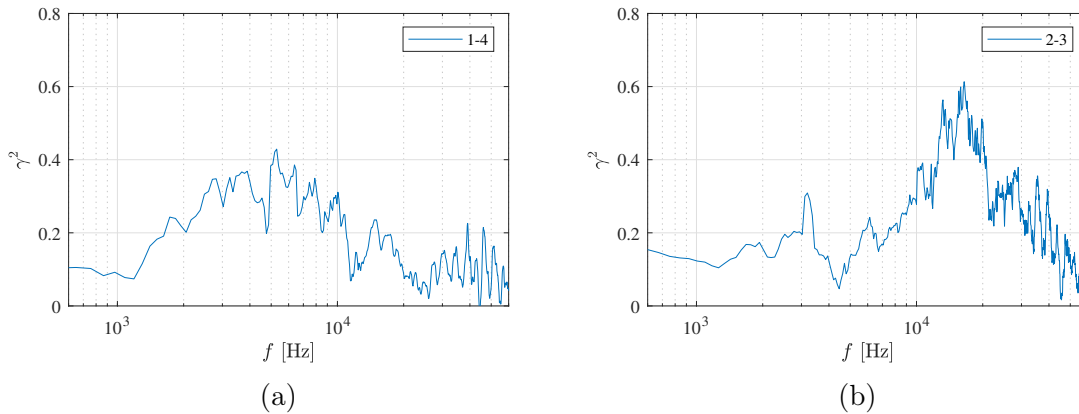
Figure 5.21: Coherence between the pressure fluctuations at the monitor points 1 and 4 (a) and the monitor points 2 and 3 (b).

5.4.3 Dynamic mode tracking

The humps observed in Figure 5.19 can be further investigated using a mode tracking technique, which is known as Dynamic Mode Tracking (DMT) [214].

Figure 5.22 shows DMT results calculated from the density in the LES around three different frequencies, $f_1 = 4000$ Hz, $f_2 = 6620$ Hz and $f_3 = 16000$ Hz, with a frequency window width of 2000 Hz. Two axial cuts upstream of the rotor blade, two spanwise positions (50% and 80% of the rotor span) and two longitudinal cuts are shown. The first longitudinal cut passes close to the leading edge of the rotor and the second cut crosses the rotor blade at about 70% of the chord length. The frequencies f_1 and f_2 are located in the frequency range of the first hump in the WPS spectrum, whereas f_3 is located in the range of the second hump. The frequency f_2 corresponds to the second harmonic of the vane passing frequency (these analyzes are performed in the rotor frame).

The dominant acoustic mode at $f_1 = 4000$ Hz exhibits large amplitudes close to the tip gap region in the longitudinal cut that crosses the blade close to the leading edge (region "A" in Figure 5.22 (a)). The amplitude of this mode increases from 50% of the rotor blade to the blade tip. This mode propagates in the upstream direction with decaying amplitude and with an inclination angle of about -50° with respect to the rotation axis (as shown by the dashed lines in Figure 5.22 (a)).

At the second frequency ($f_2 = 6620$ Hz), a dominant acoustic mode seems to be generated downstream of the rotor blade and to propagate in the upstream direction, through the blade passage. This mode can be associated with the harmonic of the rotor-stator interaction noise, which is related to the interaction between the periodic rotor wakes and the stator vanes. Similar behavior is observed at both longitudinal cuts.

The third DMT mode, at a frequency of $f_3 = 16000$ Hz, exhibits a more complex pattern. Two acoustic modes seem to be dominant at the longitudinal cut crossing the blade at 70% of the chord length (Figure 5.22 (f)). The first mode is generated from the lower part of the blade close to the hub and propagates in the upstream direction (dashed lines "2" in Figure 5.22 (f)). The second mode is generated at the blade tip where large amplitudes are observed. Two lobes ("B" and "C" in Figure 5.22 (f)) are noticed. This mode is also propagating in the upstream direction (dashed lines "1" in Figure 5.22) with a larger angle than the inclination angle of the dominant mode at $f_1 = 4000$ Hz.

Consequently, when the DMT results are combined with the tip leakage flow topology
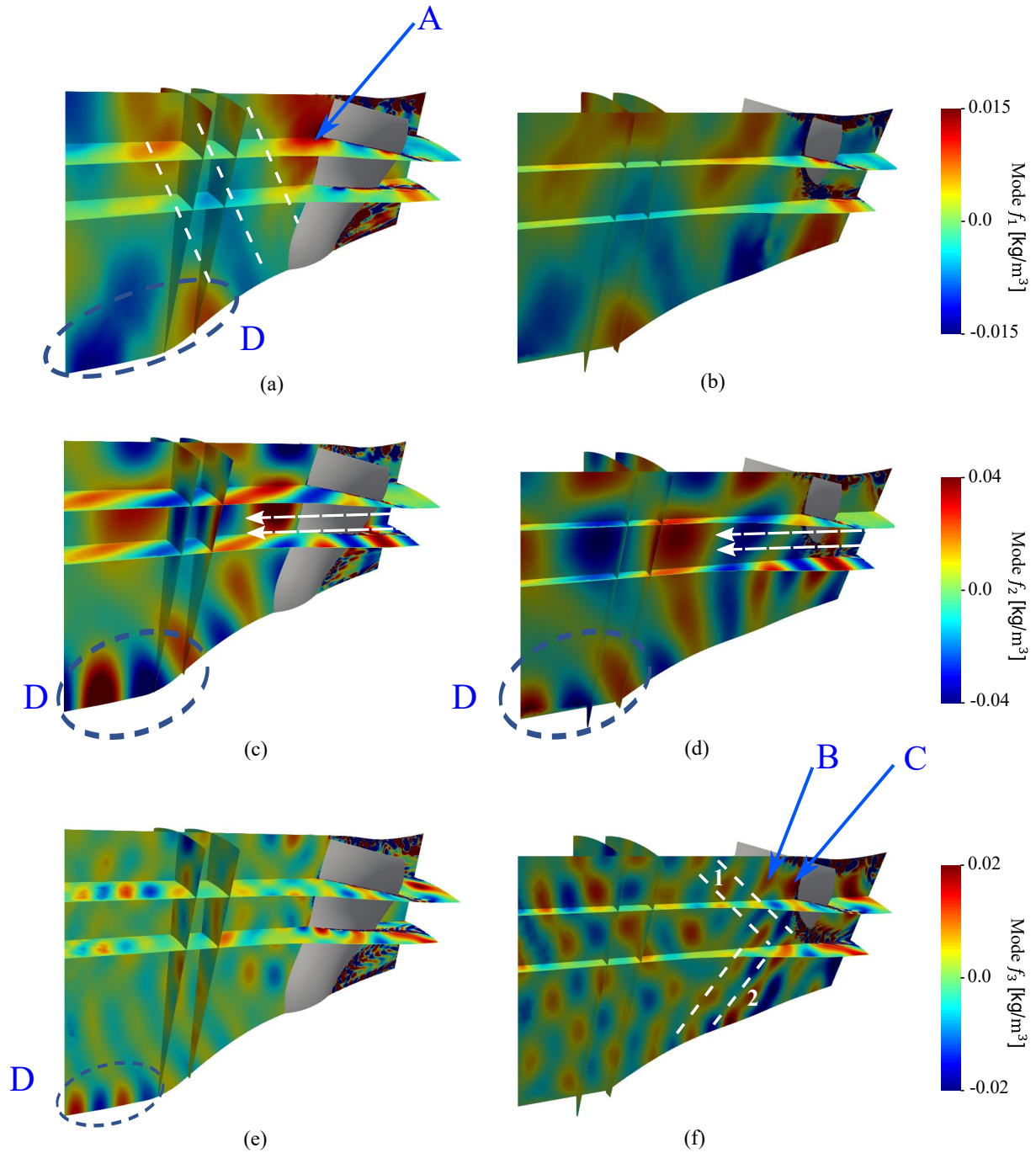
Figure 5.22: Spatial distribution of the density modes using the DMT technique. (a) & (b) Mode f_1. (c) & (d) Mode f_2. (e) & (f) Mode f_3.
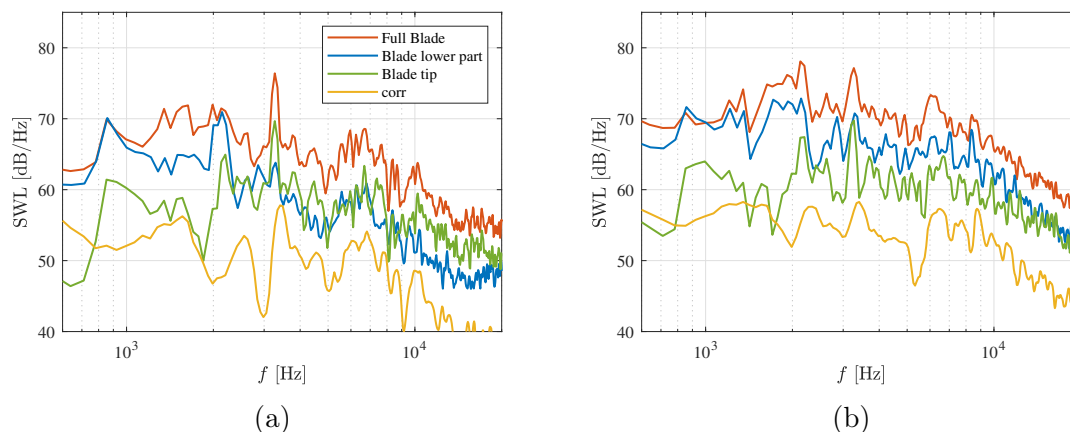
Figure 5.23: Sound power level spectra from the Ffowcs Williams and Hawkings (FWH) analogy for the full blade, the tip gap region, the low part of the blade and the cross-correlation part between them. (a) Upstream propagation direction. (b) Downstream propagation direction.

in Figures 5.3 and 5.4 and with the wall pressure and acoustic spectra in Figures 5.19 and 5.23, the first mode at f_1 can be related to the first tip leakage vortex formed at about 20% of the chord length, whereas one of the dominant modes at f_3 can be related to the tip vortices TLV2, IV and TSV, generated at about 70% of the chord length.

The amplitude of the different modes increases close to the hub in the region where the annular duct changes to a cylindrical duct (region "D" in Figure 5.22), which may be due to the mode matching between these two duct shapes.

Finally, it should be noted that the mesh size and the numerical setup are able to properly resolve the acoustic waves up to three chord lengths upstream of the rotor blades, even at high frequency.

5.4.4 Far field acoustic prediction

The far-field noise is predicted using the Ffowcs Williams and Hawkings (FWH) analogy, based on the unsteady pressure field, recorded on the solid surface of the fan blade. The sampling frequency is 80 kHz and the unsteady recording is made over four rotor revolutions. The advanced time approach of the formulation of Casalino [29] and Najafi-Yazd *et al.* [180] is adopted. Only the blade surface is used for the computation of the loading noise sources, since the noise sources are localized at the surfaces (Figure 5.15). This is justified by the low Mach numbers, especially in the tip gap region. The acoustic propagation is computed using the free-field Green's function with uniform flow. The far-field sound power level spectrum is obtained using Welch's method and Hann windows with 50% overlap.

In order to estimate the influence of the tip leakage flow on the far-field acoustic predictions, the blade is split into two parts. The upper 15% of the blade surface is considered to compute the tip flow contribution to the far-field noise. The size of this region is chosen to be large enough to contain all the contribution of the blade tip vortices (see Figure 5.11 for instance). The second part corresponds to the remaining part of the blade surface, where the influence of the tip flow is negligible. The full power spectral density of the far-field acoustic pressure from the full blade can be represented as the sum

of power spectral densities of the corresponding parts ($(S_{pp})_{\text{tip}}$ and $(S_{pp})_{\text{low}}$) and their cross-spectral density ($(S_{pp})_{\text{cross}}$) as follows,

$$(S_{pp})_{\text{blade}} = (S_{pp})_{\text{tip}} + (S_{pp})_{\text{low}} + 2(S_{pp})_{\text{cross}} \tag{5.3}$$

Figure 5.23 presents the sound power spectra at the intake and exhaust sections obtained from the different parts of the blade, the full blade (denoted "Full Blade"), the blade tip region (the upper 15% of the blade surface denoted "Blade tip"), the remaining part of the blade (denoted "Blade lower part") and the cross-correlation term (denoted "corr"). For both intake and exhaust sections, the cross-correlation spectrum is relatively small compared to the other contributions, particularly at mid to high frequencies.

At the intake section, the lower part of the blade dominates the spectrum below 2 kHz. The difference between the lower and the tip parts is about 10 dB in this frequency range. From 2 kHz to 10 kHz, comparable levels are observed between the tip and the lower parts, whereas larger SWL values for the blade tip spectrum are obtained at frequencies beyond 10 kHz. In this frequency range, the difference between the tip and the lower part is about 5 dB. Based on the coherence analysis made in Figure 5.21, the increase of the noise contribution of the tip region from 2 kHz to 10 kHz is associated to the noise source due to the interaction of the TLV1 generated at one blade with the trailing edge of the adjacent blade. Also, the increase in the SWL levels for frequencies beyond 10 kHz is related to the noise source due to the interaction of the tip vortices TLV2, IV and TSV with the trailing edge of the blade.

At the exhaust section, the contribution of the lower part dominates the noise spectrum over the frequency range from 0.6 kHz to 14 kHz. Up to 2 kHz, the difference of the noise levels between the lower and the tip parts is about 10 dB. This difference is reduced at higher frequencies, and reaches about 5 dB between 2 kHz and 10 kHz and about 2 dB from 10 kHz to 14 kHz. Similar levels between the two parts are obtained at frequencies beyond 14 kHz. As noted for the intake section, this behavior can also be explained by the two noise mechanisms at the tip region due to interactions between the tip vortices and the blade trailing edges.

Finally, it should be noted that even though (i) the pressure and velocity fluctuations exhibit larger levels in the tip gap region than in the lower part of the blade (Section 6.3) and that (ii) the instantaneous contours of the dilatation rate show a dominant noise source in the tip gap region (Figure 5.14), the tip gap noise mainly contributes to the upstream direction at high frequencies.

Tip leakage flow: aeroacoustic analysis ———————— Summary

- Instantaneous contours of the dilatation rate show a dominant noise source in the tip gap region. This noise source propagates in the upstream and downstream directions.

- The tip gap noise source is located at the trailing edge of the rotor due to two mechanisms:

    – The interaction of a part of the TLV1 generated at one blade with the

trailing edge of the adjacent blade.

– The interaction of the tip vortices TLV2, TSV and IV generated at one blade with the trailing edge of the same blade.

- Larger P_{rms} values are observed at the trailing edge over the suction side than over the pressure side, which suggests that the noise emissions due to the interaction of the tip vortices TLV2, TSV and IV with the trailing edge at the suction side may be more efficient than the interaction of the TLV1 with the trailing edge of the adjacent blade on the pressure side.

- The wall pressure spectra in the tip gap region exhibit two main humps; the first hump extends from 2 kHz to 9 kHz and the second one extends from 10 kHz to 25 kHz.

- The coherence between several monitor points in the tip gap region shows that the first hump can be associated to the interaction of the TLV1 with the trailing edge of the adjacent blade and the second hump to the interaction of the tip vortices TLV2, TSV and IV with the trailing edge.

- A dynamic mode tracking technique, performed around frequencies in the range of the first and the second humps, shows modes generated in the tip gap region and propagating in the upstream direction.

- The contribution of the tip gap noise to the far-field noise is seen mainly at high frequencies in the upstream direction.

5.5 Conclusion

In this chapter, a wall-modeled LES was performed over a scale model UHBR fan stage at approach conditions, with an emphasis on analyzing the tip leakage flow topology and the associated tip gap noise. In order to reduce the computational cost, a periodic sector with a single blade and two OGVs is considered. The mesh is designed to ensure that the acoustic waves can be propagated to all monitor points in the frequency range of interest.

A complex flow is observed in the tip gap region. The vortical structures are identified using iso-surfaces of the instantaneous and time averaged Q-criterion. Several tip vortices appear; (i) a horse-shoe vortex (HSV) is present close to the leading edge of the blade, (ii) a first tip leakage vortex (TLV1) is generated at about 20% to 30% of the chord length from the leading edge, (iii) a tip separation vortex (TSV) and a second tip leakage vortex (TLV2), alongside with an induced vortex (IV) are formed at approximately 70% of the chord length. This position corresponds to the region of large pressure difference between the blade sides, which is observed on the isentropic Mach number. The helicity, which is the normalized dot product of the vorticity and velocity vectors, shows that the induced

vortex rotates in the opposite direction of the other tip vortices. The complex tip flow topology can be explained by the blade profile at the tip, which was designed to operate at transsonic regime but is investigated here in subsonic conditions.

The tip vortices are characterized by reduced streamwise and pitchwise velocities and by a significant sign change in the radial velocity component. These vortices are also identified by large values of the streamwise and pitchwise vorticity components, which suggests that the tip vortical structures evolve in a helical way. The velocity fluctuations and the turbulent kinetic energy, as well as the loss in turbulent kinetic energy, which measures the viscous dissipation rate in the turbulent kinetic energy equation and the losses due to friction irreversibilities in the entropy equation, also exhibit large values in the tip gap region.

The trajectory of the tip vortices TLV2, IV and TSV is analyzed by means of the vorticity magnitude. Three main directions are observed; (i) the first direction between 60% to 70% of the chord length is parallel to the blade tip and corresponds to the evolution of the TSV, (ii) the second direction between 70% to 110% of the chord length forms an angle of about 30° with the blade tip chord and corresponds to the interaction of the TSV with the TLV2 and IV, and (iii) the third direction beyond 110%c is parallel to the blade's wakes and corresponds to the interaction of the tip vortices TLV2, TSV and IV with the first tip leakage vortex TLV1 and with the main flow. The vorticity magnitudes rapidly decay further downstream and in the radial direction.

Instantaneous contours of the dilatation rate and RMS pressure fluctuations are used to identify the location of the main noise sources. Since the Mach number in the present study is relatively low and due to the absence of shock waves, the main noise sources are located at the blade surface. A significant noise source is observed in the tip gap region at the trailing edge, which is associated with two mechanisms; (i) the interaction of a part of the TLV1 generated at one blade with the trailing edge of the adjacent blade and (ii) the interaction of the tip vortices TLV2, TSV and IV generated at one blade with the trailing edge of the same blade. The latter mechanism generates a more efficient noise source on the blade surface. The wall pressure spectra in the tip gap region exhibit two main humps; the first hump extends from 2 kHz to 9 kHz and the second one extends from 10 kHz to 25 kHz. Using a coherence study between several monitor points in the tip gap region, these humps are associated to the interaction mechanisms between the tip vortices and the blade surface. The first hump is related to the interaction of the TLV1 with the trailing edge of the adjacent blade and the second hump to the interaction of the tip vortices TLV2, TSV and IV with the trailing edge.

Additionally, a dynamic mode tracking (DMT) technique is performed to follow the spatial evolution of the dominant modes at three different frequencies. The DMT results at the first and third considered frequencies, which are in the frequency ranges of the first and second humps of the wall pressure spectra, respectively, show dominant modes generated from the blade tip region. The second frequency used for the DMT corresponds to the second harmonic of the vane passing frequency and shows a dominant mode generated downstream of the rotor blade, which can be related to the rotor-stator interaction noise and propagating in the upstream direction.

Finally, the acoustic far-field is computed using the Ffowcs Williams and Hawkings' analogy. To compare the contributions of the different noise sources to the far-field noise, the blade is split into two regions; the outer 15% of the blade, which corresponds to the blade tip, and the remaining part. This decomposition shows that the main contributions of the tip gap noise are visible in the frequency ranges of the humps in the wall pressure

spectra. It also shows that the tip gap noise becomes a significant noise source in the present configuration at high frequencies (beyond 2 kHz) and in the upstream direction.

Chapter 6

Aeroacoustic analysis of the ECL5 fan stage

Introduction

In this chapter, the aeroacoustic results of the (full-span) sector LES and the (full-span) 360° LES configurations are presented. Wall-modeled large eddy simulations (LES) of the fan/OGV stage are performed at approach conditions on an unstructured grid that is refined for direct noise propagation.

To justify the use of the wall-model assumption for the full-span configurations, comparisons between wall-resolved (WR) and wall-modeled (WM) computations are performed on the radial-slice sector LES configuration.

On the (full-span) sector configuration, a good agreement is found between LES and RANS aerodynamic results. However, some differences can be found in the blade tip region and near the hub, where large coherent structures appear. Additionally, a small recirculation bubble can be observed from approximately 60% of the fan blade span in the LES.

In this chapter, the broadband noise from the (full-span) sector LES configuration is directly computed from the fully-compressible LES solver and compared with predictions from available analytical models [276]. The input data for the analytical models, such as mean and turbulent flow statistics, are obtained from the LES computation. A good agreement is found for the predicted sound power levels between direct LES noise predictions and the LES-informed analytical models. However, some discrepancies can be observed at low and high frequencies. These might be attributed to the additional noise sources that are present in the LES, which are not considered by the analytical models. To characterize the origins of these differences, the contribution of different noise mechanisms, particularly noise sources associated with the fan blades, is investigated. The blade surface is split into two parts and the Ffowcs Williams and Hawkings (FWH) acoustic analogy, based on the pressure fluctuations on the solid surfaces of each part, is used.

The impact of the periodic boundary conditions is finally assessed by comparing results from the (full-span) sector and 360° LES configurations. The acoustic azimuthal decomposition, which can only be estimated using the (full-span) 360° LES configuration is presented. The evolution of the coherence function in the azimuthal direction is also studied, particularly between points located in separate blade channels.

The chapter is organized as follows. Section 6.1 presents a literature review of previous studies on the rotor-stator interaction noise and trailing edge noise mechanisms in a fan stage. Section 6.2 presents the assessment of the wall-model (WM) assumption for the prediction of the aerodynamic results. The flow topology and the aerodynamic results are presented in Section 6.3. Noise predictions from the two methodologies, i.e. the direct LES noise computation and the LES-informed analytical models, are discussed in Section 6.4. Finally, the impact of the periodic boundary conditions on the flow parameters and noise emission, assessed by performing a (full-span) 360° LES, are presented in Section 6.5.

6.1 State of the art

Several mechanisms can produce broadband noise, such as the interaction of the inlet turbulence with the rotor blades, vortex noise in the tip region of the rotor, self noise and rotor-stator interaction noise. The tip vortex noise is studied in details in Chapter 5. If a laminar recirculation bubble appears on the fan blades, it can be considered as a source of self noise and is addressed in Chapter 4. Another self noise mechanism is the trailing edge noise, which is generated by the turbulence in boundary layers diffracted by trailing edges of the blades and vanes. Rotor-stator interaction noise results from the interaction of turbulence in the rotor wakes with the leading edges of the stator, which generates an unsteady loading on the vanes. The rotor-stator interaction noise mechanism is often considered to be the dominant noise source of the fan stage at approach condition [193, 144]. The two main noise mechanisms studied in this chapter are the rotor-stator interaction (RSI) noise and the trailing edge (TE) noise.

Over the past few decades, several techniques have been developed to model and predict both trailing edge and rotor-stator interaction noise [176, 175]. Recent progress in computing resources has allowed for a detailed description of the turbulent flow in turbomachinery applications using high-fidelity simulations, such as large eddy simulation (LES) and direct numerical simulation (DNS). These numerical simulations can describe the turbulent structures in the flow that produce broadband noise. The DNS is still limited to applications at low Reynolds numbers and to academic configurations due to its expensive computational cost. LES is preferred for the current study to model complex flows in a fan stage, with sufficient accuracy, at an acceptable computational cost. Using LES, several methodologies can be used to predict the noise sources and acoustic emissions in the fan stage. The present study focuses on three different methodologies, (i) LES-informed analytical models, (ii) LES coupled with an acoustic analogy and (iii) LES direct noise computations.

Several analytical models are available for the prediction of fan broadband noise [176, 144]. Initial analytical models considered either the turbulent flow impinging on the leading edge of an isolated airfoil or the diffraction of a turbulent boundary layer at the airfoil TE [8, 7, 223]. The use of such models to predict fan broadband noise requires the assumption that the contributions of each blade and vane are incoherent and can thus

simply be summed up. This may be appropriate for low solidity rotors and stators, such as in open-rotor engines. However, cascade effects due to the high solidity of blades and vanes in ducted fan stages may have to be accounted for.

The rotor-stator interaction noise models used in this study, which account for the cascade effects, were developed by Hanson [93] and Posson *et al.* [209, 207]. These models are based on the previous work of Glegg [70] and have been developed to predict the rotor-stator interaction noise from cascade configurations and non-uniform flows in the spanwise direction through the use of the strip theory. In Hanson's model, the acoustic waves from each strip of the vanes are propagated into the free-field by assuming a uniform mean flow. In Posson's model, the unsteady loading from the vanes is used as a dipole source term in an in-duct acoustic analogy [213, 207, 153]. Thus, duct wall effects are accounted for when using Posson's model, whereas these are neglected in Hanson's model.

The trailing edge noise model adopted in this study is based on Amiet's work, which describes the scattering of pressure fluctuations from a turbulent boundary layer at the trailing edge [9, 223]. An in-duct acoustic analogy is used for the noise propagation.

For comparison purposes, LES mean and turbulent flow parameters from the rotor wakes and the boundary layers are used as inputs for these analytical models in the present study.

Noise predictions from analytical models are compared to direct noise computations from LES. The latter do not rely on assumptions that are made in analytical models, such as flat plate airfoils, uniform mean flows and isotropic turbulence. The direct noise computation from the LES requires a specific mesh refinement and numerical setup, which increases the computational cost when compared to analytical models or hybrid methods using an acoustic analogy for the noise propagation. However, an increased accuracy in noise predictions can be expected from direct noise predictions.

The third approach used in this Chapter is usually referred to as a hybrid approach. It couples an unsteady flow simulation, an LES in the present study, with an acoustic analogy, such as the Ffowcs Williams and Hawkings (FWH) [276] analogy, to predict the acoustic far-field. The unsteady loading on the surfaces of the blades and vanes is obtained from the unsteady flow simulation and is used in the acoustic analogy. The noise is propagated using a Green's function, which is only known for canonical cases, such as free-field, uniform flow and annular cylindrical ducts. This can induce some uncertainties in the noise propagation. Such a hybrid approach has been successfully applied for the prediction of fan noise operating at low Mach numbers in previous studies [213, 146, 167]. The Ffowcs Williams and Hawkings (FWH) [276] analogy based on the pressure fluctuations on the surfaces of the blades and vanes, and using the free-field Green's function for a uniform flow, is adopted in the present Chapter. This approach is used to separate the contributions of different noise mechanisms by splitting the blade surface into different parts and analyzing the contributions of each part to the total noise.

6.2 Numerical assessment of the WM-LES

WR- and WM-LES are performed on the radial-slice sector LES configuration to assess the validity of the WM assumption for the prediction of the aerodynamic results. The properties of the two meshes used for this study are given in Table 6.1 (RaSlice-WM and RaSlice-WR).

In Chapter 4, WR- and WM-LES are compared at a mass flow rate of 20 kg/s, and several discrepancies are particularly observed close to the leading edge of the rotor blade,

Table 6.1: Mesh properties for different LES grids. x^+, y^+ and z^+ are the maximum dimensionless cell-distances in the streamwise, normal and spanwise directions respectively. "RaSlice" corresponds to the radial slice cases, and "FullSpan" to the full-span case.

	RaSlice-WM	RaSlice-WR	FullSpan-WM
Number of cells $[10^6]$	40	80	95
x^+/z^+	250	35	150
y^+	30	1.0	25
Number of prism layers	10	16	10
expansion ratio	1.1	1.06	1.1
Time step $[10^{-8}\text{s}]$	2.8	0.8	2.8
CPUh/blade passage $[10^3]$	50	280	105

(a)   (b)
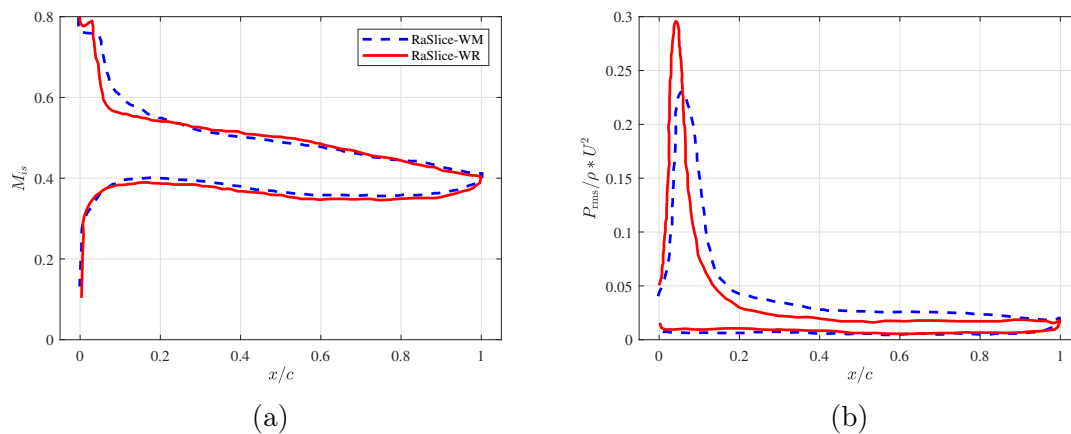
Figure 6.1: Chordwise distribution of (a) isentropic Mach number M_{is} and (b) RMS pressure fluctuations P_{rms}, along the rotor blade at mid-span.

in the recirculation bubble region. In the present chapter, a larger mass flow rate is adopted in order to minimize the influence of the recirculation bubble on the noise emission and to study in details the other noise sources (RSI and TE noise sources). The operating point is at approach condition (55%Nn) and corresponds to a mass flow rate of 21.8 kg/s.

Figure 6.1 shows numerical results from WM and WR cases for the isentropic Mach number, M_{is}, and the root-mean-square of the pressure fluctuations, P_{rms}, along the rotor blade surface. The distributions of M_{is} and P_{rms} on the pressure side, where the boundary layer remains laminar, are very similar for both WR- and WM-LES. On the suction side, a flow separation zone can be identified by a flat region of isentropic Mach number near the leading edge. It should be noted that high levels of pressure fluctuations are also observed in that region. Some discrepancies between WM and WR results can be found for both M_{is} and P_{rms} in this region. A slightly longer bubble, identified by a larger flat region of M_{is} close to the leading edge, with lower peak of P_{rms}, is predicted by the WM case in comparison with the WR case. These differences remain small and localized in the P_{rms} peak region. Moreover, it can be noted that for the full-span configurations at the considered operating point, a separation of the flow is only observed over a limited spanwise extent (between 60% and 85% of the rotor span), and not along the whole span. Overall, this justifies the use of the WM assumption, for the full-span LES configurations.

Table 6.2: Mass flow rates and total pressure ratios, obtained from the different simulations at approach condition.

	$\dot{m}$ [kg/s]	Π
(full-span) sector RANS	21.86	1.091
(full-span) sector LES	21.82	1.099
(full-span) 360° LES	21.80	1.101

6.3 Aerodynamic results

In this section, the aerodynamic results for the (full-span) sector LES are presented. Some comparisons with RANS results are also shown.

6.3.1 Global performance parameters

Table C.1 presents the global performance parameters (mass flow rate $\dot{m}$ and total pressure ratio Π) at approach condition, obtained from the RANS and the different LES. the rotor span. Similar values are obtained for the different cases, which allows the comparison of the results. It should be recalled that the (full-span) 360° LES configuration corresponds to the original configuration composed of 16 rotor blades and 31 stator vanes, whereas the (full-span) sector RANS and LES configurations correspond to the modified configuration composed of 16 rotor blades and 32 stator vanes. The good agreement of $\dot{m}$ and Π between the (full-span) sector and 360° LES shows the validity of the method used to modify the vanes count, as described in Chapter 2.

6.3.2 Instantaneous results

The two broadband noise mechanisms that are studied in this chapter, i.e. the rotor-stator interaction noise and the trailing edge noise, are directly related to the turbulent flows in the fan/OGV inter-stage, and close to the fan and OGV surfaces. Figure 6.2 shows an isosurface of the instantaneous Q-criterion ($Qc^2/U^2 = 10$). The iso-surface is colored by the vorticity magnitude. This provides a qualitative description of the turbulent structures developing in the boundary layers and the wakes. Boundary layer transition can be observed near the leading edges of the blade and vanes along the whole span. Small turbulent structures can be seen downstream of the transition regions. Such structures are diffracted at the trailing edges of the blades and vanes and generate trailing edge noise. The turbulent structures in the rotor wakes impinge on the leading edges of the stator, which generates rotor-stator interaction noise. On the rotor blade surface, a small recirculation bubble can be found at approximately 60% of the span, which is characterized by a high vorticity magnitude and leads to the boundary-layer transition in this region. It is observed in Chapter 4 that such a recirculation bubble is generated due to a relatively high angle of attack upstream of the rotor blade. Finally, a small corner-separation and a tip-leakage vortex can be observed where large turbulent structures are found.
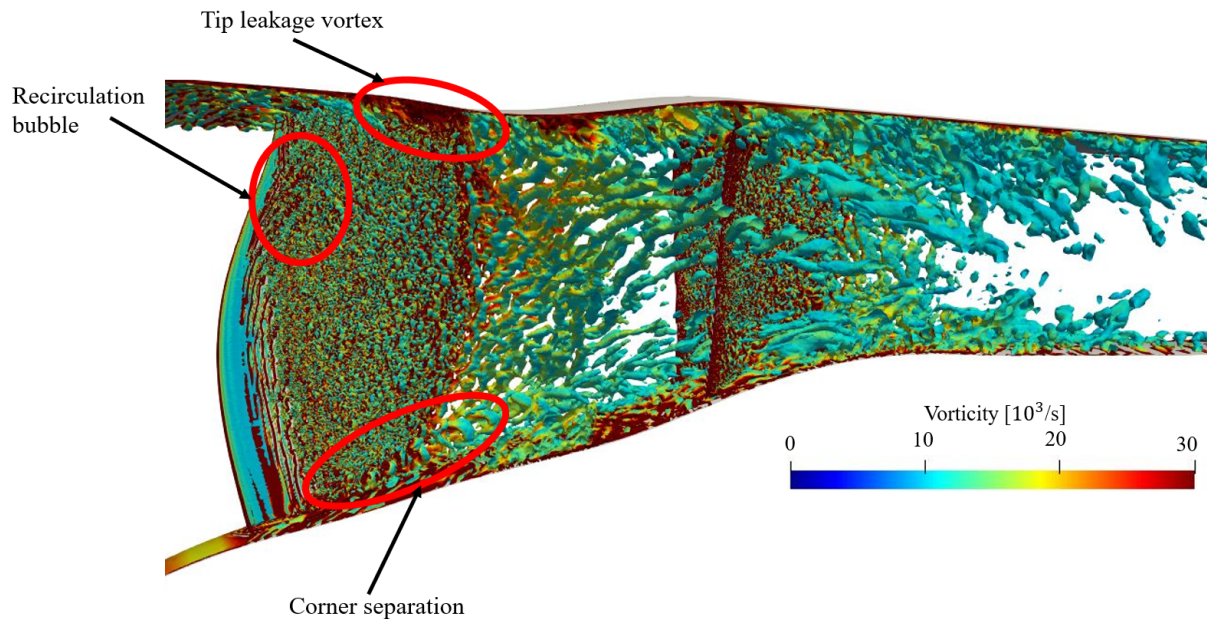
Figure 6.2: Iso-surface of Q-criterion ($Qc^2/U^2 = 10$), colored by the vorticity magnitude, for the full-span sector LES.

6.3.3 Mean quantities

Figure 6.3 presents contours of the averaged streamwise velocity component, u, and the turbulent kinetic energy, k_t, at different spanwise positions. In the rotor domain, the averaging is performed in the rotating reference frame, whereas it is performed in the fixed reference frame in the stator domain. This explains the discontinuity observed at the interface between both domains. For the different spanwise positions, the region of high streamwise velocity component on the suction side of the fan can be associated with the blade loading. Moving from hub to tip, this region is shifted towards the trailing edge and its extent decreases. This is mainly due to the geometry of the fan blade profiles near the tip, which are designed to operate in a transsonic regime at large radii for the nominal fan speed (100%Nn). Indeed, the camber is reduced from hub to tip, and the maximum camber position is shifted over the suction side of the blade towards the trailing edge. At nominal speed, the flow is transsonic near the fan tip, and the pressure difference between the pressure and the suction sides is dominated by shock waves. In the present LES, at 55Nn, the flow remains subsonic and the blade loading depends on the angle of attack and the camber.

The transition of the boundary layers to turbulence can be seen from the contours of k_t. For all the spanwise positions, the boundary layer remains laminar over the pressure side of the blade. At 80% of the blade span, a small recirculation bubble can be observed close to the leading edge on the suction side of the rotor blade. This corresponds to a small region of negative streamwise velocity in Figure 6.3 (c) and to the high vorticity magnitudes in Figure 6.2. The recirculation bubble leads to an earlier transition of the boundary layer to turbulence, compared to the transition at 30% and 50% of the blade span. Additionally, the rotor and stator wake widths seem to remain nearly constant along the span, despite the presence of a small separation region and the increase of the relative speed in the upper half of the span. This may be explained by the decrease of the blade thickness as the radial position increases, which aims at reducing the blade

200
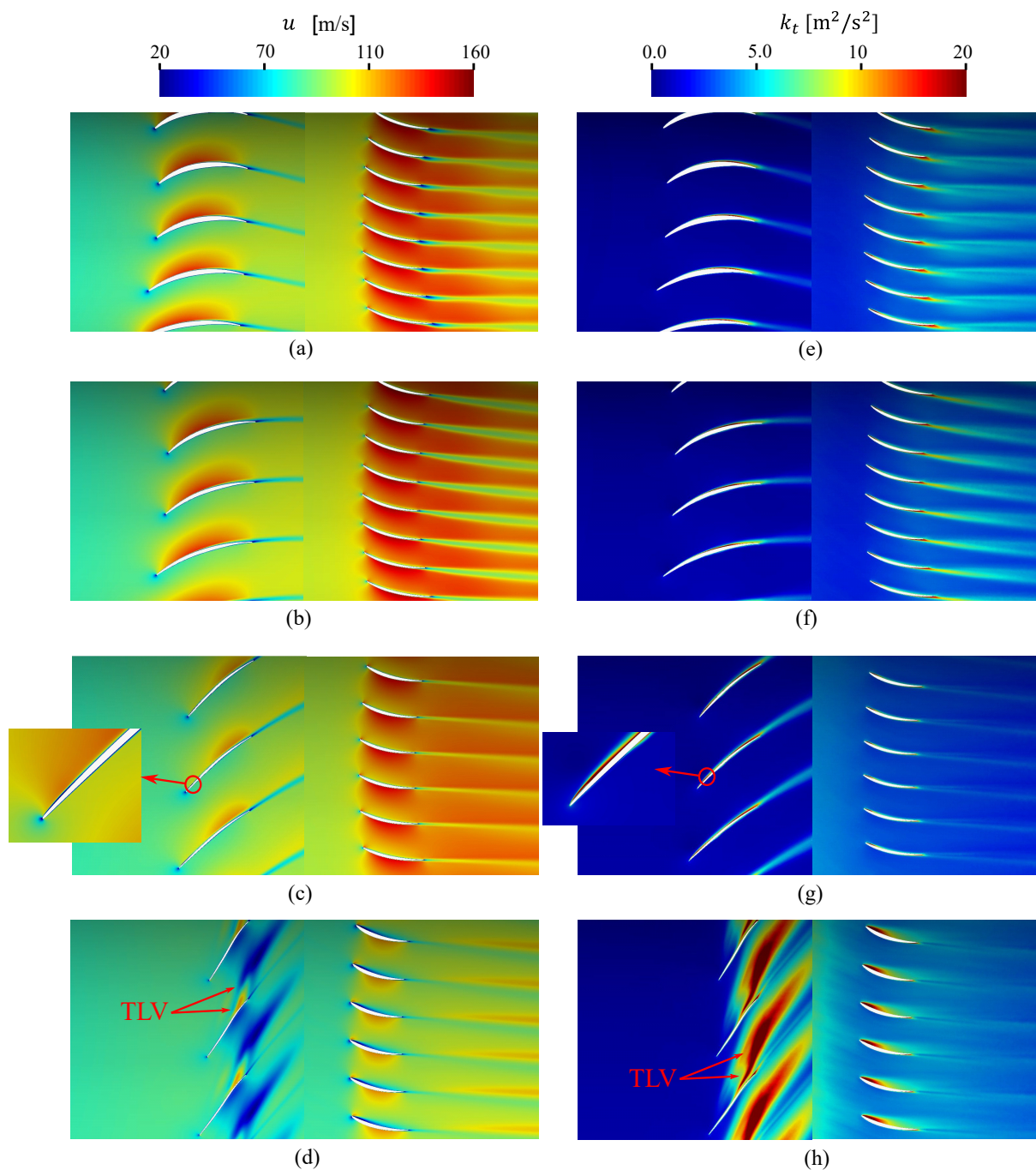
Figure 6.3: Contours of the averaged streamwise velocity (left) and the turbulent kinetic energy (right) from WM-LES, for various spanwise positions: (a,e) 30%, (b,f) 50%, (c,g) 80% and (d,h) 99%.
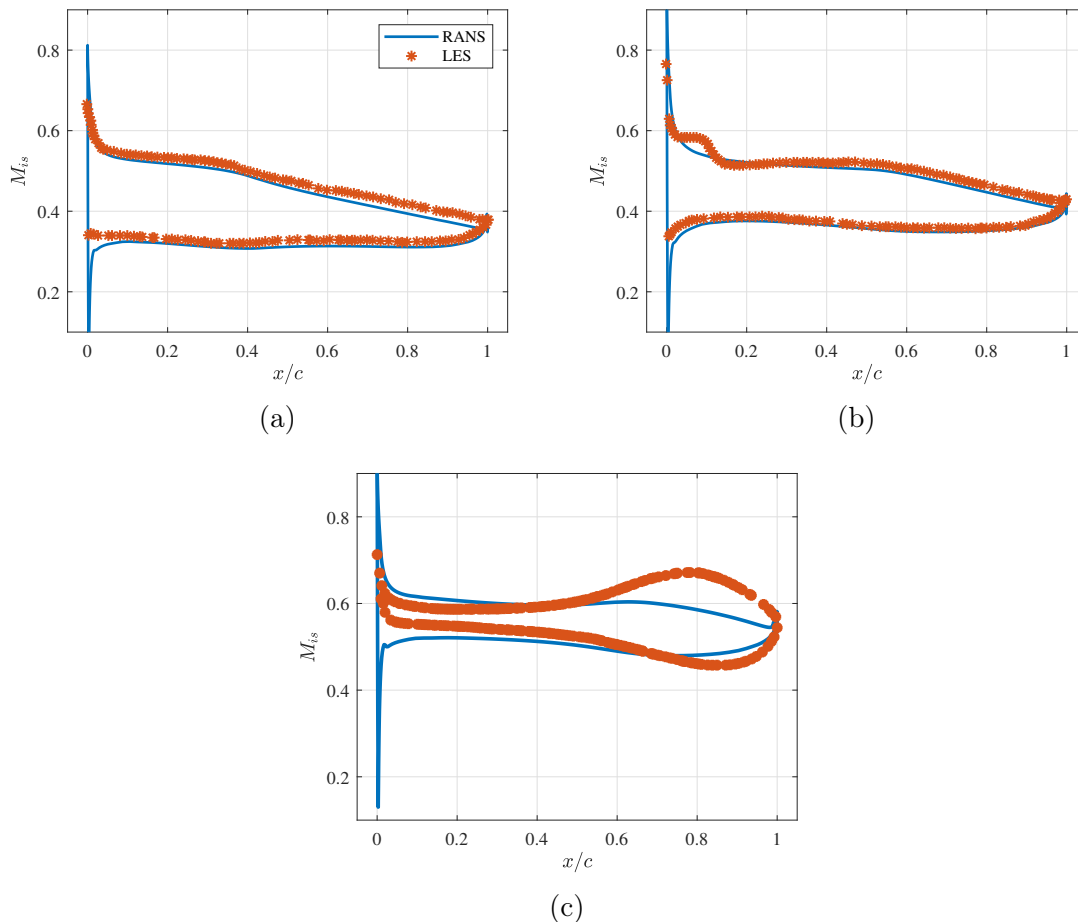
Figure 6.4: Comparison between the RANS and LES predictions of the average isentropic Mach number around the fan blade at (a) 50%, (b) 80% and (c) 95% of the rotor span.

deformation due to centrifugal forces at nominal speed and limit the flow acceleration at the tip.

At 99% of the span (Figures 6.3 (d) and 6.3 (h)), the flow topology can be observed in the blade tip region. The tip flow topology is extensively studied in Chapter 5. A complex flow can be seen in this region, which is produced by the formation of a tip-leakage vortex (TLV). The TLV can be identified by the low streamwise velocity and is characterized by large levels of turbulent kinetic energy. Unlike previous studies on the tip leakage flow in a fan stage at approach condition [121, 140], the TLV appears relatively close to the trailing edge. This may be related to the blade tip geometry and the tip clearance, which is larger than 1% of the chord length and increases towards the trailing edge. Furthermore, the blade profile at the tip presents a significant change in the slope between the leading edge and the maximum camber position, the profile is relatively flat and thin, and the position of the maximum camber is located at 70% of the chord length.

Figure 6.4 shows a comparison of the distributions of isentropic Mach number, M_{is}, from LES and RANS, over the rotor blade surface, for various spanwise positions. Similar results are obtained between LES and RANS at the radial positions of 50% and 80% of the rotor span, except in the region close to the leading edge on the suction side at 80% of the rotor span. In this region, a plateau can be seen for the LES, which shows the apparition of a small recirculation bubble, as discussed in Figures 6.2 and 6.3. When comparing these two spanwise positions, a small hump is observed between $x/c = 0.4$ and
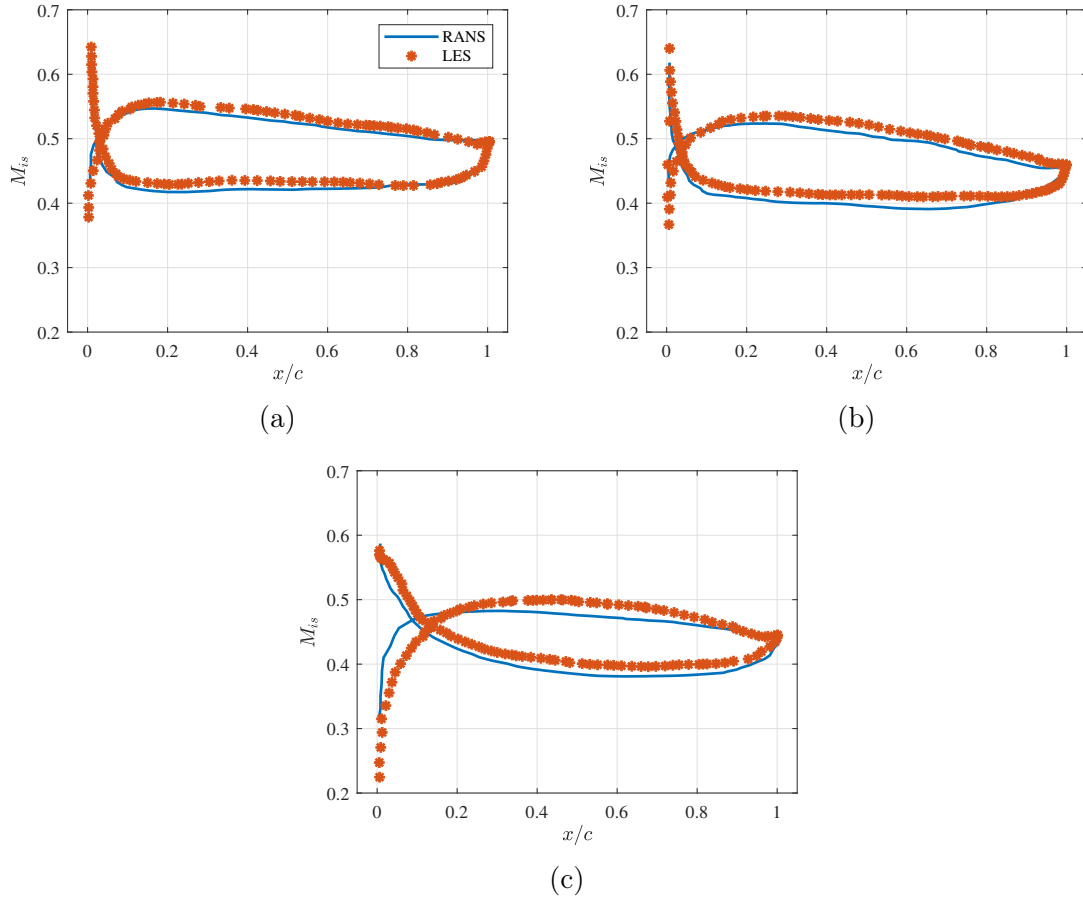
Figure 6.5: Comparison between the RANS and LES predictions of the average isentropic Mach number around the OGV, at (a) 50%, (b) 80% and (c) 95% of the stator span.

$x/c = 0.6$ on the suction side of the blade at 80% of the span, which confirms that as the radius increases the blade loading is shifted towards the trailing edge (see Figure 6.3).

Significant differences can be observed at 95% of the rotor span between RANS and LES, particularly on the blade suction side. This spanwise position is much closer to the tip gap region and is affected by the tip leakage flow, as pointed out in Chapter 5. The RANS computation predicts a slightly larger pressure difference between the leading edge and 40% of the chord length, than the LES. An important increase of the pressure difference between the two sides of the blade is only observed for the LES between 60% of the chord length and the trailing edge.

The distribution of M_{is} obtained by the LES can be associated to the blade shape at the tip, that was designed to operate at transsonic regimes and presents a significant camber evolution. As previously mentioned, between the leading edge and the maximum camber position, the blade profile is relatively flat and thin, and the position of the maximum camber is located at 70% of the chord length, which is unusual for subsonic profiles.

As shown in Chapter 5, a complex flow topology in the blade tip region is observed, where different tip vortices appear. The RANS computation does not properly capture this complex behavior of the flow, which may explain the differences between RANS and LES at this spanwise position.

The distributions of the isentropic Mach number around the stator vane at different

(a)

(b)

(c)
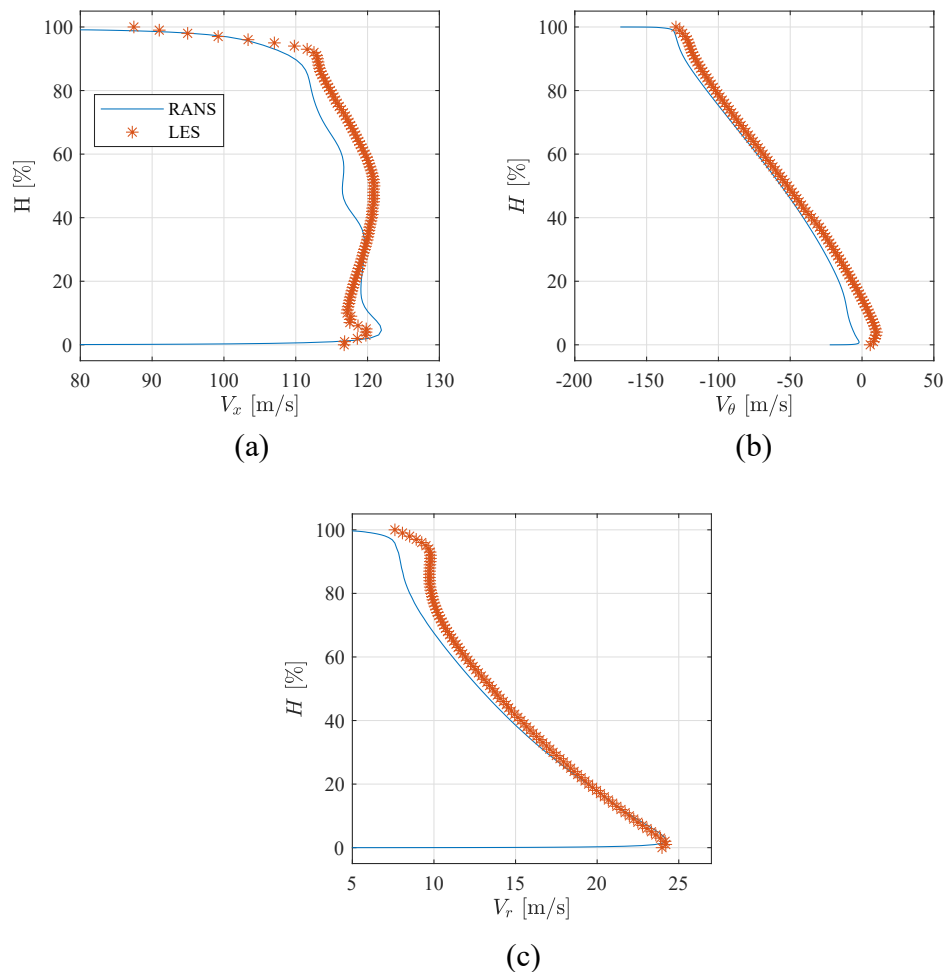
Figure 6.6: Comparison between the RANS and LES predictions of the radial profiles of the velocity components in the rotor wake.

spanwise positions are compared between RANS and LES in Figure 6.5. For both cases, the distributions of M_{is} from the suction and pressure sides intersect close to the leading edge. This suggests that the incidence angle of the stator is negative, which may be a result of the operating conditions (55%Nn) of the present simulation. Similar results are obtained between RANS and LES at 50% and 80% of the stator span, whereas some discrepancies can be found at 95%. This may be due to differences in the tip-leakage flow topology and casing boundary layers between RANS and LES.

The radial distributions of the mean flow velocity components in the rotor wake, V_x, V_θ and V_r, from LES and RANS simulations, are presented in Figure 6.6. These velocity profiles are obtained from the circumferential average of the mean velocity field at $0.5c$ downstream of the rotor trailing edge. A good agreement can be observed between the LES and RANS results for the three velocity components. In both LES and RANS approaches, a sudden increase in V_x can be seen close to the hub, below 10% of the span, which may correspond to the corner separation in Figure 6.2. When compared to the LES results, V_x is slightly overpredicted by RANS below 20% of the rotor span, whereas it is underpredicted above 40% of the span. The blade tip region is characterized by a deficit of V_x near the shroud. The radial extent of this region is larger with RANS, which may be explained by the limitations of RANS turbulence modeling in this highly vortical flow

204
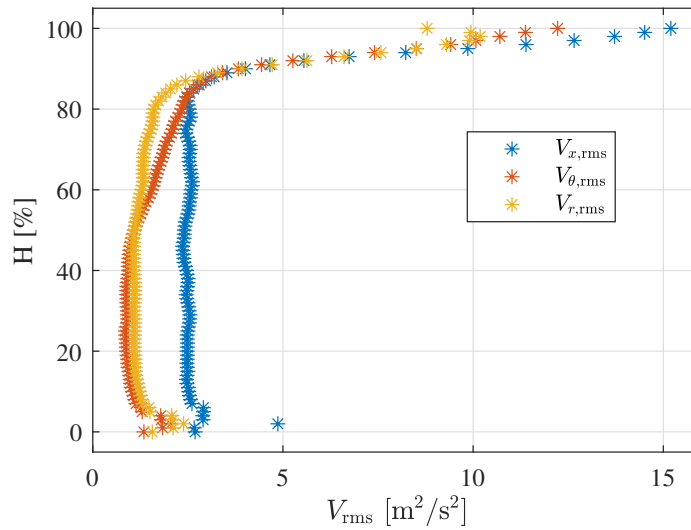
Figure 6.7: Radial profiles of the RMS velocity fluctuations, downstream of the rotor, obtained from the LES.

region. Some differences can also be observed for V_r above 50% of the span, which may be caused by the presence of the recirculation bubble in the LES in this region and the misprediction of the TLV region by RANS.

The radial distributions of the RMS velocity fluctuations in the rotor wake, $V_{x,\mathrm{rms}}$, $V_{\theta,\mathrm{rms}}$ and $V_{r,\mathrm{rms}}$, from the LES, are presented in Figure 6.7. These RMS profiles are obtained from the circumferential average of the RMS velocity fluctuations field at $0.5c$ downstream of the rotor trailing edge. Up to 85% of the rotor span, comparable levels of the azimuthal and radial components of the velocity fluctuations are observed, whereas larger values are obtained for the axial component. For the three components, the effects of the corner separation and the tip flow vortices are identified by an increase of velocity fluctuations close to hub and shroud, respectively. In the recirculation bubble region, between 60% and 85% of the rotor span, the tangential component exhibits larger values.

The azimuthal profiles of the time-averaged velocity components, their RMS values, and the turbulent kinetic energy, are plotted at $0.5c$ downstream of the rotor trailing edge, for different spanwise positions in Figures 6.8 to 6.13. The profiles of the velocity components and the turbulent kinetic energy obtained from the LES are compared to RANS results.

At 30% of the rotor span (Figure 6.8), a good agreement is observed between RANS and LES results. For the RANS results, a slightly larger wake width with a smaller velocity deficit can be observed, compared to the LES results. Similar turbulent kinetic energy profiles are also obtained at this spanwise position (Figure 6.9 (b)). Regarding the RMS velocity fluctuations, the axial component, $V_{x,\mathrm{rms}}$, exhibits larger levels than the radial and tangential components, $V_{r,\mathrm{rms}}$ and $V_{\theta,\mathrm{rms}}$, in both the wake and the background turbulence region (Figure 6.9 (a)).

As the radius increases, larger discrepancies are observed between RANS and LES results. At 50% of the rotor span (Figure 6.10), the RANS predicts a larger wake width and velocity deficit. The turbulent kinetic energy (Figure 6.11 (b)) exhibits larger values in the LES compared to the RANS in the wake region and smaller values in the background turbulence region. This may be explained by the turbulence injection at the inlet used only
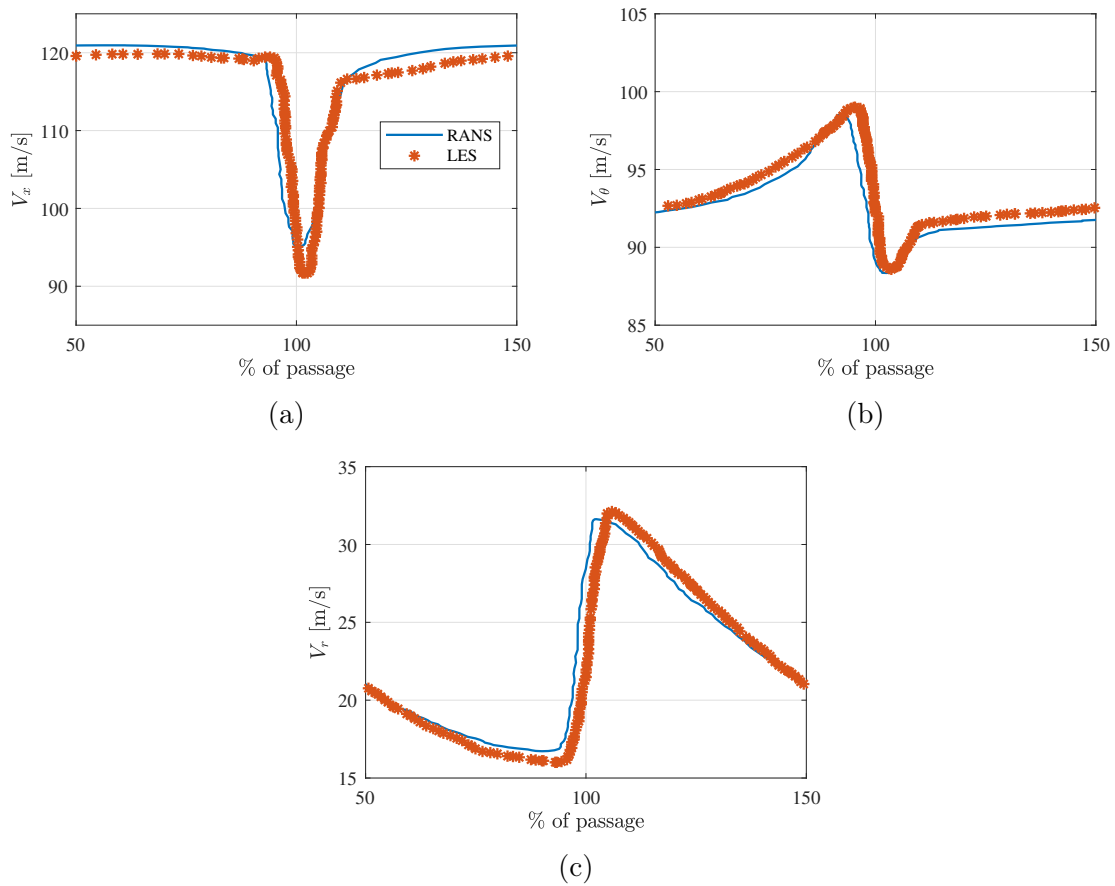
Figure 6.8: Comparison between the RANS and LES predictions of the azimuthal profiles of the averaged velocity components, at 30% of the rotor span. (a) Axial velocity. (b) Tangential velocity. (c) Radial velocity.
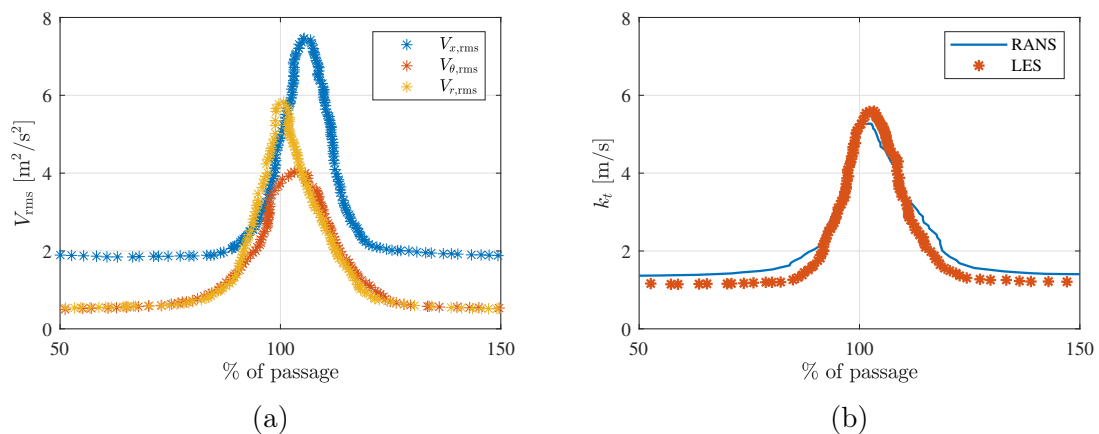
Figure 6.9: Azimuthal profiles of the (a) RMS velocity fluctuations obtained from the LES and (b) the turbulent kinetic energy, obtained from the LES and RANS, downstream of the rotor, at 30% of the rotor span.
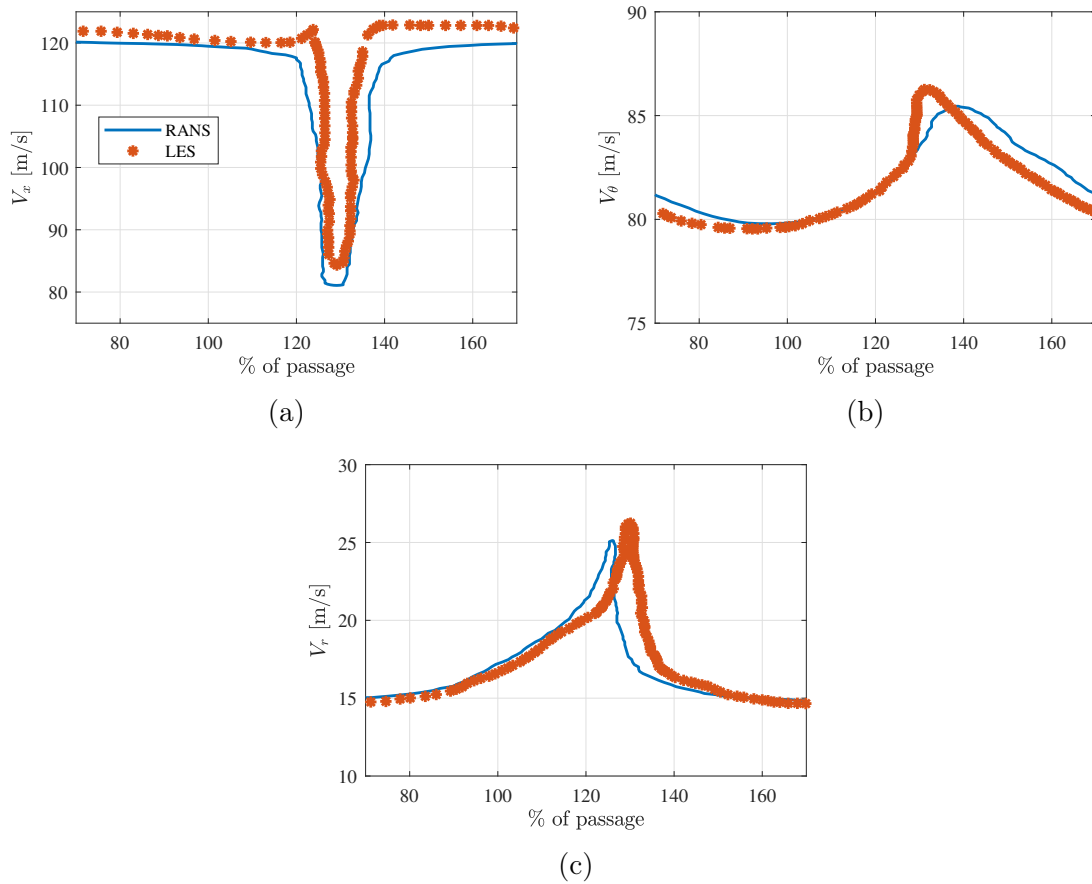
Figure 6.10: Comparison between the RANS and LES predictions of the azimuthal profiles of the averaged velocity components, at 50% of the rotor span. (a) Axial velocity. (b) Tangential velocity. (c) Radial velocity.
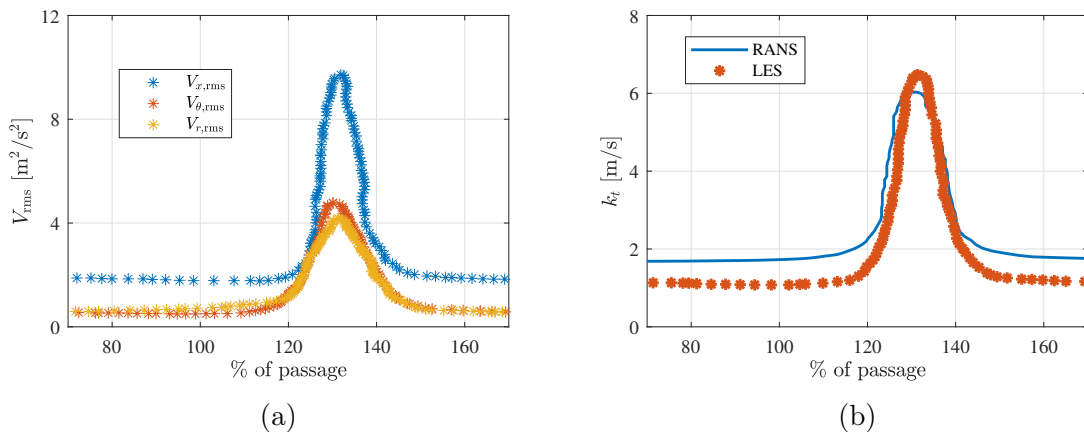
Figure 6.11: Azimuthal profiles of the (a) RMS velocity fluctuations obtained from the LES and (b) the turbulent kinetic energy, obtained from the LES and RANS, downstream of the rotor, at 50% of the rotor span.
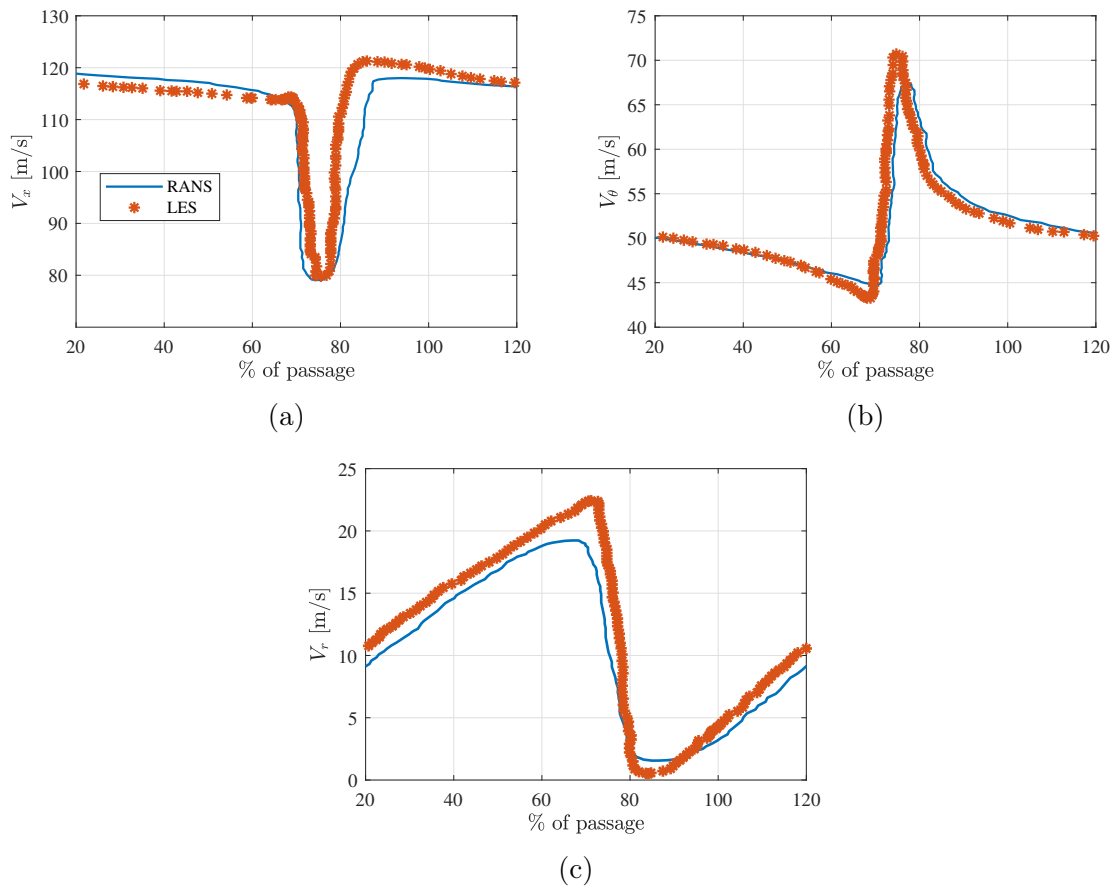
Figure 6.12: Comparison between the RANS and LES predictions of the azimuthal profiles of the averaged velocity components, at 80% of the rotor span. (a) Axial velocity. (b) Tangential velocity. (c) Radial velocity.
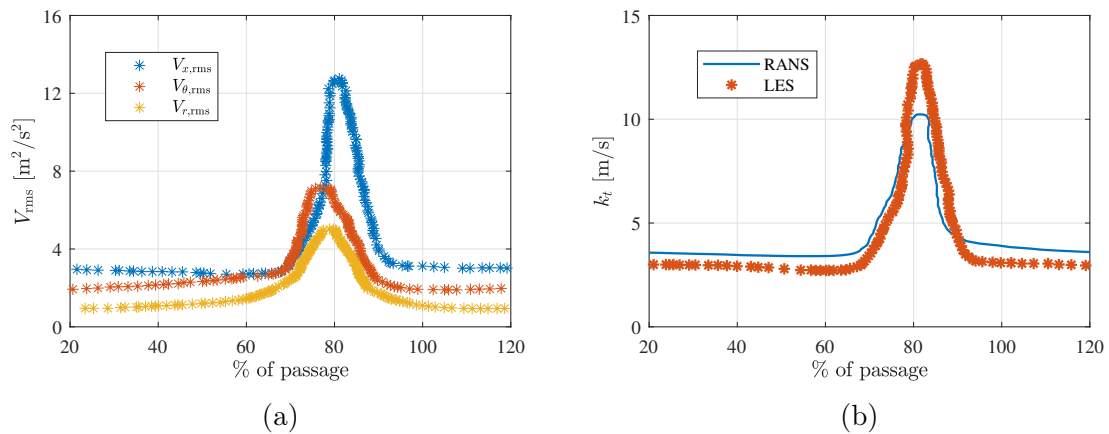
Figure 6.13: Azimuthal profiles of the (a) RMS velocity fluctuations obtained from the LES and (b) the turbulent kinetic energy, obtained from the LES and RANS, downstream of the rotor, at 80% of the rotor span.

for the RANS simulation. No turbulence is injected in the LES cases, due to the limited turbulence intensity expected in the experimental campaign (less than 1%). Similar levels of the tangential and radial RMS velocity fluctuations are observed in both the wake and background turbulence regions, whereas the axial RMS velocity component is still larger at this radial position.

At 80% of the rotor span (Figure 6.12), both RANS and LES predict a similar velocity deficit, but the wake width is larger in the RANS. At this spanwise position, the LES predicts larger values of the turbulent kinetic energy in the wake region (Figure 6.13 (b)), which may be explained by the apparition of a recirculation bubble close to the leading edge of the blade only in the LES. At this spanwise position, the RMS fluctuations of the tangential velocity component are larger than those of the radial component.

When comparing the different spanwise positions, the wake width seems to be relatively unchanged in the LES, which is consistent with the observations in Figure 6.3. At 80% of the rotor span, the levels of the turbulent kinetic energy are significantly larger than the levels at 30% and 50% in the LES, which may be due to the presence of a recirculation bubble at this spanwise position. The recirculation bubble seems to mainly generate axial and tangential RMS velocity fluctuations.

Aerodynamic analysis ———————————————————————— **Summary**

Turbulent structures.

- A good transition of the boundary layers is observed close to the leading edges of the rotor blade and stator vanes all along the whole span. Downstream of the transition, the fine turbulent structures are diffracted at the trailing edges, which will generate trailing edge noise.

- The turbulent structures in the rotor wakes impinge on the leading edges of the stator vanes, which will be responsible for rotor-stator interaction noise.

- Several secondary flows appear on the rotor blade: a recirculation bubble studied in details in Chapter 4, a tip-leakage vortex, extensively studied in Chapter 5, and a corner separation at the hub.

Mean quantities.

- When moving from hub to shroud, the blade loading is shifted towards the trailing edge of the fan blades. This is mainly due to the geometry of the blade profiles, designed to operate at transsonic regime, which is unusual for subsonic flow conditions.

- The boundary layer remains laminar on the pressure side of the blade.

- At 60% of the rotor span, a recirculation bubble appears close to the leading edge of the rotor blade.

- At 99% of the rotor span, the tip-leakage vortex can be identified by a region of low streamwise velocity, and is characterized by large levels of turbulent kinetic energy.

Pressure distribution.

- Overall, similar distributions of the isentropic Mach number are obtained from the LES and RANS computations for different spanwise positions on the blade and vane surfaces.

- On the rotor blade, some discrepancies are found close to the leading edge of the rotor in the recirculation bubble region, because RANS does not predict the apparition of this bubble.

- At 99% of the rotor span, significant differences are found between the RANS and LES results. For the LES, the isentropic Mach distribution shows a small pressure difference between the two sides of the blade close to the leading edge and a much larger one between 60% and 90% of the chord length.

- On the stator vanes, the isentropic Mach distributions show that the incidence angle of the stator is negative.

Radial profiles in the interstage region.

- Overall good agreement of the velocity profiles in the interstage region is obtained between LES and RANS.

- Differences are mainly observed in the corner separation, recirculation bubble, and blade tip regions.

- The RMS azimuthal velocity fluctuations show a small increase in the corner separation and the recirculation bubble regions, and a strong increase in the blade tip region.

Azimuthal profiles in the interstage region.

- Overall good agreement of the velocity profiles in the rotor wake region at different spanwise positions is obtained between LES and RANS, with a slightly smaller wake width in the LES.

- LES predicts larger levels of the turbulent kinetic energy in the wake region than RANS, whereas lower levels are obtained in the background turbulence region.

6.4 Aeroacoustic results

6.4.1 Noise sources

In the present study, the Mach number is relatively low and the flow remains subsonic all along the span of the blades and vanes. Dipolar noise sources, which are related to force fluctuations on the blade and vane surfaces, are thus expected to be dominant [90, 135]. Consequently, the RMS pressure fluctuations, presented in Figure 6.14, can be seen as an indicator of the presence of noise sources from the fan and OGVs. Large values of $P_{\rm rms}$ are observed in the recirculation bubble and the rotor tip regions, which is consistent with
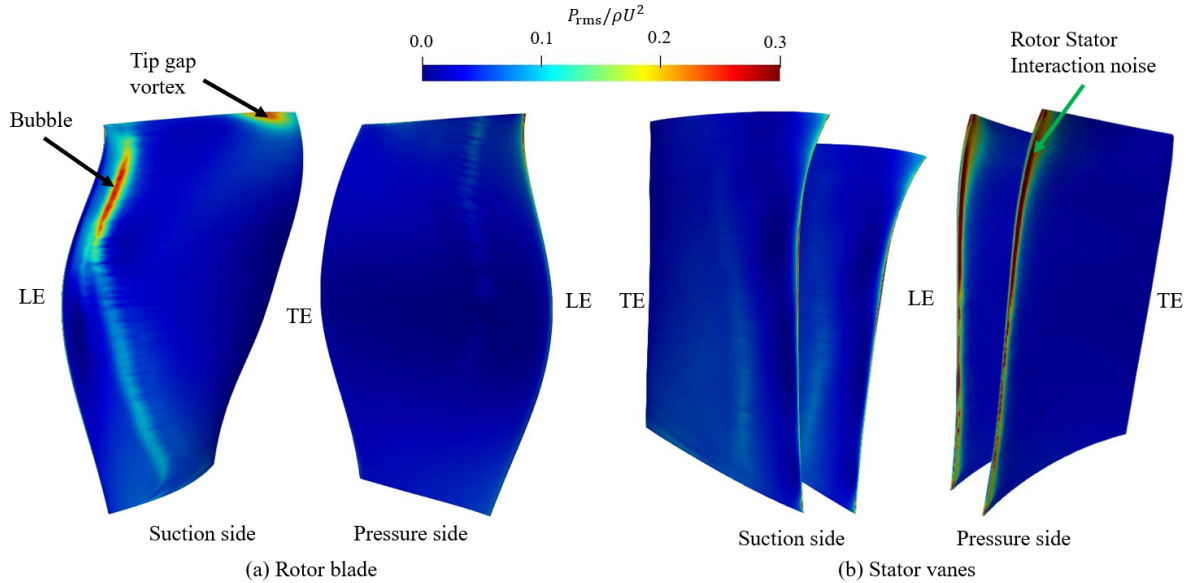
Figure 6.14: RMS pressure fluctuations on (a) the fan and (b) OGVs.

the location of intense turbulent structures, as shown in Figure 6.2. High P_{rms} values can also be found along the leading edge of the OGVs, which is related to the rotor-stator interaction noise. It should be noted that no boundary layer separation is visible on the OGVs. However, the highest levels of P_{rms} are located on the pressure side of the OGVs. This suggests that the effective angle of attack of the stator is below 0°, which is consistent with the distributions of isentropic Mach number on the stator vane in Figure 6.5.

The instantaneous dilatation rate contours, $\nabla.u$, are shown in Figure 6.15 at 80% of the rotor span. The dilatation rate is useful to identify the flow perturbations that may be considered as noise mechanisms. Hydrodynamic perturbations are shown in the boundary layers and in the wakes. When observing the wave-fronts outside of these regions, two main noise sources can be identified: the trailing edge noise generated at the trailing edges of the rotor blades and stator vanes, and the rotor-stator interaction noise generated at the leading edges of the stator vanes. It is expected that, because of the relatively low Mach number and the absence of shock waves, quadrupole noise sources associated with the turbulent wakes are negligible when compared to the dipole sources at the trailing edges and the leading edges.

6.4.2 Input data for the rotor-stator interaction noise analytical models

The rotor-stator interaction noise is computed using the flow statistics upstream of the stator leading edge extracted from the LES. The input parameters are: (i) the axial velocity and the velocity magnitude, (ii) the turbulent kinetic energy and turbulence integral length scale, and (iii) the wake half-width. These parameters are extracted at a distance of $0.03c$ upstream of the stator leading edge, which is sufficient to avoid a significant distortion of the turbulence near the stator [242, 65].

The radial distributions of absolute velocity magnitude, V_{abs}, and turbulent kinetic energy, k_t, from LES and RANS simulations, are compared in Figure 6.16. Both parameters show similar trends between LES and RANS simulations, except in the corner separation region, where larger values are obtained from the RANS simulation, and in

$$\nabla . \boldsymbol{u} \; [1/s]$$
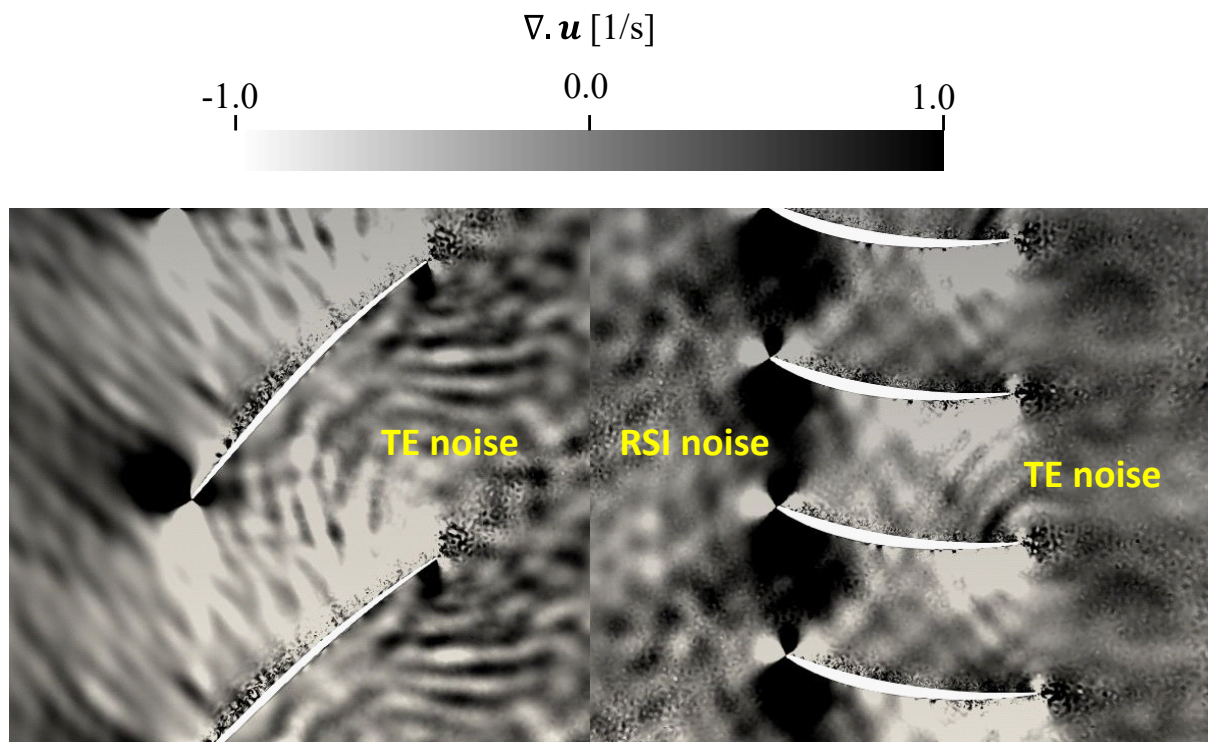
Figure 6.15: Instantaneous contours of the dilatation rate in a blade-to-blade view at 80% of the rotor span. (LES).

the recirculation bubble and tip regions, where the RANS simulation predicts lower values. Additionally, when compared to the LES, a slight over-prediction of k_t is observed between 20% and 60% of the span for the RANS simulation, which may be due to the difference in the turbulence intensity injected at the inlet plane between the LES and the RANS simulations (a turbulence intensity of 0.5% is injected in the RANS simulation, whereas no turbulence is prescribed in the LES).

In order to calculate the axial integral length scale, three different approaches are used in this work. The first approach, which is adopted for the RANS simulation, was proposed by Pope [204] and gives an estimate of the turbulence length scale, λ_p, based on the turbulent variables k_t and ω_t as follows,

$$\lambda_p = C_{Re} \frac{\sqrt{k_t}}{C_\mu \omega_t}, \tag{6.1}$$

where ω_t is the dissipation rate of the turbulent kinetic energy, $C_{Re} = 0.43$, and $C_\mu = 0.09$.

The second approach is based on the empirical law of Jurdic *et al.* [114] and requires the estimation of the wake width L_w, from the numerical simulation. In order to extract the wake width, a Gaussian shape is usually assumed for the wake, based either on the absolute velocity deficit or on the turbulence kinetic energy. In the present work a Gaussian fit is performed on the turbulence kinetic energy, as shown in Figure 6.17 at 50% of the rotor span. L_w corresponds then to the full width at half maximum of the Gaussian function used for the fitting process. L_w is computed using the standard deviation σ_G of the Gaussian function as: $L_w = 2\sqrt{2ln(2)}\sigma$.

The turbulence length scale in this case, λ_j, is given as,

$$\lambda_j = 0.21 L_w. \tag{6.2}$$

212

(a)

(b)
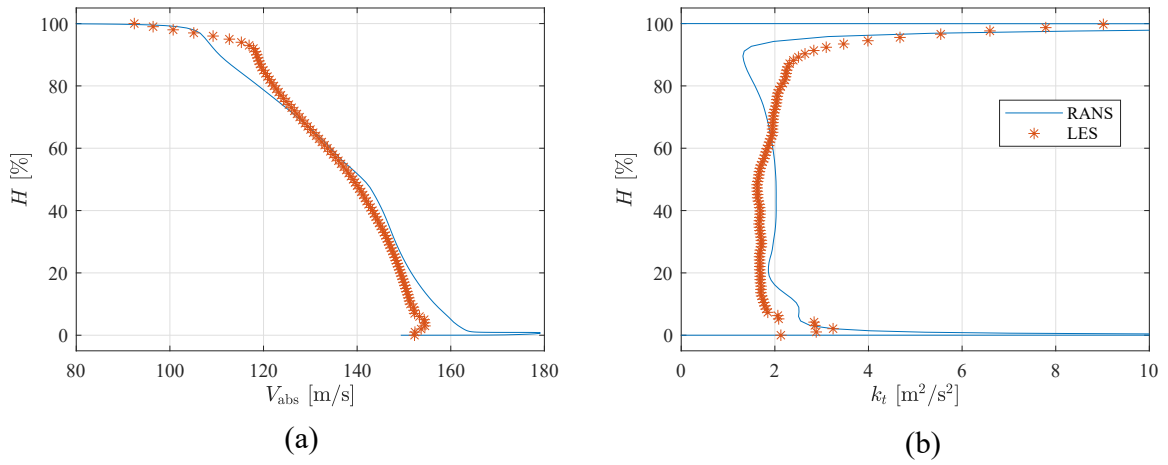
Figure 6.16: Comparison of (a) the absolute velocity magnitude V_{abs}, and (b) the turbulent kinetic energy k_t, extracted from RANS and LES, at $0.03c$ upstream of the stator leading edge.
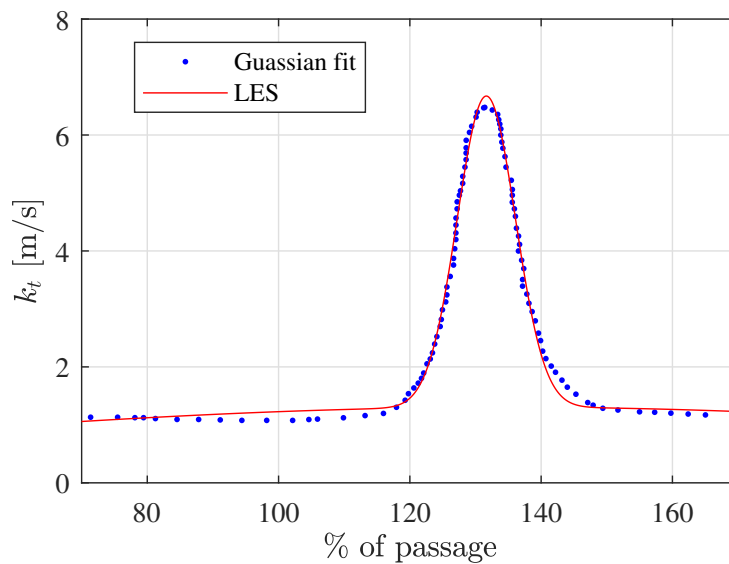
Figure 6.17: Wake extraction using a Gaussian fit.
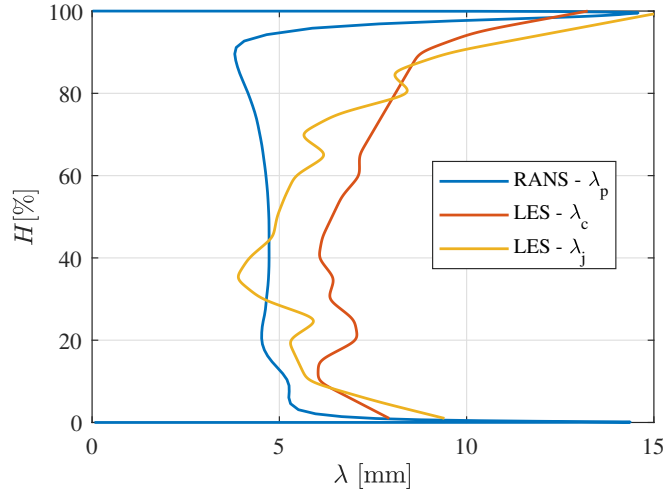
Figure 6.18: Comparison of different turbulence length scale estimates, extracted from LES and RANS simulations.

The third approach is based on Taylor's frozen turbulence assumption [204, 114], which assumes that the turbulent structures are convected unchanged by the mean flow. Temporal recordings collected on an axial cut upstream of the stator are used to calculate the autocorrelation function, $R_{V_x V_x}$, from LES as follows,

$$R_{V_x V_x}(\mathbf{x}, \tau) = \frac{\overline{V_x'(\mathbf{x}, t) V_x'(\mathbf{x}, t + \tau)}}{V_{x,\mathrm{rms}}(\mathbf{x})^2}, \tag{6.3}$$

where $V_x'(\mathbf{x}, t)$ is the axial velocity fluctuation at position $\mathbf{x}$ and time t, and $V_{x,\mathrm{rms}}(\mathbf{x})$ corresponds to the RMS of the axial velocity fluctuation. The temporal integral scale λ_t can then be computed as,

$$\lambda_t = \int_{\tau=0}^{\infty} R_{V_x V_x}(\mathbf{x}, \tau) d\tau, \tag{6.4}$$

and using Taylor's frozen turbulence assumption, the turbulence length scale λ_c can finally be computed as,

$$\lambda_c = \overline{V_x} \lambda_t, \tag{6.5}$$

where $\overline{V_x}$ is the circumferentially-averaged axial velocity component at a distance of $0.03c$ upstream of the stator leading edge.

The radial distributions of the different turbulence length scale estimates, λ_p, λ_j, λ_c, are presented in Figure 6.18. The levels are consistent between the different approaches but some discrepancies can be observed. Overall, similar trends are obtained for λ_c and λ_j, showing an increase in the length scale above 50% of the span, which can be explained by the recirculation bubble on the fan blade and the tip-leakage flow. The absence of the recirculation bubble for the RANS can partially explain the uniform behavior of λ_p from 50% to 90% of the rotor span and the differences with λ_c and λ_j.

In Figure 6.19, the turbulence velocity spectrum in the streamwise direction, Φ_{uu}, is extracted upstream of the stator leading edge at mid-span from the LES, and compared to the model of Liepmann as detailed in [205], given as:

$$\Phi_{uu} = \frac{2\lambda_c}{\pi^2} \frac{k_x^2 + k_z^2}{(1 + \lambda_c^2 k_s^2)^3}, \tag{6.6}$$

214
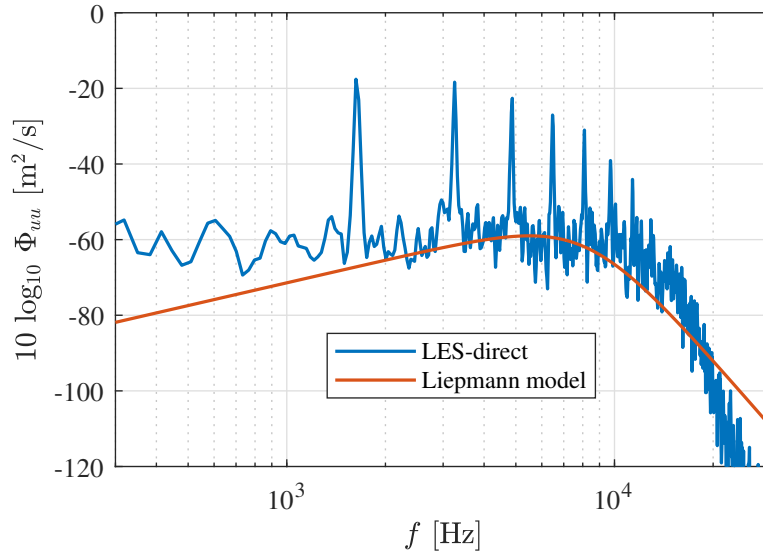
Figure 6.19: Comparison of the turbulence velocity spectrum of the streamwise velocity component, upstream of the stator leading edge, at 50% stator span, between the LES and Liepmann's model.

where $k_s^2 = k_x^2 + k_y^2 + k_z^2$. It should be noted that Φ_{uu} is an input for the analytical models of rotor-stator interaction noise. The tones that appear in the turbulence spectrum from LES correspond to the BPF and its harmonics. From 2 kHz to 8 kHz, a good agreement can be found with the model of Liepmann. Larger values for the LES at high frequencies (8-20 kHz) are observed. Φ_{uu} is also overpredicted at low frequencies (below 2 kHz) in the LES results, which may be due to the computational domain size in the azimuthal direction and the simulation time.

6.4.3   Input data for the trailing edge noise analytical model

The trailing edge noise is computed using the flow properties in the boundary layers close to the trailing edges of the rotor blade and stator vanes. The two parameters for the trailing edge noise analytical model are (i) the wall pressure spectrum, Φ_{pp}, and (ii) the spanwise correlation length, l_z. These parameters can also be estimated using empirical laws, for which the input data, such as the boundary-layer thickness, are extracted from the LES. Figures 6.20 and 6.21 present the radial distributions of several boundary-layer parameters, which are extracted on the suction side at $0.02c$ upstream of the rotor and stator trailing edges, respectively. The displacement thickness is defined as,

$$\delta_1 = \int_0^\infty (1 - \frac{\rho u_b}{\rho_0 U_0}) \mathrm{d}n. \tag{6.7}$$

The momentum thickness is defined as,

$$\delta_2 = \int_0^\infty \frac{\rho u_b}{\rho_0 U_0}(1 - \frac{u_b}{U_0}) \mathrm{d}n, \tag{6.8}$$

and the shape factor $H_{12} = \delta_1/\delta_2$, where n is the distance to the suction side surface of the blade, ρ_0 is the free-stream density, U_0 is the velocity magnitude outside the boundary

(a)

(b)
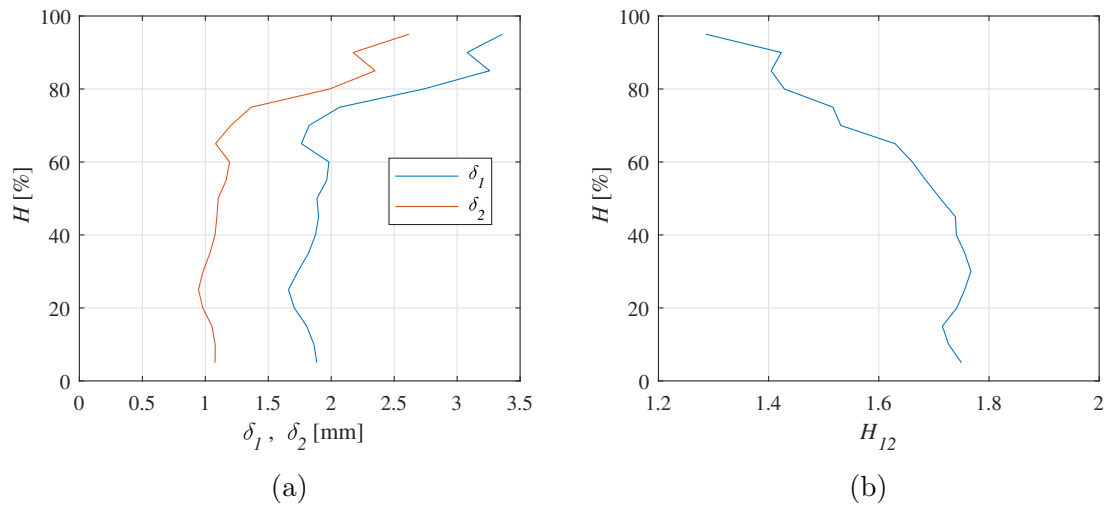
Figure 6.20: Radial distributions of the boundary-layer parameters on the rotor suction side, $0.02c$ upstream of the trailing edge. (a) Boundary layer displacement and momentum thicknesses δ_1 and δ_2, respectively, and (b) shape factor H_{12}.

(a)

(b)
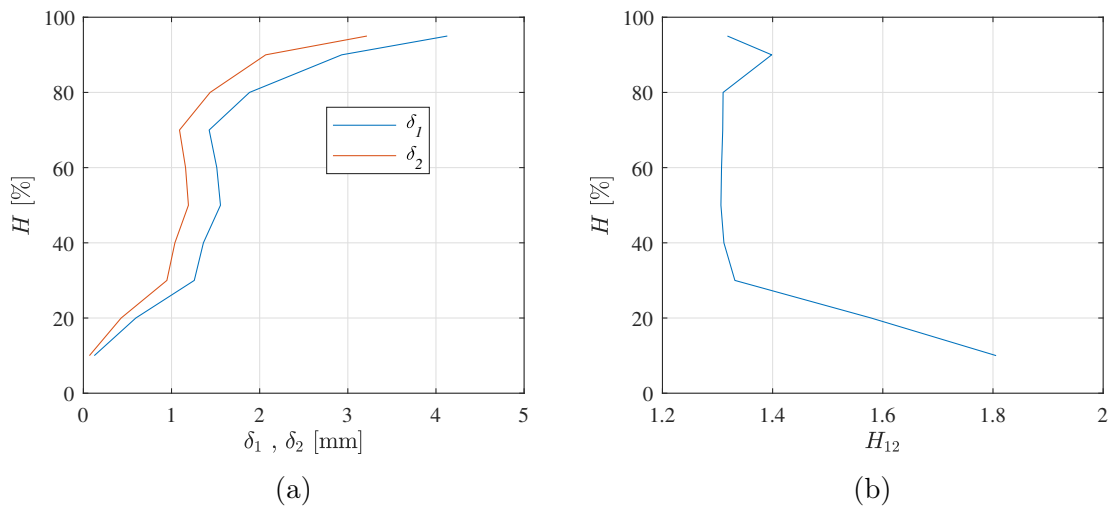
Figure 6.21: Radial distributions of the boundary-layer parameters on the stator suction side, $0.02c$ upstream of the trailing edge. (a) Boundary layer displacement and momentum thicknesses δ_1 and δ_2, respectively, and (b) shape factor H_{12}.
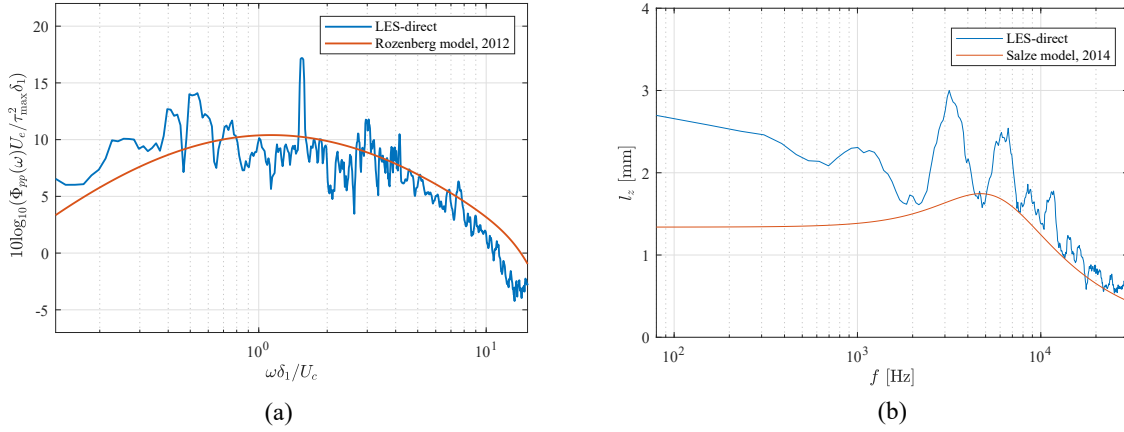
Figure 6.22: Input parameters for Amiet's trailing-edge noise model at mid-span of the rotor blade, from the direct LES approach and empirical models. (a) Wall pressure spectrum. (b) Spanwise correlation length.
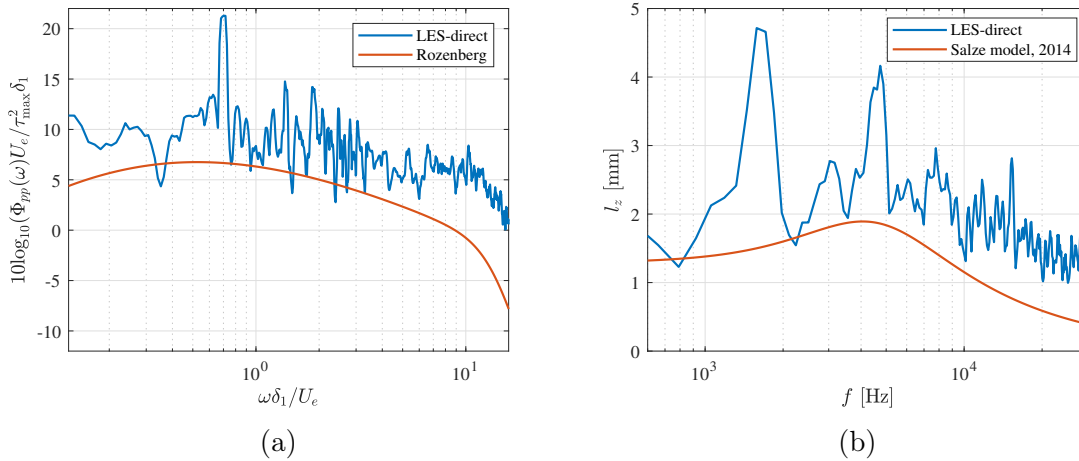
Figure 6.23: Input parameters for Amiet's trailing edge noise model at mid-span of a stator vane, from the direct LES approach and empirical models. (a) Wall pressure spectrum. (b) Spanwise correlation length.

layer, and ρ and u_b are the density and the velocity magnitude within the boundary layer, respectively.

On both the rotor blade and the stator vane, the boundary-layer displacement and momentum thicknesses show a similar behavior, and both indicate that there is a significant increase in the boundary layer thicknesses above 70% of the span. In this region on the rotor blade, the shape factor shows an important reduction, from 1.67 at 60% of the rotor span to 1.3 close to the tip region. This behavior can be explained by the high levels of turbulence intensity in the boundary layers at rotor spans higher than 60%, due to the recirculation bubble and the tip leakage flow. This may also explain the increase in the boundary layer thicknesses on the stator vanes directly downstream. A more uniform distribution of the shape factor on the stator vane is observed between 30% to 80% of the stator span, which corresponds to fully turbulent boundary layer.

The wall pressure spectra use the empirical model of Rozenberg *et al.* [229], which is based on the model of Goody [73], and includes the effects of the Reynolds number

and the adverse pressure gradient (as described in Chapter 3). Figures 6.22 (a) and 6.23 (a) show the comparison of the wall pressure spectra at mid-span of the rotor blade and stator vane, respectively, from the LES (LES-direct) and Rozenberg's model [229]. On the rotor blade, a similar trend is observed for both predictions. The LES results retrieve the main slopes of the wall pressure spectrum described in Chapter 3 over the whole frequency range, with a slope of 1.8 at low frequencies ($\omega\delta_1/U_c < 0.5$), -1.1 in the overlap region ($0.6 < \omega\delta_1/U_c < 6$) and -5.2 at high frequencies ($\omega\delta_1/U_c > 8$). On the stator vane, the LES predicts larger levels of the wall pressure spectrum over the whole frequency range. Similar trends are obtained between the two approaches in the overlap region ($0.6 < \omega\delta_1/U_c < 6$). At larger frequency, a small hump is observed in the LES results from $\omega\delta_1/U_c = 6$ to $\omega\delta_1/U_c = 11$.

The spanwise correlation length uses the empirical model of Salze *et al.* [234], which is based on the model of Efimtsov *et al.* [57]. In the direct LES approach, l_z is estimated from the coherence function γ between two points at the same axial position and separated by a spanwise distance Δz as follows,

$$l_z(\omega) = \int_0^{+\infty} \sqrt{\gamma^2(\Delta z, \omega)} d\Delta z. \tag{6.9}$$

In order to use Amiet's trailing edge noise model [9, 223], the blade and the vane are discretized by 20 radial strips. Then, Amiet's model is applied to each strip and the contributions of the strips are added incoherently. The value of l_z used for each strip is calculated using unsteady data collected from the LES, and the integral in Eq.6.9 is performed over the span of each strip.

Figures 6.22 (b) and 6.23 (b) present the comparison of the spanwise correlation length, l_z, at mid-span of the rotor blade and stator vane, respectively, from the LES (LES-direct) and the model of Salze *et al.* [234]. On the rotor blade, peaks can be observed for the direct LES approach at approximately 3200 Hz, 6400 Hz and 9600 Hz. The frequencies of these peaks correspond to the first three harmonics of the vane passing frequency VPF $= V\Omega/60$, where Ω is the fan rotation speed in RPM, and $V = 32$ corresponds to the number of vanes in the full stage of the modified configuration corresponding to the (full-span) sector LES. Since the monitor points collect data in the rotating frame, the presence of these peaks can be associated with the periodic interaction of the rotor wakes with the stator vanes. Overall, a good agreement is observed between the predictions directly obtained from the LES (LES-direct) and the model of Salze *et al.* [234] at high frequencies ($f > 4\,\mathrm{kHz}$). An over-prediction of the LES results at low frequencies compared to Salze's model [234] can be observed. This may be explained by the limited computational time used for the computation of the correlation length.

As for the wall pressure spectrum, on the stator vane (Figure 6.23 (a)), the spanwise correlation length exhibits larger values in the LES when compared to the model of Salze *et al.* [234], even at high frequencies. Several peaks appear in the LES approach at the blade passing frequency (BPF $= 1655$ Hz) and harmonics. Salze's model [234] considers the diffraction of a turbulent boundary layer by a sharp trailing edge. In the LES, other mechanisms generating disturbances in the boundary layers, such as the impact on the stator vanes of the rotor wakes and tip vortices, can be found. This may partly explain the differences between the two approaches and the larger values of l_z obtained in the LES, when compared to Salze's model [234]. Additionally, the limited computational time can also partly explain the larger values obtained in the LES, particularly at low frequencies.
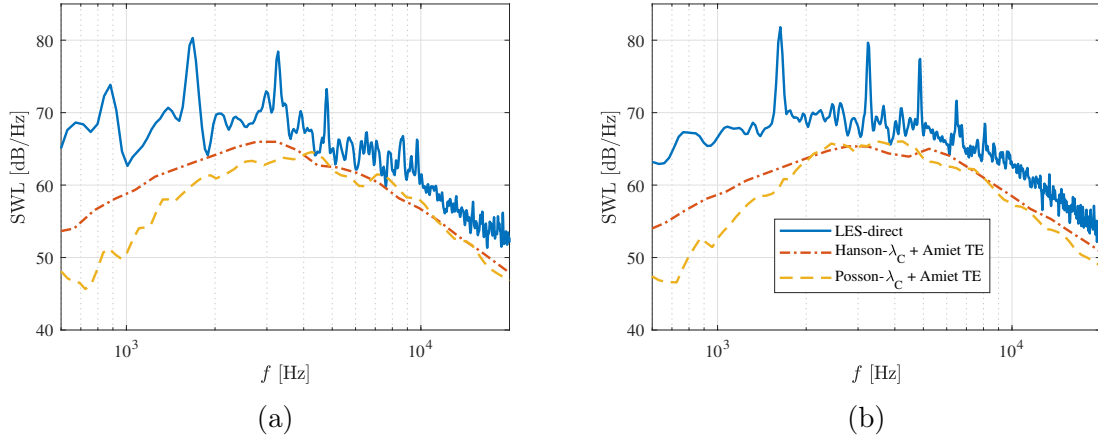
Figure 6.24: Sound power levels from the direct LES approach and the analytical models at (a) the intake and (b) the exhaust sections.

6.4.4 Noise prediction

The direct noise computation of the sound power levels from the LES is compared to the predictions of the analytical models. For the analytical modeling, the code *Optibrui* is used and the contributions of both the rotor-stator interaction noise, which is analytically predicted by Hanson's [93] and Posson's [209, 207] models, and the trailing edge noise from the rotor blades and stator vanes, which is modeled by Amiet's trailing edge model [9, 223], are added. The rotor blades and stator vanes are discretized by 20 radial strips. For the rotor-stator interaction noise, the input data described in Section 6.4.2 are extracted from the LES at a distance of $0.03c$ upstream of the stator leading edge for each strip. For the trailing edge noise, the input data described in Section 6.4.3 are extracted at 98 % of the chord length on the suction side of the rotor blades and the stator vanes for each strip.

For the direct LES predictions, the acoustic power is computed by integrating the acoustic intensity I_a over a duct section and can be written as:

$$\text{SWL} = \int_0^{2\pi} \int_{R_h}^{R_s} I_a r \mathrm{d}r \mathrm{d}\theta. \tag{6.10}$$

For homentropic fluid, the acoustic intensity can expressed as:

$$I_a = \left(\frac{p'}{\rho_0} + U_0 V_x'^{\pm} \right) \left(\rho_0 V_x'^{\pm} + U_0 \rho'^{\pm} \right). \tag{6.11}$$

Unsteady probes are located in the duct upstream of the rotor (intake section at two chord lengths upstream of the rotor) and downstream of the stator (exhaust section at two chord lengths downstream of the stator), where the mesh remains sufficiently refined to properly propagate the acoustic waves. The locations of the extraction planes are chosen such that the hub radius remains nearly constant upstream and downstream of the intake and exhaust sections, respectively. $V_x'^{-}$ is considered at the inlet section and $V_x'^{+}$ at the exhaust section.

A comparison of the sound power levels (SWL) from the two approaches is shown in Figure 6.24. A fairly good agreement is obtained between the approaches. An underprediction of the sound levels from the analytical models can be observed over the whole
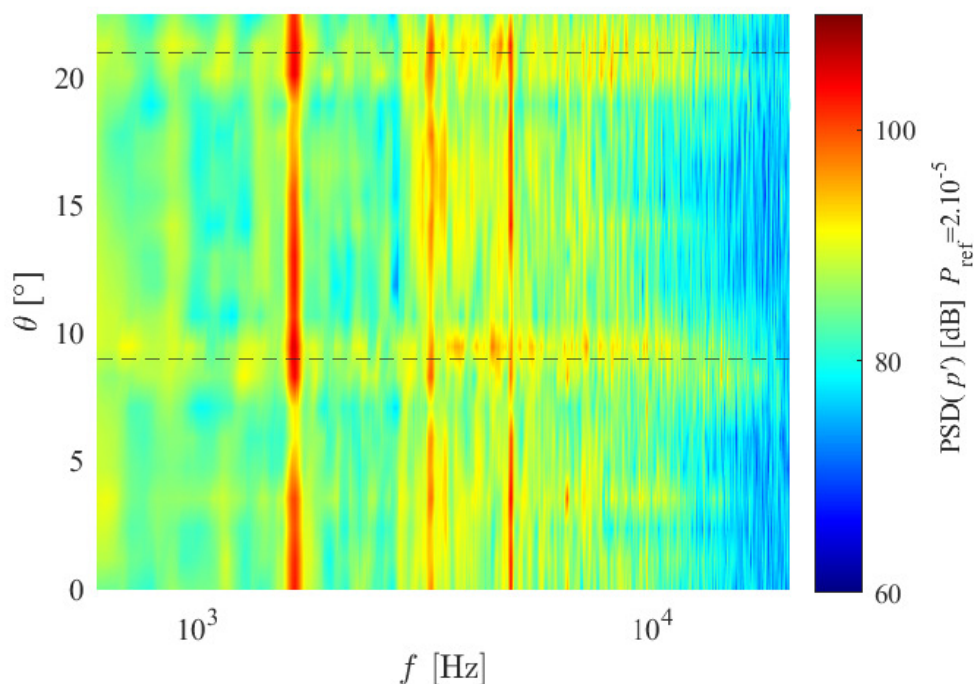
Figure 6.25: Power spectral density at 80% of the stator span at the exhaust section.

frequency range. This may be partially explained by additional noise sources that are present in the LES and are not modeled by the analytical models, such as the tip gap noise (due to the tip leakage vortex shown in Figures 6.2 and 6.14). At the exhaust section, the stator wakes may also contribute the pressure and velocity fluctuations used to compute the acoustic power. Figure 6.25 shows the PSD of the pressure fluctuations at 80% of the stator span at the exhaust section. Large PSD values are observed at the BPF and its harmonics. Additionally, at two azimuthal positions (shown by the dashed lines), relatively large PSD levels are also observed over a wide range of frequencies. These positions correspond the stator wakes.

Finally, comparing the rotor-stator interaction noise analytical models in Figure 6.24, the predictions from Posson's model [209, 207] are lower, especially at low frequencies, which may be due to duct cut-off effects that are included in Posson's model and are neglected in Hanson's model.

6.4.5 Noise contributions

The contributions of the two noise mechanisms, the rotor-stator interaction noise and the trailing edge noise, are compared in Figure 6.26 using the analytical models. The trailing edge noise from the rotor blades and the stator vanes is computed using Amiet's trailing edge noise model [9, 223]. The rotor-stator interaction noise is predicted by Hanson's [93] and Posson's [209, 207] models. At mid-to-high frequencies (beyond 2 kHz), the sound power levels due to the rotor-stator interaction noise are significantly larger than the levels due to the trailing edge noise (a difference of about 16 dB/Hz). Comparable sound power levels are obtained for the two mechanisms below 1.8 kHz.

In order to further compare the noise emissions due to the different noise sources on the rotor blade, the blade is split in two different parts and the far-field noise is predicted
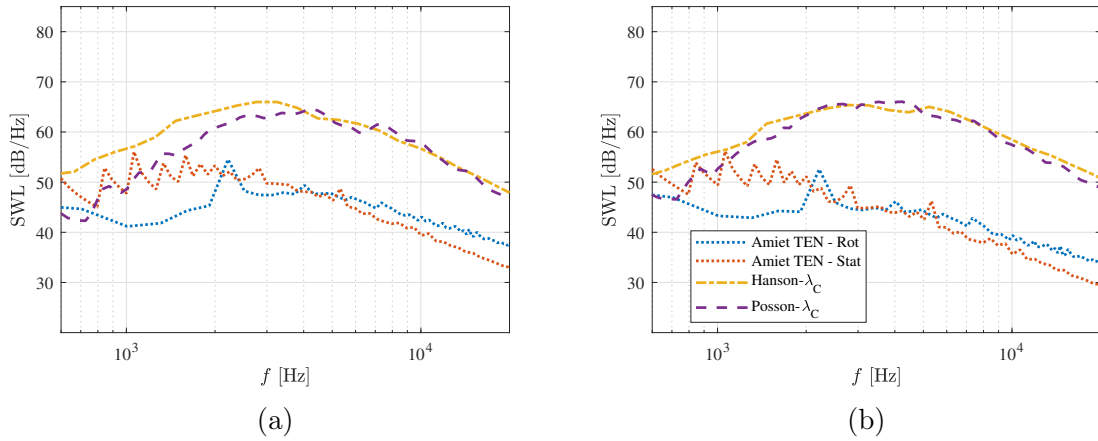
Figure 6.26: Sound power levels from the different analytical models at (a) the intake and (b) the exhaust sections.
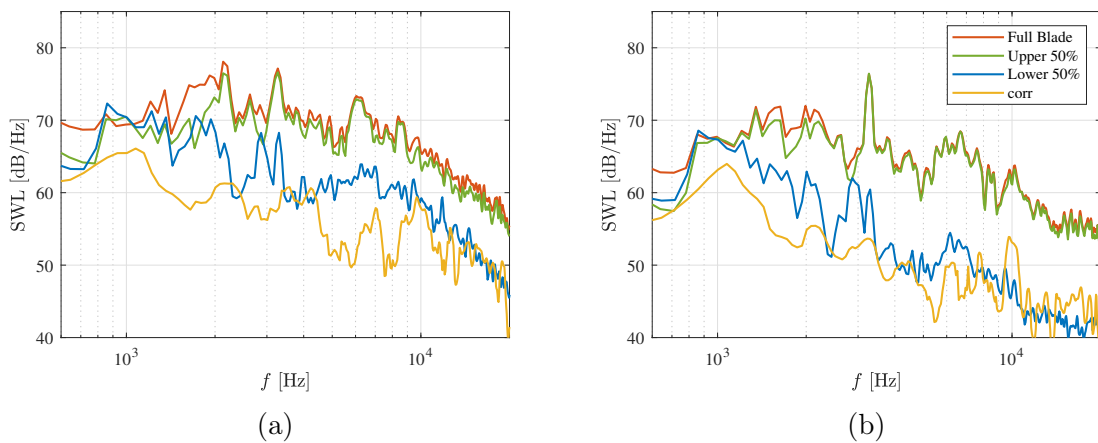
Figure 6.27: Sound power level spectra from the Ffowcs Williams and Hawkings (FWH) analogy for the full blade, the upper 50% of the blade, the lower 50% and the cross-correlation part between them at (a) the intake and (b) the exhaust sections.

using the Ffowcs Williams and Hawkings (FWH) analogy [276]. This may help us to understand the differences in the noise levels between the noise predictions from the direct LES approach and the analytical models in Figure 6.24.

The FWH analogy is based on the unsteady pressure field, recorded on the solid surface of the fan blade for the computation of the loading noise source, since the noise sources are localized at the surfaces. This is justified by the low Mach numbers and the absence of shock waves. The sampling frequency is 80 kHz and the unsteady recording is made over four rotor revolutions. The advanced time approach of Casalino [29] and Najafi-Yazd *et al.* [180] is adopted. The acoustic propagation is computed using the free-field Green's function. The far-field sound power level spectrum is obtained with a periodogram using Welch's method and a Hann window with 50% overlap between the segments.

The blade is split into two parts. For both parts, the contribution of the trailing edge noise is computed. The lower 50% of the blade surface also includes the contribution of the corner separation noise to the far-field noise. In the remaining part (the upper 50% of the blade surface), two main secondary flows are observed, the recirculation bubble and the tip-leakage vortex (see Figure 6.2). These are expected to dominate the far-field noise emissions from the upper part of the blade.

The power spectral density of the far-field acoustic pressure from the full blade can be calculated as the sum of the power spectral densities of the parts $((S_{pp})_i)$ and their cross-spectral density $((S_{pp})_{\text{cross}})$ as follows,

$$(S_{pp})_{\text{blade}} = \sum (S_{pp})_i + 2(S_{pp})_{\text{cross}} \tag{6.12}$$

Figure 6.27 presents the sound power spectra at the intake and exhaust sections obtained from the different parts of the blade, the full blade (denoted "Full Blade"), the blade upper region (the upper 50% of the blade surface denoted "Upper 50%"), the remaining part of the blade (denoted "Lower 50%"), and the cross-correlation term (denoted "corr"). For both intake and exhaust sections, the cross-correlation spectrum is relatively small compared to the other contributions, particularly at mid to high frequencies.

The noise contributions from the blade upper part dominate the noise spectra beyond 2 kHz at the inlet section and 1.5 kHz at the exhaust section. On the upper part of the blade surface, two secondary flows particularly generate pressure fluctuations: the tip-leakage flow and the recirculation bubble. At lower frequencies, comparable sound power levels are observed from the upper and lower parts. Consequently, the differences at low frequencies (below 2 kHz) observed in Figure 6.24, between the direct noise prediction and the predictions using the analytical models, may be explained by the noise emissions related to the corner separation vortex, which is the dominant source of pressure fluctuations in the lower part of the blade.

To obtain the contribution of the tip-leakage noise, the blade is also split into two parts in Chapter 5: the upper 15% of the blade surface, to compute the tip-gap noise contribution to the far-field, and the remaining lower part of the blade. It is seen that the contribution of the tip-gap noise to the total noise emissions is significant at mid to high frequencies, particularly at the intake section. Consequently, the differences at high frequencies (particularly beyond 10 kHz) observed in Figure 6.24 between the direct noise prediction and the predictions using the analytical models, may be explained by the noise emissions related to the tip flow vortices. More specifically these noise emissions may be related to the interaction of the tip vortices TLV2, TSV and IV generated on each blade with the trailing edge of the same blade, as explained in Chapter 5.

Aeroacoustic results ———————————————————————— **Summary**

Noise sources

The main noise sources, identified using the RMS pressure fluctuations on the surfaces of the blades and the vanes and the dilatation rate on a blade-to-blade view, are:

- the trailing edge noise,

- the rotor-stator interaction noise,

- the separation noise (due to the recirculation bubble),

- and the tip-gap noise.

Input parameters for the rotor-stator interaction noise models

- The input parameters are extracted as close as possible to the stator leading edge.

- The turbulence length-scale is estimated using three approaches:

  - Jurdic's approach, based on the wake width, estimated from the LES.
  - The temporal autocorrelation of the axial velocity fluctuations with Taylor's frozen turbulence hypothesis, estimated from the LES.
  - Pope's approach, based on the turbulent variables, k_t and ω_t, estimated from the RANS.

  Similar trends are obtained for Jurdic's and the autocorrelation approaches, with an increase of the turbulence length scale close to the hub, the tip and in the recirculation bubble region. Pope's approach, using RANS data, shows a more uniform radial profile all along the span.

Input parameters for the trailing edge noise model

- The input parameters are extracted close to the trailing edges of the rotor blades and stator vanes, at $0.98c$ from the leading edge.

- The wall pressure spectra are extracted from the LES and compared to the model of Rozenberg [229], which includes the effects of the Reynolds number and the adverse pressure gradient.

- The spanwise correlation length is computed from the coherence function obtained from unsteady fluctuations in the LES, and compared to the model of Salze [234].

All the input data for the model, such as the boundary layer thicknesses and the wall friction coefficient, are extracted from the LES. Similar trends are observed for the two main inputs on the rotor blades and the stator vanes. On the vanes, the LES predicts larger levels of wall pressure fluctuations and larger values of the spanwise correlation length over the whole frequency range.

Comparison between direct LES and analytical models for noise prediction

- The sound power levels are computed from the LES and compared to LES-informed analytical models: Amiet's model [9, 223] for the trailing edge noise coupled with either Hanson's [93] or Posson's [209, 207] models for the rotor-stator interaction noise.

- Good overall agreement is obtained between the LES and the analytical models over the whole frequency range.

- The analytical models predict lower sound power levels over the whole frequency range, when compared to the LES, which suggests the presence of additional noise sources in the LES.

- Lower sound power levels are obtained with Posson's model [209, 207] compared to Hanson's model [93], which may be due to cut-off duct modes that are only considered by Posson's model [209, 207].

Noise contributions

The contribution from the different noise sources to the total far-field noise emissions are compared using the analytical models and the Ffowcs Williams and Hawkings (FWH) acoustic analogy [276].

- The contributions of the trailing edge noise obtained from Amiet's model [9, 223] for the rotor and the stator are compared to the rotor-stator interaction noise obtained from Posson's [209, 207] and Hanson's [93] models. The influence of the trailing edge noise to the far-field noise is only significant at low frequencies (below 1.8 kHz).

- The blade is split into its lower and upper 50% of the span. The noise contributions from each part are compared using the Ffowcs Williams and Hawkings (FWH) acoustic analogy [276], based on the surface pressure fluctuations obtained from the LES. The lower part of the blade, which seems to be dominated by the corner separation noise, has only a significant influence at low frequencies (below 2 kHz).

6.5 Comparison between the sector and 360° LES: effects of imposed periodicity

In this section, the impact of the periodic boundary conditions on the flow field and the far-field noise emissions is assessed by comparing the results from the (full-span) sector LES and (full-span) 360° LES. The azimuthal coherence function between monitor points in several sectors and the noise modal content at the intake and exhaust sections, which can only be obtained in the (full-span) 360° LES configuration, are also presented. The (full-span) 360° LES is still in progress and the computational time used for the presented results corresponds to one fan rotation. Thus, only preliminary results are discussed. The mean and turbulent results, and the coherence functions in the (full-span) 360° LES are obtained from the circumferential average of these quantities.

6.5.1 Instantaneous results

Figures 6.28 to 6.30 show an isosurface of the Q-criterion ($Qc^2/U^2 = 10$) for the (full-span) 360° LES configuration. In these figures, the iso-surface is colored by the vorticity magnitude. A qualitative description of the turbulent structures developing in the boundary layers and the wakes can be obtained. A similar flow topology as for the (full-span) sector LES (Figure 6.2) is observed. The transition of the boundary layers can be observed near the leading edges of the blades and vanes all along the span. Small turbulent structures can be seen downstream of the transition regions. In addition to the turbulent structures, Figure 6.31 shows contours of the instantaneous dilatation rate ($\nabla \cdot \mathbf{u}$) at a radial cut of 99% of the rotor span. The wave-fronts propagating in the upstream and downstream directions shows the capability of 360° LES to capture the noise propagation in the refined-mesh region around the fan stage. It should be noted that there is no acoustic reflection from the upstream and downstream boundaries of the domain.

An iso-surface with a larger value of the Q-criterion is presented in Figure 6.32 for the (full-span) 360° LES configuration. The Q-criterion represents the difference between the rotational and the strain effects. When increasing the value of the Q-criterion, only the most intense vortices can be observed. For $\overline{Q}c^2/U_0^2 = 1000$ in Figure 6.32, only the turbulent structures in the tip gap and in the boundary layers on the blades, vanes and in the interstage region can be identified. Furthermore, as the value of the iso-surface of the Q-criterion is increased, the visible turbulent structures are characterized by larger vorticity magnitudes.

6.5.2 Mean quantities

Figure 6.33 shows a comparison of the distributions of isentropic Mach number, M_{is}, from the periodic sector LES and the 360° LES, along the rotor blade surface, for various spanwise positions. Similar results are obtained between the two configurations at the radial positions of 50% and 80% of the rotor span. The small recirculation bubble, observed by a flat region close to the leading edge on the suction side at 80% of the rotor span, is similarly captured for both configurations.

The spanwise position at 98% of the rotor span is much closer to the tip gap region and is affected by the tip leakage flow, as it is pointed out in Chapter 5. For both configurations, the pressure difference between the leading edge and 40% of the chord length is similar. Some differences between the two configurations are observed between
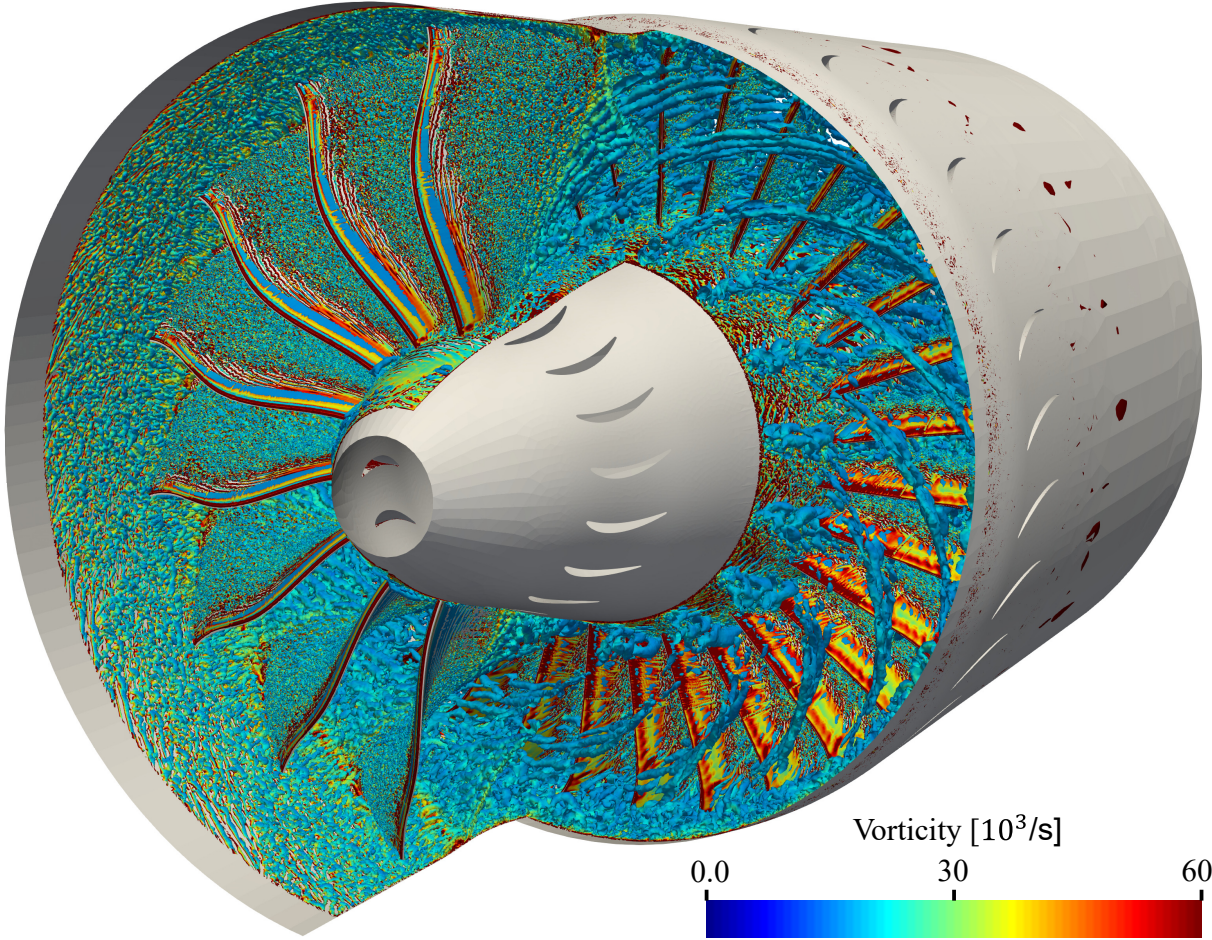
Figure 6.28: Iso-surface of Q-criterion ($Qc^2/U^2 = 10$) around of the rotor and the stator, colored by the vorticity magnitude, for the (full-span) 360° LES configuration. View from an observer upstream of the fan looking at the suction side of the rotor blades.
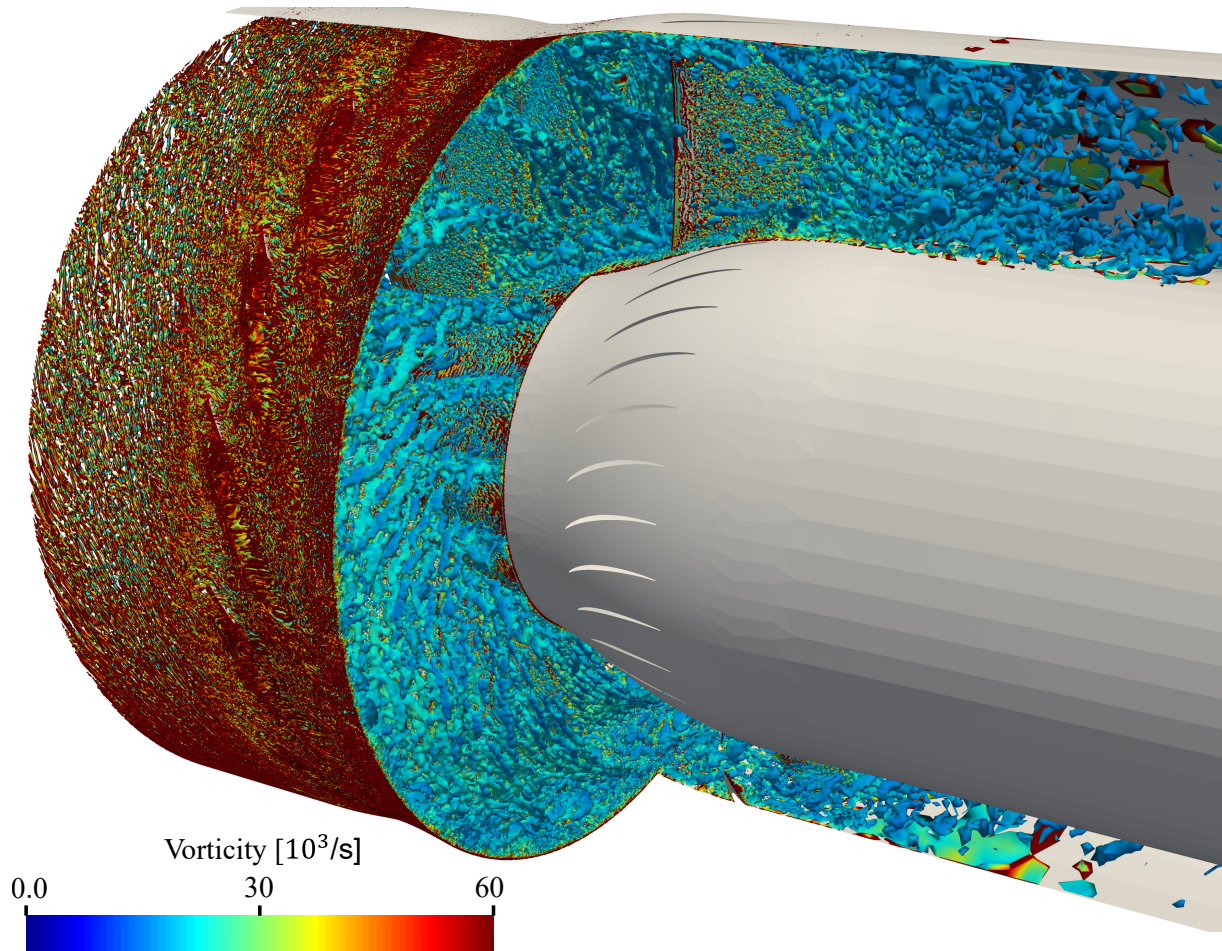
Figure 6.29: Iso-surface of Q-criterion ($Qc^2/U^2 = 10$) around of the rotor and the stator, colored by the vorticity magnitude, for the (full-span) 360° LES configuration. View from an observer downstream of the OGV looking at the pressure side of the stator vanes.
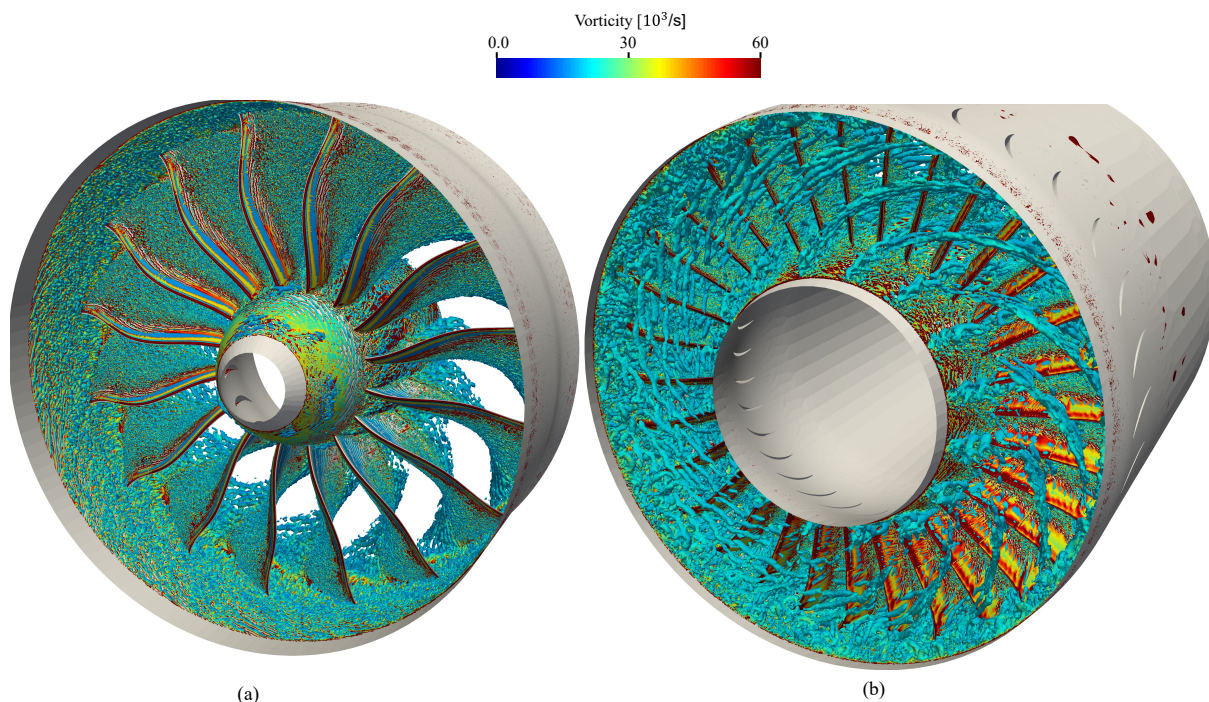
Figure 6.30: Iso-surface of Q-criterion ($Qc^2/U^2 = 10$), colored by the vorticity magnitude, for the (full-span) 360° LES. View from an observer upstream of the fan (a) and the OGV (b).

60% of the chord length and the trailing edge. For the periodic sector LES, a larger pressure difference is observed in this region, compared to the 360° LES configuration. This suggests a difference in the tip flow topology, but may also be due to an insufficient statistical convergence of the 360° LES.

Figure 6.34 shows a comparison of the distributions of isentropic Mach number, M_{is}, from the periodic sector LES and the 360° LES, along the stator vane surface, for various spanwise positions. Similar results are obtained from both configurations, except at 98% of the stator span close to the leading edge, where small differences can be noticed. A small plateau of M_{is} is observed in the 360° LES, on the pressure side between $0.05c$ and $0.1c$, probably associated to a small recirculation bubble. For the periodic sector LES, a direct transition of the boundary layer at the leading edge is observed.

The radial distributions of the mean velocity components in the interstage, V_x, V_θ and V_r, from the (full-span) sector and 360° LES configurations, are presented in Figure 6.35. These time-averaged velocity profiles are also calculated from the circumferential average of the velocity field at $0.5c$ downstream of the rotor trailing edge. The two configurations present similar results for the velocity components all along the span. A slight difference in V_r is observed from 60% to 90% of the rotor span.

The radial distributions of the RMS velocity fluctuations in the interstage, $V_{x,rms}$, $V_{\theta,rel,rms}$ and $V_{r,rms}$, from the (full-span) sector and 360° LES configurations, are presented in Figure 6.36. These RMS profiles are obtained from the circumferential average of the RMS velocity fluctuations at $0.5c$ downstream of the rotor trailing edge. Significant differences are observed between the two configurations. The periodic sector predicts larger RMS velocity fluctuations, particularly from the hub to 85% of the rotor span. Moreover, the increase of $V_{\theta,rel,rms}$ from 50% to 85% is more pronounced for the periodic sector compared to the 360° configuration. In the blade tip region (from 85% to the
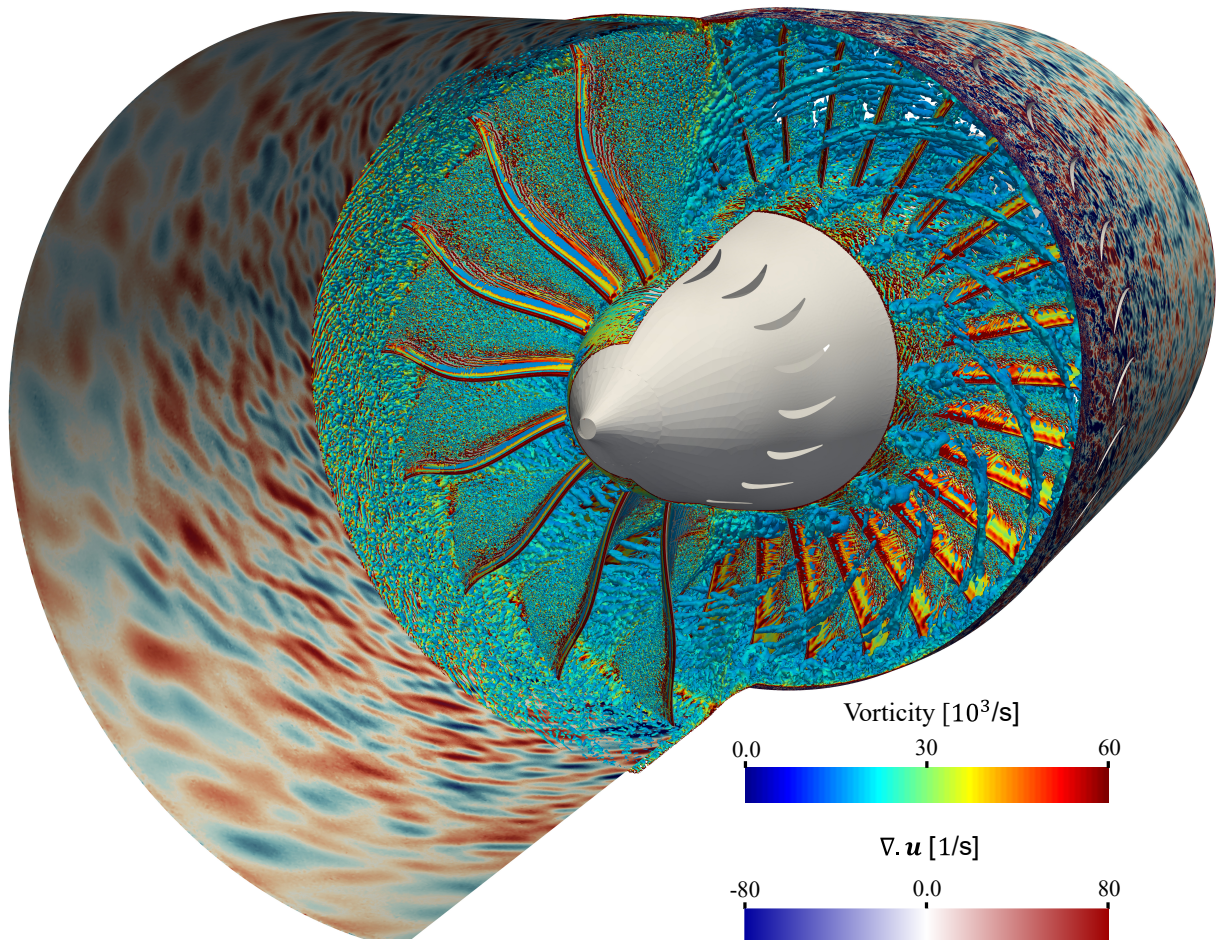
Figure 6.31: Instantaneous contours of dilatation rate at 99% of the rotor span and iso-surface of Q-criterion ($Qc^2/U^2 = 10$) around of the rotor and the stator, colored by the vorticity magnitude, for the (full-span) 360° LES configuration. View from an observer upstream of the fan looking at the suction side of the rotor blades.
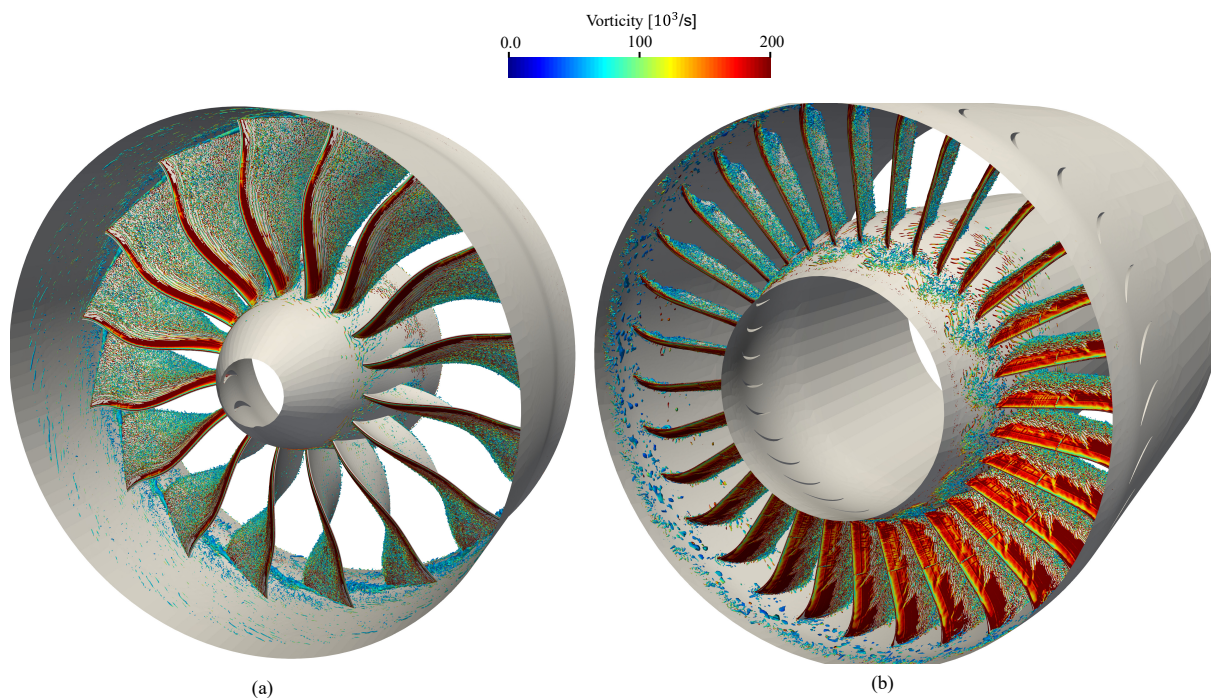
Figure 6.32: Iso-surface of Q-criterion ($Qc^2/U^2 = 1000$), colored by the vorticity magnitude, for the (full-span) 360° LES. View from an observer upstream of the fan (a) and the OGV (b).

shroud), similar velocity fluctuations are observed for the two configurations.

6.5.3 Azimuthal coherence

One of the main limitations of a periodic sector computation consists in the perfect correlation between the periodic sectors. However, the 360° LES configuration allows to obtain a full description of the correlations in the azimuthal direction, since no artificial periodicity is applied. Figure 6.38 presents the two-point coherence functions of the pressure fluctuations between monitor points at different azimuthal positions γ_θ. The positions of the monitor points are shown in Figure 6.37, on an axial cut at $0.5c$ downstream of the rotor trailing edge.

Figure 6.38 (a) presents a comparison between the coherences from the periodic sector and 360° LES, using the monitor points Ptθ1 and Ptθ2, which are within the same sector. For the 360° results, the coherence is averaged over 16 azimuthal positions. At low and mid frequencies, smaller coherence levels are obtained in the 360° LES configuration. This results from the artificial correlation induced between the lateral planes by the periodic condition in the sector LES, affecting the largest scales and lowest frequencies. At high frequencies (above 10 kHz), the coherence does not reach zero due to the lack of the computational time, particularly for the 360° LES.

Figure 6.38 (b) presents the coherences between the monitor points (in the rotating frame) Ptθ1, Ptθ4, Ptθ5 and Ptθ6, shown in Figure 6.37. The monitor point Ptθ1 is considered as a reference for the coherence, and the points Ptθ4, Ptθ5 and Ptθ6 are at $\Delta\theta$, $2\Delta\theta$ and $3\Delta\theta$, respectively, from Ptθ1, where $\Delta\theta = 2\pi/16$ corresponds to the angular extent of a sector.

The VPF and its harmonics are visible. Over a large frequency range, the coherence
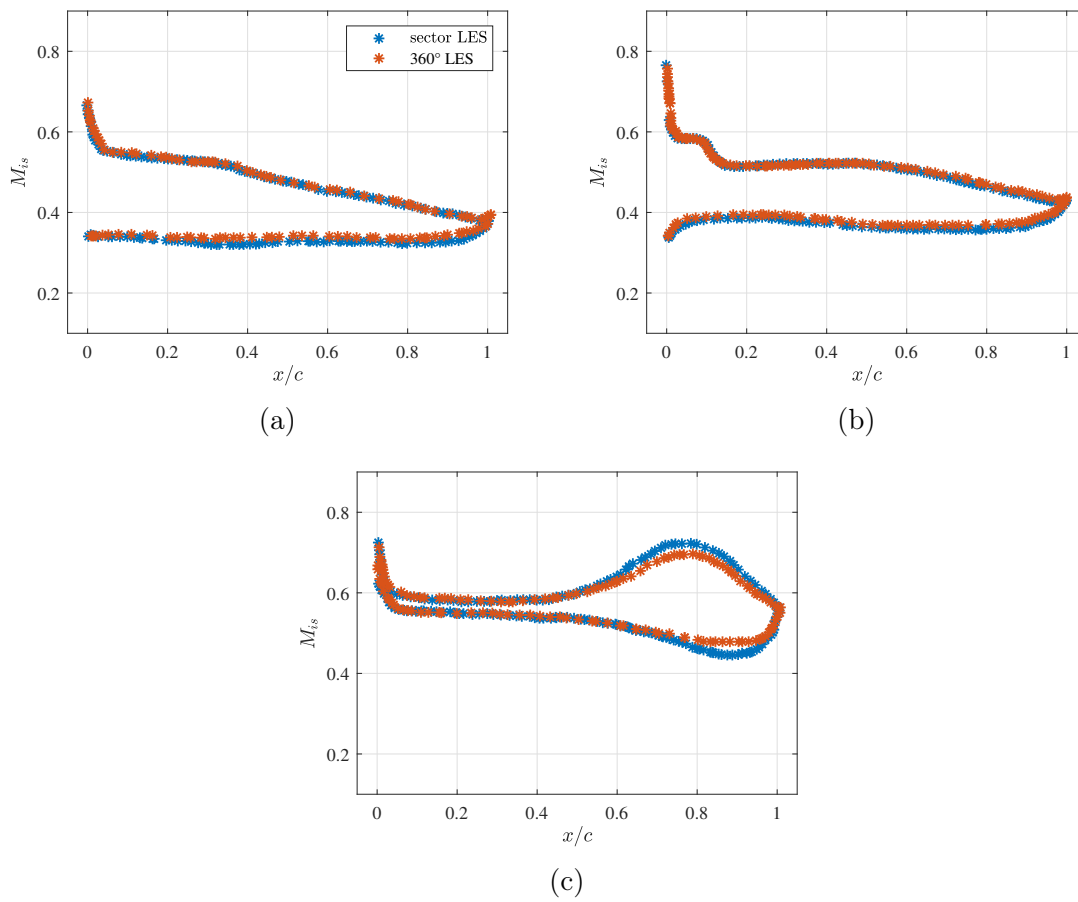
Figure 6.33: Comparison between the periodic sector LES and the 360° LES, for the prediction of the average isentropic Mach number around the fan blade, at (a) 50%, (b) 80% and (c) 98% of the rotor span.

(a)

(b)

(c)
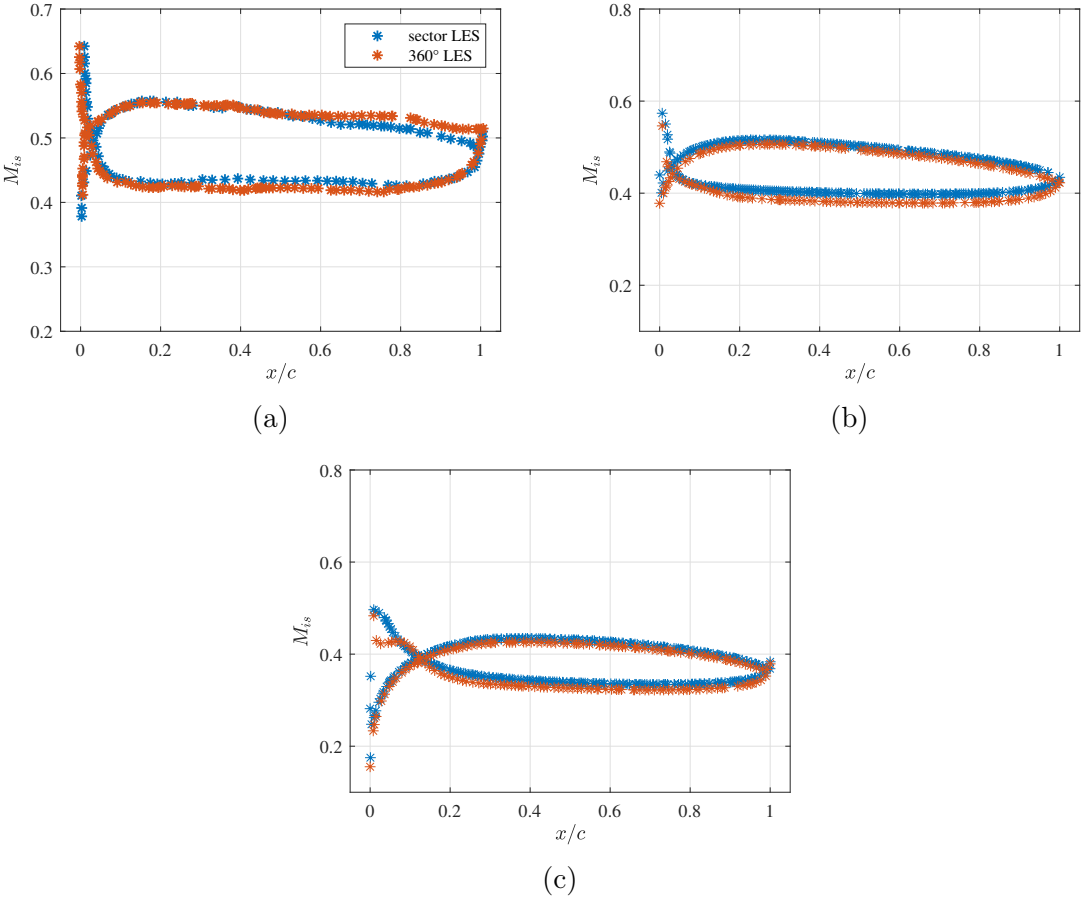
Figure 6.34: Comparison between the periodic sector LES and the 360° LES, for the prediction of the average isentropic Mach number around the stator vane, at (a) 50%, (b) 80% and (c) 98% of the stator span.
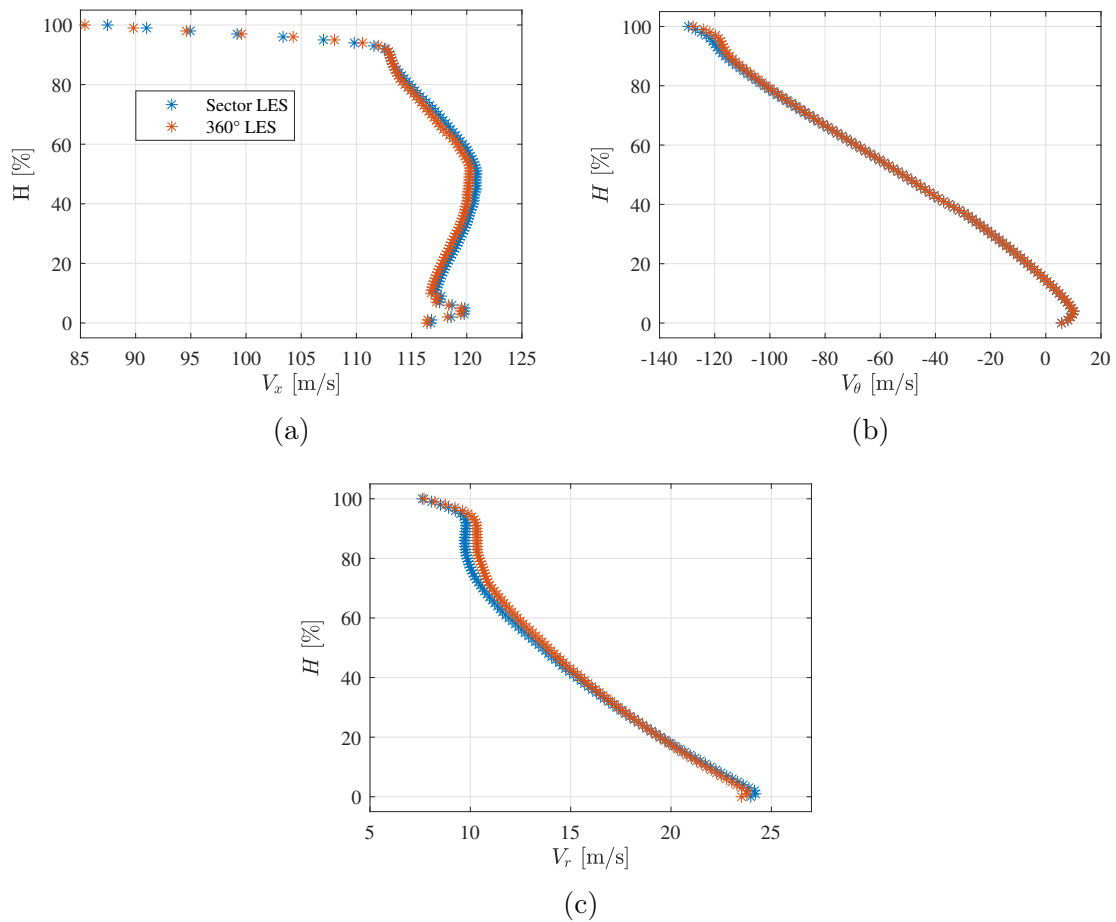
Figure 6.35: Comparison between the periodic sector LES and the 360° LES of the radial profiles of the velocity components in the interstage.

(a)

(b)

(c)
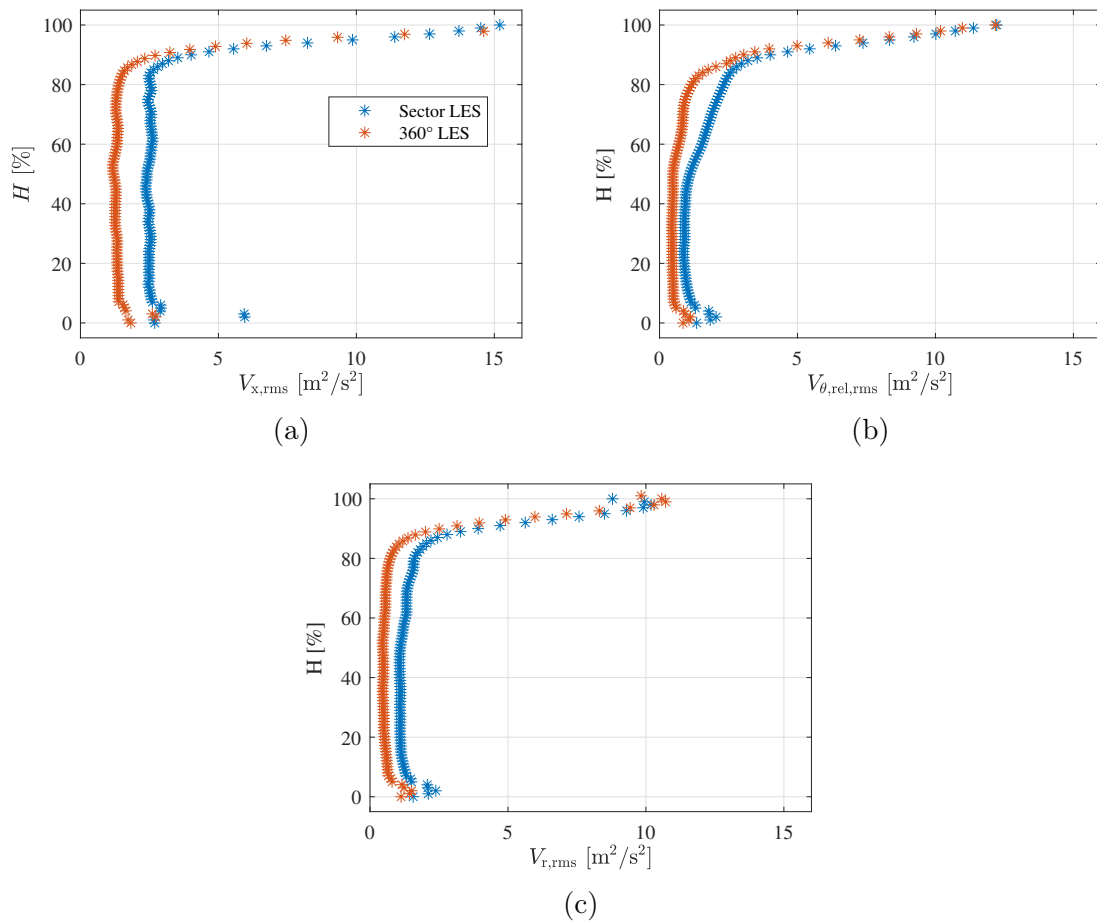
Figure 6.36: Comparison between the periodic sector LES and the 360° LES of the radial profiles of the RMS velocity fluctuations in the interstage.
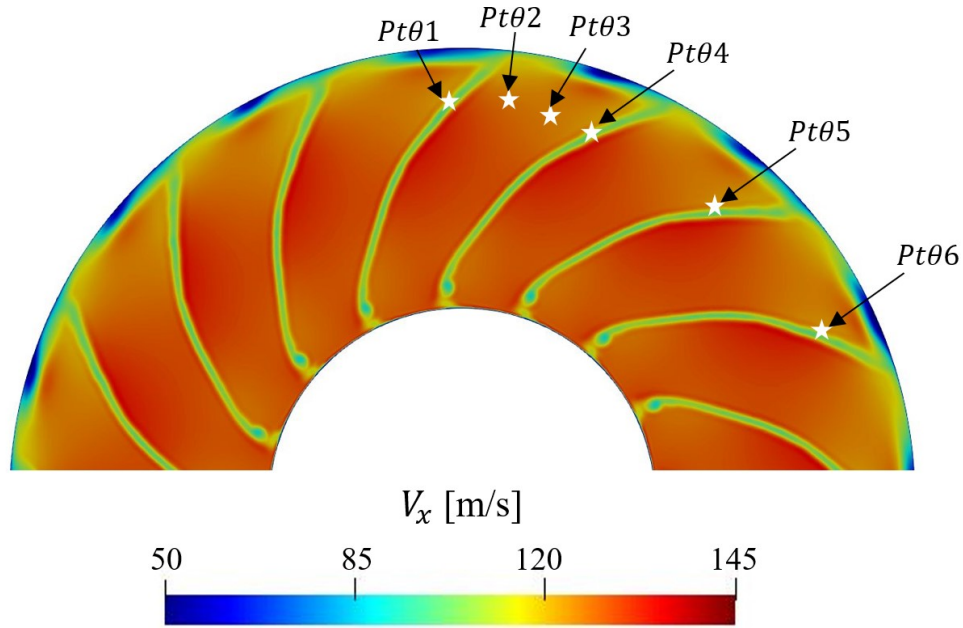
Figure 6.37: Contours of the axial component of the averaged velocity field in the interstage region, obtained from the 360° LES configuration. The star symbols indicate the monitor points used to compute the two-point coherences function in the azimuthal direction.
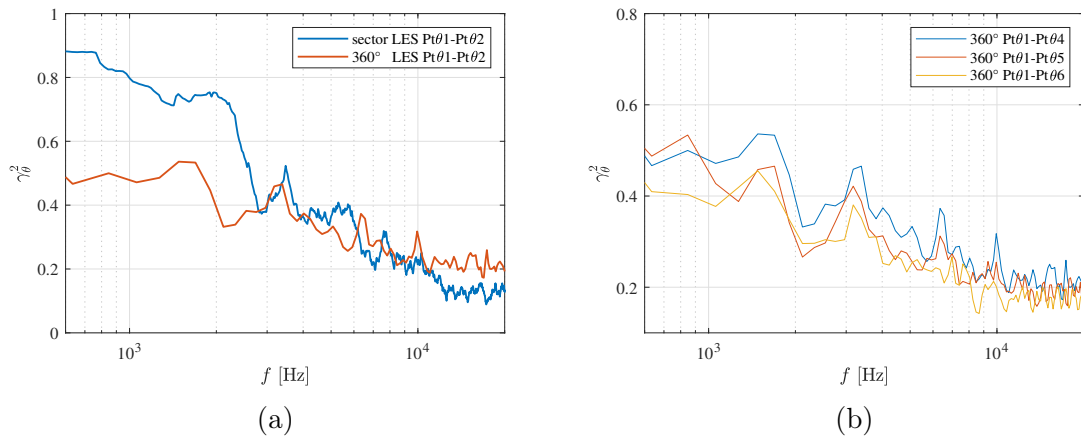
Figure 6.38: Coherence functions between two points at different azimuthal positions in the interstage. (a) Comparison between results from the periodic sector and the 360° LES configurations. (b) Comparison between different azimuthal distances, from the 360° LES configuration.
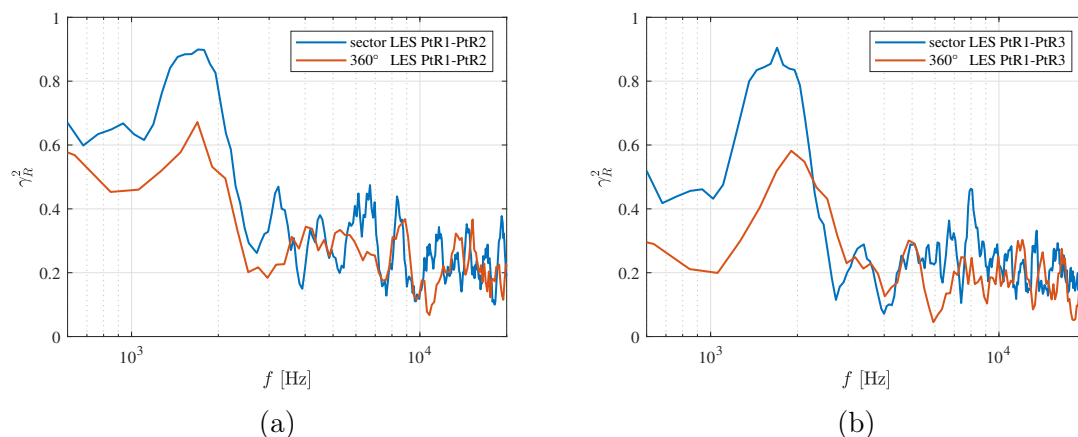
Figure 6.39: Comparison between the periodic sector LES and the 360° LES predictions of the coherence function, between two points at different radial positions downstream of the rotor.

decreases with the angular distance between the monitor points. At low frequency (below 1.5kHz), large coherence levels are obtained. The coherence quickly decreases with the frequency and reaches about 0.2. This means that the mid and high frequencies are not correlated. The coherence does not reach 0 at high frequencies due to the limited computational time used to compute the coherence.

6.5.4 Radial coherence

The two-point coherence functions of the pressure fluctuations between monitor points (in the stator domain) at different radial positions γ_R (PtR1, PtR2 and PtR3, at 20%, 40% and 60% of the stator span, respectively), from the (full-span) sector and the 360° LES configurations, are compared in Figure 6.39 at one chord length downstream of the rotor. The coherence from the 360° LES is obtained by averaging the pressure signal over 16 azimuthal positions. For both configurations, tones at the BPF and its harmonics are observed. For the 360° LES configuration, smaller coherence levels are obtained, compared to the periodic sector LES, particularly at low to mid frequencies. This can be explained by the suppression of the artificial correlation induced by the periodic boundary conditions in the azimuthal direction, and converted in the radial direction by the flow structures.

6.5.5 Modal decomposition - Preliminary results

One of the main advantages of the (full-span) 360° LES, compared to the (full-span) sector LES, is the ability to perform a complete azimuthal decomposition of the acoustic field radiated by the fan stage. However, at the time of redaction of this thesis, only one rotor rotation has been performed for the modal decomposition. Preliminary results are shown here and the analysis will only be qualitative. Quantitative results are expected subsequently to the thesis

The azimuthal modal contents at the intake and exhaust sections are presented in Figure 6.40, at 95% of the rotor span. 200 azimuthal monitor points at one rotor chord length upstream of the rotor and one stator chord length downstream of the stator are
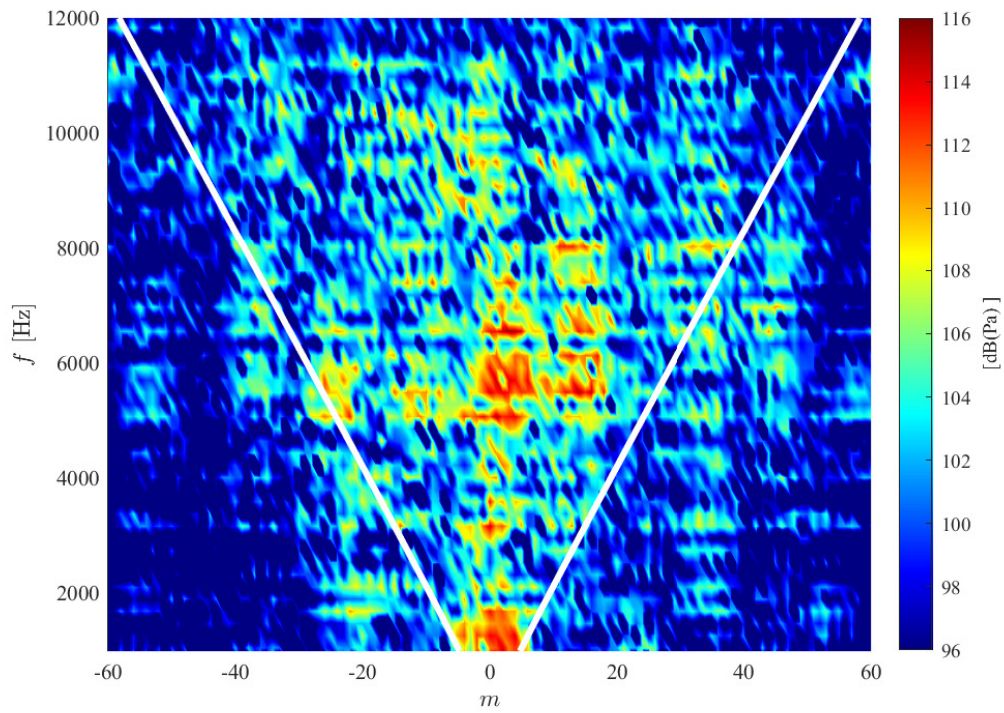
(a)
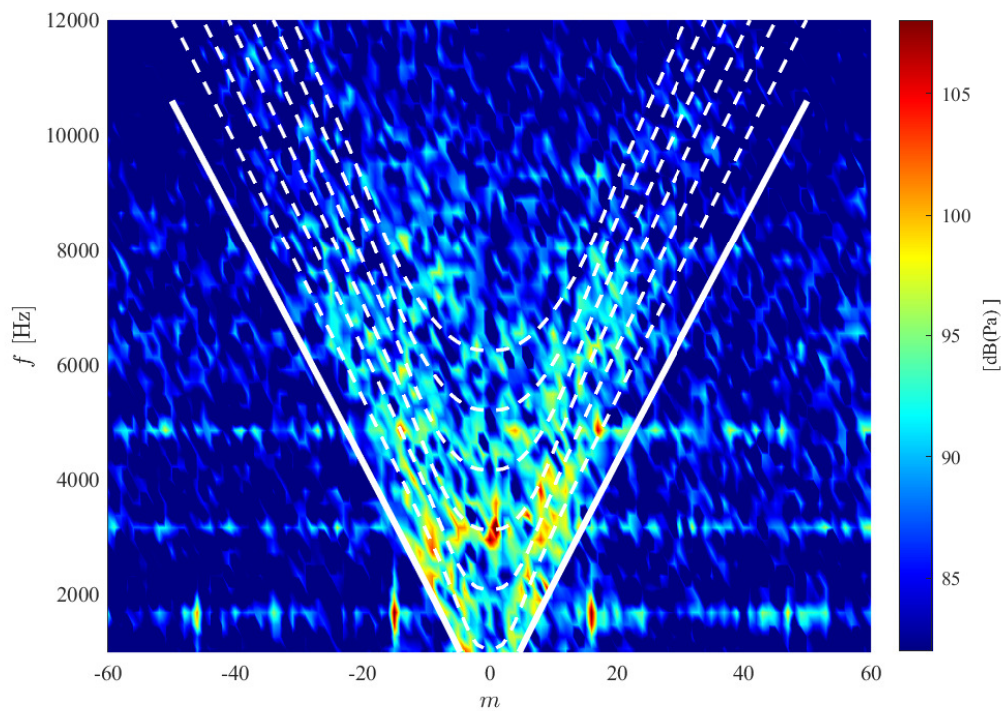
(b)

Figure 6.40: Azimuthal mode detection plots at the (a) intake and (b) exhaust sections. The frequency is plotted against the azimuthal mode order m, and the modes are colored by their amplitude. Preliminary results.
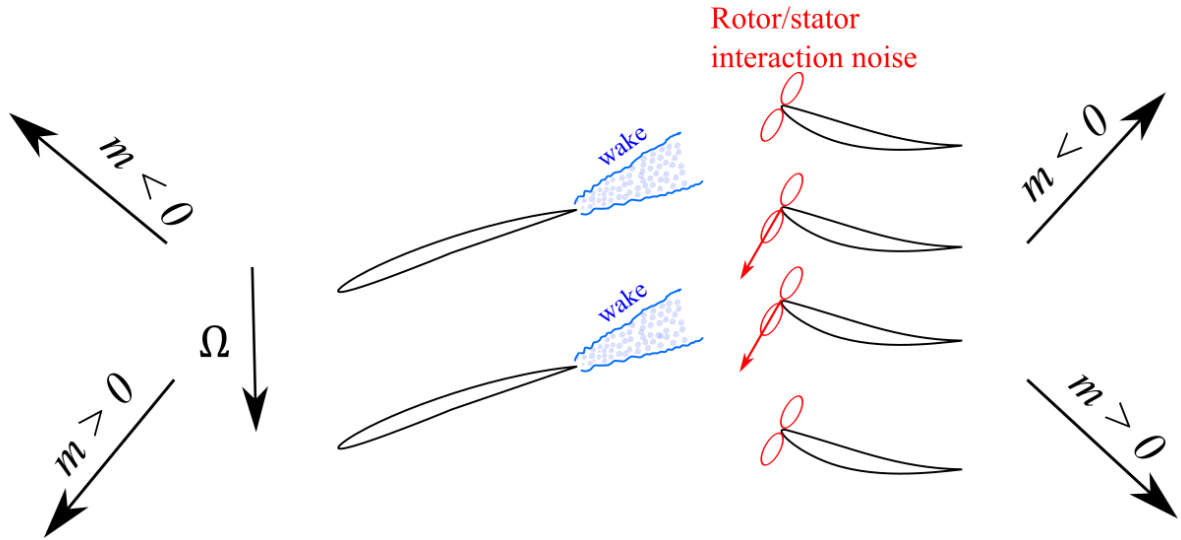
Figure 6.41: A blade to blade schematic view of the fan/OGV stage illustrating the equivalent dipoles of the rotor-stator interaction noise on the leading edge of the stator vanes. The picture shows two rotor blades and four stator vanes. The direction of rotation is represented by the Ω arrow. The direction of co- and counter-rotating modes propagating upstream or downstream of the stage are also depicted.

used (the different monitor points are presented in Appendix E). The white solid line corresponds to the theoretical cut-off frequency of each azimuthal mode of order m for the first radial mode, $j = 0$, in an annular duct, as detailed in Chapter 1, and given by:

$$\omega_c = c_0 \beta K_{mj}, \qquad (6.13)$$

where K_{mj} is the Eigenvalue of the duct mode (m,j) and $\beta = \sqrt{1 - M^2}$ is the compressibility parameter. The white dashed lines correspond to the cut-off frequencies of the radial modes of orders ranging from $j = 1$ to $j = 6$.

Over the whole range of azimuthal modes, large modal amplitudes can be observed at the BPF and its harmonics. Moreover, The modal amplitudes are concentrated in the mode-frequency cut-on triangle, as expected (inside the V-shape delimited by the solid white lines). The cut-off modes are thus well attenuated, particularly at the exhaust section.

At the intake section (Figure 6.40 (a)), the modal content is seen to be slightly dominated by co-rotating modes ($m > 0$, which rotate in the same direction as the rotor). This co-rotating mode distribution was also observed experimentally on a fan stage at approach condition [194] and was related to the rotor-stator interaction noise source at the stator leading edge. This can be explained by observing the direction of the dipolar sources corresponding to the rotor-stator interaction noise, as shown in Figure 6.41. It can be seen that the dipole main lobes of the rotor-stator interaction noise sources at the leading edges of the stator vanes are aligned with the direction of the mode propagation.

Unlike the intake modal content, no clear trend towards the co-rotating or counter-rotating modes can be observed at the exhaust section in Figure 6.40 (b). It can be noticed that the slope of the actual V-shape containing the cut-on modes is slightly steeper than the theoretical cut-on/cut-off boundary represented by the solid white lines. For some azimuthal orders m, large amplitudes are visible at frequencies corresponding to the cut-
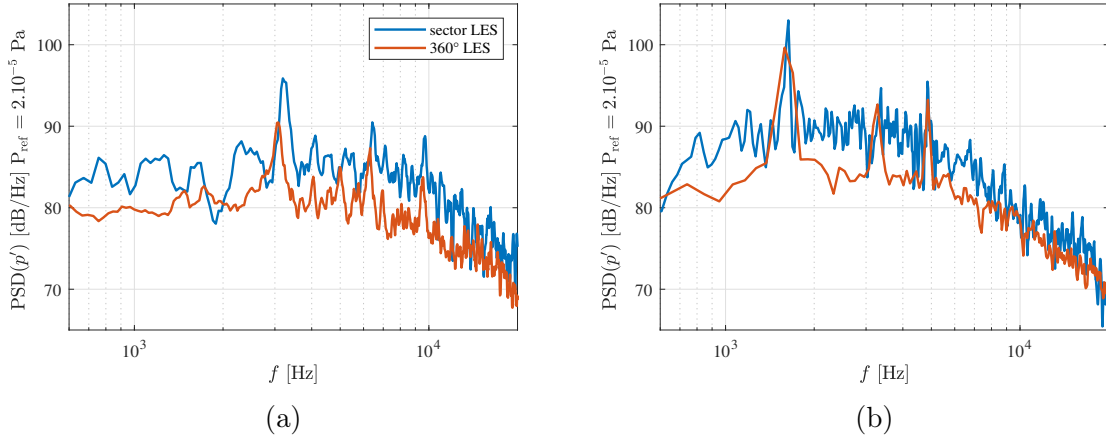
Figure 6.42: PSD of the pressure fluctuations at 95% of the span estimated from the periodic sector LES and the 360° LES at (a) the intake and (b) the exhaust sections.

off frequencies of the different radial modes (dashed lines in Figure 6.40). The azimuthal modes under the first dashed curve correspond to the first radial mode $j = 0$. At about 2 kHz, the radial mode $j = 1$ switch on, where large amplitudes can be observed. This behavior continues with more and more radial modes switching on.

A more quantitative analysis is expected subsequently, with a better convergence of the modal decomposition.

6.5.6 Far-field noise predictions

Figure 6.42 presents a comparison of the power spectral density (PSD) of the pressure fluctuations estimated from the (full-span) periodic sector LES and the 360° LES configurations using direct noise propagation in LES at 95% of span. At the intake section, the PSD is computed in the rotating frame, whereas at the exhaust section it is computed in the stationary frame. The PSD from the 360° LES are obtained by averaging over 16 azimuthal positions. Since the vane count is different between the two configurations (32 for the periodic case and 31 for the 360° configuration), the vane passing frequency (in Figure 6.42 (a)) is lower for the 360° LES (3126 Hz) compared to the periodic sector LES (3226 Hz). Lower PSD values are obtained from the (full-span) 360° LES, compared to the (full-span) sector LES, over the whole frequency range at both the intake and the exhaust sections. This noise reduction is related to (i) the reduced RMS velocity fluctuations in the wake region (as seen in Figure 6.36), which would lead to lower amplitudes of the rotor stator interaction noise, (ii) the reduced coherence levels within each sector and between the different sectors (as shown in Figures 6.39 and 6.38) and (iii) the smaller vane count (31 instead of 32). Further convergence of the (full-span) 360° LES will help to discriminate between those effects.

Comparison between the sector and 360° LES: effects of imposed periodicity ———————————————————————— **Summary**

The (full-span) sector LES and the (full-span) 360° LES have been compared.

Instantaneous and mean quantities

- As for the periodic sector LES, the 360° LES shows a good transition of the boundary layers all along the span of the blades and vanes. Downstream of the transition, small turbulent structures are observed.

- The isentropic Mach number shows similar results between the two configurations, except in the rotor blade-tip region, where a slightly smaller pressure difference is obtained by the 360° LES, from $0.4c$ down to the trailing edge.

- Similar radial mean velocity distributions are observed from both configurations.

- Smaller RMS velocity fluctuations are observed in the 360° LES.

Coherence

- Smaller azimuthal and radial coherence levels are observed in the 360° LES at low and mid frequencies.

- The coherences do not vanish at high frequencies, probably due to the limited computational time used to compute the coherences.

Modal content - Preliminary results

- The modal amplitudes are mostly located in the mode-frequency cut-on triangle.

- At the intake section, the modal content is slightly dominated by co-rotating modes.

- At the exhaust section, for some azimuthal orders m, large amplitudes are visible at frequencies corresponding to the cut-off frequencies of the different radial modes.

Far-field sound power level

- Lower PSD levels are obtained in the 360° LES, both upstream and downstream of the fan/OGV stage, compared to the periodic sector LES, over the whole range of frequencies.

6.6 Conclusions

In the present study, two broadband noise mechanisms in an UHBR fan/OGV stage have been investigated at approach conditions, using high-fidelity LES and analytical models. The mesh is carefully refined to meet both turbulent requirements, especially in the boundary layers and wakes, and acoustic requirements, away from the walls, which allow for a direct computation of the noise from the LES in the fan stage.

Several mean and turbulent flow quantities obtained from the LES have been compared to a RANS simulation of the same configuration. The aerodynamic results show a good agreement between both numerical approaches, except in highly turbulent regions such as near the blade tip, the corner separation near the blade hub, and the recirculation bubble region. The latter extends from 60% to 90% of the rotor span and is only observed in the LES.

Sound power levels deduced directly from the LES are compared with LES-informed analytical models. The input data for the models are obtained from the LES. Two analytical models are used for the rotor-stator interaction noise: Hanson's model [93] and Posson's model [209, 207]. Different approaches are used to estimate the turbulence length scale upstream of the stator leading edge. Similar trends are obtained with the two approaches relying on the LES data: Jurdic's model [114] and the autocorrelation function, associated with Taylor's frozen turbulence assumption [204, 114]. The turbulence velocity spectrum of the streamwise velocity component is also extracted from the LES and compared to Liepmann's model [205].

The analytical trailing-edge noise model used in this study is based on Amiet's work [9, 223] and describes the scattering of pressure fluctuations from an incident boundary layer at a sharp trailing edge. The main input parameters of this model are the wall pressure spectrum and the spanwise correlation length. Each of these parameters is extracted from the LES on the suction side of the rotor blades and stator vanes, close to the trailing edges, and is fitted with empirical models from the literature, for which the input data are also taken from the LES. The wall pressure spectrum is fitted with Rozenberg's model [229], which includes the effects of the Reynolds number and the adverse pressure gradient. When the direct LES spectrum is compared to the spectrum predicted by Rozenberg's model at the rotor mid-span, a good match is found with slightly larger values for the model at mid to high frequencies. The spanwise correlation length is fitted with the model of Salze *et al.* [234] and the results from both the LES and Salze's model are compared at the rotor and stator mid-spans. On the rotor surface, a good agreement is obtained at mid to high frequencies. On the stator surface, both the wall pressure spectrum and the spanwise correlation length exhibit larger values in the LES compared to the empirical models.

The predictions using the rotor-stator interaction noise and the trailing-edge noise analytical models underestimate the total noise when compared to the LES results, over the whole frequency range. This suggests the presence of additional noise sources in the LES, such as the tip leakage noise and the corner separation noise, that are not reproduced by these analytical models. To characterize the contribution of each mechanism in the LES, the blade is split into two parts and the Ffowcs Williams and Hawkings (FWH) [276] acoustic analogy is used over each part. The tip leakage noise is seen to particularly dominate at mid to high frequencies (beyond 2 kHz), whereas the corner separation noise contributes at low frequencies (below 2 kHz).

Finally, the influence of the periodic boundary conditions on the flow topology and

noise emissions is investigated by comparing the (full-span) sector and 360° LES configurations. The boundary-layer transition and mean velocity components show similar results for both configurations. Some differences are found for the RMS velocity fluctuations in the rotor wake region, with lower values in the 360° LES. The 360° LES also predicts smaller coherence levels, particularly at low to mid frequencies. The well-refined 360° configuration allows us to analyze the acoustic modal content in the fan stage. Due to the lack of sampling time for the modal decomposition, only preliminary results are presented. At the inlet section, the modal content is slightly dominated by co-rotating modes. At the exhaust section, high modal amplitudes are observed at frequencies where additional radial modes become cut-on. The PSD of the pressure fluctuations are also compared between the two configurations. The 360° configuration shows lower levels over a large range of frequencies.

> **Note**
>
> A part of the results of this Chapter were presented at the 28th AIAA/CEAS Aeroacoustics Conference in 2022 [2].

Conclusions and perspectives

Conclusions

PhD thesis objectives

The main objective of this PhD thesis was the investigation of the dominant noise mechanisms of a modern aero-engine fan stage, at approach condition, using large-eddy simulations (LES). The different noise mechanisms studied in this work are the following.

- Rotor-stator interaction noise. This noise mechanism is located at the stator leading edge. It is generated by the interaction of the rotor wakes with the stator vanes.

- Trailing edge noise. This noise mechanism is generated by the diffraction of the turbulent boundary layers at the trailing edges of the blades and vanes.

- Laminar separation noise. This noise mechanism is generated by the formation of a recirculation bubble close to the leading edge of the rotor, at partial operating conditions.

- Tip gap noise. This noise mechanism is generated by the interaction of the tip vortices with the rotor blades.

Another objective was the definition of a set of generic guidelines and best-practices for the numerical setup of LES in order to perform high-fidelity simulations that are able to model both the turbulent flow and the acoustic propagation in a fan stage. These guidelines rely on a parametric study that was conducted during the PhD.

PhD thesis methodology

This study was divided into 2 main steps that are presented below.

- The first step focused on a parametric study that included several LES numerical parameters for a flat plate configuration and a comparison with analytical models.

- The second step used the optimal numerical setup that had been previously validated to perform a number of LES on a fan/OGV stage. To this end, three configurations of increasing complexity and computational cost were considered.

  - The first configuration corresponds to a radial slice of a periodic sector of the fan stage, which contains one fan blade and two OGVs.

- The second configuration corresponds to a (full-span) periodic sector of the fan stage.

- The third configuration corresponds to the (full-span) 360° configuration with all the blades and vanes.

Noise prediction techniques

- LES-informed analytical models. The input data for the analytical models have been extracted from the LES computations. This approach has been used for the prediction of the rotor-stator interaction noise and the trailing edge noise.

- Hybrid numerical approaches. The computation of the aerodynamic sources and the noise propagation step are decoupled. This approach is based on the coupling of a LES with the acoustic analogy of Ffowcs Williams & Hawkings [277]. It has been mainly used to separate the contributions of the different noise mechanisms in the fan stage.

- Direct noise computation. LES has been used in the current study to compute both the flow field and the noise propagation in the fan stage. This method requires a specific numerical setup, particularly a well refined mesh and a sufficiently precise numerical scheme. This leads to a relatively high computational cost. Since it relies on less assumptions than the other noise prediction techniques used in this work, this method is considered as the most accurate one. This approach has been used for the prediction of the different noise mechanisms studied in this PhD thesis.

Main results of the parametric study

In this phase, the main noise mechanisms have been investigated separately: trailing edge noise and turbulence interaction noise. The main results of the parametric study are summarized in the following.

- Boundary layer's transition.

  - Mesh type. A prismatic mesh leads to a better boundary layer transition than a tetrahedral one.

  - Near wall refinement. For WM-LES, a value of y^+ of 25 is seen to be appropriate.

  - Trip properties. A trip height equal to 4 times the boundary layer displacement thickness and located at 10% of the chord length shows appropriate transition of the boundary layers.

- Spanwise correlation length. Periodic boundary conditions in the spanwise direction and a spanwise extent of 10% of the chord length have shown appropriate results when compared to empirical models.

- Noise propagation. In order to properly propagate the acoustic waves in the fan stage, 13 cells per acoustic wavelength are required for the specific numerical setup adopted in this study (particularly for the third-order numerical scheme TTGC).

Based on the results of this study, a pre-dimensioning tool called LESCOTT has been developed. LESCOTT allows the user to determine the mesh size in each region of interest of the computational domain and provides a quick estimation of the computational time of LES for fan/OGV stage applications.

Main results of fan/OGV stage LES

In this phase, the different noise mechanisms have been studied separately.

- The laminar separation noise was particularly investigated using the radial slice sector LES configuration. High-frequency peaks in the noise spectra are associated with the recirculation bubble. The effects of the mass flow rate and angle of attack on the characteristics of the recirculation bubble and noise have been extensively studied. As the mass flow rate decreases, the size of the bubble increases, the bubble shifts towards downstream locations, and high levels of wall pressure fluctuations can be found along the suction side of the blade. The frequencies of the tones from the bubble decrease with the mass flow rate, and the amplitudes of the tones increase. The noise radiated at these tones is associated to a vortex shedding mechanism.

  The development of the boundary layer and the wake is influenced by the presence of a recirculation bubble and its size. For a low mass flow rate and a large recirculation bubble, both the boundary layer thickness on the suction side and the wake width increase. Consequently, the trailing edge noise and the rotor-stator interaction noise mechanisms are affected by the presence of a recirculation bubble.

- The tip gap noise was particularly investigated using the (full-span) sector configuration. A complex flow is observed in the blade tip region with several tip vortices; (i) a horse-shoe vortex (HSV) is present close to the leading edge of the blade, (ii) a first tip leakage vortex (TLV1) is generated at about 25% of the chord length, (iii) a tip separation vortex (TSV) and a second tip leakage vortex (TLV2), alongside with an induced vortex (IV), are formed at approximately 70% of the chord length. These vortices are characterized by reduced streamwise velocities but large values of the velocity fluctuations, vorticity magnitude, and turbulent kinetic energy.

  A significant noise source is observed in the tip gap region at the trailing edge, associated with two main humps in the wall pressure spectra (WPS) in the blade tip region. The first hump is related to the interaction of a part of the TLV1 generated at one blade with the trailing edge of the adjacent blade, and the second hump to the interaction of the tip vortices TLV2, TSV and IV generated at one blade with the trailing edge of the same blade. The contribution of the tip gap noise to the far-field noise is also seen in the frequency range of the two WPS humps.

- The rotor-stator interaction noise and the trailing edge noise mechanisms were particularly studied using the (full-span) sector LES configuration. Some comparisons were also made with results from the (full-span) 360° LES. The unstructured grid is well refined for direct noise propagation. The broadband noise from the (full-span) sector LES configuration has been directly computed from the fully-compressible LES solver and compared with predictions from available analytical models. The input data for the analytical models, such as mean and turbulent flow statistics, has been obtained from the LES computation. A good agreement is found for the

predicted sound power levels between direct LES noise predictions and the LES-informed analytical models. However, some discrepancies can be observed that might be attributed to the additional noise sources that are present in the LES, and not considered by the analytical models. The contributions from some noise mechanisms have been evaluated using the Ffowcs Williams and Hawkings (FWH) acoustic analogy [276]. The corner separation noise is seen to mostly contributes at low frequencies, whereas the tip gap noise is revealed at mid and high frequencies.

In order to assess the impact of periodic boundary conditions on the flow field and noise emissions, a comparison between aeroacoustic results from the (full-span) sector and 360° LES configurations was finally presented. Furthermore, the azimuthal modal contents upstream of the rotor and downstream of the stator, which can only be estimated using the 360° configuration, were qualitatively analyzed using preliminary results.

Perspectives

The present study has shown the capability of several approaches to investigate noise mechanisms in a fan stage of future generation. It also made it possible to highlight some of the limitations of the adopted methods and identify some further analyses to be conducted in future works.

Prediction tools

- Broadband noise prediction using LES-informed analytical models. A way to increase the reliability of this approach is to use less stringent assumptions. Some of the possible improvements are listed in the following.

  - The classic infinite flat plate assumption could be replaced by a formulation that takes into account the camber and the thickness of the blades and vanes.
  - The free-field and in-duct propagation techniques only consider a mean axial flow while a swirled flow would be more realistic in the inter-stage region.
  - The in-duct propagation technique also considers an infinite duct of constant section, whereas a duct with a slowly varying cross-section would be more appropriate.
  - Accounting for the rotor shielding effect and the multiple reflections between the rotor and the stator could also enhance the model accuracy.

  The computational costs and the complexity induced by adding these features in the models must however be balanced with the gain of accuracy they induce so that this approach remains affordable and fast.

- Hybrid numerical approach. In the present study, the Ffowcs Williams & Hawkings (FWH) acoustic analogy [276] was used. Some improvements of the adopted approach are listed in the following.

  - The acoustic propagation is computed using the free-field Green's function. The FWH's acoustic analogy can be generalized to Green's functions taking into account an annular duct geometry.

– The noise is propagated in a uniform flow, which may induce some errors in the case of highly swirled flows. A swirled flow could thus be considered in the Green's function instead of a uniform flow.

– Only the blade surface is used for the computation of the noise sources. This approach is only valid for low Mach number flows. An improvement of this method relies on the use of a porous closed surface, which encloses all the acoustic sources. This extends the original FWH analogy to permeable control surfaces and allows to account for quadrupole sources.

Physical results

- Separation noise. The effects of a separation bubble on the fan noise emissions were studied in details upstream of the rotor blades using the radial-slice LES configuration. Some further analyses can be performed.

  – Some tones are also identified in the acoustic spectra downstream of the stator. The stator vanes may have important effects on the noise propagation. It is important to properly relate these tones to the noise emissions due to the recirculation bubble and to identify the influence of the stator.

  – The comparisons between WM- and WR-LES are limited to aerodynamic results. It may be interesting to investigate the influence of the WM on the noise signature of the recirculation bubble.

  – A WR-LES on the (full-span) sector configuration may be performed at a flow rate for which a large recirculation bubble is expected, with a significant noise signature. This would allow to study the contribution of the separation noise in a fan stage in presence of other more classical fan noise sources, such as tip gap noise and corner separation noise.

- Tip gap noise. The tip leakage flow topology and the tip gap noise have been studied in details using the (full-span) periodic sector LES configuration. A complex and highly turbulent flow is observed. The noise from each blade is partly generated by the interactions of the tip vortices from adjacent blades with the trailing edge of the blade. It may be interesting to study the influence of the periodic boundary conditions on the tip gap noise and particularly on the noise generated by these interactions, by comparing the results from the (full-span) periodic sector and 360° LES configurations.

- Impact of the periodic boundary conditions.

  – A more detailed comparison of both (i) the turbulent variables, such as the turbulence length scales in the rotor wakes and downstream of the stator, and (ii) the contributions of the different noise mechanisms, between the (full-span) sector and 360° LES configurations could be performed.

  – Once the unsteady recordings from the (full-span) 360° LES are sufficient, the modal content upstream of the rotor and downstream of the stator could be quantitatively analyzed.

Appendix A

The basis of Amiet's theory for flat plates

> **Introduction**
>
> This section presents the basis of Amiet's leading edge model for a single flat plate configuration. This model is used in Chapter 3.

Contents

A.1 The basis of Amiet's theory

In Amiet's model, the airfoil is assimilated to a flat plate with zero thickness, incidence and camber. Let's consider a chord length of $c = 2b$, and a span of $2d$ placed in a turbulent flow with a mean velocity magnitude U. The x axis is in the streamwise/chordwise direction, aligned with U, y is the crosswise direction and z the spanwise direction. The origin of the coordinates system is at the center of the airfoil. The turbulence upstream of the plate is assumed to be frozen and represented in terms of its spectral wavenumber components, k_x and k_z, as illustrated in Figure A.1. Only the normal component of the velocity fluctuations, v', contributes to the radiated noise generated when the flow interacts with the plate. This component, which is called the gust, can be written as,

$$v'(x, z, t) = \int_{-\infty}^{+\infty} \int_{-\infty}^{+\infty} \hat{\hat{v'}}(k_x, k_z) e^{i(k_x x + k_z z - \omega t)} dk_x dk_z \tag{A.1}$$

where ω is the angular frequency given by $\omega = k_x U$ (due to the frozen turbulence assumption) and $\hat{\hat{v'}}$ is the spatial double Fourier transform of v'. Using this spectral description
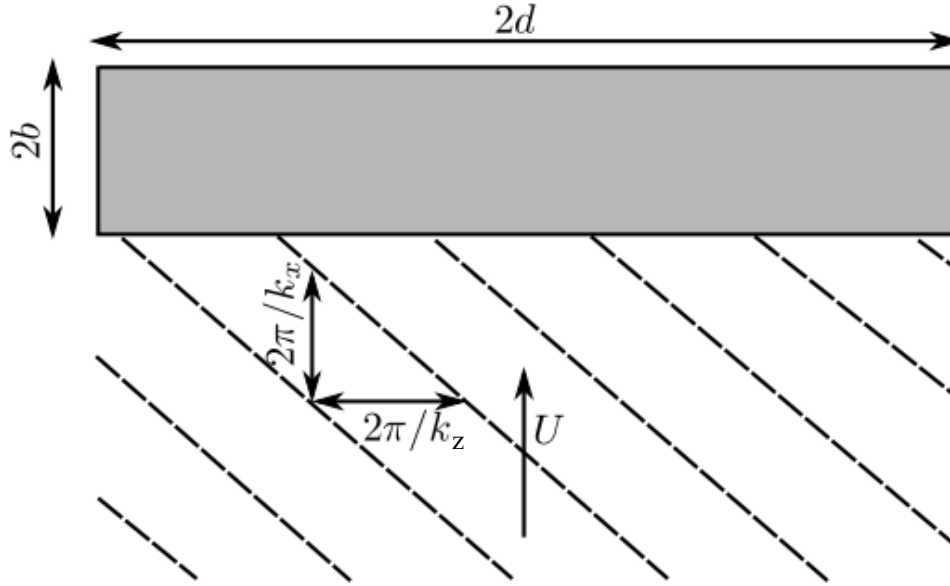
Figure A.1: Schematic view of a single skewed gust sweeping over an airfoil.

of the incident velocity fluctuations, the instantaneous response of the flat plate can be evaluated. The instantaneous pressure jump can be written as,

$$\Delta p'(x, z, t) = 2\pi \rho_\infty U \int_{-\infty}^{+\infty} \int_{-\infty}^{+\infty} \hat{\hat{v}}'(k_x, k_z) g(x, k_x, k_z) e^{i(k_x U t - k_z z)} dk_x dk_z \qquad (A.2)$$

where $g(x, k_x, k_z)$ is the transfer function between the impacting gust and the airfoil pressure jump. This function can be obtained by iteratively solving scattering problems at the airfoil edges [190]. The main leading edge scattering is obtained by assuming that the airfoil extends toward infinity in the downstream direction. It is then corrected by a trailing edge back-scattering contribution, to account for the finite chord length of the plate. The system of partial differential equations that arise at each iteration in this multiple scattering problem is solved using Schwarzschild's solution [220]. As a result, the transfer function g is obtained as the sum of the two contributions, the diffraction at the leading-edge g_1 and the correction at the trailing-edge g_2 , with $g = g_1 + g_2$.

The acoustic response of the airfoil subject to incoming turbulence involves the radiation of spanwise and chordwise distributed dipoles on the airfoil surface. Let us consider the coordinates of the observer defined as $x = (x, y, z)$ and the local coordinates on the airfoil surface defined as $x_0 = (x_0, y_0, z_0)$. The local system of coordinates is located at the center of the airfoil, with $y_0 = 0$ as the airfoil surface is infinitively thin and aligned on the (x, z) plane. The sound radiation of a single dipole placed on the airfoil for a particular angular frequency ω (and wavenumber $k = \omega/c_0$, c_0 being the speed of sound) is given by [48],

$$p(x, v; x_0) = \frac{ikx_t.\hat{F}(x_0, v)}{4\pi\sigma_s^2} e^{-ik\sigma_t} \left(1 + \frac{1}{ik\sigma_s}\right) \qquad (A.3)$$

where $\sigma_s = \sqrt{(x - x_0)^2 + \beta^2((z - z_0)^2 + y^2)}$, $\beta = \sqrt{1 - M^2}$, $M = U/c_0$ the Mack number, $x_t = (((x - x_0) - M\sigma_s)/\beta^2; y; z - z_0)$ the position of the receiver, taking into account convection effects, $\sigma_t = (\sigma_s - M(x - x_0))/\beta^2$ the propagation distance and $\hat{F}$ is the force vector in the Fourier domain, corresponding to the dipole strength. Note that the

factor $1/(ik\sigma_s$ corresponds to the acoustical near-field contribution, which only becomes significant when the distance from the receiver is of the order of magnitude of the acoustic wavelength. This term is neglected in the far-field Amiet's formulation. Then, the power spectral density of the radiated noise from the plate in the far-field will be given by,

$$S_{pp} = (\frac{ky\rho_\infty c}{2\sigma_s^2})^2 \frac{ULπ}{2} \int_{-\infty}^{+\infty} [\frac{sin^2(L/2(\frac{kz}{\sigma_s} - k_y))}{\pi L/2(\frac{kY}{\sigma_s} - k_y)^2}]L(x,k_x,k_z)^2\Phi_{vv}(k_x,k_z)dk_z \qquad (A.4)$$

where $L(x,k_x,k_z)$ is the total aeroacoustic transfer function calculated using the transfer function $g(x,k_x,k_z)$ and $\Phi_{vv}(k_x,k_z)$ is the turbulence spectrum of the normal velocity fluctuations. By making the assumption of an infinite span, one can obtain,

$$[\frac{sin^2(L/2(\frac{kz}{\sigma_s} - k_z))}{\pi L/2(\frac{kz}{\sigma_s} - k_z)^2}] = \delta(\frac{kz}{\sigma_s} - k_z) \qquad (A.5)$$

The integral will thus be removed. The power spectral density will finally be given (for an observer situated in the span medium plan $z = 0$) by,

$$S_{pp} = (\frac{ky\rho_\infty c}{2\sigma_s^2})^2 \frac{ULπ}{2} L(x,k_x,0)^2\Phi_{ww}(k_x,0) \qquad (A.6)$$

The same procedure is carried out for Amiet's trailing edge model [7]. Instead of considering a vortical velocity field impinging on the leading edge as an input gust, an incident aerodynamic wall pressure field is convected over the trailing edge. The disturbance pressure then acts as equivalent acoustic sources and the far-field pressure are calculated by means of a radiation integral. All the details of the derivation of this model can be found in [223].

A.2 Effects of the plate's thickness

The effects of the plate's thickness on the noise prediction by a turbulence interaction model based on the Amiet's theory have been addressed by many authors in the literature [190, 169, 185]. It is shown that the model over-predicts the emitted noise for thick airfoils. This over-prediction increases with the incoming velocity magnitude decrease and is more pronounced at high frequencies. Indeed, high frequencies are excited by statistically larger turbulent eddies when the mean flow speed increases, whereas the integral length scale of the incoming turbulence remains nearly constant with the flow speed. The thickness effects are expected to occur for eddies of the same order or smaller than the leading edge thickness. Consequently, the noise reduction due to thickness effects is delayed to higher frequencies when the flow speed increases.

By considering the difference between Amiet's theory for thin airfoils and the sound far-field measurements for various airfoil thicknesses in the same flow taken by different authors [190, 169, 185], a linear reduction can be noticed up to a certain reduced frequency, $f\zeta/U \approx 100$, where $\zeta = \frac{(\Lambda/e)_{ref}}{(\Lambda/e)}$, the index 'ref' standing for the NACA 0012 airfoil in Paterson and Amiet's [190] experiment taken as reference. The reduction Δ_{dB} is proportional to the relative thickness and inversely proportional to Λ_t/e (which is the ratio between the integral length scale Λ_t and the thickness e) and the flow speed U, with

the assumption of flow similarity. Δ_{dB} can be given by [169]

$$\Delta_{dB} \approx \frac{(e/c)}{(e/c)_{ref}} \frac{f}{U} \frac{(\Lambda_t/e)_{ref}}{(\Lambda_t/e)} \tag{A.7}$$

In order to reduce the thickness effects in the LES computation in Chapter 3, the flow speed and the plate's thickness are taken in a way to delay the effects of the thickness to frequencies not captured by the considered mesh.

B

LESCOTT pre-dimensioning tool

> **Introduction**
>
> LESCOTT stands for "Large Eddy Simulations COnfiguration Tool for Turbomachinery". LESCOTT is a pre-dimensioning tool for the LES setup in turbomachinery applications. It is based on the results of the parametric study performed in Chapter 2. LESCOTT allows the user to:
>
> - determine the mesh size in each region of interest of the computational domain (boundary layers, wakes, tip gap region, acoustic propagation regions) based on both turbulent and acoustic criteria, for a given numerical scheme and mesh topology (including dissipation and dispersion properties).
>
> - obtain a quick estimation of the computational time of LES for fan/OGV stage applications.
>
> This section presents the assumptions and the general methodology used in LESCOTT. An application on the ECL5 fan/OGV stage is also shown to predict the mesh size and the computational cost of the (full-span) periodic sector LES and the (full-span) 360° LES configurations.

Contents

B.1 Assumptions

In order to obtain a quick estimation tool for the mesh size and the computation cost of the LES, several assumptions are considered.

- The rotor blades and stator vanes are assimilated to symmetric flat plates.

- Turbulence is considered homogeneous and isotropic.

- The turbulence intensity is considered as a percentage of the mean velocity magnitude of the flow in each region of the domain.

- The integral length scale is considered of the order of an interblade distance.

B.2   Input parameters

The input parameters for LESCOTT, that are related to the rotor blades and stator vanes and their domains, are listed as follows,

- Flow properties.

  - Mach number and temperature of the flow.
  - Turbulent intensity in the tip region and in the wakes as a percentage of the freestream velocity magnitude.

- Geometric properties.

  - Chord and span length.
  - Interblade distance.
  - Position of the rotor and stator cascades.
  - Blade tip size.
  - Blade's and vane's count.
  - Domain length and radii of hub and the shroud.

- Mesh properties.

  - Desired mean values of the dimensionless wall distances, x^+, y^+ and z^+.
  - Number of prismatic layers.
  - Stretching ratio.

- Cut-off frequencies

  - Desired cut-off frequency of the acoustic spectra.
  - A multiplicative constant of the Taylor's micro-scale.

Some global input parameters are also prescribed:

- Performance of the cluster, defined as the number of iterations per hour per one calculating processor for a given mesh of 10^6 cells.

- Numerical scheme: LW [197] or TTGC [43].

- CFL number.

- Cluster: Newton, Occigen or Irene.

- Total number of rotations of the fan.

- Speed of rotation RPM.

- Periodicity angle (360° for a full stage).
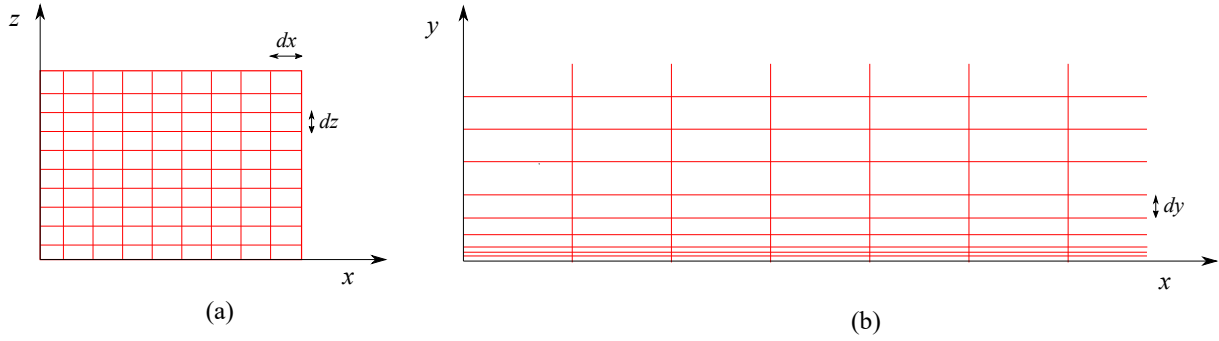
Figure B.1: Near wall mesh structure.

Table B.1: Wall mesh requirements for LES [266, 199, 3].

Parameter	WR-LES	WM-LES
dx^+	50-150	100-600
dy^+	1	20-30
dz^+	10-40	100-300
nb. layers	16-24	8-12
stretching ratio	1.03-1.06	1.1-1.15

B.3   Mesh generation

The computational domain is composed of different regions, presented below.

- Near wall region. The mesh size in this region is determined by the non-dimensional wall normal distances in the boundary layers of the rotor blades, the stator vanes, the hub and the shroud.

- Region away from the walls. This region is also composed of three parts, upstream of the rotor, in the interstage region between the rotor and the stator and downstream of the stator. In each region, the mesh should properly propagate the acoustic waves and correctly describe the turbulent wakes.

- Transition region between the near wall mesh and the volume mesh away from the walls.

- Rotor tip region.

B.3.1   Near wall mesh refinement

For a given cell count near the walls, Chapter 3 shows that prismatic cells give a higher accuracy in the prediction of the boundary layer characteristics than tetrahedral cells, in terms of velocity profiles and wall pressure fluctuating spectra. Consequently, prismatic cells are used on the walls of the rotor blades, the stotor vanes, the hub and the shroud.

Let N_{BL} be the near wall mesh count. N_{BL} can be estimated as the sum of the surface cells on the walls N_S and the prismatic cells in the vicinity of the walls N_P. N_S is determined using the axial and spanwise dimensionless wall distances (x^+ and z^+) and N_P using the normal wall distance (y^+). Using the CentaurSoft to generate the mesh, the axial and spanwise wall distances should be equal ($\Delta x = \Delta z$). The values that should

255

prescribed for $x^+ = z^+$ and y^+ depend on the type of the LES computation, whether it is a Wall-Resolved (WR) LES or a Wall-Modeled (WM) LES and are recalled in Table B.1. For WM-LES, the accuracy of these values is assessed in Chapter 3. Using these values, the wall normal distances on the walls can be given as,

$$\Delta y = \frac{y^+ \nu}{u_\tau}, \tag{B.1}$$

where ν is the kinematic viscosity and u_τ is the friction velocity, given as,

$$u_\tau = \sqrt{\frac{\tau}{\rho}}, \tag{B.2}$$

where ρ is the density of the fluid and τ is the shear stress, given as,

$$\tau = 0.5 \rho U_0^2 C_f, \tag{B.3}$$

where U_0 is the mean velocity magnitude of the free-stream flow and C_f is the friction coefficient. C_f is estimated using the law of Michel cited in [17, 45]. The laws of Michel are derived from a $1/7^{\text{th}}$ power law velocity profile (see Schlichting [243]) with coefficients tuned to better match experimental data. C_f is then given as,

$$C_f = 0.0368 Re_c^{\frac{1}{6}}, \tag{B.4}$$

where Re_c is the chord based Reynolds number.

The normal distance of the prismatic cells progressively increases in the y-direction (Figure B.1 (b)) with a typical stretching ratio given in Table B.1 for WR- and WM-LES. The number of prismatic layers in the y-direction (N_{prism}) is then chosen in a way to ensure that the boundary layers are contained in the prismatic region. Typical values are given in Table B.1 for WM- and WR-LES.

Δ_x and Δ_z can then be obtained as,

$$\Delta_x = \Delta_z = \Delta y \frac{x^+}{y^+}. \tag{B.5}$$

The number of points on the surfaces can then be estimated by,

$$N_S = N_{S,Sh} + N_{S,H} + N_{S,B} + N_{S,V}, \tag{B.6}$$

where

$$N_{S,Sh} = L_{Sh} * 2\pi R_S h / d_{x,Sh}^2$$

is the number of cells on the surface of the shroud,

$$N_{S,H} = L_{Sh} * 2\pi R_H / d_{x,H}^2$$

is the number of cells on the surface of the hub,

$$N_{S,B} = 2 * c_B * Sp_B / d_{x,B}^2 * N_B$$

and

$$N_{S,V} = 2 * c_V * Sp_V / d_{x,V}^2 * N_V$$

are the number of cells on the surfaces of the blades and the vanes. L and R are the length and the radius of the shroud (subscript Sh) and the hub (subscript H). c, Sp and N are the chord length, the span and the blade or vane count, and the subscripts B and V refer to Blade and Vane, respectively. The factor 2 in $N_{S,B}$ and $N_{S,V}$ accounts for the two sides of the blades and the vanes.

The number of prismatic cells can then be deduced by,

$$N_P = N_S * N_{\text{prism}}. \tag{B.7}$$

B.3.2 Mesh refinement away from the walls

The mesh refinement away from the walls is based on both turbulent and acoustic criteria.

- Turbulent criterion. The LES subgrid scale models, presented in Chapter 1, are developed to properly operate in the inertial zone of the Kolmogorov energetic cascade. This means that the mesh size should ensure a cut-off frequency of the LES that lies within the inertial region of the turbulent spectrum. This region is usually characterized by the Taylor micro-scale λ_{Ta}. The quality of the simulation directly depends on the cell size with respect to λ_{Ta}.

  The Taylor micro-scale can be estimated using the turbulent integral scale λ_t as,

  $$\lambda_{Ta} = \lambda_t Re_t^{-0.5} \tag{B.8}$$

  where Re_t is given as,

  $$Re_t = \frac{TI\lambda_t}{\nu} \tag{B.9}$$

  where TI is the turbulent intensity. λ_t is taken equal to the interblade spacing and TI equal to 5% of the freestream velocity magnitude.

  The mesh size required for this criterion can then be given as,

  $$\Delta x_{\text{turb}} = \frac{A\lambda_{Ta}}{C_{\text{Shannon}}N_{\lambda,\text{turb}}} \tag{B.10}$$

  where A is a constant, C_{Shannon} is the Shannon coefficient and $N_{\lambda,\text{turb}}$ accounts for the dissipation and dispersion properties of the numerical scheme. For Lax-Wandroff [197] second order numerical scheme, $N_{\lambda,\text{turb}}$ is taken equal to 26 and for TTGC [43] third order numerical scheme $N_{\lambda,\text{turb}}$ is taken equal to 15. According to Chapter 2, a value of $A = 30$ is adopted. This means that the mesh size is limited to 30 times the Taylor micro-scale λ_{Ta} to reduce the computational cost while providing a sufficiently good resolution for the turbulent structures. C_{Shannon} is taken equal to 2 in order to ensure that the Shannon's criterion is respected.

- Acoustic criterion. In order to properly propagate the acoustic waves over a certain distance in the fan stage, the mesh size should be correctly refined in the regions of interest.

  The acoustic propagation also depends on the numerical scheme, the mesh type and the artificial viscosity rate. In Chapter 3 a parametric study is performed using the TTGC [43] third order numerical scheme and for a given numerical setup and mesh type to identify the required mesh refinement. It is shown that $N_{\lambda_{ac}} = 13$ points
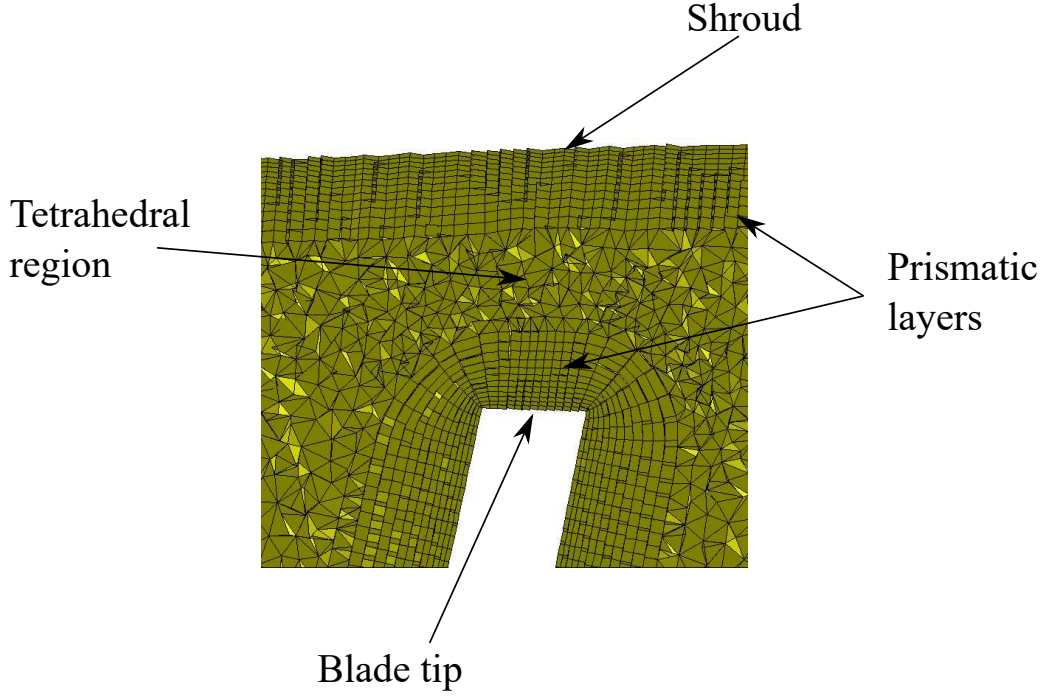
Figure B.2: Mesh structure in the blade tip.

per acoustic wavelength are required to accurately capture acoustic waves over a distance of $8c$ from the leading edge of the plate, and up to a frequency of 20 kHz. This corresponds to a distance of 47 acoustic wavelengths.

The acoustic wavelength λ_c also depends on the direction of propagation of the acoustic wave. The mesh size required for this criterion is then different whether upstream ($\Delta x_{ac,up}$) or downstream ($\Delta x_{ac,dw}$) propagating waves are considered and can be given as,

$$\Delta x_{ac,up} = \frac{c_0(1-M)}{C_{\text{Shannon}}N_{\lambda_{ac}}f_{\text{target}}}, \quad \Delta x_{ac,up} = \frac{c_0}{C_{\text{Shannon}}N_{\lambda_{ac}}f_{\text{target}}} \tag{B.11}$$

where c_0 is the speed of sound, M is a characteristic Mach number of flow in the region of interest and f_{target} is the desired cut-off frequency of the acoustic waves due to the mesh size. C_{Shannon} is taken equal to 2 in order to ensure that the Shannon's criterion is respected.

Tetrahedral elements are used in the regions away from the wall. Equilateral tetrahedral cells are considered and the volume of tetrahedron V_{tetra} can be given as,

$$V_{\text{tetra}} = \frac{\sqrt{12}}{3}L_{\text{tetra}}^3, \tag{B.12}$$

where L_{tetra} is the length of a side of the triangle. L_{tetra} is taken as the minimum between Δx_{turb} and Δx_{ac}.

The number of elements in a region of volume V_{region} is determined by,

$$N_{\text{tetra}} = \frac{V_{\text{region}}}{V_{\text{tetra}}}. \tag{B.13}$$

Table B.2: Performance of different clusters given in number of iterations per hour for a mesh of 10^6 cells.

Cluster	LW	TTGC
Newton	580	230
Occigen	585	235
Irene	600	250

B.3.3   Mesh refinement in the blade tip

In turbimachiney applications, the blade tip exhibits a highly turbulent complex flow. The mesh in this region should be sufficiently refined to properly resolve the small turbulent structures that may appear. As shown in Figure B.2, the mesh in this region is formed of two prismatic and one tetrahedral regions. The mesh size in the prismatic regions is determined by the near wall mesh refinement method described in Section B.3.1 and the tetrahedral region by the mesh refinement away from the wall method described in Section B.3.2.

In the blade tip region, the friction coefficient in Eq.B.3 is multiplied by 1.5 (as seen in Chapter 5) and the turbulent intensity is taken as 20% of the freestream velocity magnitude.

B.4   Computational cost

A quick estimation of the computational cost for LES in complex turbomachiney applications is an important task in the pre-processing step. The computational cost cost depends on the total number of cells in the computational domain N_{tot}, the total number of iterations to reach statistical and mean convergence N_{ite}, and the performance of the cluster perfo,

$$\text{cost} = N_{\text{tot}} \cdot N_{\text{ite}} \cdot \text{perfo} \tag{B.14}$$

N_{tot} is the sum of the mesh cells on the surfaces on the blades, vanes, shroud and hub, and away from the walls, as determined in Section B.3.

N_{ite} is determined in a way to reach a certain number of rotations of the fan n_{rot},

$$N_{\text{ite}} = \frac{60 \cdot n_{\text{rot}}}{RPM \cdot \Delta_t} \tag{B.15}$$

where Δ_t is the time step of the LES computation that is determined by the acoustic time and can be estimated using the CFL criterion as follows,

$$\text{CFL} = \frac{|U_0 + c_0|_{\text{max}} \Delta t}{\Delta x_{\text{min}}} = 0.7. \tag{B.16}$$

The performance of the cluster is an approximation of the mean efficiency of the cluster for one million mesh cells (in other terms, perfo is the number of iterations per hour per one calculating processor for a given mesh of 10^6 cells). For a given mesh type using TurboAVBP, the performance mainly depends on the cluster used and the numerical scheme. It is given in Table B.2 for two numerical schemes (LW [197] and TTGC [43]) and three clusters (Newton, Occigen and Irene).

Table B.3: Geometric parameters of the ECL5 configuration.

Parameter	Rotor	Stator
Mean chord [mm]	92	70
span [mm]	177.8	138
Mean interblade distance [mm]	64.8	38.2
Tip size [mm]	1.5	0.0
Blade/vane count	16	31

B.5   Application on the ECL5 fan stage

LESCOTT is used to determine the mesh size in each region of the computational domain and to estimate the computational cost of the (full-span) periodic sector LES and the (full-span) 360° LES configurations.

The input parameters and the output estimations are given in Tables B.3 and B.4. The optimal number of processors mainly depends on the mesh size. For TurboAVBP and for the specific mesh type, a ratio of 10^6 can be used between the total number of cells in the mesh and the optimal number of processors. The ratio between the required number of processors and the number of processors per node (28 for Occigen and 128 for Irene) should be an integer.

Table B.4: Input and output parameters.

	Parameter	(full-span) sector LES	(full-span) 360° LES
Flow parameters	Mach number	0.3	0.3
	Temperature [K]	300	300
	TI in the wakes [%]	5	5
	TI in the tip [%]	15	15
Mesh parameters	x^+	100	100
	y^+	25	25
	z^+	100	100
	Number of prismatic layers	12	12
	Stretching ratio	1.1	1.1
Cut-off frequencies	Constant A	30	30
	Acoustic cut-off frequency [kHz]	20	20
Global parameters	Performance	235	250
	Numerical scheme	TTGC	TTGC
	CFL	0.7	0.7
	Cluster	Occigen	Irene
	Number of rotation	10	10
	Rotation speed [RPM]	6050	6050
	Periodicity [°]	360	22.5
	Vane count	32	31
Output estimations	N_{tot} [10^6]	90	1400
	Δ_t [s]	$2.5 \cdot 10^8$	$2.5 \cdot 10^8$
	N_{ite} [10^6]	3.2	3.2
	cost [10^6] CPUh	1.2	20
	Number of processors	1036	15360
	Real time [months]	5.5	6.5

Assessment of the impact of the OGV rescaling

Introduction

For the radial slice and (full-span) periodic sector LES configurations, the original 16 blades and 31 vanes configuration of the ECL5 fan stage is modified to 32 vanes in order to be able to simulate one rotor blade and 2 stator vanes configuration and use periodic boundary conditions. This yields a significant reduction of the computational cost with respect to a full-stage LES.

This section is dedicated to the assessment of the impact of the OGV rescaling on the performance parameters and some radial distributions in the fan stage by comparing between 31 and 32 vanes configurations using RANS computations.

Contents

Table C.1: Fan-OGV stage pressure ratio obtained from the RANS simulations at approach condition.

	Pressure ratio	Isentropic efficiency [%]
Original	1.082	85.8
Rescaled	1.082	85.9

(a)

(b)

(c)
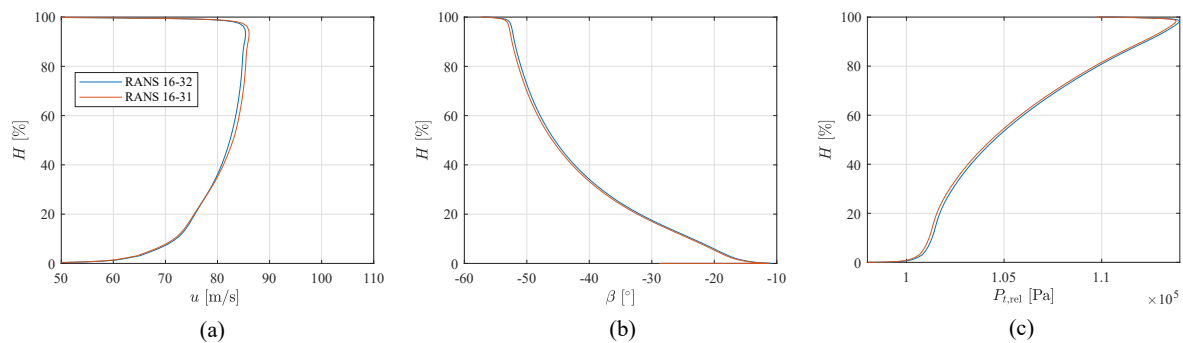
Figure C.1: Comparison between the original (16-31) and the modified (16-32) configurations of the radial distributions of averaged (a) absolute streamwise velocity u, (b) relative flow angle β and (c) relative total pressure $P_{t,\text{rel}}$, for $\dot{m} = 19$ kg/s, over an axial cut at one mid-span rotor chord length upstream of the rotor blades.

(a)

(b)

(c)
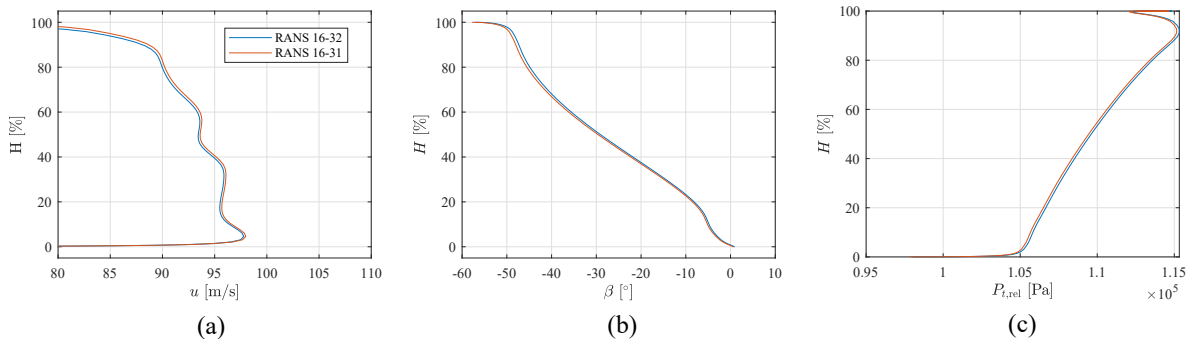
Figure C.2: Comparison between the original (16-31) and the modified (16-32) configurations of the radial distributions of averaged (a) absolute streamwise velocity u, (b) relative flow angle β and (c) relative total pressure $P_{t,\text{rel}}$, for $\dot{m} = 19$ kg/s, over an axial cut at 0.5 mid-span rotor chord length downstream of the rotor blades.
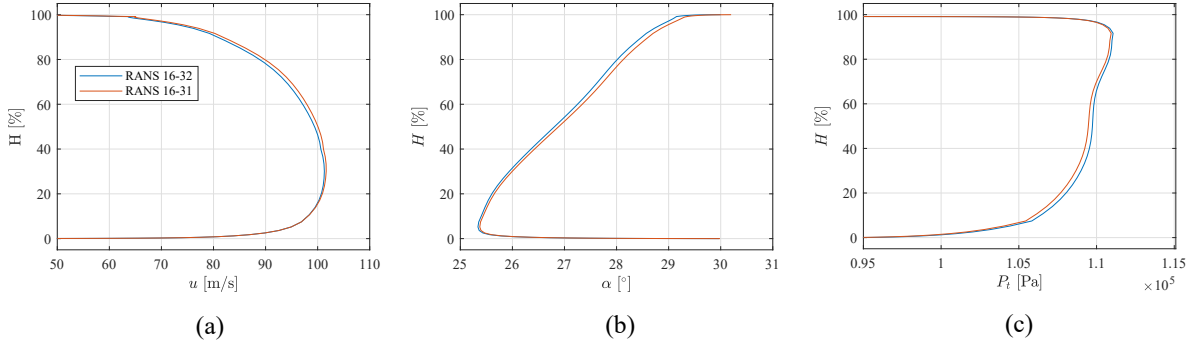
Figure C.3: Comparison between the original (16-31) and the modified (16-32) configurations of the radial distributions of averaged (a) absolute streamwise velocity u, (b) absolute flow angle α and (c) absolute total pressure P_t, for $\dot{m} = 19$ kg/s, over an axial cut at one mid-span stator chord length downstream of the stator vanes.

C.1 Performance parameters

For both the rescaled and the original configurations, the mass flow rate is prescribed at the outlet section. The fan/OGV stage pressure ratio and isentropic efficiency at approach condition (at 55Nn) for the original and rescaled configurations are presented in Table C.1. A relatively small mass flow rate ($\dot{m} = 19$ kg/s) is used for this comparison, where the highest discrepancies are expected to occur. As it can be noticed, the OGV rescaling has a negligible impact on the performance parameters.

C.2 Radial distributions

A comparison between the original configuration (16-31) and the modified one (16-32) for the radial distributions of the streamwise velocity, relative and absolute flow angles, and total pressure is presented in Figures C.1, C.2 and C.3 at a number of axial planes upstream of the rotor, between the rotor and the stator, and downstream of the stator, respectively. An averaging is performed in the azimuthal direction. A good agreement can be found for the different parameters, with slight discrepancies mainly downstream of the stator vanes.

Appendix D

Boundary layer thickness

> **Introduction**
>
> The prediction of the boundary layer thicknesses is seen to be an important step for the study of the effects of the recirculation bubble on the flow topology in the fan stage in Chapter 4 and for the modeling of the trailing edge noise using Amiet's trailing edge model [7] in Chapters 3 and 6.
>
> Several techniques are available to predict the boundary layer thicknesses. This section presents the most relevant ones, with the emphasis on those used in this work.

D.1   Estimation methods

For external flows over airfoils, the boundary layer thickness can be determined using techniques that start in the inviscid and undisturbed flow, and progressively approach the viscous layer based on a suitable criterion. Such methods are limited for turbomachinery applications since even the flow outside of the boundary layers is usually significantly disturbed and can exhibit velocity profile inversions. Consequently, several estimation processes of the boundary layer thickness based on criteria starting from the wall have been developed. The following sections present the most relevant ones.

The flow variables of interest are interpolated on the wall normal lines originating from each point of the considered surface. The different methods presented in the following are applied to estimate the boundary layer thickness and to obtain a mean thickness value that corresponds to an averaged value of the different estimates.

D.1.1   Velocity gradient based method

Boundary layers can be limited to the region where the flow encounters strong variation in the streamwise velocity component close to the walls. The streamwise velocity remains almost constant far from the walls. The boundary layer thickness can thus be estimated using methods based on the variations of the velocity profile in the direction normal to the walls. A profile point N is considered as the edge of the boundary layer if the following

relation is fulfilled.

$$\left| \left[\frac{\mathrm{d}u}{\mathrm{d}y} \right]_N \right| < \alpha, \quad \left| \left[\frac{\mathrm{d}u}{\mathrm{d}y} \right]_N - \left[\frac{\mathrm{d}u}{\mathrm{d}y} \right]_{N-1} \right| < \beta \tag{D.1}$$

where u is the streamwise velocity component, y is the wall normal direction, N and $N-1$ are consecutive profile points, $N-1$ being closer to the wall, and α and β are user-defined constants. For the boundary layer estimations in the present work, $\alpha = 0.01$ and $\beta = 0.0001$.

D.1.2 Stock-Haase method

To estimate the boundary layer thickness, Stock and Haase [256] defined a diagnostic function F defined as,

$$F = y^a \left[\frac{\partial u}{\partial y} \right]^b, \tag{D.2}$$

where a and b are constants.

The boundary layer thickness δ can be given as,

$$\delta = \epsilon_1 y_{\mathrm{max}}, \tag{D.3}$$

where ϵ_1 is a constant and y_{max} is the wall distance for which $F = F_{\mathrm{max}}$. The constants, a, b and ϵ_1 are evaluated by Colas [42] for a turbulent boundary layer and can be given as,

$$a = b = 1, \quad \epsilon_1 = 1.936. \tag{D.4}$$

D.1.3 Method based on the relative difference between the isentropic velocity and the velocity magnitude

The velocity magnitude is computed as,

$$U = \sqrt{V_x^2 + V_y^2 + V_z^2}, \tag{D.5}$$

where V_x, V_y and V_z are the velocity components in the three directions x, y and z.

The isentropic velocity is the velocity that would be obtained without any losses in the flow, including those induced by the frictions on the walls and can be computed as,

$$V_i = U_0 \sqrt{\frac{2}{(\gamma - 1)M_0^2} \cdot \left(1 - (0.5\frac{2(P - P_0)}{\rho_0 U_0^2}\gamma M_0^2 + 1)^{(\gamma-1)/\gamma}\right) + 1} \tag{D.6}$$

where P is the static pressure, P_0, ρ_0 and M_0 are the freestream pressure, density and Mach number, respectively.

The edge of the boundary layer is then defined as the first point from the wall that satisfies the following relation,

$$\frac{|U - V_i|}{U} < \epsilon_{V_i}, \quad \epsilon_{V_i} = 2.5 \cdot 10^{-3} \tag{D.7}$$

D.1.4 Method based the on relative difference between the isentropic Mach number and the actual Mach number

The isentropic Mach number M_{is} corresponds to the Mach number that would be observed without any losses in the flow, including those induced by the frictions on the walls, and is defined as follows,

$$M_{is} = \sqrt{\left(\left(\frac{P_0}{P}\right)^{\frac{\gamma-1}{\gamma}} - 1\right)\frac{2}{\gamma-1}} \tag{D.8}$$

The edge of the boundary layer should verify the following relation,

$$\frac{|M_{is} - M|}{M_{is}} < \epsilon_{M_{is}}, \quad \epsilon_{M_{is}} = 0.01. \tag{D.9}$$

D.2 Boundary layer thicknesses

Several boundary layer thicknesses can be computed.

- The displacement thickness δ_1 is the wall normal distance representing the lower edge of a hypothetical inviscid fluid of uniform velocity U_0 that has the same flow rate as occurs in the real fluid with the boundary layer. δ_1 is defined as,

$$\delta_1 = \int_0^\delta (1 - \frac{\rho U}{\rho_0 U_0})\mathrm{dn}. \tag{D.10}$$

- The momentum thickness δ_2 is the wall normal distance representing the lower edge of a hypothetical inviscid fluid of uniform velocity U_0 that has the same momentum flow rate as occurs in the real fluid with the boundary layer. δ_2 is defined as,

$$\delta_2 = \int_0^\delta \frac{\rho U}{\rho_0 U_0}(1 - \frac{U}{U_0})\mathrm{dn}, \tag{D.11}$$

where n is the wall normal distance to the suction side surface of the blade, and ρ and U are the density and the velocity magnitude in the boundary layer, respectively.

A shape factor $H_{12} = \delta_1/\delta_2$ can also be defined, which allows to easily differentiate laminar and turbulent flow.

E

Unsteady monitor points

> **Introduction**
>
> The location of the different monitor points used for the unsteady recordings in the LES configurations are presented in this section.

Monitor points location

The monitor points are located in specific regions of the domain. Figures E.1 and E.2 show some of these points, representative of each region in the (full-span) 360° and the the (full-span) sector configurations. For all the figures, the monitor points are presented by pink bullets. All the monitor points are placed in the refined regions of the mesh. The different regions where the monitor points are placed are the following.

- Upstream of the rotor and downstream of the stator. Several monitor points are located upstream of the rotor and downstream of the stator. At the axial positions (x_1 and x_2) where the monitor points are presented in Figure E.1, 20 radial points and 200 azimuthal points at each radial position are used (only 8 azimuthal positions are presented). From the inlet section up to position x_1, the radii of the spinner and the hub remain constant, and from position x_2 down to the outlet section, the radii of the hub and the shroud remain constant.

  These monitor points are used to compute the sound power levels upstream of the rotor and downstream of the stator, respectively, and to perform a radial and azimuthal modal decomposition by projecting the pressure signal on the analytical duct modes described in Chapter 1.

- Rotor blades and stator vanes. Several monitor points are located on both sides of the rotor blades and stator vanes. On each blade and vane, 20 spanwise positions and 10 axial points at each spanwise position are used (only two spanwise positions on the suction side of the rotor and the pressure side of the stator are presented in Figure E.2, respectively).

  These monitor points are used to evaluate the state of the boundary layers on the rotor blades and the stator vanes by computing the wall pressure spectra and the turbulence correlation lengths. These parameters obtained at the trailing edge are
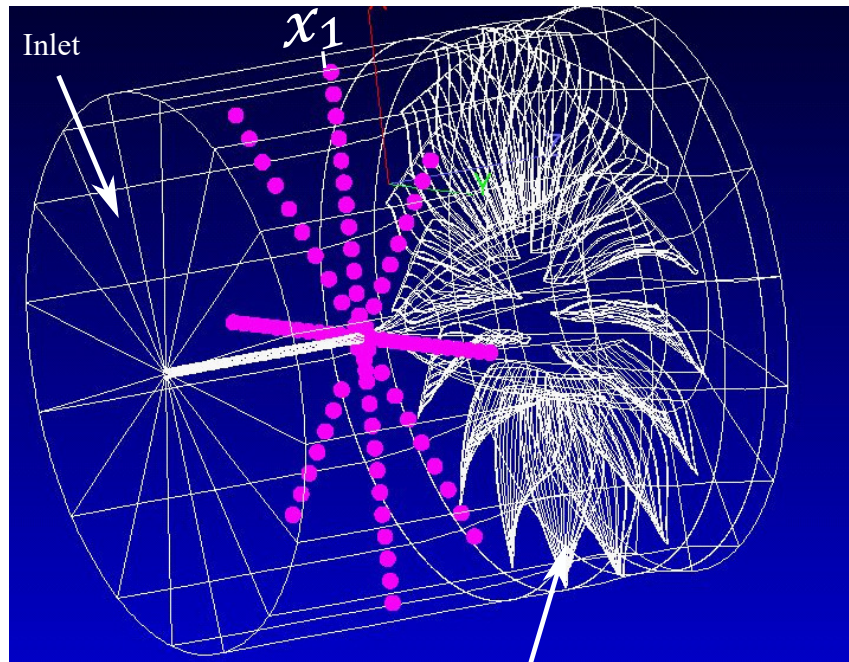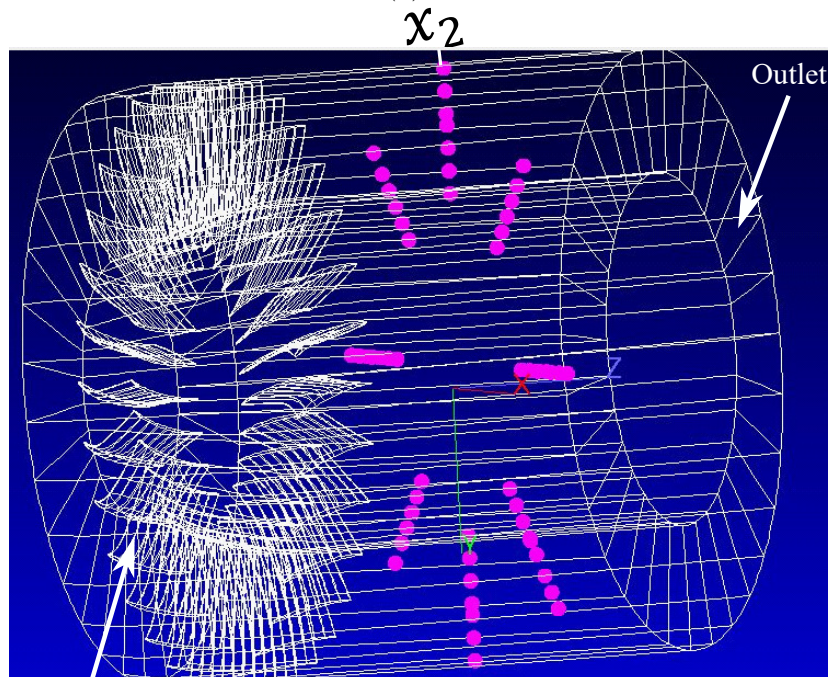
Figure E.1: Location of some monitor points in the (full-span) 360° configuration of the ECL5 fan/OGV stage. (a) Rotor domain. (b) Stator domain.
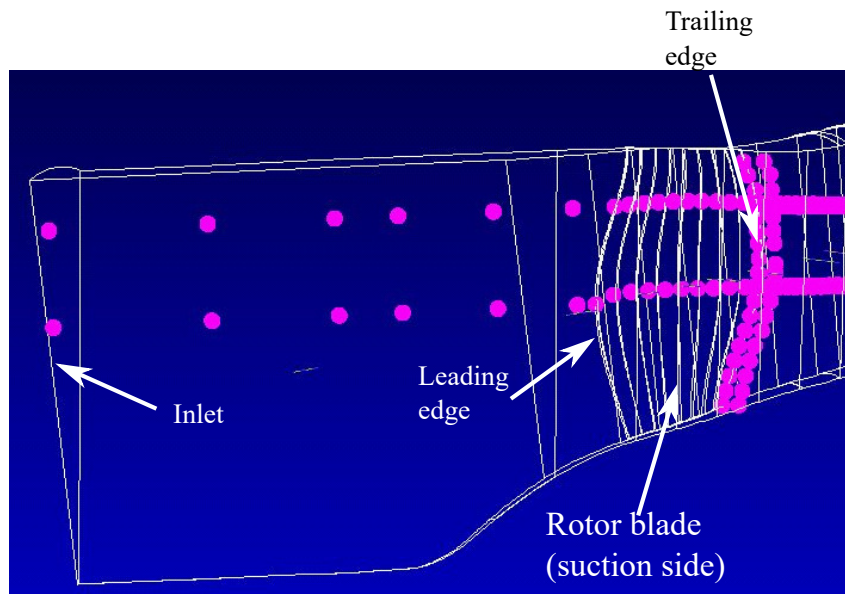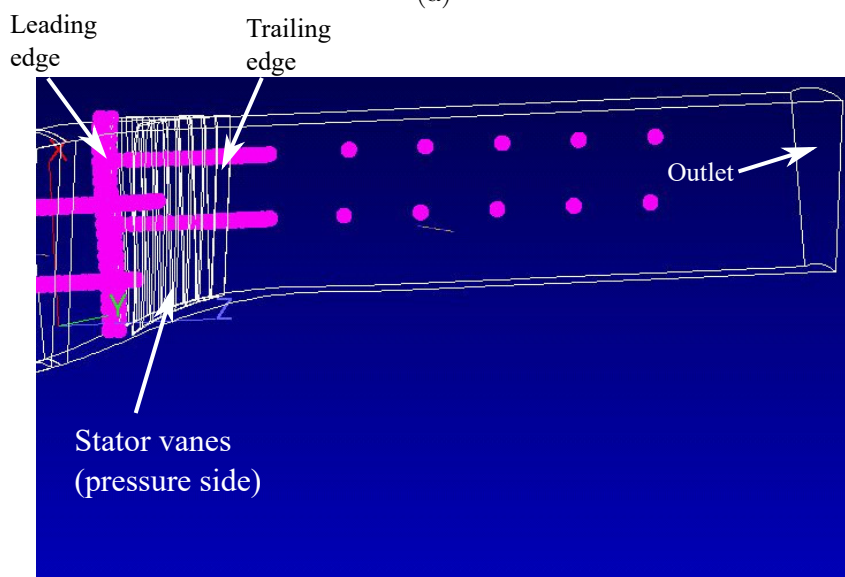
Figure E.2: Location of some monitor points in a periodic sector of the computational domain of the ECL5 fan/OGV stage. (a) Rotor domain. (b) Stator domain.

the main input data for Amiet's trailing edge model [9]. These monitor points also allow to characterize the frequency content of the recirculation bubble at 80% of the rotor span, the tip leakage flow and the corner separation close to the hub.

- Blade tip. A complex flow topology, know as a double leakage flow, is observed in the blade tip region in Chapter 5. The trajectory of the different tip vortices is not predictable before preforming the computation. Thus, several monitor points are located in the tip region. Some of these points are represented in Figure E.3 (a).

  These monitor points are used to evaluate the state of the flow in the blade tip region by computing the wall pressure spectra at the blade tip surface for different axial positions and the coherence between several points in this region. This helps to identify the frequency content of the different vortices in the blade tip region and to clarify the dominant noise source mechanisms.

- wakes regions. Several monitor points are located in the rotor and stator wakes regions. In the rotor's wake region, 20 axial points are located for 3 azimuthal and two spanwise locations, as shown in Figure E.3 (b). In the stator's wake region, 10 axial points for 3 azimuthal and two spanwise locations. A radial distribution of monitor points is also placed directly downstream of the rotor blades and upstream of the stator vanes.

  These monitor points allow to characterize the state of the wakes by computing the velocity fluctuating spectra and the turbulence correlation lengths. Upstream of the stator, these two parameters are the most important inputs for Amiet's leading edge model [8].
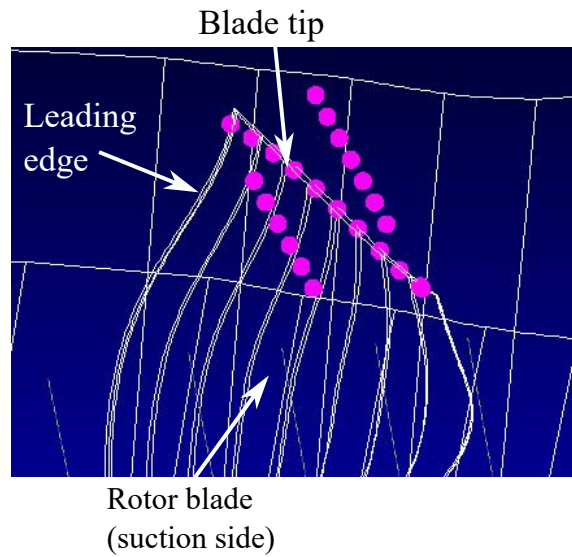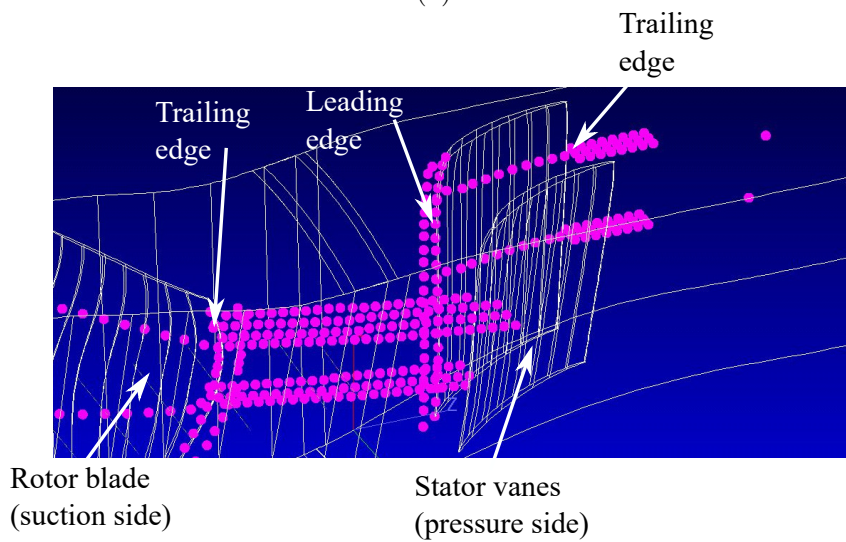
Figure E.3: Location of some monitor points in a periodic sector of the computational domain of the ECL5 fan/OGV stage. (a) Blade tip region. (b) Rotor and stator wake regions.

Bibliography

[1] J. AL-AM, V. CLAIR, A. GIAUQUE, J. BOUDET, and F. GEA-AGUILERA, Effet du débit sur le bruit propre d'un étage soufflante/redresseur en régime d'approche, in *Congrès des Jeunes Chercheurs en Mécanique - Méca-J*, en ligne, France, 2021. Available at https://hal.archives-ouvertes.fr/hal-03356145. (Cited on page 159)

[2] J. AL AM, V. CLAIR, A. GIAUQUE, J. BOUDET, and F. GEA-AGUILERA, Direct noise predictions of fan broadband noise using les and analytical models, in *28th AIAA/CEAS Aeroacoustics 2022 Conference*, 2022, p. 2882. https://doi.org/10.2514/6.2022-2882. (Cited on page 242)

[3] J. AL-AM, V. CLAIR, A. GIAUQUE, J. BOUDET, and F. GEA-AGUILERA, A parametric study on the LES numerical setup to investigate fan/OGV broadband noise, *International Journal of Turbomachinery, Propulsion and Power* **6** no. 2 (2021). https://doi.org/10.3390/ijtpp6020012. (Cited on pages xxiv, 79, 115, and 255)

[4] J. AL-AM, V. CLAIR, A. GIAUQUE, J. BOUDET, and F. GEA-AGUILERA, Effet du débit sur le bruit propre d'un étage soufflante-redresseur en présence dune bulle de recirculation, in *16th Congrès Français d'Acoustique*, à Marseille, France, 2022. (Cited on page 159)

[5] J. AL-AM, V. CLAIR, A. GIAUQUE, J. BOUDET, and F. GEA-AGUILERA, On the effects of a separation bubble on fan noise, *Journal of Sound and Vibration* **537** (2022). https://doi.org/10.1016/j.jsv.2022.117180. (Cited on pages 14 and 159)

[6] I. E. ALBER, Turbulent wake of a thin, flat plate, *AIAA journal* **18** no. 9 (1980), 1044–1051. https://doi.org/10.2514/3.50853. (Cited on page 110)

[7] R. AMIET, Noise due to turbulent flow past a trailing edge, *Journal of Sound and Vibration* **47** no. 3 (1976), 387–393. https://doi.org/10.1016/0022-460X(76)90948-2. (Cited on pages 13, 33, 34, 38, 73, 95, 115, 196, 251, and 267)

[8] R. K. AMIET, Acoustic radiation from an airfoil in a turbulent stream, *Journal of Sound and Vibration* **41** no. 4 (1975), 407–420. https://doi.org/10.1016/S0022-460X(75)80105-2. (Cited on pages 29, 33, 34, 73, 79, 196, and 274)

[9] R. K. AMIET, Noise due to turbulent flow past a trailing edge, *Journal of sound and vibration* **47** no. 3 (1976), 387–393. https://doi.org/10.1016/0022-460X(76)90948-2. (Cited on pages 197, 218, 219, 220, 224, 241, and 274)

[10] P. J. BADDOO and L. J. AYTON, An analytic solution for gust–cascade interaction noise including effects of realistic aerofoil geometry, *Journal of Fluid Mechanics* **886** (2020). https://doi.org/10.1017/jfm.2019.1016. (Cited on page 30)

[11] M. BEHN and U. TAPKEN, Investigation of sound generation and transmission effects through the acat1 fan stage using compressed sensing-based mode analysis, in *25th AIAA/CEAS Aeroacoustics Conference*, 2019, p. 2502. https://doi.org/10.2514/6.2019-2502. (Cited on page 14)

[12] A. BEJAN, Entropy generation minimization: The new thermodynamics of finite-size devices and finite-time processes, *Journal of Applied Physics* **79** no. 3 (1996), 1191–1218. https://doi.org/10.1063/1.362674. (Cited on page 174)

[13] S. BHUSHAN and D. WALTERS, A dynamic hybrid reynolds-averaged navier stokes–large eddy simulation modeling framework, *Physics of Fluids* **24** no. 1 (2012), 015103. https://doi.org/10.1063/1.3676737. (Cited on page 21)

[14] V. BONNEAU, *Prévision du bruit d'interaction tonal et à large bande d'une souf-flante de nouvelle génération en régime subsonique*, Ph.D. thesis, Poitiers, 2015. (Cited on pages xi, 12, and 13)

[15] V. BONNEAU, C. POLACSEK, L. CASTILLON, J. MARTY, Y. GERVAIS, and S. MOREAU, Turbofan broadband noise predictions using a 3-d zdes rotor blade approach, in *22nd AIAA/CEAS Aeroacoustics Conference*, 2016, p. 2950. https://doi.org/10.2514/6.2016-2950. (Cited on page 21)

[16] J. BOUDET and A. GIAUQUE, Adaptation and evaluation of a weak recycling strategy for inflow boundary layers in large-eddy simulation, *Computers & Fluids* **203** (2020), 104489. https://doi.org/10.1016/j.compfluid.2020.104489. (Cited on page 100)

[17] J. BOUDET, J.-F. MONIER, and F. GAO, Implementation of a roughness element to trip transition in large-eddy simulation, *Journal of Thermal Science* **24** no. 1 (2015), 30–36. https://doi.org/10.1007/s11630-015-0752-8. (Cited on pages 57, 100, 130, and 256)

[18] J. BOUDET, A. CAHUZAC, P. KAUSCHE, and M. C. JACOB, Zonal Large-Eddy Simulation of a Fan Tip-Clearance Flow, With Evidence of Vortex Wandering, *Journal of Turbomachinery* **137** no. 6 (2015). https://doi.org/10.1115/1.4028668. (Cited on pages 168 and 185)

[19] J. BOUDET, J. CARO, B. LI, E. JONDEAU, and M. C. JACOB, Zonal large-eddy simulation of a tip leakage flow, *International Journal of Aeroacoustics* **15** no. 6-7 (2016), 646–661. https://doi.org/10.1177/1475472X16659215. (Cited on pages 162, 163, and 164)

[20] P. BRADSHAW, 'inactive' motion and pressure fluctuations in turbulent boundary layers, *Journal of Fluid Mechanics* **30** no. 2 (1967), 241–258. https://doi.org/10.1017/S0022112067001417. (Cited on page 184)

[21] P. BRADSHAW, Prediction of the turbulent near-wake of a symmetrical aerofoil, *AIAA Journal* **8** no. 8 (1970), 1507–1508. https://doi.org/10.2514/3.5931. (Cited on page 110)

[22] C. BRANDSTETTER, V. PAGÈS, P. DUQUESNE, X. OTTAVY, P. FERRAND, S. AUBERT, and L. BLANC, UHBR open-test-case fan ECL5/CATANA part 1: geometry and aerodynamic performance, in *14th European Conference on Turbomachinery Fluid dynamics & Thermodynamics*, Gdansk, Poland, 2021. Available at https://hal.archives-ouvertes.fr/hal-03257374. (Cited on pages 49 and 55)

[23] T. F. BROOKS, D. S. POPE, and M. A. MARCOLINI, *Airfoil self-noise and prediction*, Tech. report, NASA technical report, 1989. (Cited on page 33)

[24] H. BROUWER and P. SIJTSMA, Phased array beamforming to identify broadband noise sources in the interstage section of a turbofan engine, in *25th AIAA/CEAS Aeroacoustics Conference*, 2019, p. 2669. https://doi.org/10.2514/6.2019-2669. (Cited on page 14)

[25] A. CADER, C. POLACSEK, T. LE GARREC, R. BARRIER, F. BENJAMIN, and M. C. JACOB, Numerical prediction of rotor-stator interaction noise using 3d caa with synthetic turbulence injection, in *2018 AIAA/CEAS Aeroacoustics Conference*, 2018, p. 4190. https://doi.org/10.2514/6.2018-4190. (Cited on page 14)

[26] R. CAMUSSI, J. GRILLIAT, G. CAPUTI-GENNARO, and M. C. JACOB, Experimental study of a tip leakage flow: wavelet analysis of pressure fluctuations, *Journal of Fluid Mechanics* **660** (2010), 87–113. https://doi.org/10.1017/S0022112010002570. (Cited on pages 14 and 163)

[27] S. CANT, Sb pope, turbulent flows, 2000. (Cited on page 79)

[28] T. CAROLUS, T. ZHU, and M. STURM, A low pressure axial fan for benchmarking prediction methods for aerodynamic performance and sound, in *Proceedings of International Conference of Fan Noise, Technology and Numerical Methods, Lyon*, 2015. (Cited on page 163)

[29] D. CASALINO, An advanced time approach for acoustic analogy predictions, *Journal of Sound and Vibration* **261** no. 4 (2003), 583–612. https://doi.org/10.1016/S0022-460X(02)00986-0. (Cited on pages 189 and 222)

[30] D. CASALINO, A. HAZIR, and A. MANN, Turbofan broadband noise prediction using the lattice boltzmann method, *AIAA Journal* **56** no. 2 (2018), 609–628. https://doi.org/10.2514/1.J055674. (Cited on page 120)

[31] L. CASTILLO, X. WANG, and W. K. GEORGE, Separation Criterion for Turbulent Boundary Layers Via Similarity Analysis , *Journal of Fluids Engineering* **126** no. 3 (2004), 297–304. https://doi.org/10.1115/1.1758262. (Cited on page 94)

[32] I. CELIK, M. KLEIN, and J. JANICKA, Assessment Measures for Engineering LES Applications, *Journal of Fluids Engineering* **131** no. 3 (2009). https://doi.org/10.1115/1.3059703. (Cited on page 67)

[33] K. CHANDIRAMANI, Diffraction of evanescent waves, with applications to aerodynamically scattered sound and radiation from unbaffled plates, *The Journal of the Acoustical Society of America* **55** no. 1 (1974), 19–29. https://doi.org/10.1121/1.1919471. (Cited on page 33)

[34] D. R. CHAPMAN and G. D. KUHN, The limiting behaviour of turbulence near a wall, *Journal of Fluid Mechanics* **170** (1986), 265–292. https://doi.org/10.1017/S0022112086000885. (Cited on page 24)

[35] D. M. CHASE, Sound radiated by turbulent flow off a rigid half-plane as obtained from a wavevector spectrum of hydrodynamic pressure, *The Journal of the Acoustical Society of America* **52** no. 3B (1972), 1011–1023. https://doi.org/10.1121/1.1913170. (Cited on page 33)

[36] D. M. CHASE, Noise radiated from an edge in turbulent flow, *AIAA journal* **13** no. 8 (1975), 1041–1047. https://doi.org/10.2514/3.60502. (Cited on page 33)

[37] D. CHASE, Modeling the wavevector-frequency spectrum of turbulent boundary layer wall pressure, *Journal of Sound and Vibration* **70** no. 1 (1980), 29–67. https://doi.org/10.1016/0022-460X(80)90553-2. (Cited on page 95)

[38] H.-W. D. CHIANG and S. FLEETER, Prediction of oscillating thick cambered aerofoil aerodynamics by a locally analytic method, *International journal for numerical methods in fluids* **8** no. 8 (1988), 913–931. https://doi.org/10.1002/fld.1650080804. (Cited on page 87)

[39] H. CHOI and P. MOIN, Grid-point requirements for large eddy simulation: Chapman's estimates revisited, *Physics of fluids* **24** no. 1 (2012), 011702. https://doi.org/10.1063/1.3676783. (Cited on page 20)

[40] R. CHRISTIE, S. RAMIREZ, and D. G. MACMANUS, Aero-engine installation modelling and the impact on overall flight performance, in *Advanced aero concepts, design and operations conference*, **27**, 2014. (Cited on pages xi and 2)

[41] J. CHRISTOPHE, *Application of hybrid methods to high frequency aeroacoustics*, Ph.D. thesis, 2011. (Cited on pages 72, 73, and 80)

[42] D. COLES, The law of the wake in the turbulent boundary layer, *Journal of Fluid Mechanics* **1** no. 2 (1956), 191–226. https://doi.org/10.1017/S0022112056000135. (Cited on page 268)

[43] O. COLIN and M. RUDGYARD, Development of high-order Taylor-Galerkin schemes for LES, *Journal of Computational Physics* **162** no. 2 (2000), 338–371. https://doi.org/10.1006/jcph.2000.6538. (Cited on pages 42, 55, 254, 257, and 259)

[44] G. M. CORCOS, The structure of the turbulent pressure field in boundary-layer flows, *Journal of Fluid Mechanics* **18** no. 3 (1964), 353–378. https://doi.org/10.1017/S002211206400026X. (Cited on pages 34, 97, and 105)

[45] J. COUSTEIX, *Aâerodynamique: Turbulence et Couche Limite*, Cépaduès-editions, 1989. (Cited on pages xiii, 93, and 256)

[46] D. CRIGHTON, Computational aeroacoustics for low mach number flows, in *Computational aeroacoustics*, Springer, 1993, pp. 50–68. https://doi.org/10.1007/978-1-4613-8342-0_3. (Cited on page 38)

[47] D. CRIGHTON and F. LEPPINGTON, Scattering of aerodynamic noise by a semi-infinite compliant plate, *Journal of Fluid Mechanics* **43** no. 4 (1970), 721–736. https://doi.org/10.1017/S0022112070002690. (Cited on page 33)

[48] N. CURLE, The influence of solid boundaries upon aerodynamic sound, *Proceedings of the Royal Society of London. Series A. Mathematical and Physical Sciences* **231** no. 1187 (1955), 505–514. https://doi.org/10.1098/rspa.1955.0191. (Cited on pages 36 and 250)

[49] G. DAVILLER, M. BREBION, P. XAVIER, G. STAFFELBACH, J.-D. MÜLLER, and T. POINSOT, A mesh adaptation strategy to predict pressure losses in les of swirled flows, *Flow, Turbulence and Combustion* **99** no. 1 (2017), 93–118. https://doi.org/10.1007/s10494-017-9808-z. (Cited on pages xvii, 172, and 173)

[50] J. DE LABORDERIE and S. MOREAU, Prediction of tonal ducted fan noise, *Journal of Sound and Vibration* **372** (2016), 105–132. https://doi.org/10.1016/j.jsv.2016.02.032. (Cited on page 13)

[51] J. D. L. DE LABORDERIE, *Approches analytiques et numériques pour la prédiction du bruit tonal et large bande de soufflantes de turboréacteurs*, Ph.D. thesis, Université de Sherbrooke, 2013. (Cited on pages xi and 31)

[52] M. DEUSE and R. D. SANDBERG, Different noise generation mechanisms of a controlled diffusion aerofoil and their dependence on Mach number, *Journal of Sound and Vibration* **476** (2020), 1–12. https://doi.org/10.1016/j.jsv.2020.115317. (Cited on pages 14, 119, and 120)

[53] S. S. DIWAN and O. N. RAMESH, On the origin of the inflectional instability of a laminar separation bubble, *Journal of Fluid Mechanics* **629** (2009), 263–298. https://doi.org/10.1017/S002211200900634X. (Cited on pages 118 and 119)

[54] S. S. DIWAN and O. RAMESH, Laminar separation bubbles: Dynamics and control, *Sadhana* **32** no. 1 (2007), 103–109. https://doi.org/10.1007/s12046-007-0009-7. (Cited on pages 14, 118, and 119)

[55] M. DRELA, Xfoil: An analysis and design system for low Reynolds number airfoils, in *Low Reynolds number aerodynamics*, **54**, Springer Berlin Heidelberg, 1989, pp. 1–12. https://doi.org/10.1007/978-3-642-84010-4_1. (Cited on page 138)

[56] M. DRELA and M. B. GILES, Viscous-inviscid analysis of transonic and low Reynolds number airfoils, *AIAA Journal* **25** no. 10 (1987), 1347–1355. https://doi.org/10.2514/3.9789. (Cited on page 138)

[57] B. M. EFIMTSOV, Characteristics of the field of turbulent wall pressure fluctuations at large reynolds numbers, in *Sov. Phys. Acoust.*, **28**, 1982, pp. 289–292. (Cited on pages 34, 97, 98, 105, and 218)

[58] E. ENVIA, Fan noise reduction: an overview, *International Journal of Aeroacoustics* **1** no. 1 (2002), 43–64. https://doi.org/10.1260/1475472021502668. (Cited on pages 14 and 164)

[59] I. Evers and N. Peake, *Noise generation by high-frequency gusts interacting with an airfoil in transonic flow*, *Journal of Fluid Mechanics* **411** (2000), 91–130. https://doi.org/10.1017/S0022112099008095. (Cited on page 29)

[60] L. Filotas, *Oblique compressible sears function*, *AIAA Journal* **12** no. 11 (1974), 1601–1603. https://doi.org/10.2514/3.49556. (Cited on page 29)

[61] A. C. Foley and P. C. Ivey, *3D laser transit measurements of the tip clearance vortex in a compressor rotor blade row*, in *Turbo Expo: Power for Land, Sea, and Air*, 1996. https://doi.org/10.1115/96-GT-506. (Cited on page 162)

[62] B. François, S. Bouley, M. Roger, and S. Moreau, *Analytical models based on a mode-matching technique for turbulence impingement noise on axial-flow outlet guide vanes*, in *22nd AIAA/CEAS Aeroacoustics Conference*, 2016, p. 2947. https://doi.org/10.2514/6.2016-2947. (Cited on page 14)

[63] T. Fukano, Y. Kodama, and Y. Senoo, *Noise generated by low pressure axial flow fans, i: Modeling of the turbulent noise*, *Journal of Sound and Vibration* **50** no. 1 (1977), 63–74. https://doi.org/10.1016/0022-460X(77)90551-X. (Cited on page 33)

[64] M. Furukawa, M. Inoue, K. Saiki, and K. Yamada, *The Role of Tip Leakage Vortex Breakdown in Compressor Rotor Aerodynamics*, *Journal of Turbomachinery* **121** no. 3 (1999), 469–480. https://doi.org/10.1115/1.2841339. (Cited on page 164)

[65] F. Gea-Aguilera, *Aerodynamic and aeroacoustic modelling of engine fan broadband noise*, Ph.D. thesis, University of Southampton, 2017. (Cited on pages 14 and 211)

[66] F. Gea-Aguilera, J. Gill, and X. Zhang, *On the effects of fan wake modelling and vane design on cascade noise*, *Journal of Sound and Vibration* **459** (2019), 114859. https://doi.org/10.1016/j.jsv.2019.114859. (Cited on page 14)

[67] J. Gershfeld, *Leading edge noise from thick foils in turbulent flows*, *The Journal of the Acoustical Society of America* **116** no. 3 (2004), 1416–1426. https://doi.org/10.1121/1.1780575. (Cited on page 86)

[68] J. Gill, X. Zhang, and P. Joseph, *Symmetric airfoil geometry effects on leading edge noise*, *The Journal of the Acoustical Society of America* **134** no. 4 (2013), 2669–2680. https://doi.org/10.1121/1.4818769. (Cited on pages 77, 86, and 87)

[69] S. Glegg, *The response of a swept blade row to a three-dimensional gust*, *Journal of Sound and Vibration* **227** no. 1 (1999), 29–64. https://doi.org/10.1006/jsvi.1999.2327. (Cited on pages 30 and 32)

[70] S. A. Glegg, *The response of a swept blade row to a three-dimensional gust*, *Journal of Sound and Vibration* **227** no. 1 (1999), 29–64. https://doi.org/10.1006/jsvi.1999.2327. (Cited on page 197)

[71] M. Goldstein, *Aeroacoustics*, *Advanced book program*, McGraw-Hill International Book Company, 1976. Available at https://books.google.com.lb/books?id=HY1TAAAAMAAJ. (Cited on pages 30, 33, and 37)

[72] I. GONZALEZ-MARTINO and D. CASALINO, Fan tonal and broadband noise simulations at transonic operating conditions using lattice-boltzmann methods, in *2018 AIAA/CEAS aeroacoustics conference*, 2018, p. 3919. https://doi.org/10.2514/6.2018-3919. (Cited on page 13)

[73] M. GOODY, Empirical spectral model of surface pressure fluctuations, *AIAA Journal* **42** no. 9 (2004), 1788–1794. https://doi.org/10.2514/1.9433. (Cited on pages 34 and 217)

[74] M. GOODY, Empirical spectral model of surface pressure fluctuations, *AIAA Journal* **42** no. 9 (2004), 1788–1794. https://doi.org/10.2514/1.9433. (Cited on pages 95, 96, and 99)

[75] N. GOURDAIN, Prediction of the unsteady turbulent flow in an axial compressor stage. part 1: Comparison of unsteady rans and les with experiments, *Computers & Fluids* **106** (2015), 119–129. https://doi.org/10.1016/j.compfluid.2014.09.052. (Cited on page 19)

[76] N. GOURDAIN, Prediction of the unsteady turbulent flow in an axial compressor stage. part 2: Analysis of unsteady rans and les data, *Computers & Fluids* **106** (2015), 67–78. https://doi.org/10.1016/j.compfluid.2014.09.044. (Cited on page 19)

[77] N. GOURDAIN, S. BURGUBURU, F. LEBOEUF, and G. J. MICHON, Simulation of rotating stall in a whole stage of an axial compressor, *Computers & Fluids* **39** no. 9 (2010), 1644–1655. https://doi.org/10.1016/j.compfluid.2010.05.017. (Cited on page 19)

[78] N. GOURDAIN and F. LEBOEUF, Unsteady Simulation of an Axial Compressor Stage With Casing and Blade Passive Treatments, *Journal of Turbomachinery* **131** no. 2 (2009). https://doi.org/10.1115/1.2988156. (Cited on page 19)

[79] S. GRACE, I. GONZALEZ-MARTINO, and D. CASALINO, Analysis of fan-stage gap-flow data to inform simulation of fan broadband noise, *Philosophical Transactions of the Royal Society A* **377** no. 2159 (2019), 20190080. https://doi.org/10.1098/rsta.2019.0080. (Cited on page 14)

[80] S. GRACE, D. SONDAK, W. EVERSMAN, and M. CANNAMELA, Hybrid prediction of fan tonal noise, in *14th AIAA/CEAS Aeroacoustics Conference (29th AIAA Aeroacoustics Conference)*, 2008, p. 2992. https://doi.org/10.2514/6.2008-2992. (Cited on page 13)

[81] S. GRACE, A. WIXOM, J. WINKLER, D. SONDAK, and M. LOGUE, Fan broadband interaction noise modeling, in *18th AIAA/CEAS Aeroacoustics Conference (33rd AIAA Aeroacoustics Conference)*, 2012, p. 2269. https://doi.org/10.2514/6.2012-2269. (Cited on page 14)

[82] S. M. GRACE, Influence of model parameters and the vane response method on a low-order prediction of fan broadband noise, *International Journal of Aeroacoustics* **15** no. 1-2 (2016), 131–143. https://doi.org/10.1177/1475472X15627407. (Cited on page 31)

[83] S. GRACE, Unsteady blade response: the bvi model vs. the gust model, in *Proceedings of the 7th AIAA/CEAS Aeroacoustics Conference, numéro AIAA-2001-2209*, 2001. https://doi.org/10.2514/6.2001-2209. (Cited on page 72)

[84] B. GRESCHNER, J. GRILLIAT, M. C. JACOB, and F. THIELE, Measurements and wall modeled les simulation of trailing edge noise caused by a turbulent boundary layer, *International Journal of Aeroacoustics* **9** no. 3 (2010), 329–355. https://doi.org/10.1260/1475-472X.9.3.329. (Cited on pages 13 and 14)

[85] J. GRILLIAT, *Contribution à l'étude aéroacoustique des écoulements de jeu*, Theses, Ecole Centrale de Lyon, December 2009. Available at https://tel.archives-ouvertes.fr/tel-00564497. (Cited on page 163)

[86] J. GRILLIAT, M. JACOB, R. CAMUSSI, and G. CAPUTI-GENNARO, Tip leakage experiment-part one: Aerodynamic and acoustic measurements, in *13th AIAA/CEAS Aeroacoustics Conference (28th AIAA Aeroacoustics Conference)*, 2007, p. 3684. https://doi.org/10.2514/6.2007-3684. (Cited on page 163)

[87] J. GRILLIAT, M. JACOB, E. JONDEAU, M. ROGER, and R. CAMUSSI, Broaband noise prediction models and measurements of tip leakage flows, in *14th AIAA/CEAS Aeroacoustics Conference (29th AIAA Aeroacoustics Conference)*, 2008, p. 2845. https://doi.org/10.2514/6.2008-2845. (Cited on pages 14 and 163)

[88] A. GUEDEL, M. ROBITU, N. DESCHARMES, D. AMOR, and J. GUILLARD, Prediction of the blade trailing-edge noise of an axial flow fan, *Turbo Expo: Power for Land, Sea, and Air* **4**, 2011, pp. 355–365. https://doi.org/10.1115/GT2011-45256. (Cited on pages 34, 97, and 105)

[89] S. GUERIN, C. A. KISSNER, B. KAJASA, R. JARON, M. BEHN, B. PARDOWITZ, U. TAPKEN, S. HAKANSSON, R. MEYER, and L. ENGHARDT, Noise prediction of the acat1 fan with a rans-informed analytical method: success and challenge, in *25th AIAA/CEAS aeroacoustics conference*, 2019, p. 2500. https://doi.org/10.2514/6.2019-2500. (Cited on page 14)

[90] D. HANSON and M. FINK, The importance of quadrupole sources in prediction of transonic tip speed propeller noise, *Journal of Sound and Vibration* **62** no. 1 (1979), 19–38. https://doi.org/10.1016/0022-460X(79)90554-6. (Cited on pages 181 and 210)

[91] D. HANSON and K. HORAN, Turbulence/cascade interaction-spectra of inflow, cascade response, and noise, in *4th AIAA/CEAS Aeroacoustics Conference*, 1998, p. 2319. https://doi.org/10.2514/6.1998-2319. (Cited on page 30)

[92] D. B. HANSON, Spectrum of rotor noise caused by atmospheric turbulence, *The Journal of the Acoustical Society of America* **56** no. 1 (1974), 110–126. https://doi.org/10.1121/1.1903241. (Cited on page 14)

[93] D. B. HANSON, *Theory for broadband noise of rotor and stator cascades with inhomogeneous inflow turbulence including effects of lean and sweep*, National Aeronautics and Space Administration, Glenn Research Center, CR-2001-210762, 2001. (Cited on pages 14, 30, 32, 38, 197, 219, 220, 224, and 241)

[94] C. Ho and P. Huerre, Perturbed free shear layers, *Annual Review of Fluid Mechanics* **16** no. 1 (1984), 365–422. https://doi.org/10.1146/annurev.fl.16.010184.002053. (Cited on page 119)

[95] M. S. Howe, A review of the theory of trailing edge noise, *Journal of sound and vibration* **61** no. 3 (1978), 437–465. https://doi.org/10.1016/0022-460X(78)90391-7. (Cited on pages 13, 14, and 33)

[96] M. S. Howe, Edge-source acoustic green's function for an airfoil of arbitrary chord, with application to trailing-edge noise, *Quarterly Journal of Mechanics and Applied Mathematics* **54** no. 1 (2001), 139–155. https://doi.org/10.1093/qjmam/54.1.139. (Cited on pages 33 and 34)

[97] M. S. Howe and M. S. Howe, *Acoustics of fluid-structure interactions*, Cambridge university press, 1998. (Cited on page 95)

[98] H. Hu and Z. Yang, An Experimental Study of the Laminar Flow Separation on a Low-Reynolds-Number Airfoil, *Journal of Fluids Engineering* **130** no. 5 (2008). https://doi.org/10.1115/1.2907416. (Cited on pages 14 and 119)

[99] H. H. Hubbard, *Aeroacoustics of flight vehicles: theory and practice*, **1258**, NASA Office of Management, Scientific and Technical Information Program, 1991. (Cited on pages xi and 11)

[100] J. Huber and S. Illa, Jet noise assessment and sensitivity at aircraft level, in *13th AIAA/CEAS Aeroacoustics Conference (28th AIAA Aeroacoustics Conference)*, 2007, p. 3728. https://doi.org/10.2514/6.2007-3728. (Cited on pages xi and 4)

[101] C. Hughes, Aerodynamic performance of scale-model turbofan outlet guide vanes designed for low noise, in *40th AIAA aerospace sciences meeting & exhibit*, 2002, p. 374. https://doi.org/10.2514/6.2002-374. (Cited on pages 14 and 164)

[102] C. Hughes, R. Jeracki, R. Woodward, and C. Miller, Fan noise source diagnostic test-rotor alone aerodynamic performance results, in *8th AIAA/CEAS Aeroacoustics Conference & Exhibit*, 2002, p. 2426. https://doi.org/10.2514/6.2002-2426. (Cited on page 14)

[103] Y. Hwang, W. K. Bonness, and S. A. Hambric, Comparison of semi-empirical models for turbulent boundary layer wall pressure spectra, *Journal of Sound and Vibration* **319** no. 1 (2009), 199–217. https://doi.org/10.1016/j.jsv.2008.06.002. (Cited on pages 95 and 96)

[104] M. Inoue and M. Kuroumaru, Structure of tip clearance flow in an isolated axial compressor rotor, *Journal of Turbomachinery* **111** no. 3 (1989), 250–256. https://doi.org/10.1115/1.3262263. (Cited on pages xi and 15)

[105] M. Inoue, M. Kuroumaru, and M. Fukuhara, Behavior of Tip Leakage Flow Behind an Axial Compressor Rotor, *Journal of Engineering for Gas Turbines and Power* **108** no. 1 (1986), 7–14. https://doi.org/10.1115/1.3239889. (Cited on page 162)

[106] M. C. Jacob, J. Grilliat, R. Camussi, and G. C. Gennaro, Aeroacoustic investigation of a single airfoil tip leakage flow, *International Journal of Aeroacoustics* **9** no. 3 (2010), 253–272. https://doi.org/10.1260/1475-472X.9.3.253. (Cited on pages 14 and 163)

[107] M. Jacob, M. Ciardi, L. Gamet, B. Greschner, Y. Moon, and I. Vallet, Assessment of cfd broadband noise predictions on a rod-airfoil benchmark computation, in *14th AIAA/CEAS Aeroacoustics Conference (29th AIAA Aeroacoustics Conference)*, 2008, p. 2899. https://doi.org/10.2514/6.2008-2899. (Cited on page 14)

[108] M. C. Jacob, E. Jondeau, and B. Li, Time-resolved piv measurements of a tip leakage flow, *International Journal of Aeroacoustics* **15** no. 6-7 (2016), 662–685. https://doi.org/10.1177/1475472X16659384. (Cited on pages 14 and 163)

[109] P. Jaiswal, Y. Pasco, G. Yakhina, and S. Moreau, Experimental investigation of aerofoil tonal noise at low mach number, *Journal of Fluid Mechanics* **932** (2022). https://doi.org/10.1017/jfm.2021.1018. (Cited on page 120)

[110] A. Jameson, Origins and further development of the jameson–schmidt–turkel scheme, *AIAA Journal* **55** no. 5 (2017), 1487–1510. https://doi.org/10.2514/1.J055493. (Cited on page 53)

[111] R. Jaron, A. Moreau, and S. Guerin, Rans-informed fan noise prediction: separation and extrapolation of rotor wake and potential field, in *20th AIAA/CEAS aeroacoustics conference*, 2014, p. 2946. https://doi.org/10.2514/6.2014-2946. (Cited on page 13)

[112] J. Jiménez, S. Hoyas, M. P. Simens, and Y. Mizuno, Turbulent boundary layers and channels at moderate reynolds numbers, *Journal of Fluid Mechanics* **657** (2010), 335–360. https://doi.org/10.1017/S0022112010001370. (Cited on pages 100 and 103)

[113] L. E. Jones, N. D. Sandham, and R. D. Sandberg, Acoustic source identification for transitional airfoil flows using cross correlations, *AIAA Journal* **48** no. 10 (2010), 2299–2312. https://doi.org/10.2514/1.J050345. (Cited on pages 14 and 119)

[114] V. Jurdic, P. Joseph, and J. Antoni, Investigation of rotor wake turbulence through cyclostationary spectral analysis, *AIAA Journal* **47** no. 9 (2009), 2022–2030. https://doi.org/10.2514/1.36728. (Cited on pages 212, 214, and 241)

[115] F. Kameier and W. Neise, Experimental study of tip clearance losses and noise in axial turbomachines and their reduction, *Journal of Turbomachinery* **119** no. 3 (1997), 460–471. https://doi.org/10.1115/1.2841145. (Cited on pages 162 and 163)

[116] F. Kameler, T. Nawrot, and W. Neise, Experimental investigation of tip clearance noise in axial flow machines, in *14th DGLR/AIAA Aeroacoustics Conference*, **1**, 1992, pp. 250–259. (Cited on page 163)

[117] S. KANG and C. HIRSCH, Experimental Study on the Three-Dimensional Flow Within a Compressor Cascade With Tip Clearance: Part II—The Tip Leakage Vortex, *Journal of Turbomachinery* **115** no. 3 (1993), 444–450. https://doi.org/10.1115/1.2929271. (Cited on page 163)

[118] S. KANG and C. HIRSCH, Experimental Study on the Three-Dimensional Flow Within a Compressor Cascade With Tip Clearance: Part I—Velocity and Pressure Fields, *Journal of Turbomachinery* **115** no. 3 (1993), 435–443. https://doi.org/10.1115/1.2929270. (Cited on page 163)

[119] S. KANG and C. HIRSCH, Tip Leakage Flow in Linear Compressor Cascade, *Journal of Turbomachinery* **116** no. 4 (1994), 657–664. https://doi.org/10.1115/1.2929458. (Cited on page 163)

[120] W. L. KEITH, D. A. HURDIS, and B. M. ABRAHAM, A Comparison of Turbulent Boundary Layer Wall-Pressure Spectra, *Journal of Fluids Engineering* **114** no. 3 (1992), 338–347. https://doi.org/10.1115/1.2910035. (Cited on page 95)

[121] P. KHOLODOV and S. MOREAU, Identification of noise sources in a realistic turbofan rotor using large eddy simulation, *Acoustics* **2** no. 3 (2020), 691–706. https://doi.org/10.3390/acoustics2030037. (Cited on pages 162, 164, 168, and 202)

[122] P. KHOLODOV, C. PÉREZ ARROYO, M. SANJOSÉ, and S. MOREAU, Fan broadband noise computation at transonic regime, in *25th AIAA/CEAS Aeroacoustics Conference*, 2019, p. 2714. https://doi.org/10.2514/6.2019-2714. (Cited on page 20)

[123] P. KHOLODOV, M. SANJOSE, and S. MOREAU, Tip flow evolution in a turbofan rotor for broadband noise diagnostic, in *AIAA AVIATION 2020 FORUM*, 2020, p. 2521. https://doi.org/10.2514/6.2020-2521. (Cited on pages 164 and 165)

[124] D. KIM, G.-S. LEE, and C. CHEONG, Inflow broadband noise from an isolated symmetric airfoil interacting with incident turbulence, *Journal of Fluids and Structures* **55** (2015), 428–450. https://doi.org/10.1016/j.jfluidstructs.2015.03.015. (Cited on pages 77 and 87)

[125] J. KIM, P. MOIN, and R. MOSER, Turbulence statistics in fully developed channel flow at low reynolds number, *Journal of fluid mechanics* **177** (1987), 133–166. https://doi.org/10.1017/S0022112087000892. (Cited on page 20)

[126] J. KIM, P. MOIN, and R. MOSER, Turbulence statistics in fully developed channel flow at low reynolds number, *Journal of Fluid Mechanics* **177** (1987), 133–166. https://doi.org/10.1017/S0022112087000892. (Cited on page 37)

[127] C. A. KISSNER, S. GUÉRIN, and M. BEHN, Assessment of a 2d synthetic turbulence method for predicting the acat1 fan's broadband noise, in *25th AIAA/CEAS Aeroacoustics Conference*, 2019, p. 2501. https://doi.org/10.2514/6.2019-2501. (Cited on page 14)

[128] R. Koch, M. Sanjose, and S. Moreau, Numerical investigation of noise sources in a single airfoil tip-leakage flow, in *25th AIAA/CEAS Aeroacoustics Conference*, 2019, p. 2625. https://doi.org/10.2514/6.2019-2625. (Cited on pages 163 and 185)

[129] R. Koch, M. Sanjosé, and S. Moreau, Large-eddy simulation of a linear compressor cascade with tip gap: Aerodynamic and acoustic analysis, in *AIAA AVIATION 2021 FORUM*, 2021, p. 2312. https://doi.org/10.2514/6.2021-2312. (Cited on pages 164 and 184)

[130] R. Koch, M. Sanjosé, and S. Moreau, Large-eddy simulation of a single airfoil tip-leakage flow, *AIAA Journal* **59** no. 7 (2021), 2546–2557. https://doi.org/10.2514/1.J060057. (Cited on page 163)

[131] W. Koch, On the transmission of sound waves through a blade row, *Journal of Sound and Vibration* **18** no. 1 (1971), 111–128. https://doi.org/10.1016/0022-460X(71)90635-3. (Cited on page 30)

[132] F. Kock and H. Herwig, Entropy production calculation for turbulent shear flows and their implementation in cfd codes, *International Journal of Heat and Fluid Flow* **26** no. 4 (2005), 672–680, CHT'04. https://doi.org/10.1016/j.ijheatfluidflow.2005.03.005. (Cited on page 174)

[133] R. H. Kraichnan, Diffusion by a random velocity field, *The physics of fluids* **13** no. 1 (1970), 22–31. https://doi.org/10.1063/1.1692799. (Cited on pages 73 and 125)

[134] K. Kucukcoskun, J. Christophe, C. Schram, J. Anthoine, and M. Tournour, A geometrical near-field extension of amiet's theory for spanwise varying incoming turbulence noise and broadband noise scattering, *ISMA paper 2010* **690** (2010), 4. (Cited on pages 72 and 73)

[135] K. Kücükcoskun, *Prediction of free and scattered acoustic fields of low-speed fans*, Theses, Ecole Centrale de Lyon, March 2012. Available at https://tel.archives-ouvertes.fr/tel-00758274. (Cited on pages 181 and 210)

[136] J. W. Kurelek, M. Kotsonis, and S. Yarusevych, Transition in a separation bubble under tonal and broadband acoustic excitation, *Journal of Fluid Mechanics* **853** (2018), 1–36. https://doi.org/10.1017/jfm.2018.546. (Cited on pages 14, 119, and 120)

[137] J. de Laborderie, V. Blandeau, T. Node-Langlois, and S. Moreau, Extension of a fan tonal noise cascade model for camber effects, *AIAA Journal* **53** no. 4 (2015), 863–876. https://doi.org/10.2514/1.J053266. (Cited on pages 13 and 31)

[138] B. Lakshminarayana, M. Zaccaria, and B. Marathe, The Structure of Tip Clearance Flow in Axial Flow Compressors, *Journal of Turbomachinery* **117** no. 3 (1995), 336–347. https://doi.org/10.1115/1.2835667. (Cited on page 164)

[139] D. LALLIER-DANIELS, M. PIELLARD, B. COUTTY, and S. MOREAU, Aeroacoustic study of an axial engine cooling module using lattice-boltzmann simulations and the ffowcs williams and hawkings' analogy, *European Journal of Mechanics - B/Fluids* **61** (2017), 244–254. https://doi.org/10.1016/j.euromechflu.2016.10.008. (Cited on page 163)

[140] D. LAMIDEL, G. DAVILLER, M. ROGER, and H. POSSON, Numerical prediction of the aerodynamics and acoustics of a tip leakage flow using large-eddy simulation, *International Journal of Turbomachinery, Propulsion and Power* **6** (2021). https://doi.org/10.3390/ijtpp6030027. (Cited on pages 163, 168, 185, and 202)

[141] T. LAW and A. DOWLING, Reduction of aeroengine tonal noise using scattering from a multi-segmented liner, in *14th AIAA/CEAS Aeroacoustics Conference (29th AIAA Aeroacoustics Conference)*, 2008. https://doi.org/10.2514/6.2008-2978. (Cited on page 11)

[142] C.-S. LEE, W. PANG, S. SRIGRAROM, D.-B. WANG, and F.-B. HSIAO, Classification of airfoils by abnormal behavior of lift curves at low reynolds number, in *24th AIAA Applied Aerodynamics Conference*, 2006, p. 3179. https://doi.org/10.2514/6.2006-3179. (Cited on pages 14 and 119)

[143] T. LEONARD, M. SANJOSÉ, S. MOREAU, and F. DUCHAINE, Large eddy simulation of a scale-model turbofan for fan noise source diagnostic, in *22nd AIAA/CEAS Aeroacoustics Conference*, 2016, p. 3000. (Cited on page 20)

[144] D. LEWIS, J. DE LABORDERIE, M. SANJOSÉ, S. MOREAU, M. C. JACOB, and V. MASSON, Parametric study on state-of-the-art analytical models for fan broadband interaction noise predictions, *Journal of Sound and Vibration* **514** (2021). https://doi.org/10.1016/j.jsv.2021.116423. (Cited on pages 12 and 196)

[145] D. LEWIS, S. MOREAU, and M. C. JACOB, On the use of RANS-informed analytical models to perform broadband rotor-stator interaction noise predictions, in *25th AIAA/CEAS Aeroacoustics Conference*, 2019. https://doi.org/10.2514/6.2019-2667. (Cited on pages 14 and 120)

[146] D. LEWIS, S. MOREAU, M. C. JACOB, and M. SANJOSÉ, ACAT1 fan stage broadband noise prediction using large-eddy simulation and analytical models, *AIAA Journal* **60** no. 1 (2022), 360–380. https://doi.org/10.2514/1.J060163. (Cited on pages 34, 120, and 197)

[147] M. J. LIGHTHILL, On sound generated aerodynamically i. general theory, *Proceedings of the Royal Society of London. Series A. Mathematical and Physical Sciences* **211** no. 1107 (1952), 564–587. https://doi.org/10.1098/rspa.1952.0060. (Cited on pages 1, 10, 35, and 36)

[148] M. J. LIGHTHILL, On sound generated aerodynamically ii. turbulence as a source of sound, *Proceedings of the Royal Society of London. Series A. Mathematical and Physical Sciences* **222** no. 1148 (1954), 1–32. https://doi.org/10.1098/rspa.1954.0049. (Cited on pages 1, 10, 33, 35, and 36)

[149] G. LODATO, P. DOMINGO, and L. VERVISCH, Three-dimensional boundary conditions for direct and large-eddy simulation of compressible viscous flows, *Journal of Computational Physics* **227** no. 10 (2008), 5105–5143. https://doi.org/10.1016/j.jcp.2008.01.038. (Cited on pages 45 and 47)

[150] S. MAGNE, S. MOREAU, and A. BERRY, Subharmonic tonal noise from backflow vortices radiated by a low-speed ring fan in uniform inlet flow, *The Journal of the Acoustical Society of America* **137** no. 1 (2015), 228–237. https://doi.org/10.1121/1.4904489. (Cited on page 15)

[151] R. MANI and G. HORVAY, Sound transmission through blade, *Journal of Sound and Vibration* **12** no. 1 (1970), 59–83. https://doi.org/10.1016/0022-460X(70)90048-9. (Cited on page 30)

[152] A. MANN, M.-S. KIM, J. WU, F. PÉROT, J. GRILLIAT, M. C. JACOB, and M. COLMAN, Airfoil tip leakage aeroacoustics predictions using a lattice boltzmann based method, in *22nd AIAA/CEAS Aeroacoustics Conference*, 2016, p. 2825. https://doi.org/10.2514/6.2016-2825. (Cited on page 163)

[153] V. MASSON, H. POSSON, M. SANJOSE, T. LÉONARD, S. MOREAU, and M. ROGER, Fan-ogv interaction broadband noise prediction in a rigid annular duct with swirling and sheared mean flow, in *22nd AIAA/CEAS Aeroacoustics Conference*, 2016. https://doi.org/10.2514/6.2016-2944. (Cited on pages 30, 32, and 197)

[154] J. MATHEWS and N. PEAKE, The acoustic green's function for swirling flow with variable entropy in a lined duct, *Journal of Sound and Vibration* **419** (2018), 630–653. https://doi.org/10.1016/j.jsv.2017.08.010. (Cited on page 30)

[155] D. M. MCELIGOT, E. J. WALSH, E. LAURIEN, and P. R. SPALART, Entropy Generation in the Viscous Parts of Turbulent Boundary Layers, *Journal of Fluids Engineering* **130** no. 6 (2008). https://doi.org/10.1115/1.2928376. (Cited on page 174)

[156] B. E. MCGRATH and R. L. SIMPSON, *Some features of surface pressure fluctuations in turbulent boundary layers with zero and favorable pressure gradients*, Tech. report, NASA, 1987. Available at https://ntrs.nasa.gov/api/citations/19870008970/downloads/19870008970.pdf. (Cited on page 184)

[157] F. R. MENTER, Two-equation eddy-viscosity turbulence models for engineering applications, *AIAA journal* **32** no. 8 (1994), 1598–1605. https://doi.org/10.2514/3.12149. (Cited on page 53)

[158] R. K. MEYER, S. HAKANSSON, W. HAGE, and L. ENGHARDT, Instantaneous flow field measurements in the interstage section between a fan and the outlet guiding vanes at different axial positions, in *13 th European Conference on Turbomachinery Fluid dynamics & Thermodynamics*, EUROPEAN TURBOMACHINERY SOCIETY, 2019. https://doi.org/10.29008/ETC2019-330. (Cited on page 14)

[159] M. MICHARD, M. JACOB, and N. GROSJEAN, An experimental characterization of the flow past an airfoil in the wake of a circular rod, in *Fluids Engineering Division Summer Meeting*, **36150**, 2002, pp. 1143–1149. https://doi.org/10.1115/FEDSM2002-31344. (Cited on page 14)

[160] V. MICHELASSI, L.-W. CHEN, R. PICHLER, and R. D. SANDBERG, Compressible direct numerical simulation of low-pressure turbines—part ii: Effect of inflow disturbances, *Journal of Turbomachinery* **137** no. 7 (2015), 071005. https://doi.org/10.1115/1.4029126. (Cited on page 20)

[161] V. MICHELASSI, L.-W. CHEN, R. PICHLER, and R. D. SANDBERG, Compressible Direct Numerical Simulation of Low-Pressure Turbines—Part II: Effect of Inflow Disturbances, *Journal of Turbomachinery* **137** no. 7 (2015). https://doi.org/10.1115/1.4029126. (Cited on page 37)

[162] V. MICHELASSI, J. WISSINK, and W. RODI, Analysis of dns and les of flow in a low pressure turbine cascade with incoming wakes and comparison with experiments, *Flow, turbulence and combustion* **69** no. 3 (2002), 295–329. https://doi.org/10.1023/A:1027334303200. (Cited on pages 20 and 37)

[163] T. MICHELIS, S. YARUSEVYCH, and M. KOTSONIS, On the origin of spanwise vortex deformations in laminar separation bubbles, *Journal of Fluid Mechanics* **841** (2018), 81–108. https://doi.org/10.1017/jfm.2018.91. (Cited on pages 14, 119, and 120)

[164] P. MOIN and J. KIM, Numerical investigation of turbulent channel flow, *Journal of Fluid Mechanics* **118** (1982), 341–377. https://doi.org/10.1017/S0022112082001116. (Cited on page 23)

[165] P. MOIN, K. SQUIRES, W. CABOT, and S. LEE, A dynamic subgrid-scale model for compressible turbulence and scalar transport, *Physics of Fluids A: Fluid Dynamics* **3** no. 11 (1991), 2746–2757. (Cited on pages 23, 98, and 106)

[166] S. MOREAU, Turbomachinery-related aeroacoustic modelling and simulation, in *Proceedings of the 17th International Conference on Fluid Flow Technologies, Budapest, Hungary*, 2018, pp. 4–7. (Cited on pages xi, 1, and 3)

[167] S. MOREAU, A review of turbomachinery noise: from analytical models to high-fidelity simulations, *Fundamentals of High Lift for Future Civil Aircraft* (2021), 579–595. https://doi.org/10.1007/978-3-030-52429-6_35. (Cited on page 197)

[168] S. MOREAU, M. HENNER, G. IACCARINO, M. WANG, and M. ROGER, Analysis of flow conditions in freejet experiments for studying airfoil self-noise, *AIAA journal* **41** no. 10 (2003), 1895–1905. https://doi.org/10.2514/2.1905. (Cited on pages 14 and 119)

[169] S. MOREAU and M. ROGER, Effect of angle of attack and airfoil shape on turbulence-interaction noise, in *11th AIAA/CEAS aeroacoustics conference*, 2005. https://doi.org/10.2514/6.2005-2973. (Cited on pages 29, 72, 251, and 252)

[170] S. MOREAU and M. ROGER, Competing broadband noise mechanisms in low-speed axial fans, *AIAA journal* **45** no. 1 (2007), 48–57. https://doi.org/10.2514/1.14583. (Cited on pages 13 and 14)

[171] S. MOREAU and M. ROGER, Back-scattering correction and further extensions of amiet's trailing-edge noise model. part ii: Application, *Journal of Sound and vibration* **323** no. 1-2 (2009), 397–425. https://doi.org/10.1016/j.jsv.2008.11.051. (Cited on pages 13 and 14)

[172] S. MOREAU and M. SANJOSE, Sub-harmonic broadband humps and tip noise in low-speed ring fans, *The Journal of the Acoustical Society of America* **139** no. 1 (2016), 118–127. https://doi.org/10.1121/1.4939493. (Cited on page 15)

[173] S. MOREAU, M. SANJOSÉ, F. PEROT, and M.-S.KIM, Direct self-noise simulation of the installed controlled diffusion airfoil, *17th AIAA/CEAS Aeroacoustics Conference (32nd AIAA Aeroacoustics Conference)* (2011), 2716. https://doi.org/10.2514/6.2011-2716. (Cited on pages 37 and 120)

[174] S. MOREAU, Turbomachinery noise predictions: Present and future, *Acoustics* **1** no. 1 (2019), 92–116. https://doi.org/10.3390/acoustics1010008. (Cited on pages 29, 30, and 164)

[175] S. MOREAU, Turbomachinery noise predictions: present and future, *Acoustics* **1** no. 1 (2019), 92–116. https://doi.org/10.3390/acoustics1010008. (Cited on page 196)

[176] S. MOREAU and M. ROGER, Advanced noise modeling for future propulsion systems, *International Journal of Aeroacoustics* **17** no. 6-8 (2018), 576–599. https://doi.org/10.1177/1475472X18789005. (Cited on pages xi, 29, 30, and 196)

[177] C. MUTHANNA and W. J. DEVENPORT, Wake of a compressor cascade with tip gap, part 1: Mean flow and turbulence structure, *AIAA journal* **42** no. 11 (2004), 2320–2331. https://doi.org/10.2514/1.5270. (Cited on page 164)

[178] M. R. MYERS and E. J. KERSCHEN, Influence of camber on sound generation by airfoils interacting with high-frequency gusts, *Journal of Fluid Mechanics* **353** (1997), 221–259. https://doi.org/10.1017/S0022112097007349. (Cited on page 29)

[179] Y. NA and P. MOIN, The structure of wall-pressure fluctuations in turbulent boundary layers with adverse pressure gradient and separation, *Journal of Fluid Mechanics* **377** (1998), 347–373. https://doi.org/10.1017/S0022112098003218. (Cited on page 184)

[180] A. NAJAFI-YAZDI, G. A. BRÈS, and L. MONGEAU, An acoustic analogy formulation for moving sources in uniformly moving media, *Proceedings of the Royal Society A: Mathematical, Physical and Engineering Sciences* **467** no. 2125 (2011), 144–165. https://doi.org/10.1098/rspa.2010.0172. (Cited on pages 189 and 222)

[181] M. NALLASAMY and E. ENVIA, Computation of rotor wake turbulence noise, *Journal of sound and vibration* **282** no. 3-5 (2005), 649–678. https://doi.org/10.1016/j.jsv.2004.03.062. (Cited on page 14)

[182] F. NICOUD and F. DUCROS, Subgrid-scale stress modelling based on the square of the velocity gradient tensor, *Flow, turbulence and Combustion* **62** no. 3 (1999), 183–200. https://doi.org/10.1023/A:1009995426001. (Cited on pages 23, 84, 98, 106, and 115)

[183] F. NICOUD, H. B. TODA, O. CABRIT, S. BOSE, and J. LEE, Using singular values to build a subgrid-scale model for large eddy simulations, *Physics of fluids* **23** no. 8 (2011). https://doi.org/10.1063/1.3623274. (Cited on pages 23, 42, 55, 84, 98, 106, and 115)

[184] N. Odier, F. Duchaine, L. Gicquel, G. Staffelbach, A. Thacker, N. García Rosa, G. Dufour, and J.-D. Muller, *Evaluation of integral turbulence scale through the fan stage of a turbofan using hot wire anemometry and large eddy simulation*, in *Turbo Expo: Power for Land, Sea, and Air*, **51012**, American Society of Mechanical Engineers, 2018, p. V02CT42A021. https://doi.org/10.1115/GT2018-75741. (Cited on page 20)

[185] S. Oerlemans and P. Migliore, *Aeroacoustic wind tunnel tests of wind turbine airfoils*, in *10th AIAA/CEAS Aeroacoustics Conference*, 2004, p. 3042. https://doi.org/10.2514/6.2004-3042. (Cited on page 251)

[186] M. O'meara and T. J. Mueller, *Laminar separation bubble characteristics on an airfoil at low reynolds numbers*, *AIAA journal* **25** no. 8 (1987), 1033–1041. https://doi.org/10.2514/3.9739. (Cited on pages xiv, 118, and 119)

[187] V. Pagès, P. Duquesne, X. Ottavy, P. Ferrand, S. Aubert, L. Blanc, and C. Brandstetter, *UHBR open-test-case fan ECL5/CATANA part 2: mechanical and aeroelastic stability analysis*, in *14th European Conference on Turbomachinery Fluid dynamics & Thermodynamics*, Gdansk, Poland, 2021. Available at https://hal.archives-ouvertes.fr/hal-03257377. (Cited on pages 49 and 55)

[188] R. Parker, *Paper 1: relation between blade row spacing and potential flow interaction effects in turbomachines*, in *Proceedings of the Institution of Mechanical Engineers, Conference Proceedings*, **184**, Sage Publications Sage UK: London, England, 1969, pp. 1–8. https://doi.org/10.1243/PIME_CONF_1969_184_176_02. (Cited on page 13)

[189] C. Paruchuri, J. R. Gill, N. Subramanian, P. Joseph, C. Vanderwel, X. Zhang, and B. Ganapathisubramani, *Aerofoil geometry effects on turbulence interaction noise*, in *21st AIAA/CEAS Aeroacoustics Conference*, 2015, p. 2830. https://doi.org/10.2514/6.2015-2830. (Cited on page 86)

[190] R. Paterson and R. Amiet, *Acoustic radiation and surface pressure characteristics of an airfoil due to incident turbulence*, in *3rd Aeroacoustics Conference*, 1976. https://doi.org/10.2514/6.1976-571. (Cited on pages 14, 29, 72, 79, 250, and 251)

[191] N. Peake, *The interaction between a high-frequency gust and a blade row*, *Journal of Fluid Mechanics* **241** (1992), 261–289. https://doi.org/10.1017/S0022112092002039. (Cited on page 30)

[192] N. Peake, *Elements of aviation acoustics*, *The Aeronautical Journal* **98** no. 980 (1994), 405–406. https://doi.org/10.1017/S0001924000027056. (Cited on page 11)

[193] N. Peake and A. B. Parry, *Modern challenges facing turbomachinery aeroacoustics*, *Annual Review of Fluid Mechanics* **44** (2012), 227–248. https://doi.org/10.1146/annurev-fluid-120710-101231. (Cited on pages 11, 12, 14, and 196)

[194] A. Pereira and M. C. Jacob, *Modal analysis of in-duct fan broadband noise via an iterative bayesian inverse approach*, *Journal of Sound and Vibration* **520** (2022).

`https://doi.org/https://doi.org/10.1016/j.jsv.2021.116633`. (Cited on page 238)

[195] M. Pestana, A. Pereira, E. Salze, J. Thisse, M. Sanjosé, E. Jondeau, P. Souchotte, M. Roger, S. Moreau, J. Regnard, and others, Aeroacoustics of an axial ducted low mach-number stage: numerical and experimental investigation, in *23rd AIAA/CEAS Aeroacoustics Conference*, 2017, p. 3215. `https://doi.org/10.2514/6.2017-3215`. (Cited on pages 13 and 19)

[196] M. Pestana, M. Sanjosé, S. Moreau, M. Roger, and M. Gruber, Assessment of the impact of a heterogeneous stator on the noise of an axial-flow low mach-number stage, in *25th AIAA/CEAS Aeroacoustics Conference*, 2019, p. 2589. `https://doi.org/10.2514/6.2019-2589`. (Cited on page 13)

[197] B. W. Peter D. Lax, Difference schemes for hyperbolic equations with high order of accuracy, *Communications on Pure and Applied Mathematics* **17** no. 3 (1964), 381–398. `https://doi.org/10.1002/cpa.3160170311`. (Cited on pages 254, 257, and 259)

[198] S. Peth, J. H. Seo, Y. J. Moon, M. C. Jacob, and F. Thiele, Computation of aerodynamic noise for rod wake-airfoil interactions, in *ECCOMAS CFD 2006: Proceedings of the European Conference on Computational Fluid Dynamics, Egmond aan Zee, The Netherlands, September 5-8, 2006*, Delft University of Technology; European Community on Computational Methods . . . , 2006. `https://doi.org/10.1016/B978-044453035-6/50004-3`. (Cited on page 14)

[199] U. Piomelli, Large eddy simulations in 2030 and beyond, *Philosophical Transactions of the Royal Society A: Mathematical, Physical and Engineering Sciences* **372** no. 2022 (2014), 20130320. `https://doi.org/10.1098/rsta.2013.0320`. (Cited on pages xxiv, 129, and 255)

[200] G. Podboy, M. Krupar, S. Helland, and C. Hughes, Steady and unsteady flow field measurements within a nasa 22 inch fan model, in *40th AIAA Aerospace Sciences Meeting & Exhibit*, 2002, p. 1033. `https://doi.org/10.2514/6.2002-1033`. (Cited on pages 14 and 164)

[201] G. Podboy, M. Krupar, C. Hughes, and R. Woodward, Fan noise source diagnostic test-ldv measured flow field results, in *8th AIAA/CEAS Aeroacoustics Conference & Exhibit*, 2002, p. 2431. `https://doi.org/10.2514/6.2002-2431`. (Cited on pages 14 and 164)

[202] T. Poinsot and S. Lele, Boundary conditions for direct simulations of compressible viscous flows, *Journal of Computational Physics* **101** no. 1 (1992), 104–129. `https://doi.org/10.1016/0021-9991(92)90046-2`. (Cited on pages 45, 47, and 55)

[203] C. Polacsek, V. Clair, T. Le Garrec, G. Reboul, and M. C. Jacob, Numerical predictions of turbulence/cascade-interaction noise using computational aeroacoustics with a stochastic model, *AIAA Journal* **53** no. 12 (2015), 3551–3566. `https://doi.org/10.2514/1.J053896`. (Cited on page 14)

[204] S. B. POPE, *Turbulent Flows*, Cambridge University Press, 2000. https://doi.org/10.1017/CBO9780511840531. (Cited on pages 19, 212, 214, and 241)

[205] H. POSSON, S. MOREAU, and M. ROGER, Broadband noise prediction of fan outlet guide vane using a cascade response function, *Journal of Sound and Vibration* **330** no. 25 (2011), 6153–6183. https://doi.org/10.1016/j.jsv.2011.07.040. (Cited on pages 214 and 241)

[206] H. POSSON and N. PEAKE, The acoustic analogy in an annular duct with swirling mean flow, *Journal of Fluid Mechanics* **726** (2013), 439–475. https://doi.org/10.1017/jfm.2013.210. (Cited on page 30)

[207] H. POSSON, S. MOREAU, and M. ROGER, On the use of a uniformly valid analytical cascade response function for fan broadband noise predictions, *Journal of Sound and Vibration* **329** no. 18 (2010), 3721–3743. https://doi.org/10.1016/j.jsv.2010.03.009. (Cited on pages 14, 30, 32, 34, 38, 197, 219, 220, 224, and 241)

[208] H. POSSON, S. MOREAU, and M. ROGER, Broadband noise prediction of fan outlet guide vane using a cascade response function, *Journal of Sound and Vibration* **330** no. 25 (2011), 6153–6183. https://doi.org/10.1016/j.jsv.2011.07.040. (Cited on pages 14, 32, and 38)

[209] H. POSSON, M. ROGER, and S. MOREAU, On a uniformly valid analytical rectilinear cascade response function, *Journal of Fluid Mechanics* **663** (2010), 22–52. https://doi.org/10.1017/S0022112010003368. (Cited on pages 14, 30, 32, 34, 38, 197, 219, 220, 224, and 241)

[210] A. POWELL, On the aerodynamic noise of a rigid flat plate moving at zero incidence, *The Journal of the Acoustical Society of America* **31** no. 12 (1959), 1649–1653. https://doi.org/10.1121/1.1907674. (Cited on page 33)

[211] S. PRÖBSTING and S. YARUSEVYCH, Laminar separation bubble development on an airfoil emitting tonal noise, *Journal of Fluid Mechanics* **780** (2015), 167–191. https://doi.org/10.1017/jfm.2015.427. (Cited on pages 14, 119, and 120)

[212] P. PUDDU, Tip leakage flow characteristics downstream of an axial flow fan, in *Turbo Expo: Power for Land, Sea, and Air*, 1996. https://doi.org/10.1115/96-GT-508. (Cited on page 162)

[213] C. PÉREZ ARROYO, T. LEONARD, M. SANJOSÉ, S. MOREAU, and F. DUCHAINE, Large eddy simulation of a scale-model turbofan for fan noise source diagnostic, *Journal of Sound and Vibration* **445** (2019), 64–76. https://doi.org/10.1016/j.jsv.2019.01.005. (Cited on pages 14, 20, 34, 120, 164, and 197)

[214] M. QUEGUINEUR, L. GICQUEL, F. DUPUY, A. MISDARIIS, and G. STAFFELBACH, Dynamic mode tracking and control with a relaxation method, *Physics of Fluids* **31** no. 3 (2019). https://doi.org/10.1063/1.5085474. (Cited on pages 144, 157, and 187)

[215] M. M. RAI and N. K. MADAVAN, Multi-Airfoil Navier–Stokes Simulations of Turbine Rotor–Stator Interaction, *Journal of Turbomachinery* **112** no. 3 (1990), 377–384. https://doi.org/10.1115/1.2927670. (Cited on page 55)

[216] D. A. Rains, *Tip clearance flows in axial compressors and pumps*, Ph.D. thesis, California Institute of Technology, 1954. https://doi.org/10.7907/MR84-WZ87. (Cited on page 162)

[217] B. Ramaprian, V. Patel, and M. Sastry, The symmetric turbulent wake of a flat plate, *AIAA journal* **20** no. 9 (1982), 1228–1235. https://doi.org/10.2514/3.7972. (Cited on pages 110 and 113)

[218] R.D. Sandberg, L. Jones, N. Sandham, and P. Joseph, Direct numerical simulations of tonal noise generated by laminar flow past airfoils, *Journal of Sound and Vibration* **320** no. 4 (2009), 838–858. https://doi.org/10.1016/j.jsv.2008.09.003. (Cited on pages 14 and 119)

[219] R.D. Sandberg and N. D. Sandham, Direct numerical simulation of turbulent flow past a trailing edge and the associated noise generation, *Journal of Fluid Mechanics* **596** (2008), 353–385. https://doi.org/10.1017/S0022112007009561. (Cited on pages 14 and 119)

[220] G. Reboul, *Modélisation du bruit à large bande de soufflantes de turboréacteurs.*, Ph.D. thesis, 2010. (Cited on page 250)

[221] G. Reboul, A. Cader, C. Polacsek, T. Le Garrec, R. Barrier, and N. Ben Nasr, Caa prediction of rotor-stator interaction using synthetic turbulence: Application to a low-noise serrated ogv, in *23rd AIAA/CEAS Aeroacoustics Conference*, 2017, p. 3714. https://doi.org/10.2514/6.2017-3714. (Cited on page 14)

[222] M. Ricci, R. Pacciani, M. Marconcini, and A. Arnone, Prediction of tip leakage vortex dynamics in an axial compressor cascade using RANS analyses, in *Turbo Expo: Power for Land, Sea, and Air*, 2020. https://doi.org/10.1115/GT2020-14797. (Cited on page 164)

[223] M. Roger and S. Moreau, Back-scattering correction and further extensions of Amiet's trailing-edge noise model. Part 1: theory, *Journal of Sound and vibration* **286** no. 3 (2005), 477–506. https://doi.org/10.1016/j.jsv.2004.10.054. (Cited on pages 13, 34, 38, 73, 196, 197, 218, 219, 220, 224, 241, and 251)

[224] M. Roger and S. Moreau, Extensions and limitations of analytical airfoil broadband noise models, *International Journal of Aeroacoustics* **9** no. 3 (2010), 273–305. https://doi.org/10.1260/1475-472X.9.3.273. (Cited on page 13)

[225] M. Roger, S. Moreau, and A. Guedel, Broadband fan noise prediction using single-airfoil theory, *Noise control engineering journal* **54** no. 1 (2006), 5–14. https://doi.org/10.3397/1.2888773. (Cited on page 29)

[226] M. Roger and S. Serafini, Interaction noise from a thin annulus in a circular jet, in *11th AIAA/CEAS Aeroacoustics Conference*, 2005, p. 2958. https://doi.org/10.2514/6.2005-2958. (Cited on page 79)

[227] Y. Rozenberg, *Modélisation analytique du bruit aérodynamique à large bande des machines tournantes : utilisation de calculs moyennés de mécanique des fluides*, Theses, Ecole Centrale de Lyon, December 2007. Available at https://tel.archives-ouvertes.fr/tel-00678225. (Cited on page 184)

[228] Y. ROZENBERG, G. ROBERT, and S. MOREAU, Wall-pressure spectral model including the adverse pressure gradient effects, *AIAA journal* **50** no. 10 (2012), 2168–2179. https://doi.org/10.2514/1.J051500. (Cited on pages xiii, 34, 94, 95, 96, and 184)

[229] Y. ROZENBERG, G. ROBERT, and S. MOREAU, Wall-pressure spectral model including the adverse pressure gradient effects, *AIAA Journal* **50** no. 10 (2012), 2168–2179. https://doi.org/10.2514/1.J051500. (Cited on pages 217, 218, 223, and 241)

[230] Y. ROZENBERG, M. ROGER, and S. MOREAU, Rotating blade trailing-edge noise: Experimental validation of analytical model, *AIAA journal* **48** no. 5 (2010), 951–962. https://doi.org/10.2514/1.43840. (Cited on page 184)

[231] K. RÉGIS, S. MARLÈNE, and M. STÉPHANE, Aerodynamic investigation of a linear cascade with tip gap using large-eddy simulation, *Journal of the Global Power and Propulsion Society* **5** (2021), 39–49. https://doi.org/10.33737/jgpps/133601. (Cited on page 164)

[232] P. SAGAUT, *Large eddy simulation for incompressible flows: an introduction*, Springer Science & Business Media, 2006. (Cited on pages xi and 22)

[233] É. SALZE, C. BAILLY, O. MARSDEN, E. JONDEAU, and D. JUVÉ, An experimental characterisation of wall pressure wavevector-frequency spectra in the presence of pressure gradients, in *20th AIAA/CEAS Aeroacoustics Conference*, 2014, p. 2909. https://doi.org/10.2514/6.2014-2909. (Cited on pages 34, 96, 98, 105, 106, 114, and 115)

[234] É. SALZE, C. BAILLY, O. MARSDEN, E. JONDEAU, and D. JUVÉ, An experimental characterisation of wall pressure wavevector-frequency spectra in the presence of pressure gradients, in *20th AIAA/CEAS Aeroacoustics Conference*, 2014, p. 2909. https://doi.org/10.2514/6.2014-2909. (Cited on pages 218, 223, and 241)

[235] R. SANDBERG, Compressible-flow DNS with application to airfoil noise, *Flow, Turbulence and Combustion* **95** no. 2 (2015), 211–229. https://doi.org/10.1007/s10494-015-9617-1. (Cited on page 20)

[236] R. D. SANDBERG, V. MICHELASSI, R. PICHLER, L. CHEN, and R. JOHNSTONE, Compressible Direct Numerical Simulation of Low-Pressure Turbines—Part I: Methodology, *Journal of Turbomachinery* **137** no. 5 (2015). https://doi.org/10.1115/1.4028731. (Cited on page 37)

[237] N. D. SANDHAM, Transitional separation bubbles and unsteady aspects of aerofoil stall, *The Aeronautical Journal (1968)* **112** no. 1133 (2008), 395–404. https://doi.org/10.1017/S0001924000002359. (Cited on page 118)

[238] M. SANJOSE, M. DAROUKH, W. MAGNET, J. DE LABORDERIE, S. MOREAU, and A. MANN, Tonal fan noise prediction and validation on the ANCF configuration, *Noise Control Engineering Journal* **63** no. 6 (2015), 552–561. (Cited on pages 13 and 19)

[239] M. Sanjosé, S. Moreau, M. Pestana, and M. Roger, Effect of weak outlet-guide-vane heterogeneity on rotor–stator tonal noise, *AIAA Journal* **55** no. 10 (2017), 3440–3457. https://doi.org/10.2514/1.J055525. (Cited on page 13)

[240] M. Sanjose, A. Towne, P. Jaiswal, S. Moreau, S. Lele, and A. Mann, Modal analysis of the laminar boundary layer instability and tonal noise of an airfoil at reynolds number 150,000, *International Journal of Aeroacoustics* **18** no. 2-3 (2019), 317–350. https://doi.org/10.1177/1475472X18812798. (Cited on page 120)

[241] L. D. Santana, J. Christophe, C. Schram, and W. Desmet, A rapid distortion theory modified turbulence spectra for semi-analytical airfoil noise prediction, *Journal of Sound and Vibration* **383** (2016), 349–363. https://doi.org/10.1016/j.jsv.2016.07.026. (Cited on page 77)

[242] L. D. Santana, J. Christophe, C. Schram, and W. Desmet, A rapid distortion theory modified turbulence spectra for semi-analytical airfoil noise prediction, *Journal of Sound and Vibration* **383** (2016), 349–363. https://doi.org/10.1016/j.jsv.2016.07.026. (Cited on page 211)

[243] H. Schlichting and J. Kestin, *Boundary layer theory*, **121**, Springer, 1961. (Cited on page 256)

[244] P. Schmitt, T. Poinsot, B. Schuermans, and K. P. Geigle, Large-eddy simulation and experimental study of heat transfer, nitric oxide emissions and combustion instability in a swirled turbulent high-pressure burner, *Journal of Fluid Mechanics* **570** (2007), 17–46. https://doi.org/10.1017/S0022112006003156. (Cited on page 57)

[245] T. Schonfeld and M. Rudgyard, Steady and unsteady flow simulations using the hybrid flow solver AVBP, *AIAA Journal* **37** no. 11 (1999), 1378–1385. https://doi.org/10.2514/2.636. (Cited on pages 42 and 55)

[246] W. R. Sears, Some aspects of non-stationary airfoil theory and its practical application, *Journal of the Aeronautical Sciences* **8** no. 3 (1941), 104–108. https://doi.org/10.2514/8.10655. (Cited on page 29)

[247] A. Shabbir, C. R. Berndt, and A. Breeze-Stringfellow, Turbomachine airfoil to reduce laminar separation, 2021, US Patent, Pub. No.: US 2021/0156258 A1. (Cited on page 120)

[248] S.-x. Shi, Y.-z. Liu, and J.-m. Chen, An experimental study of flow around a bio-inspired airfoil at Reynolds number 2.0×10^3, *Journal of Hydrodynamics* **24** no. 3 (2012), 410–419. https://doi.org/10.1016/S1001-6058(11)60262-X. (Cited on pages 14 and 119)

[249] S. Shubham, R. D. Sandberg, S. Moreau, and H. Wu, Surface pressure spectrum variation with Mach number on a CD airfoil, *Journal of Sound and Vibration* **526** (2022). https://doi.org/10.1016/j.jsv.2022.116762. (Cited on pages 14, 119, and 120)

[250] J. SMAGORINSKY, General circulation experiments with the primitive equations: I. the basic experiment, *Monthly weather review* **91** no. 3 (1963), 99–164. `https://doi.org/10.1175/1520-0493(1963)091<0099:GCEWTP>2.3.CO;2`. (Cited on pages 23 and 84)

[251] A. SMIRNOV, S. SHI, and I. CELIK, Random Flow Generation Technique for Large Eddy Simulations and Particle-Dynamics Modeling , *Journal of Fluids Engineering* **123** no. 2 (2001), 359–371. `https://doi.org/10.1115/1.1369598`. (Cited on pages 73 and 125)

[252] A. SMOL'YAKOV, A new model for the cross spectrum and wavenumber-frequency spectrum of turbulent pressure fluctuations in a boundary layer, *Acoustical Physics* **52** no. 3 (2006), 331–337. `https://doi.org/10.1134/S1063771006030146`. (Cited on page 96)

[253] P. R. SPALART, S. DECK, M. L. SHUR, K. D. SQUIRES, M. K. STRELETS, and A. TRAVIN, A new version of detached-eddy simulation, resistant to ambiguous grid densities, *Theoretical and computational fluid dynamics* **20** no. 3 (2006), 181–195. `https://doi.org/10.1007/s00162-006-0015-0`. (Cited on page 21)

[254] J. K. STAUBS, *Real airfoil effects on leading edge noise*, Ph.D. thesis, Virginia Tech, 2008. (Cited on page 86)

[255] R. C. STAUTER, Measurement of the Three-Dimensional Tip Region Flow Field in an Axial Compressor, *Journal of Turbomachinery* **115** no. 3 (1993), 468–476. `https://doi.org/10.1115/1.2929275`. (Cited on page 162)

[256] H. W. STOCK and W. HAASE, Feasibility study of e transition prediction in navier-stokes methods for airfoils, *AIAA journal* **37** no. 10 (1999), 1187–1196. `https://doi.org/10.2514/2.612`. (Cited on page 268)

[257] J. A. STORER and N. A. CUMPSTY, Tip Leakage Flow in Axial Compressors, *Journal of Turbomachinery* **113** no. 2 (1991), 252–259. `https://doi.org/10.1115/1.2929095`. (Cited on pages 162 and 164)

[258] C. TAM and N. REDDY, Sound generated in the vicinity of the trailing edge of an upper surface blown flap, *Journal of Sound and Vibration* **52** no. 2 (1977), 211–232. `https://doi.org/10.1016/0022-460X(77)90641-1`. (Cited on page 33)

[259] U. TAPKEN, M. BEHN, M. SPITALNY, and B. PARDOWITZ, Radial mode breakdown of the acat1 fan broadband noise generation in the bypass duct using a sparse sensor array, in *25th AIAA/CEAS Aeroacoustics Conference*, 2019, p. 2525. `https://doi.org/10.2514/6.2019-2525`. (Cited on page 14)

[260] J. TYLER and T. SOFRIN, Axial flow compressor noise studies, *Society of Automotive Engineers Transactions* **70** (1962), 309–332. `https://doi.org/10.4271/620532.`. (Cited on page 11)

[261] J. TYLER and T. SOFRIN, Axial flow compressor noise studies, *Society of Automotive Engineers Transactions* **70** (1962), 309–332. `https://doi.org/10.4271/620532.`. (Cited on pages 12, 13, and 141)

[262] H. UEDA and J. O. HINZE, Fine-structure turbulence in the wall region of a turbulent boundary layer, *Journal of Fluid Mechanics* **67** no. 1 (1975), 125–143. https://doi.org/10.1017/S0022112075000201. (Cited on page 79)

[263] E. R. VAN DRIEST, Turbulent boundary layer in compressible fluids, *Journal of the Aeronautical Sciences* **18** no. 3 (1951), 145–160. https://doi.org/10.2514/8.1895. (Cited on pages 94, 99, and 103)

[264] J. VENTOSA-MOLINA, M. LANGE, R. MAILACH, and J. FRÖHLICH, Study of Relative Endwall Motion Effects in a Compressor Cascade Through Direct Numerical Simulations, *Journal of Turbomachinery* **143** no. 1 (2020). https://doi.org/10.1115/1.4049101. (Cited on page 164)

[265] C. VENTRES, M. THEOBALD, and W. MARK, Turbofan noise generation. volume 1: Analysis, *NASA STI/Recon Technical Report N* **83** (1982), 15041. (Cited on page 14)

[266] C. WAGNER, T. HÜTTL, and P. SAGAUT, *Large-Eddy Simulation for Acoustics*, *Cambridge Aerospace Series*, Cambridge University Press, 2007. https://doi.org/10.1017/CBO9780511546143. (Cited on pages xxiv, 44, 129, and 255)

[267] G. WANG, F. DUCHAINE, D. PAPADOGIANNIS, I. DURAN, S. MOREAU, and L. Y. GICQUEL, An overset grid method for large eddy simulation of turbomachinery stages, *Journal of Computational Physics* **274** (2014), 333–355. https://doi.org/10.1016/j.jcp.2014.06.006. (Cited on pages 20 and 55)

[268] G. WANG, S. MOREAU, F. DUCHAINE, J. DE LABORDERIE, and L. GICQUEL, Les investigation of aerodynamics performance in an axial compressor stage, in *22nd Annual Conference of the CFD Society of Canada, Toronto, Canada, June*, Citeseer, 2014, pp. 1–4. (Cited on page 20)

[269] G. WANG, S. MOREAU, F. DUCHAINE, N. GOURDAIN, and L. GICQUEL, Large eddy simulations of the mt1 high-pressure turbine using turboavbp, in *Proceeding of 21st Annual Conference of the CFD Society of Canada, Sherbrooke, Quebec, Canada*, 2013, pp. 70–106. (Cited on page 20)

[270] G. WANG, M. SANJOSE, S. MOREAU, D. PAPADOGIANNIS, F. DUCHAINE, and L. GICQUEL, Noise mechanisms in a transonic high-pressure turbine stage, *International Journal of Aeroacoustics* **15** no. 1-2 (2016), 144–161. https://doi.org/10.1177/1475472X16630870. (Cited on page 20)

[271] G. WANG, F. YANG, K. WU, Y. MA, C. PENG, T. LIU, and L.-P. WANG, Estimation of the dissipation rate of turbulent kinetic energy: A review, *Chemical Engineering Science* **229** (2021). https://doi.org/10.1016/j.ces.2020.116133. (Cited on page 174)

[272] Y. WANG and W. J. DEVENPORT, Wake of a compressor cascade with tip gap, part 2: effects of endwall motion, *AIAA journal* **42** no. 11 (2004), 2332–2340. https://doi.org/10.2514/1.5272. (Cited on page 164)

[273] J. H. WATMUFF, Evolution of a wave packet into vortex loops in a laminar separation bubble, *Journal of Fluid Mechanics* **397** (1999), 119–169. https://doi.org/10.1017/S0022112099006138. (Cited on page 119)

[274] C. W. Wenger, W. J. Devenport, K. S. Wittmer, and C. Muthanna, Wake of a compressor cascade with tip gap, part 3: Two point statistics, *AIAA journal* **42** no. 11 (2004), 2341–2346. https://doi.org/10.2514/1.842. (Cited on page 164)

[275] D. C. Wilcox, Reassessment of the scale-determining equation for advanced turbulence models, *AIAA journal* **26** no. 11 (1988), 1299–1310. https://doi.org/10.2514/3.10041. (Cited on page 53)

[276] J. F. Williams and L. Hall, Aerodynamic sound generation by turbulent flow in the vicinity of a scattering half plane, *Journal of fluid mechanics* **40** no. 4 (1970), 657–670. https://doi.org/10.1017/S0022112070000368. (Cited on pages 13, 14, 33, 195, 197, 222, 224, 241, and 246)

[277] J. F. Williams and D. L. Hawkings, Sound generation by turbulence and surfaces in arbitrary motion, *Philosophical Transactions for the Royal Society of London. Series A, Mathematical and Physical Sciences* (1969), 321–342. https://doi.org/10.1098/rsta.1969.0031. (Cited on pages 10, 35, 36, 37, 38, 39, 40, and 244)

[278] W. W. Willmarth and F. W. Roos, Resolution and structure of the wall pressure field beneath a turbulent boundary layer, *Journal of Fluid Mechanics* **22** no. 1 (1965), 81–94. https://doi.org/10.1017/S0022112065000599. (Cited on page 95)

[279] J. G. Wissink and W. Rodi, Direct numerical simulation of flow and heat transfer in a turbine cascade with incoming wakes, *Journal of Fluid Mechanics* **569** (2006), 209–247. https://doi.org/10.1017/S002211200600262X. (Cited on page 20)

[280] J. G. Wissink and W. Rodi, Direct numerical simulation of flow and heat transfer in a turbine cascade with incoming wakes, *Journal of Fluid Mechanics* **569** (2006), 209–247. https://doi.org/10.1017/S002211200600262X. (Cited on page 37)

[281] R. Woodward, C. Hughes, R. Jeracki, and C. Miller, Fan noise source diagnostic test–far-field acoustic results, in *8th AIAA/CEAS Aeroacoustics Conference & Exhibit*, 2002, p. 2427. https://doi.org/10.2514/6.2002-2427. (Cited on page 164)

[282] H. Wu, S. Moreau, and R. D. Sandberg, On the noise generated by a controlled-diffusion aerofoil at rec= 1.5× 105, *Journal of Sound and Vibration* **487** (2020), 115620. (Cited on page 129)

[283] H. Wu, M. Sanjosé, S. Moreau, and R. D. Sandberg, Direct numerical simulation of the self-noise radiated by the installed controlled-diffusion airfoil at transitional Reynolds number, in *2018 AIAA/CEAS Aeroacoustics Conference*, 2018. https://doi.org/10.2514/6.2018-3797. (Cited on pages 14, 37, and 119)

[284] X. Wu and P. A. Durbin, Evidence of longitudinal vortices evolved from distorted wakes in a turbine passage, *Journal of Fluid Mechanics* **446** (2001), 199–228. https://doi.org/10.1017/S0022112001005717. (Cited on page 20)

[285] X. WU and P. A. DURBIN, *Evidence of longitudinal vortices evolved from distorted wakes in a turbine passage*, *Journal of Fluid Mechanics* **446** (2001), 199–228. https://doi.org/10.1017/S0022112001005717. (Cited on page 37)

[286] D. YOU, M. WANG, P. MOIN, and R. MITTAL, *Large-eddy simulation analysis of mechanisms for viscous losses in a turbomachinery tip-clearance flow*, *Journal of Fluid Mechanics* **586** (2007), 177–204. https://doi.org/10.1017/S0022112007006842. (Cited on pages 162, 164, and 168)

[287] T. ZHU and T. H. CAROLUS, *Experimental and unsteady numerical investigation of the tip clearance noise of an axial fan*, in *ASME Turbine Blade Tip Symposium*, 2013. https://doi.org/10.1115/TBTS2013-2034. (Cited on page 163)

[288] T. ZHU, D. LALLIER-DANIELS, M. SANJOSÉ, S. MOREAU, and T. CAROLUS, *Rotating coherent flow structures as a source for narrowband tip clearance noise from axial fans*, *Journal of Sound and Vibration* **417** (2018), 198–215. https://doi.org/10.1016/j.jsv.2017.11.014. (Cited on page 163)

[289] W. C. ZIERKE, K. J. FARRELL, and W. A. STRAKA, *Measurements of the Tip Clearance Flow for a High-Reynolds-Number Axial-Flow Rotor*, *Journal of Turbomachinery* **117** no. 4 (1995), 522–532. https://doi.org/10.1115/1.2836564. (Cited on page 162)

AUTORISATION DE SOUTENANCE

Vu les dispositions de l'arrêté du 25 mai 2016 modifié par l'arrêté du 26 août 2022,

Vu la demande du directeur de thèse

Monsieur J. BOUDET

et les rapports de

Mme M. SANJOSE
Professeure - Département de Génie Mécanique - Ecole de Technologie Supérieure
Université du Québec - Canada

et de

M. V. MOUREAU
Chargé de recherche HDR - CORIA - Avenue de l'Université - BP 12
76801 Saint-Etienne-du-Rouvray

Monsieur AL AM Jean

est autorisé à soutenir une thèse pour l'obtention du grade de **DOCTEUR**

Ecole doctorale Mécanique, Energétique, Génie civil, Acoustique

Fait à Ecully, le 1er décembre 2022

Pour le directeur de l'Ecole centrale de Lyon
Le directeur des Formations

Grégory VIAL